Patrick Vogt · Guy Le Lay Editors

# Silicene

Prediction, Synthesis, Application



### NanoScience and Technology

### Series editors

Phaedon Avouris, IBM Research, Yorktown Heights, USA Bharat Bhushan, The Ohio State University, Columbus, USA Dieter Bimberg, Technical University of Berlin, Berlin, Germany Cun-Zheng Ning, Arizona State University, Tempe, USA Klaus von Klitzing, Max Planck Institute for Solid State Research, Stuttgart, Germany Roland Wiesendanger, University of Hamburg, Hamburg, Germany The series NanoScience and Technology is focused on the fascinating nano-world, mesoscopic physics, analysis with atomic resolution, nano and quantum-effect devices, nanomechanics and atomic-scale processes. All the basic aspects and technology-oriented developments in this emerging discipline are covered by comprehensive and timely books. The series constitutes a survey of the relevant special topics, which are presented by leading experts in the field. These books will appeal to researchers, engineers, and advanced students.

More information about this series at http://www.springer.com/series/3705

Patrick Vogt · Guy Le Lay Editors

## Silicene

Prediction, Synthesis, Application



Editors
Patrick Vogt
Institut für Physik
Technische Universität Chemnitz
Chemnitz, Germany

Guy Le Lay CNRS, PIIM UMR 7345 Aix-Marseille University Marseille, France

ISSN 1434-4904 ISSN 2197-7127 (electronic) NanoScience and Technology ISBN 978-3-319-99962-3 ISBN 978-3-319-99964-7 (eBook) https://doi.org/10.1007/978-3-319-99964-7

Library of Congress Control Number: 2018953713

#### © Springer Nature Switzerland AG 2018

This work is subject to copyright. All rights are reserved by the Publisher, whether the whole or part of the material is concerned, specifically the rights of translation, reprinting, reuse of illustrations, recitation, broadcasting, reproduction on microfilms or in any other physical way, and transmission or information storage and retrieval, electronic adaptation, computer software, or by similar or dissimilar methodology now known or hereafter developed.

The use of general descriptive names, registered names, trademarks, service marks, etc. in this publication does not imply, even in the absence of a specific statement, that such names are exempt from the relevant protective laws and regulations and therefore free for general use.

The publisher, the authors, and the editors are safe to assume that the advice and information in this book are believed to be true and accurate at the date of publication. Neither the publisher nor the authors or the editors give a warranty, express or implied, with respect to the material contained herein or for any errors or omissions that may have been made. The publisher remains neutral with regard to jurisdictional claims in published maps and institutional affiliations.

This Springer imprint is published by the registered company Springer Nature Switzerland AG The registered company address is: Gewerbestrasse 11, 6330 Cham, Switzerland

### **Preface**

### **Elemental 2D Materials Beyond Graphene**

Nano-structures, objects limited in one or more dimensions to the nanometre scale, form the basis of nanotechnology, a research field initiated by the famous talk of Richard Feynman in 1959, entitled "There is plenty of room at the bottom". In this talk, Richard Feynman did not only describe the enormous impact that nanotechnology would have for technological applications but underlined also the necessity of microscopic imaging on an atomic scale, meaning the visualisation of single atoms.

Such an enormous resolution was achieved through the invention of the scanning tunnelling microscope by Gerd Binnig and Heinrich Rohrer; they were awarded the Nobel Prize in Physics in 1986. This microscope allowed for the first time to image single atoms of a solid surface, opening the door for the investigation of all sorts of crystalline nano-objects. As a natural consequence, the understanding of solid matter on an atomic scale has enormously evolved and formation, structuring and manipulation of nano-objects came into focus.

These nano-objects can be described as quasi-0D, -1D or -2D allotropes of chemically the same 3D crystal, where the dimensionality is one of the most defining material parameters. This means that the identical material exhibits drastically different properties depending on its dimensionality, making the dimensionality a key-parameter for the development of new pioneering concepts for technological applications. Although quasi-0D and -1D objects had been well investigated and understood, two-dimensional crystals were experimentally unknown before the discovery of graphene in 2004, awarded the 2010 Nobel Prize in Physics. This first purely 2D material consists of carbon atoms arranged in a 2D hexagonal honeycomb structure, and was obtained by exfoliating single atomic layers from a parent graphite crystal using a piece of sticky tape. The origin for its purely 2D atomic arrangement is the preferential sp<sup>2</sup> hybridization of carbon atoms, a fundamental aspect for organic chemistry.

Symmetry and dimensionality make graphene to stand out by its resulting peculiar physical properties. For instance, the electrons in graphene behave like vi Preface

massless relativistic particles, the so-called Dirac-fermions. Consequently, graphene has a very high electron mobility, making it an ideal candidate for the application in electronic devices. The missing electronic band gap in graphene is the only drawback and hinders its application in logic devices. In the years after its discovery, a multitude of technological applications of graphene was envisaged, ranging from ultrafast transistors to the replacements of silicon- based computer technology.

Such optimistic expectations have motivated the search for other, maybe similar, 2D materials, which exhibit an intrinsic electronic band gap and can be exfoliated from natural layered crystals, in analogy to graphite and graphene. These layered materials have strong in-plane bonds and weaker van der Waals coupling between the atomic layers, allowing their exfoliation. The family of transition metal dichalcogenide monolayers was the next group of 2D materials and initially explored by a large number of researchers, nicely illustrated for MoS<sub>2</sub>, the material, which gave birth to the first single-layer transistors in early 2011.

Deviating from this exfoliation approach of binary compounds, around that time only a few research groups were striving to create novel mono-elemental 2D materials synthetically. Already in 1994, 10 years before the advent of graphene, the possible existence of 2D silicon and germanium analogues to graphene had been suggested theoretically. These 2D materials were later coined silicene and germanene, though having a slightly buckled atomic honeycomb structure because of the different preferential hybridization state of the Si and Ge atoms in comparison to C atoms in graphene.

It was only in 2012, that silicene was synthesized, under ultrahigh vacuum conditions on a silver (111) single crystal by Si molecular beam epitaxy, and, in parallel, on zirconium diboride thin films grown on Si(111) substrates by Si segregation through the film. This realization has faced many hurdles, and the properties of the resulting 2D Si layers have been discussed controversially in the literature. This dispute included its mere potential existence, its practical feasibility and its notation as silicene. In fact, the layers grown epitaxially on a supporting substrate material differ compared to the theoretically calculated properties of so-called freestanding silicene. The latter is only a theoretical concept, as its existence has not been demonstrated yet. However, it turned out that even though influenced by the substrate the 2D character of epitaxial silicene clearly contributes to its fundamental properties.

Quickly after its synthesis, the first silicene transistor—with a single-layer channel—operating at room temperature, with ambipolar character and good mobilities, was reported in 2015. The synthesis of epitaxial silicene further launched an intensive search for finding ways to epitaxially synthesize other group-IV materials based on germanium and tin, named germanene and stanene (from the latin word for tin: stannum), respectively. The synthesis of germanene was reported in 2014, of stanene in 2015. By this endeavour, a new burgeoning field took the stage, with the young family of buckled 2D elemental materials. A cornucopia of unprecedented outstanding properties are predicted for these materials, resulting from their slightly buckled atomic structure and a significant spin—orbit interaction in their atomic constituents.

Preface vii

Those expectations range from the tunability of their electronic band gap, the modification of their electronic properties by functionalization, to their 2D topological properties. The latter opens the way to a quantum spin Hall effect at accessible temperatures (if not even, room temperature). The evolution of topologically non-trivial properties will be more robust for the heavier constituting elements, because of the related stronger spin—orbit interaction, further strengthened by the larger buckling. Topological properties are envisaged to enable entirely new concepts in electronic devices and their prediction and description was awarded the 2016 Nobel Prize in physics.

In this book, the theoretical background and predictions, the growth and synthesis of 1D and 2D Si-structures, their properties and application for electronic devices such as a field effect transistor and the synthesis of other elemental 2D materials, like germanene are presented and discussed by key international experts.

Chemnitz, Germany Marseille, France Patrick Vogt Guy Le Lay

### Contents

1	A Vi	ision on Organosilicon Chemistry and Silicene	1
	Deep	othi Jose, Chandra Chowdhury and Ayan Datta	
	1.1	Aromatic Molecules and Silicon Substituted Cyclic Rings	1
	1.2	Chemical Bonding: Unsaturated Carbon Systems Versus	
		Silicon Systems	5
	1.3	Effect of Buckling Distortions in Si <sub>6</sub> Rings: The Psuedo	
		Jahn-Teller (PJT) Effect	7
	1.4	Chemical Functionalization on Silicon Rings to Make	
		Them Planar	9
	1.5	Electron and Hole Transport in Silicene	11
	1.6	Reactivity of Silicene Towards Hydrogen and Band	
		Gap Tuning	13
	1.7	Tip Enhanced Raman Spectroscopy (TERS) as a Probe	
		for the Buckling Distortion in Silicene	16
	Refe	rences	20
2	Dens	sity-Functional and Tight-Binding Theory of Silicene	
	and	Silicane	23
	V. Z	ólyomi, N. D. Drummond, J. R. Wallbank and V. I. Fal'ko	
	2.1	Introduction	23
	2.2	First-Principles Theory of Silicene and Silicane	25
		2.2.1 Structure, Stability, and Electronic Band Structure	
		of Silicene	25
		2.2.2 Structure, Stability, and Electronic Band Structure	
		of Silicane	28
	2.3	Tight-Binding Description of Silicene and Silicane	30
		2.3.1 All-Valence Tight-Binding Model of Silicene	30
		2.3.2 All-Valence Tight-Binding Model of Silicane	31
	2.4	Silicene in a Transverse External Electric Field	34

x Contents

	2.5	SO Coupling and Topological Phase Transition
		in Silicene
		2.5.1 SO Induced Band Gap in Silicene
		2.5.2 Transition from Topological Insulator to Band
		Insulator State
	2.6	Summary
	Refe	rences
3	Elect	tronic and Topological Properties of Silicene, Germanene
	and	Stanene
	Moto	ohiko Ezawa
	3.1	Introduction
	3.2	Graphene and Silicene
		3.2.1 Graphene
		3.2.2 Silicene and Tunable Band Gap
		3.2.3 Generalized Dirac Mass Terms
	3.3	Berry Curvature and Chern Number
		3.3.1 TKNN Formula
		3.3.2 Berry Curvature in Centrosymmetric System
		3.3.3 Pontryagin Number
		3.3.4 Classification of Topological Insulators
	3.4	Topological Edges
	5.4	3.4.1 Bulk-Edge Correspondence
		3.4.2 Herical Edges and Chiral Edges
		3.4.3 Inner Edges
		3.4.4 Topological Kirchhoff Law
	3.5	Topological Quantum Field-Effect Transistor
	3.6	Impurity Effects to Topological Quantum Field-Effect
	3.0	
		3.6.1 QSH Phase
	2.7	3.6.2 QVH Phase
	3.7	Phosphorene and Anisotropic Honeycomb Lattice
		3.7.1 Band Structure of Anisotropic Honeycomb
		Nanoribbons
		3.7.2 Topological Origin of Flat Bands
		3.7.3 Wave Function and Energy Spectrum
		of Edge States
	Refe	rences
4		cal Properties of Silicene and Related Materials
		First Principles
	Fried	lhelm Bechstedt, Lars Matthes, Paola Gori and Olivia Pulci
	4.1	Introduction
	4 2	Theoretical and Numerical Methods

Contents xi

		4.2.1 Atomic and Electronic Structure	74
		4.2.2 Frequency-Dependent Dielectric Function	76
		4.2.3 Dielectric Function and Optical Conductivity	
		of Individual Sheets	77
		4.2.4 Optical Properties of Atomically Thin Films	80
	4.3	Spectra of Silicene, Germanene, and Stanene	83
		4.3.1 Influence of Many-Body Effects	83
		4.3.2 General Frequency Dependence	85
		4.3.3 Low-Frequency Absorbance	86
		4.3.4 Influence of Spin-Orbit Interaction	89
		4.3.5 Reflection, Transmission, and Absorption:	
		Global Spectra	91
	4.4	Influence of Multiple Layers	92
		4.4.1 Graphene Bilayer	92
		4.4.2 Silicene Bilayers	94
	4.5	Summary and Conclusions	96
	Refe	rences	97
5	Svnt	hesis of Silicene	99
		Le Lay, Dmytro Solonenko and Patrick Vogt	
	5.1	Introduction	99
	5.2	The Silver Track	100
	5.3	Ag(111) Mimicking a Honeycomb Lattice	103
	5.4	Growth Mode and Structure Formation of Si on the Ag(111)	
		Surface	103
	5.5	Multilayer Silicene	106
	5.6	Silicene Segregated on ZrB <sub>2</sub> Thin Films	109
	5.7	Synthesis of Silicene on Other Metallic Substrates	110
	5.8	Concluding Remarks	111
	Refe	rences	111
6	C: N	anoribbons: From 1D to 3D Nanostructures	115
U		a De Padova, Bruno Olivieri, Claudio Quaresima	113
		Carlo Ottaviani	
	6.1	Introduction	115
	6.2	Silicene Nanoribbons: From a Theoretical Point of View	116
	6.3	The Birth of SiNRs: 1D, 2D and 3D Silicene	110
	0.5	Nano-structures on Ag(110)	118
		6.3.1 Isolated SiNRs and Nanodots	118
		6.3.2 Two-Dimensional Array of SiNRs	119
	6.4	Oxidation of Isolated SiNRs on Ag(110)	119
	6.5	Electronic Properties of 1D SiNRs and 2D Arrays	11)
	0.5	of SiNRs	121
	6.6	Multilaver SiNRs	121

xii Contents

	6.7	Discussion	123
	6.8	Summary	126
	Refer	rences	126
7		erties of Monolayer Silicene on Ag(111)	129
	7.1	Introduction	129
	7.1	Expected Properties of Epitaxial Silicene	131
	7.3	Formation of 2D Si-Structures on Ag(111)	132
	7.5	7.3.1 Temperature-Dependence of the Si Growth	132
		on Ag(111)	134
	7.4	Epitaxial $(3 \times 3)$ Silicene	137
	,	7.4.1 Atomic Structure	137
		7.4.2 Electronic Properties	143
		7.4.3 Vibrational Properties	145
		7.4.4 Temperature Dependence of the Vibrational	
		Modes	149
		7.4.5 Electron-Phonon Coupling	151
	7.5	Other 2D Si Phases on Ag(111)	152
		7.5.1 The Si- $(\sqrt{13} \times \sqrt{13})$ Phase	152
		7.5.2 The Si " $(2\sqrt{3} \times 2\sqrt{3})$ " Phase on Ag(111)	153
	7.6	Stability of Silicene Layers on Ag(111)	155
	7.7	Summary and Outlook	156
	Refer	rences	157
0	Atom		
8		nic and Electronic Structure of Silicene on Ag: neoretical Perspective	159
		nur Cahangirov and Angel Rubio	139
	8.1	The 3 × 3 Reconstruction	160
	8.2	The Nature of the Linear Bands	162
	8.3	The $\sqrt{3} \times \sqrt{3}$ Reconstruction	164
	8.4	Multilayer Silicene	169
		rences	176
9		ene on Ag(111) at Low Temperatures	179
	_	Cheng, Lan Chen and Kehui Wu	170
	9.1	Introduction	179
	9.2	Electronic Structure of the $4 \times 4$ Phase by STS	181
	9.3	The $\sqrt{3} \times \sqrt{3}$ Phase	183
		9.3.1 Dirac Fermions Evidenced by Quasi-particle	
		Interference in the $\sqrt{3} \times \sqrt{3}$ Phase	184
		9.3.2 Dynamic Phase Transition of the $\sqrt{3} \times \sqrt{3}$ Phase	189
		9.3.3 Multilayer Silicene on Ag(111)	192

Contents xiii

	9.4		94
	Refer	ences	94
10		nesis of Silicene on Alternative Substrates	97
	10.1 10.2	Silicene/Substrate Interaction: Weak van der Waals	97
		E	98
	10.3	E	204
	10.4	$\epsilon$	206
	Refer	ences	208
11		<b>ce Functionalization of Silicene</b>	211
	11.1	Introduction	211
	11.2	, .	212
	11.3	$\epsilon$	221
	11.4		226
	11.5	1	230
	Refer	ences 2	231
12	Enca	psulated Silicene Field-Effect Transistors	235
	Li Ta	o, Eugenio Cinquanta, Carlo Grazianetti, Alessandro Molle	
	and D	Deji Akinwande	
	12.1		235
	12.2	Epitaxy of Silicene on Cleavable Ag (111)/Mica	
			237
	12.3	Air-Stability of Silicene Post Synthesis and During	
			239
		2 5 11 6	239
			240
	12.4	Silicene Devices: Fabrication, Measurement and Electronic	
		1	242
		12.4.1 Silicene Encapsulated Delamination and Native	
		Č , , ,	242
		12.4.2 Electrical Characterization of Silicene Field-Effect	
			244
		12.4.3 Fundamental Physics Revealed by Prelim	140
	10.5		249
	12.5	· · · · · · · · · · · · · · · · · · ·	250 251
		ences ()	, J I

xiv Contents

13	Gern	nanene: Silicene's Twin Sister	55
	Pante	lis Bampoulis, Lijie Zhang, Qirong Yao, Rik van Bremen,	
	Caspa	ar J. Walhout, Adil Acun, Arie van Houselt	
	and F	Iarold J. W. Zandvliet	
	13.1	Introduction	55
	13.2	Germanene	57
		13.2.1 First-Principles Calculations	57
		13.2.2 Synthesis	58
	13.3	Future Experiments	61
		13.3.1 Anomalous Quantum Hall Effect	61
		13.3.2 Quantum Spin Hall Effect	63
		13.3.3 Topological Phase Transitions and Band	
		Gap Engineering	64
	13.4	Conclusions and Outlook	65
	Refer	ences	66
Ind	ex	20	69

### **Contributors**

**Adil Acun** Physics of Interfaces and Nanomaterials, MESA+ Institute for Nanotechnology, University of Twente, Enschede, The Netherlands

V. V. Afanas'ev Department of Physics and Astronomy, University of Leuven, Louvain, Belgium

**Deji Akinwande** Microelectronics Research Centre, The University of Texas at Austin, Austin, TX, USA

**Pantelis Bampoulis** Physics of Interfaces and Nanomaterials, MESA+ Institute for Nanotechnology, University of Twente, Enschede, The Netherlands

**Friedhelm Bechstedt** Institut für Festkörpertheorie und -optik, Friedrich-Schiller-Universität Jena, Jena, Germany

**Seymur Cahangirov** UNAM - National Nanotechnology Research Center, Bilkent University, Ankara, Turkey

**Lan Chen** Institute of Physics, Chinese Academy of Sciences, Haidian District, Beijing, China

**Peng Cheng** Institute of Physics, Chinese Academy of Sciences, Haidian District, Beijing, China

**Chandra Chowdhury** Department of Spectroscopy, Indian Association for the Cultivation of Science, Jadavpur, West Bengal, India

Eugenio Cinquanta Laboratorio MDM, IMM-CNR, Catania, Italy

**Ayan Datta** Department of Spectroscopy, Indian Association for the Cultivation of Science, Jadavpur, West Bengal, India

**Paola De Padova** Aix Marseille University, IMéRA, Marseille, France; Consiglio Nazionale delle Ricerche-ISM, Rome, Italy

N. D. Drummond Physics Department, Lancaster University, Lancaster, UK

xvi Contributors

Motohiko Ezawa Department of Applied Physics, University of Tokyo, Tokyo, Japan

V. I. Fal'ko National Graphene Institute, University of Manchester, Manchester, UK

Paola Gori Dipartimento di Ingegneria, Università "RomaTre", Roma, Italy

Carlo Grazianetti Laboratorio MDM, IMM-CNR, Catania, Italy

**M. Houssa** Department of Physics and Astronomy, University of Leuven, Louvain, Belgium

**Deepthi Jose** Department of Chemistry, Providence Women's College, Calicut, Kerala, India

Guy Le Lay CNRS, PIIM UMR 7345, Aix-Marseille University, Marseille, France

**Lars Matthes** Institut für Festkörpertheorie und -optik, Friedrich-Schiller-Universität Jena, Jena, Germany

Alessandro Molle Laboratorio MDM, IMM-CNR, Catania, Italy

Bruno Olivieri Consiglio Nazionale delle Ricerche-ISAC, Rome, Italy

Carlo Ottaviani Consiglio Nazionale delle Ricerche-ISM, Rome, Italy

**Olivia Pulci** Dipartimento di Fisica, Università di Roma "Tor Vergata", Roma, Italy

Claudio Quaresima Consiglio Nazionale delle Ricerche-ISM, Rome, Italy

**Angel Rubio** Max Planck Institute for the Structure and Dynamics of Matter and Center for Free-Electron Laser Science, Hamburg, Germany; Nano-Bio Spectroscopy Group and ETSF, Dpto. Fisica de Materiales, Universidad del País Vasco, CFM CSIC-UPV/EHU-MPC and DIPC, San Sebastián, Spain

**E.** Scalise Department of Materials Science, University of Milano-Bicocca, Milano, Italy

**Dmytro Solonenko** Institut für Physik, Technische Universität Chemnitz, Chemnitz, Germany

**A. Stesmans** Department of Physics and Astronomy, University of Leuven, Louvain, Belgium

**Li Tao** Microelectronics Research Centre, The University of Texas at Austin, Austin, TX, USA; School of Materials Science and Engineering, Southeast University, Nanjing, China

**Rik van Bremen** Physics of Interfaces and Nanomaterials, MESA+ Institute for Nanotechnology, University of Twente, Enschede, The Netherlands

Contributors xvii

**Arie van Houselt** Physics of Interfaces and Nanomaterials, MESA+ Institute for Nanotechnology, University of Twente, Enschede, The Netherlands

**Patrick Vogt** Institut für Physik, Technische Universität Chemnitz, Chemnitz, Germany

**Caspar J. Walhout** Physics of Interfaces and Nanomaterials, MESA+ Institute for Nanotechnology, University of Twente, Enschede, The Netherlands

**J. R. Wallbank** National Graphene Institute, University of Manchester, Manchester, UK

Kehui Wu Institute of Physics, Chinese Academy of Sciences, Beijing, Haidian, China

**Qirong Yao** Physics of Interfaces and Nanomaterials, MESA+ Institute for Nanotechnology, University of Twente, Enschede, The Netherlands

**Harold J. W. Zandvliet** Physics of Interfaces and Nanomaterials, MESA+ Institute for Nanotechnology, University of Twente, Enschede, The Netherlands

**Lijie Zhang** Physics of Interfaces and Nanomaterials, MESA+ Institute for Nanotechnology, University of Twente, Enschede, The Netherlands

**Jijun Zhao** Key Laboratory of Materials Modification by Laser, Ion and Electron Beams, Dalian University of Technology, Dalian, China

V. Zólyomi National Graphene Institute, University of Manchester, Manchester, UK

## Chapter 1 A Vision on Organosilicon Chemistry and Silicene



1

Deepthi Jose, Chandra Chowdhury and Ayan Datta

Abstract Replacement of carbon atoms from aromatic molecules and their two-dimensional extended analogues (graphene) have been predicted to have interesting structural diversity and tunable electronic properties. Recent progress in the experimental realization of such systems is discussed along with a conceptual understanding of the structural properties of planar organosilicon compounds and silicene. Psuedo Jahn-Teller (PJT) distortion is shown to contribute to the buckling distortions in silicene which make them excellent materials for band-gap tuning through hydrogenation. Chemical doping of silicene by cations is suggested to be a strategy to suppress buckling of silicene and regain its perfect planar two-dimensional silicon framework. TERS spectroscopy is proposed as a tool to probe the presence or absence of buckling distortions in silicene and cation doped silicene respectively.

## 1.1 Aromatic Molecules and Silicon Substituted Cyclic Rings

The concept of aromaticity or the special stability of cyclic  $\pi$ -conjugated molecules occupies a special position in chemistry. Such molecules are associated with their unusual stability. Manifestation of this stability is seen in their reluctance to undergo several reactions like hydrogenation and oxidation which are much more facile for non-conjugated cyclic molecules. Structurally these molecules are symmetric and vibrationally stable towards distortions to lower symmetry configurations [1]. In 1930s, Hückel proposed a simple model analogous to the tight-binding model popular in solid-state physics for simple cyclic  $\pi$ -conjugated molecules and proposed that

D. Jose

Department of Chemistry, Providence Women's College, Calicut 673009, Kerala, India e-mail: alphydeepthi@gmail.com

C. Chowdhury · A. Datta (☒)
Department of Spectroscopy, Indian Association for the Cultivation of Science, Jadavpur 700032, West Bengal, India e-mail: spad@iacs.res.in

cyclic molecules with  $(4n+2)\pi$  electrons (where n=0,1,2...) should be stabilized due to aromaticity [2–4]. As shown in Table 1.1, several such molecules with integer multiples of n have been synthesized chemically and characterized by various spectroscopic tools. Of particular mention should be the X-Ray diffraction studies that have shown that these structures are highly symmetric and the bond length alterations (BLA,  $\Delta r$ ) are typically less than 1–2%. The concept of stitching small aromatic molecules in-plane to generate massive two-dimensional graphene like two dimensional materials has been achieved experimentally. Müllen and co-workers have designed atomistically precise graphene nanoribbons based on bottom up synthesis starting from a simple anthracene molecule [5] (linear (n=3) in Table 1.1).

Therefore, for generating two dimensional silicon analogue of benzene namely silicene, one should have a clear understanding of small benzene like silicon rings which might be fused to generate large silicene flakes. In fact, it is with this aim that several groups have pursued the synthesis of silicon substituted aromatic and fused aromatic systems.

In Fig. 1.1, we enlist the experimentally synthesized silicon substituted aromatic molecule. Such sila-aromatic molecules are kinetically labile towards atmospheric oxidation. Therefore, a general experimental strategy to synthesize such molecules has been to use bulky protecting groups which create hydrophobic pockets around these molecules. Tokitoh and co-workers have synthesized silabenzene and silanaphthalene [6, 7] (structures 1(a), 1(b)) and B3LYP/6-31G(d) calculations have revealed that there is a small energy difference between Dewar silabenzene and silabenzvalene, while the planar silabenzene is by far the most stable among the isomers. Jutzi et al. have synthesized the 1,1-dimethyl SiC<sub>5</sub>H<sub>5</sub> anion (structure 1(c)) which based on structural and qualitative molecular orbital theory calculations has been shown to be aromatic [8]. Sasamori and co-workers have synthesized 9-silaphenanthrene. Crystal structure analysis of 9-silaphenanthrene have shown that the structure remains planar (structure 1(d)) [9]. Based on NMR chemical shifts and NICS calculations, the authors concluded that 9-silaphenanthrene has delocalized  $14\pi$  electron aromatic configuration. Tanabe et al. have synthesized 1,1'-Disila-4,4'-biphenyl (structure 1(e)) [10]. X-ray studies show that both the phenyl rings remain planar and the twist angle of the central C-C bonds between the silaaromatic rings are 41° which is similar to that of biphenyl (45°). The UV-vis spectrum of 1,1'-Disila-4,4'-biphenyl showed a red shift and a massive six times enhancement in absorbance compared to that of Tbt-substituted silabenzene. This therefore suggests the existence of extended conjugation through the single bond connecting two silaaromatic rings, a concept well-known in the realms of carbon based on aromatic systems.

A significant experimental achievement in this area has been the synthesis of an isomer of hexasilabenzene by Abersfelder and co-workers [11]. They synthesized dark green crystals of an isomer of  $Si_6R_6$  ( $R\!=\!\text{Tip}, 2, 4, 6$ -triisopropylphenyl and 2, 6-diisopropylphenyl) by the reduction of unsymmetrically substituted trichlorocyclotrisilane (see Fig. 1.2). It has a chair-like conformation in accordance with the theoretical results [12, 13]. Authors propose the term dismutational aromaticity to explain the bonding pattern of this molecule. In order to quantify the aromaticity of the molecule, they calculated the nucleus-independent chemical shift, NICS(0),

 Table 1.1 Existence cyclic stable molecules in line with the predictions from the Hückel model

n	Molecule	Structure and Symmetry
0	Cyclopropyl cation	D <sub>3h</sub>
1	Benzene	$D_{6h}$
2	Naphthalene	$D_{2h}$
3	Anthracene (linear)	$D_{2h}$
3	Phenanthrene (bent)	$C_{2v}$
6	Coronene (circular) (Hückel antiaromatic)	D <sub>6h</sub>
∞	Graphene (flat 2D lattice)	C <sub>s</sub>

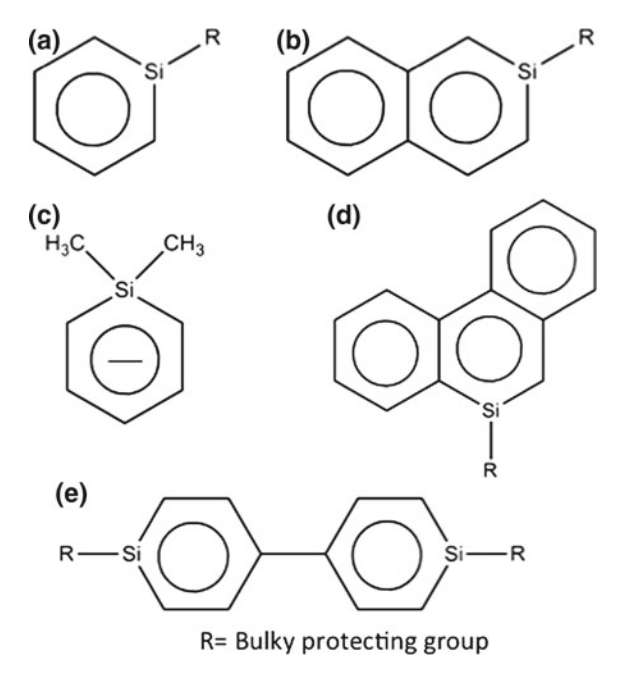
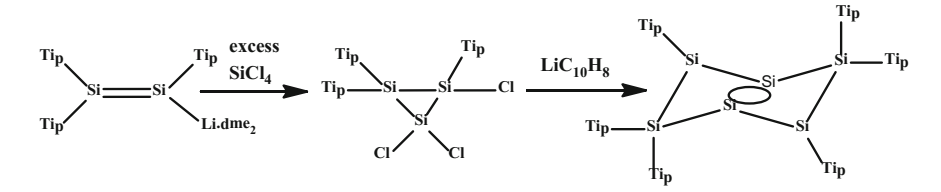
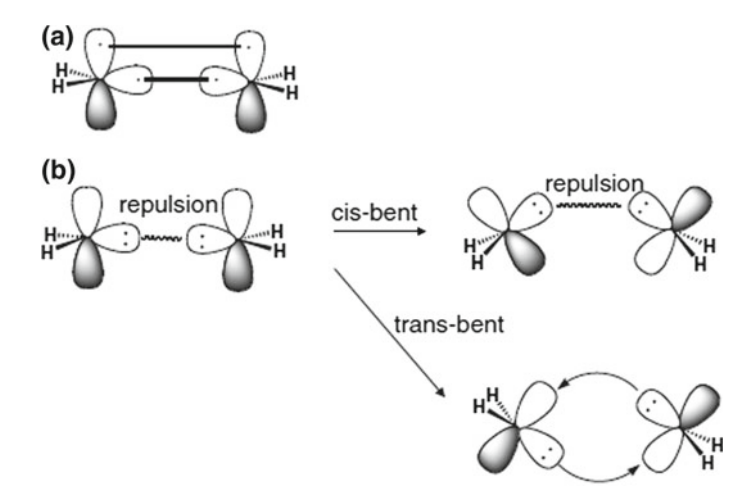


Fig. 1.1 Experimentally synthesized Sila-aromatic molecules



**Fig. 1.2** Synthesis of the tricyclic isomer of hexasilabenzene (Tip: 2,4,6-triisopropylphenyl; Li.dme<sub>2</sub>: 1,2-dimethoxyethane solvated Li)

at the center of the  $Si_4$  ring (-23.8 ppm), which indicates substantial aromaticity (benzene  $\sim -10$  ppm) but may also include shielding effects from the  $\sigma$ -framework. To estimate these latter effects, they also computed the NICS(0) value for the hypothetical saturated hydrogenation product of the molecule,  $Si_6R_6H_6$ . This in silico reduction has the effect of sequestering the two Si lone pair electrons and hence suppressing the dismutational resonance. The result (-6.4 ppm) suggests that the strongly diatropic NICS(0) value of  $Si_6R_6$  is truly due to aromaticity.



**Fig. 1.3** a Bonding in planar H<sub>2</sub>C=CH<sub>2</sub> **b** Bonding in trans-bent H<sub>2</sub>Si=SiH<sub>2</sub>. Reproduced with permission from [14]

## 1.2 Chemical Bonding: Unsaturated Carbon Systems Versus Silicon Systems

The contrasting behavior of the unsaturated carbon systems and their heavier analogues have been discussed in details by Nagase recently [14]. Here we mention the basic features which lead to different structures in silicenes and other two dimensional materials.

One might envision bonding in CH<sub>2</sub>=CH<sub>2</sub> or higher unsaturated organic molecules as composed of interaction between two or more CH<sub>2</sub> fragments. As shown in Fig. 1.3a, each of these  $CH_2$  units have two unpaired electrons (S=1, triplet). These two unpaired electrons are located in a hybridized  $sp^2$  orbital and a perpendicular  $p_z$ orbital respectively. So, as these fragments are brought closer, a maximum overlap between these two orbitals occurs when the overall H<sub>2</sub>C=CH<sub>2</sub> unit adapts a perfectly planar configuration (a  $D_{2h}$  point group). However, this case is altered in Silicon hydrides. The ground state of SiH<sub>2</sub> does not contain unpaired electrons (S=0, singlet). So, the two free electrons pair up and are localized as a lone-pair in the  $sp^2$ hybrid orbital (Fig. 1.3b). Hence, now approach of the two SiH<sub>2</sub> units along the shortest path should lead to strong electron-electron repulsion between the two filled orbitals. The only way to form a H<sub>2</sub>Si=SiH<sub>2</sub> bond will be to distort the structure either in a *cis-bent* or a *trans-bent* fashion. Clearly, a cis-bent structure should still possess this repulsion albeit in a relatively weaker angular fashion. Therefore, the best orientation of the H<sub>2</sub>Si=SiH<sub>2</sub> unit is the distorted trans-bent structure. It is important to remember that even though the H<sub>2</sub>Si=SiH<sub>2</sub> bond has a formal bond order of two, the trans-bent distortion leads to a weaker and hence, relatively longer double bonded system.

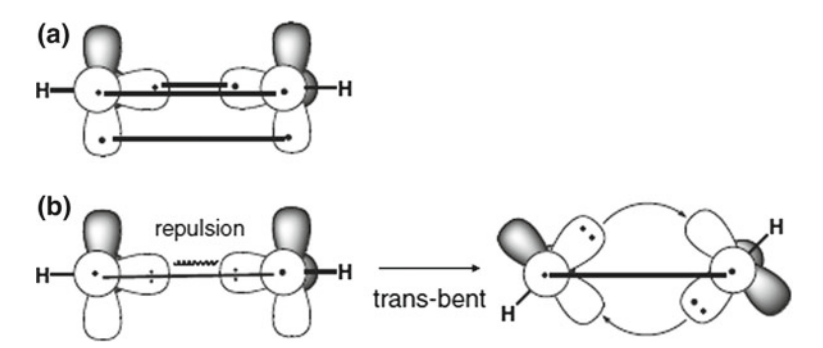


Fig. 1.4 a Bonding in linear HC≡CH b Bonding in trans-bent HSi≡SiH. Reproduced with permission from [14]

Similar to the ethylenic units, the silicon substituted acetylenes, HSi≡SiH also have a trans-bent structure. For both CH and SiH, the ground state has one unpaired electron (S = 1/2, doublet). However, for CH, the excitation energy required to possess three unpaired electrons (S = 3/2, quartet) is very small (~16.7 kcal/mol). Hence, the CH unit undergoes excitation to reach to a quartet state which facilitates it form three carbon-carbon (one  $\sigma$  and two  $\pi$ ) bonds. This results in a gain in binding energy of 228.5 kcal/mol, a more than ten fold gain compared to the loss in terms of the excitation energy. The formation of a triple bond in HE

EH is shown schematically in Fig. 1.4a. This results in linear HC $\equiv$ CH molecule ( $D_{\infty h}$  point group). For SiH, the doublet-quartet excitation energy is much more (~36.4 kcal/mol). Also, the strength of a linear triple bonded HSi=SiH is expected to be smaller due to poor overlap between the two diffused  $3p_z$  orbitals (formation of one  $\sigma$  bond) and two diffused  $3p_x$  and  $3p_y$  (formation of two  $\pi$  bond, perpendicular to the  $\sigma$  bond and with respect to each other). Therefore, the SiH units prefer to react by orienting their lone-pairs as far as possible as with respect to each other resulting in a trans-bent structure as shown in Fig. 1.4b.

One might understand the preference of the HSi $\equiv$ SiH systems to possess transbent geometries from the pseudo Jahn-Teller effects (PJTE) [15–17]. As shown in Fig. 1.5, formation of a triple bonded HE $\equiv$ EH unit (E=C, Si) involves filling up of a pair of electrons in one  $\sigma$ -orbital and two pairs of electrons in the in-plane ( $\pi_{in}$ ) and out of plane ( $\pi_{out}$ ) orbitals of  $\pi$ -symmetry. Distortion along the transbent normal mode,  $Q(\pi_g)$  leads to a symmetry allowed mixing of the filled  $\pi_{in}$  orbital ( $\pi_u$  symmetry) and the empty  $\sigma^*$  orbital ( $\sigma_u$  symmetry). In the case of C<sub>2</sub>H<sub>2</sub>, calculations at B3LYP/aug-cc-PVTZ level show that the energy separation between the  $\pi_{in}$  orbital and the  $\sigma^*$  orbital is 8.4 eV making this interaction extremely weak to effectively result in a structural distortion. However, for Si<sub>2</sub>H<sub>2</sub>, the  $\pi_{in}$ - $\sigma^*$  gap is only 3.6 eV at the same level of theory. This causes structural instability for the D<sub> $\infty$ h</sub> linear structure in Si<sub>2</sub>H<sub>2</sub> with an imaginary distortion mode ( $\omega_{\pi g}$  = 610.8i cm<sup>-1</sup>) which on relaxation leads to the trans-bent structure of Si<sub>2</sub>H<sub>2</sub> of a lower C<sub>2h</sub> symmetry. Therefore, a small gap between the filled state (occupied molecular orbital,

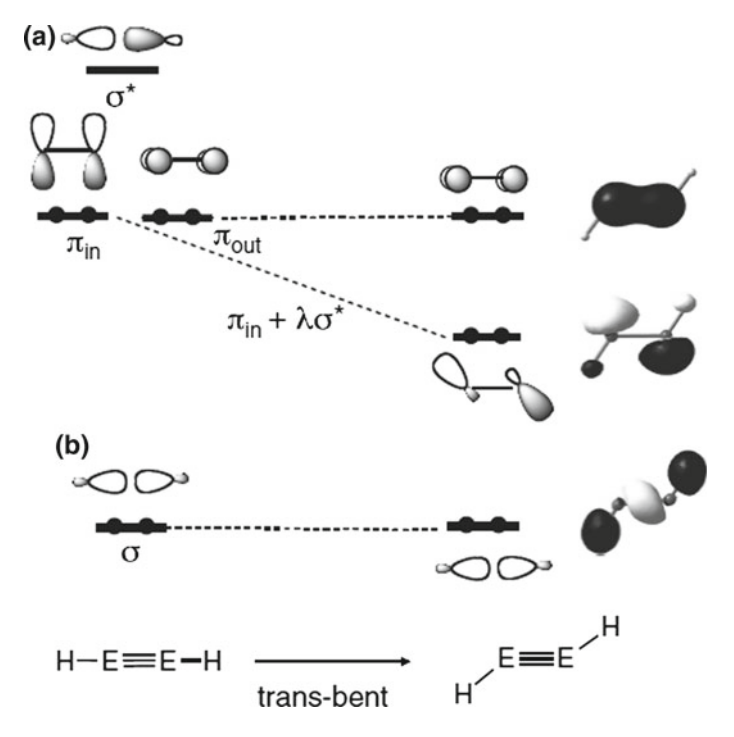


Fig. 1.5 a Bonding in linear HC≡CH b Bonding in trans-bent HSi≡SiH. Reproduced with permission from [14]

OMO) and the empty state (unoccupied molecular orbital, UMO) leads to structural instability in linear HSi $\equiv$ SiH systems. Such distortions belong to the general class of molecular distortions arising out of small OMO-UMO gaps, a *prime-facie* condition for PJT distortions. In fact, the preference for various heavier analogues of benzene like hexasilabenzene and hexagermanabenzene to have a distorted  $D_{3d}$  geometry instead of the expected planar  $D_{6h}$  geometry has been explained by us based on PJT effect [18]. We discuss this in details in the next section.

## 1.3 Effect of Buckling Distortions in Si<sub>6</sub> Rings: The Psuedo Jahn-Teller (PJT) Effect

Ab initio calculations predict buckled honeycomb geometry for silicene unlike graphene even though it possess similar electronic properties [19, 20]. The symmetry breaking in silicenes by buckling removes the instability associated with the planar high-symmetry structure. Such an instability of high-symmetry geometries of molecular systems is attributed to pseudo-Jahn–Teller (PJT) effect [15, 16]. As suggested by Bersuker, the vibronic coupling between the nondegenerate electronic

states of proper symmetry resulting in nonsymmetric vibrations leads to PJT effect [17, 21, 22]. The sufficiently strong coupling between the unoccupied molecular orbitals (UMOs) with occupied molecular orbitals (OMOs) has been identified and proved to be the source of distortions in many molecular systems [17, 23, 24]. The PJT effect can be suppressed by adding electrons to the UMOs, by increasing the energy gap between the interacting UMO and OMO, or by the isolobal substitution of atom or a group with their more electronegative analogues [25–27]. Puckering in silicene makes it more versatile since, besides having all the exotic properties of graphene, tuning the band gap is much easier [28, 29]. Unlike the ripples in graphene, which are disordered, silicene is puckered in each of the six membered ring and is symmetric across the surface. Because this short-range puckering has a pronounced effect on the electronic properties of silicene it is important to explore the fundamental aspects of puckering distortions and the factors that lead to puckering in silicene. A proper understanding of the buckling distortions is crucial to appreciate the novel properties of silicene and to tune it for various applications.

The silicene clusters gain stability on puckering with increase in the number of rings from  $Si_6H_6$  to  $Si_{70}H_{22}$  [30]. As shown in Fig. 1.6, the puckering angle  $\phi$  (the dihedral angles between the atoms 1, 2, 3, and 4) for the optimized geometry of  $Si_6H_6$  at B3PW91/TZVP is 33.7° and that for  $Si_{70}H_{22}$  is 35.6°. Periodic calculations for silicene using VASP plane wave based DFT code find the puckering angle for the optimized silicene sheet is about 36.8° (part c of Fig. 1.6). The puckering distortion in the smallest silicene cluster hexasilabenzene is preserved as such in silicene sheets. The structure, stability and aromaticity of isomers of hexasilabenzene has been studied extensively by various research groups [12, 31, 32]. Among the various isomers hexasilaprismane is computed to be the global minimum in the potential energy surface. The silicon analogue of benzene is 22.7 kJ/mol less stable than hexasilaprismane at CCSD(T)/cc-pVTZ level [33]. Because this  $D_{3d}$  structure is the smallest puckered repeating unit for silicene clusters and sheets, we chose chairlike hexasilabenzene for understanding the puckering distortions.

The strong vibronic coupling of nondegenerate orbitals that are sufficiently close in energy leads to vibrational instability in high symmetry configurations. The symmetry requirement for PJT effect is that the direct product of the symmetries of the nondegenerate orbitals should contain the symmetry of the instability path [34]. The onset of new covalence when a high symmetric configuration moves to a low symmetry configuration is responsible for PJT effect. Its well established in the literature that the planar hexasilabenzene is not a minimum energy isomer and has a vibrational instability (128.8i at M05-2X/6-31+G(d,p) level of theory) that leads to a  $C_3$ puckered structure [12, 31]. The Si-Si bond length increases from 2.21 to 2.23 Å as hexasilabenzene gets puckered, which is still less than the single Si-Si bond length of 2.35 Å. The planar hexasilabenzene is in  ${}^{1}A_{1g}$  electronic structure. The distortion along the unstable  $b_{2g}$  vibrational mode results in the chairlike  $D_{3d}$  structure and the  $b_{2g}$  mode becomes totally symmetric (a) mode. The vibronic coupling between the OMO-UMO pairs: HOMO and LUMO+2, HOMO-1 and LUMO+3 and/or HOMO-4 and LUMO can lead to the distortion of the  $D_{6h}$  structure. The product of the symmetries of OMO-UMO orbitals are:

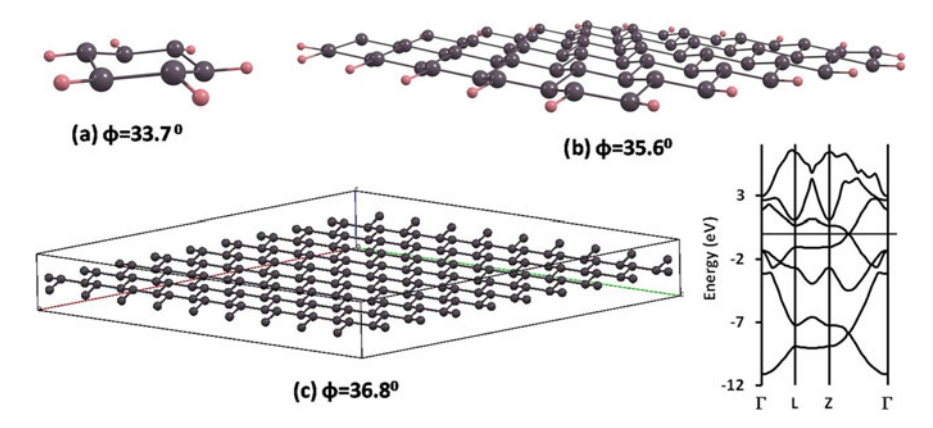


Fig. 1.6 Puckering Angle  $\phi$  for a Si<sub>6</sub>H<sub>6</sub>, b Large 2D molecular fragment: Si<sub>70</sub>H<sub>22</sub>, and c Infinite 2D Silicene Sheet with the computed band structure exhibiting the Dirac Cone. Reproduced with permission from [18]

HOMO and LUMO + 2:  $e_{1g} \times e_{2g} = b_{1g} + b_{2g} + e_{1g}$ HOMO-1 and LUMO + 3:  $a_{2u} \times b_{1u} = b_{2g}$ HOMO-4 and LUMO :  $e_{1u} \times e_{2u} = b_{1g} + b_{2g} + e_{1g}$ .

The energy gap between these OMO-UMO pairs are 6.83, 8.90, and 9.52 eV, respectively. The vibronic coupling in the OMO-UMO pairs HOMO-1 and LUMO+3 and HOMO-4 and LUMO can be neglected because the energy gap is significantly high. As shown in part a of Fig. 1.7, the PJT distortion due to the coupling between HOMO and LUMO+2 orbitals leads to the puckered  $D_{3d}$  geometry of hexasilabenzene. In the case of planar hexasilabenzene, the overlap of  $\sigma$  and  $\pi$  orbitals is zero. But puckering leads to  $\sigma$ - $\pi$  mixing resulting in a new covalence.

## 1.4 Chemical Functionalization on Silicon Rings to Make Them Planar

The cation– $\pi$  interactions are widespread and have considerable significance in molecular biology, drug discovery, and supramolecular chemistry [35, 36]. Experimental and theoretical investigations have shown that the cation– $\pi$  binding energies depend on the substituents on the aromatic surface and position and electronegativity of the cation [37, 38]. The origin of cation– $\pi$  interactions in benzene and other aromatic molecules has been mainly attributed to the electrostatic interaction and induction energy [39, 40]. Sergeeva et al. have reported the flattening of pentasila-cyclopentadienide ring by suppressing pseudo Jahn–Teller effect using Mg<sup>2+</sup> ions [26]. Ab initio calculations by Zdetsis predict that Si<sub>6</sub> can be made planar through

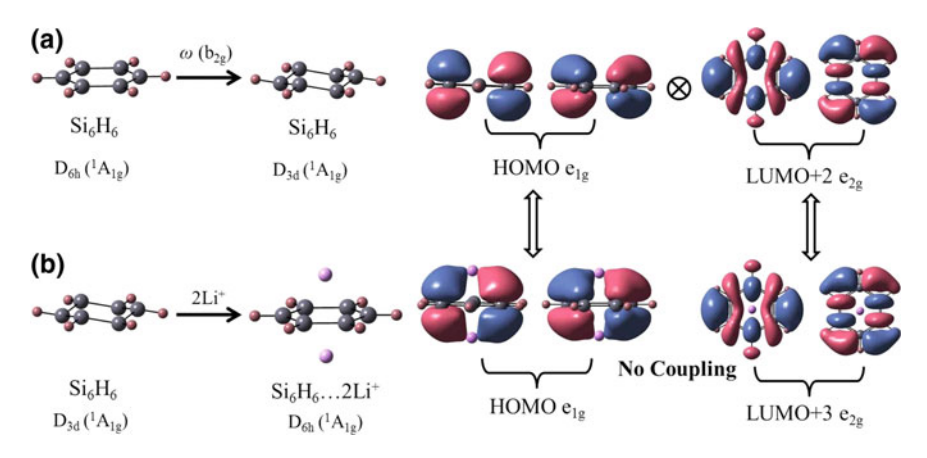
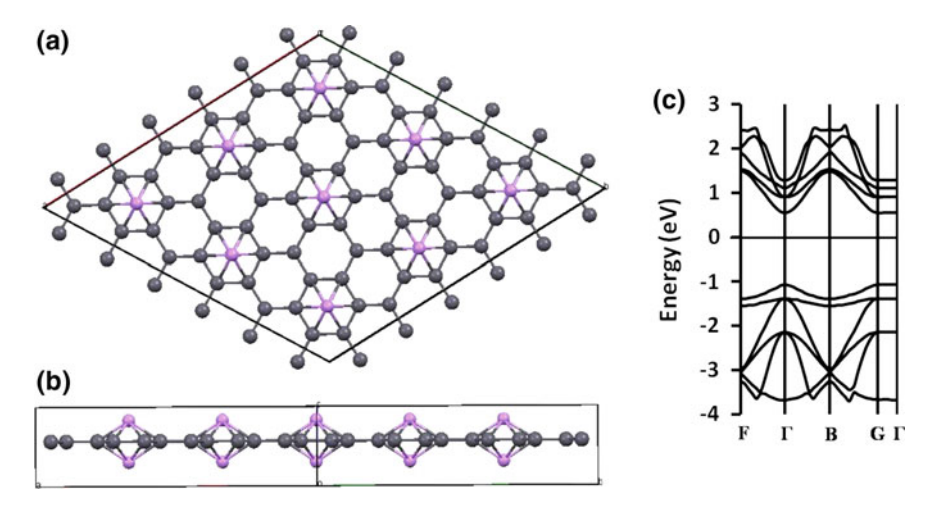


Fig. 1.7 a Onset of puckering from  $D_{6h} \rightarrow D_{3d}$  via  $b_{2g}$  distortion in hexasilabenzene. The corresponding OMO and UMO involved in this vibronic mixing associated PJT are also shown. b Suppression of distortion in hexasilabenzene.···2Li<sup>+</sup>. The 1–1 correspondence between the OMO and UMO are shown with respect to the undoped hexasilabenzene. (Calculations were done at M05-2X/6-31+g(d,p) level.) Reproduced with permission from [18]

the reduction of Si<sub>6</sub><sup>6</sup>- anion in the presence of counter cations. The resulting Si<sub>6</sub>Li<sub>6</sub> is planar, stable, and aromatic [41]. We performed DFT calculations to investigate whether the  $\pi$ -surface of hexasilabenzene can bind a metal ion. In the presence of Li<sup>+</sup>, the puckered Si<sub>6</sub> ring of hexasilabenzene becomes planar to form a stable  $C_{6v}$  Si<sub>6</sub>H<sub>6</sub>···Li<sup>+</sup> complex. The BSSE corrected binding energy for hexasilabenzene with Li<sup>+</sup> is -45.3 kcal/mol. The corresponding value for benzene...Li<sup>+</sup> complex is -39.9 kcal/mol. The distance between the metal ion and the centroid of the ring is 1.94 Å. Li<sup>+</sup> ion not only binds with hexasilabenzene more strongly than benzene but also suppresses the PJT distortion in hexasilabenzene ring. The energy gap of the OMO-UMO pair of hexasilabenzene increased from 6.83 to 7.37 eV in the presence of a Li<sup>+</sup> ion. The increase in energy gap in presence of Li<sup>+</sup> is sufficient enough to quench the coupling of OMO-UMO pair thereby suppressing the PJT effect along the  $b_{2g}$  mode. The  $\pi$ -surface of aromatic rings can be tuned to accommodate two cations [42]. We calculated the binding energy of hexasilabenzene with two Li+ ions. Unlike benzene for which binding of two cations on either side of the aromatic ring is endothermic, hexasilabenzene forms a stable  $D_{6h}$  Si<sub>6</sub>H<sub>6</sub>····2Li<sup>+</sup> complex and the BSSE corrected binding energy is -3.5 kcal/mol. The distance between the metal ion and the centroid of the ring is 2.18 Å. The electrostatic field from the two Li<sup>+</sup> ions increases the OMO-UMO energy gap to 7.68 eV restoring high symmetry  $D_{6h}$  structure of hexasilabenzene. Part b of Fig. 1.7 shows the suppression of PJT distortion of hexasilabenzene in the presence of two Li+ ions. The one-to-one correspondence between the OMO and UMO of hexasilabenzene and the 2:1 Li+ doped hexasilabenzene are also shown.

Inspired by the results for planarization for hexasilabenzene on mono and di lithiation, material with planar silicene sheet decorated with Li<sup>+</sup> were designed and



**Fig. 1.8** a Transverse view, **b** lateral view of optimized Li+decorated silicene sheet, **c** its band structure (at the GGA/PBE level with plane wave basis). Reproduced with permission from [18]

periodic calculations were performed for such extended system. The unit cell was constructed such that the Li<sup>+</sup> ions bind to the top and bottom surface of alternate hexasilicon ring. In agreement with the results of hexasilabenzene, the silicene sheet turns planar in the presence of Li<sup>+</sup> ions. The transverse and lateral view of a  $3 \times 3$  supercell of the optimized Li<sup>+</sup> decorated silicene cluster is shown in Fig. 1.8. The presence of Li<sup>+</sup> ions open up the band gap in silicene (part c of Fig. 1.5). The band gaps for silicene···Li<sup>+</sup> and silicene···2Li<sup>+</sup> are calculated to be 1.29 and 1.25 eV, respectively. The band gaps are estimated to be 1.70 and 2.14 eV (1.62 and 2.10 eV) at HSE06 and B3LYP hybrid levels of calculations for silicene···Li<sup>+</sup> (silicene···2Li<sup>+</sup>), respectively.

### 1.5 Electron and Hole Transport in Silicene

The Reorganization Energy ( $\lambda$ ) can give an insight into the charge transfer properties of the system. The reorganization energy is a key factor controlling the rate of charge transport in a system within an incoherent charge transport method. The energy required for the structural changes of the molecule when an electron is added or removed is the internal reorganization energy, and the external reorganization energy is due to structural modifications in the surrounding medium during the electron transfer process. The molecules with small reorganization energies are in high demand due to their numerous applications in the electronic and optoelectronic industries. The internal reorganization energy for the silicenes has been calculated at B3PW91/TZVP level using the relation [43]:

$$\lambda_{\text{hole/electron}} = (E_{\pm}^* - E_{\pm}) + (E_{\text{cation/anion}}^* - E)$$

where E is the energy of neutral state in the neutral geometry,  $E_{\text{cation/anion}}^*$  is the energy of the neutral state in the cationic/anionic geometry,  $E_{+}$  is the energy of cationic/anionic state in that geometry and  $E_{+}^{*}$  is the energy of cationic/anionic state in the neutral geometry. The reorganization energy for the silicenes in the are reported in Table 1.2. For all the silicenes the  $\lambda_{hole}$  value is smaller than  $\lambda_{electron}$ . This is an important result, since polyacenes are also known to be hole conductors. The  $\lambda_{hole}$  values for PAH,  $C_{10}H_8$ ,  $C_{14}H_{10}$ ,  $C_{18}H_{12}$  and  $C_{22}H_{14}$  at B3LYP/6-31G\*\* are 0.18, 0.14, 0.11 and 0.97 eV, respectively [44]. This is in good agreement with the values that we calculated for the corresponding silicon analogues Si<sub>10</sub>H<sub>8</sub> (0.16 eV),  $Si_{14}H_{10}$  (0.13 eV),  $Si_{18}H_{12}$  (0.12 eV) and  $Si_{22}H_{14}$  (0.10 eV). Therefore, silicenes might be considered as "sister molecules" to polyacenes. The reorganization energy decreases as the value of m and n increases, which can be utilized for a wide variety of applications in electronics. The  $\lambda_{hole}$  and  $\lambda_{electron}$  values for various silicenes suggest that with the increase in the values of m and n, silicenes show amphiphilic character. The puckering in the dihedral of peripheral hexasilicene rings increases with the addition of an electron and decreases with the removal of an electron compared to the neutral species. This difference is negligible as the number of rings increase, which implies that the charges get delocalized for larger clusters.

It is important to note that bulk Si is known to exist in only  $sp^3$  covalently link diamond-like structure, [45] which might be visualized as layers of puckered silicenes stacked over one another with the  $C_3$  distortions arising from the additional interlayer Si–Si bonds. This is in contrast to carbon that exists additionally in the pure  $sp^2$  graphite structure. Thus, the absence of any other allotrope of Si similar to the graphite form in carbon can be attributed to the puckering distortion that renders  $\pi$ -stacking interactions ineffective through the loss of planarity in each six-membered ring, and favors an  $sp^3$  bonding environment. Also, the diamond structure of Si ensures that Si–Si interaction energies are identical both along the layer and in between the layers. To understand the interaction between the layers, the bonding energies of the interlayer structures were computed at the same level of theory. Basis set superposition error (BSSE) was corrected using the counterpoise correction (CP) method [46].

For the dimers the Si–Si bond length varies between 2.37 and 2.39 Å along the interlayer for different sized systems, which is comparable with the bulk Si–Si bond length of 2.35 Å. The Si–Si bond length in between the layers are in the range 2.38–2.47 Å. A HOMO-LUMO gap of 2–3 eV suggests semiconducting behavior for the dimers. A higher value of the HOMO–LUMO gap compared to the corresponding monomers indicates that delocalization is more in the plane. The transfer integral in between the monomers for the dimer was calculated using the relation [47, 48].

$$t_{\text{hole}} = 1/2\{E(\text{HOMO}) - E(\text{HOMO} - 1)\}$$
  
 $t_{\text{electron}} = 1/2\{E(\text{LUMO} + 1) - E(\text{LUMO})\}$ 

Si70H22

35.6

Molecule	Average puckering	Binding energy/atom	HOMO- LUMO	$\lambda_{ m hole}$	$\lambda_{electron}$
	angle		Gap		
Si <sub>6</sub> H <sub>6</sub>	33.7	-0.90	3.22	0.26	0.96
Si <sub>10</sub> H <sub>8</sub>	34.3	-0.93	2.26	0.16	0.47
Si <sub>14</sub> H <sub>10</sub>	34.4	-0.94	1.68	0.13	0.25
Si <sub>14</sub> H <sub>10</sub>	34.8	-0.95	2.21	0.16	0.48
Si <sub>18</sub> H <sub>12</sub>	34.3	-0.95	1.31	0.12	0.15
Si <sub>22</sub> H <sub>14</sub>	34.3	-0.95	1.06	0.10	0.14
Si <sub>16</sub> H <sub>10</sub>	35.0	-0.97	1.80	0.13	0.31
Si <sub>22</sub> H <sub>12</sub>	35.2	-0.98	1.35	0.11	0.22
Si <sub>28</sub> H <sub>14</sub>	35.2	-0.99	1.03	0.12	0.17
$Si_{24}H_{12}$	36.7	-1.00	1.89	0.11	0.20
$Si_{30}H_{14}$	35.4	-1.00	1.02	0.09	0.18
Si <sub>34</sub> H <sub>16</sub>	35.2	-0.99	0.80	0.08	0.16
Si <sub>38</sub> H <sub>16</sub>	35.4	-1.00	0.78	0.08	0.15
Si <sub>46</sub> H <sub>18</sub>	35.5	-1.01	0.60	0.08	0.17
Si <sub>48</sub> H <sub>18</sub>	35.5	-1.01	0.59	0.07	0.13
Si <sub>58</sub> H <sub>20</sub>	35.6	-1.02	0.44	0.06	0.11

**Table 1.2** Binding energy per Si atom (eV), point group, HOMO-LUMO (eV), reorganization energy for silicenes of various nuclearities at B3PW91/6-31G(d) level of theory

The binding energies, reorganization energies, HOMO–LUMO gaps and the transfer integral for the dimers are given in Table 1.3. The binding energies calculated at B3PW91 and M05-2X levels are consistent with each other, which implies that dispersion interactions do not make a significant contribution in stabilizing the silicene dimers, unlike in the carbon analogues. The structures for the stacked dimers of the monomeric layers are shown in Fig. 1.9. One clearly observes that unlike  $\pi$ -stacking interactions in PAH, covalent Si–Si bonding stabilizes the interlayer bonding. It is interesting to note that both the  $t_{\text{hole}}$  and  $t_{\text{electron}}$  are about 20% of that for organic molecules like TTF, TCNQ, BTQBT, benzene and naphthalene [47, 49]. The lower values of the transfer integrals arise due to smaller spacing between the valence and conduction levels as a consequence of the more diffused orbitals on silicon compared to carbon.

0.33

0.06

0.10

### 1.6 Reactivity of Silicene Towards Hydrogen and Band Gap Tuning

-1.03

It has been already reported that the hydrogenation of a single-layer of graphene causes remarkable changes in the electronic and atomic structures, and in the trans-

**Table 1.3** Binding energy of the co-facial dimers (in eV), hole and electron reorganization energies (in eV) HOMO–LUMO (eV) and hole and electron transfer integrals (in eV) for silicenes of various nuclearities at B3PW91/6-31G(d) level of theory

Dimer	Binding	$\lambda_{hole}$	λ <sub>electron</sub>	НОМО-	Transfer integral	Transfer integral
	energy per			LUMO	$(t_{ m hole})$	$(t_{ m electron})$
	monomer			gap		
$Si_{12}H_{12}$	-3.6	0.27	1.51	2.0	0.05	0.08
Si <sub>20</sub> H <sub>16</sub>	-9.2	0.90	0.35	3.1	0.15	0.17
$Si_{28}H_{20} \\$	-12.3	0.76	0.34	2.8	0.11	0.03
$Si_{28}H_{20} \\$	-12.0	0.56	0.28	2.5	0.19	0.21
$Si_{32}H_{20}$	-13.0	0.52	0.15	2.3	0.15	0.019
$Si_{36}H_{24}$	-15.7	0.64	0.27	2.6	0.03	0.05
Si <sub>44</sub> H <sub>24</sub>	-16.6	0.56	0.16	2.0	0.04	0.06
Si <sub>44</sub> H <sub>28</sub>	-17.1	1.16	1.36	1.8	0.03	0.07

port properties. The successful synthesis of hydrogenated graphene (graphane) was first accomplished by Elias et al. [50]. Though the hydrogenation process is reversible, the graphane formed with  $sp^3$  hybridized carbon atoms in the lattice is stable at room temperature for many days. It is crystalline and retains the hexagonal lattice, but the periodicity is considerably shorter compared to graphene. The hydrogenation increases the energy gap in graphane and conductance becomes temperature dependent. Annealing the graphane at high temperature restores many of the fundamental properties of graphene, like metallic state, the lattice spacing and the quantum Hall effect. An earlier theoretical calculation by Sofo et al. predicted that the chair-like conformer, with hydrogen atoms bonded to carbon on both sides of the plane in an alternating manner, is more stable than a boat-like conformer in which a pair of hydrogen atoms occupy alternate positions. Graphane also has a very high volumetric and gravimetric hydrogen density, and hence has promising applications [51]. It is interesting to study the feasibility of the hydrogenation reaction of silicenes and its effect on the different properties and structure of silicene. The stability of hydrogenated silicon fullerenes has been studied by various research groups, and they are proven to have a potential hydrogen storage capacity. An efficient and low cost storage material for hydrogen is a major challenge for the current scientific community, and this is an area of active research. The US Department of Energy hydrogen storage system targeted a 6.0 weight percent gravimetric capacity and a volumetric capacity of 0.045 kg L<sup>-1</sup> for the year 2010 [52]. Previous first principle calculations by Cao et al. revealed that silicon nanotubes are better candidates for hydrogen storage compared to iso-diameter carbon nanotubes. The denser and more localized electron clouds of silicon nanotubes can adsorb hydrogen more strongly [53].

The structures of silicenes with different nuclearity were optimized after saturating all the bonds with hydrogen atoms. The heat of hydrogenation is calculated using the relation  $\Delta H = H(\mathrm{Si}_a \mathrm{H}_{b+c}) - (H(\mathrm{Si}_a \mathrm{H}_b) + c/2 \mathrm{H}_2)$ , where c is the number of hydrogen molecules added for complete saturation (see Fig. 1.10). The result shows that the

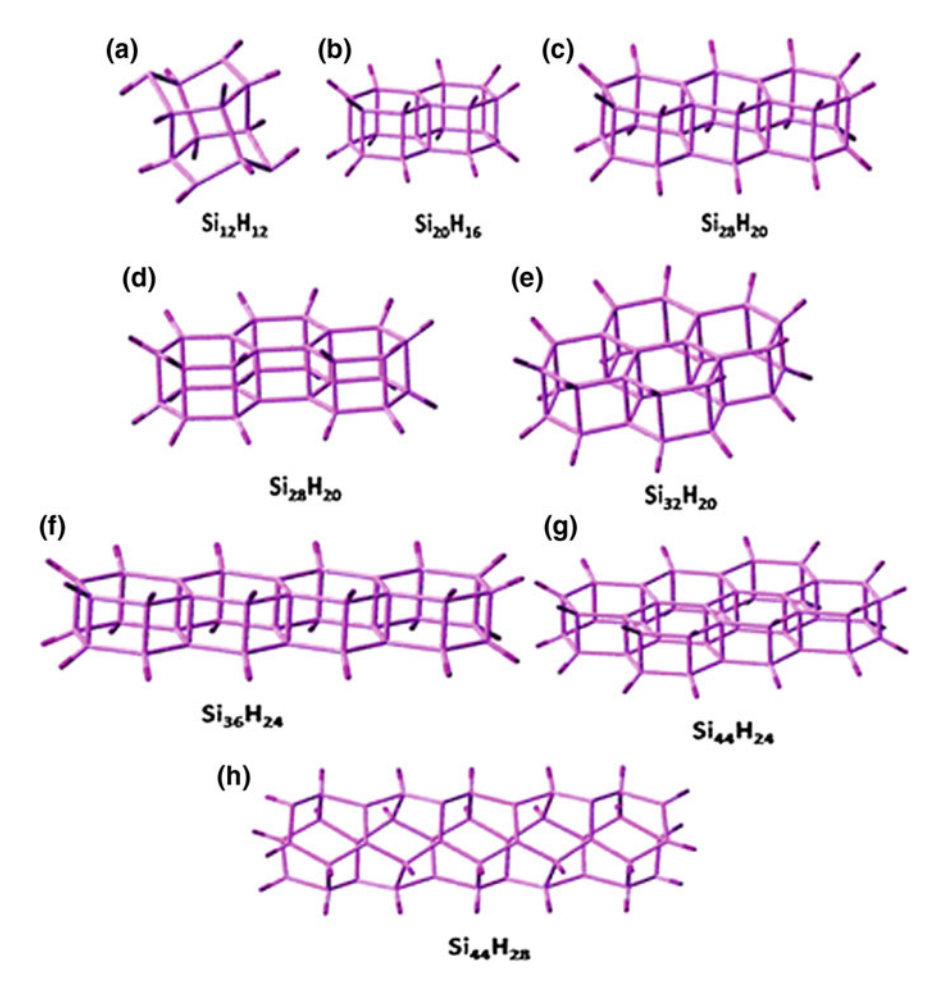


**Fig. 1.9** The optimized "tiffin-box like" structures for the stacked dimers of the silicene strips at B3PW91/6-31 G(d) level of theory. Reproduced from [30] with permission from PCCP Owner Societies

reaction is more exothermic than the carbon counterparts. The heat of hydrogenation for benzene, naphthalene, anthracene and phenanthrene is -2.16 eV, 3.5 eV, 5.0 eV and 4.7 eV, respectively, [54] which in the silicon world for  $Si_6H_6$ ,  $Si_{10}H_8$ , the anthracene analogue of Si,  $Si_{14}H_{10}$  and the phenanthrene analogue of Si,  $Si_{14}H_{10}$ , are -4.63, -7.48, -10.40 and -10.25 eV. The instability of  $sp^2$ silicon in silicene compared to  $sp^2$  carbon in graphene makes hydrogenation more feasible in the case of silicene. The weight percent of hydrogen for various silicenes (values for carbon analogues in the parenthesis) are given in Table 1.4, and it ranges from 6.6 to 4.5%. The preference of Si to be in an  $sp^3$  environment rather than an  $sp^2$  environment is evident from the structural parameters. The Si–Si bond length in hydrogenated

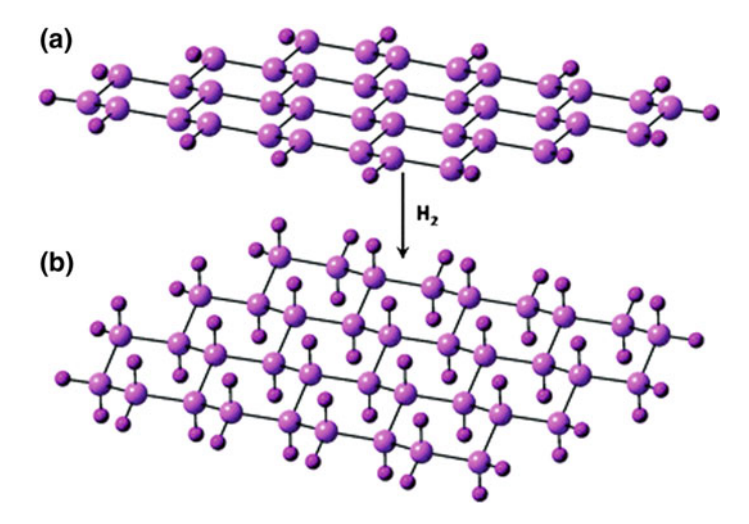


**Fig. 1.10** Schematic representation of structural changes in silicene clusters on hydrogenation. Reproduced from [30] with permission from PCCP Owner Societies

silicenes is between 2.35 and 2.36 Å, which agrees well with the standard value of 2.35 Å. The Si–Si–Si bond angles are in the range 110–111°, and Si–Si–H bond angles range between 107 and 109°. The HOMO–LUMO gap and polarizability of the hydrogenated silicenes are also given in Table 1.4. All the silicanes under our study have HOMO–LUMO gaps greater than 4 eV, indicating a shift from the zero gap semiconductor realm to that of wide gap semiconductors. The increase of the band gap during saturation of silicenes with hydrogens can be used for band gap tuning by controlled saturation by hydrogen. Though the storage capacities of these clusters are comparatively lower than PAH, coupled with their band engineering properties silicenes can be seen as promising materials.

## 1.7 Tip Enhanced Raman Spectroscopy (TERS) as a Probe for the Buckling Distortion in Silicene

Raman spectroscopy is a significant tool for the characterization of 2D materials. The Raman spectrum of graphene has been shown to evolve with the number of layers and can be effectively used to differentiate monolayer, bilayer and multilayer graphene [55]. This non-destructive technique is also sensitive towards the quality of layers, doping level and defects in the graphene sheet [56]. Scalise et al. have calculated the Raman spectrum of free standing silicene and germanene and also the nanoribbons of Si and Ge [57]. They found that silicene shows an intense G-like peak at 570 cm<sup>-1</sup>. Corresponding to the D peak in graphene, Si nanoribbons show a peak at 515 cm<sup>-1</sup>. Cinquanta et al. have reported the Raman spectrum of epitaxial silicene [58]. They found that the interaction of Si atoms with the Ag(111)

<del>-</del> -	`	ilicanes) of various nuclea		D 1 1 1 111	C
Species	Heat of	Heat of	HOMO-	Polarizability	% wt. of
	hydrogena-	hydrogenation/Si-atom	LUMO gap	(a.u.)	hydrogen
	tion		(eV)		
	(eV)				
$Si_{6}H_{12} \\$	-4.63	-0.77	6.97	175.63	6.6
$Si_{10}H_{18} \\$	-7.48	-0.75	5.96	307.51	6.0
$Si_{14}H_{24}$	-10.40	-0.74	5.35	425.41	5.7
Si <sub>14</sub> H <sub>24</sub>	-10.25	-0.73	5.54	445.59	5.7
Si <sub>18</sub> H <sub>30</sub>	-13.34	-0.74	5.00	606.28	5.6
Si <sub>22</sub> H <sub>36</sub>	-16.29	-0.74	4.78	766.09	5.5
Si <sub>16</sub> H <sub>16</sub>	-11.35	-0.71	5.48	507.29	3.4
Si <sub>22</sub> H <sub>34</sub>	-15.61	-0.71	5.01	734.18	5.2
Si <sub>28</sub> H <sub>42</sub>	-19.77	-0.71	4.70	969.62	5.0
Si <sub>24</sub> H <sub>36</sub>	-17.70	-0.74	5.12	798.21	5.0
Si <sub>30</sub> H <sub>44</sub>	-20.94	-0.70	4.81	1037.82	5.0
Si <sub>34</sub> H <sub>50</sub>	-23.95	-0.70	4.49	1214.41	5.0
Si <sub>38</sub> H <sub>54</sub>	-26.32	-0.69	4.54	1357.97	4.8
Si <sub>46</sub> H <sub>64</sub>	-31.68	-0.69	4.37	1690.37	4.7
Si <sub>48</sub> H <sub>66</sub>	-32.87	-0.68	4.45	1766.55	4.7
Si <sub>58</sub> H <sub>78</sub>	-39.46	-0.68	4.28	2189.89	4.6
SizoHo2	-47.23	-0.67	4.22	2040.75	4.5

**Table 1.4** Heat of hydrogenation, HOMO–LUMO gap, polarizability and weight percent of H for hydrogenated silicenes (silicenes) of various nuclearities

surface distorts the low buckled silicene structure and enlarges the unit cell. The intense sharp peak at  $516~\rm cm^{-1}$  resembling the G-peak of graphene is a fingerprint of silicene. Calculations have been performed on free standing silicene clusters to capture the signature of buckling distortion in the Raman spectrum and enhance the intensity of this particular normal mode using metal clusters [59]. The vertical displacement of alternate Si atoms of each hexagonal ring along the  $C_{3v}$  axis leads to the buckling distortion in silicene. Since the dipole moment of the molecule is not changing during the buckling distortion, infrared (IR) spectroscopy cannot track this effect.

The vibrational frequencies and Raman intensities for various clusters of silicene were calculated. In order to examine the effect of metal clusters on Raman intensity, the silicene clusters:  $Si_6H_6$ ,  $Si_{14}H_{10}$  and the fused cluster  $Si_{18}H_{12}$  were chosen. The clusters of gold and silver are considered to be adsorbed on the silicene surface. The  $M_2$ ,  $M_4$  and  $M_{20}$  clusters of Au and Ag were placed at a distance of 2.5 Å from the center of mass of silicene clusters from the tip of the cluster as shown in Fig. 1.11. The distance of 2.5 Å is selected based on the most stable vertical configuration of the metal dimer  $(M_2)$ . The ECP basis set LANL08(f) [60–62] available from the EMSL Basis Set Exchange Library [63, 64] was employed for the metal atoms.

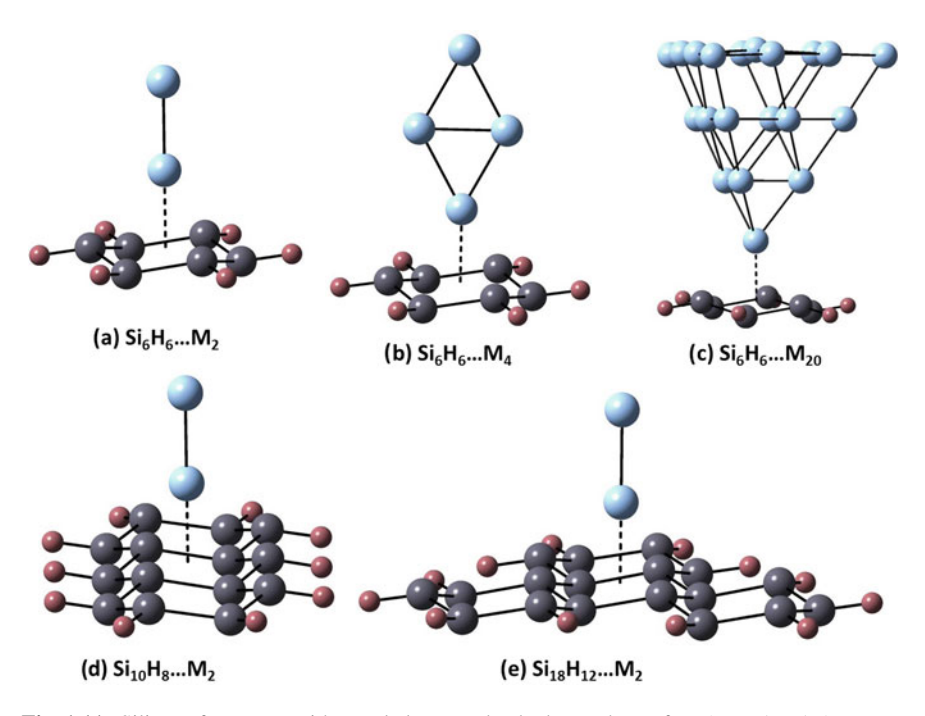


Fig. 1.11 Silicene fragments with metal clusters adsorbed over the surface (M = Au, Ag). Reproduced from [59] with permission from PCCP Owner Societies

The high sensitivity of surface-enhanced Raman scattering (SERS) has made it a powerful analytical technique [65-67]. The combination of scanning probe microscopy (SPM) and SERS, Tip-enhanced Raman scattering (TERS), is promising with added advantages like uniform enhancement of the signal at all sample locations, high spatial resolution, coupling of topographic features with spectroscopic data, quantitative measurement of SERS etc. [68, 69]. In TERS, the SPM tip is an externally tunable hot spot and one can effectively use it to enhance the Raman signal. Clusters of silver and gold to model the tip and study its effect on the Raman spectra of the silicene cluster. The buckling frequency, Raman scattering activity, enhancement in the scattering activity and binding energy for the silicene clusters Si<sub>6</sub>H<sub>6</sub>, Si<sub>14</sub>H<sub>24</sub> and Si<sub>18</sub>H<sub>12</sub> in the presence of metal clusters are given in Table 1.5. The enhancement in the scattering activity is calculated as the ratio of scattering activity for the buckling mode of the silicene...metal complex to the scattering activity of the most prominent buckling mode of the corresponding silicene cluster. While, the enhancements are modest (in between 2-5 times increase), the enhancements increase with an increase in the size of the metal cluster. For example, for hexasilabenzene (Si<sub>6</sub>H<sub>6</sub>) the enhancement increases from 1.1 to 4 times as a gold cluster increases in size from a simple linear dimer to a tetrahedral Au<sub>20</sub>. Much stronger manifestation occurs when the tip is considered to be silver. The enhancement increases from 3 times to 17 times as the size of the Ag cluster increases from 2 to 20.

Species	Buckling frequency (cm <sup>-1</sup> )	Scattering activity (S.A) (A <sup>4</sup> /AMU)	Enhancement in S.A	Binding energy (kcal mol <sup>-1</sup> )
Si <sub>6</sub> H <sub>6</sub> Au <sub>2</sub>	104	25.87	1.1	-26.0
Si <sub>6</sub> H <sub>6</sub> Au <sub>4</sub>	97	52.11	2.22	-22.3
Si <sub>6</sub> H <sub>6</sub> Au <sub>20</sub>	100	95.24	4.05	-25.4
Si <sub>6</sub> H <sub>6</sub> Ag <sub>2</sub>	100	75.28	3.21	-18.0
Si <sub>6</sub> H <sub>6</sub> Ag <sub>4</sub>	80	169.84	7.23	-14.1
Si <sub>6</sub> H <sub>6</sub> Ag <sub>20</sub>	109	402.08	17.1	-18.6
Si <sub>14</sub> H <sub>10</sub> Au <sub>2</sub>	139	76.75	1.36	-25.3
Si <sub>14</sub> H <sub>10</sub> Ag <sub>2</sub>	142	103.5	1.84	-17.7
Si <sub>18</sub> H <sub>12</sub> Au <sub>2</sub>	97	18.38	1.47	-22.5
Si <sub>18</sub> H <sub>12</sub> Ag <sub>2</sub>	131	91.43	1.81	-15.3

**Table 1.5** The buckling frequency, scattering activity, enhancement in scattering activity and binding energy for silicene fragments in the presence of metal clusters at the M05-2X/TZVP level of theory

### **Outlook and Future Perspectives**

The bottom up design of two dimensional silicon based materials from basic starting point namely silicon substituted benzene and stitching atoms with perfection along a honeycomb is challenging. Over the last decade, synthetic chemist aided by concepts of theoretical chemistry have been able to design higher order molecular fragments of fused aromatic molecules where the carbon atoms have been replaced by silicon. One should expect bigger molecular fragments with 10–15 fused six membered rings of silicon being synthesized.

Calculations and experiments have now established that unlike graphene, silicene will be buckled which is understood on the basis of Psuedo Jahn-Teller distortions in silicon systems. Computational studies predict that intercalation of cations between the silicene layers led to suppression of the buckling distortion and the graphene like structural feature can be regained. Aromatic organosilicon compounds have excellent transport properties and the band gap can be tuned by chemical functionalization. One might anticipate that rapid progress in synthesis of such molecules would provide new insights into various aspects of the rich chemistry of silicon based aromatic compounds. The possibility of depositing such molecules on bulk silicon substrates should lead to devices which can be easily integrated into existing silicon microstructures and should show superior performance under ambient conditions. Such a rational design of new materials based on molecular properties should generate excitement in the evolving area of molecular materials. A deeper understanding of the basic forces between the substrate and the molecules can minimize dissipation channels in the charge separation processes and would further augment the discovery of new phases of in two-dimensional silicon physics. Clearly, such systems provide 20 D. Jose et al.

a possibility of synergy between chemical synthesis, computational materials design and exotic physical properties.

Acknowledgements The authors are thankful to long-term discussions in the area of molecular vibrations in silicon systems to Alexander Boldyrev, Issac B. Bersuker and G. Narahari Sastry. Funding from INSA, DST, BRNS is duly acknowledged. Computational resources of the IACS-CRAY supercomputer for many of the calculations is highly appreciated.

#### References

- 1. M. Sainsbury, Aromatic Chemistry (Oxford Science Publications, Oxford, 1992)
- 2. E. Hückel, Z. Physik 72, 310 (1931)
- 3. E. Hückel, Z. Physik **70**, 204 (1931)
- 4. E. Hückel, Z. Physik **76**, 628 (1932)
- 5. J. Cai, P. Ruffieux, R. Jaafar, M. Bieri, T. Braun, S. Blankenburg, M. Muoth, A.P. Seitsonen, M. Saleh, X. Feng, K. Mullen, R. Fasel, Nature **466**, 470 (2010)
- 6. K. Wakita, N. Tokitoh, R. Okazaki, S. Nagase, Angew. Chem. Int. Ed. 39, 634 (2000)
- 7. N. Tokitoh, K. Wakita, R. Okazaki, S. Nagase, P. von Ragué Schleyer, H. Jiao, J. Am. Chem. Soc. 119, 6951 (1997)
- 8. P. Jutzi, M. Meyer, H.V.R. Dias, P.P. Power, J. Am. Chem. Soc. 112, 4841 (1990)
- 9. N. Tokitoh, A. Shinohara, T. Matsumoto, T. Sasamori, N. Takeda, Y. Furukawa, Organometallics 26, 4048 (2007)
- 10. Y. Tanabe, Y. Mizuhata, N. Tokitoh, Organometallics 29, 721 (2010)
- 11. K. Abersfelder, A.J.P. White, H.S. Rzepa, D. Scheschkewitz, Science 327, 564 (2010)
- 12. S. Nagase, H. Teramae, T. Kudo, J. Chem. Phys. **86**, 4513 (1987)
- 13. K.K. Baldridge, O. Uzan, J.M.L. Martin, Organometallics 19, 1477 (2000)
- 14. S. Nagase, Bull. Chem. Soc. Jpn 87, 167 (2014)
- 15. W.D. Hobey, J. Chem. Phys. 43, 2187 (1965)
- 16. L. Blancafort, M.J. Bearpark, M.A. Robb, Mol. Phys. 104, 2007 (2006)
- 17. I.B. Bersuker, Chem. Rev. **113**, 1351 (2013)
- 18. D. Jose, A. Datta, J. Phys. Chem. C 116, 24639 (2012)
- 19. H. Şahin, S. Cahangirov, M. Topsakal, E. Bekaroglu, E. Akturk, R.T. Senger, S. Ciraci, Phys. Rev. B 80, 155453 (2009)
- 20. G.G. Guzmán-Verri, L.C. Lew Yan Voon, Phys. Rev. B **76**, 075131 (2007)
- 21. I. Bersuker, *The Jahn-Teller Effect* (Cambridge University Press, 2006)
- 22. P. Garcia-Fernandez, I.B. Bersuker, J.E. Boggs, J. Chem. Phys. **124**, 044321 (2006)
- 23. H.J. Worner, F. Merkt, J. Chem. Phys. **127**, 034303 (2007)
- 24. Y. Liu, S. Kumari, M. Roudjane, S. Li, D.-S. Yang, J. Chem. Phys. 136, 134310 (2012)
- 25. K. Pokhodnya, C. Olson, X. Dai, D.L. Schulz, P. Boudjouk, A.P. Sergeeva, A.I. Boldyrev, J. Chem. Phys. 134, 014105 (2011)
- 26. A.P. Sergeeva, A.I. Boldyrev, Organometallics 29, 3951 (2010)
- 27. T.R. Galeev, A.I. Boldyrev, Phys. Chem. Chem. Phys. **13**, 20549 (2011)
- 28. M. Houssa, G. Pourtois, V.V. Afanas'ev, A. Stesmans, Appl. Phys. Lett. 97, 112106 (2010)
- 29. M. Ezawa, New J. Phys. **14**, 033003 (2012)
- 30. D. Jose, A. Datta, Phys. Chem. Chem. Phys. 13, 7304 (2011)
- 31. Z. Slanina, Chem. Phys. Lett. **161**, 175 (1989)
- 32. C. Gerdes, T. Müller, Angew. Chem. Int. Ed. 49, 4860 (2010)
- 33. T. Szilvási, T. Veszprémi, Organometallics 31, 3207 (2012)
- 34. R.G. Pearson, Proc. Natl. Acad. Sci. **72**, 2104 (1975)
- 35. J.C. Ma, D.A. Dougherty, Chem. Rev. 97, 1303 (1997)
- 36. D.A. Dougherty, Science 271, 163 (1996)

- C.A. Hunter, C.M.R. Low, C. Rotger, J.G. Vinter, C. Zonta, Proc. Natl. Acad. Sci. 99, 4873 (2002)
- 38. S.E. Wheeler, K.N. Houk, J. Am. Chem. Soc. 131, 3126 (2009)
- 39. S. Mecozzi, A.P. West, D.A. Dougherty, J. Am. Chem. Soc. 118, 2307 (1996)
- 40. S. Tsuzuki, M. Yoshida, T. Uchimaru, M. Mikami, J. Phys. Chem. A 105, 769 (2001)
- 41. A.D. Zdetsis, J. Chem. Phys. **127**, 214306 (2007)
- 42. S.A. Abraham, D. Jose, A. Datta, ChemPhysChem **13**, 695 (2012)
- 43. G.R. Hutchison, M.A. Ratner, T.J. Marks, J. Am. Chem. Soc. 127, 2339 (2005)
- 44. J.-L. Brédas, D. Beljonne, V. Coropceanu, J. Cornil, Chem. Rev. 104, 4971 (2004)
- 45. O. Marra, C. William, Handbook of Semiconductor Silicon Technology (1990)
- 46. S.F. Boys, F. Bernardi, Mol. Phys. 19, 553 (1970)
- 47. J. Huang, M. Kertesz, J. Chem. Phys. 122, 234707 (2005)
- 48. A. Datta, S. Mohakud, S.K. Pati, J. Mater. Chem. 17, 1933 (2007)
- 49. A. Datta, S. Mohakud, S.K. Pati, J. Chem. Phys. 126, 144710 (2007)
- D.C. Elias, R.R. Nair, T.M.G. Mohiuddin, S.V. Morozov, P. Blake, M.P. Halsall, A.C. Ferrari,
   D.W. Boukhvalov, M.I. Katsnelson, A.K. Geim, K.S. Novoselov, Science 323, 610 (2009)
- 51. J.O. Sofo, A.S. Chaudhari, G.D. Barber, Phys. Rev. B **75**, 153401 (2007)
- 52. M. Hu, X. Zhang, D. Poulikakos, Phys. Rev. B 87, 195417 (2013)
- 53. J. Lan, D. Cheng, D. Cao, W. Wang, J. Phys. Chem. C 112, 5598 (2008)
- 54. J.P. Lowe, K.A. Peterson, Quantum Chemistry, 3rd edn. (Elsevier, USA, 2006)
- A.C. Ferrari, J.C. Meyer, V. Scardaci, C. Casiraghi, M. Lazzeri, F. Mauri, S. Piscanec, D. Jiang, K.S. Novoselov, S. Roth, A.K. Geim, Phys. Rev. Lett. 97, 187401 (2006)
- 56. A.C. Ferrari, Solid State Commun. 143, 47 (2007)
- E. Scalise, M. Houssa, G. Pourtois, B. Broek, V. Afanas'ev, A. Stesmans, Nano Res. 6, 19 (2013)
- E. Cinquanta, E. Scalise, D. Chiappe, C. Grazianetti, B.V.D. Broek, M. Houssa, M. Fanciulli,
   A. Molle, arXiv:1212.5422 [cond-mat.mes-hall]
- 59. D. Jose, A. Nijamudheen, A. Datta, Phys. Chem. Chem. Phys. 15, 8700 (2013)
- 60. P.J. Hay, W.R. Wadt, J. Chem. Phys. 82, 299 (1985)
- 61. L.E. Roy, P.J. Hay, R.L. Martin, J. Chem. Theory Comput. 4, 1029 (2008)
- 62. A.W. Ehlers, M. Böhme, S. Dapprich, A. Gobbi, A. Höllwarth, V. Jonas, K.F. Köhler, R. Stegmann, A. Veldkamp, G. Frenking, Chem. Phys. Lett. **208**, 111 (1993)
- 63. D. Feller, J. Comput. Chem. 17, 1571 (1996)
- K.L. Schuchardt, B.T. Didier, T. Elsethagen, L. Sun, V. Gurumoorthi, J. Chase, J. Li, T.L. Windus, J. Chem. Inf. Model. 47, 1045 (2007)
- 65. M. Moskovits, Rev. Mod. Phys. 57, 783 (1985)
- 66. K. Kneipp, H. Kneipp, I. Itzkan, R.R. Dasari, M.S. Feld, Chem. Rev. 99, 2957 (1999)
- 67. S.E.J. Bell, N.M.S. Sirimuthu, Chem. Soc. Rev. **37**, 1012 (2008)
- 68. R.M. Stöckle, Y.D. Suh, V. Deckert, R. Zenobi, Chem. Phys. Lett. 318, 131 (2000)
- 69. E. Bailo, V. Deckert, Chem. Soc. Rev. 37, 921 (2008)

# Chapter 2 Density-Functional and Tight-Binding Theory of Silicene and Silicane



V. Zólyomi, N. D. Drummond, J. R. Wallbank and V. I. Fal'ko

Abstract A combination of density functional theory and a tight-binding model offers a robust means to describe the structure, vibrations, and electronic states of silicene. In this chapter we give an overview of the electronic structure and phonon dispersions of silicene and its fully hydrogenated derivative, silicane. We discuss the dynamical stability of the buckled silicene and silicane lattices and we present their phonon dispersions. We discuss the first-principles electronic band structure of ideal, free-standing silicene, paying particular attention to the small band gap opened by spin—orbit coupling, which renders the material a topological insulator. We look at the tight-binding description of silicene and examine the effects of an external electric field which, above a critical electric field, counters the spin—orbit gap and triggers a phase transition into a band-insulator state in which the band gap is linearly tunable by the electric field. We also present the tight-binding description of silicane which, parameterised by density functional theory, sheds light on the importance of long-range hopping in this material.

#### 2.1 Introduction

Two-dimensional (2D) crystals exist in a broad variety of forms, perhaps the simplest of which is graphene [1, 2]. Forming an atomically thin honeycomb lattice with two atoms in its unit cell, it is a high-symmetry 2D crystal with versatile physical properties. The next simplest 2D crystal comes to us in the form of the silicon equivalent of graphene: *silicene* [3, 4]. The difference in structure between graphene

V. Zólyomi · J. R. Wallbank · V. I. Fal'ko (⊠)

National Graphene Institute, University of Manchester, Booth Street East,

Manchester M13 9PL, UK

e-mail: vladimir.falko@manchester.ac.uk

N. D. Drummond

Physics Department, Lancaster University, Lancaster LA1 4YB, UK

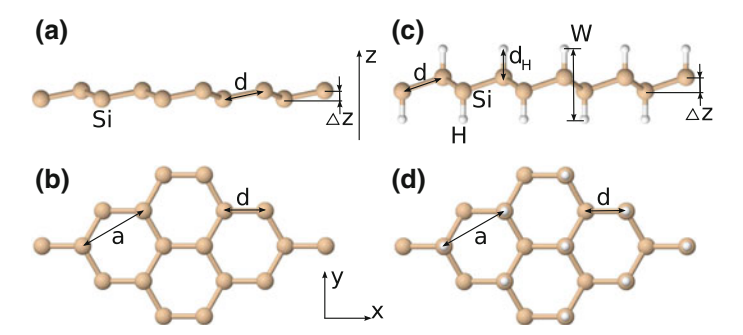


Fig. 2.1 Atomic structure of silicene (a side view, b top view) and silicane (c side view, d top view). The key structural parameters are marked in the figure: a is the lattice parameter, d is the Si–Si bond length,  $\Delta z$  is the sublattice buckling,  $d_{\rm H}$  is the Si–H bond length, and W is the width of the silicane sheet. The structural parameters are summarised in Table 2.1

and silicene takes the form of a sublattice buckling, illustrated in Fig. 2.1. The *A* and *B* sublattices of the crystal do not lie in the same plane. For this reason, silicene has reduced symmetry in comparison to graphene, which has important consequences for its physical properties.

Silicene does not occur in nature, but monolayers have been synthesised on Ag(111) surfaces [5–13]. Due to the similarity of the lattice structures, the band structure of silicene resembles that of graphene, featuring Dirac-type electron dispersion in the vicinity of the corners of its hexagonal Brillouin zone (BZ) [14]. Moreover, silicene has been shown theoretically to be metastable as a free-standing 2D crystal [3, 4], implying that it is possible to transfer silicene onto an insulating substrate and gate it electrically. Recently, a silicene field-effect transistor was fabricated by capping the silicene with  $Al_2O_3$  before transferring it off the Ag(111) surface on which it was grown [13].

The similarity between graphene and silicene arises from the fact that C and Si belong to the same group in the periodic table of elements. However, Si has a larger ionic radius, which promotes  $sp^3$  hybridisation, whereas  $sp^2$  hybridisation is energetically more favourable in C. As a result, in a 2D layer of Si atoms, the bonding is formed by mixed  $sp^2$  and  $sp^3$  hybridisation. Hence silicene is slightly buckled, with one of the two sublattices of the honeycomb lattice being displaced vertically with respect to the other, as shown in Fig. 2.1. Such buckling creates new possibilities for manipulating the dispersion of electrons in silicene and opening an electrically controlled sublattice-asymmetry band gap [15]. In fact, by applying an external electric field to silicene it becomes a semiconductor with a tunable band gap  $\Delta$  that can reach tens of meV before the 2D crystal loses structural stability [4]. But even at zero electric field, silicene is a gapped material, due to the Kane–Mele spin–orbit (SO) coupling [16] for electrons on a honeycomb lattice, which opens a small SO-gap at the Brillouin zone corner and renders the material a topological insulator [17, 18].

The ability to open a band gap in silicene highlights one of the limitations in the practical applicability of monolayer graphene, namely that it has no band gap. Due to the lack of a sub-lattice buckling, the SO-gap in graphene is negligible, and no gap appears upon the application of an electric field, either. Hence plenty of research has gone into insulating and semiconducting 2D crystals, such as boron nitride [19, 20], transition metal dichalcogenides [21–31], and III–VI chalcogenides [32–35].

Yet band-gap engineering in graphene has also been shown to be possible by chemical means, as complete hydrogenation turns graphene into a gapped material. The resulting material, graphane [36]  $(C_2H_2)$  has a buckled honeycomb structure with a single hydrogen atom attached to each carbon site on alternating sides of the sheet. Experiment [37] has shown that few-layer germanane  $(Ge_2H_2)$ , hydrogenated germanene, can be synthesised, expanding the family of atomic 2D materials. It is expected that silicane will be stable as well. Density functional theory (DFT) predicts that not only is silicane stable, but it exhibits a sizable indirect band gap and a strongly anisotropic conduction-band edge, which is a consequence of long-range hopping interactions within the crystal [38].

In this chapter we overview the properties of silicene and silicane as revealed by DFT and a tight-binding model, highlighting the tunable band gap of silicene in an external electric field.

# 2.2 First-Principles Theory of Silicene and Silicane

# 2.2.1 Structure, Stability, and Electronic Band Structure of Silicene

In the optimal structure of silicene the z-coordinates of the two Si atoms in the unit cell (the A and B sublattices) differ by a finite distance  $\Delta z$ , shown in Fig. 2.1 and Table 2.1. This metastable lattice is the same as the "low-buckled" structure found by Cahangirov et al. [3]. The parameters were obtained as follows.

First-principles DFT was employed to calculate the optimal structure of free-standing silicene, using the CASTEP [39, 40] and VASP [41] plane-wave-basis codes,

<b>Table 2.1</b> Structural parameters of silicene and silicane (see Fig. 2.1) in Å units according to density							
functional theory are summarised below. The local density approximation (LDA) and Perdew-							
Burke-Ernzerhof (PBE) exchange-correlation functionals are used							
Crystal	Method	a	d	$\Delta z$	$d_{ m H}$	W	

Crystal	Method	a	d	$\Delta z$	$d_{ m H}$	W
Silicene	LDA	3.83	2.21	0.44		
Silicene	PBE	3.87	2.23	0.45		
Silicane	LDA	3.78	2.31	0.74	1.51	3.76
Silicane	PBE	3.84	2.34	0.74	1.51	3.76

**Table 2.2** Silicene structural and electronic parameters: lattice constant a, sublattice buckling  $\Delta z$  (the difference between the z coordinates of the A and B sublattices), and Fermi velocity v

Method	a (Å)	Δz (Å)	$v (10^5 \text{ ms}^{-1})$
PBE (CASTEP)	3.86	0.45	5.27
PBE (VASP)	3.87	0.45	5.31
PBE [15]	3.87	0.46	
LDA (CASTEP)	3.82	0.44	5.34
LDA (VASP)	3.83	0.44	5.38
LDA [3]	3.83	0.44	≈10
LDA [47]	3.86	0.44	
HSE06 (VASP)	3.85	0.36	6.75

employing ultrasoft pseudopotentials and the projector-augmented-wave (PAW) method, respectively. For the exchange-correlation functional the local density approximation (LDA), the Perdew–Burke–Ernzerhof (PBE) generalised gradient approximation [42], and the screened Heyd–Scuseria–Ernzerhof 06 (HSE06) hybrid functionals were used [43, 44].

All plane-wave DFT total energies were corrected for finite-basis error [45] and it was verified that the residual dependence of the total energy on the plane-wave cutoff energy is negligible. Ultrasoft pseudopotentials were used throughout, except where otherwise stated. The silicene system was made artificially periodic in the z direction (normal to the silicene layer). The atomic structure was obtained by relaxing the lattice parameter and atom positions within DFT.

To evaluate the Fermi velocity shown in Table 2.2 the DFT band structure was calculated using a  $53 \times 53$  **k**-point grid and a plane-wave cutoff energy of 816 eV in a cell of length  $L_z=26.46$  Å. Then Eq. (17) of [46] was fitted to the highest occupied and lowest unoccupied bands within a circular region around the K point; the Fermi velocity is one of the fitting parameters. The radius of the circular region was 6% of the length of the reciprocal lattice vectors; the Fermi velocity was converged with respect to this radius.

The experimental measurement of the structural properties of silicene is invariably affected by the Ag(111) substrate on which the silicene is grown. A detailed discussion of theoretically and experimentally determined structural properties of silicene on various substrates can be found in [48].

By calculating the DFT phonon dispersion it has been verified [3, 4] that free-standing monolayer silicene is dynamically stable: no imaginary frequencies appear anywhere in the BZ. The results of such an analysis are summarised in Fig. 2.2. This stability proves that, as a metastable 2D crystal, silicene can be transferred onto an insulating substrate, where its electronic properties can be studied and manipulated.

The geometry optimisation and band-structure calculations were performed with both the CASTEP [39, 40] and VASP [41] codes, to verify that the results are in good agreement. The PAW method [49] was used in the VASP calculations, whereas ultrasoft pseudopotentials were used in the CASTEP calculations. As can be seen in

Fig. 2.2 DFT-PBE phonon dispersion curves for silicene in zero external field and at an external transverse electric field of  $E_z=0.51$  VÅ $^{-1}$ . In both cases the calculations were performed using the method of finite displacements, with the atomic displacements being 0.0423 Å, in a supercell consisting of  $3\times3$  primitive cells with a  $20\times20$  **k**-point grid in the primitive cell

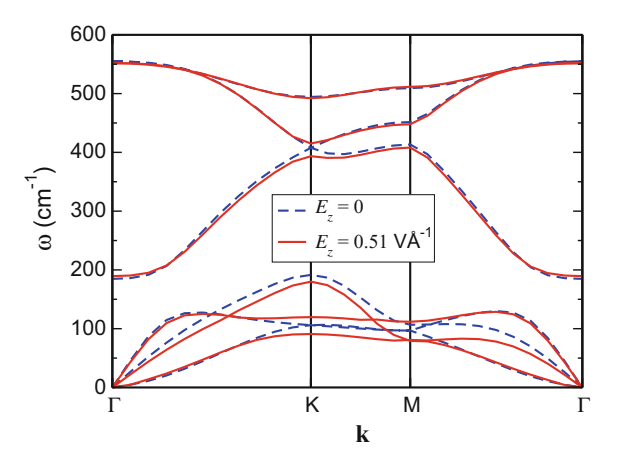


Table 2.2, the geometries predicted by the two codes agree well, and it was verified that the phonon dispersions obtained with the two codes are virtually identical when the same parameters are used. It was also verified that the phonon dispersion curves are converged with respect to supercell size.

The calculated electronic band structure of a "free" silicene layer is shown in Fig. 2.3. As expected, it resembles the band structure of graphene; in particular it shows the linear Dirac-type dispersion of electrons near the K points, where the Fermi level in undoped silicene is found.

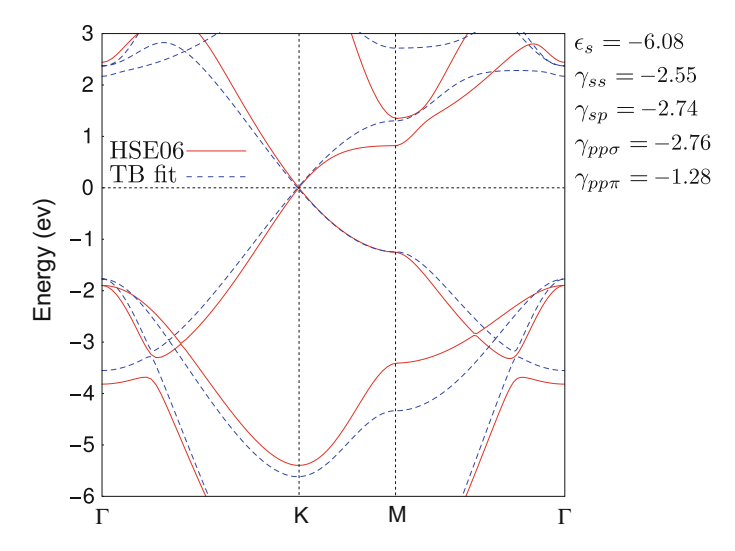


Fig. 2.3 HSE06 band structure of freestanding silicene compared to a tight-binding fit as described in the text. Tight-binding model parameters are listed on the right hand side

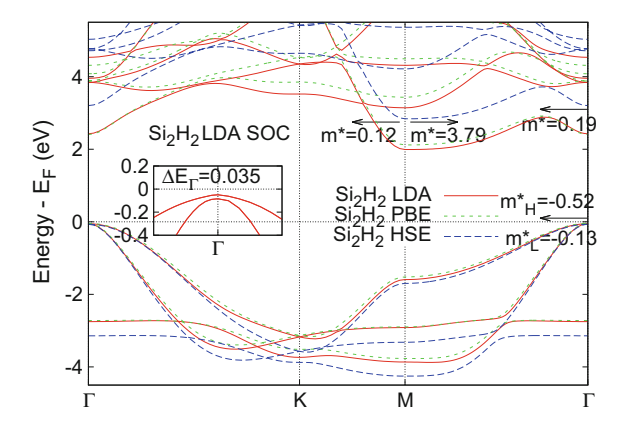


Fig. 2.4 Band structure of silicane. The zero of energy is taken to be the Fermi level and the top of the valence band is marked with a horizontal line. The effect of SO coupling at the  $\Gamma$  point is illustrated in the inset. Effective masses (in units of electron mass) in the HSE06 calculations are provided in the conduction band at M and  $\Gamma$ , and in the valence band at  $\Gamma$  (where the H and L subscript refers to the heavy and light effective mass). There is almost no sign of anisotropy in the effective masses at  $\Gamma$ . In comparison to the literature on graphene, an LDA study found a small anisotropy in both the valence and conduction band of graphane [58], while an earlier generalised gradient approximation study makes no mention of any such anisotropy [56]

# 2.2.2 Structure, Stability, and Electronic Band Structure of Silicane

To obtain the optimal crystal structure, the phonon dispersions, and the electronic band structure of silicane, the VASP [41] plane-wave-basis code was used and the plane-wave cutoff energy was set to 500 eV. A  $12 \times 12$  Monkhorst–Pack **k**-point grid was used for geometry optimisations while a  $24 \times 24$  grid was used to calculate the band structures. The vertical separation of periodic images of the monolayer was set to 15 Å. The force tolerance in the optimisation was 0.005 eV/Å. Phonons were calculated with the force-constant approach in a  $3 \times 3$  supercell. For an estimate of the band gap, the HSE06 exact-exchange functional was used.

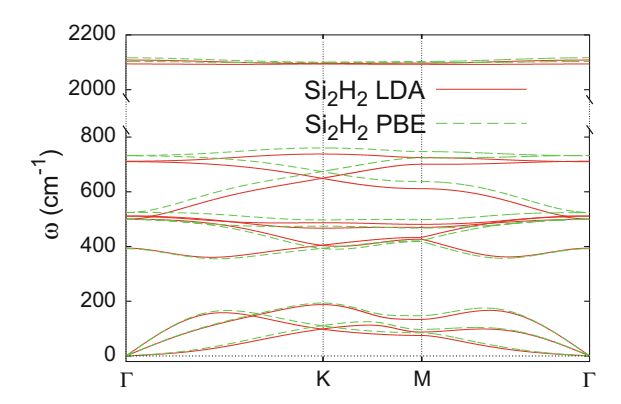
The relaxed structure of silicane [38] is very similar to that of graphane, as illustrated in Fig. 2.1. The bond lengths (see Table 2.1) obtained with the PBE functional are systematically larger than those optimised with the LDA, as expected [50]. Note that the hydrogenation is accompanied by a significant increase in the magnitude of the sublattice buckling when compared to silicene. Lattice constants and sublattice bucklings agree with previous literature to within  $\pm 5\%$  and  $\pm 10\%$ , respectively [51–55].

The calculated electronic band structures are plotted in Fig. 2.4. One important difference between graphane [56] and silicane is that in the latter material a band appears close to the conduction-band edge at the M point. In fact the conduction-band minimum of silicane is at the M point, making silicane an indirect-gap semiconductor.

r Hr B B Hr					
	$\Gamma$	M			
Silicane val.	$0.23(p_x^{Si} + p_y^{Si})$	$0.05p_x^{Si} + 0.16p_y^{Si}$			
Silicane cond.	$0.09s^{Si} + 0.05p_z^{Si} + 0.03s^{H}$	$0.07s^{Si} + 0.01p_x^{Si}$			
		$+0.01p_{y}^{Si}+0.03p_{z}^{Si}$			

**Table 2.3** Orbital decomposition of the valence and conduction bands of silicane at the  $\Gamma$  and M points according to the local density approximation

**Fig. 2.5** Phonon dispersion of silicane



The band gap of silicane is 2.91 eV according to the HSE06 functional, which is expected to underestimate the gap by no more than 10% [57]. Note that the conduction band is anisotropic at the M point with a heavy effective mass in the  $M-\Gamma$  direction. The finding that the band gap of silicane is indirect is supported by a variety of methods ranging from semilocal DFT through hybrid functionals to single-shot GW [51, 52, 54, 55].

Now we discuss the orbital composition of the valence and conduction bands of silicane (see Table 2.3). At the  $\Gamma$  point the valence band consists of Si  $p_x$  and  $p_y$  orbitals, while the conduction band is predominantly Si s and  $p_z$ . However, at the M point the conduction band also contains Si  $p_x$  and  $p_y$  contributions. The H s orbital also contributes to the valence band in silicane at the M point. This means that for a tight-binding description of silicane an all-valence description is required taking into account the s,  $p_x$ ,  $p_y$ , and  $p_z$  orbitals of Si, as well as the H s orbital. This is a direct consequence of the sublattice buckling; an all-valence model is already needed for the description of the silicene lattice (excluding the H orbitals, naturally) [63].

While a full geometry optimisation of silicane yields an energetically stable configuration, it is necessary to examine its phonon dispersion in order to ascertain whether that configuration is dynamically stable. The phonon dispersion reveals that silicane is stable as there is no sign of any dynamical instability anywhere along the high-symmetry lines of the Brillouin zone (see Fig. 2.5).

The so-called chair-like structure shown in Fig. 2.1 corresponds to the case when H atoms alternate on the two sides of the sheet such that for each sublattice the H atom is on a fixed side. In the so-called boat configuration, which is not considered

here, the H atoms alternate in pairs instead, which slightly increases the unit cell size. The latter has been shown to be notably less stable than the chair configuration in the case of graphane [56]; nevertheless the boat configuration of silicane has been found to be stable [52].

### 2.3 Tight-Binding Description of Silicene and Silicane

## 2.3.1 All-Valence Tight-Binding Model of Silicene

The unit cell of silicene comprises two Si atoms in a honeycomb lattice, and the A and B sublattices of Si atoms exhibit a buckling. The minimum tight-binding model required to describe the band structure in the entire Brillouin zone is an all-valence nearest-neighbour model that takes into account four orbitals per Si atom (one s and three p orbitals). The tight-binding Hamiltonian is

$$H = H_0 + H_1, (2.1)$$

where

$$H_{0} = \sum_{i} \left[ \varepsilon_{s} a_{i}^{+} a_{i} + \varepsilon_{p} \sum_{\alpha} \left( b_{i\alpha}^{+} b_{i\alpha} \right) \right]$$

$$H_{1} = \gamma_{ss} a_{A}^{+} a_{B} + \sum_{\alpha} \left\{ \gamma_{sp} v_{\alpha}^{AB} a_{A}^{+} b_{B\alpha} + \gamma_{pp\sigma} \left( v_{\alpha}^{AB} \right)^{2} b_{A\alpha}^{+} b_{B\alpha} + \gamma_{pp\pi} \left[ 1 - \left( v_{\alpha}^{AB} \right)^{2} \right] b_{A\alpha}^{+} b_{B\alpha} \right\}$$

$$+ \sum_{\alpha \neq \beta} \left( \gamma_{pp\sigma} v_{\alpha}^{AB} v_{\beta}^{AB} b_{A\alpha}^{+} b_{B\beta} - \gamma_{pp\pi} v_{\alpha}^{AB} v_{\beta}^{AB} b_{A\alpha}^{+} b_{B\beta} \right) + h.c. \qquad (2.2)$$

Here,  $a^+$  and a are the creation and annihilation operators of the s electrons of Si,  $b^+$  and b are the same for the p electrons of Si. In  $H_0$ , parameters  $\varepsilon_s$  and  $\varepsilon_p$  are the on-site energies of the s and p orbitals of Si. In  $H_1$ ,  $\gamma_{ss}$ ,  $\gamma_{sp}$ ,  $\gamma_{pp\sigma}$ , and  $\gamma_{pp\pi}$  are the nearest-neighbour hoppings between Si electrons on sublattice A and sublattice B. Summations in i go over the A and B sublattices while summations in  $\alpha$  and  $\beta$  go over x, y, and z.  $v_{\alpha}^{AB}$ ,  $v_{\alpha}^{AA'}$ , and  $v_{\alpha}^{AB'}$  take into account the orientation of the p orbitals, where  $\mathbf{R}$  denotes the coordinates of the atoms. The Hamiltonian in the Slater–Koster approach [59], shown with solid lines separating the A and B sublattice contributions, has the form of an  $8 \times 8$  matrix:

$$\begin{pmatrix} \varepsilon_{s} & & & H_{ss} & H_{sy} & H_{sz} \\ & \varepsilon_{p} & & H_{sx} & H_{xx} & H_{xy} & H_{xz} \\ & & \varepsilon_{p} & & H_{sx} & H_{xx} & H_{xy} & H_{xz} \\ & & & \varepsilon_{p} & H_{sy} & H_{xy} & H_{yz} \\ \hline H_{ss}^{*} & H_{sx}^{*} & H_{sy}^{*} & H_{sz}^{*} & \varepsilon_{s} \\ & & & H_{ss}^{*} & H_{xx}^{*} & H_{xy}^{*} & H_{xz}^{*} \\ H_{sy}^{*} & H_{xy}^{*} & H_{yy}^{*} & H_{yz}^{*} \\ H_{sy}^{*} & H_{xy}^{*} & H_{yy}^{*} & H_{zz}^{*} \\ H_{sz}^{*} & H_{xz}^{*} & H_{yz}^{*} & H_{zz}^{*} \\ \end{bmatrix},$$

$$(2.3)$$

where

$$H_{ss} = \gamma_{ss} \sum_{R} e^{i\mathbf{k} \cdot (\mathbf{R}_{Si}^{\mathbf{A}} - \mathbf{R}_{Si}^{\mathbf{B}})}, \tag{2.4}$$

$$\begin{split} H_{s\alpha} &= \gamma_{sp} \sum_{B} v_{\alpha}^{AB} e^{i\mathbf{k}\cdot(\mathbf{R}_{Si}^{\mathbf{A}} - \mathbf{R}_{Si}^{\mathbf{B}})}, \\ H_{\alpha\alpha} &= \gamma_{pp\sigma} \sum_{B} (v_{\alpha}^{AB})^{2} e^{i\mathbf{k}\cdot(\mathbf{R}_{Si}^{\mathbf{A}} - \mathbf{R}_{Si}^{\mathbf{B}})} + \gamma_{pp\pi} \sum_{B} \left[1 - (v_{\alpha}^{AB})^{2}\right] e^{i\mathbf{k}\cdot(\mathbf{R}_{Si}^{\mathbf{A}} - \mathbf{R}_{Si}^{\mathbf{B}})}, \\ H_{\alpha\beta} &= \gamma_{pp\sigma} \sum_{B} v_{\alpha}^{AB} v_{\beta}^{AB} e^{i\mathbf{k}\cdot(\mathbf{R}_{Si}^{\mathbf{A}} - \mathbf{R}_{Si}^{\mathbf{B}})} \\ &- \gamma_{pp\pi} \sum_{B} v_{\alpha}^{AB} v_{\beta}^{AB} e^{i\mathbf{k}\cdot(\mathbf{R}_{Si}^{\mathbf{A}} - \mathbf{R}_{Si}^{\mathbf{B}})} \text{for } \alpha \neq \beta. \end{split} \tag{2.5}$$

The total number of parameters in this model is six, but one can choose one of the on-site energies to be zero to set the Fermi level, leaving five parameters to fit. The resulting model can be used to provide a simple, semiempirical reproduction of first-principles band structures.

After fitting the model to the HSE06 band structure of silicene, the following values are obtained for the parameters:  $\varepsilon_s = -6.08 \, \mathrm{eV}$ ,  $\gamma_{ss} = -2.55 \, \mathrm{eV}$ ,  $\gamma_{sp} = -2.74 \, \mathrm{eV}$ ,  $\gamma_{pp\sigma} = -2.76 \, \mathrm{eV}$ , and  $\gamma_{pp\pi} = -1.28 \, \mathrm{eV}$ .

# 2.3.2 All-Valence Tight-Binding Model of Silicane

Silicane has a honeycomb lattice as depicted in Fig. 2.1. The unit cell comprises two Si atoms and two H atoms, and the A and B sublattices of Si atoms exhibit a buckling. The minimum tight-binding model needed to describe the band structure in the entire Brillouin zone is an all-valence second-nearest-neighbour model that takes into account four orbitals per Si atom (one s and three p orbitals) and the s orbital of hydrogen. The tight-binding Hamiltonian is

$$H = H_{0} + H_{1} + H_{2}$$

$$H_{0} = \sum_{i} (\varepsilon_{s}a_{i}^{+}a_{i} + \varepsilon_{p} \sum_{\alpha} (b_{i\alpha}^{+}b_{i\alpha}) + \varepsilon_{s}Hc_{i}^{+}c_{i})$$

$$H_{1} = \sum_{i} (\gamma_{s}H_{s}c_{i}^{+}a_{i}) + \gamma_{ss}a_{A}^{+}a_{B} + \sum_{\alpha} (\gamma_{sp}v_{\alpha}^{AB}a_{A}^{+}b_{B\alpha} + \gamma_{pp\sigma}(v_{\alpha}^{AB})^{2}b_{A\alpha}^{+}b_{B\alpha} + \gamma_{pp\pi}(1 - (v_{\alpha}^{AB})^{2})b_{A\alpha}^{+}b_{B\alpha}) + \sum_{\alpha \neq \beta} (\gamma_{pp\sigma}v_{\alpha}^{AB}v_{\beta}^{AB}b_{A\alpha}^{+}b_{B\beta} - \gamma_{pp\pi}v_{\alpha}^{AB}v_{\beta}^{AB}b_{A\alpha}^{+}b_{B\beta}) + \sum_{\alpha \neq \beta} \gamma_{s}H_{p}v_{\alpha}^{AB}c_{A}^{+}b_{B\alpha} + h.c.$$

$$H_{2} = \sum_{i} (\gamma_{ss}'a_{i}^{+}a_{i'} + \sum_{\alpha} (\gamma_{sp}'v_{\alpha}^{AA'}a_{i}^{+}b_{i'\alpha} + \gamma_{pp\sigma}'(v_{\alpha}^{AA'})^{2}b_{A\alpha}^{+}b_{A'\alpha} + \gamma_{pp\pi}'(1 - (v_{\alpha}^{AA'})^{2})b_{A\alpha}^{+}b_{A'\alpha}) + \sum_{\alpha \neq \beta} (\gamma_{pp\sigma}'v_{\alpha}^{AA'}v_{\beta}^{AA'}b_{A\alpha}^{+}b_{A'\beta} - \gamma_{pp\pi}'v_{\alpha}^{AA'}v_{\beta}^{AA'}b_{A\alpha}^{+}b_{A'\beta}) + \gamma_{s}H_{s}c_{\alpha}^{+}a_{B} + \sum_{\alpha} \gamma_{s}H_{p}v_{\alpha}^{AB'}c_{A}^{+}b_{B\alpha} + h.c.$$

$$v_{\alpha}^{AB} = (\mathbf{R}_{Si}^{A} - \mathbf{R}_{Si}^{B})_{\alpha}/|\mathbf{R}_{Si}^{A} - \mathbf{R}_{Si}^{B}|$$

$$v_{\alpha}^{AA'} = (\mathbf{R}_{Si}^{A} - \mathbf{R}_{Si}^{B})_{\alpha}/|\mathbf{R}_{Si}^{A} - \mathbf{R}_{Si}^{B}|$$

$$v_{\alpha}^{AB'} = (\mathbf{R}_{Si}^{A} - \mathbf{R}_{Si}^{B})_{\alpha}/|\mathbf{R}_{Si}^{A} - \mathbf{R}_{Si}^{A'}|$$

$$\begin{pmatrix} H_{ss}' & H_{sx}' & H_{sy}' & H_{sz}' & H_{ss} & H_{sx} & H_{sy} & H_{sz} & H_{s^{H}s} & H_{s^{H}s}' \\ H_{sx}' & H_{xx}' & H_{xy}' & H_{xz}' & H_{sx} & H_{xx} & H_{xy} & H_{xz} & H_{s^{H}s} \\ H_{sy}' & H_{xy}' & H_{yy}' & H_{yz}' & H_{sy} & H_{xy} & H_{yy} & H_{yz} \\ H_{sz}' & H_{xy}' & H_{yz}' & H_{zz}' & H_{sy} & H_{xy} & H_{yy} & H_{yz} \\ H_{sz}' & H_{xz}' & H_{yz}' & H_{z}' & H_{sz} & H_{xz} & H_{yz} & H_{zz} & H_{s^{H}p} & H_{s^{H}z}' \\ H_{ss}' & H_{sx}' & H_{sy}' & H_{sz}' & H_{ss}' & H_{sx}' & H_{sy}' & H_{sz}' & H_{s^{H}s}' & H_{s^{H}s}' \\ H_{sx}' & H_{xx}' & H_{xy}' & H_{xz}' & H_{sx}' & H_{xy}' & H_{xz}' & H_{s^{H}s}' & H_{s^{H}s}' \\ H_{sy}' & H_{xz}' & H_{yz}' & H_{zz}' & H_{sx}' & H_{xy}' & H_{yy}' & H_{zz}' & H_{s^{H}z}' & H_{s^{H}p}' \\ H_{sx}' & H_{xx}' & H_{sy}' & H_{sx}' & H_{sx}' & H_{sx}' & H_{sx}' & H_{s^{H}z}' & H_{s^{H}s}' \\ H_{sx}' & H_{sx}' \\ H_{sx}' & H_{sx}' \\ H_{sx}' & H_{sx}' \\ H_{sx}' & H_{sx}' \\ H_{sx}' & H_{sx}' & H_{sx}' & H_{sx}' & H_{sx}' & H_{sx}' & H_{sx}' \\ H_{sx}' & H_{sx}' & H_{sx}' & H_{sx}' & H_{sx}' & H_{sx}' & H_{sx}' \\ H_{sx}' & H_{sx}' & H_{sx}' & H_{sx}' & H_{sx}' & H_{sx}' & H_{sx}' \\ H_{sx}' & H_{sx}' & H_{sx}' & H_{sx}' & H_{sx}' & H_{sx}' & H_{sx}' \\ H_{sx}' & H_{sx}' \\ H_{sx}' & H_{sx}' & H_{sx}' & H_{sx}' & H_{sx}' & H_{sx}' & H_{sx}' \\ H_{sx}' & H_{sx}' & H_{sx}' & H_{sx}' & H_{sx}' & H_{sx}' & H_{sx}' \\ H_{sx}' & H_{sx}' \\ H_{sx}' & H_{sx}' \\ H_{sx}' & H_{sx}' \\ H_{sx}' & H_{sx}' \\ H_{sx}' & H_{sx}' & H_{sx}' & H_{s$$

where

$$H_{ss} = \gamma_{ss} \sum_{B} e^{i\mathbf{k}(\mathbf{R}_{Si}^{\mathbf{A}} - \mathbf{R}_{Si}^{\mathbf{B}})}, H_{s^{\mathbf{H}}s} = \gamma_{s^{\mathbf{H}}s}, H_{s^{\mathbf{H}}p} = \gamma_{s^{\mathbf{H}}p}$$

$$H_{s\alpha} = \gamma_{sp} \sum_{B} v_{\alpha}^{AB} e^{i\mathbf{k}(\mathbf{R}_{Si}^{\mathbf{A}} - \mathbf{R}_{Si}^{\mathbf{B}})}, H_{s\alpha}' = \gamma_{sp}' \sum_{A} v_{\alpha}^{AA'} e^{i\mathbf{k}(\mathbf{R}_{Si}^{\mathbf{A}} - \mathbf{R}_{Si}^{\mathbf{A}'})}$$

$$H_{\alpha\alpha} = \gamma_{pp\sigma} \sum_{B} (v_{\alpha}^{AB})^{2} e^{i\mathbf{k}(\mathbf{R}_{Si}^{\mathbf{A}} - \mathbf{R}_{Si}^{\mathbf{B}})} + \gamma_{pp\pi} \sum_{B} (1 - (v_{\alpha}^{AB})^{2}) e^{i\mathbf{k}(\mathbf{R}_{Si}^{\mathbf{A}} - \mathbf{R}_{Si}^{\mathbf{B}})}$$

$$H_{\alpha\beta} = \gamma_{pp\sigma} \sum_{B} v_{\alpha}^{AB} v_{\beta}^{AB} e^{i\mathbf{k}(\mathbf{R}_{Si}^{\mathbf{A}} - \mathbf{R}_{Si}^{\mathbf{B}})} - \gamma_{pp\pi} \sum_{B} v_{\alpha}^{AB} v_{\beta}^{AB} e^{i\mathbf{k}(\mathbf{R}_{Si}^{\mathbf{A}} - \mathbf{R}_{Si}^{\mathbf{B}})}, \alpha \neq \beta$$

$$H_{\alpha\alpha}' = \varepsilon_{p} + \gamma_{pp\sigma}' \sum_{A} (v_{\alpha}^{AA'})^{2} e^{i\mathbf{k}(\mathbf{R}_{Si}^{\mathbf{A}} - \mathbf{R}_{Si}^{\mathbf{A}'})} + \gamma_{pp\pi}' \sum_{A} (1 - (v_{\alpha}^{AA'})^{2}) e^{i\mathbf{k}(\mathbf{R}_{Si}^{\mathbf{A}} - \mathbf{R}_{Si}^{\mathbf{A}'})}$$

$$H_{\alpha\beta}' = \gamma_{pp\sigma}' \sum_{A} v_{\alpha}^{AA'} v_{\beta}^{AA'} e^{i\mathbf{k}(\mathbf{R}_{Si}^{\mathbf{A}} - \mathbf{R}_{Si}^{\mathbf{A}'})} - \gamma_{pp\pi}' \sum_{A} v_{\alpha}^{AA'} v_{\beta}^{AA'} e^{i\mathbf{k}(\mathbf{R}_{Si}^{\mathbf{A}} - \mathbf{R}_{Si}^{\mathbf{A}'})}, \alpha \neq \beta$$

$$H_{s^{\mathbf{H}}s}' = \gamma_{s^{\mathbf{H}}s}' \sum_{B} e^{i\mathbf{k}(\mathbf{R}_{Si}^{\mathbf{A}} - \mathbf{R}_{H}^{\mathbf{B}'})}, H_{s^{\mathbf{H}}s^{\mathbf{H}}}' = \varepsilon_{s}^{\mathbf{H}} + \gamma_{s^{\mathbf{H}}s^{\mathbf{H}}}' \sum_{A} e^{i\mathbf{k}(\mathbf{R}_{Si}^{\mathbf{A}} - \mathbf{R}_{Si}^{\mathbf{A}'})}$$

$$H_{s^{\mathbf{H}}\alpha}' = \gamma_{s^{\mathbf{H}p}}' \sum_{B} v_{\alpha}^{AB'} e^{i\mathbf{k}(\mathbf{R}_{Si}^{\mathbf{A}} - \mathbf{R}_{H}^{\mathbf{B}'})}, H_{ss}' = \varepsilon_{s} + \gamma_{ss}' \sum_{A} e^{i\mathbf{k}(\mathbf{R}_{Si}^{\mathbf{A}} - \mathbf{R}_{Si}^{\mathbf{A}'})}$$

$$(2.8)$$

The total number of parameters in this model is sixteen, but one can choose one of the on-site energies to be zero to set the Fermi level, leaving fifteen parameters to fit. The resulting model can be used to provide a simple semiempirical reproduction of first-principles band structures.

Using the HSE06 band structures as reference, the tight-binding band structure can reproduce the entirety of the DFT valence band and the vicinity of the conduction band at both the  $\Gamma$  and M points (see Fig. 2.6) to within  $\approx$ 1 eV of the band edge. It is important to note here that if second-nearest-neighbour interactions are neglected, the valence band can still be reproduced to within several eV of the band edge, but the behaviour of the conduction band at the M point cannot, which indicates that the second-nearest-neighbour interactions are responsible for the minimum in the

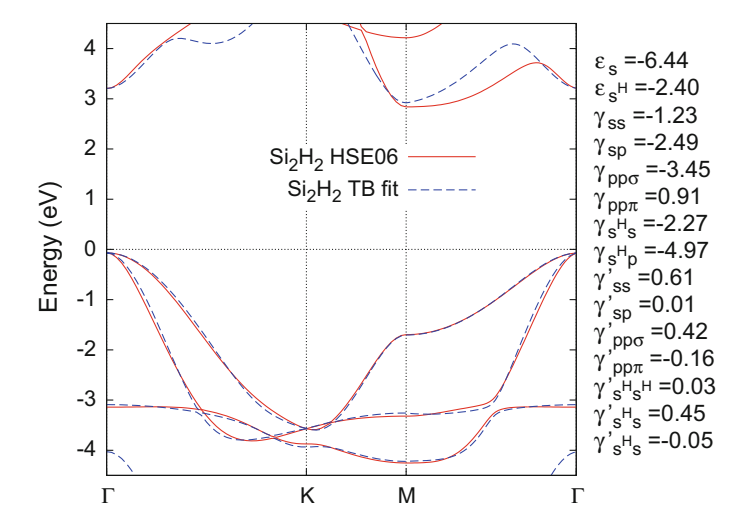


Fig. 2.6 Tight-binding band structure of silicane compared with the HSE06 DFT bands. The parameters of the model are shown in the legend in units of eV. The reference energy level is set by  $\varepsilon_p=0$ 

conduction band at the M point. Also, the d-shell of Si is likely to affect states in the conduction band. The best fit is achieved with the parameters listed in the legend of Fig. 2.6; the fitting was optimised to give a quantitative description of the valence band and the conduction band near the  $\Gamma$  and the M point.

#### 2.4 Silicene in a Transverse External Electric Field

To exploit the weak buckling of silicene, one can apply an external electric field  $E_z$  in the z direction, as shown in Fig. 2.7. The main effect of such an electric field is to break the symmetry between the A and B sublattices of silicene's honeycomb structure and hence to open a gap  $\Delta$  in the band structure at the hexagonal BZ points K and K'. In the framework of a simplified nearest-neighbour tight-binding model, which can be thought of as an expansion of the tight-binding model in Sect. 2.3.1 for small wave vectors around the corner of the Brillouin zone, this manifests itself in the form of an energy correction to the on-site energies that is positive for sublattice A and negative for B. This difference in on-site energies  $\Delta = \mathcal{E}_A - \mathcal{E}_B$  leads to a spectrum with a gap for electrons in the vicinity of the corners of the BZ:  $\mathcal{E}_{\pm} = \pm \sqrt{(\Delta/2)^2 + |v\mathbf{p}|^2}$ , where  $\mathbf{p}$  is the electron "valley" momentum relative to the BZ corner. Opening a gap in graphene by these means would be impossible because the A and B sublattices lie in the same plane.

A naïve estimate of the electric-field-induced gap in silicene can be made using first-order perturbation theory by diagonalising a 2  $\times$  2 Hamiltonian matrix at  $\mathbf{p} \rightarrow \mathbf{0}$ ,

**Fig. 2.7** Sketch of silicene in an external electric field, with an illustration of the charge density for the highest occupied valence band in the vicinity of the *K* point

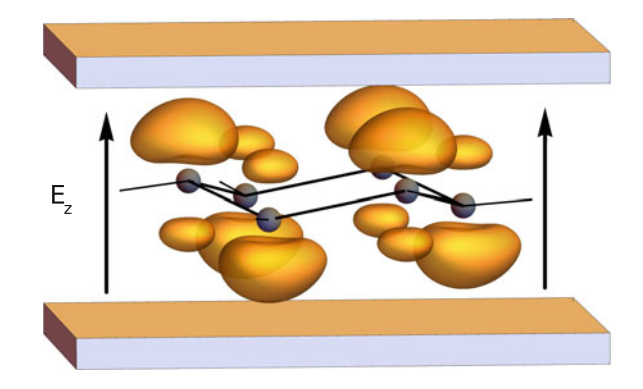
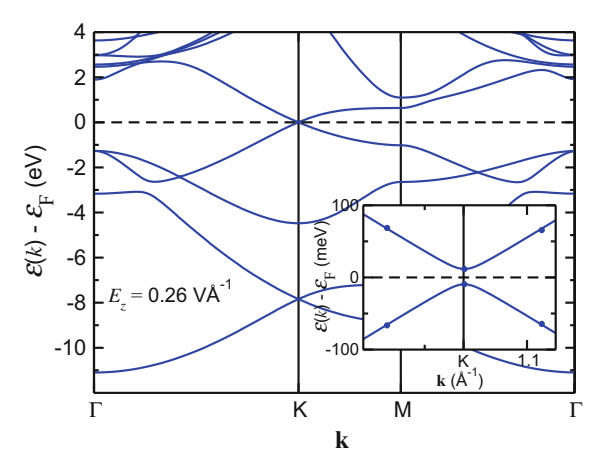


**Fig. 2.8** DFT-PBE band structure for silicene in a cell of length  $L_z=26.5$  Å with a plane-wave cutoff energy of 816 eV and a  $53 \times 53$  **k**-point grid in  $E_z=0.26$  VÅ $^{-1}$  external electric field. The zero of the external potential is in the centre of the silicene layer. The dashed line shows the Fermi energy and the inset shows the spectrum near the Fermi level in the vicinity of the K point



$$\delta \mathcal{H}(E_z) = e E_z \begin{bmatrix} \langle \psi_K^- | z | \psi_K^- \rangle & \langle \psi_K^- | z | \psi_K^+ \rangle \\ \langle \psi_K^+ | z | \psi_K^- \rangle & \langle \psi_K^+ | z | \psi_K^+ \rangle \end{bmatrix}. \tag{2.9}$$

Here,  $\psi_K^{\pm}$  are the degenerate lowest unoccupied and highest occupied Kohn–Sham orbitals at the K point at  $E_z=0$ , and z=0 corresponds to the mid-plane of the buckled lattice. This suggests a band gap which opens linearly with the electric field at a rate  $d\Delta/dE_z=0.554$  and 0.573 eÅ for the wave functions  $\psi_K$  found using the LDA and PBE functionals, respectively.

The estimate is in fact only an upper limit for the rate at which the band gap opens, since it neglects screening by the polarisation of the *A* and *B* sublattices. In order to obtain an accurate value of the rate at which a band gap can be opened with an electric field, fully self-consistent calculations of the DFT band structure in the presence of an electric field must be carried out. A typical result of such a calculation is shown in Fig. 2.8. At small electric fields, relaxing the structure in the presence of the field does not have a significant effect on the band gap, but the screening of the electric potential by the sublattice polarisation of the electron states

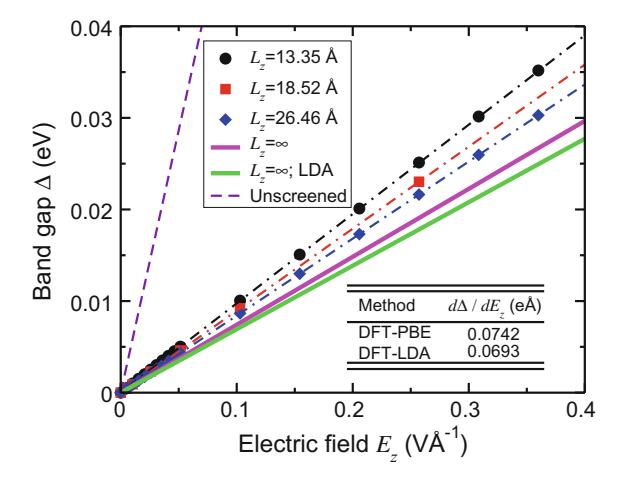


Fig. 2.9 DFT gap against applied electric field  $E_z$  for silicene with a plane-wave cutoff energy of 816 eV and a 53 × 53 k-point grid. Unless otherwise stated, the PBE functional was used. The box length in the z direction was varied from  $L_z=13.35$  Å to 26.46 Å. The results have been extrapolated to the limit  $L_z \to \infty$  of infinite box length (solid lines). Unscreened band gaps calculated using perturbation theory are also shown. The inset table shows the calculated rate at which the band gap opens

makes a substantial difference. The DFT-calculated gaps are gathered in Fig. 2.9. The variation of the band gap  $\Delta$  at K with electric field  $E_z$  is almost perfectly linear for fields up to  $E_z \approx 1 \text{ VÅ}^{-1}$ . The results for the rate  $d\Delta/dE_z$  at which a gap is opened are shown in the table inset in Fig. 2.9. The eightfold difference between the self-consistent and the unscreened values of  $d\Delta/dE_z$  indicates that the system exhibits a strong sublattice polarisability.

Applying a transverse electric field  $E_z$  in a periodic simulation cell results in a sawtooth potential in the out-of-plane (z) direction. This creates a triangular quantum well in the vacuum region between periodic images of the silicene layer. If a plane-wave basis set is used, the formation of a quasi-2D electron gas in this spurious quantum well can in principle be described; however, for the cell lengths used and the electric fields considered in Fig. 2.8, these quantum-well states are unoccupied, as demonstrated by the absence of quadratic bands at  $\Gamma$  in the vicinity of the Fermi energy. Hence at low  $E_z$  the electric-field-induced band gap can be reliably calculated using a plane-wave basis, and a linear dependence of the field-induced gap on  $E_z$  is obtained. It is found that the gap for a given  $E_z$  varies with the length of the cell in the z direction; however, the gap can be extrapolated to infinite layer separation using a series of cell lengths that are sufficiently short that no spurious quantum-well states are found close to the Fermi energy.

Several DFT-PBE calculations of the rate at which the gap opens in the presence of a transverse electric field have been reported. Plane-wave basis DFT-PBE calculations yield a rate of 0.0742 eÅ [4], while localised basis set calculations give values between

0.157 eÅ [15] and  $\approx 0.1$  eÅ [62], which agree to within an order of magnitude. The plane-wave results are illustrated in Fig. 2.8.

It is important to note that the electric field does not simply open a linearly tunable band gap but can also slightly alter the structure, or in extremely large fields it can destabilise it. It was demonstrated [4] by reoptimisation of the geometry in the presence of an electric field that the material is stable in fields up to at least  $E_z \approx 0.4$   $V\rm{\AA}^{-1}$ .

Figure 2.2 demonstrates what happens to the phonon dispersion in the presence of the electric field. The main effects of a small  $E_z$  on the phonon dispersion curve are (i) to lift some degeneracies at K and M and (ii) to soften one of the acoustic branches, but without making the frequency imaginary. Under much higher electric fields, the honeycomb structure of silicene becomes unstable:  $E_z \geq 2.6 \,\mathrm{VÅ}^{-1}$  causes the lattice parameter to increase without bound when the structure is relaxed. In the phonon calculations, the box length was  $L_z = 19.05 \,\mathrm{Å}$  and the plane-wave cutoff energy was 435 eV. This is slightly different from how the phonons were calculated without the presence of an electric field, because the error due to a finite box length  $L_z$  is potentially much larger in the presence of a transverse electric field.

# 2.5 SO Coupling and Topological Phase Transition in Silicene

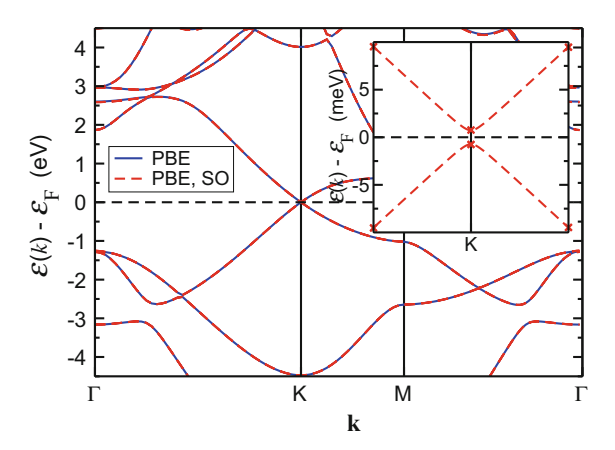
The effects of SO coupling on the band structures of silicene and silicane yield quite different results. In the case of silicane, which is an indirect-gap semiconductor, the effect of SO coupling is limited to splitting some of the bands as shown in the inset in Fig. 2.4. In the case of the semimetal silicene, on the other hand, the effect is much more important, especially when considering the behaviour of the material in an electric field.

# 2.5.1 SO Induced Band Gap in Silicene

The PBE band structure of silicene with SO coupling explicitly included in the Hamiltonian is shown in Fig. 2.10. The functional predicts an SO gap of the order of a few meV at the *K* point, while the rest of the band structure barely differs from the nonrelativistic case, in agreement with the LDA functional. The calculated LDA and PBE SO gaps are 1.4 meV and 1.5 meV, respectively, in agreement with the literature [60].

The SO calculations were performed with a plane-wave cutoff of 500 eV and a  $24 \times 24$  **k**-point grid. The length of the simulation box has negligible influence on the SO gap: the gap is the same with simulation box lengths of 15 and 30 Å up to numerical accuracy.

Fig. 2.10 DFT-PBE and DFT-LDA band structures with and without SO coupling taken into account. The inset shows the bands around the K point, revealing a small band gap induced by SO coupling. The width of the bottom panel corresponds to 1/200 of the  $\Gamma$ -K line



# 2.5.2 Transition from Topological Insulator to Band Insulator State

In the theory of Dirac electrons on the honeycomb lattice, the SO gap is accounted for by the Kane–Mele term describing, e.g., intrinsic SO coupling in graphene [16]. The Kane–Mele SO coupling and the electric-field induced A–B sublattice asymmetry for electrons in the vicinity of the BZ corners  $K_{\pm} = (\pm 4\pi/(3a), 0)$  in silicene can be incorporated in the Hamiltonian

$$H_{K_{\pm}} = v\mathbf{p} \cdot \sigma + \Delta_{\text{SO}} s_z \sigma_z + \frac{1}{2} \xi \Delta_z \sigma_z, \tag{2.10}$$

where  $\xi=\pm 1$  distinguishes between the two valleys,  $K_+$  and  $K_-$ , in silicene's spectrum. Here, the Pauli matrices  $\sigma_x$ ,  $\sigma_y$ , and  $\sigma_z$  act in the space of the electrons' amplitudes on orbitals attributed to the A and B sublattices,  $(\psi_A, \psi_B)$  for the valley at  $K_+$  and  $(\psi_B, -\psi_A)$  for the valley at  $K_-$ . In (2.10),  $s_z$  is the electron spin operator normal to the silicene plane, and  $\Delta_{SO}$  and  $\Delta_z$  are the DFT-calculated SO-coupling and electric-field induced gaps.

The Hamiltonian of (2.10) generically describes the transition between the 2D topological and band-gap insulators. Its spectrum,

$$\mathcal{E}_{\uparrow\pm} = \pm \sqrt{\frac{1}{4} (\Delta_{SO} + \xi \Delta_z)^2 + v^2 p^2},$$

$$\mathcal{E}_{\downarrow\pm} = \pm \sqrt{\frac{1}{4} (\Delta_{SO} - \xi \Delta_z)^2 + v^2 p^2},$$
(2.11)

includes two gapped branches, one with a larger gap  $|\Delta_{SO} + \Delta_z|$  and another with a smaller gap  $|\Delta_{SO} - \Delta_z|$ . At a critical external electric field  $E_z^c \approx 20$  mVÅ<sup>-1</sup>,  $\Delta_{SO} = \Delta_z$ , and the smaller gap closes, marking a transition from a topological

insulator [16–18] at  $\Delta_{SO} > \Delta_z$  to a simple band insulator at  $\Delta_{SO} < \Delta_z$ . The difference between these two states of silicene is that the topological insulator state supports a gapless spectrum of edge states for the electrons, in contrast to a simple insulator, where the existence of gapless edge states is not protected by topology. However, something similar to the topological properties of Dirac electrons may show up even in the band insulator state of silicene: an interface between two differently gated regions, with electric fields  $E_z$  and  $-E_z$  (where  $E_z \gg E_z^c$ ), should support a one-dimensional gapless band with an almost linear dispersion of electrons [61].

# 2.6 Summary

As illustrated in this chapter, silicene and silicane are prime examples of 2D materials with rich physics and great application potential. The topological insulator ground state of silicene and its electric field induced transformation into a band insulator with a tunable band gap certainly warrants future study of this fascinating material, while the indirect semiconductor silicane could potentially see good use in silicon-based semiconductor technology.

#### References

- K.S. Novoselov, A.K. Geim, S.V. Morozov, D. Jiang, Y. Zhang, S.V. Dubonos, I.V. Grigorieva, A.A. Firsov, Science 306, 666 (2004)
- 2. A.K. Geim, K.S. Novoselov, Nat. Mater. 6, 183 (2007)
- 3. S. Cahangirov, M. Topsakal, E. Aktürk, H. Şahin, S. Ciraci, Phys. Rev. Lett. 102, 236804 (2009)
- 4. N.D. Drummond, V. Zólyomi, V.I. Fal'ko, Phys. Rev. B 85, 075423 (2012)
- P. Vogt, P. De Padova, C. Quaresima, J. Avila, E. Frantzeskakis, M.C. Asensio, A. Resta, B. Ealet, G. Le Lay, Phys. Rev. Lett. 108, 155501 (2012)
- B. Feng, Z. Ding, S. Meng, Y. Yao, X. He, P. Cheng, L. Chen, K. Wu, Nano Lett. 12, 3507 (2012)
- L. Chen, C.-C. Liu, B. Feng, X. He, P. Cheng, Z. Ding, S. Meng, Y. Yao, K. Wu, Phys. Rev. Lett. 109, 056804 (2012)
- 8. C.L. Lin, R. Arafune, K. Kawahara, M. Kanno, N. Tsukahara, E. Minamitani, Y. Kim, M. Kawai, N. Takagi, Phys. Rev. Lett. **110**, 076801 (2013)
- L. Chen, H. Li, B. Feng, Z. Ding, J. Qiu, P. Cheng, K. Wu, S. Meng, Phys. Rev. Lett. 110, 085504 (2013)
- P. De Padova, P. Vogt, A. Resta, J. Avila, I. Razado-Colambo, C. Quaresima, C. Ottaviani, B. Olivieri, T. Bruhn, T. Hirahara, T. Shirai, S. Hasegawa, M.C. Asensio, G. Le Lay, Appl. Phys. Lett. 102, 163106 (2013)
- A. Resta, T. Leoni, C. Barth, A. Ranguis, C. Becker, T. Bruhn, P. Vogt, G. Le Lay, Sci. Rep. 3, 2399 (2013)
- 12. A.J. Mannix, B. Kiraly, B.L. Fisher, M.C. Hersam, N.P. Guisinger, ACS Nano 8, 7538 (2014)
- L. Tao, E. Cinquanta, D. Chiappe, C. Grazianetti, M. Fanciulli, M. Dubey, A. Molle, D. Akinwande, Nat. Nanotechnol. 10, 227 (2015)
- 14. P.R. Wallace, Phys. Rev. 71, 622 (1947)
- Z. Ni, Q. Liu, K. Tang, J. Zheng, J. Zhou, R. Qin, Z. Gao, D. Yu, J. Lu, Nano Lett. 12, 113 (2012)

- 16. C.L. Kane, E.J. Mele, Phys. Rev. Lett. 95, 226801 (2005)
- 17. M.Z. Hasan, C.L. Kane, Rev. Mod. Phys. 82, 3045 (2010)
- 18. X.-L. Qi, S.-C. Zhang, Rev. Mod. Phys. 83, 1057 (2011)
- 19. Y. Kubota, K. Watanabe, O. Tsuda, T. Taniguchi, Science 317, 932 (2007)
- M.P. Levendorf, C.-J. Kim, L. Brown, P.Y. Huang, R.W. Havener, D.A. Muller, J. Park, Nature 488, 627 (2012)
- 21. K.F. Mak, C. Lee, J. Hone, J. Shan, T.F. Heinz, Phys. Rev. Lett. 105, 136805 (2010)
- B. Radisavljevic, A. Radenovic, J. Brivio, V. Giacometti, A. Kis, Nat. Nanotechnol. 6, 147 (2011)
- 23. B. Radisavljevic, M.B. Whitwick, A. Kis, ACS Nano 5, 9934 (2011)
- T. Georgiou, R. Jalil, B.D. Belle, L. Britnell, R.V. Gorbachev, S.V. Morozov, Y.-J. Kim, A. Gholinia, S.J. Haigh, O. Makarovsky, L. Eaves, L.A. Ponomarenko, A.K. Geim, K.S. Novoselov, A. Mishchenko, Nat. Nanotechnol. 8, 100 (2013)
- J.N. Coleman, M. Lotya, A. O'Neill, S.D. Bergin, P.J. King, U. Khan, K. Young, A. Gaucher,
   S. De, R.J. Smith, I.V. Shvets, S.K. Arora, G. Stanton, H.-Y. Kim, K. Lee, G.T. Kim, G.S.
   Duesberg, T. Hallam, J.J. Boland, J.J. Wang, J.F. Donegan, J.C. Grunlan, G. Moriarty, A.
   Shmeliov, R.J. Nicholls, J.M. Perkins, E.M. Grieveson, K. Theuwissen, D.W. McComb, P.D.
   Nellist, V. Nicolosi, Science 331, 568 (2011)
- 26. C. Ataca, H. Sahin, S. Ciraci, J. Phys. Chem. C 116, 8983 (2012)
- 27. D. Braga, L.I. Gutiérrez, H. Berger, A.F. Morpurgo, Nano Lett. 12, 5218 (2012)
- A. Kormányos, V. Zólyomi, N.D. Drummond, P. Rakyta, G. Burkard, V.I. Fal'ko, Phys. Rev. B 88, 045416 (2013)
- 29. A. Kormányos, V. Zólyomi, N.D. Drummond, G. Burkard, Phys. Rev. X 4, 011034 (2014)
- A. Kormányos, G. Burkard, M. Gmitra, J. Fabian, V. Zólyomi, N.D. Drummond, V. I. Fal'ko, 2D Mater. 2, 022001 (2015)
- D. MacNeill, C. Heikes, K.F. Mak, Z. Anderson, A. Kormányos, V. Zólyomi, J. Park, D.C. Ralph, Phys. Rev. Lett. 114, 037401 (2015)
- 32. V. Zólyomi, N.D. Drummond, V.I. Fal'ko, Phys. Rev. B 87, 195403 (2013)
- 33. V. Zólyomi, N.D. Drummond, V.I. Fal'ko, Phys. Rev. B 89, 205416 (2014)
- F. Liu, H. Shimotani, H. Shang, T. Kanagasekaran, V. Zólyomi, N. Drummond, V.I. Fal'ko, K. Tanigaki, ACS Nano 8, 752 (2014)
- G.W. Mudd, A. Patanè, Z.R. Kudrynskyi, M.W. Fay, O. Makarovsky, L. Eaves, Z.D. Kovalyuk,
   V. Zólyomi, V. Falko, Appl. Phys. Lett. 105, 221909 (2014)
- D.C. Elias, R.R. Nair, T.M.G. Mohiuddin, S.V. Morozov, P. Blake, M.P. Halsall, A.C. Ferrari,
   D.W. Boukhyalov, M.I. Katsnelson, A.K. Geim, K.S. Novoselov, Science 323, 610 (2009)
- E. Bianco, S. Butler, S. Jiang, O.D. Restrepo, W. Windl, J.E. Goldberger, ACS Nano 7, 4414 (2013)
- 38. V. Zólyomi, J.R. Wallbank, V.I. Fal'ko, 2D Mater. 1, 011005 (2014)
- S.J. Clark, M.D. Segall, C.J. Pickard, P.J. Hasnip, M.I.J. Probert, K. Refson, M.C. Payne, Z. Kristallogr. 220, 567 (2005)
- 40. K. Refson, P.R. Tulip, S.J. Clark, Phys. Rev. B 73, 155114 (2006)
- 41. G. Kresse, J. Furthmüller, Phys. Rev. B 54, 11169 (1996)
- 42. J.P. Perdew, K. Burke, M. Ernzerhof, Phys. Rev. Lett. 77, 3865 (1996)
- 43. J. Heyd, G.E. Scuseria, M. Ernzerhof, J. Chem. Phys. 118, 8207 (2003)
- 44. A.V. Krukau, O.A. Vydrov, A.F. Izmaylov, G.E. Scuseria, J. Chem. Phys. 125, 224106 (2006)
- 45. G.P. Francis, M.C. Payne, J. Phys.: Condens. Matter 2, 4395 (1990)
- 46. R. Winkler, U. Zülicke, Phys. Rev. B 82, 245313 (2010)
- 47. L. Pan, H.J. Liu, Y.W. Wen, X.J. Tan, H.Y. Lv, J. Shi, X.F. Tang, Phys. Lett. A 375, 614 (2011)
- 48. M. Houssa, A. Dimoulas, A. Molle, J. Phys.: Condens. Matter 27, 253002 (2015)
- 49. P.E. Blöchl, Phys. Rev. B **50**, 17953 (1994)
- 50. F. Favot, A.D. Corso, Phys. Rev. B 60, 11427 (1999)
- 51. L.C. Lew Yan Voon, E. Sandberg, S. Aga, A.A. Farajian, Appl. Phys. Lett. 97, 163114 (2010)
- 52. M. Houssa, E. Scalise, K. Sankaran, G. Pourtois, V.V. Afanas'ev, A. Stesmans, Appl. Phys. Lett. 98, 223107 (2011)

- 53. J.C. Garcia, D.B. de Lima, L.V.C. Assali, J.F. Justo, J. Phys. Chem. C 115, 13242 (2011)
- O. Pulci, P. Gori, M. Marsili, V. Garbuio, R. Del Sole, F. Bechstedt, Eur. Phys. Lett. 98, 37004 (2012)
- 55. W. Wei, T. Jacob, Phys. Rev. B 88, 045203 (2013)
- 56. J.O. Sofo, A.S. Chaudhari, G.D. Barber, Phys. Rev. B **75**, 153401 (2007)
- 57. S. Park, B. Lee, S.H. Jeon, S. Han, Curr. Appl. Phys. 11, S337 (2011)
- 58. L. Liu, Z. Shen, Appl. Phys. Lett. 95, 252104 (2009)
- 59. J.C. Slater, G.F. Koster, Phys. Rev. 94, 1498 (1954)
- 60. C.-C. Liu, W. Feng, Y. Yao, Phys. Rev. Lett. 107, 076802 (2011)
- 61. G.W. Semenoff, V. Semenoff, F. Zhou, Phys. Rev. Lett. 101, 087204 (2008)
- 62. H. Hakan Gürel, V. Ongun Özcelik, S. Ciraci, J. Phys. Condens. Matter 25, 305007 (2013)
- 63. C.-C. Liu, H. Jiang, Y. Yao, Phys. Rev. B 84, 195430 (2011)

# Chapter 3 Electronic and Topological Properties of Silicene, Germanene and Stanene



Motohiko Ezawa

**Abstract** In this chapter, we review the recent progress on electronic and topological properties of monolayer topological insulators including silicene, germanene and stanene. We start with the description of the topological nature of the general Dirac system and then apply it to silicene by introducing the spin and valley degrees of freedom. Based on them, we classify all topological insulators in the general honeycomb system. We discuss topological electronics based on honeycomb systems. We introduce the topological Kirchhoff law, which is a conservation law of topological edge states. Field effect topological transistor is proposed based on the topological edge states. We show that the conductance is quantized even in the presence of random distributed impurities. Monolayer topological insulators will be a key for future topological electronics and spin-valleytronics.

#### 3.1 Introduction

Monolayer materials provide us with a most active field of two-dimensional electron systems. The success of graphene initiated an extensive search for other monolayer materials. In particular, monolayer topological materials are fascinating, realizing topological insulators and topological superconductors [1]. We theoretically investigate those described by a honeycomb system with Dirac mass terms, where various topological phases are indexed by Chern numbers determined by Dirac mass terms. Silicene, germanene and stanene are the best examples, which are topological insulators made of silicon, germanium and tin, respectively.

Silicene, germanene and stanene are the best examples, which are topological insulators made of silicon, germanium and tin, respectively. A manufacture of silicene on Ag substrate excited the study of silicene [2]. A recent experiment has

successfully demonstrated that silicene acts as a field effect transistor at room temperature [3], which will undoubtedly accelerate the study of silicene and related materials. An intriguing feature is that the band gap of silicene is controllable even locally by applying the gate voltage locally [4, 5]. It induces a topological phase transition from a quantum spin-Hall (QSH) insulator to quantum valley-Hall (QVH) insulator. It exhibits various interesting topological phases such as quantum anomalous Hall (QAH) insulator induced by exchange coupling to ferromagnet [6] and photo-irradiation [7]. The edge states can be controlled by gate voltage, which will act as a field effect topological transistor [8].

We present a generic scheme of the classification of topological insulators in topological honeycomb systems. The topological edge states are also classified. They satisfy the "topological Kirchhoff's law", which is the conservation law of the topological numbers carried by the topological edge states at the junction [9]. This conservation law will be a basic law of future topological electronic devices. We also propose topological spin-valleytronics, which uses the spin and valley degrees of freedom for future electronics applications.

Part of this chapter (Sects. 3.1–3.6) has already been published in [10], reproduced here with kind permission of Società Italiana di Fisica. Copyright (2018) by the Italian Physical Society.

## 3.2 Graphene and Silicene

The basic structure of graphene and silicene is a honeycomb lattice. It consists of two triangular sublattices made of inequivalent lattice sites A and B (Fig. 3.1a). The reciplocal lattice is also a honeycomb lattice in the momentum space (Fig. 3.1b), which constitutes the Brilloin zone.

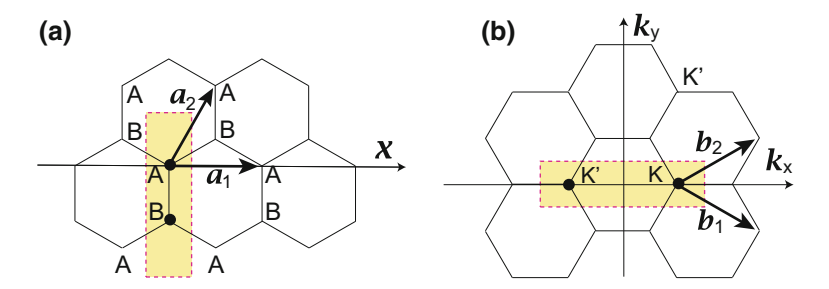


Fig. 3.1 a The honeycomb structure, made of two fundamental vectors  $\mathbf{a}_1$  and  $\mathbf{a}_2$ , consists of two sublattices made of A and B sites. A dotted rectangular represents a unit cell. b The reciprocal lattice is also a honeycomb lattice. A dotted rectangular represents a unit cell, which contains two inequivalent points K and K'

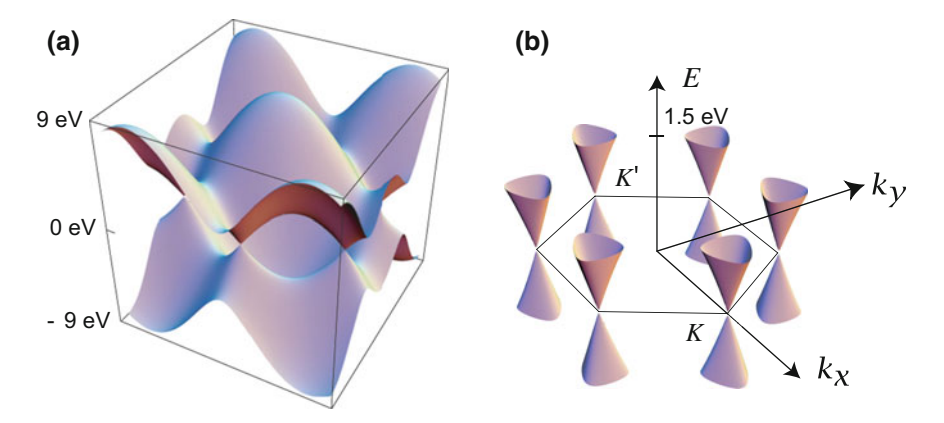


Fig. 3.2 Band structure of graphene. a Six valleys are seen in this figure. b The gap is closed at the K and K' points, where the band structure looks like a cone. It is called the Dirac cone because the dispersion is linear

# 3.2.1 Graphene

Graphene is described by the simplest tight-binding model on a honeycomb lattice [11, 12],

$$\hat{H}_0 = -t \sum_{\langle i,j \rangle s} c_{is}^{\dagger} c_{js}, \tag{3.1}$$

where  $c_{is}^{\dagger}$  creates an electron with spin polarization  $s = \uparrow \downarrow$  at site  $i, \langle i, j \rangle$  runs over all the nearest neighbor hopping sites, and t is the transfer energy. By diagonalizing the Hamiltonian we obtain the band structure, which we illustrate in Fig. 3.2a. It consists of valleys or cones near the Fermi surface. The cones touch the Fermi surface at two inequivalent points, that is, the K and K' points in the Brillouin zone (Fig. 3.2b).

We are interested in physics near the Fermi energy. To derive the relevant Hamiltonian, we rewrite (3.1) as

$$\hat{H}_{0} = t \sum_{s} \int d^{2}k' \left( c_{\mathrm{A}s}^{\dagger}, c_{\mathrm{B}s}^{\dagger} \right) \begin{pmatrix} 0 & f\left(\mathbf{k'}\right) \\ f^{*}\left(\mathbf{k'}\right) & 0 \end{pmatrix} \begin{pmatrix} c_{\mathrm{A}s} \\ c_{\mathrm{B}s} \end{pmatrix}$$
(3.2)

in the momentum space, with  $s = \pm$  being the spin index, and

$$f(\mathbf{k}') = e^{-iak_y'/\sqrt{3}} + 2e^{iak_y'/2\sqrt{3}}\cos\frac{ak_x'}{2}.$$
 (3.3)

The energy spectrum is obtained as

$$E(\mathbf{k}') = t\sqrt{1 + 4\cos\frac{ak_x'}{2}\cos\frac{\sqrt{3}ak_y'}{2} + 4\cos^2\frac{ak_x'}{2}}.$$
 (3.4)

The gap closes at  $\mathbf{k}' = \mathbf{K}_{\eta}$  with

$$\mathbf{K}_{\eta} = \frac{1}{a} \left( \eta \frac{4\pi}{3}, 0 \right) \quad \text{with} \quad \eta = \pm, \tag{3.5}$$

which are the K and K' points.

We make the Taylor expansion of (3.3) around  $\mathbf{k}' = \mathbf{K}_{\eta}$ . By setting  $\mathbf{k}' = \mathbf{K}_{\eta} + \mathbf{k}$ , we obtain

$$f\left(\mathbf{k} + \mathbf{K}_{\eta}\right) = \eta k_x - i k_y \quad \text{for} \quad |\mathbf{k}| \ll a^{-1}, \tag{3.6}$$

and the dispersion is linear,

$$E\left(\mathbf{k} + \mathbf{K}_{\eta}\right) = \pm \hbar v_{\mathrm{F}} \sqrt{k_{x}^{2} + k_{y}^{2}}.$$
(3.7)

Hence, the low-energy physic near the Fermi energy is described by the Dirac theory,

$$H_s^{\eta} = \begin{pmatrix} 0 & \hbar v_{\mathrm{F}} (\eta k_x - i k_y) \\ \hbar v_{\mathrm{F}} (\eta k_x + i k_y) & 0 \end{pmatrix} = \hbar v_{\mathrm{F}} (\eta k_x \tau_x + k_y \tau_y), \tag{3.8}$$

where  $v_{\rm F} = \frac{\sqrt{3}}{2\hbar}at$  is the Fermi velocity.

The K and K' points are also referred to as the  $K_{\eta}$  points or the Dirac points. The cone-shaped parts of the energy spectrum are referred to as the Dirac cones (Figs. 3.2 and 3.3a2). We note that the number of the Dirac cones is always even in the tight-binding theory, which is known as the Nielsen-Ninomiya theorem [13] (Table 3.1).

# 3.2.2 Silicene and Tunable Band Gap

The basic nature of silicene is described also by the tight-binding model (3.1). There are two additional features. One is the presence of the spin-orbit interaction, which makes silicene a topological insulator [14, 15]. The other is its buckled structure with a layer separation between the two sublattices (Fig. 3.3b1) [4]. This freedom allows us to tune the gap by introducing a potential difference between the two sublattices. When we apply electric field  $E_z$  perpendicular to silicene, the tight-binding Hamiltonian reads

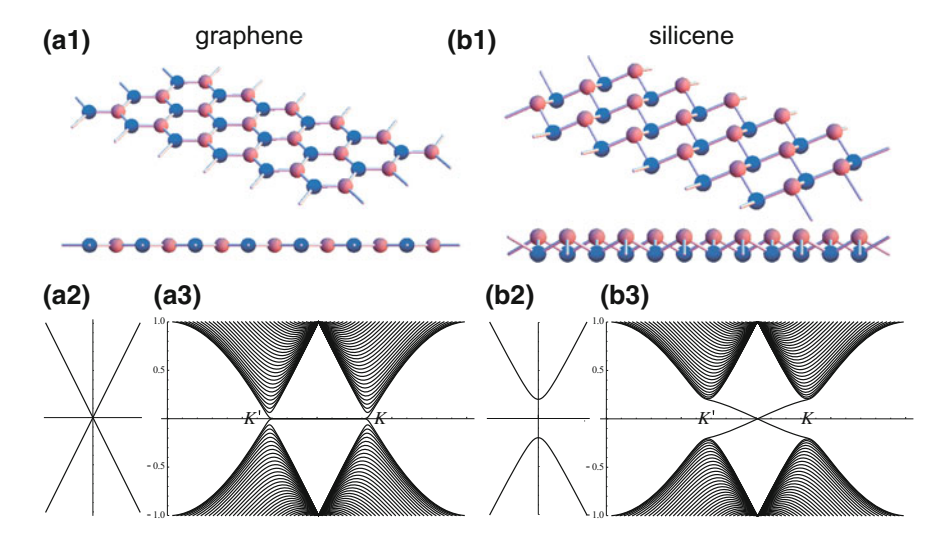


**Fig. 3.3** a1 The lattice structure of graphene is planar, but b1 that of silicene is buckled. Red and blue balls represent A and B sites. a2 The band gap of graphene is closed, where the dispersion is linear near the Fermi energy. b2 The band gap of silicene is open. a3 A flat line connecting the K and K' points represents gapless flat edge modes in a nanoribbon. It contains fourfold degenerate edge states for up/down-spin and left/right movers. b3 Two lines connecting the tips of the Dirac cones represents edge modes of a nanoribbon. Each line contains twofold degenerate edge states

$$\hat{H} = -t \sum_{\langle i,j \rangle s} c_{is}^{\dagger} c_{js} + i \frac{\lambda_{SO}}{3\sqrt{3}} \sum_{\langle \langle i,j \rangle \rangle s} s \nu_{ij} c_{is}^{\dagger} c_{js} - \ell \sum_{is} \mu_i E_z c_{is}^{\dagger} c_{is}, \qquad (3.9)$$

where  $\langle \langle i, j \rangle \rangle$  run over all the next-nearest neighbor hopping sites. The spin index stands for  $s = \uparrow \downarrow$  for indices and for  $s = \pm$  within equations. It describes germanene and stanene as well.

We explain each term. (i) The first term represents the usual nearest-neighbor hopping with the transfer energy t. (ii) The second term represents the effective SO coupling with  $\lambda_{\rm SO}$ , where  $\nu_{ij}=+1$  if the next-nearest-neighboring hopping is anticlockwise and  $\nu_{ij}=-1$  if it is clockwise with respect to the positive z axis [16]. (iii) The third term represents the staggered sublattice potential with  $\mu_i=+1$  (-1) for the A (B) site [4]. Explicit values of these parameters are summarized in the Table 3.1. By diagonalizing the Hamiltonian by setting  $E_z=0$ , we obtain the band structure illustrated as in Fig. 3.3b2. The prominent feature is that the gap is open due to the SO interaction, and hence silicene is an insulator. A large SO interaction with  $\lambda_{\rm SO}=0.3\,{\rm eV}$  is materialized in functionalized stanene [17], which will be a topological insulator at room temperature.

The low-energy physic near the Fermi energy is derived from the tight-binding model. It is given by the Dirac Hamiltonian (3.8) together with the diagonal mass term,

<b>Table 3.1</b> The parameters characterising graphene, silicene and germanene. Here, $v_F$ is in the unit
of $10^5$ m/s, and $\lambda_{SO}$ in the unit of meV. $\ell$ is the buckle height, while $\theta$ is the bond angle. Taken from
[14]

	t (eV)	υ	a (Å)	$\lambda_{ ext{SO}}$	$\ell$	$\theta$
Graphene	2.8	9.8	2.46	$10^{-3}$	0	90
Silicene	1.6	5.5	3.86	3.9	0.23	101.7
Germanene	1.3	4.6	4.02	43	0.33	106.5
Stanene	1.3	4.9	4.70	100	0.40	107.1

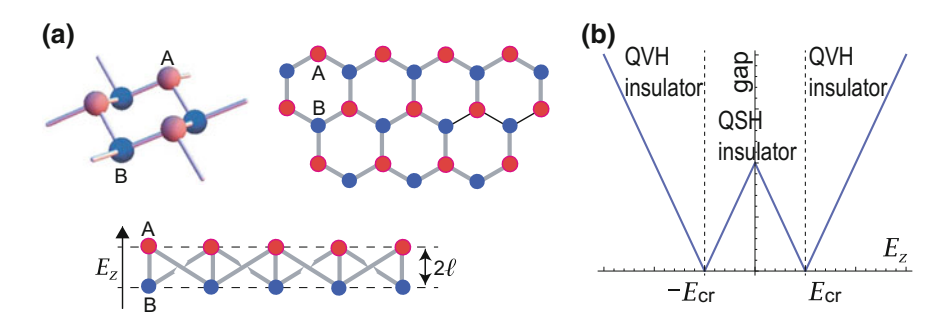


Fig. 3.4 a Bird's eye view, top view and side view of silicene. b Ellectrically tunable band gap of silicene. The states for  $|E| > E_{cr}$  and  $|E| < E_{cr}$  are a quantum valley Hall (QVH) insulator and a quantum spin Hall (QSH) insulator, respectively. See Table 3.2 for explanation for these

$$H_s^{\eta} = \begin{pmatrix} \Delta_s^{\eta} & \hbar v_{\rm F} (\eta k_x - i k_y) \\ \hbar v_{\rm F} (\eta k_x + i k_y) & -\Delta_s^{\eta} \end{pmatrix} = \hbar v_{\rm F} (\eta k_x \tau_x + k_y \tau_y) + \Delta_s^{\eta} \tau_z, \quad (3.10)$$

where

$$\Delta_{\rm s}^{\eta} = \eta s \lambda_{\rm SO} - \ell E_{\rm z} \equiv -\ell (E_{\rm z} - \eta s E_{\rm cr}), \tag{3.11}$$

and

$$E_{\rm cr} \equiv \lambda_{\rm SO}/\ell.$$
 (3.12)

Here,  $\lambda_{SO}$  is the SOI strength,  $\ell$  is the separation between the A and B sublattices, and  $E_z$  is the applied perpendicular electric field.

The energy spectrum reads

$$E(\mathbf{k}) = \pm \sqrt{(\hbar v_{\rm F} k)^2 + \left(\Delta_s^{\eta}\right)^2}.$$
 (3.13)

The gap is given by  $2|\Delta_s^{\eta}| = 2\ell |E_z - \eta s E_{cr}|$ .

It is important that the band gap is tunable by controlling external electric field  $E_z$ . The gap is open when  $E_z=0$ . As  $|E_z|$  increases, the gap become narrower (Fig. 3.4), and it closes at  $E_z=\eta s E_{\rm cr}$ , where silicene is semimetallic just as in graphene. As  $|E_z|$  increases further, the gap opens again.

#### 3.2.3 Generalized Dirac Mass Terms

There are actually other ways to control the band gap by introducing other interactions to silicene. Since each Dirac cone is indexed by two parameters  $\eta = \pm$  and  $s = \pm$ , the most general Dirac mass must have the following expression,

$$\Delta_s^{\eta} = \eta s \lambda_{SO} - \lambda_V + \eta \lambda_H + s \lambda_{SX}, \tag{3.14}$$

so that it has four independent parameters,  $\lambda_{SO}$ ,  $\lambda_V$ ,  $\lambda_H$  and  $\lambda_{SX}$ . We have already discussed the first two terms representing the SO interaction and the sublattice staggered potential with  $\lambda_V = \ell E_z$ . The third term describes the Haldane interaction induced by the photo-irradiation, where  $\lambda_\Omega = \hbar v_F^2 \mathcal{A}^2 \Omega^{-1}$  with  $\Omega$  the frequency and  $\mathcal{A}$  the dimensionless intensity [7]. The fourth term describes the antiferromagnetic exchange magnetization [18]. We may write down the tight-binding terms that yield the fourth and fifth terms [18],

$$i\frac{\lambda_H}{3\sqrt{3}}\sum_{\langle\langle i,j\rangle\rangle s}\nu_{ij}c_{is}^{\dagger}c_{js}, \quad \lambda_{SX}\sum_{is}s\mu_ic_{is}^{\dagger}c_{is}. \tag{3.15}$$

There are a variety of 2D materials whose low-energy physics is described by the Dirac Hamiltonian (3.10) with the Dirac mass (3.14). We call them general honeycomb systems. Examples are monolayer antiferromagnetic manganese chalcogenophosphates (MnPX<sub>3</sub>, X = S, Se) [19] and perovskite G-type antiferromagnetic insulators grown along the [111] direction [20].

# 3.3 Berry Curvature and Chern Number

#### 3.3.1 TKNN Formula

According to the Kubo formula, the Hall conductance is given by

$$\sigma_{xy} = -i\hbar e^{2} \int d^{2}k \sum_{n\neq m} \frac{f(E_{n}(\mathbf{k}))}{(E_{n}(\mathbf{k}) - E_{m}(\mathbf{k}))^{2}} \times \left[ \langle \psi_{n}(\mathbf{k}) | v_{x} | \psi_{m}(\mathbf{k}) \rangle \langle \psi_{m}(\mathbf{k}) | v_{y} | \psi_{n}(\mathbf{k}) \rangle - \langle \psi_{n}(\mathbf{k}) | v_{y} | \psi_{m}(\mathbf{k}) \rangle \langle \psi_{m}(\mathbf{k}) | v_{x} | \psi_{n}(\mathbf{k}) \rangle \right], \quad (3.16)$$

where  $f(E_n(\mathbf{k}))$  is the Fermi distribution function, and the states are subject to the condition  $\langle \psi_m(\mathbf{k}) | \psi_n(\mathbf{k}) \rangle = \delta_{mn}$ . By using the Hellmann-Feynman theorem

$$\langle \psi_m(\mathbf{k}) | v_\mu | \psi_n(\mathbf{k}) \rangle = \frac{1}{\hbar} (E_n(\mathbf{k}) - E_m(\mathbf{k})) \langle \psi_m(\mathbf{k}) | \partial_{k_\mu} | \psi_n(\mathbf{k}) \rangle, \qquad (3.17)$$

the Hall conductance is rewritten as

$$\sigma_{xy} = \frac{ie^2}{\hbar} \int d^2k \sum_{n \neq m} f(E_n(\mathbf{k})) \left[ \langle \psi_n(\mathbf{k}) | \partial_{k_x} \psi_m(\mathbf{k}) \rangle \langle \psi_m(\mathbf{k}) | \partial_{k_y} \psi_n(\mathbf{k}) \rangle - \langle \psi_n(\mathbf{k}) | \partial_{k_y} \psi_m(\mathbf{k}) \rangle \langle \psi_m(\mathbf{k}) | \partial_{k_x} \psi_n(\mathbf{k}) \rangle \right].$$
(3.18)

Here it should be noticed that the sum can be extended to include the states with n = m.

Making the use of the relation

$$\langle \psi_n(\mathbf{k}) | \partial_{k_x} \psi_m(\mathbf{k}) \rangle + \langle \partial_{k_x} \psi_n(\mathbf{k}) | \psi_m(\mathbf{k}) \rangle = \partial_{k_x} \langle \psi_m(\mathbf{k}) | \psi_n(\mathbf{k}) \rangle = 0,$$
 (3.19)

and the completeness condition  $\sum_{m} |\psi_{m}(\mathbf{k}) \langle \psi_{m}(\mathbf{k})| = 1$ , we obtain

$$\sigma_{xy} = \frac{e^2}{2\pi h} \sum_{n} \int d^2k f\left(E_n\left(\mathbf{k}\right)\right) F_n\left(\mathbf{k}\right), \qquad (3.20)$$

where

$$F_{n}(\mathbf{k}) = i \left[ \langle \partial_{k_{x}} \psi_{n}(\mathbf{k}) | \partial_{k_{y}} \psi_{n}(\mathbf{k}) \rangle - \langle \partial_{k_{y}} \psi_{n}(\mathbf{k}) | \partial_{k_{x}} \psi_{n}(\mathbf{k}) \rangle \right]. \tag{3.21}$$

The conductance is the sum of the contributions from various bands indexed by n. It is convenient to define a "gauge potential" in the momentum space for each band index n by

$$a_{\mu}^{n}(\mathbf{k}) = -i \langle \psi_{n}(\mathbf{k}) | \partial_{k_{\mu}} \psi_{n}(\mathbf{k}) \rangle, \tag{3.22}$$

which is properly called the Berry connection. We may rewrite (3.21) as

$$F_n(\mathbf{k}) = \partial_{k_x} a_y^n(\mathbf{k}) - \partial_{k_y} a_x^n(\mathbf{k}). \tag{3.23}$$

This is the "magnetic field", which is properly called the Berry curvature.

We consider the zero-temperature limit, where the integration is taken below the Fermi energy by setting  $f(E_n(\mathbf{k})) = 1$ . The conductance is given by

$$\sigma_{xy} = \frac{e^2}{h} \sum_{n} C_n, \tag{3.24}$$

where

$$C_n = \frac{1}{2\pi} \int d^2k \, F_n \left( \mathbf{k} \right). \tag{3.25}$$

We go on to prove that  $C_n$  is an integer. The formula (3.25) is interpreted as the integral of the Berry curvature  $F_n(\mathbf{k})$  over the first Brillouin zone, which is the total "magnetic flux". Such a quantity is called the Chern number. Using the Stokes

theorem, this can be rewritten as a contour integration along the boundary of the Brillouin zone,

$$C_n = \frac{1}{2\pi} \int d^2k \, F_n \left( \mathbf{k} \right) = \frac{1}{2\pi} \oint dk_\mu a_\mu^n \left( \mathbf{k} \right). \tag{3.26}$$

Since it is a periodic system, it follows that  $C_n = 0$  if  $a_{\mu}^n(\mathbf{k})$  is a regular function. However, the gauge potential  $a_{\mu}^n(\mathbf{k})$  can be singular though the magnetic field  $F_n(\mathbf{k})$  is regular. In this case it is necessary to choose the contour integration to avoid these singular points. Then,  $C_n$  counts the number of singularities, following the argument familiar to the theory of Dirac monopoles. The formula (3.24) is known as the TKNN formula [21].

### 3.3.2 Berry Curvature in Centrosymmetric System

We explicitly calculate the Berry connection and the Chern number in the present system. Let us first show the Berry curvature with the use of the tight-binding Hamiltonian (3.9) in Fig. 3.5. The Berry curvature is strictly localized at the K and K' points. This feature remains unchanged even if we include the extra terms (3.15). Consequently, the Dirac Hamiltonian is valid to make a topological analysis to each valley, which is indexed by the spin index s and the valley index  $\eta$ . Namely, it is possible to assign the Chern number  $C_s^{\eta}$  to each valley.

The Dirac Hamiltonian is given by (3.10), or

$$H_s^{\eta} = \begin{pmatrix} \Delta_s^{\eta} & \hbar v_{\rm F}(\eta k_x - i k_y) \\ \hbar v_{\rm F}(\eta k_x + i k_y) & -\Delta_s^{\eta} \end{pmatrix}. \tag{3.27}$$

The wave function of the valence band is given by

$$\psi_v(\mathbf{k}) = \frac{1}{N} \begin{pmatrix} \hbar v_F k (\eta k_x + i k_y) \\ -\Delta_s^{\eta} + \sqrt{(\hbar v_F k)^2 + (\Delta_s^{\eta})^2} \end{pmatrix}$$
(3.28)

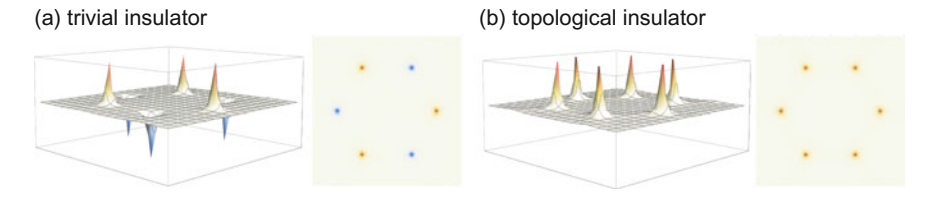


**Fig. 3.5** Berry curvature in **a** the trivial insulator and **b** the topological insulator. It is strictly localized in the vicinity of the K and K' points. The Chern number, the integration of the Berry curvature over the Brillouin zone, is zero for a trivial insulator, while it is non-zero for a topological insulator

with  $N=\sqrt{(\hbar v_{\rm F} k)^2+\left(-\Delta_s^\eta+\sqrt{(\hbar v_{\rm F} k)^2+\left(\Delta_s^\eta\right)^2}\right)^2}$ . The Berry connection is calculated as

$$a_x(\mathbf{k}) = -\eta \frac{k_y}{2k^2} (1 + g(k)), \quad a_y(\mathbf{k}) = \frac{k_x}{2k^2} (1 + g(k))$$
 (3.29)

with  $g(k) = \Delta_s^{\eta} / \sqrt{(\hbar v_F k)^2 + (\Delta_s^{\eta})^2}$ . The gauge potential  $a_{\mu}(\mathbf{k})$  has a singularity at k = 0. We make the contour integration avoiding the point k = 0. Consequently, we may calculate (3.26) explicitly as

$$C_{s_z}^{\eta} = \frac{1}{2\pi} \oint dk_{\mu} a_{\mu} (\mathbf{k}) = -\frac{\eta}{2} \operatorname{sgn}(\Delta_s^{\eta}), \tag{3.30}$$

where the Dirac mass  $\Delta_s^{\eta}$  is given by (3.14). The Chern number is quantized as  $C_s^{\eta} = \pm \frac{1}{2}$  at each Dirac point. It is insensitive to a deformation of the band structure provided the gap is open. Since there are two Dirac points, the total Chern number is an integer.

Here we present a detailed derivation of (3.30). When we adopt the Dirac Hamiltonian, the notion of the original Brillouin zone is lost. The contour integration is to be taken along the two circles at  $k \to \infty$  and k = 0, where  $g(\infty) = 0$  and  $g(0) = \Delta_s^{\eta}/|\Delta_s^{\eta}| = \operatorname{sgn}(\Delta_s^{\eta})$ . We note that

$$\frac{k_x}{k^2} = \partial_{k_y}\theta, \qquad \frac{k_y}{k^2} = -\partial_{k_x}\theta \tag{3.31}$$

in the polar coordinate,  $k_x = k \cos \theta$ ,  $k_y = k \sin \theta$ . Then,

$$C_{s_z}^{\eta} = \frac{\eta}{2\pi} \left[ \oint_{k \to \infty} d\theta \left( 1 + g(k) \right) - \oint_{k \to 0} d\theta \left( 1 + g(k) \right) \right] = -\frac{\eta}{2} \operatorname{sgn}(\Delta_s^{\eta}), \quad (3.32)$$

which is (3.30).

It is instructive to calculate the Berry curvature explicitly in the polar coordinate. Substituting (3.29) into (3.23) we obtain

$$F_s^{\eta}(\mathbf{k}) = -\eta \frac{\Delta_s^{\eta}}{2\left((\hbar v_F k)^2 + \left(\Delta_s^{\eta}\right)^2\right)^{3/2}}.$$
(3.33)

We then calculate (3.25) to reproduce (3.30). Note that there is no singularity in  $F_s^{\eta}(\mathbf{k})$ . This function reproduces the Berry curvature at each Dirac point in Fig. 3.5.

#### 3.3.3 Pontryagin Number

We present another formula to calculate the Chern number valid for the  $2 \times 2$  Hamiltonian of the form  $H = \tau \cdot \mathbf{d}(\mathbf{k})$ . We parametrize  $\mathbf{d}(\mathbf{k})$  as

$$\hat{\mathbf{d}}(\mathbf{k}) = \mathbf{d}/|\mathbf{d}| = (\sin\theta\cos\phi, \sin\theta\sin\phi, \cos\theta). \tag{3.34}$$

The eigen function of the Hamiltonian is unique and given by

$$\psi_{v}(\mathbf{k}) = \begin{pmatrix} -e^{-i\phi} \sin\frac{\theta}{2} \\ \cos\frac{\theta}{2} \end{pmatrix}. \tag{3.35}$$

The Berry connection (3.22) and the Berry curvature (3.23) are calculated as

$$a_{\mu}(\mathbf{k}) = \frac{1}{2} \left( 1 - \cos \theta \right) \partial_{k_{\mu}} \phi, \tag{3.36}$$

$$F(\mathbf{k}) = \frac{1}{2} \sin \theta \left( \partial_{k_x} \theta \partial_{k_y} \phi - \partial_{k_y} \theta \partial_{k_x} \phi \right) = \left( \frac{\partial \hat{\mathbf{d}}}{\partial k_x} \times \frac{\partial \hat{\mathbf{d}}}{\partial k_y} \right) \cdot \hat{\mathbf{d}}.$$
(3.37)

Consequently the Chern number (3.25) is equivalent to the Pontryagin number,

$$C_s^{\eta} = \frac{1}{4\pi} \int d^2k \left( \frac{\partial \hat{\mathbf{d}}}{\partial k_x} \times \frac{\partial \hat{\mathbf{d}}}{\partial k_y} \right) \cdot \hat{\mathbf{d}}. \tag{3.38}$$

The Pontryagin number counts how many times the vector  $\hat{\mathbf{d}}(\mathbf{k})$  wraps a sphere as  $k_{\mu}$  moves for  $-\infty < k_{\mu} < \infty$ . It is interesting that the Chern number is calculable solely by using the vector  $\mathbf{d}(\mathbf{k})$  in the Hamiltonian  $H = \tau \cdot \mathbf{d}(\mathbf{k})$ .

We apply the above formula to the present Hamiltonian given by (3.10), which is expressed as  $H_s^{\eta} = \tau \cdot \mathbf{d}$  with

$$\hat{\mathbf{d}}(\mathbf{k}) = \frac{1}{\sqrt{(\hbar v_F k)^2 + (\Delta_s^{\eta})^2}} \left(\hbar v_F \eta k_x, \hbar v_F k_y, \Delta_s^{\eta}\right). \tag{3.39}$$

We express  $\hat{d}_x \pm i\hat{d}_y = \sqrt{1 - \sigma^2(k)}e^{i\eta\theta}$ ,  $\hat{d}_z = \sigma(k)$  in the polar coordinate of the  $\hat{\mathbf{d}}$  (**k**) vector. Then, the Pontryagin number (3.38) is rewritten as

$$C_s^{\eta} = \frac{\eta}{4\pi} \int d^2k \ \varepsilon_{ij} \partial_i \sigma \partial_j \theta = -\frac{\eta}{2} \int_0^1 d\sigma = -\frac{\eta}{2} \operatorname{sgn}(\Delta_s^{\eta}), \tag{3.40}$$

which agrees with (3.30). The pseudospin texture  $\hat{\mathbf{d}}(\mathbf{k})$  forms a meron structure in the momentum space as k moves from k = 0 to  $k = \infty$  and  $\theta$  moves from  $\theta = 0$  to

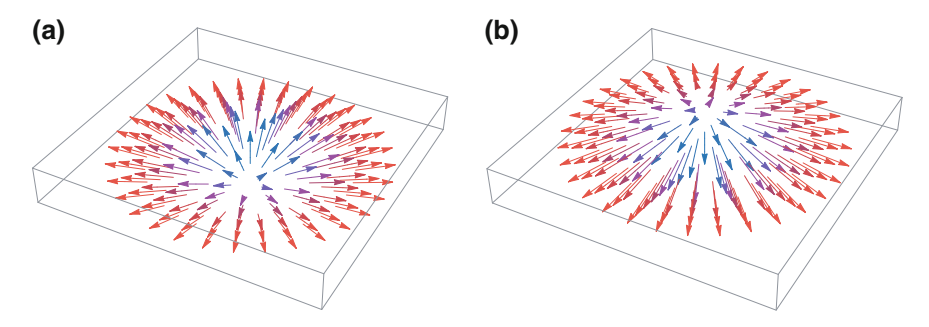


Fig. 3.6 Illustration of a meron structure in momentum space. A meron with the Pontryagin number a 1/2, whose core spin is pointing up direction,  $\mathbf{b} - 1/2$ , whose core spin is pointing down direction

 $\theta = 2\pi$ , as shown in Fig. 3.6. A meron is a topological structure which has a half integer Pontryagin number.

# 3.3.4 Classification of Topological Insulators

An insulator phase is indexed by a set of four Chern numbers  $C_s^{\eta}$ . Equivalently we may define the total Chern number C, the spin Chern number  $C_s$ , the valley Chern number  $C_v$ , and the spin-valley Chern number  $C_s v$  [9],

$$C = C_{\uparrow}^{K} + C_{\uparrow}^{K'} + C_{\downarrow}^{K} + C_{\downarrow}^{K'}, \tag{3.41}$$

$$C_s = \frac{1}{2} (C_{\uparrow}^K + C_{\uparrow}^{K'} - C_{\downarrow}^K - C_{\downarrow}^{K'}), \tag{3.42}$$

$$C_v = C_{\uparrow}^K - C_{\uparrow}^{K'} + C_{\downarrow}^K - C_{\downarrow}^{K'}, \tag{3.43}$$

$$C_{sv} = \frac{1}{2} (C_{\uparrow}^K - C_{\uparrow}^{K'} - C_{\downarrow}^K + C_{\downarrow}^{K'}). \tag{3.44}$$

Here we have used the spin index  $s=\uparrow\downarrow$  and the valley index  $\eta=K$ , K' instead of  $s=\pm$  and  $\eta=\pm$  for notational clarity. The valley Chern number and the spin-valley Chern number are well defined only in the Dirac theory. Hence, we may call  $\mathcal C$  and  $\mathcal C_s$  the genuine Chern numbers.

Possible sets of genuine Chern numbers  $(C, C_s)$  are (0, 0), (2, 0), (0, 1),  $(1, \frac{1}{2})$  up to the sign  $\pm$ . They are the trivial, quantum anomalous Hall (QAH), quantum spin Hall (QSH), spin-polarized quantum anomalous Hall (SQAH) insulators, respectively. Note that there are two-types of trivial band insulators, which are quantum valley Hall (QVH) insulator, and quantum spin-valley Hall (QSVH) insulator with antiferromagnetic (AF) order (Table 3.2).

**Table 3.2** Corresponding to the spin and valley degrees of freedom, there are 4 Chern numbers  $\mathcal{C}_{s_z}^{\eta}$ , each of which takes  $\pm \frac{1}{2}$ , Equivalently they are given by the Chern, spin Chern, valley Chern and spin-valley Chern numbers  $\mathcal{C}$ ,  $\mathcal{C}_s$ ,  $\mathcal{C}_v$  and  $\mathcal{C}_{sv}$ . They are independently controlled by the four parameters  $\lambda_{SO}$ ,  $\lambda_V$ ,  $\lambda_Q$  and  $\lambda_{SX}$ . Hence there are 16 states indexed by them. The genuin topological numbers are only  $\mathcal{C}$  and  $\mathcal{C}_s$ 

	$C_{\uparrow}^{K}$	$C_{\uparrow}^{K'}$	$C_{\downarrow}^{K}$	$C_{\downarrow}^{K'}$	C	$2C_s$	$ C_v $	$2C_{sv}$
QAH	1/2	1/2	1/2	1/2	2	0	0	0
SQAH	1/2	1/2	1/2	-1/2	1	1	1	-1
SQAH	1/2	1/2	-1/2	1/2	1	-1	1	1
QVH	1/2	1/2	-1/2	-1/2	0	0	2	0
SQAH	1/2	-1/2	1/2	1/2	1	1	-1	1
QSH	1/2	-1/2	1/2	-1/2	0	2	0	0
QSVH	1/2	-1/2	-1/2	1/2	0	0	0	2
SQAH	1/2	-1/2	-1/2	-1/2	-1	1	1	1
SQAH	-1/2	1/2	1/2	1/2	1	-1	-1	-1
QSVH	-1/2	1/2	1/2	-1/2	0	0	0	-2
QSH	-1/2	1/2	-1/2	1/2	0	-2	0	0
SQAH	-1/2	1/2	-1/2	-1/2	-1	-1	1	-1
QVH	-1/2	-1/2	1/2	1/2	0	0	-2	0
SQAH	-1/2	-1/2	1/2	-1/2	-1	1	-1	-1
SQAH	-1/2	-1/2	-1/2	1/2	-1	-1	-1	1
QAH	-1/2	-1/2	-1/2	-1/2	-2	0	0	0

# 3.4 Topological Edges

# 3.4.1 Bulk-Edge Correspondence

The most convenient way to determine if the system is topological is to employ the bulk-edge correspondence. When there are two topological distinct phases, a topological phase transition must occur between them. The band gap must close at the topological phase transition point since the topological number cannot change its quantized value without gap closing.

To reveal the emergence of gapless modes at a phase transition point, it is convenient to analyze the energy spectrum of a nanoribbon in a topological phase, because the boundary of the nanoribbon separates a topological state and the vacuum whose topological numbers are zero. Indeed, we have pointed out the emergence of gapless edge modes in silicene: See Fig. 3.3b3. We may call an edge a topological edge when it separates two topologically distinctive states.

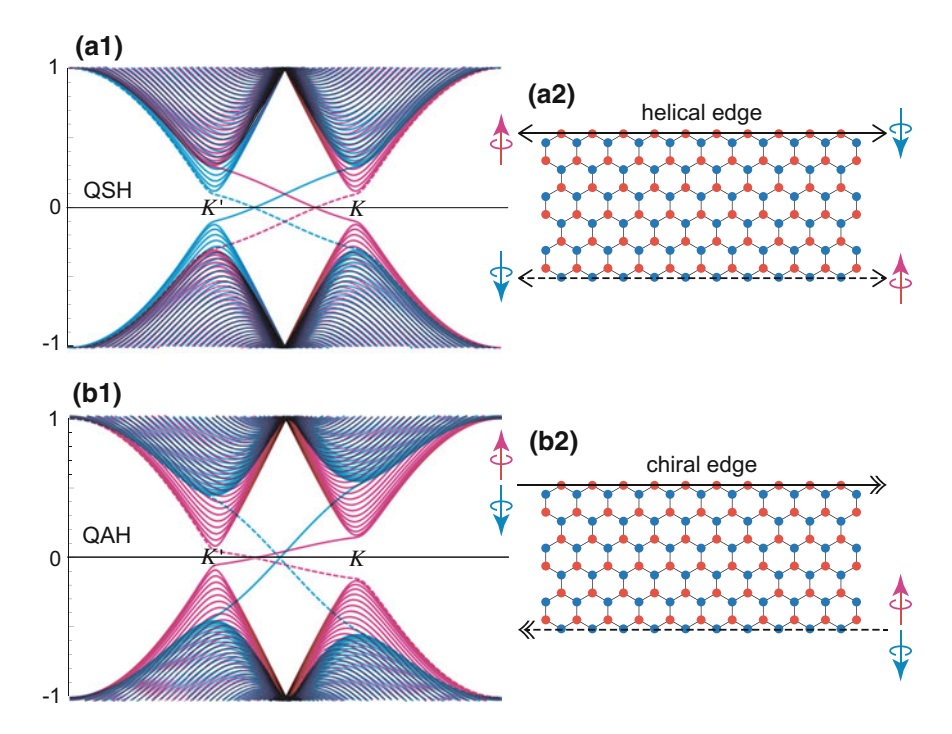


Fig. 3.7 Nanoribbon in QSH phase. We have applied  $E_z$  to differentiate the upper (A sites) and lower (B sites) edges

# 3.4.2 Herical Edges and Chiral Edges

We analyze the edge modes of silicene in the QSH phase. We resolve the degeneracy of the edge modes by applying weak electric field  $E_z$  to a nanoribbon with zigzag edges as in Fig. 3.7a. A prominent feature is the up and down spins flow into the opposite directions along each edge, implying that the edge current is a pure spin current. Such an edge is called a helical edge.

We may also analyze a silicene nanoribbon in the QAH phase. The band structure is given by Fig. 3.7b1, where we have applied weak electric field  $E_z$  to resolve the degeneracy. The spin and the current direction are shown in both edges in Fig. 3.7b2. The edge current does not convey spins. Such an edge is called a chiral edge.

# 3.4.3 Inner Edges

When a nanoribbon has only the valley Chern number and the spin-valley Chern number, no edge modes emerge because these numbers are not defined in the vacuum. Nevertheless these numbers are also topological numbers within the bulk.

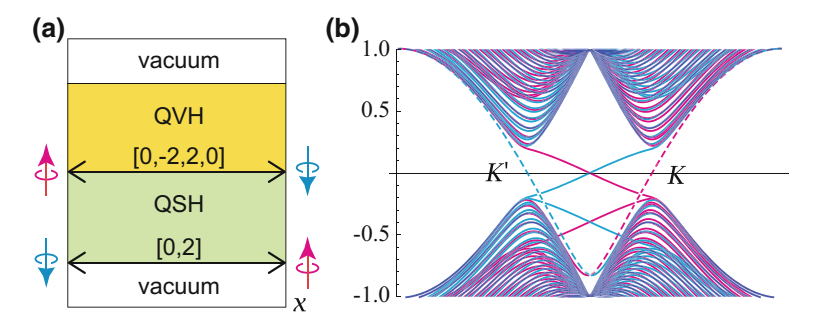


**Fig. 3.8** a Silicene nanoribbon placed parallel to the x axis. When external field  $E_z$  is applied along the y axis, the region with  $E_z > E_{\rm cr}$  becomes a QVH insulator. The inner edge between the QSH and QVH parts is helical. The outer edge below the QSH part is also helical. No gapless edge states appear along the outer edge above the QVH part. **b** The band structure of a silicene nanoribbon. Four gapless edge modes are found, which are assigned as in (a)

We may consider a junction separating two different topological phases in a single honeycomb system. We call such a junction an inner edge. In contrast we may call a real edge of a nanoribbon an outer edge. There is a crucial difference between gapless edge modes appearing along an inner edge and an outer edge. Any gapped state is indexed by a set of four topological numbers  $(C, C_s, C_v, C_{sv})$ . Consequently, an inner edge state carries a gapless edge mode indexed by the difference  $[\Delta C, \Delta C_s, \Delta C_v, \Delta C_{sv}]$  between the two adjacent gapped states. More precisely, we set  $\Delta C = C^L - C^R$  and so on, when the topological insulator with  $(C^L, C_s^L, C_v^L, C_{sv}^L)$  is on the left-hand side of the one with  $(C^R, C_s^R, C_v^R, C_{sv}^R)$ . On the other hand, an outer edge state can carry a gapless edge mode only indexed by  $[C, C_s]$  of the gapped state because the valley Chern numbers are ill defined in the vacuum.

We illustrate a nanoribbon which contains the QSH and QVH phases in Fig. 3.8, where there are two outer edges and one inner edge. As we have argued, the outer edge of the QSH part is helical, while the outer edge of the QVH part has no gapless edge modes. The nature of the inner edge is seen by analying the band structure in Fig. 3.8b. It contains only four nondegenerate gapless states. On one hand, two solid lines correspond to the helical edge between the QSH part and the vacuum. On the other hand, two dotted lines correspond to the inner edge between the QSH and QVH parts, which is also helical. It should be noted that the inner edge modes cross the Fermi energy at the K and K' points.

We construct the Dirac theory of a gapless inner-edge state [4, 9] indexed by  $\eta$  and s. It emerges along a curve where the Dirac mass vanishes,  $\Delta_s^{\eta}(x,y) = 0$ . Let us take the edge along the x axis. The zero modes emerge along the line determined by  $\Delta_s^{\eta}(y) = 0$ , when  $\Delta_s^{\eta}(y)$  changes the sign. We may set  $k_x$  =constant due to the translational invariance along the x axis

$$\left(-i\hbar v_{\rm F}\tau_y\partial_y + \Delta_s^\eta \tau_z\right)\psi = 0. \tag{3.45}$$

We seek the zero-energy solution by setting  $\psi_B = i\zeta\psi_A$  with  $\zeta = \pm 1$ . Here,  $\psi_A$  is a two-component amplitude with the up spin and down spin,  $\psi_A = (\psi_A^{\uparrow}, \psi_A^{\downarrow})$ . Setting  $\psi_A(x,y) = e^{ik_x x}\phi_A(y)$ , we obtain  $H_{\eta}\psi_A(x,y) = E_{\eta\zeta}\psi_A(x,y)$ , together with a linear dispersion relation  $E_{\eta\zeta} = \eta\zeta\hbar v_F k_x$ .

$$\left(\xi \hbar v_{\rm F} \partial_y - \Delta_s^{\eta}(y)\right) \phi_A(y) = 0. \tag{3.46}$$

We can explicitly solve this as

$$\phi_A(y) = C \exp\left[\frac{\zeta}{\hbar v_F} \int^y \Delta_s^{\eta}(y') \, dy'\right], \tag{3.47}$$

where C is the normalization constant. The sign  $\zeta$  is determined so as to make the wave function finite in the limit  $|y| \to \infty$ . This is a reminiscence of the Jackiw-Rebbi mode [22] presented for the chiral mode. The difference is the presence of the spin and valley indices in the wave function.

#### 3.4.4 Topological Kirchhoff Law

We consider a configuration where three different topological insulators meet at one point: See Fig. 3.9. In this configuration there are three edges forming a Y-junction. The condition which edges can make a Y-junction is the conservation of

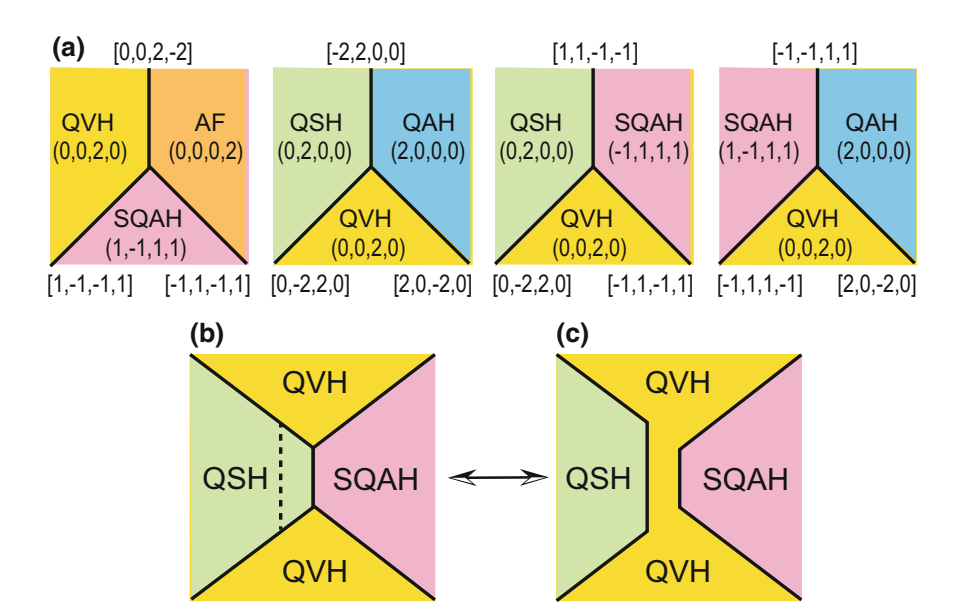


Fig. 3.9 Y junctions of topological edge currents

these topological numbers at the junction. This law is a reminiscence of the Kirchhoff law, which dictates the conservation of currents at the junction of electronic circuits. We call it the topological Kirchhoff law [9].

We present an interesting interpretation of the topological Kirchhoff law. We may regard each topological edge state as a world line of a particle carrying the four topological charges. The Y-junction may be interpreted as a scattering process of these particles. In this scattering process, the topological charges conserve. We have shown that we can control the mass of Dirac cones with the spin and valley independently in silicene.

## 3.5 Topological Quantum Field-Effect Transistor

We calculate the conductance of a nanoribbon by using the Landauer formalism. The conductance is quantized in silicene nanoribbons. Indeed, one channel has a quantized conductance  $e^2/h$ . Accordingly, the conductance is obtained by counting the number of bands. We show the conductance in Fig. 3.10. When electric field is not applied, there are helical edge states, which contribute to the conductance  $2e^2/h$  since up and down spin channels contribute to the conductance. When the electric field  $E_z$  exceeds the critical value  $E_{\rm cr}$ , the edge states disappear since the nanoribbon becomes a trivial insulator, which results in zero conductance. This means the system acts as a transistor where the "on" state can be switched to the "off" state by applying electric field. This transistor is "quantum" since the conductance is quantized, which is highly contrasted with the ordinal transistor, where the conductance is not quantized. Furthermore the conductance is topologically protected because the zero-energy edge state is topologically protected. Namely the conductance is robust against impurities due to its topological stability. Consequently we may call it a field-effect topological quantum transistor since it utilizes the minimum conductance.

The natural framework for transport calculations in nanoscopic devices is the Landauer formalism [23–26]. The conductance is given by

$$\sigma(E) = \frac{e^2}{h}T(E) \tag{3.48}$$

with the total transmission

$$T(E) = \text{Tr}[t^{\dagger}t] \tag{3.49}$$

with the transmission matrix t.

We consider a zigzag silicene nanoribbon divided into three regions: the device region, the left lead and the right lead. The size of the device region is actually irrelevant in the absence of impurities due to the ballistic transport property. The Hamiltonian is divided into submatrices

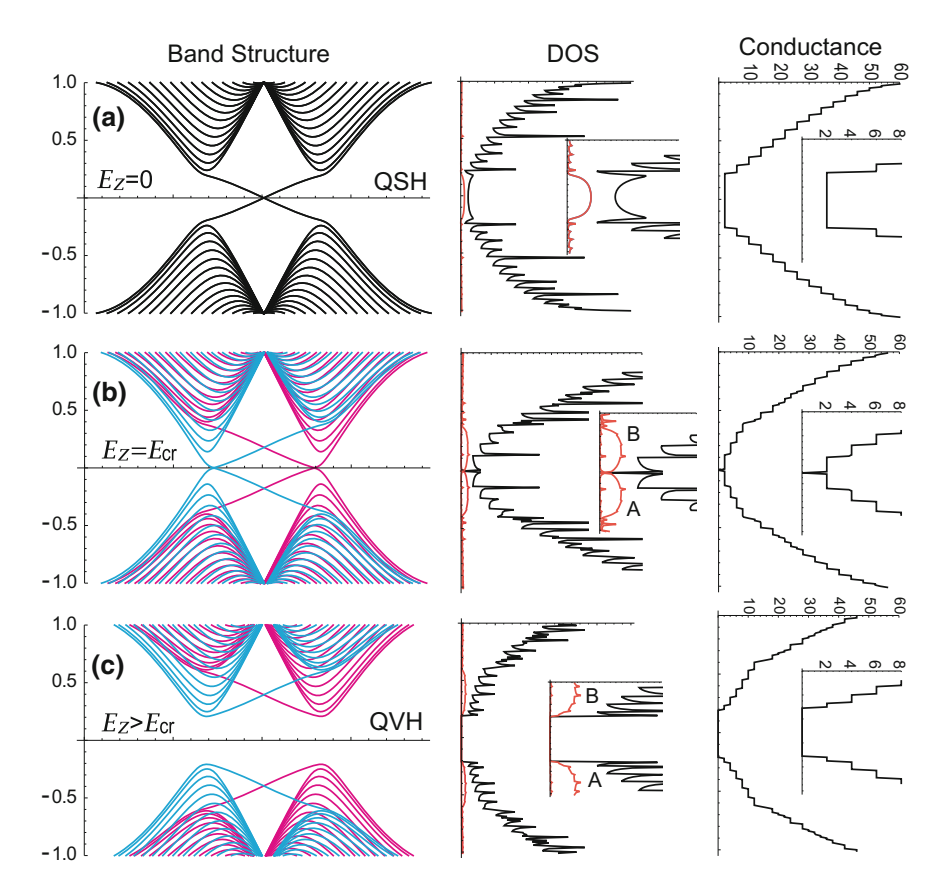


**Fig. 3.10** Band structure, DOS and conductance of zigzag silicene nanoribbons for **a** the QSH insulator phase, **b** the metallic phase at the phase transition point, and **c** the trivial insulator phase. These phases are obtained by applying electric field  $E_z$ . The phase transition occurs at  $E_z = E_{\rm cr}$ . The number of bands is 2W + 2 in the nanoribbon with width W. Here, the width is taken to be W = 31, and only a part of bands are shown. The band gap is degenerate (nondegenerate) with respect to the up (red) and down (blue) spins at  $E_z = 0$  ( $E_z > 0$ ). Van Hove singularities emerge in the DOS at the points where the band dispersion is flat. The site-resolved DOS of the up-spin state at the outmost A and B sites of a nanoribbon are shown by red curves in the insets. There are finite DOS for the zero-energy edge states in the QSH insulator. The conductance is quantized by unit of  $e^2/h$ 

$$H = \begin{pmatrix} H_{\rm L} & H_{\rm LD} & 0 \\ H_{\rm LD}^* & H_{\rm D} & H_{\rm RD} \\ 0 & H_{\rm RD}^* & H_{\rm R} \end{pmatrix}, \tag{3.50}$$

where  $H_{\rm D}$  is a finite size square matrix which dimension is equal to the number of atoms in the device region, while  $H_{\rm L}$  and  $H_{\rm R}$  are infinite size square matrices which describes the semi-infinite leads.  $H_{\rm LD}$  and  $H_{\rm RD}$  describe the coupling between the

device and leads. The Green function  $G(E) = (E - H)^{-1}$  can also be divided into submatrices as

$$G = \begin{pmatrix} G_{L} & G_{LD} & G_{LR} \\ G_{LD}^* & G_{D} & G_{RD} \\ G_{LR}^* & G_{RD}^* & G_{R} \end{pmatrix}. \tag{3.51}$$

In terms of single-particle Green's functions, the low-bias conductance  $\sigma(E)$  at the Fermi energy E is given by [23]

$$\sigma(E) = (e^2/h) \text{Tr}[\Gamma_L(E) G_D^{\dagger}(E) \Gamma_R(E) G_D(E)], \tag{3.52}$$

where  $\Gamma_{R(L)}(E) = i[\Sigma_{R(L)}(E) - \Sigma_{R(L)}^{\dagger}(E)]$  with the self-energies  $\Sigma_{L}(E)$  and  $\Sigma_{R}(E)$ , and

$$G_{\rm D}(E) = [E - H_{\rm D} - \Sigma_{\rm L}(E) - \Sigma_{\rm R}(E)]^{-1},$$
 (3.53)

with the Hamiltonian  $H_D$  for the device region. Comparing (3.49) and (3.52), we find

$$t = \Gamma_{R}(E)G_{D}(E), \tag{3.54}$$

where we have used the fact  $\Gamma_L^{\dagger}(E) = \Gamma_R(E)$ . The self-energy  $\Sigma_{L(R)}(E)$  describes the effect of the electrode on the electronic structure of the device, whose real part results in a shift of the device levels whereas the imaginary part provides a life time. They are given by

$$\Sigma_{\mathrm{L}}(E) = H_{\mathrm{LD}}^* g_{\mathrm{L}}(E) H_{\mathrm{LD}}, \quad \Sigma_{\mathrm{R}}(E) = H_{\mathrm{RD}}^* g_{\mathrm{R}}(E) H_{\mathrm{RD}},$$

together with

$$q_{\rm L}(E) = (E - H_{\rm L})^{-1}, \quad q_{\rm R}(E) = (E - H_{\rm R})^{-1}.$$
 (3.55)

Here, the dimension of  $H_L$  and  $H_R$  are infinite and we cannot obtain  $g_L(E)$  and  $g_R(E)$  as it is. This problem is solved by introducing the self energies of the lead  $\Sigma_1(E)$ ) and  $\Sigma_r(E)$  which has all information of the lead. Then we can write the semi-infinite Green function into the finite matrices

$$g_{\rm L}(E) = (E - H_0 - \Sigma_{\rm l}(E))^{-1}, \quad g_{\rm R}(E) = (E - H_0 - \Sigma_{\rm r}(E))^{-1},$$
 (3.56)

where  $H_0$  is the Hamiltonian of a unit cell in the lead. The self energies of leads are given by

$$\Sigma_{l}(E)) = H_{l}^{\dagger} \tilde{\Lambda}, \quad \Sigma_{r}(E)) = H_{l} \Lambda,$$
 (3.57)

where  $H_1$  is the coupling matrix between two neighbor unit cells in the lead  $\Lambda$  and  $\tilde{\Lambda}$  are determined by [26, 27]

$$\Lambda = t_0 + \tilde{t}_0 t_1 + \tilde{t}_0 \tilde{t}_1 t_2 + \dots + \tilde{t}_0 \tilde{t}_1 \tilde{t}_2 \dots t_n, \tag{3.58}$$

$$\tilde{\Lambda} = t_0 + t_0 \tilde{t}_1 + t_0 t_1 \tilde{t}_2 + \dots + t_0 t_1 t_2 \dots \tilde{t}_n, \tag{3.59}$$

where  $t_i$  and  $\tilde{t_i}$  are defined by the recursion relations

$$t_i = (I - t_{i-1}\tilde{t}_{i-1}\tilde{t}_{i-1}t_{i-1})^{-1}t_{i-1}^2, \tag{3.60}$$

$$t_{i} = (I - t_{i-1}\tilde{t}_{i-1}\tilde{t}_{i-1}t_{i-1})^{-1}\tilde{t}_{i-1}^{2}, \tag{3.61}$$

and

$$t_0 = (EI - H_0)^{-1} H_1^{\dagger}, \quad \tilde{t}_0 = (EI - H_0)^{-1} H_1.$$
 (3.62)

We have calculated the conductance  $\sigma(E)$  of a nanoribbon as functions of the Fermi energy E, which is controlled by doping. We give the results at electric field  $E_z = 0$ ,  $E_{cr}$  and  $2E_{cr}$  in Fig. 3.10. As E increases beyond the critical electric field  $E_{cr}$ , the Fermi level crosses a new band. A new channel opens and contributes to the conductance by  $e^2/h$  for each spin and valley.

The local density of states (DOS) at i site reads

$$\rho_i(E) = -\pi^{-1} \text{Im}[G_D(E)_{ii}], \tag{3.63}$$

in terms of the Green function  $G_D(E)$  of the device.

# 3.6 Impurity Effects to Topological Quantum Field-Effect Transistor

We investigate the impurity problem. In practical application, a field-effect transistor must be fabricated on substrate. Impurity potential will be introduced from substrate.

The helical edge states are exactly localized at the outermost edge sites. The effects of impurities are strongest when they are present at outermost edge sites. We first examine the effects when we put one or two impurities at the zigzag edge (Fig. 3.11a, b). We find that the conductance is almost unchanged, as found in Fig. 3.11c, d. Especially, the conductance at the zero energy remains to be exactly quantized. We show the distribution of the zero-energy wave function in Fig. 3.11a, b. The wave function is strictly localized at the outermost edge sites away from impurities, while it acquires nonvanishing values also at the sites detouring the impurity sites. As a result the quantization of the conductance is maintained.

Now we introduce the disorder potential by

$$H_{\rm imp} = \sum_{i} U_i c_i^{\dagger} c_i, \tag{3.64}$$

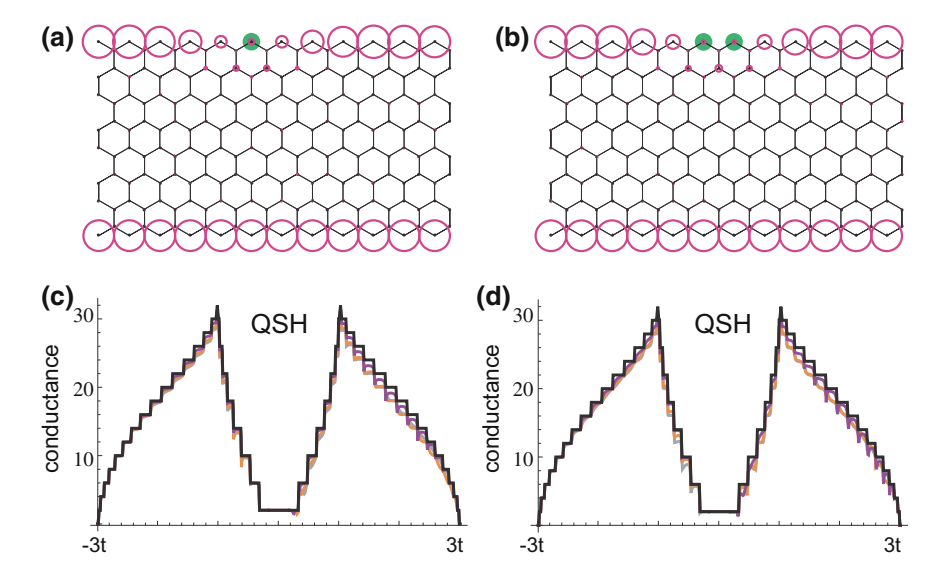


Fig. 3.11 Local DOS with **a** one impurity and **b** two impurities at the edge in the QSH phase. We set  $\lambda_{SO} = 0.2t$ , W = 7, L = 12 and V = t. The red circles denote the local DOS. The radius of the green (blue) disks denote the impurity strength with positive (negative) values. Conductance with **c** one impurity and **d** two impurities. The zero energy conductance due to the helical edge is robust against impurities. We take W = 15 and L = 12. The vertical axis is the conductance in unit of  $e^2/h$ 

where  $U_i$  takes a random distribution such that  $-V < U_i < V$ . We illustrate nanoribbons with small and large impurity strengths in Fig. 3.12a, b.

# 3.6.1 QSH Phase

We investigate the robustness of the helical edge states in the QSH phase. We show the conductance as a function of the energy in Fig. 3.12c. It is quantized when V=0, but it is reduced and not quantized in general for  $V \neq 0$ . It is greatly reduced away from the half filling. However, the conductance around the Fermi energy remains quantized below a certain impurity strength. This is understood as follows. The conductance at  $|E| < \lambda_{SO}$  is due to the helical edge states. The helical edge states are robust against impurities since it is topologically protected.

# 3.6.2 *QVH Phase*

We investigate the conductance in the QVH phase by applying electric field  $E_z = 2\lambda_{SO}$ . The helical edge states are absent and the conductance becomes zero in

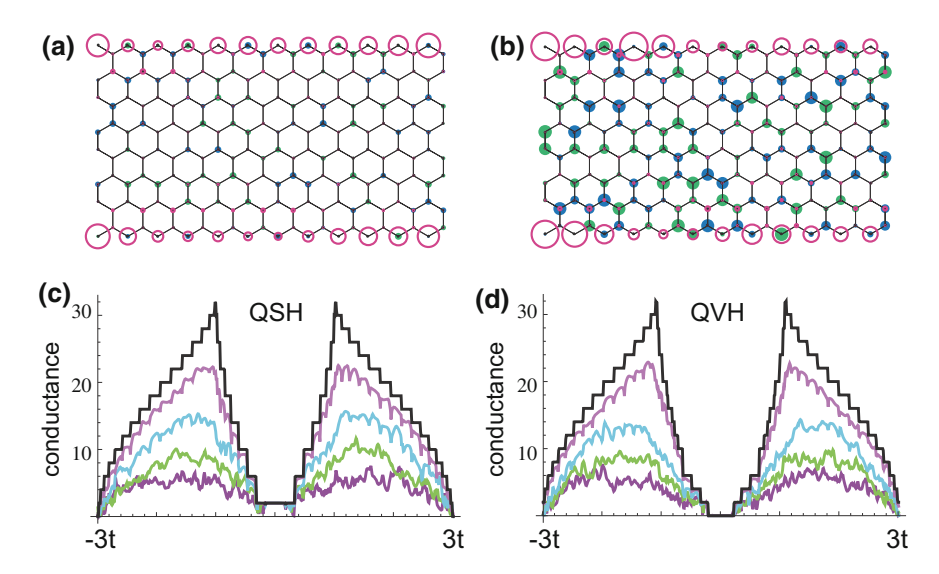


Fig. 3.12 Local DOS at the Fermi energy for **a** small impurity strength  $V=2\lambda_{\rm SO}$  and **b** strong impurity strength  $V=5\lambda_{\rm SO}$ . We set  $\lambda_{\rm SO}=0.2t$ , W=7 and L=12. The red circles denote the local DOS. The radius of the green (blue) disks denote the impurity strength with positive (negative) values. Conductance as a function of the energy for various impurity strength  $V/\lambda_{\rm SO}=0,1,2,3,4$  in **c** the QSH phase and **d** the QVH phase  $(E=2\lambda_{\rm SO})$ . The zero energy conductance due to the helical edge is robust against impurities. We take W=15 and L=12. The vertical axis is the conductance in unit of  $e^2/h$ 

the pure system, as shown in Fig. 3.10b. We show the conductance with impurities in Fig. 3.12d. The conductance inside the bulk band gap remains to be exactly zero even when the impurities are introduced. On the other hand, the conductance outside the band gap is similar to that of the QSH phase.

In order to investigate the reason why the conductance is quantized even in the presence of impurities, we analyze the local DOS at the Fermi energy. Fig. 3.12a shows the local DOS for small impurities, while Fig. 3.12b shows that for large impurities. We find the helical edges survive for small impurities although its magnitude of local DOS fluctuates. However the helical edges is largely deformed for large impurities.

We next discuss the zero-energy conductance as a function of the impurity strength V by changing the width and the length of a nanoribbon. In Fig. 3.13a, we show the zero-energy conductance for various width with the length fixed. The conductance is found to be robust for wider nanoribbons. In Fig. 3.13b, we show the zero-energy conductance for various length with the width fixed. The conductance is robust for shorter nanoribbons. It is important that the conductance is quantized even for values larger than  $\lambda_{\rm SO}$  in certain cases.

We have investigated the impurity effects to the topological transistor, which will be important for practical applications. It is shown that the topological edge states are very robust against impurities, which is highly contrasted with the ordinary transistor.

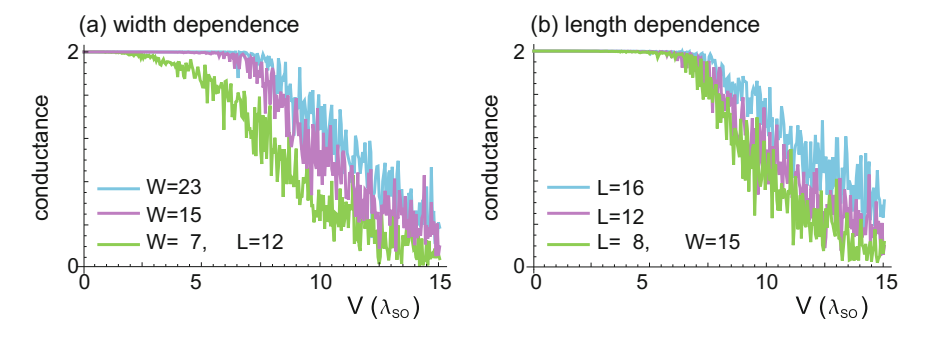


Fig. 3.13 Zero-energy conductance as a function of the impurity strength V a for W=7, 15, 23 with the fixed Length L=12 and b for L=8, 12, 16 for the fixed W=15. The horizontal axis is the impurity strength V in unit of  $\lambda_{SO}$ . We have taken  $\lambda_{SO}=0.2t$ . The vertical axis is the conductance in unit of  $e^2/h$ . The zero-energy conductance is quantized even at a much higher impurity strength than  $\lambda_{SO}$ 

This robustness enables us to make fault tolerant devices. Our results will open a new field of topological electronics based on topological edge states.

#### 3.7 Phosphorene and Anisotropic Honeycomb Lattice

We investigate the honeycomb system where the hoppings are anisotropic. The Hamiltonian is modified as

$$\hat{H} = \sum_{s} \int d^{2}k' \left( c_{A}^{\dagger}, c_{B}^{\dagger} \right) \begin{pmatrix} 0 & f\left(\mathbf{k'}\right) \\ f^{*}\left(\mathbf{k'}\right) & 0 \end{pmatrix} \begin{pmatrix} c_{A} \\ c_{B} \end{pmatrix}, \tag{3.65}$$

with

$$f(\mathbf{k}') = t_1 e^{-iak_y'/\sqrt{3}} + 2t_2 e^{iak_y'/2\sqrt{3}} \cos \frac{ak_x'}{2}.$$
 (3.66)

The energy spectrum reads

$$E\left(\mathbf{k}'\right) = |f\left(\mathbf{k}'\right)| = \sqrt{t_1^2 + 4t_1t_2\cos\frac{ak_x'}{2}\cos\frac{\sqrt{3}ak_y'}{2} + 4t_2^2\cos^2\frac{ak_x'}{2}}.$$
 (3.67)

We show the band structure in Fig. 3.14. The gap closes at

$$\mathbf{K}_{\xi} = \frac{1}{a} \left( \frac{2}{\pi} \arctan\left( -\frac{t_1}{2t_2}, \xi \frac{\sqrt{4t_2^2 - t_1^2}}{2t_2} \right), 0 \right), \tag{3.68}$$

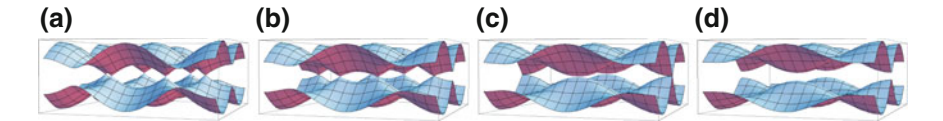


**Fig. 3.14** The band structure of the anisotropic honeycomb lattice for  $\mathbf{a} t_1 = 1$ ,  $\mathbf{b} t_1 = 1.5$ ,  $\mathbf{c} t_1 = 2$  and  $\mathbf{d} t_1 = 2.5$ . We have set  $t_2 = 1$ . Two inequivalent Dirac cones merge at  $t_1 = 2t_2$  and the system becomes gapped for  $t_1 > 2t_2$ 

when  $4t_2^2 - t_1^2 < 0$ . These two points merge at  $4t_2^2 - t_1^2 = 0$ . On the other hand, there are no solutions for  $4t_2^2 - t_1^2 < 0$ , which means that the system is gapped.

We make the Taylor expansion of (3.66) around **M** point. By setting  $\mathbf{k}' = \mathbf{M} + \mathbf{k}$ , we obtain

$$f(\mathbf{k} + \mathbf{M}) = m + uk_x^2 - ivk_y$$
 for  $|\mathbf{k}| \ll a^{-1}$ , (3.69)

with

$$m = t_1 - 2t_2, \qquad u = \frac{\pi^2}{4}t_2, \qquad v = \frac{\pi}{\sqrt{3}}(t_1 + t_2).$$
 (3.70)

Hence, the low-energy physics near the Fermi energy is described by

$$H = \left(m + uk_x^2\right)\tau_x + vk_y\tau_y. \tag{3.71}$$

The dispersion is linear along the  $k_y$ -axis, while it is parabolic along the  $k_x$ -axis

$$E\left(\mathbf{k} + \mathbf{K}_{\xi}\right) = \pm \sqrt{\left(m + uk_{x}^{2}\right)^{2} + v^{2}k_{y}^{2}}.$$
(3.72)

The gap closes at m = 0. This type of Hamiltonian and energy dispersion are naturally realized in phosphorene, monolayer black phosphorus [28].

# 3.7.1 Band Structure of Anisotropic Honeycomb Nanoribbons

We investigate the change of the band structure of nanoribbon by changing the parameter  $t_2$  continuously with  $t_1$  being fixed [28]. We show the band structure with (a) the zigzag-zigzag edges, (b) the zigzag-beard edges, and (c) the beard-beard edges in Fig. 3.15 for typical values of  $t_1$  and  $t_2$ .

(i) We start with the case  $t_2 = |t_1|$ , where the energy spectrum (3.67) becomes that of graphene with two Dirac cones at the K and K' points. The perfect flat band emerges and connects the K and K' points, that is, it lies for (a)  $-\pi \le ak \le -\frac{2}{3}\pi$  and  $\frac{2}{3}\pi \le ak \le \pi$ ; (b)  $-\pi \le ak \le \pi$ ; (c)  $-\frac{2}{3}\pi \le ak \le \frac{2}{3}\pi$ . It is attached to the bulk band. See Fig. 3.15a-c.

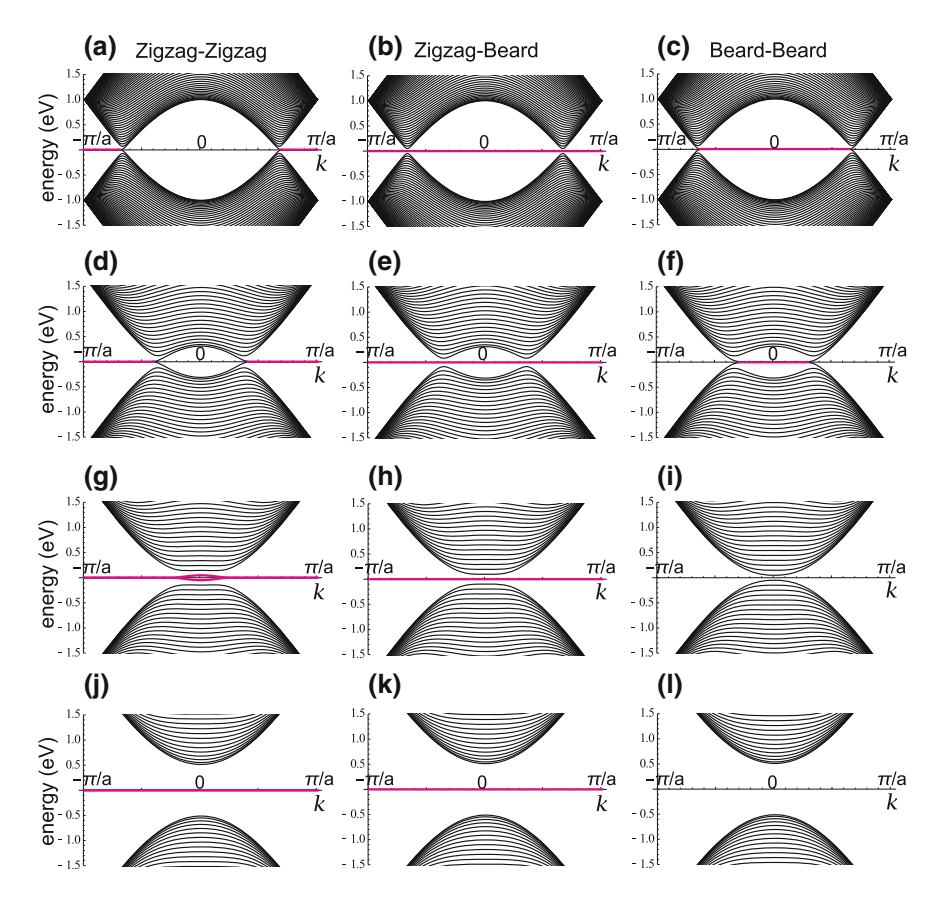


**Fig. 3.15** Band structure of anisotropic honeycomb nanoribbons. The flat edge states are marked in magenta. We have also set  $\mathbf{a}$ - $\mathbf{c}$   $t_1 = 1$ ,  $\mathbf{d}$ - $\mathbf{f}$   $t_1 = 1.7$ ,  $\mathbf{g}$ - $\mathbf{i}$   $t_1 = 2$ ,  $\mathbf{j}$ - $\mathbf{l}$   $t_1 = 2.5$ . The unit cell contains 144 atoms. We have set  $t_2 = 1$ 

- (ii) As we increase  $t_2$  but keeping  $t_1$  fixed, the two Dirac points move towards k = 0, as is clear from (3.68). The flat band keeps to be present and connect the two Dirac points. See Fig. 3.15d–f.
- (iii) At  $|t_2| = 2 |t_1|$ , the two Dirac points merge into one Dirac point at k = 0, as implied by (3.68). The flat band touches the bulk band at k = 0 for the zigzagzigzag nanoribbon and the zigzag-beard nanoribbon, but disappears from the beard-beard nanoribbon. See Fig. 3.15g-i.
- (iv) For  $|t_2| > 2 |t_1|$ , the bulk band shifts away from the Fermi level. The flat band is disconnected from the bulk band for the zigzag-zigzag nanoribbon and the zigzag-beard nanoribbon, where it extends over all region  $-\pi \le k \le \pi$ . On the other hand, the edge band becomes a part of the bulk band and disappears from the Fermi level for the beard-beard nanoribbon. See Fig. 3.15j–l.

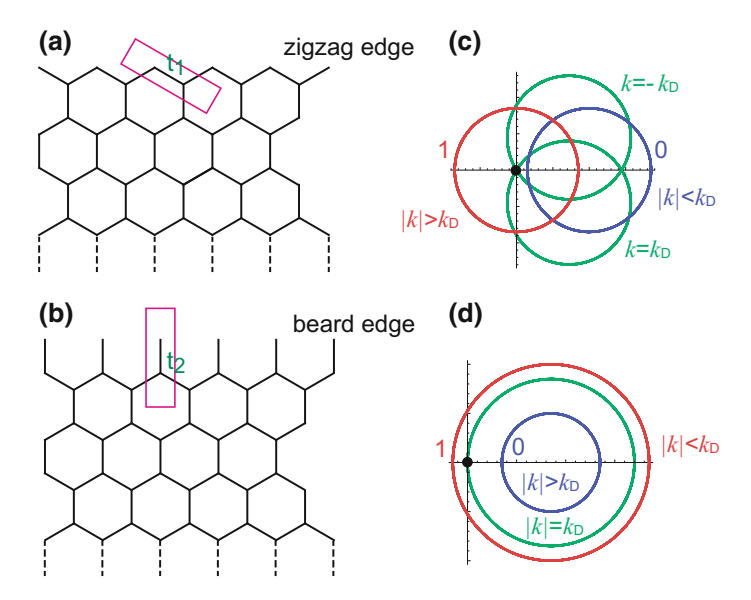


**Fig. 3.16** Unit cells and winding numbers for the zigzag and beard edges. It is necessary to make a gauge fixing in the Hamiltonian so that the hopping between the two atoms in the unit cell becomes real, namely, **a**  $t_1$  for the zigzag edge and **b**  $t_2$  for the beard edge. **c**, **d** The winding number reads  $N_{\text{wind}}(k) = 1$  if the loop encircles the origin (red circle), and  $N_{\text{wind}}(k) = 0$  if not (blue circle). The origin is represented by a dot, where the Hamiltonian is ill defined

# 3.7.2 Topological Origin of Flat Bands

The topological origin of the flat band has been discussed in graphene [29]. It is straightforward to apply the reasoning to the anisotropic honeycomb-lattice model (3.65). We consider one-dimensional Hamiltonian  $H_k(k_x)$  in the  $k_x$  space, which is given by the 2-band model (3.65) at a fixed value of  $k \equiv k_y$ . We analyze the topological property of this one-dimensional Hamiltonian. Because the  $k_x$  space is a circle due to the periodic condition, the homotopy class is  $\pi_1(S^1) = \mathbb{Z}$ .

We write the Hamiltonian as

$$H_k(k_x) = \begin{pmatrix} 0 & F_k(k_x) \\ F_k^*(k_x) & 0 \end{pmatrix}.$$
 (3.73)

It is important to remark that the gauge degree of freedom is present in this Hamiltonian. Indeed the phase of the term  $F_k(k_x)$  is irrelevant for the energy spectrum of the bulk system. However, this is not the case for the analysis of a nanoribbon since the way of taking the unit cell is inherent to the type of nanoribbon, as illustrated in Fig. 3.16. It is necessary to make a gauge fixing so that the hopping between the two atoms in the unit cell becomes real, namely,  $t_1$  for the zigzag edge and  $t_2$  for the beard edge.

For the zigzag edge we thus make the gauge fixing such that

$$F_k(k_x) = e^{-i(\frac{1}{2\sqrt{3}}a_xk_x + \frac{1}{2}ak)}(f_1 + f_2) = t_1\left(1 + e^{-iak}\right) + t_2e^{-i\frac{1}{2}\left(\sqrt{3}a_xk_x - ak\right)}, \quad (3.74)$$

where the parameter k corresponds to the momentum of zigzag nanoribbons. Here,  $t_1$  for the link in the unit cell and  $e^{-iak}t_1$  for the neighboring link (Fig. 3.16a). The topological number of the one-dimensional system is given by

$$N_{\text{wind}}(k) = \frac{1}{2\pi i} \oint dk_x \, \partial_{k_x} \log F_k(k_x). \tag{3.75}$$

By an explicit evaluation,  $N_{\text{wind}}(k)$  is found to take only two values;  $N_{\text{wind}} = 1$  for  $|k| < k_{\text{D}}$ , and  $N_{\text{wind}} = 0$  for  $\pi \ge |k| > k_{\text{D}}$ . We may interpret this as the winding number as follows. We consider the complex plane for  $F_k(k_x) = |F_k(k_x)| \exp[i\Theta_k(k_x)]$ . The quantity  $N_{\text{wind}}(k)$  counts how many times the complex number  $F_k(k_x)$  winds around the origin as  $k_x$  moves from 0 to  $2\pi/a$  for a fixed value of k. Note that the origin implies  $F_k(k_x) = 0$ , where the Hamiltonian is ill defined. We have shown such a loop for typical values of k in Fig. 3.16b, where the horizontal axis is for  $\text{Re}[F_k(k_x)]$  and the vertical axis is for  $\text{Im}[F_k(k_x)]$ ,

$$Re[F_k(k_x)] = t_1(1 + \cos ak) + t_2 \cos \frac{1}{2} \left( \sqrt{3}a_x k_x - ak \right), \tag{3.76}$$

$$Im[F_k(k_x)] = t_1 \sin ak + t_2 \sin \frac{1}{2} \left( \sqrt{3} a_x k_x - ak \right).$$
 (3.77)

The loop surrounds the origin and  $N_{\text{wind}}(k) = 1$  when  $-\pi \le k < -k_{\text{D}}$  and  $k_{\text{D}} < k \le \pi$ , while it does not and  $N_{\text{wind}}(k) = 0$  when  $|k| < k_{\text{D}}$ : The loop touches the origin when  $k = \pm k_{\text{D}}$ . We have demonstrated that the system is topological for  $|k| > k_{\text{D}}$  and trivial for  $|k| < k_{\text{D}}$ .

We next appeal to the bulk-edge correspondence to the topological system. When we cut the bulk along the y direction, the one-dimensional system has an edge. Since the edge separates a topological insulator and the trivial state (i.e., the vacuum state), the gap must close at the edge, namely, there must appear a gapless edge mode. The gapless edge mode appears for all  $|k| < k_{\rm D}$ , implying the emergence of a flat band connecting the two Dirac points given by (3.68).

For the beard edge we make the gauge fixing such that

$$F_k(k_x) = e^{i\frac{1}{\sqrt{3}}a_x k_x} (f_1 + f_2), \tag{3.78}$$

and carry out an analogous argument. See Fig. 3.16. We reach at the conclusion that a flat band appears for  $|k| > k_D$  and connects the two Dirac points given by (3.68) but in an opposite way to the case of the zigzag edge.

## 3.7.3 Wave Function and Energy Spectrum of Edge States

We have explained how the flat band appears in the anisotropic honeycomb-lattice model. The flat band corresponds to the quasi-flat band in the original Hamiltonian (3.65).

We construct an analytic form of the wave function at the zero-energy state in the anisotropic honeycomb-lattice model (3.65) as follows. We label the wave function of the atom on the outer most site as  $\psi_1$ , and that of the atom next to it as  $\psi_2$ , and as so on. The total wave function is  $\psi = \{\psi_1, \psi_2, \dots, \psi_N\}$  if there are N atoms across the nanoribbon. The Hamiltonian is explicitly written as

$$H = \begin{pmatrix} 0 & t_1 g & 0 & 0 & \cdots \\ t_1 g^* & 0 & t_2 & 0 & \cdots \\ 0 & t_2 & 0 & t_1 g & \cdots \\ 0 & 0 & t_1 g^* & 0 & \cdots \\ \cdots & \cdots & \cdots & \cdots \end{pmatrix}, \tag{3.79}$$

with  $g=1+e^{-iak}$ . The eigenvalue problem  $H\psi=0$  is easily solved [30], yielding  $\psi_{2n}=0$  and  $\psi_{2n+1}=\left[t_1\left(1+e^{iak}\right)/t_2\right]^n\psi_1$ . By solving the Hamiltonian matrix recursively from the outer most site, we obtain the analytic form of the local density of states of the wave function for odd site j,

$$|\psi(j)| = \alpha^j \sqrt{1 - \alpha^2},\tag{3.80}$$

with  $\alpha = 2|t_1|(\cos\frac{ak}{2})/|t_2|$ . The wave function is zero for even site. It is perfectly localized at the outer most site when  $ak = \pi$ , and describes the flat band.

#### References

- M. Ezawa, Antiferromagnetic topological superconductor and electrically controllable Majorana fermions. Phys. Rev. Lett. 114, 056403 (2015)
- P. Vogt, P. De Padova, C. Quaresima, J. Avila, E. Frantzeskakis, M.C. Asensio, A. Resta, B. Ealet, G. Le Lay, Silicene: compelling experimental evidence for graphenelike two-dimensional silicon. Phys. Rev. Lett. 108, 155501 (2012)
- L. Tao et al., Silicene field-effect transistors operating at room temperature. Nat. Nanotechnol. (2015). https://doi.org/10.1038/nnano.2014.325
- M. Ezawa, Topological insulator and helical zero mode in silicene under inhomogeneous electric field. New J. Phys. 14, 033003 (2012)
- N.D. Drummond, V. Zolyomi, V.I. Fal'ko, Electrically tunable band gap in silicene. Phys. Rev. B 85, 075423 (2012)
- M. Ezawa, Valley-polarized metals and quantum anomalous Hall effect in silicene. Phys. Rev. Lett 109, 055502 (2012)
- M. Ezawa, Photoinduced topological phase transition and a single Dirac-cone state in silicene. Phys. Rev. Lett. 110, 026603 (2013)
- 8. M. Ezawa, Quantized conductance and field-effect topological quantum transistor in silicene nanoribbons. Appl. Phys. Lett. **102**, 172103 (2013)

- 9. M. Ezawa, N. Nagaosa, Interference of topologically protected edge states in silicene nanoribbons. Phys. Rev. B 88, 161406 (R) (2013)
- M. Ezawa, E. Salomon, P. De Padova, D. Solonenko, P. Vogt, M.E. Dvila, A. Molle, T. Angot, G. Le Lay, Fundamentals and functionalities of silicene, germanene, and stanene. La Rivista del Nuovo Cimento 41, 175 (2018)
- R. Saito, G. Dresselhaus, M.S. Dresselhaus, *Physical Properties of Carbon Nanotubes* (Imperial College Press, London, 1998)
- M.I. Katsnelson, Graphene: Carbon in Two Dimensions (Cambridge University Press, Cambridge, 2012)
- H.B. Nielsen, M. Ninomiya, A no-go theorem for regularizing chiral fermions. Phys. Lett. B 105, 219 (1981)
- C.-C. Liu, H. Jiang, Y. Yao, Low-energy effective Hamiltonian involving spin-orbit coupling in silicene and two-dimensional germanium and tin. Phys. Rev. B 84, 195430 (2011)
- C.-C. Liu, W. Feng, Y. Yao, Quantum spin Hall effect in silicene and two-dimensional germanium. Phys. Rev. Lett. 107, 076802 (2011)
- C.L. Kane, E.J. Mele, Quantum spin Hall effect in graphene. Phys. Rev. Lett. 95, 226801 (2005); Z<sub>2</sub> topological order and the quantum spin Hall effect. Ibid 95, 146802 (2005)
- 17. Y. Xu, B. Yan, H.-J. Zhang, J. Wang, G. Xu, P. Tang, W. Duan, S.-C. Zhang, Large-gap quantum spin Hall insulators in tin films. Phys. Rev. Lett. 111, 136804 (2013)
- M. Ezawa, Spin-valleytronics in silicene: quantum spin Hall-quantum anomalous Hall insulators and single-valley semimetals. Phys. Rev. B 87, 155415 (2013)
- X. Li, T. Cao, Q. Niu, J. Shi, J. Feng, Coupling the valley degree of freedom to antiferromagnetic order. PNAS 110, 3738 (2013)
- Q.-F. Liang, L.-H. Wu, X. Hu, Electrically tunable topological state in [111] perovskite materials with an antiferromagnetic exchange field. New J. Phys. 15, 063031 (2013)
- 21. D.J. Thouless, M. Kohmoto, M.P. Nightingale, M. den Nijs, Quantized Hall conductance in a two-dimensional periodic potential. Phys. Rev. Lett. **49**, 405 (1982)
- 22. R. Jackiw, C. Rebbi, Solitons with fermion number 1/2. Phys. Rev. D 13, 3398 (1976)
- S. Datta, Electronic Transport in Mesoscopic Systems (Cambridge University Press, Cambridge, England, 1995): Quantum Transport: Atom to Transistor (Cambridge University Press, England, 2005)
- F. Muñoz-Rojas, D. Jacob, J. Fernández-Rossier, J.J. Palacios, Coherent transport in graphene nanoconstrictions. Phys. Rev. B 74, 195417 (2006)
- 25. L.P. Zârbo, B.K. Nikolić, Spatial distribution of local currents of massless Dirac fermions in quantum transport through graphene nanoribbons. EPL 80, 47001 (2007): D.A. Areshkin, B.K. Nikolić, I-V curve signatures of nonequilibrium-driven band gap collapse in magnetically ordered zigzag graphene nanoribbon two-terminal devices. Phys. Rev. B 79, 205430 (2009)
- T.C. Li, S.-P. Lu, Quantum conductance of graphene nanoribbons with edge defects. Phys. Rev. B 77, 085408 (2008)
- M.P.L. Sancho, J.M.L. Sancho, J. Rubio, Highly convergent schemes for the calculation of bulk and surface Green functions. J. Phys. F: Met. Phys. 15, 851 (1985)
- M. Ezawa, Electrically tunable conductance and edge modes in topological crystalline insulator thin films: tight-binding model analysis. New J. Phys. 16, 115004 (2014)
- S. Ryu, Y. Hatsugai, Topological origin of zero-energy edge states in particle-hole symmetric systems. Phys. Rev. Lett. 89, 077002 (2002)
- M. Kohmoto, Y. Hasegawa, Zero modes and edge states of the honeycomb lattice. Phys. Rev. B 76, 205402 (2007)

# Chapter 4 Optical Properties of Silicene and Related Materials from First Principles



Friedhelm Bechstedt, Lars Matthes, Paola Gori and Olivia Pulci

**Abstract** Slightly buckled, graphene-like honeycomb crystals made by silicon, silicene, or by other group-IV elements such as germanene and stanene represent atomically thin films, i.e., two-dimensional (2D) systems. The theoretical description of their optical properties suffers from three difficulties, (i) a thickness much smaller than the wavelength of light, (ii) their common modeling by superlattice arrangements with sufficiently large layer distances, and (iii) the inclusion of many-body effects. Here, the solutions of all problems are discussed. (i) The optical response of an individual honeycomb crystal is described by a tensor of 2D optical conductivities or dielectric functions, which are related to the optical response of the corresponding superlattice. (ii) The influence of such a sheet crystal on the transmittance, reflectance and absorbance of a layer system is described. (iii) Excitonic and quasiparticle effects are demonstrated to widely cancel each other. Silicene sheets are investigated in detail. As a consequence of the linear bands and Dirac cones the low-frequency absorbance is defined by the Sommerfeld finestructure constant. Van Hove singularities represented by critical points in the interband structure are identified at higher photon energies. Clear chemical trends along the row

F. Bechstedt (⋈) · L. Matthes

Institut für Festkörpertheorie und -optik, Friedrich-Schiller-Universität Jena, Max-Wien-Platz 1, 07743 Jena, Germany

e-mail: bechsted@ifto.physik.uni-jena.de

L. Matthes

e-mail: lars.matthes@uni-jena.de

P. Gori

Dipartimento di Ingegneria, Università "RomaTre", Via della Vasca Navale 79, 00146 Roma, Italy

e-mail: paola.gori@uniroma3.it

O. Pulci

Dipartimento di Fisica, Università di Roma "Tor Vergata", via della Ricerca Scientifica 1, 00133 Roma, Italy e-mail: olivia.pulci@roma2.infn.it

© Springer Nature Switzerland AG 2018 P. Vogt and G. Le Lay (eds.), *Silicene*, NanoScience and Technology, https://doi.org/10.1007/978-3-319-99964-7\_4

 $C \rightarrow Si \rightarrow Ge \rightarrow Sn$  are derived. The influence of multiple layers is studied for the cases of bilayer silicene and graphene.

#### 4.1 Introduction

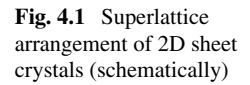
The knowledge of the optical properties of novel two-dimensional (2D) crystals made by group-IV elements Si, Ge, and Sn such as silicene, germanene, and stanene [1] is very important for both spectroscopic studies of the 2D materials and optoelectronic applications. Optical studies have been performed in a wide frequency range for the most stable 2D honeycomb structure of the group-IV element carbon (C), the graphene [2–5]. However, not only the basic optical properties of graphene, silicene and related materials are of interest. Optical studies can also help to understand the growth process or preparation of the 2D systems on certain substrates [6, 7]. This has been clearly demonstrated for silicene-like overlayers on Ag(110) and Ag(111) surfaces by surface-sensitive methods [8, 9].

Also for 2D crystals spectral features in the optical spectra can be easily related to the atomic geometry, electronic structure, and many-body effects. This has been shown for the absorbance spectrum of graphene, where the peak at 4.62 eV can been clearly related to a 2D saddle-point exciton [4]. However, the propagation of light in and through atomically thin materials films and their optical response in general are controversially discussed in literature due to the vanishing layer thickness but the request to reach macroscopic films by stacking of atomic layers. Thereby, the main problems are related to the optical response perpendicular to the 2D sheets and the formulation of the boundary conditions for electromagnetic field [1, 10–13]. The description of optical properties of silicene and related group-IV materials will be discussed in this chapter.

#### 4.2 Theoretical and Numerical Methods

#### 4.2.1 Atomic and Electronic Structure

The majority of calculations of ground-state, electronic and spectroscopic properties presented here are based on the density functional theory (DFT, see Chap. 2) as implemented in the Vienna ab initio simulation package (VASP) [14, 15]. Discussing many-body effects such as the influence of excitons we also use another implementation of DFT in the Quantum Espresso code [16]. In the first implementation exchange and correlation (XC) are described within the generalized gradient approximation (GGA) [17, 18]. Pseudopotentials for  $C1s^2$ ,  $Si1s^22s^23p^6$ ,  $Ge1s^22s^22p^63s^23p^63d^{10}$ , and  $Sn1s^22s^22p^63s^23p^63d^{10}4s^24p^64d^{10}$  cores and all-electron-like wave functions are generated within the projector-augmented wave (PAW) method [19, 20].



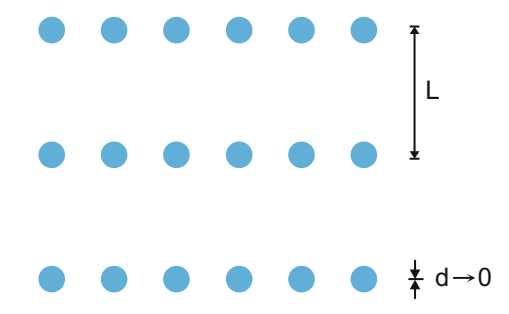


**Table 4.1** Structural (buckling  $\Delta$ , lattice constant a) and electronic (Fermi velocity  $v_F$ , SOC-induced fundamental gap  $E_g$ ) parameters. Electronic quantities are derived from hybrid HSE06 (GGA) calculations

Parameter	Graphene	Silicene	Germanene	Stanene
a (Å)	2.468	3.868	4.060	4.673
Δ (Å)	0.00	0.45	0.69	0.85
$v_F (10^6 \text{ ms}^{-1})$	1.01 (0.83)	0.65 (0.53)	0.62 (0.52)	0.55 (0.48)
$E_g \text{ (meV)}$	0.0 (0.0)	1.9 (1.5)	33 (24)	101 (73)

The wave functions between the cores are expanded in plane waves with a kinetic energy cutoff of 500 eV. In the second DFT version we use the local density approximation (LDA) [16]. Norm-conserving pseudopotentials are employed.

The isolated (free standing) C, Si, Ge, and Sn honeycomb layers are simulated by a repeated slab approximation [21], basically a graphite-like superlattice arrangement with a large superlattice period L (see Fig. 4.1). Typically a distance L=20 Å between two adjacent layers is chosen. The integration over the corresponding flat and, hence, 2D Brillouin zone (BZ) is replaced by a  $\Gamma$ -centered  $N\times N\times 1$  **k**-point mesh of the Monkhorst-Pack type [22]. For total energy calculations and structural optimizations but also calculations of the frequency-dependent dielectric function N=400 is used [23]. For freestanding group-IV honeycomb crystals the low-buckled geometries with an alternating buckling  $\Delta$  of the two atoms in a unit cell are energetically favored [24, 25], with graphene the only exception. Even when high-buckled geometries are energetically favored within a  $1\times 1$  lateral unit cell, softening of phonons branches suggests their instability. The resulting buckling values [26] are listed in Table 4.1. They demonstrate a clear chemical trend indicating a change from pure  $sp^2$  bonding (graphene) to an almost  $sp^3$  bonding (stanene).

The band structures described by the Kohn-Sham eigenvalues of the DFT-GGA or -LDA are well known. In general, the calculation of the optical properties requires the inclusion of excitation aspects, the real or virtual generation of quasielectrons and quasiholes, which are renormalized by the interaction with the other electrons, and their direct screened Coulomb attraction or unscreened electron-hole exchange interaction [27]. In many cases, solving the generalized Kohn-Sham equation with a hybrid functional, e.g. HSE06 [28], may give results which approach quasiparticle

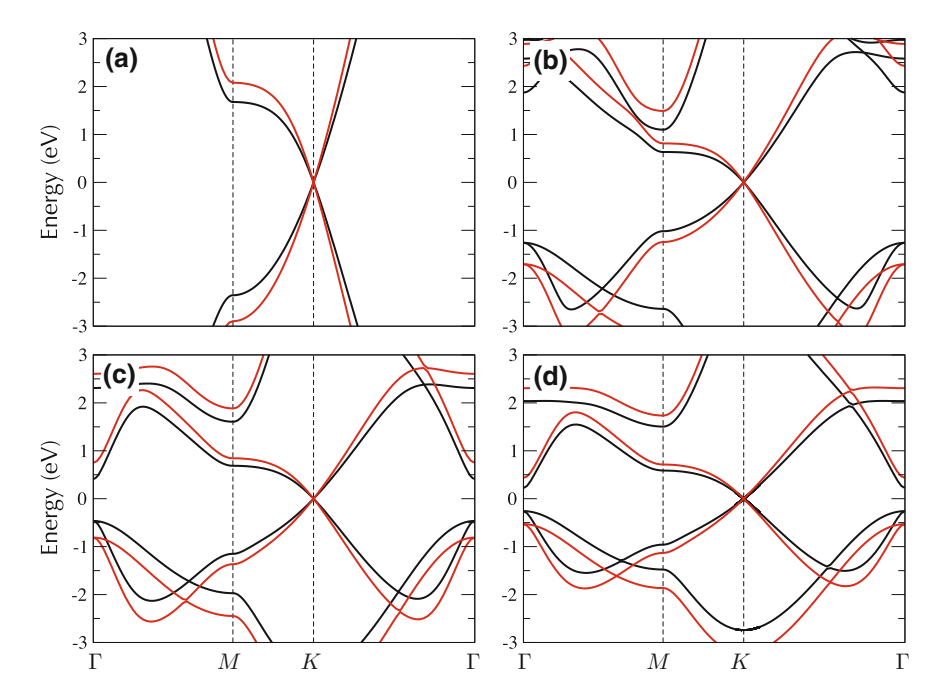


**Fig. 4.2** Comparison of the band structures along high-symmetry lines in the 2D BZ of (a) graphene, (b) silicene, (c) germanene and (d) stanene in the DFT-GGA approach (black curves) and with quasiparticle corrections in the HSE06 framework (red curves). The Fermi level is fixed at zero energy

values [29]. The resulting band structures [26] are compared in Fig. 4.2 with those derived within the DFT-GGA framework [23].

The characteristic parameters of the Dirac cones near the K (or K') points of the BZ boundary, i.e., the Fermi velocity  $v_F$  of the linear bands, and the spin-orbit-coupling (SOC)-induced gap are also listed in Table 4.1. Qualitatively band structures similar to the HSE06 ones in Fig. 4.2 are generated when quasiparticle corrections within the GW approach [27] are added to the DFT-GGA Kohn-Sham eigenvalues. The electronic parameters in Table 4.1 indicate that the linear bands vary much stronger with the wave vector in the quasiparticle picture. The increased Fermi velocity approaches the experimental value for graphene [30]. The SOC-induced gaps indicate that effects of SOC need to be mainly taken into account for heavy elements, i.e., germanene and stanene.

# 4.2.2 Frequency-Dependent Dielectric Function

The frequency-dependent optical properties of the 2D crystals are derived from the dielectric tensor  $\hat{\epsilon}_{SL}(\omega)$  of the superlattice (SL) arrangement in Fig. 4.1. In the

independent-particle approximation (IPA) or independent-quasiparticle approximation (IQPA) (also called random phase approximation (RPA)) [31] the two independent in-plane ( $\parallel$ ) and out-of-plane ( $\perp$ ) components of the dielectric tensor can be written in form of an Ehrenreich-Cohen formula for completely empty conduction (c) and filled valence (v) bands

$$\epsilon_{SL}^{\parallel/\perp}(\omega) = 1 + \frac{8\pi}{LA} \sum_{c,v} \sum_{\mathbf{k}} \left| M_{cv}^{\parallel/\perp}(\mathbf{k}) \right|^2 \sum_{\beta = \pm} \frac{1}{\varepsilon_c(\mathbf{k}) - \varepsilon_v(\mathbf{k}) + \beta(\hbar\omega + i\gamma)}$$
(4.1)

with A as the sheet area. Within the longitudinal approach [32] the optical transition matrix elements are given by

$$M_{cv}^{\parallel/\perp}(\mathbf{k}) = \lim_{\mathbf{q}_{\parallel/\perp} \to 0} \frac{e/\sqrt{4\pi\epsilon_0}}{|\mathbf{q}_{\parallel/\perp}|} \langle c\mathbf{k} \left| e^{i\mathbf{q}_{\parallel/\perp}\mathbf{r}} \right| v\mathbf{k} + \mathbf{q}_{\parallel/\perp} \rangle$$
(4.2)

for a vanishing wave vector  $\mathbf{q}_{\parallel/\perp}$  (whose direction is later identified with the light polarization) between Bloch states  $|v\mathbf{k}\rangle \to |c\mathbf{k}\rangle$  with  $\mathbf{k} \in \mathrm{BZ}$ . The excited (quasi)electron-(quasi)hole pairs possess energies  $[\varepsilon_c(\mathbf{k}) - \varepsilon_v(\mathbf{k})]$  and a lifetime  $1/\gamma$ .

Within the PAW approach the Bloch functions are all-electron functions. The corresponding Hamiltonian is local in space and, hence, the dipole matrix element (4.2) can be directly related to the optical transition matrix element of the momentum operator  $\bf p$  [27]. Equation (4.2) can be rewritten to

$$M_{cv}^{\parallel/\perp}(\mathbf{k}) = \frac{e/\sqrt{4\pi\epsilon_0}\hbar}{m} \frac{\langle c\mathbf{k}|\mathbf{p}_{\parallel/\perp}|v\mathbf{k}\rangle}{\varepsilon_c(\mathbf{k}) - \varepsilon_v(\mathbf{k})}.$$
 (4.3)

The appearance of the momentum-operator matrix element can be also interpreted as the use of the transverse gauge of the electromagnetic field.

The in-plane component of the resulting dielectric tensor is displayed in Fig. 4.3 for graphene, silicene, and germanene within the DFT-HSE06 description. The poles for  $\omega \to 0$  and the peaks arising from van Hove singularities are clearly visible. The latter spectral features can be easily explained in terms of the interband structure and joint density of states in Fig. 4.4.

# 4.2.3 Dielectric Function and Optical Conductivity of Individual Sheets

Optical response of individual sheets is mostly measured by reflection, transmission and absorption experiments. In this section, we explain how to relate the calculated superlattice dielectric function to these experimentally accessible quantities. In order to model the optical properties of individual silicene films and other sheet crystals

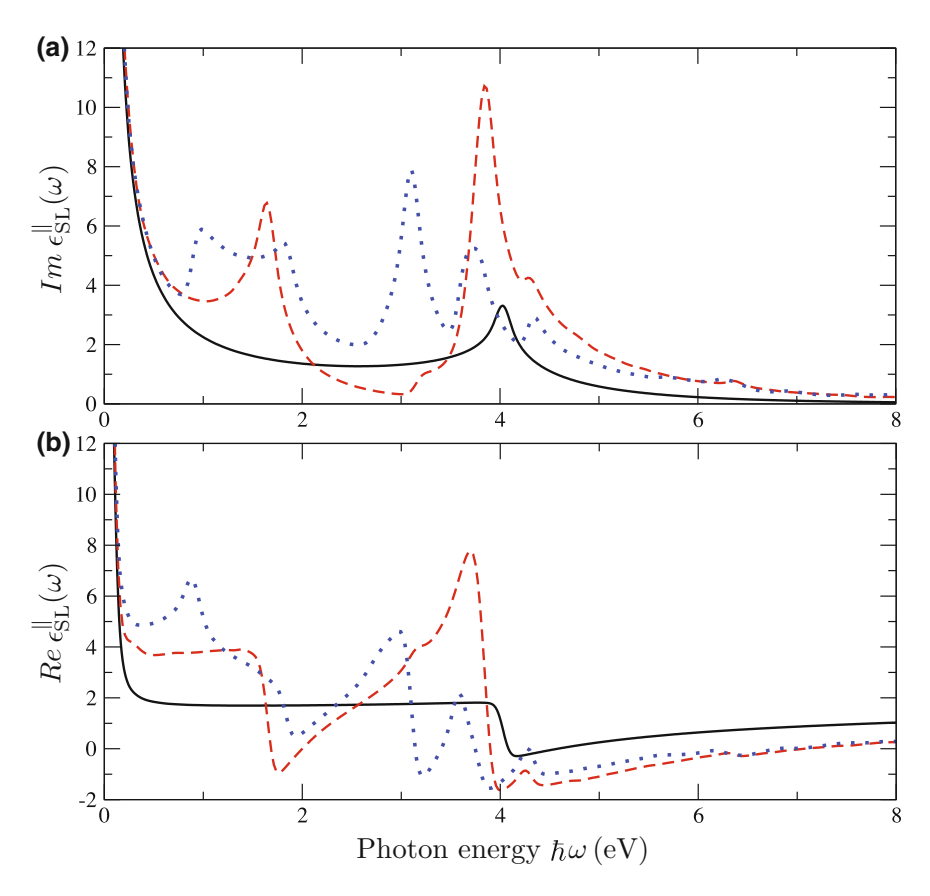


Fig. 4.3 Imaginary (a) and real (b) part of the in-plane dielectric function of the superlattices made by graphene (black solid line), silicene (red dashed line), and germanene (blue dotted line)

we reinterprete the dielectric functions (4.1) of their superlattice arrangements. Since the space between the sheets is vacuum, the tensor  $\hat{\epsilon}_{SL}(\omega)$  is directly related to that of the sheet material  $\hat{\epsilon}_{2D}(\omega)$ , if an effective thickness d of the sheet is assumed, as e.g. d=3.35 Å used in ellipsometry studies of graphene [5]. In the limit  $d\ll\lambda$  with  $\lambda=2\pi c/\omega$  the wavelength of light, the two independent components can be related to those of the superlattice within an effective-medium theory by [33]

$$\epsilon_{\text{2D}}^{\parallel}(\omega) = 1 + \frac{L}{d} \left[ \epsilon_{\text{SL}}^{\parallel}(\omega) - 1 \right],$$

$$\frac{1}{\epsilon_{\text{2D}}^{\perp}(\omega)} = 1 + \frac{L}{d} \left[ \frac{1}{\epsilon_{\text{SL}}^{\perp}(\omega)} - 1 \right].$$
(4.4)

The description (4.4) of the frequency-dependent properties of silicene or another sheet depends on the empirical thickness d. For individual atomically thin sheets

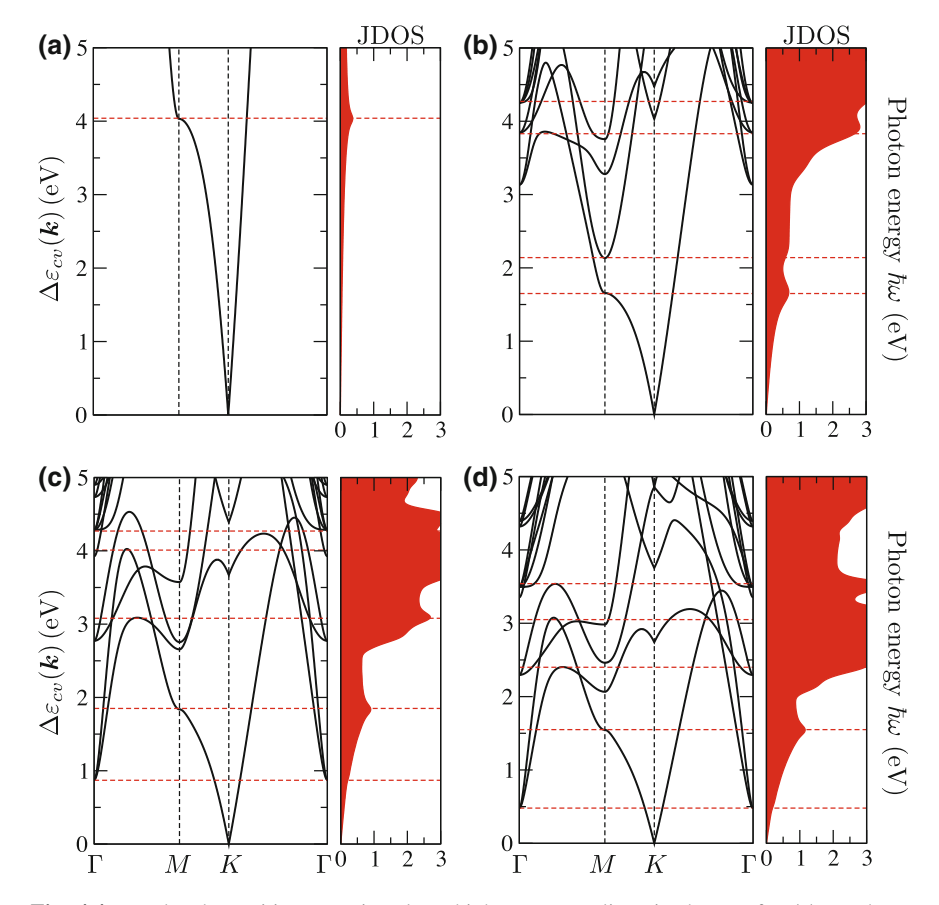


Fig. 4.4 Interband transition energies along high-symmetry lines in the BZ for (a) graphene, (b) silicene, (c) germanene, and (d) stanene. The red-dashed horizontal lines indicate energies of van Hove singularities which give peak structures in the optical spectra. The resulting joint density of states  $JDOS(\omega)$  are displayed in addition [in units  $eV^{-1}/cell$ ]

one is interested in the limit  $d \to 0$ . This limit is possible by the introduction of the optical conductivity tensor of a sheet  $\hat{\sigma}_{2D}(\omega)$ , at least for its in-plane component  $\sigma_{2D}^{\parallel}(\omega)$ . According to the Ohm law  $j_{2D}^{\parallel}(\omega) \sim \sigma_{2D}^{\parallel}(\omega)$  the in-plane current density fulfills the continuity equation in Fourier space as [10]

$$\rho_{\rm 2D}(\omega) = \mathbf{q} \cdot \mathbf{j}_{\rm 2D}^{\parallel}(\omega)/\omega \tag{4.5}$$

with  $\mathbf{q}$  the wave vector of the propagating light and  $\rho_{2D}(\omega)$  the induced (2D) surface charge density.

The in-plane conductivity is directly related to the 3D conductivity of the superlattice by

$$\sigma_{2D}^{\parallel}(\omega) = L\sigma_{SL}^{\parallel}(\omega) \tag{4.6}$$

with

$$\epsilon_{SL}^{\parallel}(\omega) = 1 + \frac{i}{\varepsilon_0 \omega} \sigma_{SL}^{\parallel}(\omega)$$
 (4.7)

according to Maxwell equations. The combination of the two equations leads to the relation

$$\sigma_{\rm 2D}^{\parallel}(\omega) = -i\varepsilon_0 \omega L \left[ \epsilon_{SL}^{\parallel}(\omega) - 1 \right], \tag{4.8}$$

which allows us to relate directly the results presented in Fig. 4.3 to a quantity characterizing the isolated sheet crystal. The prefactor  $\sim \omega$  in (4.8) cancels the pole in  $\hat{\epsilon}_{SL}(\omega)$  for  $\omega \to 0$ . Notice that  $L\left[\epsilon_{SL}^{\parallel}(\omega) - 1\right]$  is independent of L (see (4.1)).

Moreover, no ansatz for d has to be taken, since in  $\sigma_{2D}^{\parallel}(\omega)$  the thickness d does not appear explicitly.

In analogy to the different formulations (4.4) for the in-plane and out-of-plane components of the dielectric tensor, we introduce a definition of the out-of-plane conductivity different from (4.8) as

$$\sigma_{2D}^{\perp}(\omega) = -i\varepsilon_0 \omega L \left[ 1 - \frac{1}{\epsilon_{SI}^{\perp}(\omega)} \right]. \tag{4.9}$$

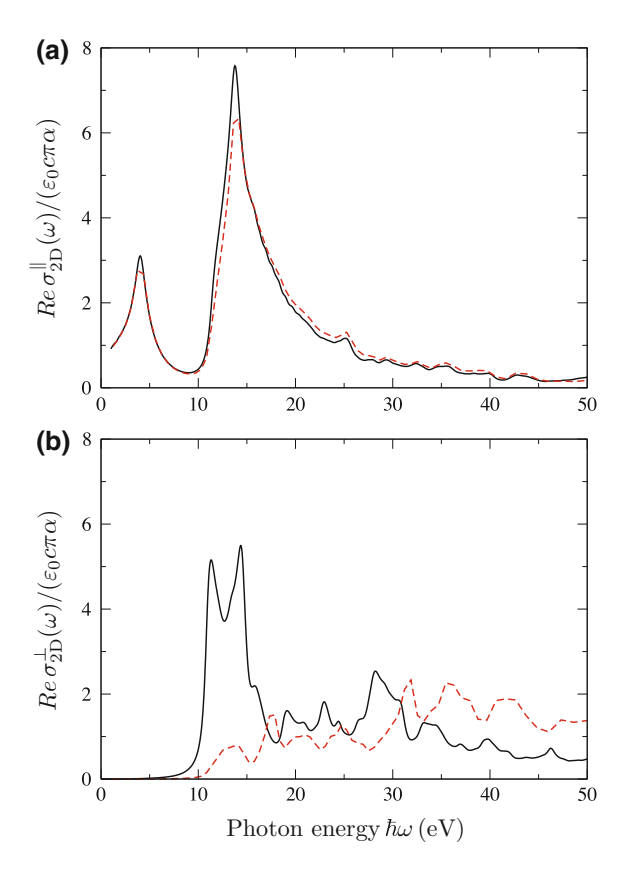
In the limit  $L \to \infty$  the two relations (4.8) and (4.9) become equivalent. In this limit it holds  $L\left[1-\frac{1}{\epsilon_{SL}^\perp}\right] \approx L\left[\epsilon_{SL}^\perp-1\right]$  using the representation (4.1). The two components of the 2D optical conductivity have different physical mean-

The two components of the 2D optical conductivity have different physical meanings. Whereas the in-plane component gives rise to an in-plane current (4.5), the out-of-plane one is associated with an electric dipole operator, which describes electron excitation along the normal direction. This fact explains the zero out-of-plane optical conductivity in a wide spectral range for not too large photon energies for unbuckled graphene (see Table 4.1) in Fig. 4.5b. In contrast to the in-plane component of the optical conductivity, only above  $\hbar\omega\approx 10$  eV the out-of-plane component has a significant magnitude. Especially interesting are the local-field effects (LFEs) [27] due to the superlattice arrangement, which further reduce the out-of-plane component in the lower-energy range. While the in-plane component is practically independent of L and LFEs, local-field effects due to the superlattice arrangement play an important role in  $\sigma_{\rm 2D}^{\perp}(\omega)$ . In general, Fig. 4.5 shows that the in-plane component is more important.

# 4.2.4 Optical Properties of Atomically Thin Films

For grazing incidence both components of the optical conductivity tensor  $\hat{\sigma}_{\text{2D}}(\omega)$  of silicene and related honeycomb sheets made by other group-IV elements play a role. The details however depend on the description of the boundary conditions for the electromagnetic field and the limit  $d \to 0$  or the use of finite thicknesses d. They are discussed in a recent paper [34] where also the different approaches

Fig. 4.5 Real parts of the (a) in-plane and (b) out-of-plane components of the optical conductivity of graphene within the independent-particle picture without (4.1) (black solid line) and with (not explicitly described) local-field effects (red dashed line). The optical conductivity is given in units of the dc conductivity  $\sigma_0 = \varepsilon_0 c$  and  $\pi \alpha$  with  $\sigma_0 \pi \alpha = e^2/(4\hbar)$  with the parameter  $\alpha$  as the Sommerfeld finestructure constant. Only results for L = 20 Å are displayed. Larger L values have only a minor influence



based on electromagnetic boundary conditions [35] with an infinitely atomically thin but conducting overlayer [1, 10] or the use of the transfer-matrix method [36] but different descriptions of a group-IV sheet [11–13] are presented.

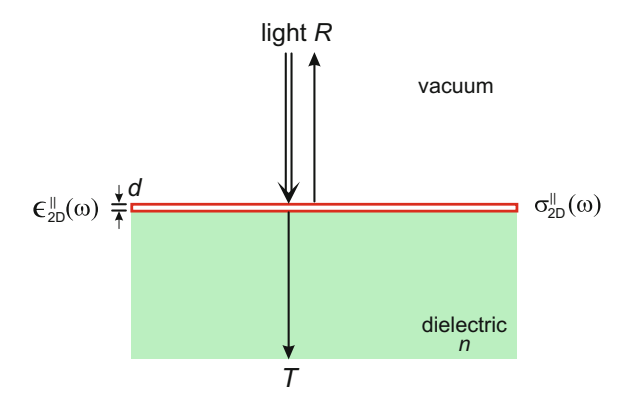
Here, we focus on the simple case of normal incidence, in which only the in-plane optical conductivity  $\sigma_{2D}^{\parallel}(\omega)$  (4.8) or the corresponding component  $\epsilon_{2D}^{\parallel}(\omega)$  (4.4) of the dielectric tensor of the sheet with an effective thickness d plays a role. We only study a three-layer system: vacuum, silicene or other group-IV sheet, and a dielectric characterized by a real refraction index n (see Fig. 4.6). The Fresnel formulas can be easily derived applying the electromagnetic boundary conditions. For reflectance R, transmittance T, and absorbance A one finds [1, 10]

$$R = \left| \frac{1 - n - \tilde{\sigma}}{1 + n + \tilde{\sigma}} \right|^2,$$

$$T = \frac{4n}{|1 + n + \tilde{\sigma}|^2},$$

$$A = 1 - R - T.$$
(4.10)

**Fig. 4.6** Light propagation in a three-layer system consisting of a 2D sheet characterized by  $\sigma_{\rm 2D}^{\parallel}(\omega)$  or  $\epsilon_{\rm 2D}^{\parallel}(\omega)$  as well as vacuum and a dielectric as substrate



with a dimensionless, normalized in-plane conductivity

$$\tilde{\sigma} = \sigma_{\text{2D}}^{\parallel}(\omega)/\varepsilon_0 c = \sqrt{\frac{\mu_0}{\varepsilon_0}} \sigma_{\text{2D}}^{\parallel}(\omega). \tag{4.11}$$

In the case of freestanding silicene or other sheet crystals the refraction index n in (4.10) has to be replaced by  $n \equiv 1$ . One obtains

$$R = \left| \frac{\tilde{\sigma}/2}{1 + \tilde{\sigma}/2} \right|^2 \approx 0,$$

$$T = \frac{1}{|1 + \tilde{\sigma}/2|^2} \approx 1 - \text{Re}\tilde{\sigma},$$

$$A = \frac{\text{Re}\tilde{\sigma}}{|1 + \tilde{\sigma}/2|^2} \approx \text{Re}\tilde{\sigma},$$
(4.12)

where also the results linearized in the optical response of the sheet are given. In the limit of vanishing reflectance of the sheet the absorbance is directly related to the in-plane optical conductivity

$$A(\omega) \approx \frac{1}{\varepsilon_0 c} \text{Re} \sigma_{\text{2D}}^{\parallel}(\omega) \approx \frac{\omega}{c} d \text{Im} \epsilon_{\text{2D}}^{\parallel}(\omega) \approx \frac{\omega}{c} L \text{Im} \epsilon_{SL}^{\parallel}(\omega). \tag{4.13}$$

Hence  $A(\omega)$  can be calculated through  $\epsilon_{SL}^{\parallel}(\omega)$  at any level of theory (independent particle, independent quasi-particle, with or without local fields, with or without excitonic effects) without any *a priori* knowledge of the sheet thickness d.

## 4.3 Spectra of Silicene, Germanene, and Stanene

# 4.3.1 Influence of Many-Body Effects

In expression (4.1) of the dielectric tensor of the sheet superlattices, excitonic effects [27] are not taken into account. In 3D systems we know that the Coulomb interactions between excited (quasi)electrons and (quasi)holes, i.e., the excitonic effects, may remarkably determine the optical properties [27], especially near the absorption edge. The excitonic effects in structures with reduced dimensionality are significantly more influenced by two factors, (i) the quantum confinement effects [37], and (ii) the less efficient electronic screening [38]. In the case of silicene and related materials there is an additional difficulty. These 2D crystals are zero-gap semiconductors. Nevertheless, to treat numerically excitonic effects we follow the standard procedure [27] also for the 2D sheets graphene, silicene, and germanene [39, 40] as done for the corresponding hydrogenated sheet crystals graphane, silicane, and germanane. In detail, it is described as a two-step procedure [41]: (i) The QP bands are calculated within the Hedin GW approximation on top of the Kohn-Sham results [27]. (ii) The matrix elements of the screened Coulomb attraction between (quasi)electrons and (quasi)holes and the unscreened electron-hole exchange are computed using the corresponding wave functions. The Bethe-Salpeter equation (BSE) is solved to obtain eigenvectors and eigenvalues of the two-particle problem that modify the dielectric function (4.1) [27]. Technically the GW calculations are performed as a one-shot approach, applying a  $50 \times 50 \times 1$  ( $90 \times 90 \times 1$ ) **k**-point mesh for the screened (exchange) part of the self-energy and the plasmon-pole approximation for the screening dynamics. The Coulomb interaction between the sheets of the superlattice is cut. In the BSE,  $50 \times 50 \times 1$  k points, four filled valence and five empty conduction bands are included. The EXC code [42] is used.

As a result the real part of the 2D optical conductivity  $\sigma_{2D}^{\parallel}(\omega)$  is presented in Fig. 4.7a for silicene in an energy range  $0.5 \text{ eV} < \hbar\omega < 6 \text{ eV}$ . It shows a two-peak structure independent of the approximation of the many-body effects. In the imaginary part (Fig. 4.7a) the peak positions appear as zeros in the energy denominators, similar to those in (4.1). According to the interband structure and the JDOS in Fig. 4.4, the first peak is mainly due the lowest optical transitions near the M points of the BZ. They represent 2D saddle points in the JDOS. The second peak consists of contributions of several minima in the interband structure at  $\Gamma$  and M. Adding the quasiparticle corrections the IQPA spectrum is blueshifted by about 0.5 eV (lower peak) or 0.9 eV (upper peak), while its lineshape nearly remains the same. The excitonic effects are ruled by the (screened) electron-hole attraction. The electron-hole exchange or optical local-field effects are negligible for the in-plane component of the optical conductivity (see discussion of Fig. 4.5). As a consequence, the excitonic effects lead to strong redshifts compensating (upper peak) or even slightly overcompensating (lower peak) the blueshift of the peaks due to QP effects. Qualitatively, the resulting BSE spectrum is very similar to the IPA spectrum due to many-body effects almost compensating each other. For that reason, the majority of the spec-

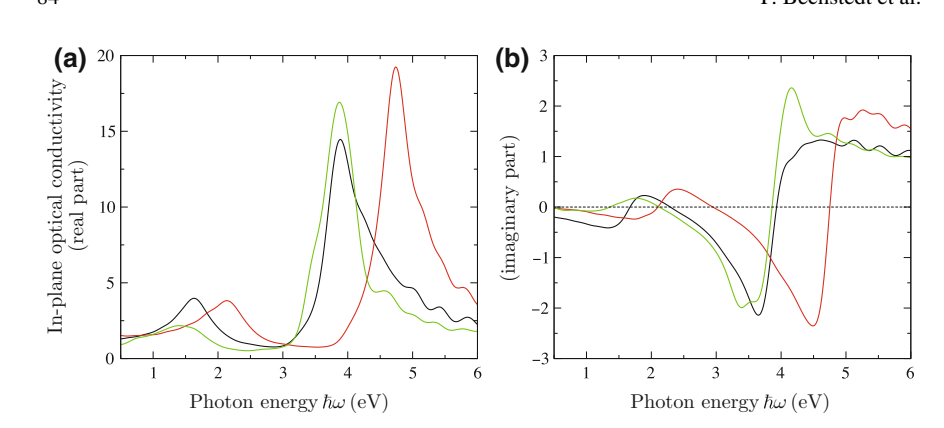


Fig. 4.7 Real part (a) and imaginary part (b) of the in-plane optical conductivity for silicene within three different approaches to the many-body effects: IPA (4.1) using the DFT-GGA electronic structure (black line), IQPA including quasiparticle GW corrections (red line), and BSE including quasiparticle and excitonic effects (green line). The optical conductivity  $\sigma_{\rm 2D}^{\parallel}(\omega)$  is given in units of the dc conductivity  $\sigma_0 = \varepsilon_0 c$  and  $\pi \alpha$  with  $\sigma_0 \pi \alpha = e^2/(4\hbar)$  with the parameter  $\alpha$  as the Sommerfeld finestructure constant

tra discussed in the following are computed within the IPA using eigenvalues and eigenfunctions of the Kohn-Sham equation or the generalized Kohn-Sham equation.

The low-energy part of  $\text{Re}\sigma_{2D}^{\parallel}(\omega)$  for  $\hbar\omega < 0.5$  eV is not shown in Fig. 4.7 for two reasons. (i) There is a technical reason. The optical spectra for vanishing photon energies  $\hbar\omega \to 0$  require a more dense **k**-point sampling around the K and K' points of the BZ because of the linear bands (see Figs. 4.2 and 4.4) resulting in the pole  $\sim 1/\omega$  (see Fig. 4.3). Non-converged calculations lead to wrong absorption spectra in the low-energy region (see e.g. Fig. 3 in [39]). (ii) However, there is also a physical reason. For systems with exciton binding energies larger than the fundamental gap (which is zero here) one expects an instability of the electronic system against the formation of charge or spin density waves or the formation of an excitonic insulator [43, 44]. A close formal similarity between the excitonic insulating state and the superconducting state has been predicted. However, physical properties of the two states are different, in particular, there is no Meissner effect in an excitonic insulator. Graphene seems to be a prototypical system because of its character as zero-gap semiconductor (also including SOC, see Table 4.1). Indeed, there are several papers on the excitonic insulator phase in graphene (see e.g. [45, 46]) but also in other materials. Nevertheless, neither the ab-initio studies [37, 40] nor the experimental investigations [2–4, 30] of the optical absorption of graphene discuss the excitonic insulator state.

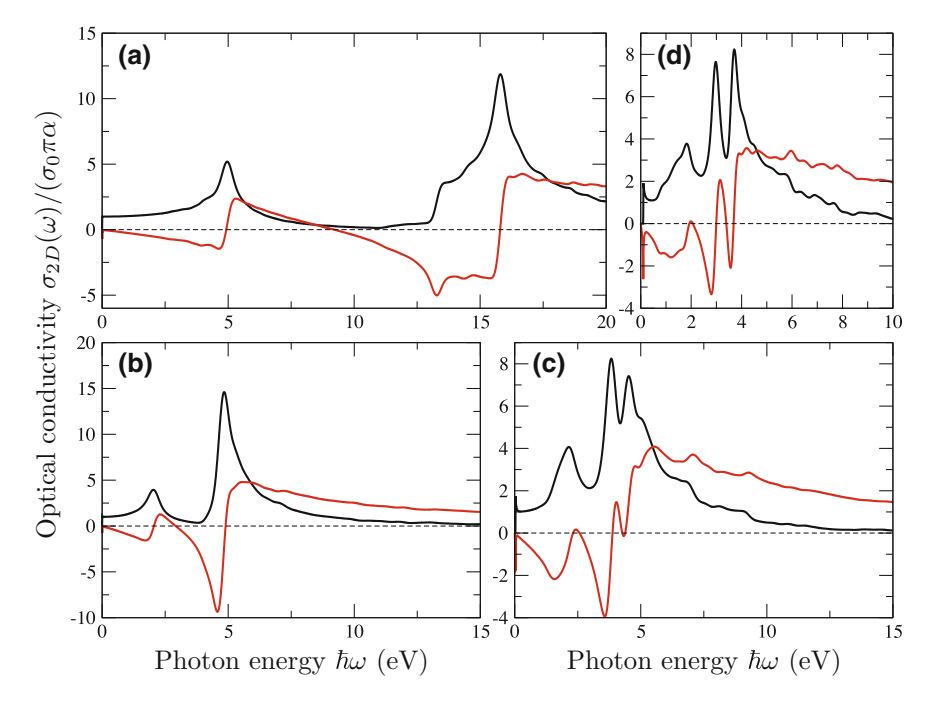


Fig. 4.8 In-plane optical conductivity in units of the dc conductivity  $\sigma_0 = \varepsilon_0 c$  and  $\pi \alpha$  of (a) graphene, (b) silicene, (c) germanene, and (d) stanene. Real part: black line, imaginary part: red line [1]

# 4.3.2 General Frequency Dependence

The optical spectra resulting from converged calculations within the IPA based on the general DFT with the HSE06 hybrid functional are shown in Fig. 4.8. Both real and imaginary part of the in-plane optical conductivity are displayed for silicene but also germanene and stanene in units of the dc conductivity  $\sigma_0 = \varepsilon_0 c$  and  $\pi \alpha$  with  $\sigma_0 \pi \alpha = e^2/(4\hbar)$  with the parameter  $\alpha$  as the Sommerfeld finestructure constant. For comparison, also the spectra of graphene are given. The spectra show general features of those of damped harmonic oscillators with two (graphene, silicene) or three (germanene, stanene) oscillators in the studied frequency range. Apart from variations due to the SOC-induced small gap (see Table 4.1) the  $\text{Re}\sigma_{\text{2D}}^{\parallel}(\omega)/(\sigma_0\pi\alpha)$  spectra tend to 1 for  $\omega \to 0$ , while the curves for  $\text{Im}\sigma_{\text{2D}}^{\parallel}(\omega)/(\sigma_0\pi\alpha)$  vanish in the long-wavelength limit. For large frequencies  $\omega \to \infty$  all spectra tend to zero. For arbitrary frequencies, even in a wide energy range up to 20 eV (graphene), or 10 eV (silicene, germanene, stanene) the most important intensity variations can be interpreted by van Hove singularities in the 2D interband structure or JDOS in Fig. 4.4 [23, 26].

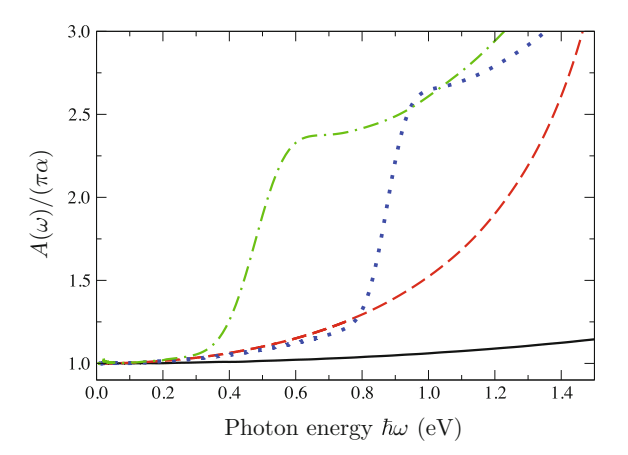
The peak positions in Fig. 4.8 are influenced by the chosen XC functional. Compared to the results obtained within the DFT-GGA approach the peaks and energy zeros are blueshifted. The blueshift of the first absorption peak in  $\operatorname{Re}\sigma_{2D}^{\parallel}(\omega)$  amounts to 1.0 eV (graphene), 0.4 eV (silicene, germanene), and 0.3 eV (stanene). The lowestenergy oscillators have been discussed in the literature. The first peak in  $\text{Re}\sigma_{2D}^{\parallel}(\omega)$ of graphene near  $\hbar\omega = 5.0$  eV (in DFT-HSE) is a consequence of 2D saddle points in the  $\pi^* - \pi$  interband structure in Fig. 4.4 located at the three M points at the BZ boundary belonging to one BZ. This peak has been clearly identified in optical absorption spectra  $A(\omega)/\pi\alpha = \text{Re}\sigma_{2D}^{\parallel}(\omega)/(\sigma_0\pi\alpha)$  (4.4) with a maximum position at  $\hbar\omega = 4.62$  eV [4]. It should have a Fano lineshape, which we, however, cannot confirm since no electron-hole coupling effects are taken into account. The corresponding peak near  $\hbar\omega = 2.0$  eV for silicene in DFT-HSE06 (Fig. 4.8) appears near  $\hbar\omega = 1.5$  eV in DFT-GGA (Fig. 4.7) and also exhibits a strong asymmetry. For germanene and stanene this peak slightly below  $\hbar\omega=2.0$  corresponds to the same type of van Hove singularities (see Fig. 4.4). The energetically lower lying  $\sigma^* - \sigma$ transition at  $\Gamma$  gives rise to minimum but is already hardly visible in the JDOS in Fig. 4.4 because of the extremely small effective interband mass. The higher peaks near 14/16 eV (C), 5 eV (Si), 4.0/4.7 (eV) (Ge), and 3.1/4.0 eV (Sn) are related to  $\sigma \to \sigma^*$  transitions mainly at the  $\Gamma$  point of the 2D BZ. These peaks are basically also related to van Hove singularities in the interband structure (not shown for graphene in Fig. 4.4). For graphene flat, i.e., dispersionless interband contributions appear along the high-symmetry lines  $\Gamma K$ ,  $\Gamma M$ , and MK, which give significant features in the JDOS.

Interestingly, the two main spectral features in the real part of the in-plane conductivity of pristine graphene agree well with the  $\pi$  and  $\pi + \sigma$  plasmon peaks found in experimental and theoretical energy loss spectra at loss energies of 4.7 and 14.6 eV [47, 48]. These findings are in rough agreement with the spectral variation of the in-plane optical conductivity in Fig. 4.8a.  $\mathrm{Im}\sigma_{2D}^{\parallel}(\omega) = 0$  near  $\hbar\omega = 5$  and 16 eV is a consequence of  $\mathrm{Re}\epsilon_{SL}^{\parallel}(\omega) \approx 1$  for large L for the superlattice arrangement of graphene sheets. As a consequence, it nearly holds  $\mathrm{Im}\epsilon_{SL}^{\parallel}(\omega) \approx -\mathrm{Im}(1/\epsilon_{SL}^{\parallel}(\omega))$ . That means that the spectral behavior of the optical absorption spectrum and the energy loss function show similarities for the 2D crystals.

# 4.3.3 Low-Frequency Absorbance

In the low-frequency limit the approximation (4.13) can be applied to describe the optical absorbance  $A(\omega)$ . The results for the four group-IV honeycomb crystals are displayed in Fig. 4.9 in units of  $\pi\alpha$ . One clearly sees that in the limit  $\hbar\omega \to 0$  the absorbance approaches to a constant  $A(\omega \to 0) = \pi\alpha$  with  $\alpha$  the Sommerfeld constant. This happens independent of the group-IV element, i.e., the sheet buckling and the relation of  $sp^2$  and  $sp^3$  bonding [23, 49]. In other words, the IR absorbance tends, in these systems, to a universal value. Only for larger frequencies the material

Fig. 4.9 Optical absorption spectrum  $A(\omega)$  calculated within the approximation of independent Kohn-Sham particles with the DFT-GGA XC functional for graphene (black solid line), silicene (red dashed line), germanene (blue dotted line), and stanene (green dashed-dotted line) versus photon energy



dependence becomes obvious as a result of the interband structure presented in Fig. 4.4, whose lowest van Hove singularities are visible for stanene, germanene, and silicene. The reason is the honeycomb symmetry which guarantees that the mainly contributing interband transition near the K and K' points and the Fermi level are dominated by  $\pi \to \pi^*$  transitions. For graphene the result  $A(0) = \pi \alpha$  is known from measurements [1, 2].

The spectra in Fig. 4.9 have been computed within the usual Fermi-liquid approximation (4.1) taking into account the complete band structure and optical interband transition matrix elements. For the lowest interband transitions  $|v\mathbf{k}\rangle \to |c\mathbf{k}\rangle$  with  $\mathbf{k}$  near K or K' and  $\hbar\omega \to 0$  the corresponding matrix elements (4.4) and interband transitions are illustrated in Fig. 4.10. All quantities have been expressed in units defined by the Fermi velocity  $v_F$  given in Table 4.1. With this normalization the relevant interband transition energies and strengths are rather similar for the four 2D sheets, graphene, silicene, germanene, and stanene. The linear variation of the bands near K and K' is obvious from the very beginning because of the appearance of Dirac cones in the band structure (see Fig. 4.2). Interestingly, the square of the in-plane optical transition matrix element is exactly given by  $(mv_F)^2$  at K and K'.

These numerical results allow an analytical investigation of the absorbance for  $\omega \to 0$ . Combining expressions (4.1), (4.3), (4.8), and (4.13) it holds for  $\omega \to 0$  [23]

$$A(\omega) = \frac{2\alpha\hbar}{m^2\omega} \int d^2(\Delta \mathbf{k}) \sum_{j=x,y} \left| \langle c\Delta \mathbf{k} | p_j | v\Delta \mathbf{k} \rangle \right|^2 \delta \left( 2\hbar v_F |\Delta \mathbf{k}| - \hbar\omega \right)$$
(4.14)

with  $\Delta \mathbf{k}$  the variation of the Bloch wave vector near a K or K' point in the BZ. For  $\Delta \mathbf{k} = 0$  in the optical transition matrix elements in (4.14) and the result in Fig. 4.10a the integral can be analytically performed. One finds

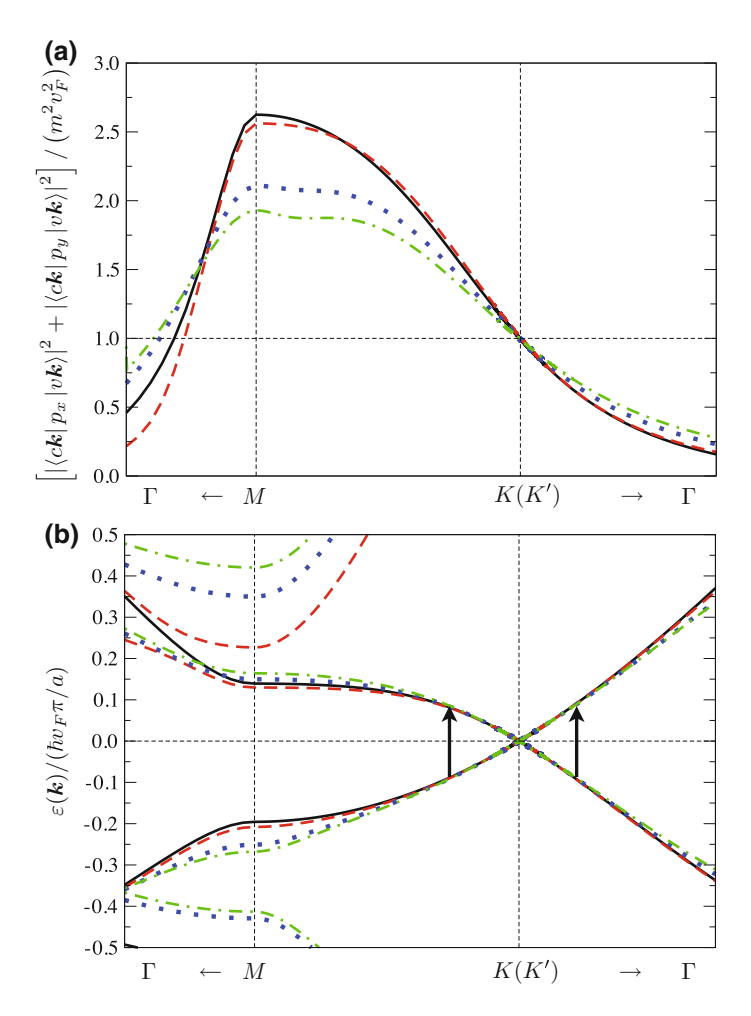
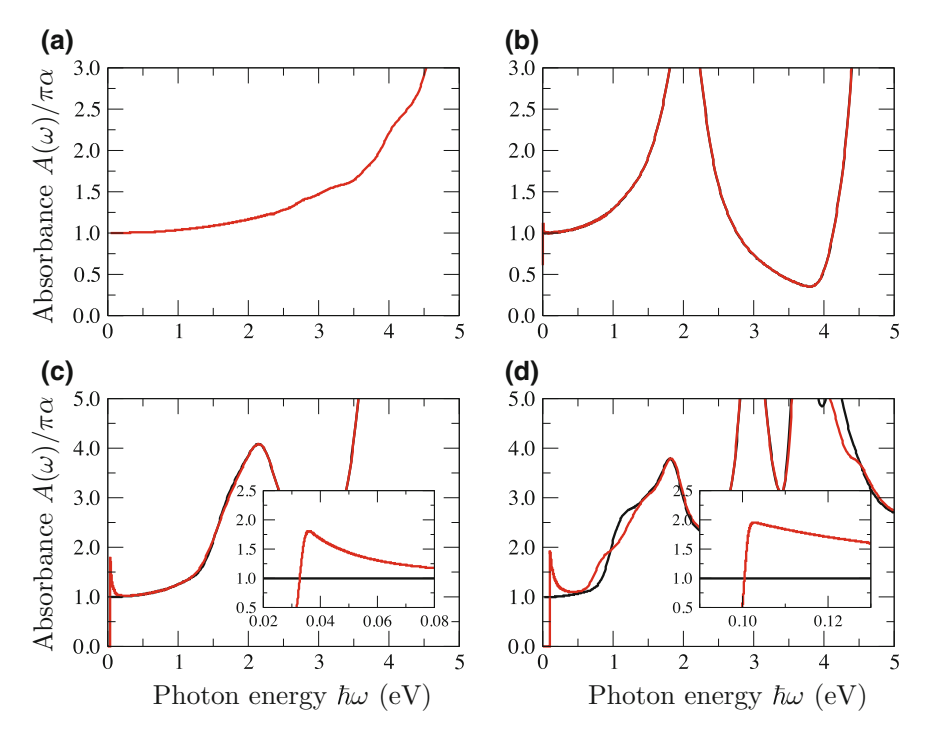


Fig. 4.10 (a) Transition matrix elements of the pure  $\pi \to \pi^*$  transitions along high-symmetry lines in the BZ for graphene (black solid line), silicene (red dashed line), germanene (blue dotted line), and stanene (green dot-dashed line). The longitudinal representation of the matrix elements (4.3) has been used in the numerical calculations. (b) For illustration, the  $\pi$  and  $\pi^*$  bands that are involved in the optical transitions are also shown. The transitions are indicated by vertical arrows

$$A(\omega) = 2\frac{\hbar v_F^2}{\omega} \alpha \frac{\pi \omega}{2\hbar v_F^2} = \pi \alpha \tag{4.15}$$

in agreement with the numerical calculations (see Fig. 4.9) and measurements, at least for graphene [2, 3].



**Fig. 4.11** Optical absorbance in units of  $\pi\alpha$  as a function of the photon energy for **(a)** graphene, **(b)** silicene, **(c)** germanene, and **(d)** stanene without (black solid lines) and with (red solid lines) spin-orbit coupling. The insets in **(c)** and **(d)** depict the region around their respective fundamental absorption edges

# 4.3.4 Influence of Spin-Orbit Interaction

The optical absorbance, more strictly speaking the real part of the in-plane optical conductivity (see expression (4.13)), as calculated within the independent-quasiparticle approximation and SOC, is displayed in Fig. 4.11. The quasiparticle corrections are computed in an approximate way by means of the non-local hybrid functional HSE06 [26].

In a wide frequency range the optical absorbance in Fig. 4.11 taking into account SOC shows a very good overall agreement with the spectrum obtained without SOC. A detailed analysis, however, reveals remarkable modifications close to the SOC-induced fundamental absorption edge related to the gap  $E_g$  given in Table 4.1. For  $\hbar\omega < E_g$  the absorption vanishes, while for  $\hbar\omega > E_g$  the absorbance is significantly increased for  $\hbar\omega \to E_g$ . This behavior is particularly pronounced for germanene (Fig. 4.11c) and stanene (Fig. 4.11d). Already for silicene (Fig. 4.11b) the SOC effects are hardly visible. Within the numerical accuracy the absorbance is increased by a factor of two at  $\hbar\omega = E_g$  due to SOC (see Fig. 4.12 for germanene). The spectral

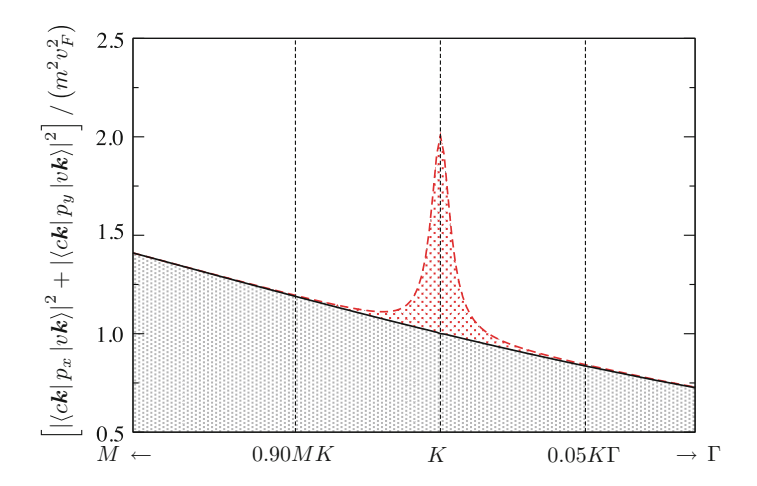


Fig. 4.12 A normalized optical matrix element of germanene without (black solid line) and with (red dashed line) spin-orbit interaction between the highest occupied and lowest occupied Bloch bands in the vicinity of K. At K, without SOC, the normalized optical matrix element approaches the ideal value 1

variation for  $\hbar\omega \stackrel{>}{\sim} E_g$  mainly represents the appearance of massive Dirac quasiparticles near the conduction band minimum and valence band maximum separated by  $E_g$ . In the vicinity of K and K' their dispersion relation is approximately given by

$$\varepsilon_{c/v}(\mathbf{k}) = \pm \left[ (E_g/2)^2 + (\hbar v_F)^2 (\Delta \mathbf{k})^2 \right]^{\frac{1}{2}}$$
(4.16)

with the 2D wave vector variation  $\Delta \mathbf{k}$ . Consequently, the effective mass of the Dirac particles is given by  $m_{c/v}^* = E_g/(2v_F^2)$ .

The frequency variation above the absorption edge is also influenced by the SOC-modified optical transition matrix element. Instead of  $(mv_F)^2$  as used in expression (4.14) it holds  $(mv_F)^2 \left\{ 1 + 1/\left[ 1 + 2\hbar^2(\Delta \mathbf{k})^2/(m^*E_g) \right] \right\}$ . Consequently we derive for the low-frequency absorbance in the presence of SOC [26]

$$A(\omega) = \pi \alpha \left[ 1 + \left( \frac{E_g}{\hbar \omega} \right)^2 \right] \Theta(\hbar \omega - E_g), \tag{4.17}$$

which approaches to the value (4.15) for vanishing SOC. Interestingly for  $E_g \ll \hbar\omega$  < interband critical points the value  $A(\omega) \approx \pi\alpha$  is recovered.

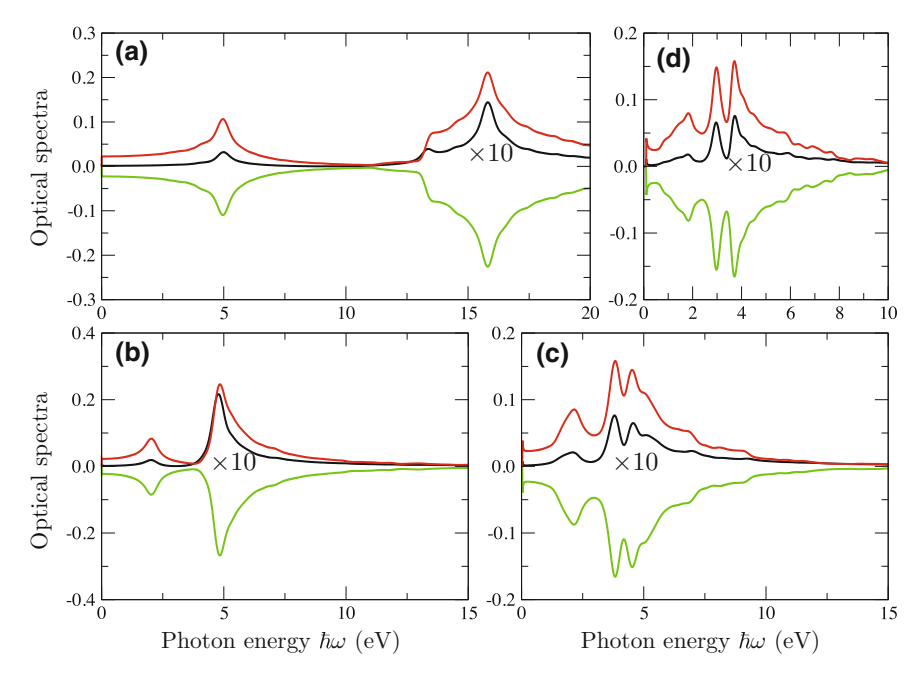


Fig. 4.13 Frequency dependence of the optical properties R (black line), T-1 (green line), and A (red line) for the four honeycomb crystals (a) graphene, (b) silicene, (c) germanene, and (d) stanene. Normal incidence and hence in-plane light polarization are assumed

# 4.3.5 Reflection, Transmission, and Absorption: Global Spectra

We investigate the optical properties of freestanding group-IV honeycomb crystals in air for normal incidence. It holds n=1 in relations (4.10). The resulting expressions show how the frequency-dependent optical conductivity  $\sigma_{2D}^{\parallel}(\omega)$  describes the optical properties of an isolated single sheet of silicene and related materials. The corresponding reflection, transmission, and absorption spectra are displayed in Fig. 4.13. According to the monatomic character of the sheet crystals the transmission  $T(\omega)$  is only weakly influenced by an isolated sheet as indicated also in expression (4.12).

The optical properties in Fig. 4.13 exhibit several common features independent of the group-IV material. The reflectance of all layers is extremely small. It may only be measurable in the frequency region of the resonances discussed in Fig. 4.8 for the real part of the optical conductivity. As a consequence the absorbance and the real part of the normalized optical conductivity agree rather well [1]. Deviations only appear for photon energies corresponding to the discussed resonances. The absorbance  $A(\omega)$  and the deviation  $[1-T(\omega)]$  from 100% transmittivity of a group-IV layer exhibit similar lineshapes and magnitudes. The strength of the absorbance is remarkable for one-atom-thick layers. This holds especially for the photon energies in the resonance

regions. The absorbance approaches extremely large values up to 0.24 (graphene, silicene) or 0.15 (germanene, stanene) in these frequency regions. The values are by more than one order of magnitude larger than the value  $\pi\alpha=0.023$  for vanishing frequencies. The major influence of the group-IV element concerns the lineshape, essentially the number and position of the optical resonances. They however agree widely with the findings for  $\text{Re}\sigma_{\text{2D}}^{\parallel}(\omega)$  discussed in Fig. 4.8.

## 4.4 Influence of Multiple Layers

#### 4.4.1 Graphene Bilayer

The above results suggest the possibility of manipulation of optical properties by deposition of not only one silicene or, in general, a group-IV honeycomb crystal, but of two or more sheets. For hydrogenated bilayer silicene the resulting exceptional optoelectronic properties have been recently predicted [50]. Even bilayer silicene has been studied on top of a Ag(111) substrate [51]. Here, we first illustrate the influence of further sheets by investigating bilayer graphene as a model system for the other 2D group-IV crystals such as silicene. Its electronic structure is known (see e.g. [40, 52]). Its optical properties have been studied by infrared spectroscopy [53].

We have optimized the atomic geometry of Bernal-stacked bilayer graphene including van der Waals interaction in the XC functional of the DFT (see [54]). In contrast to the too large layer distance of 4.4 Å within the DFT-GGA approach [17, 18], we find an interlayer spacing of 3.54 Å not too far from the experimental value 3.35 Å [55], which is close to the c-lattice constant 3.34 Å of graphite. The band structure has been computed within the DFT-GGA. It is displayed in Fig. 4.14. It shows strong qualitative similarities with the band structures given in Fig. 4.2. The main effect of the bilayer is the doubling of the number of atoms in the unit cell and band splittings due to the weak interaction between the two honeycomb layers. Most important for the infrared optical properties is the modification of the Dirac cones near the K point. Bilayer graphene is still a zero-gap semiconductor formed by one conduction band-valence band pair. The linear variation of the bands near K is however destroyed. The second conduction band-valence band pair is split away from zero energy by an energy of 50 meV which expresses the interlayer coupling. The 'split' bands are due to a bonding and antibonding combination of  $p_z$  orbitals.

The resulting real part of the in-plane optical conductivity is plotted in Fig. 4.15. Only the DFT-GGA result, i.e., the spectrum in independent-particle approximation without SOC is presented in agreement with the discussion of Fig. 4.7a. For comparison, the spectrum of two non-interacting graphene layers is shown. Three important features are visible: (i) The bilayer graphene almost keeps the intensity of the optical absorption due to two non-interacting graphene sheets (a fact that is also experimentally observed [2]). (ii) The high-energy peak related to a saddle-point van Hove singularity at M points shows a vanishing blueshift with respect to its

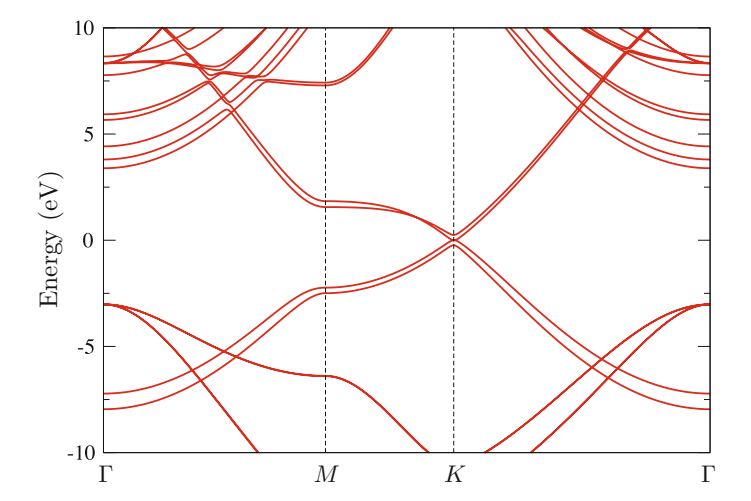


**Fig. 4.14** Band structure of Bernal-stacked bilayer graphene with an interlayer spacing of 3.54 Å within the DFT-GGA but without SOC. The Fermi level position is used as energy zero

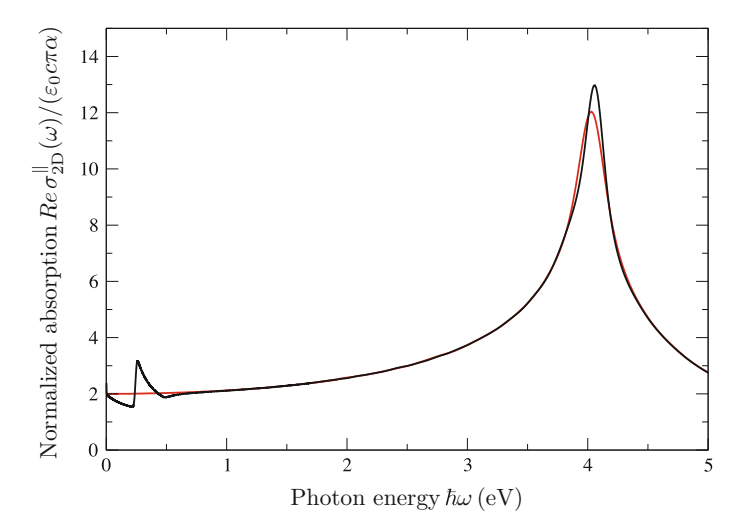


Fig. 4.15 The real part of the in-plane optical conductivity of bilayer graphene in independent-particle approximation (black line). For comparison, the curve (red line) of two non-interacting graphene layers is displayed, too. The spectra are normalized by dc conductivity  $\varepsilon_0 c$  and the value  $\pi \alpha$  of the low-frequency absorbance

position in single-layer graphene near 4 eV (in DFT-GGA). Excitonic effects only partly cancel the corresponding quasiparticle shifts (see [40]). (iii) The interband transition between the second highest valence band and second lowest conduction band at *K* generates a new feature in the joint DOS and, hence, in the absorbance in Fig. 4.15 somewhat below 0.5 eV. This is in complete agreement with transmission

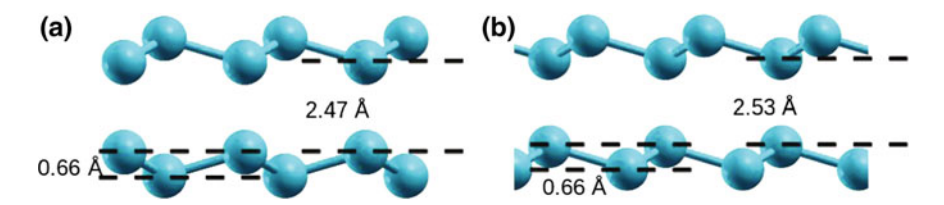


Fig. 4.16 Silicene bilayers with AA (a) and AB (b) stacking

measurements which exhibit a pronounced negative peak at  $\hbar\omega = 0.40 \text{ eV}$  [53] or a positive structure at this energy in the absorbance [4].

#### 4.4.2 Silicene Bilayers

Among the group-IV elements, silicon is the element next to carbon, which has been the dominant material of semiconductor technology. Until now there are indications for the existence of bilayer silicene on Ag(111) substrates (see [51]). For freestanding silicene bilayers we therefore take the atomic geometry from a structural optimization within the DFT-GGA for AA and AB stackings. The results are illustrated in Fig. 4.16. The in-plane lattice constant a=3.86 Å and the layer buckling  $\Delta=0.66$  Å are practically independent of the layer stacking and similar to the values for a single layer (see Table 4.1). Only the interlayer distance varies between 3.13 Å (AA stacking) and 3.19 Å (AB stacking). Nevertheless, the AB stacking is energetically favorable by 34 meV/atom over the AA stacking (see also [56]).

The electronic band structures in DFT-GGA quality are displayed in Fig. 4.17 for AA- and AB-stacked bilayer silicene. They are distinctly different from the bilayer graphene in Fig. 4.14 as far as dispersion of the bands at the K point and along the  $K-\Gamma$  direction are concerned. That occurs despite the fact that the shape of the lateral 2D unit cell in Fig. 4.16 and the 2D BZ conserve that of the isolated silicene sheet. This is especially astonishing because the 2D point-group symmetry is also conserved. For AB-stacked bilayer silicene only one of the bands remains at K. For AA stacking such band crossings occur away from the BZ boundary. As a consequence bilayer silicene with AA stacking remains a zero-gap semiconductor, whereas the AB stacking gives a metal. The main reason for differences is related to the interaction of the orbitals which do not decay anymore into pure  $p_z$  orbitals at K as in the monolayer case. The modifications are due to the buckled structure of bilayer silicene and strong interlayer covalent bonding between sheets compared to bilayer graphene with unbuckled sheets and weak van der Waals interaction. The results in general are very similar to other DFT-LDA findings [56].

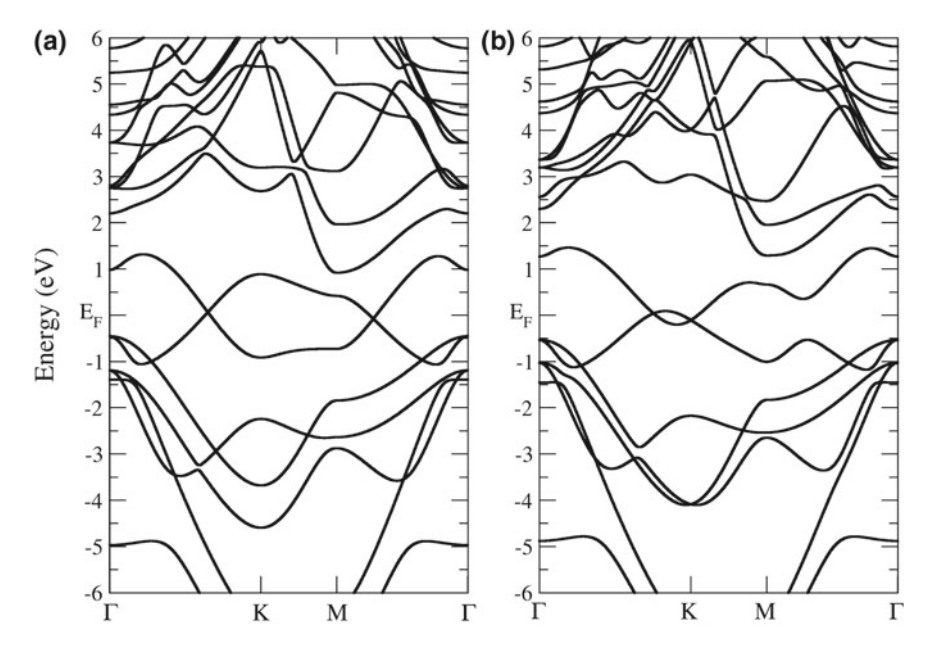


**Fig. 4.17** Band structure of AA-stacked (a) and AB-stacked (b) bilayer silicene versus high-symmetry lines in the hexagonal BZ. The Fermi level is set at 0 eV

The consequences of the electronic structures on the optical properties are described by the real part of the in-plane optical conductivity in Fig. 4.18. Only interband transitions (see (4.1)) are taken into account. The free-carrier-related intraband contributions in the AB-stacking case are neglected. The comparison of the resulting bilayer spectra with that of an isolated silicene sheet in Fig. 4.18 shows strong similarities in the higher-energy range of the  $\sigma \to \sigma^*$  transitions and considerable variations in the low-energy range of  $\pi \to \pi^*$  transitions. These observations are in line with the findings for the band structures in Fig. 4.17. Most interesting is the fact that the normalized spectrum of  $\operatorname{Re} \sigma_{2D}^{\parallel}(\omega \to 0)$  does not approach the value of 2 (in units of  $\sigma_0\pi\alpha$ ). Rather, for  $\omega \to 0$  the absorbance vanishes for AA stacking but increases for AB stacking. The low-energy peak in the monolayer spectrum that we related to  $\pi \to \pi^*$  transitions near the M point (see Fig. 4.4) is significantly modified in lineshape. The main spectral weight is shifted toward higher (lower) photon energies for AA (AB) stacking of the two silicene layers.

96 F. Bechstedt et al.

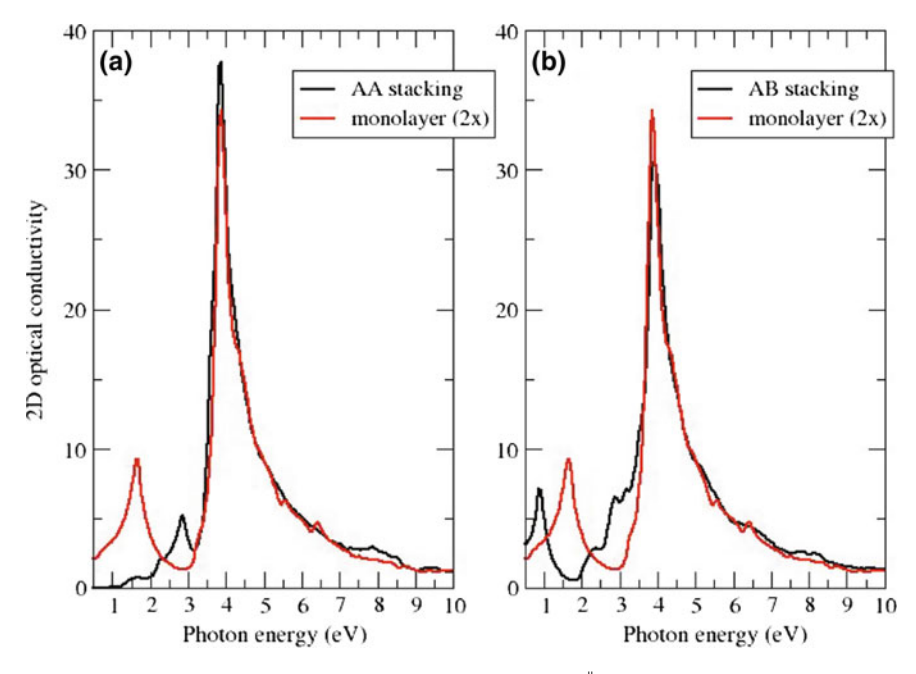


Fig. 4.18 Real part of the in-plane optical conductivity  $\operatorname{Re}\sigma_{2D}^{\parallel}(\omega)$  of AA-stacked (a) and AB-stacked (b) bilayer silicene (black lines). For comparison, the result for two non-interacting silicene layers (red lines) is also displayed. The spectra are normalized to the dc conductivity  $\varepsilon_0 c$  and  $\pi \alpha$ . Therefore, the red curves approach the value 2 for  $\omega \to 0$ 

### 4.5 Summary and Conclusions

In summary, first-principles calculations have been performed to describe the optical properties of silicene and the related materials germanene and stanene. For comparison, also spectra have been computed for graphene. The isolated 2D sheet crystals are described within a repeated arrangement of such sheets in superlattices with sufficiently large lattice constant. We have demonstrated how (i) the optical conductivity or a dielectric function of a sheet crystal can be derived from the frequency-dependent dielectric tensor of the superlattice and (ii) these quantities influence the optical reflectivity, transmittivity and absorptivity of a layered system containing a 2D crystal. We have described the difficulties to include such an atomically thin layer and the difficulties related to the out-of-plane component of the optical conductivity.

Three different approximations of the many-body effects have been studied. We found that local-field effects play a minor role, especially those due to the atomic arrangement in the sheets. Quasiparticle effects on top of the electronic structure obtained in the Kohn-Sham framework and excitonic effects, the Coulomb attraction between excited electrons and holes, tend to cancel each other. The quasiparticle blueshift is widely compensated by the redshift due to the electron-hole attraction.

Consequently, the independent-particle approximation seems to give a reasonable first approach to the optical conductivity.

In general, for low frequencies the reflectivity vanishes and the absorbance is equal to the real part of the in-plane optical conductivity. This absorbance of freestanding sheet honeycomb crystals is mainly given by  $\pi\alpha$  with  $\alpha$  the Sommerfeld finestructure constant, but modified for strong spin-orbit interaction. The result is independent of the chemical element, the layer buckling, and the bond hybridization. For higher photon energies the optical properties are ruled by interband transitions near critical points. Amazingly, the reflection, transmission and absorption show drastic changes near the resonances despite the atomically thin objects. These facts suggest the possibility to tailor optical properties of given substrates in a wide frequency range by deposition of single or multiple layers of silicene or other group-IV sheet crystals. The corresponding modifications have been illustrated for bilayer systems.

**Acknowledgements** O.P. acknowledges financial support from the EU HORIZON2020 (RISE project CoExAN GA644076).

### References

- 1. L. Matthes, O. Pulci, F. Bechstedt, New J. Phys. 16, 105007 (2014)
- R.R. Nair, P. Blake, A.N. Grigorenko, K.S. Novoselov, T.J. Booth, T. Stauber, N.M.R. Peres, A.K. Geim, Science 320, 1308 (2008)
- 3. K.F. Mak, M.Y. Sfeir, Y. Wu, C.H. Lui, J.A. Misewich, T.F. Heinz, Phys. Rev. Lett. **101**, 196405 (2008)
- 4. K.F. Mak, J. Shan, T. Heinz, Phys. Rev. Lett. 106, 046401 (2011)
- U. Wurstbauer, C. Röling, W. Wegscheider, M. Vaupel, P.H. Thiesen, D. Weis, Appl. Phys. Lett. 97, 231901 (2010)
- P. Vogt, P. de Padova, C. Quaresima, J. Avila, E. Frantzeskazis, M.C. Asensio, A. Resta, B. Ealet, G. Le Lay, Phys. Rev. Lett. 108, 155501 (2012)
- B. Feng, Z. Ding, S. Meng, Y. Yao, X. He, P. Cheng, L. Chen, K. Wu, Nano Lett. 12, 3507 (2012)
- 8. Y. Borensztein, G. Prévot, L. Masson, Phys. Rev. B 89, 245410 (2014)
- 9. G. Prévot, D. Bernard, H. Cruegel, Y. Borensztein, Appl. Phys. Lett. 105, 213106 (2014)
- 10. T. Stauber, N.M.R. Peres, A.K. Geim, Phys. Rev. B 78, 085432 (2008)
- 11. H.S. Skulason, P.E. Gaskell, T. Szkopek, Nanotechnology 21, 295709 (2010)
- 12. T. Zhan, X. Shi, Y. Dai, X. Liu, J. Zi, J. Phys.: Condens. Matter 25, 215301 (2013)
- 13. X.-H. Deng, J.-T. Liu, J.-R. Yuan, Q.-H. Liao, N.-H. Liu, EPL **109**, 27002 (2015)
- 14. G. Kresse, J. Furthmüller, Phys. Rev. B 54, 1169 (1996)
- 15. G. Kresse, J. Furthmüller, Comput. Mater. Sci. 6, 15 (1996)
- P. Giannozzi, S. Baroni, N. Bonini, M. Calandra, R. Car, C. Cavazzoni, D. Ceresoli, G.L. Chiarotti, M. Cococcioni, I. Dabo, R.M. Wentzcovitch, J. Phys.: Condens. Matter 21, 395502 (2009)
- 17. J. Perdew, *Electronic Structure of Solids '91* (Akademie-Verlag, Berlin, 1991)
- 18. J.P. Perdew, Y. Wang, Phys. Rev. B 45, 13244 (1992)
- 19. P.E. Blöchl, Phys. Rev. B 50, 17953 (1994)
- 20. G. Kresse, D. Joubert, Phys. Rev. B 59, 1758 (1999)
- 21. F. Bechstedt, Principles of Surface Physics (Springer, Berlin, 2003)
- 22. H.J. Monkhorst, D.J. Pack, Phys. Rev. B 13, 5188 (1976)

98 F. Bechstedt et al.

- 23. L. Matthes, P. Gori, O. Pulci, F. Bechstedt, Phys. Rev. B 87, 035438 (2013)
- 24. S. Cahangirov, M. Topsakal, E. Aktürk, H. Sahin, S. Ciraci, Phys. Rev. Lett. 102, 236804 (2008)
- B. van den Broek, M. Houssa, E. Scalise, G. Pourtois, V.V. Afanaasév, A. Stermans, 2D Mater. 1, 021004 (2014)
- 26. L. Matthes, O. Pulci, F. Bechstedt, J. Phys.: Condens. Matter 25, 395305 (2013)
- 27. F. Bechstedt, Many-Body Approach to Electronic Excitations (Springer, Berlin, 2015)
- 28. J. Heyd, G.E. Scuseria, M. Ernzerhof, J. Chem. Phys. 118, 8207 (2003); 124, 219906 (2006)
- 29. F. Fuchs, J. Furhtmüller, F. Bechstedt, M. Shishkin, G. Kresse, Phys. Rev. B 76, 115109 (2007)
- 30. Y. Zhang, Y.-W. Tan, H.L. Stormer, P. Kim, Nature **438**, 201 (2005)
- 31. B. Adolph, V.I. Gavrilenko, K. Tenelsen, F. Bechstedt, R. Del Sole, Phys. Rev. B 53, 9797 (1996)
- 32. M. Gajdoš, K. Hummer, G. Kresse, J. Furthmüller, F. Bechstedt, Phys. Rev. B 73, 045112 (2006)
- 33. F. Bechstedt, R. Enderlein, Superlattices Microstruct. 2, 543 (1986)
- 34. L. Matthes, O. Pulci, F. Bechstedt, Phys. Rev. B 94, 205408 (2016)
- 35. J.D. Jackson, Classical Electrodynamics (Wiley, New York, 2001)
- 36. P. Berning, in *Physics of Thin Films*, ed. by G. Hass (Academic Press, New York and London, 1963), p. 69
- 37. L. Yang, M.L. Cohen, S.G. Louie, Nano Lett. 7, 3112 (2007)
- O. Pulci, M. Marsili, V. Garbuio, P. Gori, I. Kupchak, F. Bechstedt, Phys. Status Solidi B 252, 72 (2015)
- 39. W. Wei, Y. Dai, B. Huang, T. Jacob, Phys. Chem. Chem. Phys. **15**, 8789 (2013)
- 40. L. Yang, J. Deslippe, C.-H. Park, M.L. Cohen, S.G. Louie, Phys. Rev. Lett. 103, 186802 (2009)
- 41. O. Pulci, P. Gori, M. Marsili, V. Garbuio, R. Del Sole, F. Bechstedt, EPL 98, 37004 (2012)
- 42. http://etsf.polytechnique.fr/exe/
- 43. D. Jérome, T.M. Rice, W. Kohn, Phys. Rev. 158, 462 (1967)
- 44. W. Jones, N.H. March, *Theoretical Solid State Physics*, vol. 2 (Dover Publications Inc., New York, 1985)
- 45. G.-Z. Liu, W. Li, G. Chen, Phys. Rev. B 79, 205429 (2009)
- 46. T. Stroucken, J.H. Grönqvist, S.W. Koch, Phys. Rev. B 84, 205445 (2011)
- 47. T. Eberlein, U. Bangert, R.R. Nair, R. Jones, M. Gass, A.L. Bleloch, K.S. Novoselov, A. Geim, P.R. Briddon, Phys. Rev. B 77, 233406 (2008)
- 48. V. Despoja, D. Novko, K. Dekanič, M. Sunjić, L. Marušić, Phys. Rev. B 87, 075447 (2013)
- 49. F. Bechstedt, L. Matthes, P. Gori, O. Pulci, Appl. Phys. Lett. **100**, 261906 (2012)
- 50. B. Huang, H.-X. Deng, H. Lee, M. Yoon, B.G. Sumpler, F. Liu, S.C. Smith, S.-H. Wei, Phys. Rev. X 4, 021029 (2014)
- 51. P. Pflugradt, L. Matthes, F. Bechstedt, Phys. Rev. B 89, 205428 (2014)
- 52. E.J. Nicol, J.P. Carbotte, Phys. Rev. B 77, 155409 (2008)
- Z.Q. Li, E.A. Henriksen, Z. Jiang, Z. Hao, M.C. Martin, P. Kim, H.L. Stormer, D.N. Basov, Phys. Rev. Lett. 102, 037403 (2009)
- 54. K. Lee, E.D. Murray, K. Long, B.I. Lundqvist, D.C. Langreth, Phys. Rev. B 82, 081101 (2010)
- U. Wurstbauer, C. Röling, U. Wurstbauer, W. Wegscheider, M. Vaupel, P.H. Thiesen, D. Weiss, Appl. Phys. Lett. 97, 231901 (2010)
- 56. B. Mohan, A. Kumar, P.K. Ahluwalia, Physica E **53**, 233 (2013)

## **Chapter 5 Synthesis of Silicene**



Guy Le Lay, Dmytro Solonenko and Patrick Vogt

**Abstract** The key issue for the first proof-of-principle synthesis of the two-dimensional Si allotrope, silicene, realized in 2012, was to find an appropriate substrate. Here, we give a background for the initial choice of silver single crystals, determined by decades of studies of the reverse system: silver deposited onto silicon (111) templates. Next, clever serendipity lead to another platform: ZrB<sub>2</sub> thin films grown on Si(111). Clearly, non-metallic substrates would be preferred for many practical applications, they are currently searched for. A digest of this quest is presented in this chapter.

### 5.1 Introduction

The possible existence of silicene as a standalone novel two-dimensional (2D) silicon allotrope with a *corrugated* stage was already conjectured in 1994 in Density Functional Theory (DFT) calculations by Kyozaburo Takeda and Kenji Shiraishi, ten years before the advent of graphene [1]. Such silicene layers differ from graphene, which is basically flat, have a ~0.44 nm out-of-plane buckling between the A and B sublattices. Their paper remained essentially unnoticed for many years, because most scientists did not believe in the existence of silicene [2], and, hence, did not try to synthesize it.

However, if a pristine free-standing single layer sheet of silicene has not been be discovered, silicene could still be grown on some support, for instance, metallic or semiconductor surface, as it was stressed by Nobel laureate Roald Hoffmann [3].

G. Le Lay (⊠)

CNRS, PIIM UMR 7345, Aix-Marseille University, Marseille, France

e-mail: guy.lelay@univ-amu.fr

D. Solonenko · P. Vogt

Institut für Physik, Technische Universität Chemnitz, Reichenhainer Str. 70,

09126 Chemnitz, Germany

e-mail: dmytro.solonenko@physik.tu-chemnitz.de

P. Vogt

e-mail: patrick.vogt@physik.tu-chemnitz.de

© Springer Nature Switzerland AG 2018

P. Vogt and G. Le Lay (eds.), *Silicene*, NanoScience and Technology,

100 G. Le Lay

Indeed, standalone silicene has not been realized until now, but epitaxial silicene has been synthesized on few substrates, especially, since 2012, on silver (111) single crystals [4], and on zirconium diboride (0001) thin films grown on silicon (111) [5].

This achievement has further triggered research on other silicene-like counterparts of graphene. To date, germanene [6–8], stanene [9], hafnene [10] and borophene [11], the 2D analogues for germanium, tin, hafnium and boron, have been synthesized on diverse substrates. Obviously, the family of artificial elemental two-dimensional materials, which have no layered equivalent crystal in nature, as in the cases of graphene and phosphorene [12] is rapidly growing.

In this chapter, we will review the motivation for the silver track as well as for the unexpected  $ZrB_2$  films, and highlight some relevant aspects of silicene synthesis and its characterization.

### 5.2 The Silver Track

The Ag on Si(111) couple has been—and still is—the most prototypical metal-semiconductor system for several decades, especially in the context of the Schottky barrier problem. The study of the Ag/Si(111) system was already pioneered in the seventies [13] and has become the reference example of the Stranski-Krastanov (or layer-plus-islands) growth mode. Here, three dimensional (3D) Ag crystallites develop on top a 2D Ag ad-layer forming the well-known Si(111)  $\sqrt{3} \times \sqrt{3}$ R(30°)-Ag reconstruction (in short Si(111)  $\sqrt{3}$ -Ag) [14], interpreted in terms of the so-called Honeycomb-Chained-Triangle (HCT) model at room temperature (RT) [15]. Figure 5.1 illustrates this growth by the Low Energy Electron Microscopy (LEEM) image and Low Energy Electron Diffraction (LEED) patterns [16].

At variance with most of metal/semiconductor systems, which are reactive and present a strong intermixing, the interface between silver atoms and Si(111) is unre-

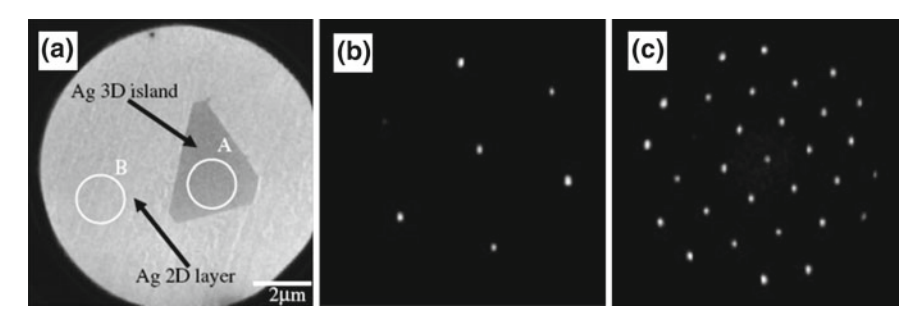


Fig. 5.1 Illustration of the Stranski-Krastanov growth mode for the prototypical Ag on Si(111) metal/semiconductor system (adapted from Fig. 5.1 of [17]). a Bright field LEEM image taken at 14.4 eV (10  $\mu$ m field of view). b and c local area LEED patterns taken at 33.2 eV obtained at circles A and B (1.3  $\mu$ m in diameters) in the LEEM image

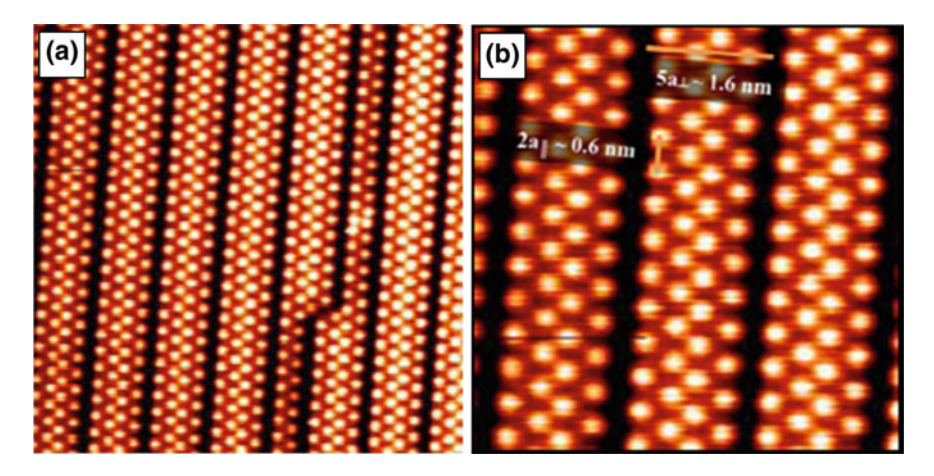


Fig. 5.2 STM images of atom-thin nanoribbons obtained upon deposition of Si onto an Ag(110) surface and forming a highly ordered 2  $\times$  5 grating (adapted from Fig. 5.2 of [22]). Left, 15  $\times$  15 nm<sup>2</sup> image acquired at T=80 K,  $V=\pm0.05$  V, I=200 nA; Right,  $6.5\times6.5$  nm<sup>2</sup> image acquired at T=5 K,  $V=\pm0.05$  V, I=200 nA

active and atomically abrupt. This specific aspect was motivation for trying to grow silicene on Ag(111) single crystals, with the guess of avoiding any detrimental interface reactions.

Clearly, nothing was guaranteed, especially, since it was known that germanium deposited onto Ag(111) forms a Ag<sub>2</sub>Ge surface alloy with a coverage of 1/3 monolayer (ML) already at RT [17]. A more favorable situation was found for Ag(110) templates, where germanium forms self-assembled germanium nano-clusters [18]. Silicon forms on the same template unique, massively parallel, one-atom-thin nanoribbons (or stripes) with a "magic" width of just 16 Å, perfectly aligned along the [1–10] direction, and organized, at completion, in a grating with a pitch of just 20 Å [19–21], as shown in Fig. 5.2.

Then, upon depositing Si (by sublimation of a piece of silicon wafer) in ultra-high vacuum on the Ag(111) surface held at ~220 °C, a Si superstructure was discovered with a  $4\times4$  periodicity with respect to primitive Ag(111)  $1\times1$  in LEED patterns and STM images. The superstructure was found to exhibit a perfect 2D growth wetting the Ag surface up until the full coverage is reached (Fig. 5.3). A structure known now as the "flower pattern" [4], the unique building block, paved the way for silicene, but does not resemble with what was naively expected for a honeycomb graphene-like Si sheet.

It was an inspiration, supported by DFT calculations and complimentary angleresolved photoelectron spectroscopy (ARPES) results, showing a linear electronic dispersion, which helped to unveil the hidden underlying honeycomb arrangement of a  $3 \times 3$  reconstructed silicene monolayer. Up to now, epitaxial silicene turns out 102 G. Le Lay

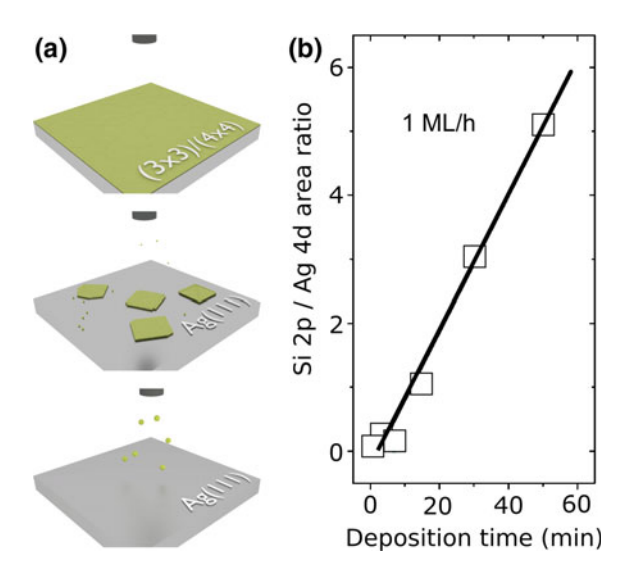


Fig. 5.3 a Sketch of the 2D growth of epitaxial silicene on Ag(111). b Si 2p/Ag 4d area ratio as a function of Si deposition time suggesting the layer-by-layer, linear, silicene growth on the Ag surface (adapted from [4]). The slope allows the determination of the silicene growth rate for the given conditions

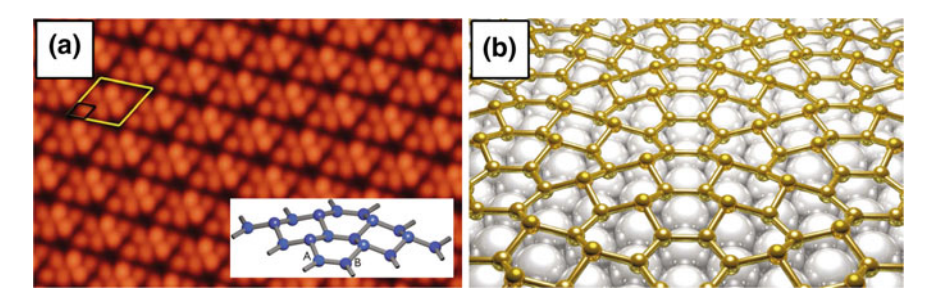


Fig. 5.4 The archetype structure of epitaxial monolayer silicene on Ag(111) (adapted from figures in [23]). a Filled states STM image (10 nm in width, tunnel current 0.55 nA, sample bias -520 mV) showing the "flower pattern", which results from protruding Si atoms within the  $3 \times 3$  reconstructed silicene monolayer (the  $3 \times 3$  supercell and the primitive  $1 \times 1$  cell are indicated in yellow and in black, respectively). Inset: perspective view of the atomic model of the  $3 \times 3$  reconstructed silicene monolayer. b An artistic rendering of the  $3 \times 3$  reconstructed silicene monolayer on Ag(111) by courtesy of Prof. Thierry Angot from Aix-Marseille University

to be always reconstructed on metallic substrates, because of the interaction and because silicene is compliant: the inherent buckling gives a great flexibility of the bond angles, favoring an adaptation in a coincidence lattice [22], as illustrated in Fig. 5.4.

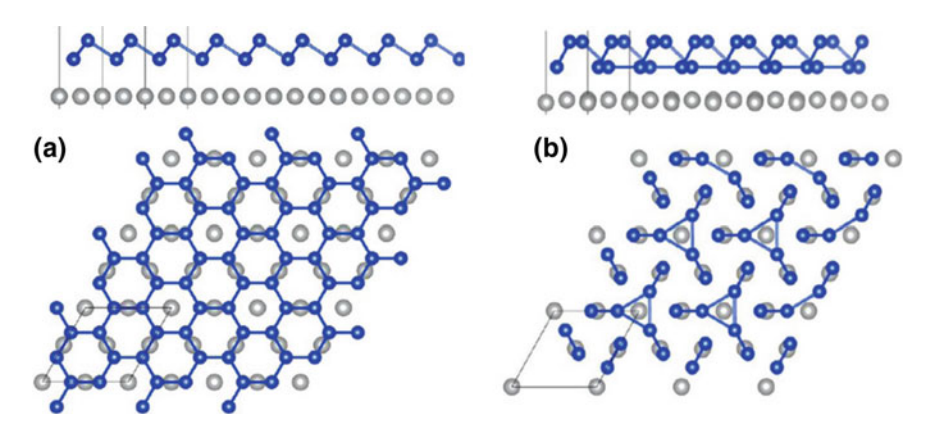


Fig. 5.5 Instability of an illusory  $3 \times 3$  silicene sheet in coincidence with a  $2\sqrt{3} \times 2\sqrt{3}$  Ag(111) supercell (adapted from [26]). a Top and side view of the starting model of the hypothetical  $3 \times 3/2\sqrt{3} \times 2\sqrt{3}$  phase for the DFT calculations. b Relaxation result showing the instability of the hypothetical phase. Blue balls: Si atoms, grey balls: Ag atoms

### **5.3** Ag(111) Mimicking a Honeycomb Lattice

The naive expectation of a simple honeycomb appearance of silicene in STM imaging can be specious. It turns out that the bare Ag(111) surface can be reversed in contrast during STM imaging, which mimics a honeycomb lattice [23]. This effect led in 2010 to the conclusion that a silicene sheet was synthesized on the basis of the STM images only [24]. The unit cell of that structure in this case was claimed to be of just ~3.29 Å, with a tiny corrugation of only 0.2 Å, in strong contrast to the values calculated for free-standing silicene, 3.83 Å and 0.44 Å, respectively [25]. Similar discrepancy was found in a value of the Si–Si distance of 0.19 nm for the newly found structure as compared to that of free-standing sheet: 0.22 nm. Indeed, this result was rapidly questioned by several experimental groups, discussed in [26]. 2D crystallography considerations and DFT calculations as well as the lack to reproduce this structure have eventually confirmed the impossibility of the formation of the claimed silicene lattice with the small ~3.29 Å parameter on Ag(111) [26], as illustrated in Fig. 5.5.

### 5.4 Growth Mode and Structure Formation of Si on the Ag(111) Surface

Lee et al. have studied and compiled a number of different structures observed in STM upon depositing diverse amounts of Si onto the bare Ag(111) surface held at various temperatures [27]. Only few of them occupy significant areas and can be reliably examined. To date, only the archetype  $3 \times 3$  structure, matching a  $4 \times 4$  Ag(111) supercell (or S1/A1 phase in Figs. 5.6 and 5.7) and showing a "flower pattern" in

104 G. Le Lay

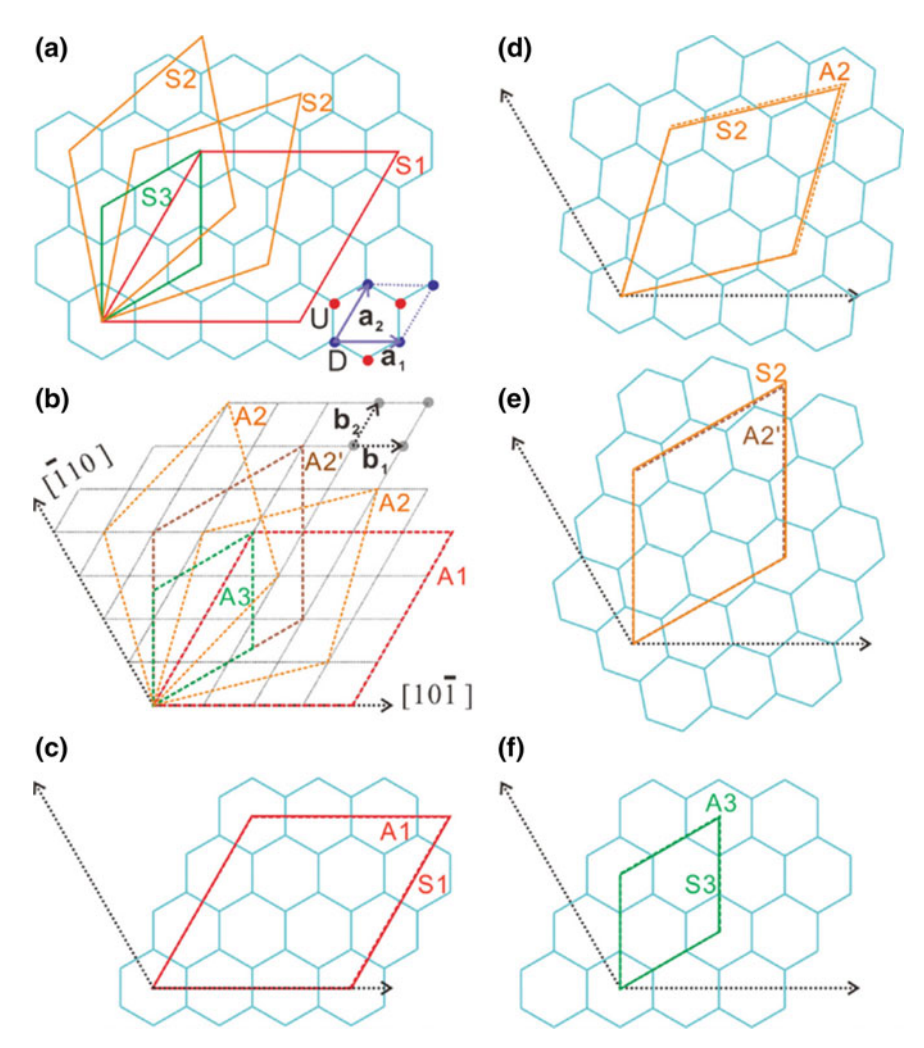
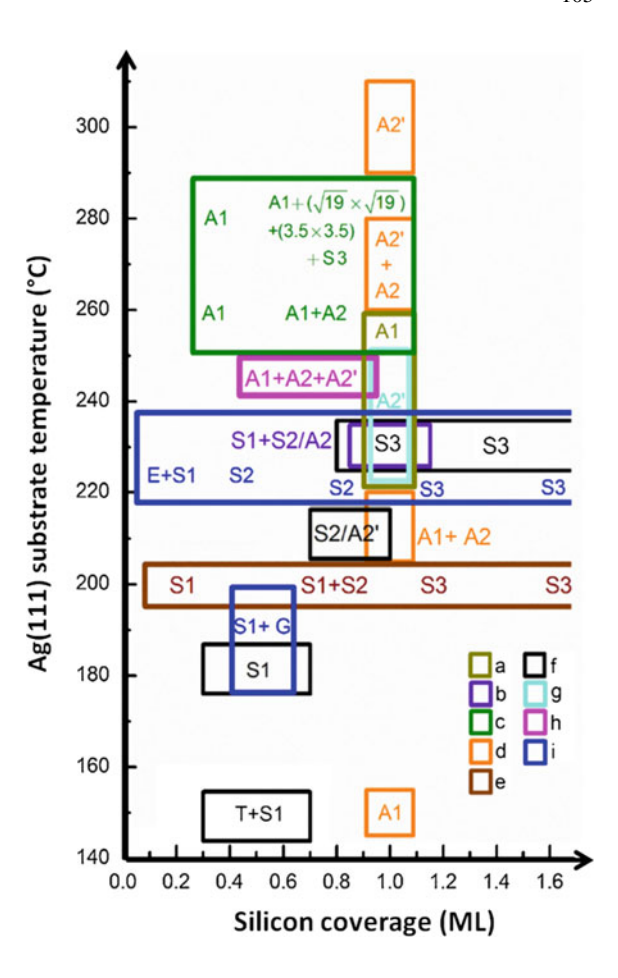


**Fig. 5.6** Various supercells using a free silicene lattice (labelled S) and a Ag(111) surface lattice (labelled A), as listed in -and adapted from [27]. Blue honeycombs represent standalone silicene lattices. In (a)  $a_1$  and  $a_2$  indicate primitive translation vectors; blue and red circles represent the lower (D) and upper (U) basis atoms, respectively. In (b)  $b_1$  and  $b_2$  are primitive vectors for the silver (111) lattice in dash gray. c-f show that a silicene-based supercell (solid rhombus) can match a corresponding Ag-based one (dashed rhombus) when the silicene lattice in blue suitably rotates wrt the fixed lattice (represented by dashed arrows) of the Ag(111) substrate

STM, has passed crucial diffraction tests. Reflection high energy positron diffraction [28] or dynamical LEED analysis [29] could confirm its honeycomb lattice and show that this structure can cover up to 95% of the substrate's surface.

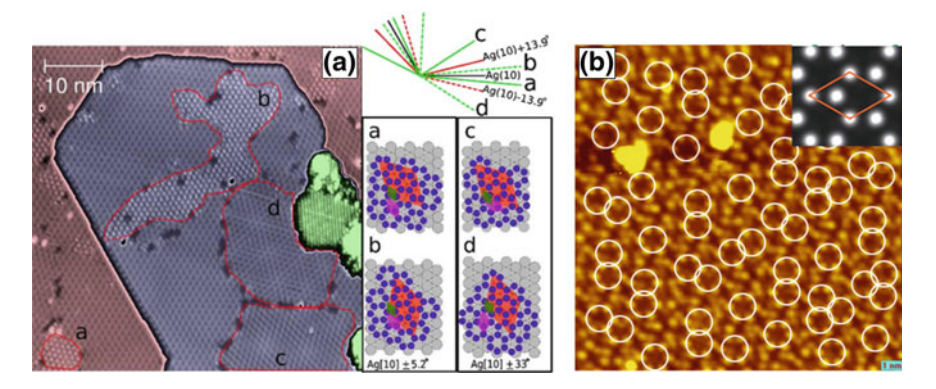
Another silicene phase, generally co-existing with the  $3 \times 3(\text{S1/A1})$ , the " $\sqrt{7} \times \sqrt{7}/\sqrt{13} \times \sqrt{13}$ " according to notations in [30] (S2/A2 in Figs. 5.6 and 5.7), can be

Fig. 5.7 Phase diagram (schematics, with the phase labels indicated in Fig. 5.6) of the observed structures as a function of substrate temperature and the Si coverage (adapted from Fig. 5.2 of [27]). E1–E4 are precursor states at domain edges in Fig. 5.7 of [27]. The blue box (i) is the work of the authors of [27], while data (a)–(i) summarize some results from the literature cited [27]



present in 4 symmetry equivalent domains on the surface, as illustrated in the STM topograph in Fig. 5.8a. DFT calculations support an assignment of this structure to silicene [31]. Yet, the in-plane lattice parameter in this 4-domain phase turns out to be slightly expanded, while the nominal surface coverage ratio would be 14/13 = 1.08, which is a bit lower than that of the archetypical phase with reference value 18/16 = 1.125 (Fig. 5.7).

Another Si structure, indicated by S2/A'2 in Figs. 5.5 and 5.6, obtained at high preparation temperatures (>250 °C) can form in extended areas, although with a highly defective appearance in STM imaging (see Fig. 5.8b). It is often referred to as  $(2\sqrt{3} \times 2\sqrt{3})$ R30° structure with regard to the Ag(111) lattice LEED, but should be better re-named as " $2\sqrt{3} \times 2\sqrt{3}$ ", since a real  $2\sqrt{3} \times 2\sqrt{3}$  periodicity is not really respected [32]. Its assignment to a similar epitaxial silicene sheet as the  $3 \times 3$  is questionable and strongly debated [33]. As a matter of fact, this structure is essentially linked to a fating of the 2D layer and finally a de-wetting process



**Fig. 5.8** Other extended structures. **a** STM image showing the four expected S2/A2 domains in addition to the archetype S1/A1 silicene structure on Ag(111); adapted from Fig. 5.4 of [30]. **b** STM image of the " $2\sqrt{3} \times 2\sqrt{3}$ " superstructure wrt Ag(111) recorded at 77 K ( $15 \times 15 \text{ nm}^2$ ,  $U_{\text{bias}} = 95.3 \text{ mV}$ , I = 0.2 nA). The aperiodic circles indicate very local honeycomb arrangements corresponding to the simulated STM image (in inset, after Fig. 5.2e of [31]) of an ideally  $\sqrt{7} \times \sqrt{7}$  reconstructed silicene sheet on a perfect  $2\sqrt{3} \times 2\sqrt{3}$ R( $30^{\circ}$ ) Ag(111) supercell

[34]. All these structures are stable under UHV conditions, once prepared, and can survive several weeks or possibly longer. Under ambient conditions, i.e. in air, the 2D Si layers are not stable and will be destroyed by oxidation or contamination processes. Nevertheless, it is a time lapse long enough to measure the characteristics of field effect transistors (FETs) operating at RT, fabricated with a single layer silicene channel [35].

### 5.5 Multilayer Silicene

Continuing the growth beyond the first  $3 \times 3$  layer in direct contact with the substrate, one obtains multilayers, which grow as successive terraces [36] (Fig. 5.9). All those terraces show an unique  $\sqrt{3} \times \sqrt{3}$  superstructure with respect to the primitive silicene cell, where protruding Si atoms arrange into honeycombs as seen in the STM images (Fig. 5.10a, b).

These multilayers exhibit a linear electronic dispersion in ARPES measurements depicted in Fig. 5.10c, a prerequisite to host Dirac fermions. The crossing point of the bands is found at ~0.3 eV below the Fermi level, which can be explained by a charge transfer from the silver substrate into the Si-multilayers, resulting in a partial filling of the  $\pi^*$  upper cone [37].

Such electronic structure is not expected for a bulk-like Si arrangement and, therefore, supported the interpretation of these multi-layer stacks as "multi-layer silicene". Similarly, to graphite, multi-layer silicene would consist of silicene monolayers weakly interacting with each other by van der Waals forces. While the first

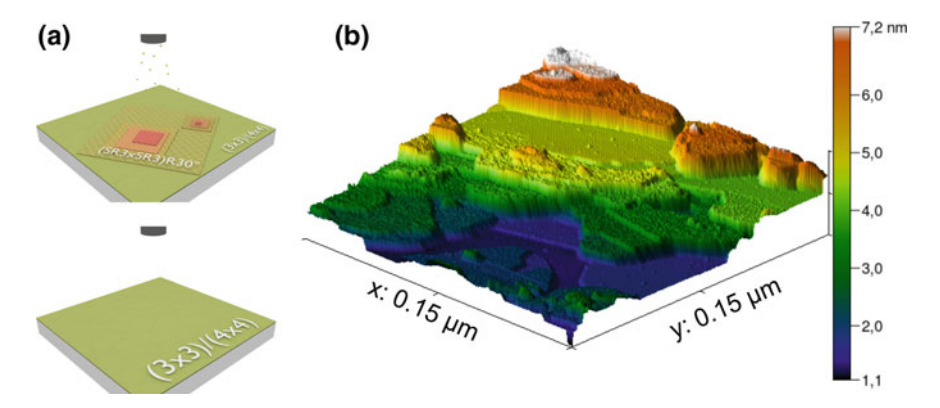


Fig. 5.9 a Sketches of the layer-plus-island growth of the  $\sqrt{3} \times \sqrt{3}$  structure on top of epitaxial silicene/Ag(111). b The stereographic STM topograph ( $U_{\text{bias}} = -1.1 \text{ V}$ ,  $I_{\text{t}} = 1.73 \text{ nA}$ ), after deposition of approximately 5 MLs of Si onto the first Si layer (adapted from [37])

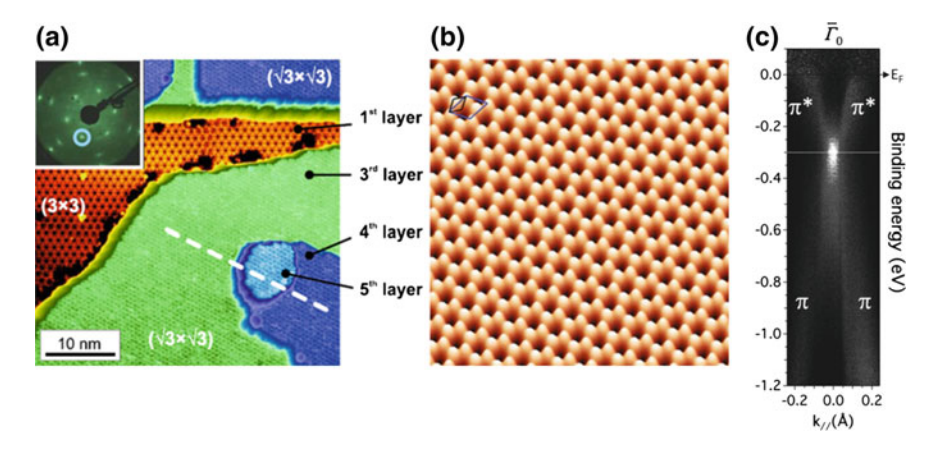


Fig. 5.10 Growth of multilayers. **a** Three well-ordered successive terraces showing the unique  $\sqrt{3} \times \sqrt{3}$  reconstruction are seen in STM imaging at ~1.5 ML additional coverage of Si onto the  $3 \times 3$  initial monolayer (Filled states:  $U_{\text{bias}} = -1.1 \text{ V}$ ,  $I_{\text{t}} = 0.54 \text{ nA}$ ; adapted from Fig. 5.2 in [27]). **b** Zoom-in at the  $\sqrt{3} \times \sqrt{3}$  structure of the terraces (9 nm × 9 nm; filled states: 0.16 nA, -560 mV; the  $\sqrt{3} \times \sqrt{3}$  supercell is indicated in blue; adapted from Fig. 5.4 of [23]). **c** Evidence of Dirac fermions in those multilayers: a Dirac cone with  $\pi$  and  $\pi^*$  states, is recorded in synchrotron radiation ARPES at the center of the Brillouin zone due to the band folding associated with the reconstruction (the Dirac point is situated at ~0.3 eV below the Fermi level  $E_{\text{F}}$ ; adapted from Fig. 5.4 of [23])

silicene wetting layer is reconstructed due to the interaction to the silver substrate, the next layers should barely experience the influence of the substrate. Such scenario implies that the upper layers should acquire properties similar to a free-standing Si sheet, seemingly in agreement with the electronic dispersions at the K points of  $\sqrt{3} \times \sqrt{3}$  layers.

108 G. Le Lay

However, the observation of the "multi-layer silicene" could also be explained considering other systems, such as Ag surface reconstruction on top of the bulk Si surface [38]. This fact as well as missing appropriate structural model of multi-layer silicene, explaining all experimental observations, casts doubt on this concept.

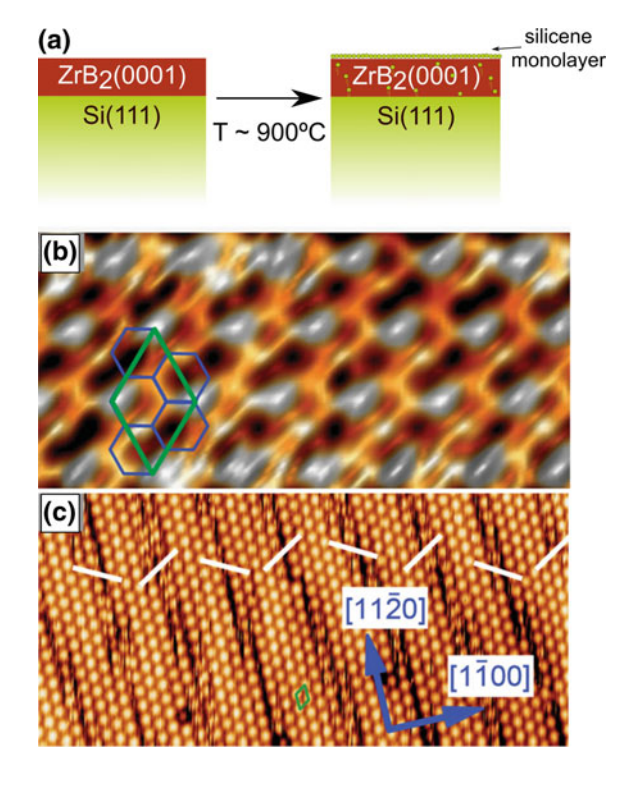
It is thus important to point out the characteristics expected for a layered silicene structure in order to identify it. One of the most important properties is the weak inter-layer interaction, which implies that the single Si layers should show properties closer to quasi-free-standing silicene if compared to epitaxial silicene on a substrate material. Similarly to graphene and graphite, the electronic band structure might still be perturbed by the presence of other layers but the atomic arrangement within the layer should show a low buckling and a clear indication of a sp<sup>2</sup>/sp<sup>3</sup> hybridization. In order to probe these structural properties X-ray diffraction has been carried out, showing conflicting results. The diffraction results of De Padova et al. give indication for a weak inter-layer interaction due to an absent contraction between the layers in the out-of-plane direction and support the interpretation as a silicene multi-layer [39]. On the other hand Curcella et al. find that the difference in the lattice constants stems from the built-in strain within bulk Si lattice, contradicting the formation of silcene multi-layers [38].

At the same time, the structural properties also alter the vibrational signature, as can be probed by Raman spectroscopy, vastly used to study graphene-based systems [40] as well as other layered materials such as transition metal dichalcogenides [41]. However, the Raman studies carried out so far for the Si multi-layer system, report a phonon mode at 523 cm<sup>-1</sup> [39, 42], a mode very close to the L(T)O mode of bulk Si at 520 cm<sup>-1</sup> [43]. Furthermore, this observation differs significantly from the A-modes (at 175 and 216 cm<sup>-1</sup>) and the E-mode (514 cm<sup>-1</sup>) observed for epitaxial silicene on Ag(111) [44] (a detailed discussion is found in Chap. 7). For a silicene multi-layer structure one would expect that the vibrational signatures gets closer to the one of free-standing silicene with an A-mode at 180 cm<sup>-1</sup> and an E-mode at 580 cm<sup>-1</sup> [25], which is obviously not the case. Yet, the Raman results do not unambiguously support the interpretation as a silicene multi-layer.

Alternative model to explain the atomic structure of the Si multi-layer include bulk-like Si crystallites with a  $(\sqrt{3} \times \sqrt{3})$ R30° Si surface reconstruction [45] or a Agterminated bulk Si surface showing the well-known Honeycomb-Chained-Triangle (HCT) model, proposed for the formation of the Ag terminated  $(\sqrt{3} \times \sqrt{3})$ R30° reconstruction formed on Si (111) [46]. Another possible explanation is the formation of silicene dumbbell double-layers [47]. In its free-standing form such dumbbell structure is energetically stable and is discussed in detail in Chap. 8.

However, so far, a clear assignment of the  $\sqrt{3} \times \sqrt{3}$  superstructure to "multi-layer silicene" emains questionable.

Fig. 5.11 a Scheme of the silicene formation on the ZrB<sub>2</sub>(0001) thin film as a result of the interdiffused Si atom surface segregation. STM images of the segregated  $\sqrt{3} \times \sqrt{3}$  silicene layer on the  $(2 \times$ 2)-reconstructed ZrB<sub>2</sub>(0001) surface at different length scales. **b**  $20 \text{ nm} \times 9.5 \text{ nm}$ ; the white lines point the directions of offsets between successive domains. c  $4.2 \text{ nm} \times 2 \text{ nm}$ . The honevcomb mesh and the  $(2 \times 2)$  unit cell are signaled by green and blue solid lines, respectively. Adapted from Fig. 5.1 of [41]



### 5.6 Silicene Segregated on ZrB<sub>2</sub> Thin Films

Another substrate, on which the formation of epitaxial silicene has been observed, is a  $ZrB_2(0001)$  metallic thin film of about 15–30 nm in thickness, grown in situ on a Si(111) substrate. Initially these layers were planned to be used as intermediate platforms for the growth of other electronic materials. However, Fleurence et al. noticed a Si segregation to the surface of  $ZrB_2$  at elevated temperatures [5]. A comprehensive characterization of the segregated layer, including STM measurements and synchrotron radiation photoemission studies as well as the support from DFT calculations demonstrated the formation of a 2D Si top-layer. The authors could show that the observed striped structure shown in Fig. 5.11 represents an epitaxial  $\sqrt{3} \times \sqrt{3}$  reconstructed epitaxial silicene sheet, matching a  $2 \times 2$   $ZrB_2(0001)$  supercell.

Although the article of Fleurence et al. [5] appeared slightly later than the report on the formation of epitaxial silicene on Ag(111) [4], the simultaneity of these studies is worth stressing, especially in view of the very different procedures to produce a silicene sheet.

On-going work on the silicene ZrB<sub>2</sub> system has been reported in a review [48], and recent results show that a single-domain epitaxial silicene sheet can be formed, an important step forward [49].

110 G. Le Lay

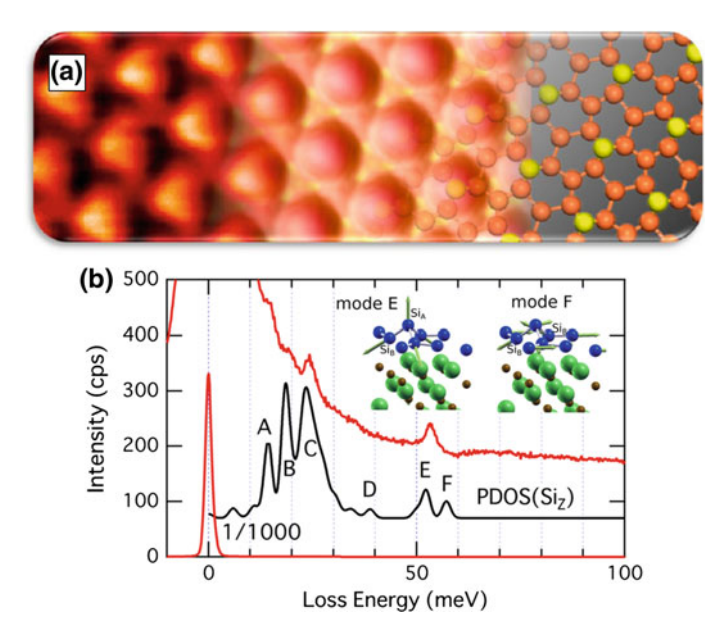


Fig. 5.12 Top vignette: illustration of the growth of silicene on the iridium (111) surface (adapted from [44]). Bottom vignette: Specular High Resolution Electron Energy Loss Spectroscopy ( $E_p = 9 \text{ eV}$ ) of the silicene layer formed on ZrC(111) (in red) and calculated Partial Density Of States of the vertical vibrations of silicene at the  $\bar{\Gamma}$  point (in black), broadened with a Gaussian of 1 meV width to simulate the experimental spectrum and arbitrarily magnified for comparison (adapted from Fig. 5.8 of [44])

### 5.7 Synthesis of Silicene on Other Metallic Substrates

In this section we will briefly summarize results on the synthesis of silicene single layers on other metallic substrates.

A  $\sqrt{3} \times \sqrt{3}$  reconstructed buckled silicene sheet matching a  $\sqrt{7} \times \sqrt{7}$  supercell of the substrate was observed on an Ir(111) substrate by Meng et al., see Fig. 5.12a, and identified through LEED and STM measurements, complemented by first-principles calculations. These calculations could confirm the 2D continuity of the adlayer, where each pair of silicon atoms shows a covalent interaction between them [50].

Similarly, Si deposition onto a ZrC(111) substrate results in a  $\sqrt{3} \times \sqrt{3}$  silicene monolayer coinciding with a 2 × 2 substrate periodicity, showing a thermal stability up to approximately 1000 K, and a relative inertness to a gas adsorption [51]. Remarkably, the phonon dispersions, measured by high resolution electron energy loss spectroscopy (HREELS), point to the existence of a covalently bonded Si–Si network. Here, at least one protruding Si atom exists in the unit cell, a result also confirmed by ab initio DFT calculations, predicting a distorted silicene structure. Especially, the dipole-active spectrum measured in the specular HREELS condition (Fig. 5.12b) agreed very well with the calculations, verifying the proposed structure.

Nearly three decades ago, Margaritondo and co-workers [52], in the course of examining the "other side" of the Schottky barrier formation process, presented the first experimental study on ordered semiconductor overlayers on single-crystal metal surfaces.

By exploring the local electronic structure using synchrotron radiation photoemission and electron energy-loss spectra, the authors found Si overlayers formed on the clean Al(111) surfaces at RT. The LEED pattern showed a  $3 \times 3$  periodicity for a Si coverage between 0.6 and 1 ML, which could reflect the formation of a silicene ad-layer, similarly to the successful growth of germanene by Derivaz et al. [8]. Indeed, this suggestion requires further experimental and theoretical confirmation.

We close this section with what we think could be a very exciting possibility. Since silicene, germanene and stanene are 2D materials suggested to be topological insulators (TIs), we propose to fabricate with them superconductor/2D TI interfaces. Superconducting proximity effects may lead to the appearance of Majorana fermions that could be searched for in vortices by Scanning Tunneling Spectroscopy (STS) measurements. Recently, Jia et al. reported the detection of a Majorana zero mode with spin selective Andreev reflection in the vortex of a TI, the topological superconductor of the Bi<sub>2</sub>Te<sub>3</sub>/NbSe<sub>2</sub> hetero-structure [53].

### **5.8 Concluding Remarks**

Overall, we have described the journey from 3D bulk silicon into the silicene flatlands. This development has sometime been harsh and strewn with pitfalls, but yet rewarding and ending up as a very exciting endeavor. Despite the success of paving the way for a number of novel artificial elemental two-dimensional materials, which did not exist in nature before, many gaps are to be filled in order to find the hidden patterns behind their formation and discoveries of new members are yet to come.

After all, the starting phase of this research has passed but the Holy Grail quest for the long-sought Majorana fermions continues, as an exciting scenario.

#### References

- 1. K. Takeda, K. Shiraishi, Phys. Rev. B **50**, 14916 (1994)
- 2. E.F. Sheka, Int. J. Quantum Chem. (2012). https://doi.org/10.1002/qua.24081
- 3. R. Hoffmann, Angew. Chem. Int. Ed. **52**, 93 (2013)
- 4. P. Vogt, P. De Padova, C. Quaresima, J. Avila, E. Frantzeskakis, M.C. Asensio, A. Resta, B. Ealet, G. Le Lay, Phys. Rev. Lett. **108**, 155501 (2012)
- A. Fleurence, R. Friedlein, T. Ozaki, H. Kawai, Y. Wang, Y. Yamada-Takamura, Phys. Rev. Lett. 108, 245501 (2012)
- 6. M.E. Dávila, L. Xian, S. Cahangirov, A. Rubioand, G. Le Lay, New J. Phys. 16, 095002 (2014)
- P. Bampoulis, L. Zhang, A. Safaei, R. van Gastel, B. Poelsema, H.J.W. Zandvliet, J. Phys.: Condens. Matter 26, 442001 (2014)

112 G. Le Lay

8. M. Derivaz, D. Dentel, R. Stephan, M.-C. Hanf, A. Mehdaoui, P. Sonnet, C. Pirri, Nano Lett. 15, 2510 (2015)

- 9. F.-F. Zhu, W.-J. Chen, Y. Xu, C.-L. Gao, D.-D. Guan, C.-H. Liu, D. Qian, S.-C. Zhang, J.-F. Jia, Nat. Mat. 14, 1020 (2015)
- L. Li, Y. Wang, S. Xie, X.-B. Li, Y.-Q. Wang, R. Wu, H. Sun, S. Zhang, H.-J. Gao, Nano Lett. 13, 4671 (2013)
- A.J. Mannix, X.-F. Zhou, B. Kiraly, J.D. Wood, D. Alducin, B.D. Myers, X. Liu, B.L. Fisher, U. Santiago, J.R. Guest, M.J. Yacaman, A. Ponce, A.R. Oganov, M.C. Hersam, N.P. Guisinger, Science 350, 1513 (2015)
- L. Li, Y. Yu, G.J. Ye, Q. Ge, X. Ou, H. Wu, D. Feng, X.H. Chen, Y. Zhang, Nat. Nanotechnol. 9, 372 (2014)
- 13. G. Le Lay, G. Quentel, J.P. Faurie, A. Masson, Thin Solid Films 35, 273 (1976)
- 14. G. Le Lay, Surface Sci. 132, 169 (1983)
- 15. S. Hasegawa, X. Tong, S. Takeda, N. Sato, T. Nagao, Prog. Surf. Sci. 60, 89 (1999)
- M. Hashimoto, F.-Z. Guo, M. Suzuki, M. Ueda, Y. Matsuoka, T. Kinoshita, K. Kobayashi, S. Shin, M. Oura, T. Takeuchi, Y. Saito, T. Matsushita, T. Yasuea, T. Koshikawa, Surf. Interface Anal. 40, 1772 (2008)
- 17. H. Oughaddou, S. Sawaya, J. Goniakowski, B. Aufray, G. Le Lay, J.M. Gay, G. Treglia, J.P. Biberian, N. Barrett, C. Guillot, A. Mayne, G. Dujardin, Phys. Rev. B **62**, 16653 (2000)
- C. Léandri, H. Oughaddou, J.M. Gay, B. Aufray, G. Le Lay, J.P. Bibérian, A. Ranguis, O. Bunk, R.L. Johnson, Surface Sci. 573, L369 (2004)
- C. Léandri, G. Le Lay, B. Aufray, C. Girardeaux, J. Avila, M.E. Dávila, M.C. Asensio, C. Ottaviani, A. Cricenti, Surface Sci. 574, L9 (2005)
- H. Sahaf, L. Masson, C. Léandri, F. Ronci, B. Aufray, G. Le Lay, Appl. Phys. Lett. 90, 263110 (2007)
- F. Ronci, S. Colonna, A. Cricenti, P. De Padova, C. Ottaviani, C. Quaresima, B. Aufray, G. Le Lay, Phys. Status Solidi C 7, 2716 (2010)
- 22. G. Le Lay, E. Salomon, T. Angot, Europhys. News 47, 17 (2016)
- 23. G. Le Lay, P. De Padova, A. Resta, T. Bruhn, P. Vogt, J. Phys. D Appl. Phys. 45, 392001 (2012)
- B. Lalmi, H. Oughaddou, H. Enriquez, A. Kara, S. Vizzini, B. Ealet, B. Aufray, Appl. Phys. Lett. 97, 223109 (2010)
- 25. S. Cahangirov, M. Topsakal, E. Aktürk, H. Sahin, S. Ciraci, Phys. Rev. Lett. 102, 236804 (2009)
- 26. G. Le Lay, S. Cahangirov, L. Xian, A. Rubio, IEEE Xplore. https://doi.org/10.1109/3m-nano. 2014.7057339
- 27. G.-W. Lee, H.-D. Chen, D.-S. Lin, Appl. Surf. Sci. 354, 187 (2015)
- 28. Y. Fukaya, I. Mochizuki, M. Maekawa, K. Wada, T. Hyodo, I. Matsuda, A. Kawasuso, Phys. Rev. B 88, 205413 (2013)
- K. Kawahara, T. Shirasawa, R. Arafune, C.-L. Lin, T. Takahashi, M. Kawai, N. Tagagi, Surface Sci. 623, 25 (2014)
- A. Resta, T. Leoni, C. Barth, A. Ranguis, C. Becker, T. Bruhn, P. Vogt, G. Le Lay, Sci. Rep. 3, 2399 (2013)
- 31. Z.-X. Guo, S. Furuya, J.-I. Iwata, A. Oshiyama, Phys. Rev. B **87**, 235435 (2013)
- 32. Z.-L. Liu, M.-X. Wang, J.-P. Xu, J.-F. Ge, G. Le Lay, P. Vogt, D. Qian, C.-L. Gao, C. Liuand, J.-F. Jia, New J. Phys. **16**, 075006 (2014)
- 33. W. Wang, W. Olovsson, R.I.G. Uhrberg, Phys. Rev. B 92, 205427 (2015)
- 34. P. Moras, T.O. Mentes, P.M. Sheverdyaeva, A. Locatelli, C. Carbone, J. Phys.: Condens. Matter 26, 185001 (2014)
- 35. L. Tao, E. Cinquanta, D. Chiappe, C. Grazianetti, M. Fanciulli, M. Dubey, A. Molle, D. Akinwande, Nat. Nanotechnol. 10, 227 (2015)
- P. Vogt, P. Capiod, M. Berthe, A. Resta, P. De Padova, T. Bruhn, G. Le Lay, B. Grandidier, Appl. Phys. Lett. 104, 021602 (2014)
- P. De Padova, J. Avila, A. Resta, I. Razado-Colambo, C. Quaresima, C. Ottaviani, B. Olivieri,
   T. Bruhn, P. Vogt, M.C. Asensio, G. Le Lay, J. Phys.: Condens. Matter 25, 382202 (2013)

- 38. A. Curcella, R. Bernard, Y. Borensztein, M. Lazzeri, A. Resta, Y. Garreau, G. Prévot, 2D Mater. 4, 025067 (2017)
- P. De Padova, A. Generosi, B. Paci, C. Ottaviani, C. Quaresima, B. Olivieri, E. Salomon, T. Angot, G. Le Lay, 2D Mater. 3, 031011 (2016)
- 40. A.C. Ferrari, D.M. Basko, Nat. Nano 8, 235 (2013)
- 41. H. Li, Q. Zhang, C.C.R. Yap, B.K. Tay, T.H.T. Edwin, A. Olivier, D. Baillargeat, Adv. Funct. Mater. 22, 1385 (2012)
- P. De Padova, C. Ottaviani, C. Quaresima, B. Olivieri, P. Imperatori, E. Salomon, T. Angot, L. Quagliano, C. Romano, A. Vona, M. Muniz-Miranda, A. Generosi, B. Paci, and G. Le Lay, 2D Mater. 1, 021003 (2014)
- 43. E. Haro, M. Balkanski, R.F. Wallis, K.H. Wanser, Phys. Rev. B 34, 5358 (1986)
- D. Solonenko, O.D. Gordan, G. Le Lay, H. Şahin, S. Cahangirov, D.R.T. Zahn, P. Vogt, 2D Mater. 4, 015008 (2017)
- B. Feng, Z. Ding, S. Meng, Y. Yao, X. He, P. Cheng, L. Chen, K. Wu, Nano Lett. 12, 3507 (2012)
- 46. T. Takahashi, S. Nakatani, N. Okamoto, T. Ishikawa, S. Kikuta, Jpn. J. Appl. Phys. 27, L753 (1988)
- 47. S. Cahangirov, V.O. Özçelik, A. Rubio, S. Ciraci, Phys. Rev. B 90, 085426 (2014)
- 48. Y. Yamada-Takamura, R. Friedlein, Sci. Technol. Adv. Mater. 15, 064404 (2014)
- 49. A. Fleurence, T.G. Gill, R. Friedlein, J.T. Sadowski, K. Aoyagi, M. Copel, R.M. Tromp, C.F. Hirjibehedin, Y. Yamada-Takamura, Appl. Phys. Lett. 108, 151902 (2016)
- L. Meng, Y. Wang, L. Zhang, S. Du, R. Wu, L. Li, Y. Zhang, G. Li, H. Zhou, W.A. Hofer, H.-J. Gao, Nano Lett. 13, 685 (2013)
- 51. T. Aizawa, S. Suehara, S. Otani, J. Phys. Chem. C 118, 23049 (2014)
- 52. Y. Chang, E. Colavita, N. Tache, G. Margaritondo, J. Vac. Sci. Technol. A 6, 1971 (1988)
- H.-H. Sun, K.-W. Zhang, L.-H. Hu, C. Li, G.-Y. Wang, H.-Y. Ma, Z.-A. Xu, C.-L. Gao, D.-D. Guan, Y.-Y. Li, C. Liu, D. Qian, Y. Zhou, L. Fu, S.-C. Li, F.-C. Zhang, J.-F. Jia, Phys. Rev. Lett. 116, 257003 (2016)

## Chapter 6 Si Nanoribbons: From 1D to 3D Nanostructures



Paola De Padova, Bruno Olivieri, Claudio Quaresima and Carlo Ottaviani

**Abstract** In this chapter we give an overview on the theoretical and experimental investigations of one-dimensional (1D), two-dimensional (2D) and three -dimensional (3D) Si nanoribbons (SiNRs) formed on the anisotropic Ag(110) substrate surface. We start by introducing briefly free-standing silicene, a silicon layer with Si atoms arranged in honeycomb lattice, with hexagonal Si-rings as structural units. These hexagonal Si units are subsequently discussed as possible candidates to explain the atomic arrangement of the experimentally synthesized Si nanoribbons on Ag(110). This interpretation is supported by properties such as the presence of the 1D projection of the  $\pi$  and  $\pi^*$  bands, forming the so-called "Dirac cones" at the K points of the Brillouin zone, the  $sp^2$ -like nature of the Si valence orbitals, and the strong resistance against oxidation. Besides these results, the atomic structure as well as the origin of the electronic properties of these Si nanoribbons are still controversially debated in the literature. We address this discussion in the last part of the chapter before summarizing it.

#### 6.1 Introduction

The  $sp^3$  hybridization of silicon (Si) atoms leads to the common covalent Si–Si bond formation in the diamond-like crystalline Si lattice. The  $sp^3$  hybridization is the energetically favourable configuration in comparison with the  $sp^2$  or the mixed  $sp^2$ - $sp^3$  hybridization, found in a honeycomb structure. This is the reason for the missing tendency of Si to form instead strong  $\sigma(\pi)$  bonds to stabilize the  $sp^2$  three-fold coordination, characteristic for carbon atoms in graphene, the two-dimensional (2D) one-atom-thin honeycomb structure of carbon [1]. Nevertheless, it is worth

P. De Padova (⊠)

Aix Marseille University, IMéRA, 2 Place le Verrier, 13004 Marseille, France e-mail: paola.depadova@ism.cnr.it

P. De Padova · C. Quaresima · C. Ottaviani Consiglio Nazionale delle Ricerche-ISM, via Fosso del Cavaliere 100, 00133 Rome, Italy

B. Olivieri

Consiglio Nazionale delle Ricerche-ISAC, via Fosso del Cavaliere 100, 00133 Rome, Italy

© Springer Nature Switzerland AG 2018

P. Vogt and G. Le Lay (eds.), *Silicene*, NanoScience and Technology, https://doi.org/10.1007/978-3-319-99964-7\_6

noting that the synthesis of layered silicon atoms in inorganic crystalline systems dates far back in time. Indeed 2D-poly[1,3,5-trihydroxocyclohexasilane], or siloxenes, a system composed by a backbone of two-dimensional Si nearly identical to the corrugated (111) double layers in crystalline Si terminated on one side by H and on the opposite side by OH groups [2–6], was prepared for the first time in the late 1863 by Wöhler [2]. Siloxene was synthesized from calcium disilicide, CaSi<sub>2</sub>, which is the only known silicide already containing the described layered Si backbone structure, from which intact Si layers were produced, by topochemical removal of calcium atoms in concentrated HCl at low temperatures [3]. Many years later, Nakano et al. prepared silicon sheets, by using another method, i.e. the chemical exfoliation of CaSi<sub>2</sub> [7]. Other examples of Si layered in inorganic crystalline systems are the alkaline-earth-metal silicides, consisting of flat Si sheets separated by ions of alkaline-earth-metal [8, 9].

In the following, the structural and electronic properties of the Si nanoribbons (SiNRs) are discussed, from a theoretical point of view in Sect. 6.2, in the framework of silicene-like units and its experimental synthesis in 1D, 2D and 3D structures in Sect. 6.3, by self-assembly of silicon on the anisotropic Ag(110) surface. At the end, the current debate on the existence of silicene SiNRs has been reported.

### 6.2 Silicene Nanoribbons: From a Theoretical Point of View

The aromatic stage of corrugated 2D Si and Ge layers [10], as well as graphitic-like silicon [11] were theoretically predicted, already some time ago. Silicene got the name in 2007 by Guzmán-Verri and Lew Yan Voon [12] as a single layer of silicon atom packed into a honeycomb lattice. It was considered the counterpart of graphene, mainly due to its calculated electronic properties, for flat [13] or low-buckled [14, 15] two-dimensional honeycomb graphene-like lattices of free-standing Si. Similarly to graphene, free-standing silicene exhibits Dirac cone-like features in the electronic dispersion, where charge carriers behave like massless Dirac fermions due to its  $\pi$  and  $\pi^*$  bands, around the K point, crossing at the Fermi level linearly [13, 14]. In addition to these fundamental properties, bare and hydrogen passivated nanoribbons of Si (SiNRs) showed remarkable similar electronic properties and magnetic characteristics, size and orientation dependent (zigzag Si nanoribbons are ferromagnetic (FM) with a FM state of  $1.62 \mu_B$ ) [14, 15].

In the last few years, many other theoretical papers on free-standing silicene nanoribbons, either in zigzag (ZSiNRs) or armchair (ASiNRs) configurations, have been reported. ASiNRs were found to be metallic or semiconducting, depending on their width, while ZSiNRs are antiferromagnetic semiconductors [16], which, in addition, under a transverse electric field, become semi-metals, showing that they have both rich electronic and magnetic properties. On the other hand, it was shown that for hydrogen terminated zigzag and armchair SiNRs edges, the length of the Si–H bond is always 0.15 nm, but the edge Si–Si bonds are shorter than the inner ones with

identical orientation, leading to a contraction of edge Si atoms [17]. This casts the interesting result that in broader ZSiNRs, an edge state can appear at the Fermi level, whereas it does not in all ASiNRs due to their dimer Si–Si edge [17]. In the same way, the predicted electronic properties of hydrogenated silicene (called "silicane") show that an energy gap opens in silicene, making it a wide band-gap semiconductor [18] (see also Sect. 6.3.2). This could be an important ingredient to tune the properties of electronic and spintronic nano-devices. In fact, quite remarkably, a giant magnetoresistance was predicted in ZSiNRs connected to two semi-infinite armchair-edged silicene electrodes, through switch of the edge spins direction of ZSiNRs, with the spin-efficiency sign-changeable by bias voltage [19].

Another intriguing issue is the effect of *n*-type and *p*-type doping on the SiNRs lattice structure, the electronic structure, the phonon spectrum, and the electron-phonon coupling, studied by first principle calculations [20]. Although the lattice is found to be very sensitive to the carrier concentration, it was stable in a wide carrier distribution [20]. ASiNRs [21], as well as ZSiNRs [22] substitutionally doped with single and double N or B atoms located at various sites ranging from the edge to the centre of the ribbon, have given that the doping is favourable at the edges of both ribbons [21, 22], making the SiNRs act as a selective tool for chemical species. In addition, N and B doping can strongly affect the electronic and magnetic properties of ZSiNRs [22], demonstrating how easy it could be to manipulate their physical properties by doping.

One of the most amazing properties of silicene NRs are their topological nontrivial characteristics. Silicene NRs could be topological insulators, a new state of quantum matter, characterized by a full insulating gap in the bulk and gapless, topologically protected edges on the surface [23, 24]. For ZSiNRs studied using ab initio simulating methods [24], novel structure properties affected by several factors, such as spin orbit coupling (SOC), spin polarization, and extended topological defects, were recently found [24]. The role of the SOC is very significant because it produces spin-dependent energy gaps in the electronic structure [24]. In the same way, the effect of many body correlation on spin and charge excitation in zigzag honeycomb nanoribbons, modelled within the Hubbard Hamiltonian, lead to a reduced spin gap and an increased charge gap, thus indicating the possibility of spin filtering applications [25]. Another opportunity to model the electronic and magnetic properties (for both ZSiNRs and ASiNRs) is offered by hybrid system, such as silicane-silicene nanoribbons [26]. Furthermore, first-principles calculation combined with quantum scattering theory showed that ribbons of silicene are DNA selective, leading to potential cheap and portable sensing device for DNA sequencing [27].

The first calculations on low dimensional Si structure supported by a substrate, which was appropriately included into the calculation scheme, were performed on Si nanoribbons epitaxially grown on the anisotropic Ag(110) surface [28], in order to deduce their atomic structure. These DFT calculations, obtained within General Gradient Approximation (GGA), provided a model basically constituted by an arched honeycomb structure of Si atoms, with Si–Si bond length of 0.223 nm, anchored along their length [1-10] on the Ag(110) surface, indicating a silicene-like structure, mediated by the silver substrate [28].

P. De Padova et al.

### 6.3 The Birth of SiNRs: 1D, 2D and 3D Silicene Nano-structures on Ag(110)

So far, 1D isolated SiNRs, called hereafter i-SiNRs, 2D grating of Si nanoribbons and 3D multilayer SiNRs were experimentally synthesised [29–38], through epitaxial growth of Si on the oriented Ag(110) surface, used as a template.

### 6.3.1 Isolated SiNRs and Nanodots

The i-SiNRs with a width of typically 1.6 (or 0.8) nm were obtained at room temperature (RT) by deposition of about 0.5 monolayer (ML) of silicon onto the clean Ag(110) surface [29, 31, 33–38]. These 1D nano-objects have typically a length of several ten nanometres and are aligned along the [-110] direction, parallel to each other (see Fig. 6.1a). Their lengths can vary from small values like 1.5 nm to more than 30 nm, with a maximum height of ~0.2 nm. For a short length of approximately 1.5 nm these structures are better described as *nanodots*.

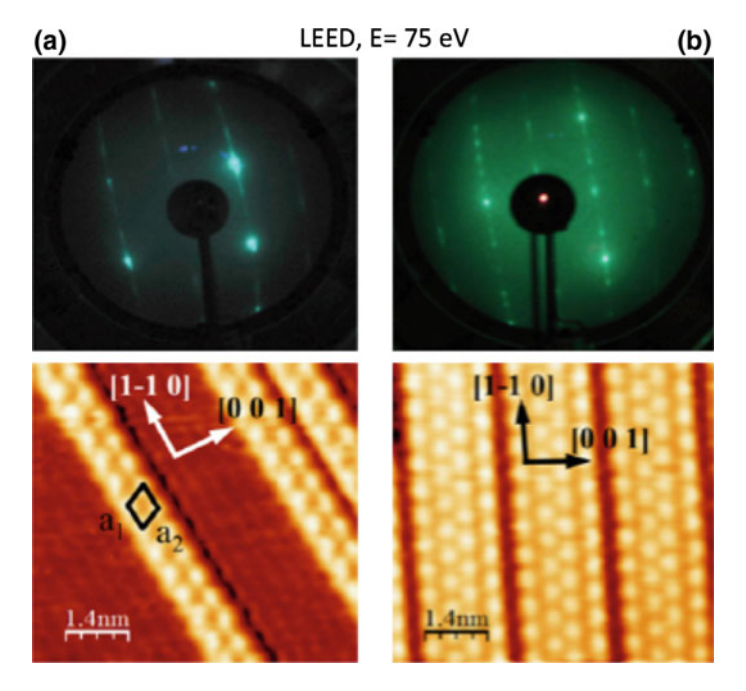


**Fig. 6.1** LEED patterns and STM images measured on isolated SiNRs. **a** and on ordered  $5 \times 2$  SiNRs array. **b** The LEED patterns are measured at an energy of 75 eV. The STM image sizes and tunnelling parameters are: **a**  $7 \times 7$  nm<sup>2</sup>; VS = -1.8 V; I = 1.2 nA; **b**  $7 \times 7$  nm<sup>2</sup>; VS = -1.1 V; I = 1.0 nA. Adapted from Fig. 6.1 of [36]

In both, real and reciprocal space, as probed by STM and LEED measurements, SiNRs show a twofold periodicity along the Ag[-110] direction (i.e., twice the Ag lattice constant,  $a_{Ag[-110]}$ ). In the perpendicular [001] direction no long-range order is found, due to different separation gaps between adjacent SiNRs within the ensemble of parallel Si ribbons [29, 38].

We note that one of the interesting properties of these SiNRs is the symmetry breaking across their widths. This leads to two self-assembling chiral species, in large left-handed and right-handed magnetic-like domains. Additionally, they show a strong metallic character observed by high-resolution synchrotron-based photoelectron spectroscopy measurements or by scanning tunnelling spectroscopy (STS) [31].

### 6.3.2 Two-Dimensional Array of SiNRs

Silicon nanoribbons grown on Ag(110) at about 520 K self-assemble by lateral compaction of the 1D Si ribbons to form, on a macroscopic scale, a 2D array with pitches of only 2 nm or 1.2 nm, for 1.6 or 0.8 nm wide SiNRs, respectively [30, 38]. These dense-SiNRs arrays display either a  $5 \times 2/5 \times 4$  periodicity in LEED patterns for 1.6 nm wide SiNRs or a  $3 \times 2$  periodicity for 0.8 wide SiNRs, depending on the substrate temperature during growth. The fourfold (×4) periodicity is the one of the inner protrusions within the SiNRs along the [1-10] Ag direction.

In Fig. 6.1a the LEED (a) patterns and filled-states STM images measured on 0.8 nm wide isolated SiNRs are displayed and in (b) for the ordered  $5 \times 2$  array with 1.6 nm wide ribbons, adapted from [36]. A comparative structural and electronic study of both, atomic and molecular hydrogen interaction with isolated versus ordered silicon nanoribbons grown on Ag(110) at RT was carried out by Dávila et al. [36]. The hydrogen absorption process and hydrogenation mechanism were found similar in both cases, i.e. for isolated or  $5 \times 2/5 \times 4$  ordered SiNRs. Atomic hydrogen strongly interacted with each silicon atom, whereas molecular hydrogen has to dissociate first, activating an etching process of the SiNRs, which forms volatile SiH<sub>x</sub> species [36].

On both isolated SiNRs and a dense array of SiNRs electron reflection energy loss spectroscopy at the Si K absorption edge (1.840 keV) show the presence of threefold Si–Si  $\sigma$  bonds [34]. This is confirmed by the very low reactivity to molecular oxygen, which underlines the formation of less reactive  $sp^2$ -like Si valence orbitals in nanoribbons [34].

### 6.4 Oxidation of Isolated SiNRs on Ag(110)

The oxidation of i-SiNRs by exposure to oxygen under ultra-high vacuum (UHV) conditions shows to be an interesting physical process [35]. Figure 6.2 displays a  $14.3 \times 14.3 \text{ nm}^2$  filled-states STM image, after a deposition of ~0.5 ML Si at RT on the Ag(110) surface and exposure to a 30 Langmuir (1  $L=1 \times 10^{-6}$  Torr per 1s) dose of oxygen [35]. The high resolution STM image shows how the massively

120 P. De Padova et al.

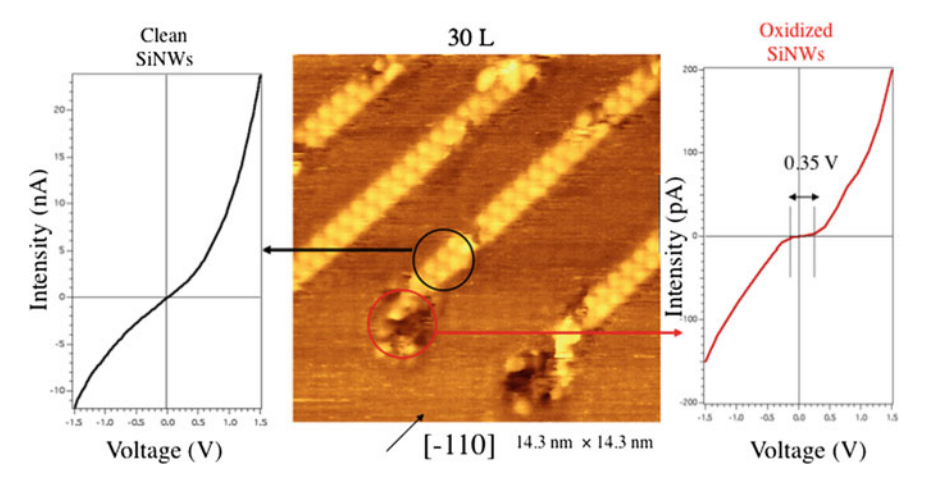


Fig. 6.2  $14.3 \times 14.3 \text{ nm}^2$  filled-states STM image (V = -1.8 V; I = 1.2 nA) of SiNRs exposed to 30 Lof O<sub>2</sub> (centre panel). The selected areas on STM image (black and red circles) denote where I-V characteristics are measured: on clean (left panel) and oxidized (right panel) SiNRs. Adapted from Fig. 6.4 of [35]

parallel SiNRs, all aligned along the [-110] direction of the Ag(110) surface, oxidize starting from their ends, described as the so-called "burning match" oxidation process [35]. It can be observed that the ends that terminate the clean SiNRs are drastically modified after oxygen exposure, showing some black voids or hollow sites (marked by circled in Fig. 6.2), indicating the onset of the oxidation process. Only these ribbon terminations are involved in the oxidation process at the beginning, whereas almost the entire rest of the SiNRs remain unchanged.

At a higher oxygen exposure  $(300\,L)$ , the oxidation of the SiNRs proceeds progressively from their ends along the ribbon, indicating an atomic structure modification preferably developing along the 1D ribbons. This SiNRs oxidation acts like a *bursting-match* process, where the terminating ends of the SiNRs can be considered as the head of the match, which reacts with the oxygen atoms. It is noteworthy that the terminating ends of the SiNRs act as the seeds of the starting oxidation process, probably due to the localization of strongly reactive dangling bonds or defects at the ends, which then propagates along the ribbons like a flame front.

To analyze the structure modification STS measurements were carried out on both the clean and the oxidized parts of the SiNRs, separated by the interface between them [35].

The left and the right panel in Fig. 6.2 display the corresponding I(V) spectra measured for the clean and the oxidized regions of the SiNRs, respectively. On the initially not oxidized part of the SiNRs, a metallic characteristic is found with rather high currents in the nA range. On the other hand, the I(V) curve acquired on the oxidized parts of the SiNRs shows a semiconducting behavior with much smaller tunneling currents in the pA range, and a gap of about 0.35 V. This behavior is an

indication for the formation of a transverse internal nano-junction between the clean and the oxidized parts of the SiNRs.

We note that, in the case of the dense 2D arrays of SiNRs the oxidation process starts only at high oxygen exposures, around  $10^4$  times higher if compared with the dose where bulk Si surfaces oxidize. This demonstrates the strong resistance of the dense SiNRs towards oxidation, underlining a  $sp^2$  character of the Si–Si bonds.

### 6.5 Electronic Properties of 1D SiNRs and 2D Arrays of SiNRs

The electronic properties of the described 1D and 2D SiNRs were studied by angleresolved photoemission spectroscopy (ARPES) [32, 38], allowing to identify states corresponding to the one-dimensional projection of the  $\pi^*$  (upper branch) and  $\pi$ (lower branch) bands, forming the Dirac cones at the K points of the BZ.

This interpretation is consistent with zigzag Si nanoribbons consisting of hexagonal silicene-like units aligned along the ribbon axis (i.e., the Ag[1-10] direction), where 4 Ag-Ag nearest neighbour distances match 3 Si–Si 2nd neighbour distances. Therefore, a k value of 1.09 Å<sup>-1</sup> v corresponds to the  $\bar{X}$  point of the Ag surface BZ, which leads to a  $\bar{\Gamma} \to \bar{K}$  value for silicene given by  $(4 \times \pi)/(3 \times \sqrt{3} \times d_{Si-Si})$ , which yields a nearest neighbour bond length of  $d_{Si-Si} = 0.224$  nm within the hexagons of the honeycomb lattice [32, 38]. This is in excellent agreement with the real space values reported above and the mean Si–Si distance  $d_{Si-Si}$  of the honeycomb-like structure from the DFT-GGA calculations [28].

### 6.6 Multilayer SiNRs

Besides the 1D SiNRs and their 2D arrays also stacked ribbons can form on the Ag(110) surface. Figure 6.3a displays a filled-states STM image showing these multilayer SiNRs, which can be seen as 3D Si nanostructures, in the following termed as 3D SiNRs [39]. As in the case of 2D dense arrays of SiNRs the 3D SiNRs are grown at a substrate temperature of ~470 K on the Ag(110) surface and are also all aligned along the [1-10] direction of the Ag(110) surface. The 3D SiNRs have widths which vary between 10 and 30 nm and heights between 2 and 5 nm and the lengths can exceed more than several hundred nanometers [39]. The line marked L in Fig. 6.3a shows for example a 3D SiNR with a length of approximately 500 nm. These thick multilayer SiNRs are regular stacks of silicon layers with a pyramidal cross section. All successive layers correspond to a step height of h ~ 0.29 nm.

It is interesting to note that, the entire Ag(110) surface is covered by a layer of single atom-thin SiNRs in the regions between those multilayer SiNRs. This shows that this layer, monolayer SiNRs acts as a template for the subsequent growth of the

122 P. De Padova et al.

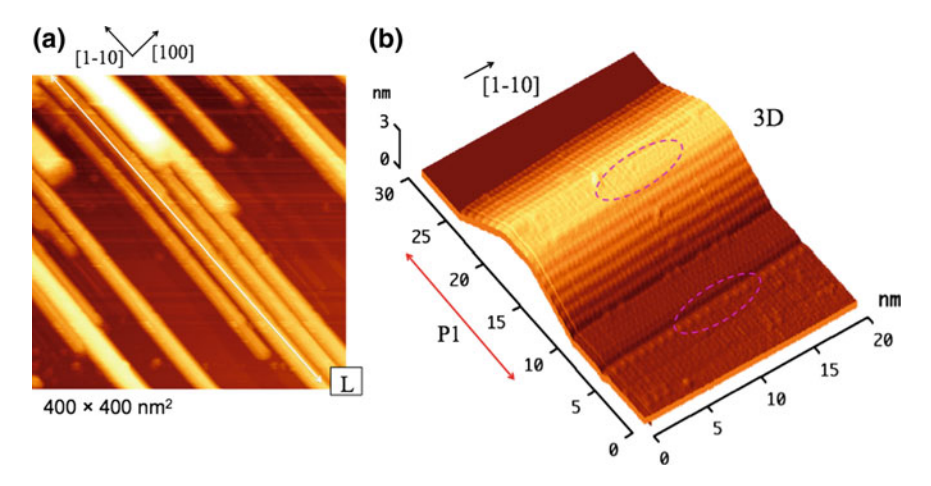


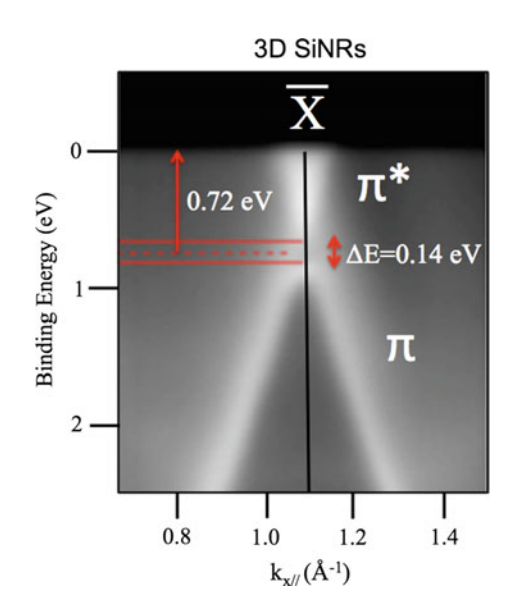
Fig. 6.3 a  $400 \times 400 \text{ nm}^2$  STM image (V = -0.6; I = 1 nA) of an ensemble of multilayer-thick SiNRs on Ag(110), L marks a length of ~500 nm. b  $30 \times 20 \text{ nm}^2$  STM 3D view (V = 0.2; I = 0.1 nA). Adapted from Fig. 6.1 of [39]

3D multilayer SiNRs. The Si atoms in the top layer of the 3D SiNRS show s similar arrangement with a  $5 \times 4$  unit cell as those within the atom-thin SiNRs located at their bottom, indicated by the two ovals in Fig. 6.3b. This observation is also supported by LEED and RHEED measurements, which show a very clear  $5 \times 4$  pattern [39].

Figure 6.4 displays ARPES measurements of the electronic dispersion from the 3D multilayer 5  $\times$  4 SiNRs recorded along their lengths, i.e. along the Ag[1-10] direction. Two types of linearly dispersing bands can be seen, one with a  $\Lambda$ -like shape (bottom) and one with a V-like shape crossing the Fermi level (top). These bands are separated by a small gap of about 0.14 eV around 0.72 eV below  $E_F$ . These bands are located in an electronic gap of the Ag(110) surface and centred at  $k_{ff}$  value of 1.087 Å $^{-1}$  i.e., exactly at the  $\bar{X}$  point of the 1D Brillouin zone for atom-thin SiNRs. The bands correspond to the 1D projection of  $\pi^*$  (upper band) and  $\pi$  (lower band) bands, similar to the Dirac cones in multilayer silicene [39].

It could be argued that the observed bands result from the layer of atom-thin SiNRs between the 3D multilayer ribbons. However, for the latter a gap of  $\sim$ 0.56 eV, centred at 0.62 eV below  $E_{\rm F}$  was found, which clearly differs from the results shown in Fig. 6.4. The upward shift and the closing of the gap of the 3D multilayer ribbons with respect to the array of atom-thin SiNRs is attributed to the increasing separation of the Si layers from the Ag(110) substrate and thus a lowering of the interaction with the substrate.

Fig. 6.4 ARPES intensities (hv = 126 eV) from multilayer-thick  $5 \times 4$  SiNRs recorded along their lengths at  $k_y = 0.4 \text{ Å}^{-1}$ , the  $(\bar{\Gamma} \to \bar{X})$  direction. A Dirac cone-like dispersion is seen at the  $\bar{X}$  point, between 0.67 and 1.5 Å<sup>-1</sup>, where one  $\Lambda$ -like band (bottom) and one V-like band (top) which crosses the Fermi level are found. Adapted from Fig. 6.3 of [39]



#### 6.7 Discussion

The results shown above demonstrate that the SiNRS formed epitaxially on the Ag(110) surface show properties that clearly differ from the properties of diamond-like bulk Si. The Si atoms in the SiNRS have a  $sp^2$ -like hybridization character, are less chemically reactive, and show two linear  $\pi^*$  and  $\pi$  electronic bands, similar to a Dirac cone. This motivated the suggestion of an atomic structure model for these ribbons, based on silicene-like hexagonal Si-rings. However, this explanation of the SiNRs by a silicene-like structure has also been questioned in the literature based on other results.

Recently, it has been suggested that the SiNRs growth on Ag(110) induce a reconstruction of the Ag(110) surface underneath the ribbons, associated with a missing row in the Ag layer [40]. In this case Ag atoms are released from the surface, induced by the growth of Si nanoribbons. Hence, the SiNRs are explained by a Si induced reconstruction of the Ag(110) surface, challenging the structural interpretation of the SiNRs within the framework of silicene. However, this model does not explain the  $sp^2$ -like hybridization of the Si atoms or the linear electronic bands.

In situ Raman spectroscopy results obtained on the 2D array of SiNRs grown on Ag(110) show four vibrational modes at 459, 440, 266, and 220 cm<sup>-1</sup> [41]. These modes differ from the calculated phonon modes of free-standing silicene layers obtained by first-principles calculations, which demonstrate an intense (G-like) peak at 575 cm<sup>-1</sup> [42] and also from the L(T)O mode of bulk Si at 520 cm<sup>-1</sup>. However, the comparison with 2D silicene is problematic because the anisotropic structure of the ribbons would certainly alter the vibrational properties. Additionally the SiNRs interact with the Ag(110) substrate which can also modify the vibrational signature

P. De Padova et al.

(see also Chap. 7). Therefore, the experimental Raman results do not exclude the explanation of the SiNRs as silicene-like structures, unambiguously.

Furthermore, silicon-induced faceting at the Ag(110) surface was investigated by STM, LEED and DFT calculations upon silicon deposition at temperatures above 460 K (up to 550 K) [43]. This temperature was high enough to allow Ag atoms to migrate or Si atom to diffuse into the Ag substrate. Two different kinds of nanostructures were described to be formed by these processes such as nanodikes and nanotrenches, protruded from or engraved on the Ag(110) substrate, respectively. Nanodikes and nanotrenches were found to be the result of silver faceting stabilized by Si atoms. It has been suggested, that these nanostructures could explain the formation of the 3D multilayer-thick SiNRs shown in Fig. 6.3 [43]. However, it is worth noting that the 3D SiNRs (in Fig. 6.3) are not in agreement with the configuration of the nanodikes because their lateral compaction (width separation between NRs) and depth between the NRs are not consistent with their height, if considered caused by Ag atoms.

The optical properties of Si nanoribbons grown on Ag(110) at 450 K at completion of the first Si overlayer were determined by in situ differential reflectance spectroscopy [44]. Here, it is found that the optical response appears to be quite different from what is expected for a layer of silicene but very similar to the dielectric function of amorphous silicon. This is in clear contradiction to the well-attested well-ordered  $5 \times 2 / 5 \times 4$  periodicity of SiNRs [29, 30, 38].

Very recently, another honeycomb-based armchair model, different to the one discussed before, was proposed for the atomic structure of both 1D and 2D Silicene nanoribbons [45, 46]. The atomic structure of these structures was determined by first principles calculations for both 1.0 and 2.0 nm wide SiNRs, as shown in Fig. 6.5 (adapted from Fig. 6.2 of [45]). In panel (a) the calculated partial density of states is shown, demonstrate quite similar electronic properties for both structures. Panel (b) shows side view top view for the two structures. The light blue balls are the topmost Ag atoms and the dark blue balls are the underlying Ag atoms. Red balls indicate upper buckled Si atoms, which can be probed by STM and the yellow balls the other Si atoms. In panel (c) the simulated (black and white) STM images are compared to the experimental (colour) STM images at different bias voltages.

The two different structures in panel (b) were found to show the best agreement with the experimental STM images. Interestingly, for both structures the central part of the nanoribbons is composed of perfect honeycomb units, extending along the [1-10] direction of Ag. The edges of both structures have armchair configurations, which are reconstructed. However, the good agreement of the STM images is not enough evidence for an unambiguous proof that these models explain the experimentally observed SiNRs. Furthermore, these models do not explain the experimentally observed electronic structures reported above. On the other hand, these electronic properties are strictly compatible with a zigzag honeycomb arrangement along the [-110] Ag(110) direction for isolated SiNRs, the dense 2D array of SiNRs and 3D SiNRs [39].

Finally, it was also suggested that an atomic structure model where Ag atoms are included in the Si nanoribbons could explain the experimentally observed ribbon on

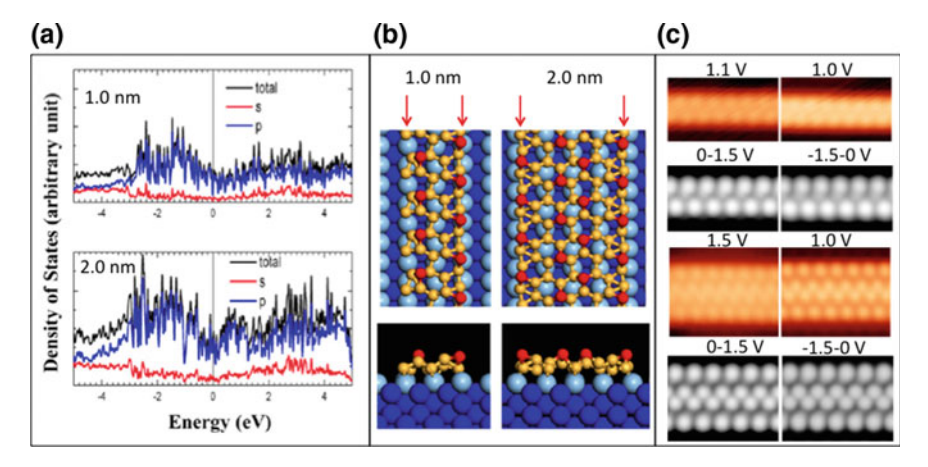


**Fig. 6.5** Panel **a** Calculated partial density of states of the relaxed SiNRs without Ag(110) for 1.0 nm and 2.0 nm wide SiNRs, respectively. Panel **b** Left: top and side view of the relaxed structural model of 1.0 nm wide SiNRs on top of Ag(110); Panel **b** Right: top and side view of the relaxed structural model of 2.0 nm wide SiNRs on top of Ag(110). Light blue balls: topmost Ag atoms; dark blue balls: underlying Ag atoms; red balls: upper buckled silicon atoms that can be probed by STM; yellow balls: other silicon atoms. Panel **c** Simulated (black and white) STM images compared with the experimental (color) STM images at different bias voltages. Adapted from Fig. 6.2 of [45]

the Ag surface. These results are based on a combination of STM results and totalenergy calculations within DFT [47]. An experimental proof for the incorporation of Ag atoms in the ribbons is so far missing.

This discussion shows, that up today, several different models have been proposed as alternative atomic model for the observed SiNRs, which differ from the silicene-like arrangements [40, 41, 43–47]. However, any model for the SiNRs needs to explain the experimental results, in particular the origin of Dirac-cone-like features for these ribbons, apparent in ARPES measurements. We underline, that other DFT calculations attribute the origin of these bands stem from the silver substrate and not the SiNRs, as an effect of band folding induced by the Si overlayer periodicity [48].

A model, very different from the ones discussed so far, was proposed recently by Cerda et al. based on DFT calculations [49]. The authors propose a unique pentagonal arrangement of the Si atoms within single- and double-strand SiNRs sitting along a missing row reconstructed Ag(110) surface. The constitutive Si pentamers, could reflect a one-dimensional form of pentasilicene, the analogue of the conjectured, but not yet synthesized, 2D pentagraphene [50]. This structure model has been supported by both synchrotron radiation SXRD and photoelectron diffraction measurements [51, 52]. This gives hopes that the puzzling search for an atomic structure model of these arrays of parallel SiNRs [29] might finally be solved, long time after they were first reported.

P. De Padova et al.

### 6.8 Summary

The content of this chapter deals with the silicon nanoribbons epitaxially grown on Ag(110) starting from their discovery up to today. We have looked over the most significant literature on these Si-based nanoribbons, including isolated (1D) SiNRs, dense 2D arrays of SiNRs nd 3D SiNRs, in order to review the currently ongoing debate, concerning the correct structure model for these ribbons. Particular attention has been paid to the further prospects about the theoretical predicted potential of this novel material system for smart devices, such as spintronic or DNA sensing devices. Free-standing and supported Si nanoribbons were revised from a theoretical point of view by including the precursor Si chemical exfoliated Si layer from the CaSi<sub>2</sub> sample.

We emphasize that several atomic arrangements for these SiNRs were proposed, but now a pentagonal moiety model that takes into account all the experimental results appears to finally explain these Si nanoribbons.

**Acknowledgements** Paola De Padova wishes to thank the IMERA (Aix-Marseille University) for the fellowship supporting her work from September 2015 to July 2016.

### References

- 1. A.K. Geim, K.S. Novoselov, Nat. Mat. 8, 183 (2007)
- 2. F. Wöhler, Ann. Chem. Pharm. 127, 257 (1863)
- 3. A. Weiss, G. Beil, H. Meyer, Z. Naturforsch. **35b**, 25 (1979)
- 4. K. Takeda, K. Shiraishi, Phys. Rev. B 39, 11028 (1989); Solid State Commun. 85, 301 (1993)
- U. Dettlaff-Weglikowska, W. Hönle, A. Molassioti-Dohms, S. Finkbeiner, J. Weber, Phys. Rev. B 56, 13132 (1997)
- 6. I. Manners, Angew. Chem. Int. Ed. Engl. 35, 1602 (1996)
- H. Nakano, T. Mitsuoka. M. Harada, K. Horibuchi, H. Nozaki, N. Takahaschi, T. Nonaka, Y. Seno, H. Nakamura, Angew. Chem. Int. Ed. 45, 6303 (2006)
- 8. K.H. Janzon, H. Schäfer, A. Weiss, Z. Anorg, Allg. Chem. 372, 87 (1970)
- 9. A.F. Wells, Structural Inorganic Chemistry, 5th edn. (Clarendon, Oxford, 1984)
- 10. K. Takeda, K. Shiraishi, Phys. Rev. B **50**, 14916 (1994)
- 11. Y.C. Wang, K. Scheerschmidt, U. Gösele, Phys. Rev. B 61, 12864 (2000)
- 12. G.G. Guzmán-Verri, L.C. Lew Yan Voon, Phys. Rev. B 76, 075131 (2007)
- 13. S. Lebègue, O. Eriksson, Phys. Rev. B 79, 115409 (2009)
- S. Cahangirov, M. Topsakal, E. Aktuerk, H. Sahin, S. Ciraci, Phys. Rev. Lett. 102, 236804 (2009)
- 15. S. Cahangirov, M. Topsakal, S. Ciraci, Phys. Rev. B 81, 95120 (2010)
- 16. Y. Ding, J. Ni, Appl. Phys. Lett. 95, 083115 (2009)
- 17. Y.L. Song, Y. Zhang, J.M. Zhang, D.-B. Lu, Appl. Surf. Sci. 256, 6313 (2010)
- M. Houssa, E. Scalise, K. Sankaran, G. Pourtois, V.V. Afanas'ev, A. Stesmans, Appl. Phys. Lett. 98, 223107 (2011)
- 19. C. Xu, Luo, Q. Liu, J. Zheng, Z. Zhang, S. Nagase, Z. Gao, J. Lu, Nanoscale 4, 3111 (2012)
- 20. Y.C. Cheng, Z.Y. Zhu, U. Schwingenschlögl, Eur. Phys. Lett. **95**, 17005 (2011)
- 21. L. Ma, J.-M. Zhang, K.-W. Xu, V. Ji, Physica B 425, 66 (2013)
- 22. L. Ma, J.-M. Zhang, K.-W. Xu, V. Ji, Physica E 60, 112 (2014)

- 23. M. Ezawa, New J. Phys. 14, 033300 (2014)
- 24. N.B. Le, T.D. Huan, L.M. Woods, Phys. Rev. Appl. 1, 054002 (2014)
- 25. S. Dutta, K. Wakabayashi, Jpn. J. Appl. Phys. 53, 06JD01 (2014)
- 26. G. Li, J. Tan, X. Liu, X. Wang, F. Li, M. Zhao, Chem. Phys. Lett. **595**, 20 (2014)
- 27. H. Sadegni, S. Bailey, C.J. Lambert, Appl. Phys. Lett. **104**, 103104 (2014)
- A. Kara, C. Léandri, M.E. Dávila, P. De Padova, B. Ealet, H. Oughaddou, B. Aufray, G. Le Lay, J. Supercond. Novel Mater. 22, 259 (2009); G. Le Lay, B. Aufray, C. Léandri, H. Oughaddou, J.P. Bibérian, P. De Padova, M.E. Dávila, B. Ealet, A. Kara, Appl. Surf. Sci. 256, 524 (2009); B. Aufray, A. Kara, S. Vizzini, H. Oughaddou, C. Léandri, B. Ealet, G. Le Lay, Appl. Phys. Lett. 96, 183102 (2010); A. Kara, S. Vizzini, C. Léandri, B. Ealet, H. Oughaddou, B. Aufray, G. Le Lay, Phys. Condens. Matter 22, 045004 (2010)
- C. Léandri, G. Le Lay, B. Aufray, C. Girardeaux, C.J. Avila, M.E. Dávila, M.C. Asensio, C. Ottaviani, A. Cricenti, Surf. Sci. Lett. 574, L9 (2005)
- H. Sahaf, L. Masson, C. Léandri, B. Aufray, G. Le Lay, F. Ronci, Appl. Phys. Lett. 90, 263110 (2007)
- 31. P. De Padova, C. Quaresima, P. Perfetti, B. Olivieri, C. Léandri, B. Aufray, S. Vizzini, G. Le Lay, Nano Lett. 8, 271 (2008)
- 32. P. De Padova et al., Appl. Phys. Lett. **96**, 261905 (2010)
- 33. F. Ronci, S. Colonna, A. Cricenti, P. De Padova, C. Ottaviani, C. Quaresima, B. Aufray, G. Le Lay, Phys. Status Solidi C 7, 2716 (2010)
- P. De Padova, C. Quaresima, B. Olivieri, P. Perfetti, G. Le Lay, Appl. Phys. Lett. 98, 081909 (2011)
- P. De Padova, C. Léandri, S. Vizzini, C. Quaresima, P. Perfetti, B. Olivieri, H. Oughaddou, B. Aufray, G. Le Lay, Nano Lett. 8, 2299 (2008)
- M.E. Dávila, A Marele, P. De Padova, I. Montero, F. Hennies, A. Pietzsch, M.N. Shariati, J.M. Gómez-Rodríguezand, G. Le Lay, Nanotechnology 23, 385703 (2012)
- 37. P. De Padova, C. Quaresima, B. Olivieri, P. Perfetti, G. Le Lay, J. Phys. D: Appl. Phys. Fast Track Commun. 44, 312001 (2011)
- 38. P. De Padova P. Perfetti, B. Olivieri, C. Quaresima, C. Ottaviani, G. Le Lay, J. Phys. Condens. Matter 24, 223001 (2012)
- 39. P. De Padova, O. Kubo, B. Olivieri, C. Quaresima, T. Nakayama, M. Aono, G. Le Lay, Nano Lett. 12, 5500 (2012)
- R. Bernard, T. Leoni, A. Wilson, T. Lelaidier, H. Sahaf, E. Moyen, L. Assaud, L. Santinacci, F. Leroy, F. Cheynis, A. Ranguis, H. Jamgotchian, C. Becker, Y. Borensztein, M. Hanbücken, G. Prévot, L. Masson, Phys. Rev. B 88, 121411 (2013)
- 41. E. Speiser, B. Buick, N. Esser, W. Richter, S. Colonna, A. Cricenti, F. Ronci, Appl. Phys. Lett. 104, 161612 (2014)
- 42. E. Scalise, M. Houssa, G. Pourtois, B. van den Broek, V. Afanas'ev, A. Stesmans, Nano Res. 6, 19 (2013)
- 43. F. Ronci, G. Serrano, P. Gori, A. Cricenti, S. Colonna, Phys. Rev. B 89, 115437 (2014)
- 44. Y. Borensztein, G, Prévot, L. Masson, Phys. Rev. B 89, 245410 (2014)
- 45. B. Feng, H. Li, S. Meng, L. Chen, K. Wu, Surf. Sci. **645**, 74 (2016)
- M.R. Tchalala, H. Enriquez, A.J. Mayne, A. Kara, G. Dujardin, M. Ait Ali, H. Oughaddou, J. Phys.: Conf. Ser. 491, 012002 (2014)
- 47. C. Hogan, S. Colonna, R. Flammini, A. Cricenti, F. Ronci, Phys. Rev. B 92, 115439 (2015)
- 48. P. Gori, O. Pulci, F. Ronci, S. Colonna, F. Bechstedt, J. Appl. Phys. 114, 113710 (2013)
- 49. J.I. Cerdá, J. Sławińska, G. Le Lay, A. Marele, J.M. Gómez-Rodríguez, M.E. Dávila, Nat. Commun. 7, 13073 (2016)
- 50. S. Zhang, J. Zhou, O. Wang, X. Chen, Y. Kawazoe, P. Jena, PNAS 112, 2372 (2015)
- G. Prévot, C. Hogan, T. Léoni, R. Bernard, E. Moyen, L. Masson, Phys. Rev. Lett. 117, 276102 (2016)
- P. Espeter, C. Keutner, P. Roese, K. Shamout, U. Berges, C. Westphal, Nanotechnology 28, 455701 (2017)

# Chapter 7 Properties of Monolayer Silicene on Ag(111)



**Patrick Vogt** 

**Abstract** The expected properties of silicene and their theoretical background have already been discussed in Chaps. 1-3 and the different ways to synthesize this new 2D material in Chap. 5. It has already been mentioned that such a synthesis requires an adequate substrate material to accommodate the formation of a one-atom-thin silicon layer. Such a material is silver, in particular the Ag(111) surface plane. In this chapter the formation and properties of silicene formed epitaxially on the  $Ag(111)(1 \times 1)$  surface are discussed. We will see that the properties of these silicene layers are modified with respect to the ones of free-standing silicene, due to the interaction with the substrate. For this reason we will refer to it as *epitaxial silicene* and look in detail at its two-dimensional (2D) character. A more detailed look at the formation of Si layers on Ag(111) shows that, depending on the specific preparation conditions, several 2D Si phase can be formed. Differences and similarities of these structures will be discussed. Furthermore, we will draw the intention on the chemical and temperature stability of these epitaxial silicene layers and unveil the limits for the silicene formation.

### 7.1 Introduction

The advent of graphene in 2004 can surely be seen as the foundation of the new class of two-dimensional (2D) materials. This was achieved by peeling off single graphene layers from a parent graphite crystal using a piece of sticky tape. In particular the unique electronic, optical, and mechanical properties of this first 2D material member have been responsible for its tremendous impact in research. One of these outstanding properties is the linear dispersion at the graphene  $\overline{K}$  points, featuring conical bands for electrons and holes which meet each other at the Fermi level and form the so-called "Dirac cones". As a consequence, the charge carriers behave like massless particles, which allows very high predicted mobilities, important for

P. Vogt

graphene's technological applicability. Accordingly, the crucial work of Andre Geim and Konstantin Novoselov, that initiated this success, was awarded the Nobel Prize in Physics in 2010.

Since this discovery researches have been trying to find or create other twodimensional materials with possibly similar properties. In particular the group-IV elements of the periodic table, such as silicon, germanium and tin, have been seen as good candidates to form also 2D-lattices besides their well-known 3D crystalline allotropes. The 2D silicon equivalent of graphene was already mentioned in a theoretical study by Takeda and Shiraishi in 1994, around 10 years prior to the discovery (or re-discovery) of graphene [1]. In 2007 the name "silicene" for such 2D Si sheets was created by Guzman-Verri and Yan Voon in another theoretical publication [2].

The main message of these theoretical studies was that a one-atom-thin hexagonal arrangement of Si atoms in a honeycomb structure is energetically stable, if it existed. However, these theoretical investigations do not say if and in which way this 2D material can be grown or synthesised. Moreover, its energetic stability does not necessarily imply its real existence. A 3D equivalent to graphite has not been found for silicon and purely 2D silicene layers cannot be generated by exfoliation methods but have to be synthesized by means of more sophisticated methods. In Chap. 5 it is shown, that a promising concept to synthesize silicene is the deposition of Si on a metal substrate, which does not interact with the Si atoms and form a silicide. A metal that fulfils this requirement is silver, and it is shown in Chap. 6 that Si nanoribbons (SiNRs) can be grown on Ag(110) substrates [3–7]. Even though the atomic structure of these Si nanoribbons has been discussed controversially for many years, it was found hat the ribbons are composed of Si atoms only, in a more  $sp^2$ -like hybridized state, a prerequisite for the formation of a real 2D structure. In order to grow real two-dimensional silicene sheets, the Ag(111) surface seems to be better suited compared to Ag(110) because it has a 6-fold symmetry that better facilitates and supports the formation of a honeycomb Si ad-layer.

The successful growth of silicene was reported in 2012 using a Ag(111) single crystal substrate [9–11],  $ZrB_2$  [12], and later Ir(111) [13] templates. In contrast to graphene, these silicene layers show a low buckling along the bonds of adjacent Si atoms, i.e. a not fully planar structure. The reason for this buckling is the fact that Si atoms energetically prefer an  $sp^3$  rather than an  $sp^2$  hybridisation. However, first principles calculations based on density functional theory (DFT) demonstrated that a low buckling does not influence the electronic properties of free-standing silicene layers, preserving the linear electronic dispersion at the  $\overline{K}$  points of the Brillouinzone [14, 15]. We will see below that the interaction with the Ag substrate has a much stronger impact on the properties of the 2D layer.

In this chapter the formation and properties of silicene formed epitaxially on the  $Ag(111)(1 \times 1)$  surface are discussed. The chapter is focused on Ag(111) as a substrate only, because it is by far the most used substrate material for the growth

<sup>&</sup>lt;sup>1</sup>In the meantime a model has been suggested, which is based on a pentagonal arrangement of Si atoms in interconnected rings, forming the SiNRs along the missing rows of the reconstructed Ag(110) surface [8].

of silicene and it is the subject of most theoretical investigations. It will be shown that the properties of these silicene layers on Ag(111) are modified with respect to the ones of free-standing silicene, due to the interaction with the substrate. For this reason we will refer to it as *epitaxial silicene* and look in detail at its two-dimensional (2D) character. A more detailed analysis of the formation of Si layers on Ag(111) shows that, depending on the specific preparation conditions, several silicene and 2D Si phases can be formed. Differences and similarities of these structures will be discussed in terms of their symmetries and fundamental structural, electronic and vibrational properties. Finally, we will draw the intention on the chemical and temperature stability of these epitaxial silicene layers and unveil the limits for the silicene formation.

### 7.2 Expected Properties of Epitaxial Silicene

One of the main differences of a 2D form of silicon in comparison to diamond-like bulk silicon is the different hybridisation state, changing form  $sp^3$  to  $sp^2$  or some where in between, i.e.  $sp^2/sp^3$ -like. Determination of the Si atom hybridisation therefore allows us to identify the formation of 2D epitaxial silicene on Ag(111). The hybridisation can experimentally be determined by diffraction methods, such as electron or X-ray diffraction, by analysing the geometric structure of the layer. This yields the angles of the bonds between nearest-neighbour Si atoms which directly allows the determination of the hybridisation. In the case of a  $sp^3$  hybridisation 3s and 1p orbital form 4 fully equivalent  $sp^3$  orbitals, equally distanced from each other in a tetragonal configuration, which results in angles  $\alpha$  between each two orbitals of  $109.5^{\circ}$ . For an  $sp^2$  configuration 2s and 1p orbital  $3sp^2$  hybrid orbitals, located in the same plane with angles  $\alpha$  of  $120^{\circ}$  between them. A hybridisation somewhere between  $sp^3$  and  $sp^2$  can then be identified by an angle between  $109.5^{\circ}$  and  $120^{\circ}$ . Besides diffraction methods also DFT calculations the verification of the bond angles and thus the hybridisation, if the correct model for the layered structure is considered.

Besides the bond angle also the bond length between the Si atoms is an important property of a 2D Si layer. This bond length was found to have a value of 0.225 nm or 0.226 nm for free-standing silicene, by Cahangirov et al. [14] and by Houssa et al., respectively, both as results of DFT calculations. These values are only approximately 5% smaller than the distance in bulk silicon (0.235 nm) and a bit larger than twice the covalent radius of silicon of 0.22 nm. Si atoms with an  $sp^2$  hybridisation are found in Si=Si double bonds of disilenes (e.g.  $H_2Si=SiH_2$ ), where the bond length has values between 0.214 and 0.229 nm [16, 17]. It is therefore reasonable to expect that the Si–Si bond length in epitaxial silicene with an  $sp^2/sp^3$  character of the Si atoms should be found between 0.22 and 0.24 nm, i.e. somewhere between purely  $sp^2$  or  $sp^3$  hybridized Si atoms.

Additional to these structural properties, a free-standing layer should also show unique electronic properties, in particular a linear dispersion at the silicene  $\overline{K}$  point. It was demonstrated by Cahangirov et al. that free-standing silicene shows such a linear

P. Vogt

dispersion, even for the case of a low buckling within the layer [14]. It can be assumed that these electronic properties should be preserved also for an epitaxial silicene layer on a substrate material, if not significantly altered by the interaction between the two. Structural modification of the 2D layer, charge transfer or the dielectric environment might influence the electronic properties. We will see below that such an interaction plays indeed a significant role for these properties of an epitaxial silicene sheet on the Ag(111) surface.

Contrary to the electronic properties the vibrational properties are more robust and should also show a two-dimensional character of the Si layer even if the interaction with the substrate cannot be neglected. By forming a 2D layer the phonon properties should fundamentally alter if compared to bulk Si. The optical phonon spectrum of the latter is characterized by the well-known triple degenerate L(T)O mode at about  $520\,\mathrm{cm^{-1}}$  at the  $\Gamma$  point [19]. In the 2D layer, this degeneracy is partly lifted since for the out-of-plane transversal optical (TO) phonon (i.e. the motion of the atoms would be perpendicular to the layer) the frequency should significantly shift towards lower frequencies. Perpendicular to the plane the atoms have no bonding partners which reduces the restoring force and thus lowers the frequency. For the in-plane modes the restoring force gets stronger because of the additional  $\pi$  bond, associated with an  $sp^2$  hybridisation. Hence, the triple degeneracy of the L(T)O mode is lifted and an out-of-plane phonon mode can be distinguished. A similar behaviour is found for graphene in comparison to 3D diamond [20].

These considerations show that a number of physical properties allow the identification the two-dimensional character of an epitaxial silicene layer. Of course, many more effects or properties would settle the two-dimensionality, such as the topological properties described in Chap. 2, but these properties are generally dependent to the structural, electronic and vibrational properties. Hence, the investigation of the latter gives already fundamental insight into the 2D character of epitaxial silicene.

### 7.3 Formation of 2D Si-Structures on Ag(111)

In Chap. 5 the growth of Si on the Ag(111) surface is described in detail and it is shown that it follows a 2D growth mode. To obtain nicely ordered 2D Si islands which eventually from 2D layers with increasing deposition the Ag substrate should have a well-defined surface structure. Well ordered Ag(111)(1  $\times$  1) surfaces are usually prepared by Ar<sup>+</sup> ion-sputtering followed by annealing at a temperature around 550 °C for approximately 30 min in order to "heal" the surface from roughness and defects created by the sputtering. Then Si is deposited on the clean substrate surface by evaporation from a heated Si-wafer as described in Chap. 5. In Fig. 7.1 the LEED

<sup>&</sup>lt;sup>2</sup>In a simple linear chain model of harmonic oscillators the frequency  $\omega$  is given proportional to  $\sqrt{\frac{D}{m}}$ , where D is the spring constant and m the mass.

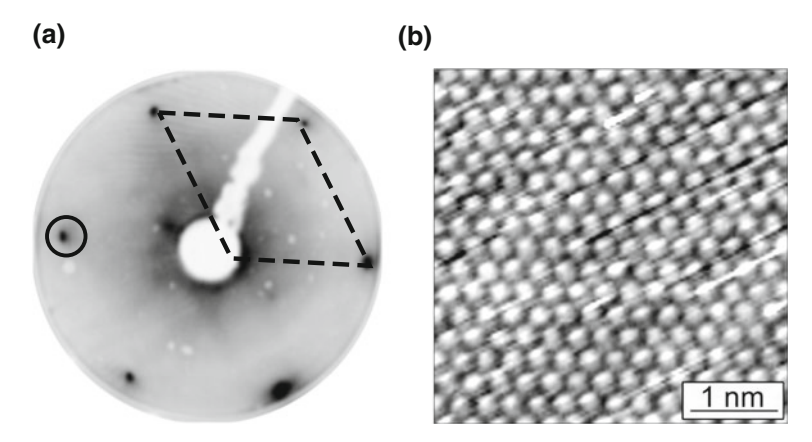


**Fig. 7.1** The Ag(111)(1 × 1) surface. **a** LEED pattern recorded on the same surface. The circle indicates the first order  $1 \times 1$  diffraction spot, the unit cell is marked by the rhombus. **b** STM image  $(U_{\text{bias}} = -1.0 \text{ V}, I = 1.08 \text{ nA})$  of Ag(111)(1 × 1)

diffraction pattern (a) and the related STM image (b) of the  $Ag(111)(1 \times 1)$  surface are shown. The STM image shows a well-ordered atomic arrangement of this surface, where the bright protrusions indicate the position of top layer Ag atoms. The sharp intense spots of the  $1 \times 1$  LEED pattern point to a good long-range order.

If Si is deposited of these ordered Ag(111) surfaces several different silicene symmetries have been reported, which strongly depend on the preparation conditions, and above all on the substrate temperature during the silicene formation [9–11, 21–23]. Among those Si atomic layers, the best investigated superstructure has a  $(4 \times 4)$  symmetry with respect to the Ag(111) surface unit cell and refers to a 2D honeycomb epitaxial silicene layer [9–11]. Various experimental techniques have been applied to study this structure and substantiate its interpretation as silicene, such as scanning tunnelling microscopy and spectroscopy (STM and STS), atomic force microscopy (nc-AFM), electron and positron diffraction, photoemission spectroscopy and Raman spectroscopy [9–11, 18, 21, 24–29].

Other 2D Si ad-layer have  $(\sqrt{13} \times \sqrt{13})R \pm 13.9^{\circ}$  and  $(2\sqrt{3} \times 2\sqrt{3})$  symmetries with respect to the Ag(111)(1 × 1) surface. Not all of these 2D Si structures are fully understood but recent in situ Raman and tip-enhanced Raman (TERS) results demonstrate their similarities to the  $(4 \times 4)$  phase [30, 31]. While, the well-ordered  $(\sqrt{13} \times \sqrt{13})R \pm 13.9^{\circ}$  Si reconstruction (existing in four differently rotated domains) is described as rotated silicene with respect to the  $(4 \times 4)$  reconstruction, the  $(2\sqrt{3} \times 2\sqrt{3})$  structure shows some inherent disorder in STM images. Additionally, the possible incorporation of Ag-atoms in these structure was suggested [32, 33], a structure that would, of course, not be in agreement with the interpretation as silicene.

## 7.3.1 Temperature-Dependence of the Si Growth on Ag(111)

The substrate temperature during the Si deposition on the Ag(111) surface plays a key role for the formation of the 2D Si-layer [9–11, 21–23]. If the deposition temperatures is below approximately 180 °C Si does not form any ordered structures on the Ag(111) template but only the formation of cluster-like Si structures. These clusters do not show any internal order and have very irregular edges. In Fig. 7.2a, a filled states STM image is shown, measured after deposition of about 0.05 monolayer (ML) of Si at room temperature (RT). The Ag(111) surface is atomically flat with homogeneously distributed Si clusters. If the amount of Si on the surface increases to 0.1 ML the size and the number of the clusters increase too, but an additional regular corrugation within the clusters is not observed by STM. This agrees also with LEED observations in Fig. 7.2c, showing no additional diffraction spots besides the ones of the Ag(111)(1 × 1) reconstruction, even for the deposition of Si equivalent to a complete ML. Raman spectra recorded after such Si deposition at room temperature give rise to a broad phonon band centred around  $480\,\mathrm{cm}^{-1}$  with a full width at

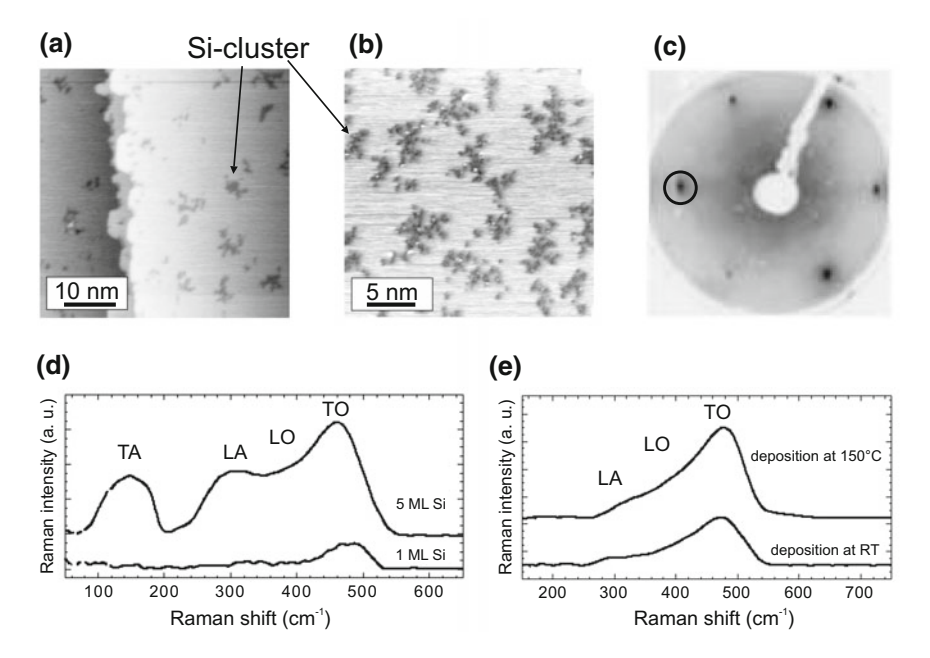


Fig. 7.2 STM image ( $U_{\rm bias} = -1.0 \text{ V}$ , I = 1.08 nA) after deposition of **a** nominal 0.05 ML and **b** nominal 0.10 ML of Si onto the Ag(111) surface at room temperature. **c** LEED pattern of the sample shown in (**b**). Only diffuse  $1 \times 1$  spots of the Ag(111) surface can be seen (black circle). **d** Raman spectra after deposition of 1 ML and 5 ML Si on Ag(111) at room temperature, showing the signature of amorphous Si. **e** Raman spectra after deposition of 1 ML Si on Ag(111) at room temperature and at 150°. Both show a very similar line shape, characteristic for a-Si (**d** and **e** adopted from [18])

half maximum (FWHM) of 78 cm<sup>-1</sup> accompanied by a weak shoulder at the lower frequency side [18]. This line shape is similar to the one of amorphous silicon (a-Si) which usually also shows less intense Raman modes around 150 and 300 cm<sup>-1</sup> [34–36]. However, because of the low deposition rate the absence of these less intense modes is expected. If the deposition of Si at RT is continued up to ~5 ML these two modes slowly evolve and the Raman spectrum becomes identical to the one of a-Si (Fig. 7.2d). These results demonstrate that the cluster-like structures observed in the STM image are associated with a-Si clusters. This picture does not change even for higher deposition temperature up to approximately 150 °C, where the Raman spectrum still shows the signature of a-Si (Fig. 7.2e).

It was suggested that Si atoms impinging at RT on the Ag(111) surface can penetrate the latter and exchange Ag atoms within the first atomic Ag layer. In this way the Si atoms would act as seeds for the growth of recessed reconstructed Si-islands including the formation of Si-Ag bonds [37]. According to [37] this process will proceed more rapidly as the size of the embedded islands increases. The LEED, STM and Raman results contradict these assumptions and demonstrate that the RT deposition only leads to the formation of a-Si clusters. In particular, the Raman results give no indication for the formation of Si-Ag bonds at room temperature. Formation of such bonds would also be associated with Raman modes at lower wavenumbers around 90 cm<sup>-1</sup> [38], which is not observed (Fig. 7.2d). These results underline the assumption that Si atoms do not favour the intermixing with Ag atoms to form a silicide, as discussed in Chap. 5. Hence, the Ag(111) surface represents an appropriate substrate for the possible synthesis of silicene.

If the substrate temperature during the Si deposition is higher than 150 °C but does not exceed 300 °C ordered 2D Si phases can form on the silver surface. The STM images in Fig. 7.3 show an overview of these different Si structures, depending on the growth temperature. At a substrate temperature around 180 °C and a Si deposition of 0.1 ML the Ag terraces start to show some decoration by locally ordered features (see Fig. 7.3a). These features do first form at the Ag step edges and then grow into the terraces if the Si deposition increases. Nonetheless, any long-range order is still not observed. This drastically changes

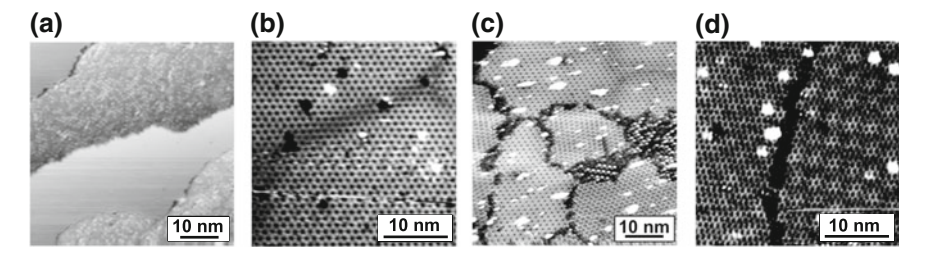


Fig. 7.3 STM topographic images ( $U_{\rm bias} = -1.0 \text{ V}$ , I = 1.08 nA) of **a** 0.1 ML of Si deposited onto Ag(111) at approximately 180 °C, 1 ML of Si deposited at 220 °C resulting in the formation of epitaxial (3 × 3) silicene, **c** 1 ML of Si deposited at 240 °C showing the formation of several 2D Si phases, and **d** 1 ML of Si deposited at 280 °C with a clear " $(2\sqrt{3} \times 2\sqrt{3})$ R30°" reconstruction

for slightly higher deposition temperatures of approximately 220 °C. Now a regular and well-ordered structure is observed in filled-states STM images (see Fig. 7.3c), after deposition of about 1.0 ML Si, covering the initial terraces of the Ag(111) surface [9–11, 21–23]. We will discuss below that this structure has a  $(4 \times 4)$ periodicity in LEED images, with respect to the integer spots of  $Ag(111)(1 \times 1)$ , and refers to an epitaxially grown silicene layer. It forms a  $(3 \times 3)$  superstructure with respect to an ideal silicene honeycomb grid, coinciding with a  $(4 \times 4)$ super cell of the Ag(111)(1  $\times$  1) surface. The structure is therefore often denoted  $(3 \times 3)/(4 \times 4)$  in the literature but will be called  $(3 \times 3)$  only, in the following. The  $(3 \times 3)$  structure is often accompanied by a second 2D Si phase which shows a  $(\sqrt{13} \times \sqrt{13})$ R  $\pm 13.9^{\circ}$  periodicity in LEED images with respect to Ag(111)(1  $\times$  1) spots. Compared to an ideal silicene grid the  $(\sqrt{13} \times \sqrt{13})R \pm 13.9^{\circ}$  phase refers to a super cell with a  $(\sqrt{7} \times \sqrt{7})R \pm 19.1^{\circ}$  periodicity and is therefore denoted as  $(\sqrt{7} \times \sqrt{7})R \pm 19.1^{\circ}/(\sqrt{13} \times \sqrt{13})R \pm 13.9^{\circ}$ . For appropriate preparation temperatures around 220° the imbalance between both domains is very clear and can be as low as 2% of the  $(\sqrt{7} \times \sqrt{7})R \pm 19.1^{\circ}/(\sqrt{13} \times \sqrt{13})R \pm 13.9^{\circ}$  phase, as determined by positron diffraction [25]. The relative distribution of both phases is temperature dependent and the amount of the  $(\sqrt{7} \times \sqrt{7})R \pm 19.1^{\circ}/(\sqrt{13} \times \sqrt{13})R \pm 13.9^{\circ}$ phase increases with increasing preparation temperatures.

The  $(\sqrt{7} \times \sqrt{7})R \pm 19.1^{\circ}/(\sqrt{13} \times \sqrt{13})R \pm 13.9^{\circ}$  structure comprises four differently structured domains, which can be distinguished clearly in STM. These four domains refer to very similar underlying silicene-like honeycomb lattices rotated by different rotation angles with respect to the Ag Ag[110] direction, respectively [24]. Contrary to the  $(3 \times 3)/(4 \times 4)$  it is not possible to prepare any of the  $(\sqrt{7} \times \sqrt{7})R \pm 19.1^{\circ}/(\sqrt{13} \times \sqrt{13})R \pm 13.9^{\circ}$  phases as a single dominant domain but are always part of a multiple-phases layer.

For deposition temperatures between 220 and 250 °C the simultaneous occurrence of multiple different Si-phases is observed by STM (Fig. 7.3c), such as the (3 × 3), the  $(\sqrt{7} \times \sqrt{7})R \pm 19.1^{\circ}/(\sqrt{13} \times \sqrt{13})R \pm 13.9^{\circ}$  and domains of a third 2D Si configuration, the so-called " $(2\sqrt{3} \times 2\sqrt{3})$ ", are found. The related LEED pattern shows a superposition of these three distinct periodicities, and slight domination of single phases results from the exact preparation temperatures.

If the preparation temperature gets closer to  $\sim\!250\,^\circ\text{C}$  the  $(2\sqrt{3}\times3\sqrt{3})$  becomes dominant and is finally observed as a single phase for deposition temperatures above 250 °C. The STM image of this phase in Fig. 7.3d shows a very characteristic Moirélike surface pattern, superimposing a smaller more detailed atomic arrangement [11, 39]. The origin of this Moiré-like pattern is the coexistence of atomically well ordered areas and disordered areas within the layer, which is discussed below in more detail. Because of the disordered areas it is not possible to describe the entire structure unambiguously by an clear translational symmetry and a related super cell and will be denoted as " $(2\sqrt{3}\times\sqrt{3})$ ", in accordance with LEED measurements.

For preparation temperatures around 300 °C the 2D growth mode of the Si adlayer changes into a 3D growth mode and 3D Si nano-particles are formed. Auger electron spectroscopy (AES) measurements demonstrate a sudden change of the Auger intensity ratio between the Si LVV and the Ag MNN Auger intensities at

this temperature [39], where L(M) represents the core level hole, the first V(N) the relaxing electron's initial state, and the second V(N) the initial energy state of the emitted electron. Thus, the Auger electron energy is characteristic for a specific element and its emission intensity can be used to determine the relative composition if more elements are present. If Si is deposited on Ag(111) the Si(LVV)/Ag(MNN) ration increases linearly for substrate temperatures below 300 °C. Around 300 °C this ratio suddenly drops in agreement with a de-wetting of the Si surface layer and the formation of Si nano-crystals. This is also in agreement with low energy electron microscopy (LEEM) measurements carried out in situ during the growth of Si on Ag(111) which show that already existing 2D Si domains start to de-wet from the surface and undergo a 2D to 3D phase transition [40]. Hence, the growth temperature of 300 °C marks the formation limit for the meta-stable 2D Si layers on Ag(111). At higher temperatures the formation of 3D Si crystals is energetically more favourable.

All of the mentioned 2D Si phases on Ag(111) can be prepared under the growth conditions described, using any sub-ML deposition up to a complete ML. This means that dominant  $(3\times3)/(4\times4)$  or " $(2\sqrt{3}\times\sqrt{3})$ " phases are also observed for a deposition of, for example, 0.5 ML of Si, leaving also plain Ag(111)(1 × 1) areas uncovered. This is expected for a 2D growth mode and supports the interpretation of these layers as real 2D structures.

In the following the different 2D Si-layers mentioned in the previous Sect. 7.3.1 will be discussed in detail concerning their atomic structure and the related electronic, optical and vibrational properties. This discussion unveils similarities and differences of these Si phases.

## 7.4 Epitaxial $(3 \times 3)$ Silicene

#### 7.4.1 Atomic Structure

After deposition of up to 1 ML Si onto the Ag(111) surface at a temperature of approximately 220 °C the surface shows the characteristic  $(3 \times 3)/(4 \times 4)$  surface periodicity in LEED (Fig. 7.4a) [9]. This periodicity can already be observed for rather low deposition amounts in the range of 1/10 of a ML but the pattern gets more intense with higher amounts. This observation is in agreement with a 2D growth mode where smaller islands start to evolve from nucleation seeds and grow larger with the amount of Si, covering more and more of the substrate surface. This interpretation is also supported by AES and XPS results discussed in Sect. 5.4, which also attest a 2D growth mode of Si on Ag(111) up to 1 ML at a growth temperature of 220 °C [9]. The STM image in Fig. 7.4c show the  $(3 \times 3)/(4 \times 4)$  Si ad-layer after a deposition of slightly less than 1 ML. The image reveals a Si layer covering the surface terraces up to the Ag step edge (top right corner). The terrace below still shows the uncovered initial Ag(111) surface. A line scan crossing the mono-atomic Ag(111) step between the two terraces (not shown) could be used to measure the height of the Si ad-layer.

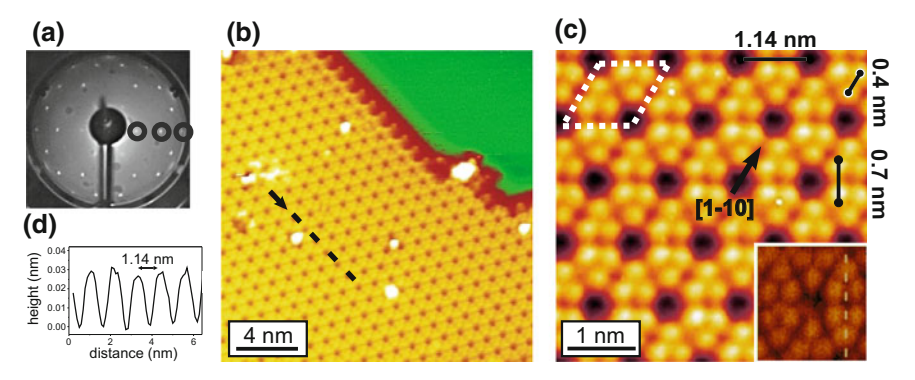


**Fig. 7.4** 2D Si layer after deposition of approximately 1ML of Si on Ag(111)(1 × 1) at a temperature of 210 °C. **a** (4 × 4) LEED pattern (27 eV), the circles indicate the (0, 1/4), (0, 1/2) and (0, 3/4). **b** Filled states STM image of the 2D Si-layer ( $U_{\rm bias} = -1.0$  V, I = 1.08 nA). Clearly visible is the honeycomb-like Si ad-layer. In the top left corned the bare Ag surface is visible. **c** High-resolution STM topograph ( $U_{\rm bias} = -1.3$  V, I = 0.35 nA) of the Si ad-layer gives rise to a "flower-like" pattern, composed of triangular structures, each consisting of three bright protrusions. The inset shows a NC-AFM images, giving rise to a very similar pattern as observed by STM. **d** Line profile along the direction indicated by the arrow in (**b**). The dark centres in the STM micrograph are separated by 1.14 nm corresponding to a 4 times the Ag(111) lattice constant in agreement with the LEED pattern in (**a**) (adopted from [9, 24, 41])

However, since the density of states of the Si ad-layer and the bare Ag(111) surface can be expected to differ significantly the observed "height" of the single steps is strongly influenced by electronic effects and depends crucially on the tunnelling voltage  $U_{\rm bias}$ . It is therefore not possible to determine the exact step height from the STM line profile. The line profile along the direction running through the dark centres of the flower pattern (indicated by the black arrow and the dashed line) is shown in Fig. 7.4d. From the profile the distance between two neighbouring dark centres can be determined and has an average value of 1.14 nm, which corresponds to four times the surface Ag(111) lattice constant and thus a  $4 \times 4$  unit cell with respect to Ag(111)(1  $\times$  1), in very good agreement with the observed LEED pattern.

Atomically resolved STM images reveal a more complex pattern of the  $(3 \times 3)/(4 \times 4)$  Si ad-layer: It is composed of the aforementioned "flower-like" features, composed of six triangular structures, each consisting of three bright protrusions. These triangles are arranged hexagonally around dark centres which form a hexagonal Bravais lattice. It is noticeable that the appearance of the  $(3 \times 3)/(4 \times 4)$  structure does not change if STM images are recorded at other sample biases between -1.4 and -0.01 V. This indicates that the STM image is probably dominated by the geometry of the layer and not by electronic effects.

In general, the intensity observed in STM images (i.e. the value of the tunelling current) depends exponentially on the distance between the STM tip and the probed sample (i.e. geometric contrast) as well as the density of states (DOS) of both (i.e. electronic contrast). Within the so-called Tersoff-Hamann approximation the

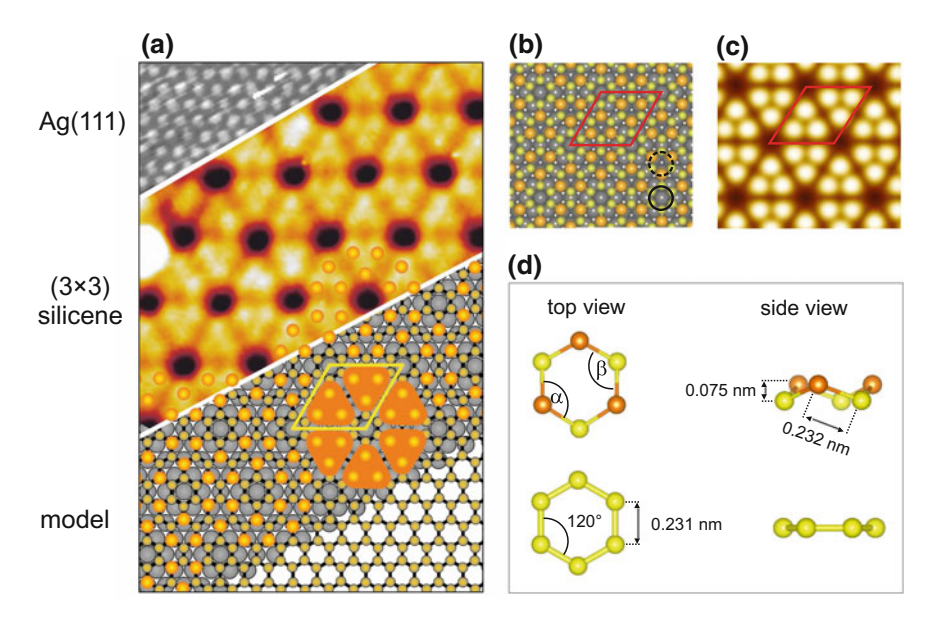


Fig. 7.5 a Atomic structure model for the 2D Si ad-layer. Top: Filled states STM image ( $U_{\rm bias} = -0.2 \, {\rm V}, I = 1.93 \, {\rm nA}$ ) of the initial clean Ag(111)(1 × 1) surface. Middle: Filled states STM image ( $U_{\rm bias} = -1.4 \, {\rm V}, I = 0.29 \, {\rm nA}$ ) of the (4 × 4) Si-ad-layer. Bottom: Model of silicene on Ag(111), Si atoms of the ball-and-stick model (right corner) sitting on top of Ag atoms are highlighted as bigger balls. DFT results for the silicene on Ag(111) model shown in (a): b the fully relaxed atomic geometries of the model in (a), c simulated STM image for the structure shown in (b), detailed top and side view of the hexagonal Si rings indicated in (b) by a dashed circle (top) and a full circle (bottom) (adopted from [9])

STM tip consists of a mathematical point source of current and the density of states at the tip is constant ( $\rho_{\text{tip}}(E) = \text{const.}$ ) [42, 43]. Here, the intensity depends on the local density of states (LDOS), which is the DOS of the sample at the position of the STM tip, revealing a signal that is based on the charge density on the sample only. But the charge density does not necessarily correspond directly to the atomic structure, but for example, to inter-atomic bonds between surface atoms or to dangling bonds. In the case of the  $(3\times3)/(4\times4)$  Si ad-layer non-contact AFM images with an atomic resolution (Fig. 7.4d) show, however, a very similar pattern as observed by STM [24]. Within these AFM images a very similar "flower-like" pattern can be observed which indeed shows the very same lateral dimensions, as observed by STM. Since AFM images are dominated by geometric factors because of the different interaction mechanism with the probed surface, the similarity of the STM and AFM images underlines strongly that the images will have to be interpreted by geometry and not by electronic effects.

Figure 7.5 explains how the observed STM and AFM images of the  $(3 \times 3)/(4 \times 4)$  structure can be explained by a single silicene-like 2D honeycomb Si sheet. The top part of Fig. 7.5 shows the bare Ag(111) surface and in the middle the 2D

Si ad-layer can be seen. At the bottom part a simple ball-and-stick model of a 2D Si honeycomb grid is shown. Within this model Si atoms form in-plane bonds to neighbouring Si atoms only. This honeycomb grid is moved atop the underlying Ag(111) surface, represented by the grey spheres, where each sphere represents a top-layer Ag atom. Covalent chemical bonds between the Si atoms of the 2D layer and the outermost Ag atoms of the Ag(111) substrate are not formed, i.e. the Si layer preserves its 2D character. Now, one has to distinguish whether the top-layer Si atoms within the honeycomb lattice are localized directly above an underlying Ag atom of the Ag(111) substrate, or between two of these underlying Ag atoms. In the first case it is assumed that the Si atom moves slightly out of the 2D Si-plane, as a result of the interaction with the Ag(111) surface. In the second case the Si ad-layer atoms moves slightly into the lattice plane. If the atoms that move out of the plane are all indicated by big orange spheres (see Fig. 7.5a) then these spheres form exactly the pattern observed in STM and AFM images. This is illustrated in Fig. 7.5a by the orange spheres which extend into the measured STM image and overlap with the bright protrusions that form the "flower-like" pattern. Note that the unit cell forms a  $(3 \times 3)$  superstructure with respect to the ideal hexagonal Si honeycomb ring (Fig. 7.5b). Therefore, the structure is referred to as  $(3 \times 3)$  only.

Based on this atomic model the in-plane Si–Si distance can be determined from the experimental STM image. From the line profile shown in Fig. 7.4d the distance D of adjacent centres was shown to have a value of 1.14 nm. From D the Si–Si in plane distance a can be calculated according to  $a = D/(3\sqrt{3})$  and has a value of  $0.22\,\mathrm{nm}\,(\pm 0.01\,\mathrm{nm})$  [9]. This is a reasonable value if compared to other Si allotropes where the Si atoms are differently hybridized as discussed in Sect. 7.2. Compared to the bond length in bulk silicon the bond shortening in epitaxial silicene is less than in carbon compounds where a C–C bond shortening between diamond  $(0.154\,\mathrm{nm})$  and graphene  $(0.142\,\mathrm{nm})$  of approximately 8% is observed [44]. However, it is still large enough to show a true  $sp^2/sp^3$  hybridisation character of the Si atoms in the silicene layer.

The energetic stability of the structure model in Fig. 7.5 has been demonstrated by ab initio calculations based on density functional theory (DFT). Different groups have reported a negative value of the total energy of this model [9, 10, 45–47], and an adhesion energy of -0.48 eV for each Si atom was reported in [9]. The formation energy of the adsorbed layer depends in principle on the chemical potential  $\mu_{\rm Si}$  ( $\mu_{\rm Ag}$ ) of the respective elements, but Pflugradt et al. showed that the (3 × 3) layer remains stable even if  $\mu_{\rm Si}$  is reasonably varied, i.e. for a wide range of chemical potentials [47].

The model of the  $(3 \times 3)$  layer after full structural relaxations is shown in Fig. 7.5b (top view) which fully supports the above made assumptions. The Si atoms of the Si honeycomb layer which are located directly above underlying Ag atoms of the Ag(111) substrate are slightly displaced normal to the layer away from the substrate, while Si atoms which are located between two or more underlying Ag atoms move closer to the substrate. This means that the Si atoms are located in two different sublattices A and B of the  $(3 \times 3)$  structure. The distance between the top (bottom) Si

**Table 7.1** Comparison of the structural values of  $(3 \times 3)$  silicene from electron and positron diffraction [25, 26] and DFT calculations [9]. Shown are the values of the buckling  $\Delta$ , the distance between the down silicene sub-lattice and the top Ag layer d, the angles  $\alpha$  and  $\beta$  from Fig. 7.5, the Si–Si bond length

Method	Δ (Å)	d (Å)	α (°)	β (°)	Si-Si (nm)	Source
DFT	0.78	2.17	110	118	0.23	From [9]
RHEPD	0.83	2.14	112	119	_	From [25]
LEED	0.74-0.77	2.18	_	-	0.23	From [26]

atoms and the average height of the first Ag layer is  $0.292 \pm 0.002$  nm and  $0.217 \pm 0.003$  nm, respectively.

The described displacement leads to the formation of the observed triangular structures in the top-layer, consisting of three Si atoms which are separated by  $0.38\,\mathrm{nm}$ . This distance agrees very well with the experimental STM observations which show the same triangular structure and a separation of approximately  $0.40\,\mathrm{nm}$ . The characteristic dark holes in the experimental STM images are explained by a ring of Si atoms, all localised in a "down" position, which mark the corners of the  $(3\times3)$  simple hexagonal surface unit cell with respect to a single silicene hexagonal ring (see Fig. 7.5a). Each unit cell contains 18 Si atoms, of which 6 are outward displaced in an "up" position and 12 are in a "down position", meaning that up and down positions are populated asymmetrically.

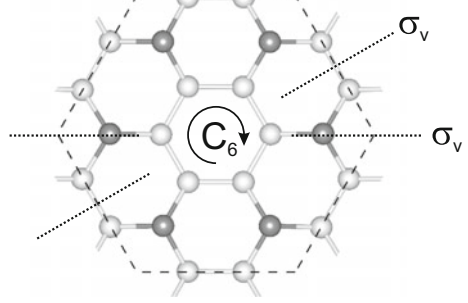
Following these calculations also the bond angles of the Si atoms can be determined, which give information on the hybridisation state of the respective atom. To illustrate this Fig. 7.5d shows the two hexagonal Si rings marked in Fig. 7.5b by black circles in more detail in top and side view. The circles refer to rings where either three atoms are in a "top" and three in a "down" position (solid line) or all six atoms are in a "down" position (dashed line), Fig. 7.5d top or bottom, respectively. In the first case the top Si atoms have bond angles of  $\approx 110^{\circ}$  ( $\alpha$ ) which are very close to an angle of  $109.5^{\circ}$  for ideally  $sp^3$ -hybridized Si atom. The down Si atoms have bond angles between  $\approx 112^{\circ}$  and  $\approx 118^{\circ}$ , indicative for a  $sp^3/sp^2$  hybridisation. For the second case all six atoms are purely  $sp^2$ -hybridized with bond angles of  $\approx 120^{\circ}$  (dashed circle). These different bond angles of the Si atoms result from the displacement of the Si atoms in z-direction caused by the interaction with the Ag(111) substrate. However, most of the atoms are  $sp^3/sp^2$  hybridized which is the equilibrium state in agreement with calculations for free-standing Si [14].

These structural values are also confirmed by different diffraction methods used to study the  $(3 \times 3)$  structure. In Table 7.1 the results for electron and positron diffraction experiments [25, 26] are compared to the DFT results from Fig. 7.5. The value  $\Delta$  describes the buckling between top and bottom Si positions, d is the height difference the centre of the down sub-lattice of the  $(3 \times 3)$  layer and the first Ag(111) layer,  $\alpha$  and  $\beta$  refer to the angles also shown in Fig. 7.5, and Si–Si is the bond length between adjacent Si atoms. The table shows a very good agreement for the angles and the distance d determined by DFT and reflection high-energy position

C<sub>6v</sub> symmetry

Fig. 7.6 Wigner-Seitz unit cell (dashed hexagon) of  $(3 \times 3)$  epitaxial silicene on Ag(111), belonging to a  $C_{6v}$ symmetry point group. The 6-fold rotation axis  $C_6$  is indicated by the arrow, the dashed lines represent two of the six mirror planes  $(\sigma_v)$ 





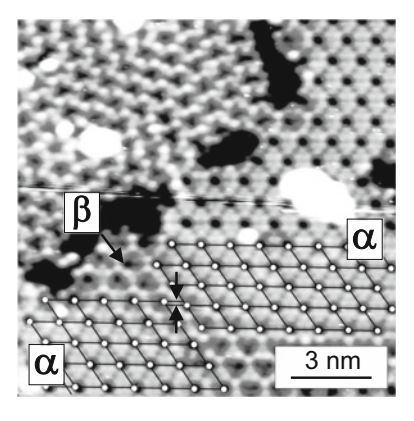
diffraction (RHEPD), and also for the Si-Si distance from DFT and LEED results. Only the buckling  $\Delta$  from RHEPD is slightly larger than from DFT and LEED results. Overall, there is a very good agreement between the DFT and the diffraction results, supporting the honeycomb-based model of epitaxial silicene.

Based on the relaxed geometry, STM images can be simulated by calculating the local electron density of states according to the Tersoff-Hamann approach [42, 43]. In Fig. 7.5c it can be seen that the simulated STM image exhibits the same structural features as observed experimentally, i.e. a hexagonal arrangement of the triangular structure around dark centres (adopted from [9]). By looking at the charge density around top and bottom Si atoms (not shown here) it is found that these atoms are electronically very similar. This means that the STM corrugation is mainly dominated by geometrical aspects rather than electronic effect which is in good agreement with the voltage-independence of the experimental STM images mentioned above. The DFT-based calculations therefore clearly support the suggested structure model and give evidence that the  $(3 \times 3)$  2D Si ad-layer refers to silicene.

Besides the symmetry reduction, caused by having 12 Si in the down and only 6 in the up sub-lattice, the unit cell is highly symmetric. In Fig. 7.6 the Wigner-Seitz cell of the epitaxial  $(3 \times 3)$  silicene layer is shown. This unit cell has a six-fold rotation axis, indicated by  $C_6$  and six mirror planes parallel to the rotation axis: three running through the corners of the hexagonal unit cell and three through the centres of the sides. Hence, the structure belongs to a  $C_{6v}$  symmetry point group [47] in contrast to low-buckled free-standing silicene which belongs to  $D_{3d}$ . The assignment of the symmetry group will be important for the interpretation of polarization dependent Raman measurements in Sect. 7.4.3.

Since the  $(3 \times 3)$  unit cell coincides with a  $(4 \times 4)$  supercell of the Ag(111) substrate surface  $(3 \times 3)$  domains can also be shifted with respect to each other by a Ag surface lattice constant. From the 2D growth mode it can be expected that different silicene domains start to grow at different seeds on the substrate layer being shifted with respect to each other. In Fig. 7.7 a filled states STM images shows such two domains. The lattice in both domains is illustrated by the black grids and the

Fig. 7.7 Filled states STM image ( $U_{\text{bias}} = -1.1 \text{ V}$ , I = 0.92 nA) of two (3 × 3) silicene domains, shifted with respect to each other by 1/4 of the Ag lattice constant (arrows)



white circles that indicate the dark centres of the  $(3 \times 3)$  structure. If the relative positions of these grids are compared it is found that they are indeed shifted with respect to each other. At the boundary between the two domains the appearance in STM varies from the typical flower-pattern. This structure is also referred to as  $\beta$ -silicene and indicates the domain boundary between two  $(3 \times 3)$  domains, also named  $\alpha$ -silicene. An atomic structure model of the  $\beta$  phase was suggested by DFT calculations and it was shown that the cohesive energy  $E_c$  for the  $\beta$  phase is 4 meV per Si atom lower than for the normal  $(3 \times 3)$  structure, i.e. the  $\alpha$  phase [48]. The  $\beta$  structure is therefore less energetically stable and found only in a very limited areas between two  $(3 \times 3)$   $\alpha$  domains, as in Fig. 7.7.

Finally, it is important to note that the results described so far show a significant influence of the substrate atomic structure on the geometry of the epitaxial silicene layer. The  $3\times 3$  superstructure formation is solely a result of the interaction with the substrate which also leads to a symmetry breaking by formation of two differently populated sub-lattices. The next paragraph will show that this interaction has also an influence on the electronic properties of epitaxial silicene, if compared to expectations for the ideal free-standing form.

# 7.4.2 Electronic Properties

An important aspect of graphene-like 2D materials are the electronic properties, in particular the electronic band structure. According to the theoretical calculations free-standing silicene should have a linear dispersion at the  $\overline{K}$  points of the BZ, the so-called "Dirac cones". An easy experimental access to measure the electronic dispersion is angle-resolved photoemission spectroscopy (ARPES). In the case of epitaxial (3 × 3) silicene on Ag(111) the  $\overline{K}$  point of silicene is located at 3/4 of the distance to the Ag  $\overline{K}$  point, because of the (3 × 3)/(4 × 4) coincidence arrangement, sketched in Fig. 7.8c. The ARPES data recorded along the Ag  $\overline{\Gamma}$  –  $\overline{K}$  direction are

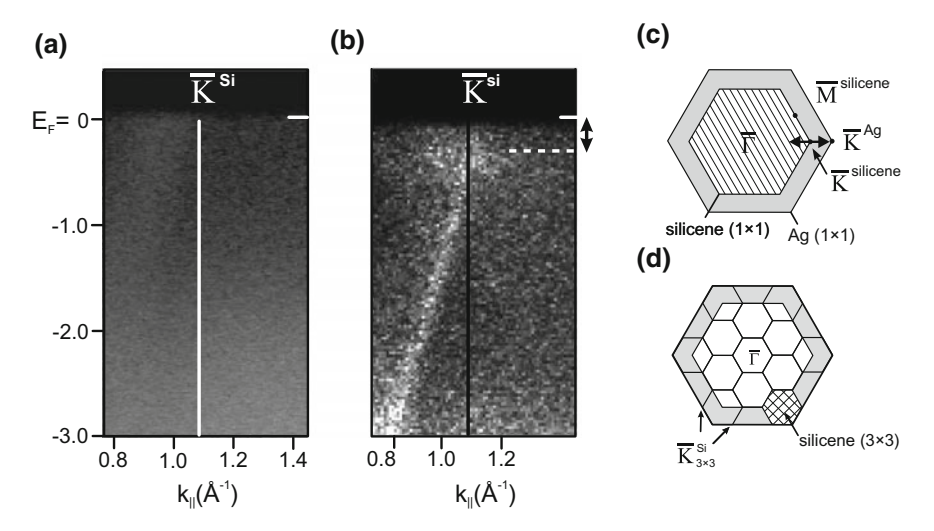


Fig. 7.8 ARPES measurements of epitaxial  $(3 \times 3)$  silicene on Ag(111). **a** ARPES intensity map for the clean Ag surface and **b** after formation of the  $(3 \times 3)$  silicene ad-layer, measured along the Ag  $\overline{\Gamma} - \overline{K}$  direction through the Si  $\overline{K}$  point. **c** Brillouin-zone (BZ) scheme of the 2D Si layer with respect to the Ag(111)1  $\times$  1 surface. **d** BZ of the  $(3 \times 3)$  supercell of epitaxial silicene, showing silicene  $\overline{K}$  points at the BZ edge of the Ag(1  $\times$  1) BZ ((a) and (b) adopted from [9])

shown in Fig. 7.8a for the clean initial Ag(111) surface and in (b) after formation of the  $(3 \times 3)$  silicene ad-layer (from [9]). The spectra are measured at an excitation energy of 126 eV, i.e. at the Cooper minimum of Ag in order to suppress strong Ag contributions and the ARPES data do not show obvious bands of the initial surface. After the silicene formation a downward-dispersing conical linear band can be identified, with an apex at the silicene  $\overline{K}$  point close to the Fermi energy  $E_F$ . Such bands were observed at different Si  $\overline{K}/\overline{K}'$  points of the surface BZ but not on the initial Ag(111) surface (Fig. 7.8a) [9]. This dispersion is partly similar to the one of graphene which initiated the interpretation that this dispersion is related to a Dirac cone of epitaxial silicene. However, there are also some differences which need to be taken into account. The linear dispersion can be described by the expression  $E = \hbar v_F k$ , where  $v_F$  is the slope of the dispersion, the so-called Fermi velocity. For epitaxial silicene  $v_F$  can be determined from Fig. 7.8 and has a value of  $v_F = 1.3 \times 10^6 \text{ ms}^{-1}$ , which is comparable to the one found for graphene and even higher [49]. This is surprising, looking at the above discussed significant interaction with the substrate material. Additionally, the linear part of the band exceeds over about 3 eV, a range much larger than in the case of graphene. The possible existence of a small band gap at  $E_F$  is also suggested by the dispersion (indicated by the arrow) but was later shown to not exist [50]. Free-standing silicene is expected to have a zero-gap, however, the opening of the gap could result from an interaction with the Ag(111) substrate, an effect already observed for graphene [51].

Soon after these first measurements of the dispersion of epitaxial silicene, the interpretation as a Dirac cone was disputed by theoretical DFT calculation. In none of these calculations a linear dispersion could be preserved due to the interaction with the substrate and breaking of the symmetry [48, 52–55]. But if the dispersion does not result from the existence of charge carriers which mimic Dirac particles, another explanation for the bands had to be given. Several such explanations were suggested, among those, the possibility that the linear band is a Ag sp band, which could occur at the silicene  $\overline{K}$  points due to back-folding of the BZ [55]. However, in this case the band would originate from bulk states which should disperse with  $k_{\perp}$ . This is experimentally disproved by showing that the observed dispersion does not change in an an energy range of  $126 \pm 5$  eV or at a photon energy of 78 eV, clearly showing that this state is localized at the interface [9]. It was later shown by Cahangirov et al. that the linear dispersion result form hybridized electronic state through the interaction between the silicene layer and the Ag substrate, localized at the interface [56]. This interpretation does not lead to contradictions with the experimental observations and details of these calculations are discussed in Sect. 8.2.

ARPES measurements in a wider range of k values also shows that the silicene-Ag interaction leads to the formation of cone-like features at the 1. BZ-edge of the Ag(111) surface (see Fig. 7.8d). At points between the Ag  $\overline{M}$  and the Ag  $\overline{K}$  points, coinciding with silicene  $\overline{K}$  points, paired cones were measured by ARPES and assigned to Dirac cones. These cones also result from the Ag-silicene interaction [57].

The absence of linear cone-like bands at the silicene  $\overline{K}$  points, as observed for graphene, has initiated a discussion if epitaxial silicene can really be interpreted as a 2D graphene like material, and actually be called "silicene". However, as explained in Sect. 7.2 the electronic properties are easily altered by an interaction, an effect also observed for graphene if the interaction with the substrate is not negligible [51]. In the next section it will be shown that the vibrational properties are more robust and fully confirm the 2D character of epitaxial silicene.

# 7.4.3 Vibrational Properties

Figure 7.9a shows the Raman spectrum of the epitaxial  $(3 \times 3)$  silicene phase recorded in situ at room temperature, adopted from [18]. Three intense narrow Raman modes are observed at 175, 216, and  $514\,\mathrm{cm^{-1}}$ . The full width at half maximum (FWHM) of these modes has values of  $15\,\mathrm{cm^{-1}}$ ,  $20\,\mathrm{cm^{-1}}$ , and  $16\,\mathrm{cm^{-1}}$ , respectively. In order to obtain this Raman spectrum the signature of amorphous Si (a-Si) was subtracted from the as-measured data. The presence of the latter is associated with the co-existence of smaller amounts of amorphous Si (a-Si) which nucleate during the Si deposition on the Ag(111) substrate at surface defects and has broad Raman bands at 350 and  $480\,\mathrm{cm^{-1}}$  [18]. This assumption is substantiated by the Si deposition on the Ag(111) surface at room temperature and oxidation of the epitaxial silicene (see also Sect. 7.6).

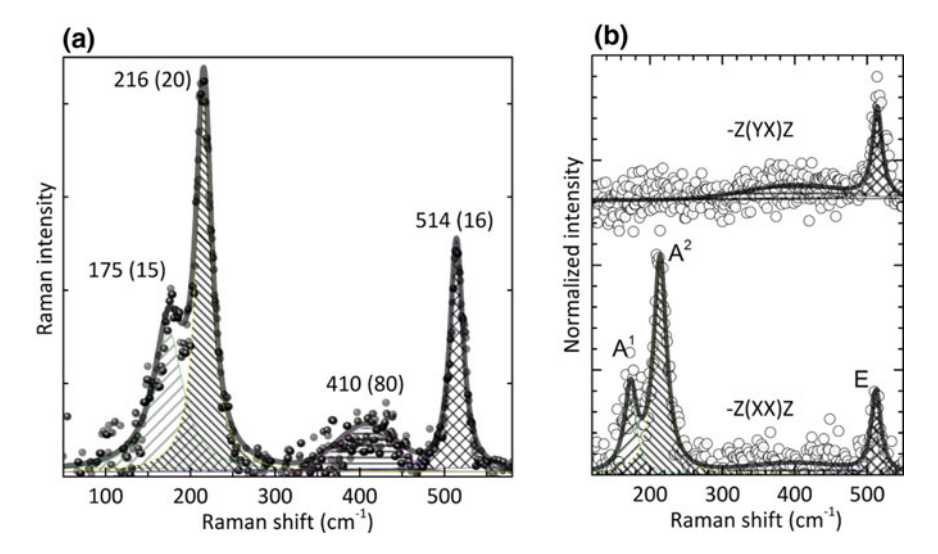


**Fig. 7.9** a Raman spectrum of epitaxial  $(3 \times 3)/(4 \times 4)$  silicene on Ag(111) showing phonon modes at 175, 216, 410, and 514 cm<sup>-1</sup> (FWHM in brackets). **b** Related Raman selection rules for parallel  $\bar{z}(xx)z$  and crossed  $\bar{z}(yx)z$  geometries (adopted from [18])

In addition to the intense phonon modes, a weak broad band around 410 cm<sup>-1</sup> can now be seen in the spectrum. This mode matches the spectral range, where a second-order phonon band of the intense mode at 216 cm<sup>-1</sup> can be expected.

Modes with frequencies close to 514 cm<sup>-1</sup> were also observed by ex situ and low temperature in situ Raman measurements with Raman shifts of 516 cm<sup>-1</sup> and 530 cm<sup>-1</sup>, respectively [58, 59]. To some extent, the significant blueshift of the latter is probably caused by the much lower temperature (77 K) during the Raman measurements. However a shift of approximately 16 cm<sup>-1</sup> is too large to be solely related to a thermal effect, as we will also see in Sect. 7.4.4. The low temperature in situ Raman measurements also found a mode close to 230 cm<sup>-1</sup> which was interpreted to be related to light scattering from domain boundaries [58]. In analogy to graphene this mode was assigned to a "*D* band". However, this is not in agreement with polarization dependent Raman measurements, discussed below.

The nature of the observed modes is elucidated by Raman selection rules, measured in two polarization geometries:  $\bar{z}(xx)z$  and  $\bar{z}(yx)z$  (Porto notation), i.e. parallel and crossed polarisations, respectively. The x,y, and z axes represent the sample coordinate system: the z axis is normal to the 2D layer, whereas x and y are the in-plane axes (x aligned along the Ag[-110] direction). With this notation the orientation of the layer with respect to the polarization vector of the laser light in the experiment is expressed. Assuming  $e_i$  and  $e_s$  to be the unit vectors of the polarisation of the incoming and scattered light, respectively, the Raman scattering intensity I of the phonon modes is proportional to

$$I \sim |e_i \cdot R \cdot e_s|^2 \tag{7.1}$$

where R is the Raman tensor. This tensor is a symmetric second rank tensor and has the same symmetry as the corresponding phonon mode. Hence, (7.1) determines whether a Raman-active phonon mode can be observed for a certain scattering geometry in terms of the incoming and scattered polarisation. Such behaviour is governed by different symmetries of the lattice vibrations associated with these modes. Thus the Raman selection rules allow us to determine the symmetry of a phonon mode by using different scattering geometries in the experiment.

The  $(3 \times 3)$  structure of the epitaxial silicene layer belongs to the  $C_{6\nu}$  symmetry point group [47], which possesses A(z),  $E_1$ , and  $E_2$  phonon symmetries. These phonon symmetries are related to the Raman tensors:

$$A(z) = \begin{pmatrix} a & 0 & 0 \\ 0 & a & 0 \\ 0 & 0 & b \end{pmatrix}; E_1 = \begin{pmatrix} 0 & 0 & c \\ 0 & 0 & c \\ c & c & 0 \end{pmatrix}; E_2 = \begin{pmatrix} d & -d & 0 \\ -d & -d & 0 \\ 0 & 0 & 0 \end{pmatrix}$$
(7.2)

For the 2D layer  $e_i$  and  $e_s$  can be aligned along the (100) or the (010) direction which gives, for example, the following selection rules for the A mode:

$$\begin{vmatrix} \begin{pmatrix} 1 \\ 0 \\ 0 \end{pmatrix} \cdot \begin{pmatrix} a & 0 & 0 \\ 0 & a & 0 \\ 0 & 0 & b \end{pmatrix} \cdot \begin{pmatrix} 1 \\ 0 \\ 0 \end{pmatrix} \begin{vmatrix} 2 \\ 0 \\ 0 \end{vmatrix}^2 = a^2; \quad \begin{vmatrix} \begin{pmatrix} 1 \\ 0 \\ 0 \end{pmatrix} \cdot \begin{pmatrix} a & 0 & 0 \\ 0 & a & 0 \\ 0 & 0 & b \end{pmatrix} \cdot \begin{pmatrix} 0 \\ 1 \\ 0 \end{pmatrix} \begin{vmatrix} 2 \\ 0 \\ 0 \end{vmatrix}^2 = 0$$
 (7.3)

This means that the A mode of epitaxial silicene can only be observed in parallel configuration, but is forbidden in crossed configuration. In contrast, the E mode is allowed in both polarization configurations. The A modes are associated with out-of-plane vibrational motions of the Si atoms, i.e. perpendicular to the 2D layer. An vibrational mode with an A symmetry can therefore not exist in a 3D Si allotrope such as diamond-like Si and is an unambiguous indication for the two dimensional character of the silicene layer. This does not only account for silicene but for 2D materials or layered materials in general, and is, for example observed for  $MoS_2$  [60],  $MoSe_2$  and  $WSe_2$ [61], and black phosphorous [62]. However, it is noteworthy that in graphene the observation of an out-of-plane mode (having a  $B_2$  symmetry) by Raman spectroscopy is symmetry forbidden, but observed by high resolution electron energy loss spectroscopy [63].

The measured polarization dependent Raman spectra of epitaxial (3 × 3) silicene on Ag(111) are depicted in Fig. 7.9b (adopted from [18]). The plot shows spectra for crossed ( $\bar{z}(yx)z$ , top) and parallel ( $\bar{z}(xx)z$ , bottom) polarization geometries and the single components are numerically fitted. The Raman mode at 514 cm<sup>-1</sup> and the broad band at 410 cm<sup>-1</sup> are clearly seen in both polarization configurations, while the two modes at 175 and 216 cm<sup>-1</sup> are only found in parallel geometry and entirely disappear in crossed geometry. In connection with the expected Raman selection rules for the  $C_{6v}$  point group shown in (7.3), these results unambiguously demonstrate that the modes at 175 cm<sup>-1</sup> and 216 cm<sup>-1</sup> have to be assigned to an A symmetry and

are denoted as  $A^1$  and  $A^2$ , respectively. The mode at  $514\,\mathrm{cm}^{-1}$  is observed in both polarization configurations and is assigned to an E symmetry, while the Raman band at  $410\,\mathrm{cm}^{-1}$  shows almost no polarization dependence expected for a second order phonon band.

The measurements of the Raman selection rules demonstrates that the observed modes of epitaxial silicene are attributed to E and A symmetries. In particular the strong dependence of the A modes on the polarization geometry underline their relation to a well-ordered crystal structure of the 2D layer. This also shows that an assignment of the A modes to disorder induced light scattering from domain boundaries [58], similar to the "D band" in graphene, can be ruled out. Domain boundaries break the long-range translational symmetry in the 2D crystal and a strong polarization dependence of the Raman modes should not be observed. In fact, a "D-type band" is not observed for epitaxial silicene in the entire spectral range between 100 and 2000 cm $^{-1}$ .

As discussed above, the symmetries of the observed Raman modes are in good agreement with theoretical expectations for free-standing silicene, according to which three optical phonon branches should be observed at  $\Gamma$ : an out-of-plane ZO mode and energetically degenerate TO and LO phonons [64-66]. On the other hand the frequencies do not fully match the theoretical calculations. While the frequency of the ZO branch is close to the experimentally observed A modes at  $\Gamma$ , the degenerate TO/LO branches should have frequencies of 562 cm<sup>-1</sup> [64], ~550 cm<sup>-1</sup> [65] or  $\sim$ 556 cm<sup>-1</sup> [66], which obviously differs from the E mode of epitaxial silicene at 514 cm<sup>-1</sup>. This discrepancy is related to the interaction between the epitaxial silicene layer and the Ag substrate. If such an interaction is accounted for within the DFT calculations it is found that the interaction with the substrate alters the phonon dispersions [18]. The phonon dispersions of the epitaxial silicene become more flat than the one of free-standing silicene due to the formation of the  $3 \times 3$  super-structure and the E mode shifts to lower frequencies. In detail: degenerate modes are found centred around 514 cm<sup>-1</sup>, belonging to the irreducible representation  $E_2$  and two normal modes that belong to the irreducible representation A are found at 173 cm<sup>-1</sup>  $(A^1)$  and  $204 \,\mathrm{cm}^{-1}$   $(A^2)$  [18]. We see that the frequencies of the degenerate LO/TO modes at the  $\Gamma$ -point is significantly lowered upon the superstructure formation, in agreement with the experimental data in Fig. 7.9.

The motion pattern of these three vibrational modes is shown by the corresponding eigenvectors in Fig. 7.10, in top and side view. It can be seen that in the case of the E mode, the three protruding atoms in the left half of the  $(3 \times 3)$  cell are moving in a in-plane direction opposite to the surrounding atoms and the atoms in the right half move opposite to the corresponding atoms in the left half of the  $(3 \times 3)$  cell. For the  $A^1$  mode, the six protruding atoms forming the "flower pattern" and the six atoms connected to them are moving downwards while the remaining six atoms move upwards while for the  $A^2$  mode, the protruding six atoms move upwards while the remaining twelve atoms move downwards. This shows that the E mode is dominated by in-plane and both A modes by out-of-plane atomic displacements, in very good agreement with the experimentally determined Raman selection rules.

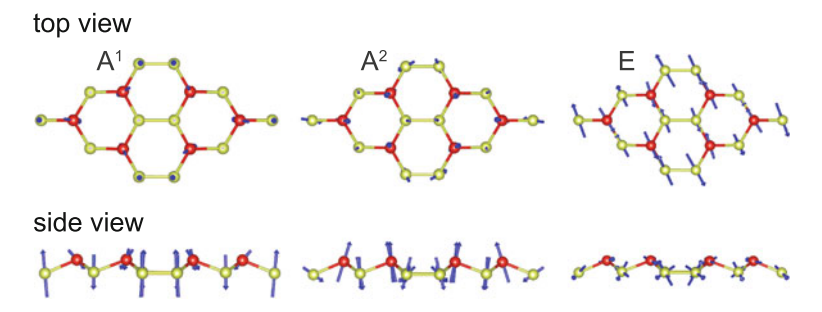


**Fig. 7.10** Top and side views of the eigenvectors of the calculated phonon modes related to the experimentally observed Raman active modes. 175, 216, 410, and 514 cm<sup>-1</sup> (adopted from [18])

In summary, it is found that the two  $A^1$  and  $A^2$  modes are clearly related to the ZO mode calculated for free-standing silicene. A modes do not exist in diamond-like Si [67, 68] or other Si allotropes and are a conclusive indicator for the 2D character of epitaxial silicene. The translational symmetry is broken perpendicular to the 2D lattice plane of epitaxial silicene, lifting the phonon triple degeneracy at the  $\Gamma$  point, in agreement with calculations for free-standing silicene [64–66] and group theory analysis shows that free-standing silicene has Raman-active modes of A and E symmetries, unlike bulk Si, which has only one zone-centre Raman mode of F symmetry [69]. The presence of two A modes for epitaxial silicene on Ag(111) in contrast to only one A mode theoretically found for free-standing silicene, is related to the much bigger unit cell of the  $(3 \times 3)$  superstructure containing more atoms. This means that there are also more atoms F in the basis, allowing for more phonon modes, since the number of possible phonon modes is equal to F

We see that the 2D vibrational properties of  $(3 \times 3)$  epitaxial silicene are indeed more robust than the electronic properties against the interaction with the substrate material. This make in situ Raman spectroscopy an ideal tool to investigate not only the two-dimensional properties by possibly also the modification by functionalisation or chemical modifications through organic and inorganic adsorbates.

# 7.4.4 Temperature Dependence of the Vibrational Modes

The 2D character of epitaxial silicene on Ag(111) has also an influence on its temperature dependent properties. Measuring the phonon bands as a function of temperature also allows to get some more inside into the electron-phonon coupling (EPC) in these 2D layers.

Figure 7.11a shows a series of Raman spectra measured at different annealing temperatures of the epitaxial  $(3 \times 3)$  silicene layer between room temperature and 500 °C. We can see that the annealing has no significant influence on the overall line shape of the Raman spectra for temperatures below  $\sim 300$  °C. For this temperatures

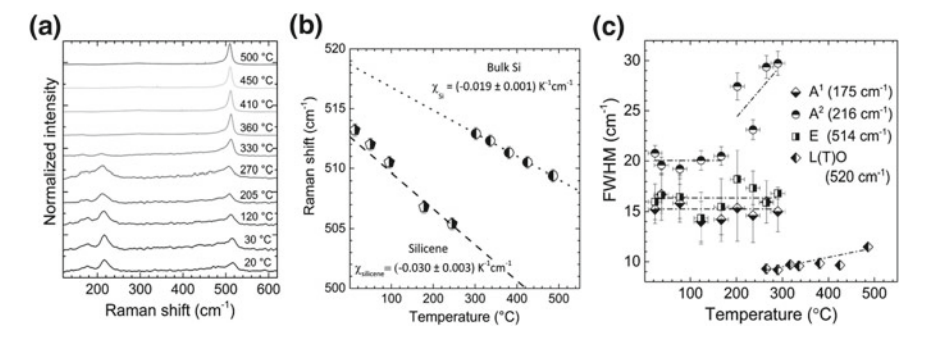


**Fig. 7.11** a Series of Raman spectra of  $(3 \times 3)$  silicene on Ag(111) measured with increasing temperatures between room temperature and 500 °C. Around 300 °C the spectral line shape changes dramatically as a result of a phase transition. **b** Determination of the thermal coefficient  $\chi$  of the *E* mode of epitaxial silicene and the L(T)O mode of the Si nano-crystallits, formed after the phase transition. **c** FWHM of the two *A* modes and the *E* mode of epitaxial silicene as a function of the temperature (adopted from [18])

ature range the two A modes ( $A^1$  and  $A^1$ ) and the E mode are seen in all spectra which show an equal increasing small shift towards lower wavenumbers with increasing temperatures. The temperature shift of the phonon frequency results from the anharmonic terms of the potential energy in the crystal lattice and is related to a change of the repelling force constant between the oscillating atoms. The observed shift is qualitatively quite similar to the ones of graphene [70], MoS<sub>2</sub> [71], or bulk Si [19, 68].

The temperature related shift can be described by the so-called first-order thermal coefficient  $\chi$  which is defined as the slope of the linear fit through the temperature dependent frequency positions of a specific phonon mode. The thermal coefficient  $\chi$  is represented by the equation:  $\omega(T) = \omega_0 + \chi \Delta T$ , where  $\omega_0$  is the Raman frequency at a reference temperature (e.g. room temperature or 0 K (by extrapolation)) and  $\Delta T$  is the temperature difference with respect to the reference temperature. For moderate temperatures this relation is normally valid and a good approximation. Figure 7.11b shows the temperature-dependent position of the E mode along with the a linear shift (dashed line), giving a value for  $\chi_{\rm silicene}$  of  $(-0.030 \pm 0.003)~{\rm K}^{-1}~{\rm cm}^{-1}$ .

At a temperature of approximately  $300\,^{\circ}\text{C}$  the line shape of the Raman spectra start to change significantly. The modes related to epitaxial silicene ( $A^1$ ,  $A^1$  and E) start to vanish and are fully gone for slightly higher temperatures while a dominating new broad mode appears around  $520\,\text{cm}^{-1}$  with an asymmetric shoulder on the lower energy side. The line shape of this new mode is characteristic for the L(T)O mode of bulk-like Si nanoparticles around  $520\,\text{cm}^{-1}$  with an asymmetric shoulder. This shoulder is caused by the spatial phonon confinement in particles smaller than 7 nm [72] and the size distribution of these nanoparticles explains the broad line width. The formation of nanoparticles indicates a structural phase transition at  $300\,^{\circ}\text{C}$  where the silicene layer transforms into these bulk-like Si particles. Such a phase transition is supported by LEEM and AFM measurements which give evidence for a de-wetting

process and a destruction of the Si ad-layer at temperatures above 300 °C [39, 40]. At the same time a broad 2nd-order band (of the L(T)O mode) appears around 950 cm<sup>-1</sup>, which is not the case for the epitaxial silicene layer [18]. The occurrence of this 2nd-order band is thus indicating the formation of Si crystallites. The thermal coefficient  $\chi_{\text{crystallites}}$  of the L(T)O phonon of the Si nanocrystallites can be determined from its temperature-dependent shift for temperatures between 300 and 500 °C (Fig. 7.11b).  $\chi_{\text{crystallites}}$  has a value of  $(-0.019 \pm 0.003) \, \text{K}^{-1} \, \text{cm}^{-1}$  which is clearly different from the thermal coefficient of the E mode of epitaxial silicene but comparable with values reported for diamond-like bulk Si [19, 68, 73] which also supports the interpretation of the described phase transition.

The results underline that the thermal coefficient of the Raman modes of epitaxial silicene on Ag(111) markedly differs from the one of bulk-like Si or bulk-like Si crystallites. A rather similar behaviour is found by comparing  $\chi$  of graphene (2D) and diamond (3D), where values of  $-0.016\,\mathrm{K^{-1}\,cm^{-1}}$  and  $-0.012\,\mathrm{K^{-1}\,cm^{-1}}$  are reported, respectively [70, 74]. Hence, in both cases one finds the same trend for the thermal coefficient if changing from their 3D forms (diamond/silicon) to their 2D forms (graphene/epitaxial silicene on Ag(111)).

## 7.4.5 Electron-Phonon Coupling

Crystals with an inherent metallicity usually show a significant interaction between the electrons and their lattice vibrations, which is mainly related to the high concentration of the free charge carriers within the lattice. Due to same reasons, such effect is expected for elemental 2D materials as well. Indeed, it was shown that graphene exhibits a significant electron-phonon coupling (EPC), by temperature dependent Raman spectroscopy [75]. It turned out that a defect-free graphene layer yields a rather broad G band. Such broadening is usually an indication for disorder, which reduces the phonon lifetime that is inversely proportional to the peak width (FWHM). If disorder can be neglected the phonon mode linewidth results from a temperature-independent part related to the electron-phonon interaction and a temperature-dependent contribution from the phonon-phonon interaction [75]. If the contribution from the electron-phonon interaction strongly dominates the FWHM is largely temperature-independent. Temperature-dependent Raman measurements could show that the width of the G mode of such a graphene layer remains invariably large, even at high temperatures. This suggests that the contribution from phononphonon interaction (phonon scattering) to the peak broadening is small in comparison to a contribution from the electron-phonon interaction (electron scattering).

In order to examine the EPC in epitaxial (3 × 3) silicene, the FWHM of the three characteristic Raman modes was measured at different sample temperatures between room temperature and 300 °C [18]. These results are illustrated in Fig. 7.11c and show a constant FWHM for the E and the  $A^1$  Raman modes of epitaxial silicene up to the phase transition temperature of 300 °C, with values of  $16 \, \text{cm}^{-1}$  and  $15 \, \text{cm}^{-1}$ , respectively. Only the  $A^2$  mode starts to broaden for temperatures exceeding  $250 \, ^{\circ}\text{C}$ ,

which might be related to the beginning formation of Si crystallites and creation of local disorder [40]. For temperatures below 250 °C A<sup>2</sup> has a constant FWHM of approximately  $20 \,\mathrm{cm}^{-1}$ . After the phase transition at  $\sim 300 \,^{\circ}\mathrm{C}$  and the appearance of Si nano-crystallites the L(T)O mode has a FWHM of around  $6 \,\mathrm{cm}^{-1}$  and broadens with increasing temperatures as expected for bulk-like Si, in consistency with data reported previously [68].

These results are similar to the afore mentioned results for graphene, but caused by a different origin of the metallicity. DFT calculations show that in a free-standing  $(3 \times 3)$  silicene layer (which is obtained in the calculations by removing the Ag and keeping the atomic arrangement within the silicene) that the bands become parabolic with a band-gap opening of a 0.3 eV [56]. This shows that the metallicity stems from charge transfer from the Ag substrate and the hybridized states at the silicene/Ag interface [56] (see also Sect. 8.2). The observed EPC should therefore depend on the silicene-substrate interaction, or in other words on the choice of the substrate material, and might be observed in future experiments.

#### 7.5 Other 2D Si Phases on Ag(111)

# 7.5.1 The Si- $(\sqrt{13} \times \sqrt{13})$ Phase

The  $(\sqrt{7} \times \sqrt{7})R \pm 19.1^{\circ}/(\sqrt{13} \times \sqrt{13})R \pm 13.9^{\circ}$  phase (in short  $(\sqrt{13} \times \sqrt{13})$ ) forms for substrate temperatures during Si deposition between 220 °C and approximately 250 °C. It always coexists with the  $(3 \times 3)/(4 \times 4)$  and the " $(2\sqrt{3} \times 2\sqrt{3})$ " R30°" superstructure and forms usually relatively small domains in the range of a few nanometres (see Fig. 7.3c). For this reason the number of different experimental results concerning this structure is limited, as most experimental techniques do not allow to probe domains of such small size. In this "multi-phase" regime, the observed spectroscopic data result from superimposed data of the single domains. Local probes such as STM show that the  $(\sqrt{7} \times \sqrt{7})R \pm 19.1^{\circ}/(\sqrt{13} \times \sqrt{13})R \pm 13.9^{\circ}$ subsidiary phase can be found in four different domains [24]. These domains are explained by four different rotation angles relative to the Ag[110] direction of an initial honeycomb lattice similar to the  $(3 \times 3)$  phase but slightly expanded. In STM imaging these phases have a very different appearance with respect to each other and the  $(3 \times 3)$ . This is reasonable, because the  $(3 \times 3)$  structure results from the displacement of Si atoms depending on the underlying position of the substrate's Ag atoms. By changing the rotation angles such displacements will also change, causing a different atomic arrangement in the top layer. It can be expected, that the physical properties of the  $(\sqrt{13} \times \sqrt{13})$  phase do not differ significantly from the ones of  $(3 \times 3)$  epitaxial silicene. This expectation is supported by recent in situ Raman and TERS measurements [30, 31].

# 7.5.2 The Si " $(2\sqrt{3} \times 2\sqrt{3})$ " Phase on Ag(111)

The " $(2\sqrt{3} \times 2\sqrt{3})$ " phase starts to form for temperatures between 220 and 250 °C and becomes the only phase observed for temperatures above 250 °C. In contrast to the before mentioned 2D Si layers the " $(2\sqrt{3} \times 2\sqrt{3})$ " phase shows a fundamental difference. Whereas the  $(3 \times 3)$  and the  $(\sqrt{13} \times \sqrt{13})$  show only statistically distributed defects or defects at domain boundaries, disorder is an intrinsic property of the " $(2\sqrt{3} \times 2\sqrt{3})$ " structure. Figure 7.12a shows a large scale STM image of this structure formed at a deposition temperature of approximately 270 °C. It is seen that the " $(2\sqrt{3} \times 2\sqrt{3})$ " phase shows a characteristic Moiré-like surface pattern superimposing a more detailed atomic structure. This Moiré-pattern has a periodicity length of about 3.3 nm, but also values of 3.7 nm have been reported [76]. These layers are covering the entire surface terraces of the Ag substrate and give the impression of good crystalline order. The LEED pattern of this surface (Fig. 7.13a) shows resemblance with a  $(2\sqrt{3} \times 2\sqrt{3})R30^{\circ}$  symmetry with respect to the Ag(111)(1 × 1) surface, with some additional spot doublets. Figure 7.13b shows the simulated diffraction pattern of an ideal  $(2\sqrt{3} \times 2\sqrt{3})R30^{\circ}$  symmetry where the arrows indicate exemplarily the same two spots observed experimentally. The notation of this structure is based on these LEED observations.

When zooming into this structure by high-resolution STM one finds an atomic arrangement which does not show a very good order [22, 39, 59, 77]. In Fig. 7.12b such an STM image is shown for a  $6 \times 6$  nm area. Within the image some areas show nicely ordered hexagonal honeycombs (marked by the arrows), but between these areas the structure is disordered. This appearance is independent from the local area on the surface and is intrinsic for the " $(2\sqrt{3} \times 2\sqrt{3})$ " phase. Because of the

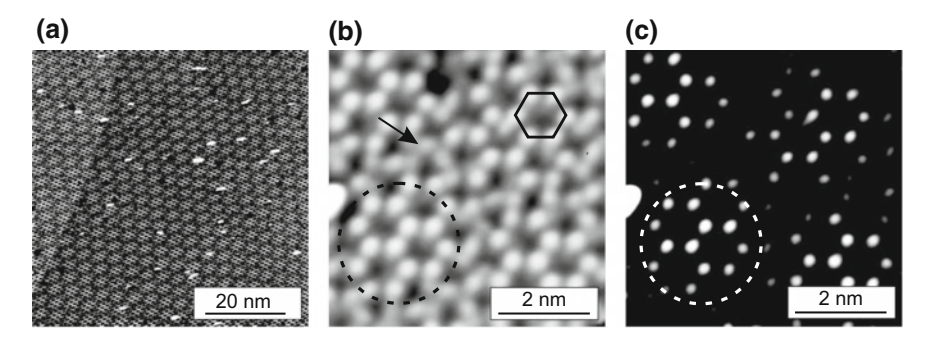
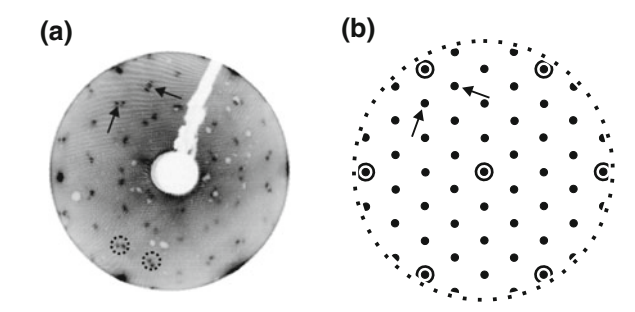


**Fig. 7.12** STM images of the Si " $(2\sqrt{3}\times2\sqrt{3})$ " phase after deposition of about 1 ML of Si on Ag(111) at approximately 270 °C. In **a** a large-scale STM image shows the characteristic This Moiré-like pattern of this phase, superimposing a more complex atomic structure. In **b** a high-resolution STM image is depicted which showing ordered (black dashed circle) and disordered areas (arrow) of the " $(2\sqrt{3}\times2\sqrt{3})$ " phase. The ordered areas comprise hexagonal honeycomb rings (white hexagon). **c** Shows the same image as in (**b**) with an artificially enhanced contrast, showing only the brighter ordered areas

Fig. 7.13 a LEED diffraction pattern of the same Si " $(2\sqrt{3} \times 2\sqrt{3})$ " structure as shown in Fig. 7.12. **b** Shows the simulated diffraction pattern of an ideal  $(2\sqrt{3} \times 2\sqrt{3})R30^\circ$  symmetry. The arrows indicate same spots in both images



disordered areas it not reasonable to assign any silicene superstructure symmetry to this structure, and it is denoted with quotation marks, as " $(2\sqrt{3} \times \sqrt{3})$ ", in accordance with the LEED pattern. The clear periodicity in LEED despite the obvious disorder of this phase, is observed because only ordered structures contribute to the diffraction pattern while disordered parts may only enhance the background signal.

In Fig. 7.12c the same image as in (b) is shown, with an artificial enhancement of the contrast. It is found that now only the ordered areas are seen, which show the same distance between them as the periodicity of the Moiré-pattern. This pattern originates from the ordered areas surrounded by less-ordered or disordered areas, where only the ordered part appear brighter in filled states STM images, and hence mimic a Moiré pattern. It has been suggested that strain relaxation of the undisturbed 2D honeycomb arrangement could cause the formation of the disordered areas [76]. Even though some structural patterns have been identified that are frequently found in disordered areas the intrinsic disorder does not allow to identify a general structure model of this phase since the translational symmetry is broken by the disorder. The ordered areas an atomic model can be constructed when viewed independently, as described in [76]. Angle-resolved photoemission spectroscopy measurements of this superstructure from Wang et al. [78] showed that its electronic band structure is mostly comprised of bands pointing to an  $sp^3$  hybridisation of its Si atoms. This agrees well with the intrinsic disorder, where Si atoms are likely  $sp^3$  hybridized, possible as a result of the relaxation.

When the substrate temperature further increases closer to 300 °C the disorder also increases [39], indicating the beginning of the distortion of epitaxial silicene, which leads to its destruction at 300 °C, caused by a dewetting process [40]. Claims that the " $(2\sqrt{3} \times 2\sqrt{3})$ " superstructure is stabilized by Ag atoms, either localised on the top or within the 2D layer [32, 33], have not been supported experimentally.

Hence, the " $(2\sqrt{3} \times 2\sqrt{3})$ " phase can be seen as a distorted epitaxial silicene layer with intrinsic disorder, also supported by recent Raman measurements [30].

## 7.6 Stability of Silicene Layers on Ag(111)

An important question for the applicability of silicene layers, for example in electronic devices, is the stability under ambient conditions or with varying temperatures.

It was already shown in Sect. 7.4.4 that annealing of an initial  $(3 \times 3)$  silicene layer on Ag(111) leads to a phase transition into bulk-like  $sp^3$  hybridized Si crystallites at around 300 °C. An AFM image of such a surface is shown in the inset Fig. 7.14b where the Si crystallites are nicely seen. The same is found if Si is deposited onto Ag(111) at substrate temperatures exceeding 300 °C. In such a case only the characteristic  $(1 \times 1)$  pattern of the Ag  $1 \times 1$  substrate surface occurs in LEED. The Raman spectra after deposition of 1 ML of Si at 290 and 350 °C (shown in Fig. 7.14a), are dominated by an narrow L(T)O diamond-like silicon band at 520 cm<sup>-1</sup> with a FWHM of 8 cm<sup>-1</sup>.

In addition, a second-order TO phonon mode at around  $900\,\mathrm{cm^{-1}}$  (not shown) shows up and further supports the bulk-like nature of the structures formed now [18]. The intensity of the L(T)O phonon mode gets higher for deposition at  $350\,\mathrm{^{\circ}C}$ , demonstrating that the sizes of the crystallites enlarge with increasing deposition temperatures.

This interpretation is further supported results by Auger electron spectroscopy measurements [39] and low-energy electron microscopy observations [40], showing the beginning of a de-wetting process of the Si layer from the Ag(111) surface around 300 °C. Thus a temperature of  $\sim 300$  °C is the high temperature limit for formation and thermal stability of 2D Si structures on Ag(111). A temperature of  $\sim 150$  °C is its low temperature limit for the formation of silicene. For lower temperatures only amorphous Si forms on the silver template. However, once a (3 × 3) epitaxial silicene

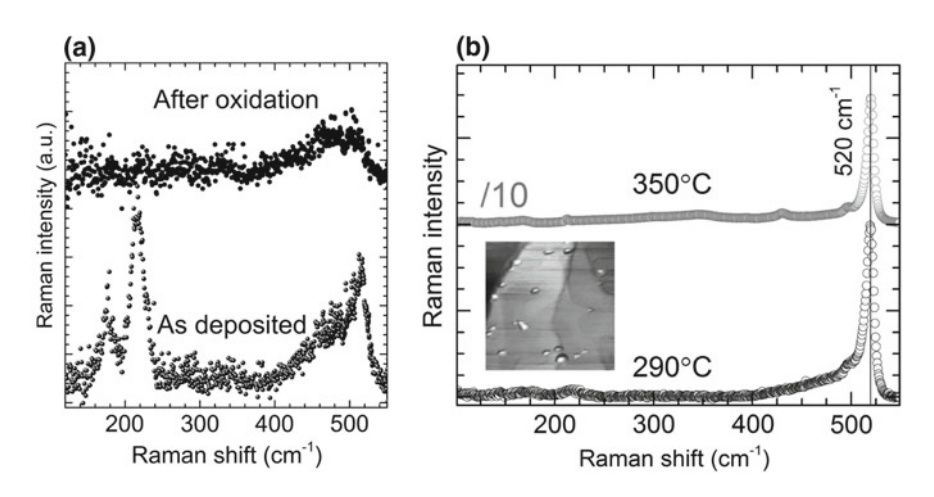


**Fig. 7.14** a Raman spectra of epitaxial  $(3 \times 3)$  before (bottom) and after (top) oxidation. **b** Overview Raman spectra after deposition of 1 ML of Si at 290 °C (bottom) and 350 °C on Ag(111). The inset shows an AFM images of an initial  $(3 \times 3)$  epitaxial silicene layer after annealing to 500 °C (adopted from [18])

layer has formed it is stable at low temperature and at least up to its preparation temperature around 220 °C.

In order to test its stability in ambient conditions the Raman signature can be utilized to detect structural changes. Figure 7.14 shows Raman spectra before and after exposure to air of an initial  $(3 \times 3)$  epitaxial silicene layer. The plot shows that the E and the two A Raman modes, characteristic for the pristine layer, fully disappear for the oxidized layer. Only the broad band of amorphous Si (discussed in Sect. 7.3.1) is still present in the spectrum. The LEED pattern of the same layer does not show any more the additional spots of the  $(3 \times 3)$  super structure. The vanishing of the Raman modes and the diffraction spots unambiguously demonstrates that the epitaxial silicene layer is destroyed in air by forming SiO<sub>2</sub>. Hence, epitaxial silicene is not stable in air or only for a very short time in the range of minutes. However, this can be sufficiently long to demonstrate its potential for electronic devices, such as a field effect transistor (see also Chap. 12).

For the transfer of epitaxial silicene layers through air they need to be chemically passivated by a protective capping layer. Such capping methods are well established and have be used long time for protecting semiconductor surface. In Chap. 12 it will be discussed that an amorphous aluminium layer can protect the silicene from oxidation.

## 7.7 Summary and Outlook

We have seen that a real two-dimensional Si layer can be synthesized on a Ag(111) substrate by Si deposition at substrate temperature between approximately 200 and  $300\,^{\circ}$ C. These layers, in particular the  $(3\times3)$  superstructure can be explain as an epitaxial silicene layer, despite the deviation of some of its properties from the purely theoretical free-standing silicene, a structure that might not exist. The influence of the substrate material cannot be neglected and influences the structural electronic and vibrational properties. Still, epitaxial silicene clearly shows 2D properties in its phonon and electronic dispersions. It is metallic and many of its properties and modifications by adsorption of inorganic and organic adsorbates have not been investigated yet. Hence, it offers an interesting 2D platform that helps to evolve the applicability of 2D materials.

The synthesis of epitaxial silicene has also initiated the search for other elemental 2D materials, and the synthesis of germanene [79] (2015) and stanene [80, 81] (2016) have been reported in the meantime (germanene is also discussed in Chap. 13). These materials show a significant spin-orbit interaction that enables fully new applications, involving, QSH or topological non-trivial properties. The search for such materials has just started, opening a new research area in the field of solid state physics.

**Acknowledgements** This work was financially supported by the Deutsche Forschungsgemeinschaft (DFG) under Heisenberg Grant No. VO1261/4-1.

#### References

- 1. K. Takeda, K. Shiraishi, Phys. Rev. B **50**, 14916 (1994)
- 2. G.G. Guzmán-Verri, L.C. Lew Yan Voon, Phys. Rev. B 76, 075131 (2007)
- 3. A. Kara et al., J. Supercond. Nov. Magn. 22, 259 (2009)
- 4. H. Sahaf et al., Appl. Phys. Lett. 90, 263110 (2007)
- 5. P. De Padova et al., Appl. Phys. Lett. **96**, 261905 (2010)
- 6. P. De Padova et al., Nano Lett. 8, 271 (2008)
- P. De Padova, C. Quaresima, B. Olivieri, P. Perfetti, G. Le Lay, Appl. Phys. Lett. 98, 081909 (2011)
- 8. J.I. Cerdá et al., Nat. Commun. 7, 13076 (2016)
- 9. P. Vogt et al., Phys. Rev. Lett. 108, 155501 (2012)
- 10. C.-L. Lin et al., Appl. Phys. Express 5, 045802 (2012)
- 11. B. Feng et al., Nano Lett. 12, 3507 (2012)
- 12. A. Fleurence et al., Phys. Rev. Lett. 108, 245501 (2012)
- 13. L. Meng et al., Nano Lett. 13, 685 (2013)
- 14. S. Cahangirov, M. Topsakal, E. Aktürk, H. Şahin, S. Ciraci, Phys. Rev. Lett. 102, 236804 (2009)
- 15. T. Suzuki, Y. Yokomizo, Physica E 42, 2820 (2010)
- M. Kira, T. Iwamoto, Progress in the chemistry of stable disilenes, in Advances in Organometallic Chemistry, ed. by R. West, A.F. Hill, vol. 54. (Elsevier, Academic Press, 2006), pp. 73–148
- 17. M. Kira, Proc. Jpn. Acad. Ser. B 88, 167 (2012)
- 18. D. Solonenko, et al., 2D Mater. 4, 015008 (2017)
- 19. T.R. Hart, R.L. Aggarwal, B. Lax, Phys. Rev. B 1, 638 (1970)
- 20. U. Monteverde et al., Carbon 91, 266 (2015)
- 21. D. Chiappe, C. Grazianetti, G. Tallarida, M. Fanciulli, A. Molle, Adv. Mat. 24, 5088 (2012)
- 22. H. Jamgotchian, J. Phys. Condens. Mat. 24, 172001 (2012)
- 23. R. Arafune et al., Surf. Sci. 608, 297 (2013)
- 24. A. Resta, Sci. Rep. 3, 2399 (2013)
- 25. Y. Fukaya et al., Phys. Rev. B 88, 205413 (2013)
- 26. K. Kawahara et al., Surf. Sci. 623, 25 (2014)
- D. Tsoutsou, E. Xenogiannopoulou, E. Golias, P. Tsipas, A. Dimoulas, Appl. Phys. Lett. 103, 231604 (2013)
- 28. J. Avila, J. Phys. Condens. Mat. 25, 262001 (2013)
- 29. P.D. Padova, J. Phys. Condens. Mat. 25, 382202 (2013)
- D. Solonenko, O.D. Gordan, G. Le Lay, D.R.T. Zahn, P. Vogt. Beilstein J. Nanotechnol. 8, 1357 (2017)
- S. Sheng, J.B. Wu, X. Cong, W. Li, J. Gou, Q. Zhong, P. Cheng, P.H. Tan, L. Chen, K. Wu. Phys. Rev. Lett. 119, 196803 (2017)
- 32. G. Prévot, R. Bernard, H. Cruguel, Y. Borensztein, Appl. Phys. Lett. 105, 213106 (2014)
- 33. R. Bernard, Y. Borensztein, H. Cruguel, M. Lazzeri, G. Prévot, Phys. Rev. B 92 (2015)
- 34. Z. Iqbal, S. Veprek, J. Phys. C Solid State Phys. 15, 377 (1982)
- 35. T. Ishidate, K. Inoue, K. Tsuji, S. Minomura, Sol. Stat. Commun. 42, 197 (1982)
- 36. K. Wu, X.Q. Yan, M.W. Chen, Appl. Phys. Lett. 91, 101903 (2007)
- 37. M. Satta, S. Colonna, R. Flammini, A. Cricenti, F. Ronci, Phys. Rev. Lett. 115, 026102 (2015)
- 38. S.H. Chou et al., J. Chem. Phys. **89**, 5177 (1988)
- 39. Z.-L. Liu, New J. Phys. 16, 075006 (2014)
- 40. A. Acun, B. Poelsema, H.J.W. Zandvliet, R.V. Gastel, Appl. Phys. Lett. 103 263119 (2013)
- 41. P. Vogt et al., Appl. Phys. Lett. 104, 021602 (2014)
- 42. J. Tersoff, D.R. Hamann, Phys. Rev. Lett. 50, 1998 (1983)
- 43. J. Tersoff, D.R. Hamann, Phys. Rev. B 31, 805 (1985)
- 44. M.K.R. Hoffmann, J. Sol. Stat. Chem. 54, 313 (1984)
- 45. D. Kaltsas, L. Tsetseris, A. Dimoulas, J. Phys. Condens. Mat. 24, 442001 (2012)
- 46. J. Gao, J. Zhao, Sci. Rep. 2, 861 (2012)

- 47. P. Pflugradt, L. Matthes, F. Bechstedt, Phys. Rev. B 89, 035403 (2014)
- 48. Z.-X. Guo, S. Furuya, J.-i. Iwata, A. Oshiyama, Phys. Rev. B 87 (2013)
- 49. K.R. Knox et al., Phys. Rev. B 78, 201408 (2008)
- 50. N.W. Johnson, Adv. Funct. Mater. 24, 5253 (2014)
- 51. S.Y. Zhou, Nat. Mater. 7, 259 (2008)
- 52. C.-L. Lin et al., Phys. Rev. Lett. 110, 076801 (2013)
- 53. S. Huang, W. Kang, L. Yang, Appl. Phys. Lett. 102, 133106 (2013)
- 54. Y.-P. Wang, H.-P. Cheng, Phys. Rev. B 87, 245430 (2013)
- 55. P. Gori, O. Pulci, F. Ronci, S. Colonna, F. Bechstedt, J. Appl. Phys. 114, 113710 (2013)
- 56. S. Cahangirov et al., Phys. Rev. B 88, 035432 (2013)
- 57. Y. Feng et al., PNAS 118, 14656–14661 (2016)
- 58. J. Zhuang et al., Phys. Rev. B **91**, 161409(R) (2015)
- 59. E. Cinquanta et al., J. Phys. Chem. C 117, 16719 (2013)
- 60. C. Lee et al., ACS Nano 4, 2695 (2010)
- 61. P. Tonndorf et al., Optics Express 21, 4908 (2013)
- 62. H.B. Ribeiro et al., Nat. Commun. 7, 12191 (2016)
- 63. A. Allard, L. Wirtz, Nano Lett. 10, 4335 (2010)
- J.-A. Yan, R. Stein, D.M. Schaefer, X.-Q. Wang, M.Y. Chou, Phys. Rev. B 88, 121403(R) (2013)
- 65. P. Gori, O. Pulci, R.d.L. Vollaro, C. Guattari, Energy Procedia 45 512 (2014)
- 66. X. Li et al., Phys. Rev. B 87, 115418 (2013)
- 67. H. Richter, Z.P. Wang, L. Ley, Sol. Stat. Commun. 39, 625 (1981)
- 68. J. Menéndez, M. Cardona, Phys. Rev. B 29, 2051 (1984)
- J. Ribeiro-Soares, R.M. Almeida, L.G. Cançado, M.S. Dresselhaus, A. Jorio, Phys. Rev. B 91, 205421 (2015)
- 70. I. Calizo, A.A. Balandin, W. Bao, F. Miao, C.N. Lau, Nano Lett. 7, 2645 (2007)
- S. Sahoo, A.P.S. Gaur, M. Ahmadi, M.J.-F. Guinel, R.S. Katiyar, J. Phys. Chem. C 117, 9042 (2013)
- 72. I.H. Campbell, P.M. Fauchet, Sol. Stat. Commun. **58**, 739 (1986)
- S. Périchon, V. Lysenko, B. Remaki, D. Barbier, B. Champagnon, J. Appl. Phys. 86, 4700 (1999)
- 74. E.S. Zouboulis, M. Grimsditch, Phys. Rev. B 43, 12490 (1991)
- 75. A.C. Ferrari, Sol. Stat. Commun. **143**, 47 (2007)
- 76. H. Jamgotchian, J. Phys. Condens. Mat. 27, 395002 (2015)
- 77. H. Jamgotchian, J. Phys. Conf. Ser. **491**, 012001 (2014)
- 78. W. Wang, W. Olovsson, R.I.G. Uhrberg, Phys. Rev. B 92, 205427 (2015)
- 79. M.E. Dávila, L. Xian, S. Cahangirov, A. Rubio, G.L. Lay, New J. Phys. 16, 095002 (2014)
- 80. F.-F. Zhu et al., Nat. Mat. 14, 1020 (2015)
- 81. S. Saxena, R.P. Chaudhary, S. Shukla, Sci. Rep. 6, 31073 (2016)

# Chapter 8 Atomic and Electronic Structure of Silicene on Ag: A Theoretical Perspective



Seymur Cahangirov and Angel Rubio

The isolation of graphene sheets from its parent crystal graphites has given the kick to experimental research on its prototypical 2D elemental cousin, silicene [1]. Unlike graphene, silicene lacks a layered parent material from which it could be derived by exfoliation. Hence, the efforts of making the silicene dream a reality were focused on epitaxial growth of silicene on substrates. The first synthesis of epitaxial silicene on silver (111) [27, 46] and zirconium diboride templates [16] and next on an iridium (111) surface [31], has boosted research on other elemental group IV graphene-like materials, namely, germanene and stanene [30, 48]. The boom is motivated by several new possibilities envisaged for future electronics, typically because of the anticipated very high mobilities for silicene and germanene [49], as well as potential optical applications [30]. It is also fuelled by their predicted robust 2D topological insulator characters [14, 28] and potential high temperature superconductor character [5, 50]. One of the most promising candidates as a substrate is Ag because from the studies of the reverse system, where Ag atoms were deposited on silicon substrate, it was known that Ag and silicon make sharp interfaces without making silicide compounds

S. Cahangirov (\simeg)

UNAM - National Nanotechnology Research Center, Bilkent University,

06800 Ankara, Turkey

URL: http://unam.bilkent.edu.tr/seymur

#### A. Rubio

Max Planck Institute for the Structure and Dynamics of Matter and Center for Free-Electron Laser Science, Luruper Chaussee 149, 22761 Hamburg, Germany

URL: http://www.mpsd.mpg.de/en/research/theo

#### A. Rubio

Nano-Bio Spectroscopy Group and ETSF, Dpto. Fisica de Materiales, Universidad del País Vasco, CFM CSIC-UPV/EHU-MPC and DIPC, 20018 San Sebastián, Spain

URL: http://nano-bio.ehu.es/

© Springer Nature Switzerland AG 2018 P. Vogt and G. Le Lay (eds.), *Silicene*, NanoScience and Technology, https://doi.org/10.1007/978-3-319-99964-7\_8 [24]. Indeed, studies on synthesiz and characterization of silicene is mainly focused on using Ag(111) as substrates and hence we think it is important to understand this particular system. In this Chapter, we present a theoretical perspective on the studies investigating the atomic and electronic structure of silicene on Ag substrates.

#### 8.1 The $3 \times 3$ Reconstruction

Silicene was synthesized for the first time on Ag(111) substrates [46]. Their STM measurements revealed the "flower pattern" originating from protruding atoms of  $3 \times 3$  reconstructed silicene matching the  $4 \times 4$  supercell of the Ag(111) surface as shown in Fig. 8.1. This structure was also confirmed by DFT calculations where the geometry optimization starting from unreconstructed  $3 \times 3$  supercell of silicene on top of  $4 \times 4$  supercell of Ag(111) slabs resulted in the reconstructed silicene that reproduced the STM image observed in experiments. Note that, while bond lengths vary from 2.34 to 2.39 Å, the angle between the bonds spans a wide range starting from 108°, which is less than the ideal  $sp^3$  bond angle, up to 120°, which is the ideal bond angle of  $sp^2$  hybridization. Each of the three protrusions seen in STM image make a group of Si atoms that belong to the same silicene sublattice. However, there are two such groups in every  $3 \times 3$  unitcell that belong to the different sublattices of silicene. This becomes evident when H is deposited on  $3 \times 3$  silicene which results in a highly asymmetric STM image due to the fact that H atoms prefer to bind only to one of the two sublattices. The atomic structure of  $3 \times 3$  phase of silicene was also confirmed by reflection high energy positron diffraction (RHEPD) as well as low energy electron diffraction (LEED) experiments [17, 23].

The archetype single layer silicene, which is the  $3 \times 3$  phase having a unique orientation, results from a delicate balance between the impinging Si flux (yielding, typically, completion in about 30 minutes), the surface diffusion of the deposited Si atoms on the bare and silicene covered areas and the competing in-diffusion toward the sub-surface. The growth is driven by these kinetic processes, which, actually, gives a very narrow substrate temperature window of about 200–220 °C [27, 46]. Here silicene forms a highly ordered structure, which can cover 95% of the crystal surface [17], because of the exact correspondence between 3 silicene basis vectors and 4 nearest neighbor Ag–Ag distances. The "flower pattern" observed both in STM and non-contact AFM imaging results from the puckered Si atoms sitting nearly on top of Ag atoms, giving a total corrugation of  $\sim$ 0.07 nm in the silicene sheet [36, 46].

Already from ~250 °C a new 2D phase of silicene develops, co-existing with domains of the  $3 \times 3/4 \times 4$  phase. Since control of the substrate temperature is not easy in this temperature regime where most pyrometers are inoperative and where thermocouples, depending on their locations, generally give improper values, in many cases, mixed  $3 \times 3/4 \times 4$  and  $\sqrt{7} \times \sqrt{7}/\sqrt{13} \times \sqrt{13}$  domains are simultaneously observed [27]. In the latter case, four rotated domains, imposed by symmetry are present, since the  $\sqrt{7} \times \sqrt{7}$  silicene domains are rotated by  $\pm 19.1^{\circ}$  with respect

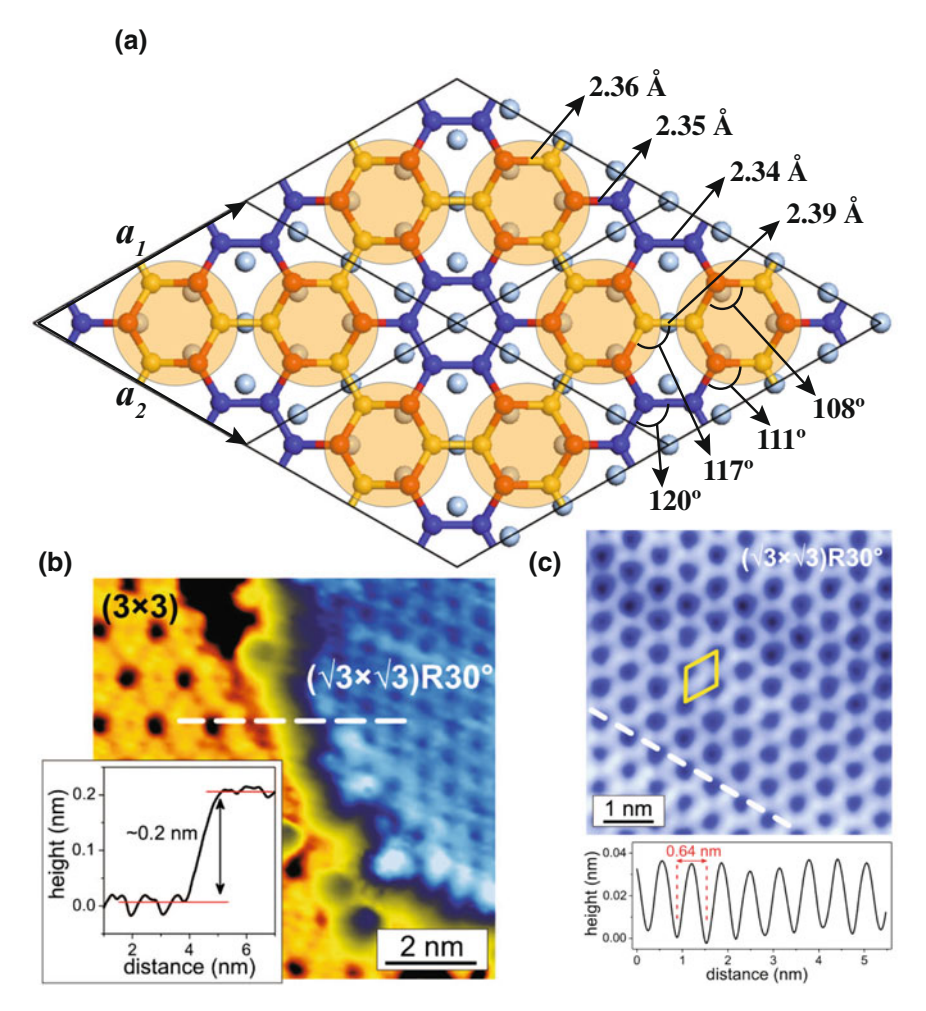


Fig. 8.1 a Top view of  $3 \times 3$  silicene matched with a  $4 \times 4$  Ag(111) surface supercell. Only the topmost atomic layer of Ag(111) is shown and represented by light blue balls. Red, yellow and blue balls represent Si atoms that are positioned near the top, hollow and the bridge sites of the Ag(111) surface. Red Si atoms that are positioned on top of Ag atoms protrude up. Yellow Si atoms are mainly interacting with the Ag atoms that sit under the bonds connecting them. When the STM resolution is not high enough, the three protruding red Si atoms are seen as a single dot represented by transparent orange circles drawn around them. These circles form large hexagons that have  $3 \times 3$  periodicity. b STM image and line profile scanning from  $3 \times 3$  to  $\sqrt{3} \times \sqrt{3}$  silicene on Ag(111). c STM image and line profile of  $\sqrt{3} \times \sqrt{3}$  silicene on Ag(111). Adapted from [45]

to each of the two  $\sqrt{13} \times \sqrt{13}$  Ag super cells, which are themselves rotated by  $\pm 13.9^\circ$  with respect to the main [-110] and alike directions of the Ag(111) surface. These domains are buckled, differently from the  $3 \times 3/4 \times 4$  case and are accordingly slightly expanded, while remaining commensurate, to accommodate a 4% reduction

in Si coverage ratio (from  $\theta_{Si} = 1.125$  for the  $3 \times 3/4 \times 4$  phase to  $\theta_{Si} = 1.077$  for this new one), signaling a self-healing process of the silicene mesh, while some of its atoms have disappeared below the surface. These four domains have been imaged simultaneously on the same STM topograph [36]. Details of these structures are discussed in Chap. 7.

#### 8.2 The Nature of the Linear Bands

There is no doubt that the linear bands are one of the most intriguing features of silicene (see Chap. 2). Indeed, angle resolved photoemission spectroscopy (ARPES) measurements of the  $3\times3$  silicene phase revealed a linear band starting 0.3 eV below the Fermi level and extending all the way down to -3 eV with a slope of  $\sim 1.3\times10^6$  m/s [46]. This linear band was not detected when silicene was absent. However the extension and slope of the linear band was too high to be attributed solely to silicene. On the other hand, scanning tunneling spectroscopy (STS) measurement performed under high magnetic field applied in perpendicular direction to the  $3\times3$  silicene on Ag substrate have shown that the peaks corresponding to the Landau levels corresponding to the presence of the Dirac fermions were absent while they were present in the highly oriented pyrolitic graphite samples [26]. This experimental result was supported by DFT calculations to conclude that Dirac fermions of ideal silicene were destroyed due to the symmetry breaking and hybridization with the Ag substrate. These results created a debate on the origin of the linear bands of silicene on silver.

The  $3 \times 3$  reconstruction of silicene forms due to the interaction with the Ag substrate and breakes the symmetry needed to preserve the linearly crossing bands at the Fermi level. This is clearly seen in the band structure of the  $3 \times 3$  reconstructed silicene isolated from the substrate presented in Fig. 8.2a. Here the band structure of the  $3 \times 3$  reconstructed silicene is unfolded into the Brillouin zone of the ideal  $1 \times 1$ silicene. Upon reconstruction, the linearly crossing bands are destroyed and instead there is a 0.3 eV gap at the K point. To interpret the ARPES experiments mentioned above, Cahangirov et al. calculated the electronic structure of  $3 \times 3$  silicene placed on top of 11 layers of  $4 \times 4$  Ag substrate [2]. Figure 8.2c shows the detailed band structure of the silicene/Ag system in the window where the experiments were performed (see Fig. 8.2b). The blue curve corresponds to the bulk Ag sp-band that should not be detected by ARPES which is sensitive to the surface states. Figure 8.2d and e show the states that have significant contribution from surface Ag states when silicene is absent and present, respectively. Here one can choose the threshold in such a way that the linear band disappears when silicene is absent and appears when it is present thereby mimicking the situation observed in ARPES experiments. This analysis suggests that the linear bands are caused by hybridization between silicene and Ag. The perpendicular momentum dependence of the electronic states was calculated by a k-projection technique and was used to calculate the contribution of silicene and Ag to the surface band created by hybridization [8]. This study provided further quan-

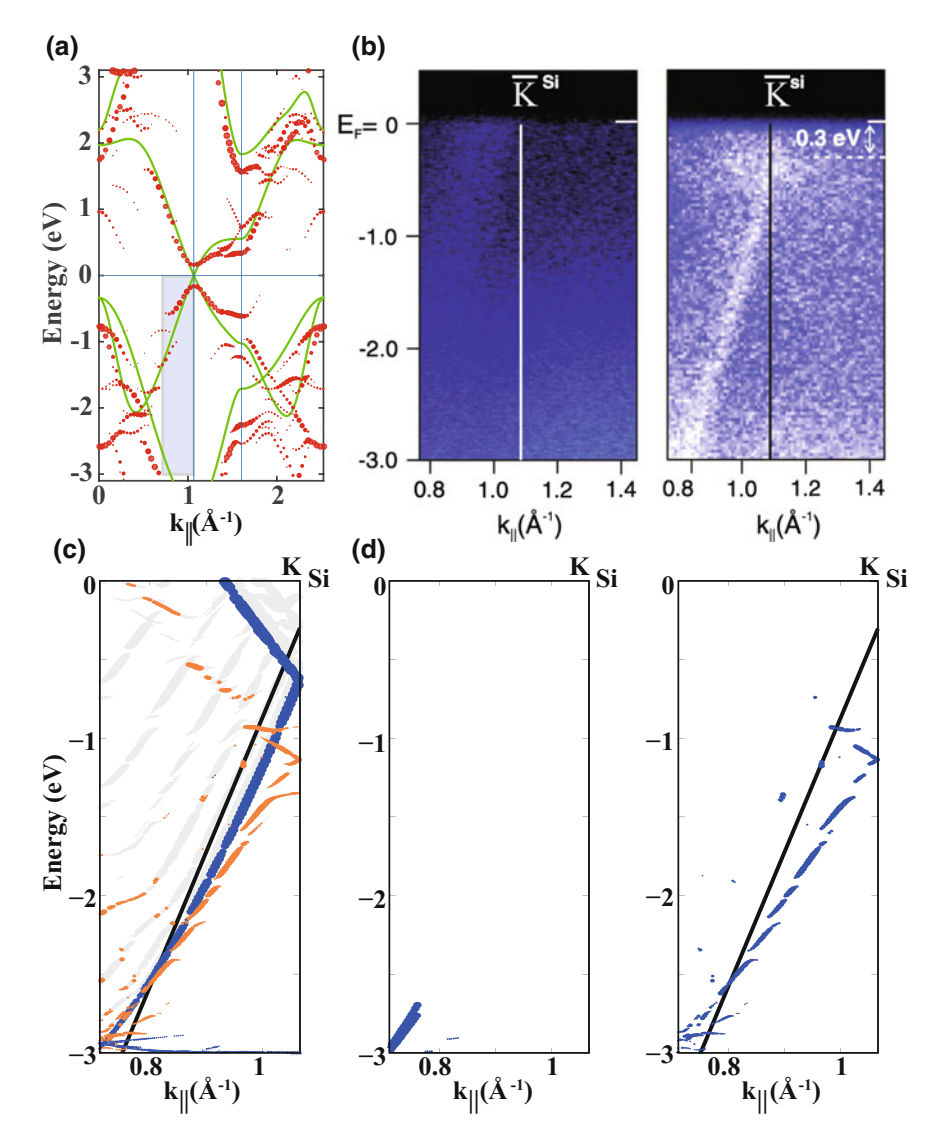


Fig. 8.2 a Band structure of reconstructed  $3 \times 3$  silicene (red dots) in the absence of Ag substrate unfolded to  $1 \times 1$  Brillouin zone of silicene. The dots radii correspond to the weight of the unfolded state. The band structure of ideally buckled silicene is shown by green lines. **b** ARPES data around the K point of  $1 \times 1$  silicene in the absence (left panel) and presence (right panel) of silicene on Ag(111) substrate (adapted from [46]). **c** Band structure of  $3 \times 3$  silicene a  $4 \times 4$  Ag(111) 11 layer slab in the experimentally relevant range shown by the shaded region in (**a**). The states contributed by 3 Ag layers in the middle of the slab represent the bulk Ag states and are shown by blue lines. Orange lines are contributed by silicene and 3 Ag layers underneath. The black line represents the experimentally observed linear band. **d** States contributed by 3 Ag layers underneath silicene in the absence (left panel) and presence (right panel) of silicene. Adapted from [2]

titative agreement with experiments while confirming the hybridized nature of the experimentally observed linear bands. The surface band created by the hybridization between silicene and Ag was detected and distinguished from the faintly visible Ag sp-bands in the ARPES measurements [43]. There are many other investigations that have reached to conclusion that the linear bands are due to hybridization between silicene and Ag [18, 47].

The search for Dirac cones is not limited to the silicene on Ag substrates. ARPES measurements performed on calcium disilicide (CaSi<sub>2</sub>) revealed a massless Dirac cone located at 2 eV below the Fermi level [32]. CaSi<sub>2</sub> can be considered as buckled silicene sandwiched between the planar atomic planes of Ca. The energy shift in the electronic states of silicene is due to significant charge transfer between Si and Ca atoms. First-principles calculations of the CaSi<sub>2</sub> structure revealed that there is, in fact, also a momentum shift in the Dirac cone away from the highly symmetric K point [13]. This is due to the symmetry breaking between the sublattice atoms of silicene and consequent asymmetric interlayer hopping. The shift in the momentum space is also accompanied with a small energy gap opening between the linearly crossing bands.

The Ag substrate plays a crucial role in growth of silicene, as seen from the previous section. This wouldn't be possible if the interaction between silicene and Ag was too weak. A first-principles study of the electronic charge density between silicene and the Ag(111) substrate has concluded that bonds between Si and Ag atoms don't have covalent character [41]. However, hybridization with Ag seems to interfere with the delicate electronic structure of silicene, as mentioned above. To avoid this, one has to develop techniques to transfer silicene to less interacting and insulating substrates. Tao et al. have taken an important step in this direction [42]. They first grew silicene on Ag and encapsulated it with alumina. Then they flipped the system upside down and etched Ag on silicene, just leaving two Ag pads that they used as metal contacts. In this way they have demonstrated that silicene can operate as an ambipolar field-effect transistor at room temperature.

# 8.3 The $\sqrt{3} \times \sqrt{3}$ Reconstruction

Another phase of silicene that is frequently observed to grow on Ag(111) substrate has a  $\sqrt{3} \times \sqrt{3}$  reconstruction with respect to silicene unitcell. Unlike the other phases mentioned above, the  $\sqrt{3} \times \sqrt{3}$  reconstructed phase of silicene is not matched by any lattice vector of the Ag(111) substrate [7, 15, 45]. The  $\sqrt{3} \times \sqrt{3}$  reconstructed silicene was first reported by Feng et al. They measured the lattice constant to be 0.64 nm which is  $\sim 5\%$  less compared to ideal silicene while the STM image was composed of bright triangular spots arranged in a  $\sqrt{3} \times \sqrt{3}$  honeycomb lattice (see Fig. 8.1). They have also shown that the same STM image persists in the second layer which hinted that the  $\sqrt{3} \times \sqrt{3}$  structure was intrinsic and not formed due to the matching with Ag substrate. Later the  $\sqrt{3} \times \sqrt{3}$  reconstruction was also observed in multilayer silicene grown on Ag(111) substrates [45]. The distance between con-

secutive layers was measured to be around 3.0–3.1 Å. The STM images presented in Fig. 8.1 shows that the distance between neighboring  $3 \times 3$  and  $\sqrt{3} \times \sqrt{3}$  silicene is only 2 Å.

Several models were proposed to describe the origin and the atomic structure of the  $\sqrt{3} \times \sqrt{3}$  reconstruction. One of them proposes that if monolayer silicene is squeezed enough, then the  $\sqrt{3} \times \sqrt{3}$  honeycomb reconstruction becomes energetically more favorable than the ideal  $1 \times 1$  buckling [7]. However, this happens if the lattice constant is squeezed down to  $\sim$ 6.3 Å and also there is no physical reason for the system to remain in this high energy state. Another model is based on the well studied Si(111)-Ag $\sqrt{3} \times \sqrt{3}$  system [12, 39]. This model also produces a  $\sqrt{3} \times \sqrt{3}$ honeycomb pattern in STM measurements (see Fig. 8.6). In this case the bright spots are originating from Ag atoms on top of Si(111). However, it is not clear how the  $3 \times 3$ structure is transformed into  $\sqrt{3} \times \sqrt{3}$  structure with Ag atoms on top and also why the lattice is compressed. Yet another model suggests that the  $\sqrt{3} \times \sqrt{3}$  honeycomb STM image is a result of the atomic scale flip-flop motion at the surface of bilayer Si(111) structure formed on top of the  $3 \times 3$  structure [19]. Here the authors suggest that there are three possible configurations and the system is alternating between two of them. Since each state produces a trigonal STM pattern, the combination of two of them should produce the expected honeycomb pattern. However, there is no clear reason why the system should choose to alternate only between two states. Furthermore, this model does not explain the 5% lattice contraction observed in experiments [7, 15, 45].

The subsequent growth of  $\sqrt{3} \times \sqrt{3}$  reconstructed silicene after formation of  $3 \times 3$  silicene was studied by DFT calculations [4]. Here we summarize results of that study. As Si atoms are deposited on Ag(111) surface they search for the optimum structure that minimizes the energy. In the absence of the Ag substrate this optimum structure is the cubic diamond structure that has a cohesive energy of 4.598 eV/atom according to DFT calculations. However, in the presence of the Ag substrate a monolayer of silicene that has primarily  $3 \times 3$  reconstruction is formed. Here, the  $3 \times 3$  supercell of silicene is matched with the  $4 \times 4$  supercell of the Ag(111) surface, as shown in the Fig. 8.1a. If we remove the Ag substrate and freeze the Si atoms of the  $3 \times 3$  reconstructed silicene to calculate its cohesive energy, it turns out to be 3.850 eV/atom, which is 108 meV lower than the buckled freestanding silicene. In fact, if we start from the freestanding  $3 \times 3$  reconstructed silicene and relax the structure, it goes to the buckled structure, meaning that it is not even a local energy minimum in the absence of the Ag substrate. However, the cohesive energy of  $3 \times 3$  structure surpasses that of the cubic diamond structure when it is placed on the Ag(111) surface. This strong interaction between silicene and the Ag substrate explains the growth of monolayer silicene instead of clustering of Si atoms into bulk structures.

The model proposed by Cahangirov et al. to explain the growth of the  $\sqrt{3} \times \sqrt{3}$  structure is based on the so called dumbbell structures. This peculiar structure emerges when a Si adatom is adsorbed on already formed silicene. As seen in Fig. 8.3, the Si adatom first attaches to dangling bonds of silicene and then forms bridge bonds with two-second neighbor Si atoms of silicene thereby increasing the coordination

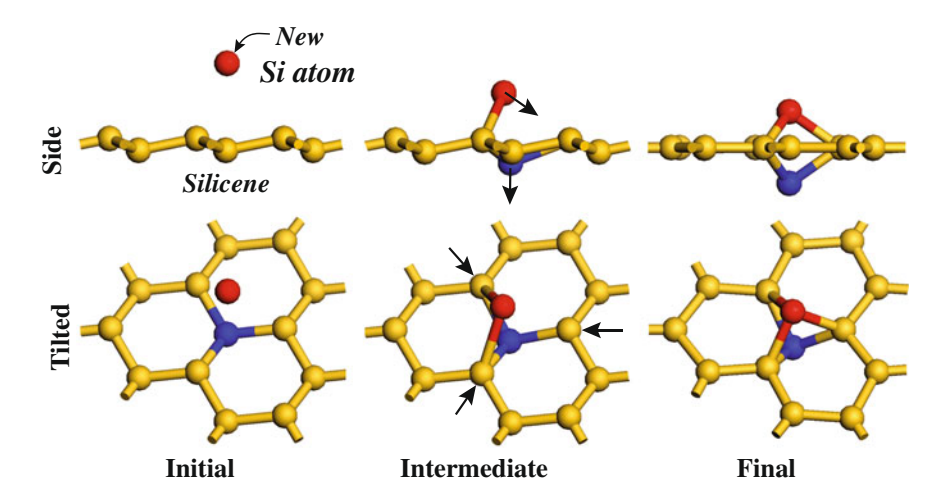
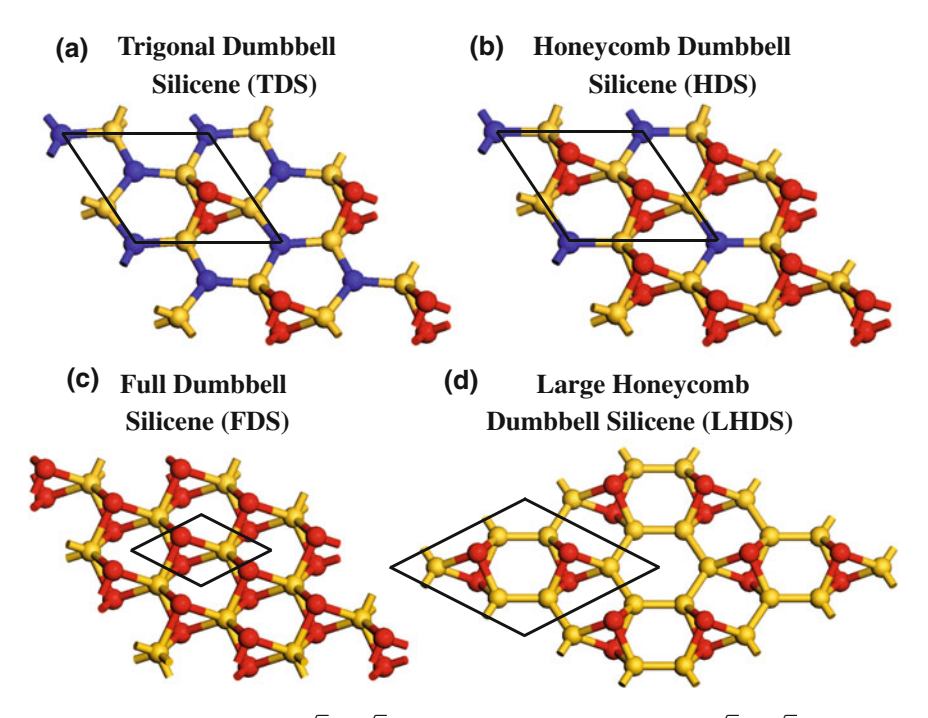


Fig. 8.3 Formation of the dumbbell building block units starting from freestanding silicene

number of these Si atoms from three to four. In search for tetrahedral orientation, these four bonds then force the atoms to move towards the directions shown in the middle panel of Fig. 8.3. As a result, the new Si adatom sits 1.38 Å above the top site of silicene while at the same time pushing down the Si atom just below it by the same amount. These two atoms are connected to other Si atoms by three bonds that are almost perpendicular to each other. The resulting geometry is called the dumbbell structure [4, 22, 34]. The dumbbell formation is an exothermic process and occurs spontaneously without need to overcome any kind of barrier. In the case of a C atom adsorbed on graphene, the dumbbell structure does not form because it is energetically less favorable compared to the configuration in which the C adatom is attached to the bridge site of graphene [35].

Calculations show that when a single dumbbell unit is placed in an  $n \times n$  unit cell the cohesive energy per Si atom is maximized when  $n = \sqrt{3}$  and decreases monotonically for  $n \ge 2$  [4]. We refer to the structure having a single dumbbell unit in the  $\sqrt{3} \times \sqrt{3}$  unit cell as trigonal dumbbell silicene (TDS) due to the trigonal lattice formed by dumbbell atoms, as shown in Fig. 8.4a [4, 22]. As seen in Table 8.1, TDS is energetically more favorable than freestanding silicene [22, 34]. Interestingly, the cohesive energy per Si atom is further increased when another dumbbell unit is created in the  $\sqrt{3} \times \sqrt{3}$  unit cell of TDS. We refer to this new structure as honeycomb dumbbell silicene (HDS) due to the honeycomb structure formed by two dumbbell units in the  $\sqrt{3} \times \sqrt{3}$  unit cell (see Fig. 8.4b).

The atomic structure of HDS is crucial to understand the  $\sqrt{3} \times \sqrt{3}$  reconstruction that emerges when silicene is epitaxially grown on Ag(111) substrates since it is in excellent agreement with contracted lattice constant and STM image measured in experiments [4, 7, 15, 45]. Adding another dumbbell unit in the  $\sqrt{3} \times \sqrt{3}$  unit cell of HDS results in a 1 × 1 structure composed of dumbbell atoms connected by sixfold



**Fig. 8.4** Atomic structure of  $\mathbf{a} \sqrt{3} \times \sqrt{3}$  trigonal dumbbell silicene (TDS),  $\mathbf{b} \sqrt{3} \times \sqrt{3}$  honeycomb dumbbell silicene (HDS),  $\mathbf{c} \ 1 \times 1$  full dumbbell silicene (FDS) and  $\mathbf{d} \ 2 \times 2$  large honeycomb dumbbell silicene (LHDS). The unit cells are delineated by solid black lines. Atoms having different environment are represented by balls having different colors

**Table 8.1** Cohesive energy and  $\sqrt{3} \times \sqrt{3}$  lattice constant of buckled silicene compared with that of dumbbell structures

***************************************						
	Silicene	TDS	LHDS	HDS	FDS	
Cohesive energy (eV/atom)	3.958	4.013	4.161	4.018	3.973	
$\frac{\sqrt{3} \times \sqrt{3}}{\text{lattice}}$ constant (Å)	6.69	6.52	6.43	6.38	6.23	

coordinated Si atoms (see Fig. 8.4c). The cohesive energy of this structure, that we refer to as full dumbbell silicene (FDS), is less than that of TDS and HDS.

We should emphasize that it is the interplay between two competing effects that makes HDS the most favorable  $\sqrt{3} \times \sqrt{3}$  structure. While formation of new dumbbells and thus new bonds increases the cohesive energy, the increase in the coordination number beyond four decreases it. As seen in Fig. 8.4, the coordination number of yellow atoms in the TDS structure is four while in HDS it is five. Apparently, the formation of a new dumbbell and hence new bonds compensates the energy required

80 7 11 11 11 11 11 11 11 11 11 11 11 11 1							
	3 × 3	TDS	LHDS	HDS			
Cohesive energy per atom (eV/atom)	4.877	4.663	4.483	4.471			
Cohesive energy per area (eV/Å <sup>2</sup> )	0.759	0.887	0.938	1.014			

**Table 8.2** Cohesive energies per Si atom and per unit area are given for the  $3 \times 3$  reconstructed silicene. TDS, LHDS, and HDS structures on the Ag(111) surface

to form the peculiar fivefold coordination. However, it fails to compensate the sixfold coordination of Si atoms forming the middle atomic layer of FDS. This arguments led us to investigate another dumbbell structure that has even larger cohesive energy per atom compared to HDS. This structure has two dumbbell units arranged in a honeycomb lattice in a  $2\times 2$  unit cell. Here the packing of dumbbell units is dense compared to TDS but sparse compared to HDS. In this structure, the honeycomb lattice formed by dumbbell units is larger compared to the one formed in HDS, hence we refer to this structure as large honeycomb dumbbell silicene (LHDS). As seen in Fig. 8.4d, the maximum coordination of Si atoms in the LHDS is four. Since there are more dumbbell units in LHDS compared to TDS and no hypervalent Si atoms as in HDS, the cohesive energy per atom of freestanding LHDS is higher than both TDS and HDS.

Unlike the  $3 \times 3$  silicene that matches the  $4 \times 4$  Ag(111) supercell, the dumbbell structures cannot be matched because their lattice constant is squeezed as the density of dumbbell units is increased as seen in Table 8.1. To include the effect of Ag, the  $4 \times$ 4 Ag(111) slab composed of five layers is first squeezed to match the lattice of the  $3 \times 10^{-2}$ 3 supercell of the dumbbell structures and then the system is optimized by keeping the Ag atoms fixed. Then the energy of the squeezed Ag substrate in the absence of Si atoms is calculated. The energy difference between these two systems gives the cohesive energies of the dumbbell structures. As seen in Table 8.2, the cohesive energy per Si atom is maximized in the  $3 \times 3$  silicene while the cohesive energy per area is maximized for the  $\sqrt{3} \times \sqrt{3}$  HDS structure. According to the model, when Si atoms are first deposited on Ag(111) substrate, they form the  $3 \times 3$  reconstructed silicene that has the highest cohesive energy per Si atom, as seen in Table 8.2. At first, the dumbbell units that spontaneously form on  $3 \times 3$  silicene diffuse and annihilate at the edges and contribute to the growth of even larger  $3 \times 3$  regions. Once  $3 \times 3$ silicene reaches sufficiently large area, the dumbbell units compete to form the most energetic structure in a given area covered by 3 × 3 silicene. To achieve the highest cohesive energy per area, the dumbbell units arrange themselves to form the  $\sqrt{3} \times \sqrt{3}$ HDS structure.

The schematic sketch of this growth model is presented in Fig. 8.5a. This picture is in accordance with experiments in which the  $\sqrt{3} \times \sqrt{3}$  structure usually appears as islands on top of the first  $3 \times 3$  silicene layer. As seen in Fig. 8.5b, d, the model also excellently reproduces the distance between  $\sqrt{3} \times \sqrt{3}$  and  $3 \times 3$  surfaces measured

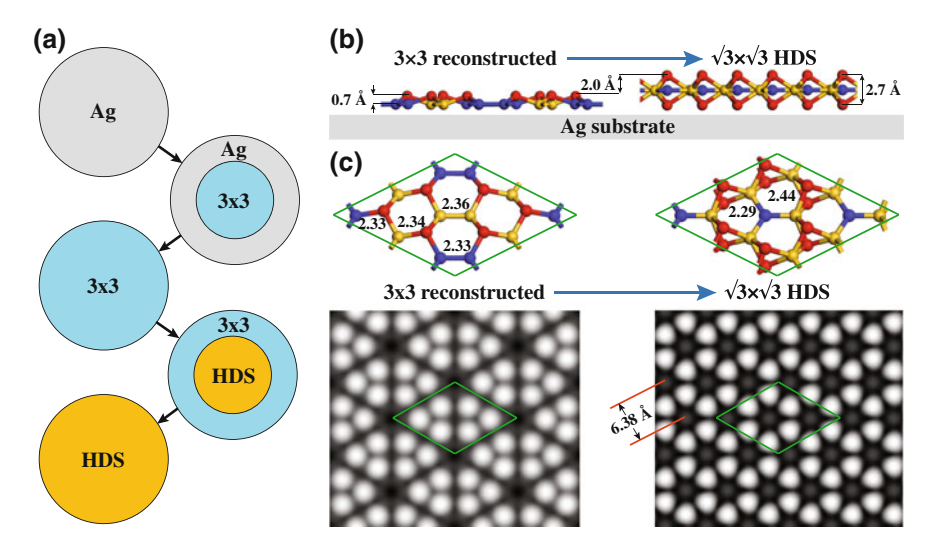


Fig. 8.5 a Growth sequence of the  $3 \times 3$  reconstructed silicene and of the HDS structure on the Ag(111) substrate. **b** Schematic depiction of the structural transformation from the  $3 \times 3$  to the  $\sqrt{3} \times \sqrt{3}$  reconstruction from the side view. **c** Tilted view of the atomic structures and calculated STM images. Green lozenges represent the  $3 \times 3$  supercell

to be  $\sim$ 2Å [45]. Furthermore, as shown in Fig. 8.5c, e, the simulated STM image of HDS has the same honeycomb pattern as the one obtained in experiments while the  $\sqrt{3} \times \sqrt{3}$  lattice constant of HDS that is calculated to be 6.38 Å, excellently matches the measured value that is  $\sim$ 6.4 Å [7, 15, 45]. Also, according to the model, the  $\sqrt{3} \times \sqrt{3}$  silicene forms by morphing the 3 × 3 and  $\sqrt{7} \times \sqrt{7}$  reconstructed monolayers and this is in agreement with two experimental observation. First, in experiments, the  $\sqrt{3} \times \sqrt{3}$  silicene appears after the 3 × 3 structure. Second, it was demonstrated that the  $\sqrt{3} \times \sqrt{3}$  structures can inherit the four domains originating from the matching of the  $\sqrt{7} \times \sqrt{7}$  silicene with  $\sqrt{13} \times \sqrt{13}$  Ag(111) supercell [37]. Finally, this model can also be extended to explain multilayers that have  $\sqrt{3} \times \sqrt{3}$  reconstruction as discussed below.

## 8.4 Multilayer Silicene

When Si deposition is prolonged beyond the formation of the first layer  $3 \times 3/4 \times 4$  or  $\sqrt{7} \times \sqrt{7}/\sqrt{13} \times \sqrt{13}$  phases and in the same conditions, growth of multi-layer silicene, which possesses a unique  $\sqrt{3} \times \sqrt{3}R(30^\circ)$  (in short  $\sqrt{3} \times \sqrt{3}$ ) structure is obtained. Such films grow in successive terraces, each showing this unique reconstruction. If growth occurs on the prototype  $3 \times 3/4 \times 4$  phase, one gets a single orientation of these terraces. Instead, if growth occurs on the initial  $\sqrt{7} \times \sqrt{7}/\sqrt{13} \times \sqrt{13}$  first layer silicene phase, rotated terraces are obtained; the rotation angles are directly

related to those of the first layer domains [37]. In angle-resolved photoemission (ARPES) measurements, these films possess a Dirac cone at the centre of the Brillouin zone due to back folding of the  $\sqrt{3} \times \sqrt{3}$  silicene superstructure with a Fermi velocity about half that of the free standing graphene [9, 11]. Vogt et al. have studied terraces with up to five layers of  $\sqrt{3} \times \sqrt{3}$  silicene. They have shown that the height difference between adjacent terraces is ~3.1 Å [45]. Using in situ a four probe scanning tunneling microscope, a sheet resistance analogous to that of thin films of graphite in nano-grains was determined. De Padova et al. took this even further and synthesized few tens monolayers of silicene with  $\sqrt{3} \times \sqrt{3}$  reconstruction. Remarkably, these multilayer silicene films survive after exposure in ambient air for a day at least, because just the very top layers are oxidized; the film underneath remains intact, as directly revealed via a graphite-like Raman signature [10]. Feng et al. have investigated bilayers of  $\sqrt{3} \times \sqrt{3}$  silicene [15]. They have measured the quasi-particle interference of electrons in the first layer due to the scattering from the islands formed by the second layer grown on top [7]. A linear dispersion with high Fermi velocity was derived from these interference patterns.

Although multilayer silicene was grown in many experiments mentioned above its atomic structure has been a subject of debate. The experiments report a 5% contracted  $\sqrt{3} \times \sqrt{3}$  structure that has a honeycomb appearance in STM imaging with a  $\sim 3.1$  Å distance between its layers. However, there is still no structural model that explains all these observations. Here we discuss the proposed models and point out their shortcomings.

The interlayer separation of multilayer silicene is very close but measurably different from that of Si(111). This inspired models of multilayer silicene that has bulk silicon-like interior with a modified surface structure. One such model is based on the Si(111)-Ag $\sqrt{3} \times \sqrt{3}$  system. The various surfaces obtained by the deposition of Ag on Si(111) substrate were studied intensively in the 1980s [12, 25, 29, 44]. One of the most favorable surfaces that were observed in experiments was the so called honeycomb-chain trimer (HCT) structure [44]. As seen in Fig. 8.6, the HCT model has a  $\sqrt{3} \times \sqrt{3}$  honeycomb STM pattern that resembles the one observed in multilayer silicene experiments. Furthermore, the interlayer separation is close to the one obtained in experiments since the bulk region is basically Si(111). The HCT structure makes transition to the so-called inequivalent triangle (IET) structure at low temperatures. This transition could explain the spontaneous symmetry breaking observed in  $\sqrt{3} \times \sqrt{3}$  silicene at low temperatures [6, 39]. Finally, it was argued that the slope of the linear portion of the S<sub>1</sub> band formed by the Si(111)-Ag $\sqrt{3} \times \sqrt{3}$  surface is comparable to that of the linear bands observed in  $\sqrt{3} \times \sqrt{3}$ silicene experiments [7, 38, 39]. However, the HCT model does not account for the contraction of the lattice constant observed in experiments. Another model inspired by the bulk silicon structure is the tristable Si(111) bilayer grown on Ag substrate [19]. Here the flip-flop motion that is suggested to give rise to the honeycomb STM topographs is not supported by convincing arguments. Also it does not explain the lattice contraction and can not be extended to multilayers.

Here we present a possible growth model of multilayer silicene that produces structures which are in a good agreement with experiments in certain respects [3].

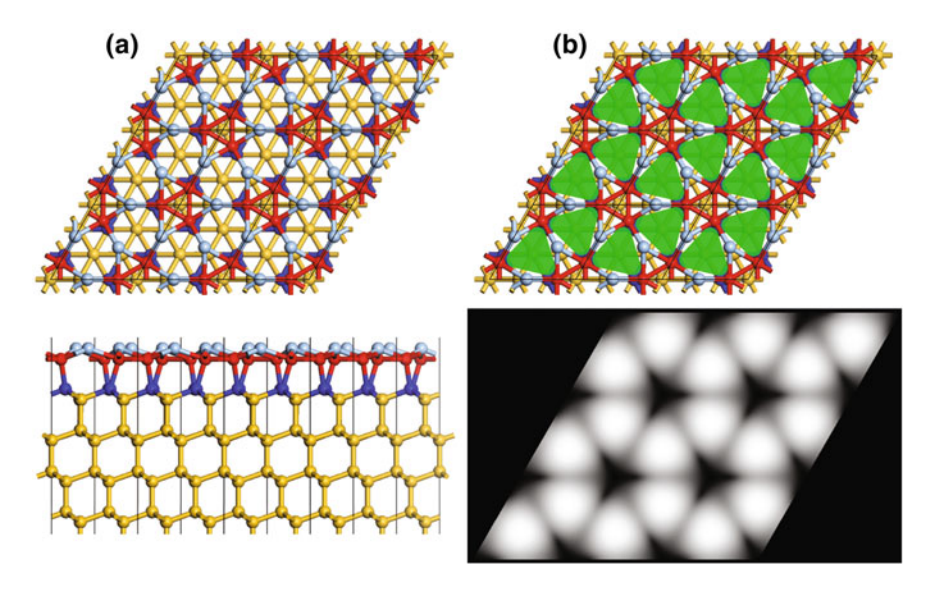


**Fig. 8.6** a Ball and stick representation of the honeycomb-chain trimer (HCT) model [44]. The top and side views are presented in the top and bottom panels, respectively. The yellow balls are Si atoms sitting in almost ideal positions of the Si(111) substrate. The topmost layer of Si atoms and the layer below them are represented by the red and the blue balls, respectively. The Ag atoms represented by the light blue balls form the topmost atomic layer of the system by attaching to Si atoms (red balls) below them. **b** Schematic and calculated STM image of HCT structure are presented in top and bottom panels, respectively. The bright triangular spots that are observed in the STM image are represented by green triangles superimposed on the top view of the ball and stick model

This model can inspire new calculations that might eventually solve the mistery of multilayer silicene. A realistic growth simulation is really hard to do because one needs to take into account many experimental parameters. It is especially hard to run a molecular dynamics simulation long enough for the atoms to explore the whole energy landscape. Instead, we present structural relaxations accompanied with educated guesses.

A silicene monolayer is first placed on top of the already formed HDS structure, as seen in Fig. 8.7a. Upon relaxation of this system, one of the dumbbell atoms in HDS transfers to the silicene layer forming a dumbbell unit there. As a result, HDS loses one dumbbell unit and becomes TDS, while silicene sheet gains one dumbbell unit and also becomes TDS. The two TDS layers become connected to each other by covalent bonds. However, the number and strength of these vertical covalent bonds are less compared to the ones formed between two (111) planes of cubic diamond silicon (cdSi).

If we continue depositing Si atoms onto the bilayer TDS system, the TDS layer on top will first transform to HDS. This HDS layer will follow the same faith as the original HDS structure, transforming itself to TDS by donating one dumbbell to create another TDS on top, which in turn will transform to yet another HDS

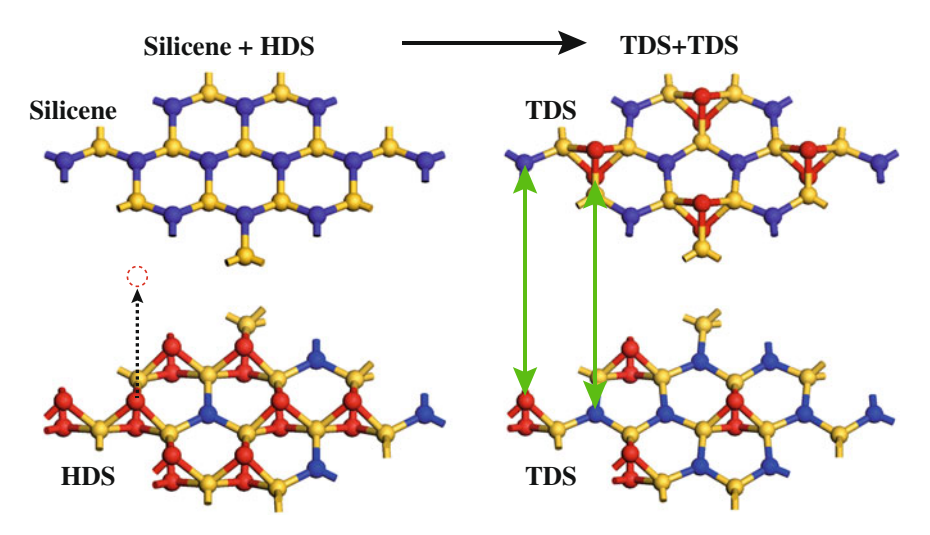


**Fig. 8.7** A possible growth mechanism of multilayer silicene or silicites. When silicene is put on top of HDS, one of the dumbbell atoms transfer to the silicene layer, as shown by dashed black arrow. As a result, two TDS layers are formed, that connect to each other through covalent bonding between atoms shown by green arrows

layer. This process will continue producing multiple TDS layers connected to each other with an HDS layer on the very top. This is in agreement with experiments that continue to see the  $\sqrt{3}\times\sqrt{3}$  honeycomb pattern in the STM measurements performed on multilayer silicene. It is possible to stack TDS layers in eclipsed or staggered fashion, as shown in Fig. 8.8a. The resulting bulk structures are named eclipsed (eLDS) and staggered (sLDS) layered dumbbel silicite, accordingly. All atoms in both eLDS and sLDS structure are fourfold coordinated. However, the covalent bonds significantly deviate from the ideal tetrahedral bonding angle of  $109^{\circ}$ . In the eLDS structure the TDS layers are just shifted by one third of their 2D unitcell vectors and stacked on top of each other. As shown in Fig. 8.8a, stacking follows ABCABC... and so on. It cannot be ABABAB... because in that case blue atoms would be connected to dumbbell atoms from both sides, which would unfavorably increase their coordination from four to five. The stacking of the sLDS structure is similar, but the layers are staggered with respect to each other. This is represented by a bar on top of the staggered layers.

Both eLDS and sLDS are open structures similar to the structure of cubic silicon. In fact, the mass densities of eLDS (2.10 g/cm³) and sLDS (2.11 g/cm³) are smaller than that of cdSi (2.28 g/cm³). The inplane lattice constant of LDS structures is 6.47 Å which is in agreement with experiments. Note that, this is the only model that accounts for inplane lattice contraction of multilayer silicene. The interlayer distance in both eLDS and sLDS structures are around 4.3 Å. This is in contrast to experiments that find the interlayer distance to be 3.1 Å. Further work needs to be done to resolve this disagreement between theory and experiment. Due to the

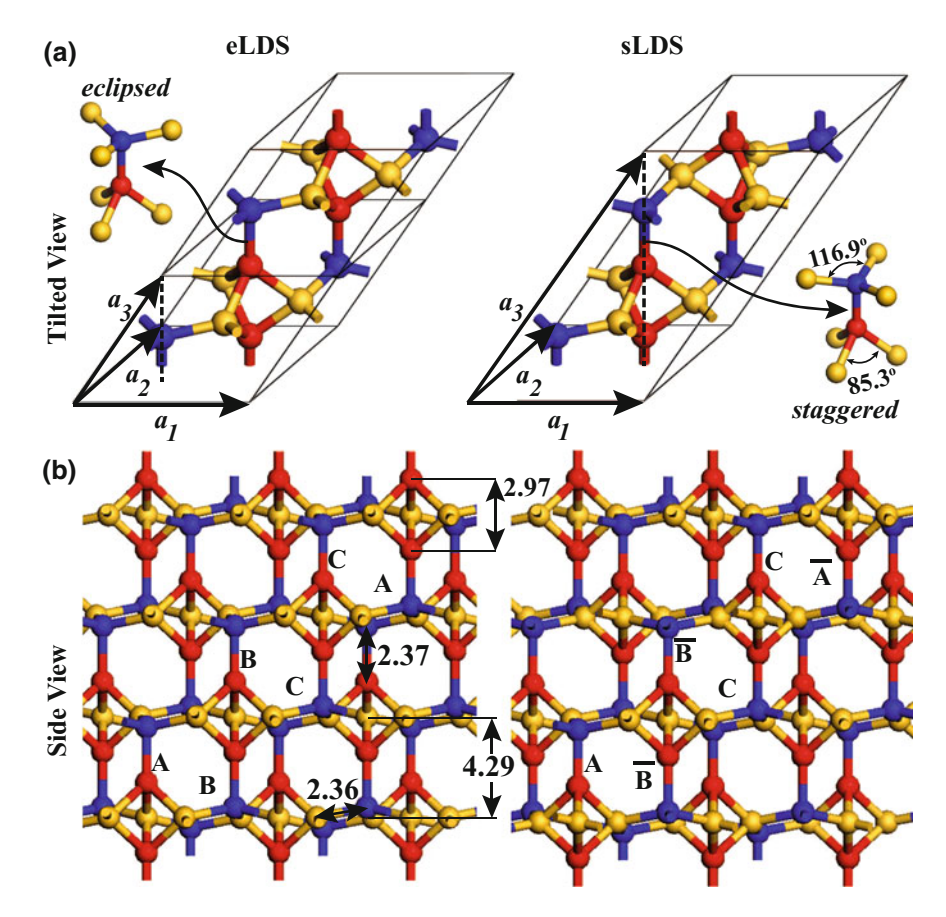
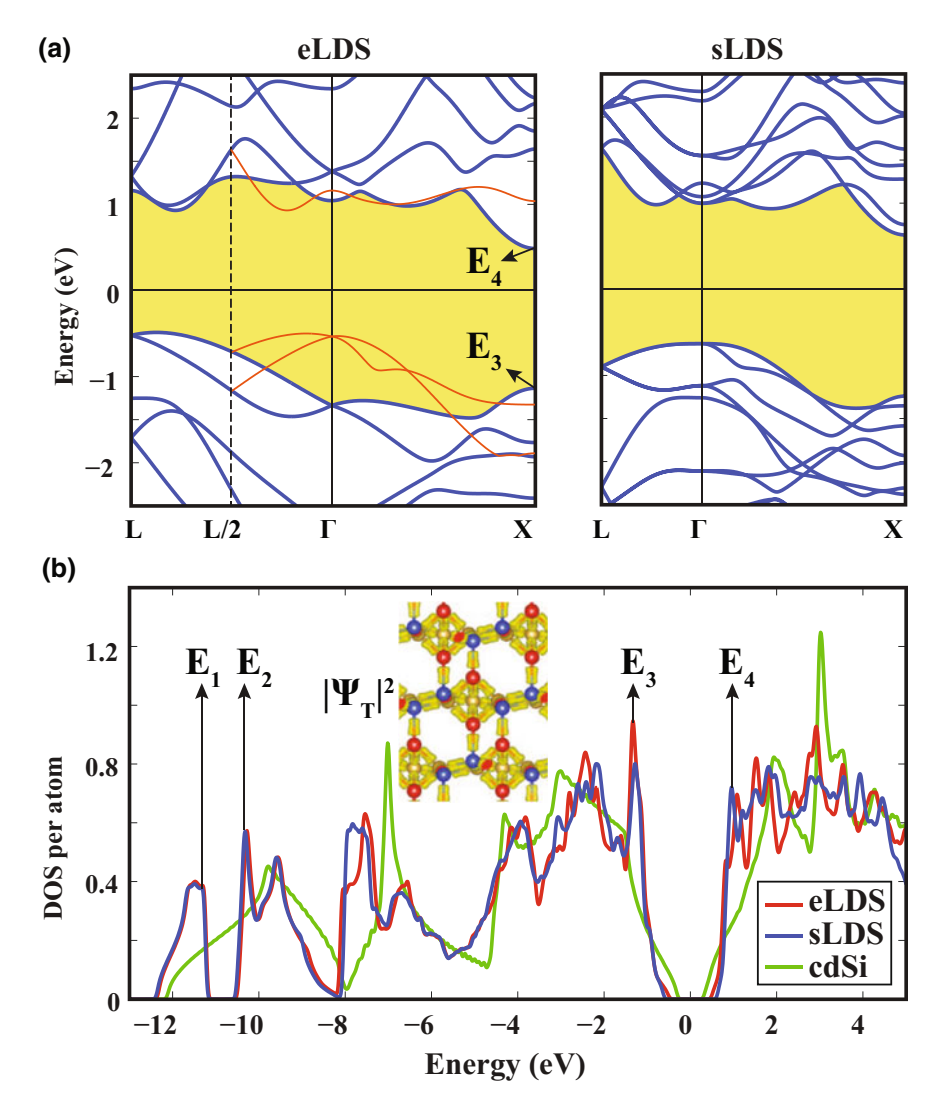


Fig. 8.8 a The double unit cell of eclipsed layered dumbbell silicite (eLDS) including N=7 Si atoms per unit cell and single unit cell of staggered layered dumbbell silicite (sLDS) including N=14 Si atoms per unit cell. b Side view showing the ABCABC... stacking of eLDS and the ABCABCA... stacking of sLDS. The bond lengths are given in Angström [3]

covalent bonds connecting LDS layers, the interlayer interaction is not like the weak van der Waals interaction found in graphite or  $MoS_2$ . However, these covalent bonds are sparse compared to those found between Si(111) layers in cubic silicon. The calculated cohesive energies are 4.42 eV and 4.43 eV per atom for eLDS and sLDS, respectively which is very close to that of cdSi (4.60 eV).

The electronic structures of eLDS and sLDS phases have indirect band gaps, which are wider than that of cdSi, as shown in Fig. 8.9a. The calculated indirect (direct) band gaps of eLDS and sLDS are 0.98 (1.43) eV and 1.26 (1.65) eV, respectively. The indirect band gap of cdSi is 0.62 eV at the DFT-PBE level while it is increased to 1.12 eV upon including many-body self-energy corrections at the  $G_0W_0$  level [21, 40]. With  $G_0W_0$  correction the indirect band gap of eLDS increased to 1.52 eV.



**Fig. 8.9** a Energy band structure of eLDS and sLDS. Zero of energy is set to the the Fermi level. Bands of eLDS folded by doubling the unit cell along  $a_3$  are shown by red lines. **b** Normalized densities of states (DOS) of eLDS, sLDS and cdSi. The isosurfaces of the total charge density shown by inset confirm the layered nature

Indirect (direct) band gaps of eLDS and sLDS calculated by HSE06 hybrid functional are  $1.92\ eV\ (2.37\ eV)$  and  $1.88\ eV\ (2.26\ eV)$ , respectively.

Owing to the different Brillouin zones it is difficult to directly compare the band structures of LDS and cdSi. Therefore the effects of the layered character on the electronic structure are sought in the normalized densities of states (DOS). Figure 8.9b

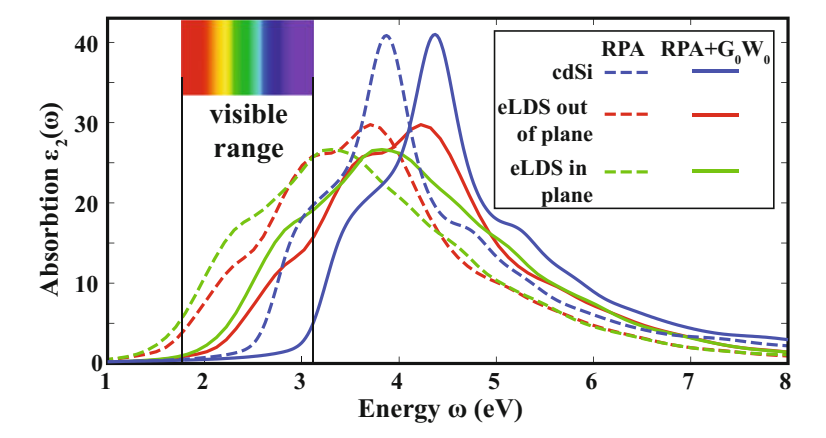


Fig.  $8.10\,$  The calculated Kohn-Sham and  $G_0W_0$  RPA optical absorption spectra for eLDS and cdSi

shows the normalized DOSs of eLDS, sLDS and cdSi. Except for some peak shifts, the DOSs of silicites are similar. Owing to the fourfold coordination of Si atoms in all structures, the overall features of DOSs of LDS structures appear to be reminiscent of that of cdSi. This confirms the fact that the overall features of the bands of cdSi can be obtained within the first nearest neighbor coupling [20]. The total charge density,  $|\Psi_T|^2$  presented by inset, depicts that electrons are mainly confined to TDS layers. This is another clear manifestation of the layered character of eLDS and sLDS phases. On the other hand, significant differences are distinguished in the details of the electronic energy structures due to deviations from tetrahedral coordination: (i) Indirect band gaps relatively larger than that of cdSi can offer promising applications in micro and nanoelectronics. (ii) Sharp peaks  $E_3$  and  $E_4$  near the edges of the valence and conduction bands, originate from the states, which are confined to TDS layers and can add critical functionalities in optoelectronic properties. (iii) A gap opens near the bottom of the valence band at  $\sim -11$  eV; its edge states are also confined to TDS layers.

The in-plane and out of plane static dielectric responses also reflect the layered nature of silicite. As a matter of fact, the calculated in-plane dielectric constant of eLDS (sLDS) is  $\varepsilon_{\parallel}=12.52$  (12.85), while its out of plane dielectric constant is  $\varepsilon_{\perp}=11.69$  (11.56). Those values are contrasted with the uniform dielectric constant,  $\varepsilon=12.19$  of cdSi. In Fig. 8.10 we present the optical absorption spectra of eLDS and cdSi calculated at the RPA level using the Kohn-Sham wave functions and  $G_0W_0$  corrected eigenvalues. The frequency dependent dielectric matrix takes different values in the in-plane and out of the plane directions of eLDS while for cdSi it is isotropic. One can see that the optical absorption of eLDS is significantly enhanced in the visible range compared to cdSi which makes it a potential candidate material for photovoltaic applications. This enhancement is still present when we rigidly shift the absorption spectra by the amount we get from  $G_0W_0$  corrections [33].

In closing, we would like to stress that, although LDS structures fail to explain the interlayer distance or metallicity of multilayer silicene, they are novel and interesting allotropes of silicon inspired by experiments. We believe that the search for a modified version of LDS model that might fully explain the multilayer silicene experiments is worth pursuing.

### References

- 1. G. Brumfiel, Sticky problem snares wonder material. Nature 495, 152–153 (2013)
- S. Cahangirov, M. Audiffred, P. Tang, A. Iacomino, W. Duan, G. Merino, A. Rubio, Electronic structure of silicene on Ag(111): strong hybridization effects. Phys. Rev. B 88, 035432 (2013)
- 3. S. Cahangirov, V.O. Özçelik, A. Rubio, S. Ciraci, Silicite: the layered allotrope of silicon. Phys. Rev. B **90**, 085426 (2014a)
- 4. S. Cahangirov, V.O. Özçelik, L. Xian, J. Avila, S. Cho, M.C. Asensio, S. Ciraci, A. Rubio, Atomic structure of the  $\sqrt{3} \times \sqrt{3}$  phase of silicene on Ag(111). Phys. Rev. B **90**, 035448 (2014b)
- L. Chen, B. Feng, K. Wu, Observation of a possible superconducting gap in silicene on Ag(111) surface. Appl. Phys. Lett. 102, 081602 (2013a)
- L. Chen, H. Li, B. Feng, Z. Ding, J. Qiu, P. Cheng, K. Wu, S. Meng, Spontaneous symmetry breaking and dynamic phase transition in monolayer silicene. Phys. Rev. Lett. 110, 085504 (2013b)
- L. Chen, C.C. Liu, B. Feng, X. He, P. Cheng, Z. Ding, S. Meng, Y. Yao, K. Wu, Evidence for Dirac fermions in a honeycomb lattice based on silicon. Phys. Rev. Lett. 109, 056804 (2012)
- M.X. Chen, M. Weinert, Revealing the substrate origin of the linear dispersion of silicene/Ag(111). Nano Lett. (2014)
- P. De Padova, J. Avila, A. Resta, I. Razado-Colambo, C. Quaresima, C. Ottaviani, B. Olivieri, T. Bruhn, P. Vogt, M.C. Asensio, G.L. Lay, The quasiparticle band dispersion in epitaxial multilayer silicene. J. Phys.: Condens. Matter 25, 382202 (2013)
- P. De Padova, C. Ottaviani, C. Quaresima, B. Olivieri, P. Imperatori, E. Salomon, T. Angot, L. Quagliano, C. Romano, A. Vona, M. Muniz-Miranda, A. Generosi, B. Paci, G.L. Lay, 24 h stability of thick multilayer silicene in air. 2D Mater. 1, 021003 (2014)
- P. De Padova, P. Vogt, A. Resta, J. Avila, I. Razado-Colambo, C. Quaresima, C. Ottaviani,
   B. Olivieri, T. Bruhn, T. Hirahara, T. Shirai, S. Hasegawa, M. Carmen Asensio, G. Le Lay,
   Evidence of Dirac fermions in multilayer silicene. Appl. Phys. Lett. 102, 163106 (2013)
- 12. Y.G. Ding, C.T. Chan, K.M. Ho, Structure of the  $(\sqrt{3} \times \sqrt{3})$ R30° Ag/Si(111) surface from first-principles calculations. Phys. Rev. Lett. **67**, 1454–1457 (1991)
- S. Dutta, K. Wakabayashi, Momentum shift of Dirac cones in the silicene-intercalated compound CaSi<sub>2</sub>. Phys. Rev. B 91, 201410 (2015)
- M. Ezawa, Valley-polarized metals and quantum anomalous Hall effect in silicene. Phys. Rev. Lett. 109, 055502 (2012)
- B. Feng, Z. Ding, S. Meng, Y. Yao, X. He, P. Cheng, L. Chen, K. Wu, Evidence of silicene in honeycomb structures of silicon on Ag(111). Nano Lett. 12, 3507–3511 (2012)
- A. Fleurence, R. Friedlein, T. Ozaki, H. Kawai, Y. Wang, Y. Yamada-Takamura, Experimental evidence for epitaxial silicene on diboride thin films. Phys. Rev. Lett. 108, 245501 (2012)
- Y. Fukaya, I. Mochizuki, M. Maekawa, K. Wada, T. Hyodo, I. Matsuda, A. Kawasuso, Structure of silicene on a Ag(111) surface studied by reflection high-energy positron diffraction. Phys. Rev. B 88, 205413 (2013)
- Z.X. Guo, S. Furuya, J.I. Iwata, A. Oshiyama, Absence and presence of Dirac electrons in silicene on substrates. Phys. Rev. B 87, 235435 (2013)

- Z.X. Guo, A. Oshiyama, Structural tristability and deep Dirac states in bilayer silicene on Ag(111) surfaces. Phys. Rev. B 89, 155418 (2014)
- 20. W.A. Harrison, S. Ciraci, Bond-orbital model II. Phys. Rev. B 10, 1516–1527 (1974)
- L. Hedin, New method for calculating the one-particle Green's function with application to the electron-gas problem. Phys. Rev. 139, A796–A823 (1965)
- D. Kaltsas, L. Tsetseris, Stability and electronic properties of ultrathin films of silicon and germanium. Phys. Chem. Chem. Phys. 15, 9710–9715 (2013)
- K. Kawahara, T. Shirasawa, R. Arafune, C.L. Lin, T. Takahashi, M. Kawai, N. Takagi, Determination of atomic positions in silicene on Ag(111) by low-energy electron diffraction. Surface Sci. 623, 25–28 (2014)
- G. Le Lay, Physics and electronics of the noble-metal/elemental-semiconductor interface formation: a status report. Surface Sci. 132, 169–204 (1983)
- 25. G. Lelay, M. Manneville, R. Kern, Cohesive energy of the two-dimensional Si(111)  $3 \times 1$  Ag and Si(111) $\sqrt{3}$ -R(30°) Ag phases of the silver (deposit)-silicon(111) (substrate) system. Surface Sci. **72**, 405–422 (1978)
- C.L. Lin, R. Arafune, K. Kawahara, M. Kanno, N. Tsukahara, E. Minamitani, Y. Kim, M. Kawai, N. Takagi, Substrate-induced symmetry breaking in silicene. Phys. Rev. Lett. 110, 076801 (2013)
- C.L. Lin, R. Arafune, K. Kawahara, N. Tsukahara, E. Minamitani, Y. Kim, N. Takagi, M. Kawai, Structure of silicene grown on Ag(111). Appl. Phys. Exp. 5, 045802 (2012)
- 28. C.C. Liu, W. Feng, Y. Yao, Quantum spin Hall effect in silicene and two-dimensional germanium. Phys. Rev. Lett. **107**, 076802 (2011)
- 29. E.J. van Loenen, J.E. Demuth, R.M. Tromp, R.J. Hamers, Local electron states and surface geometry of Si(111)- $\sqrt{3} \times \sqrt{3}$  Ag. Phys. Rev. Lett. **58**, 373–376 (1987)
- 30. L. Matthes, O. Pulci, F. Bechstedt, Massive Dirac quasiparticles in the optical absorbance of graphene, silicene, germanene, and tinene. J. Phys.: Condens. Matter 25, 395305 (2013)
- 31. L. Meng, Y. Wang, L. Zhang, S. Du, R. Wu, L. Li, Y. Zhang, G. Li, H. Zhou, W.A. Hofer, H.J. Gao, Buckled silicene formation on Ir(111). Nano Lett. 13, 685–690 (2013)
- E. Noguchi, K. Sugawara, R. Yaokawa, T. Hitosugi, H. Nakano, T. Takahashi, Direct observation of Dirac cone in multilayer silicene intercalation compound CaSi<sub>2</sub>. Adv. Mater. 27, 856–860 (2015)
- G. Onida, L. Reining, A. Rubio, Electronic excitations: density-functional versus many-body Green's-function approaches. Rev. Mod. Phys. 74, 601–659 (2002)
- 34. V.O. Özçelik, S. Ciraci, Local reconstructions of silicene induced by adatoms. J. Phys. Chem. C 117, 26305–26315 (2013)
- 35. V.O. Özçelik, H.H. Gurel, S. Ciraci, Self-healing of vacancy defects in single-layer graphene and silicene. Phys. Rev. B 88, 045440 (2013)
- 36. A. Resta, T. Leoni, C. Barth, A. Ranguis, C. Becker, T. Bruhn, P. Vogt, G.L. Lay, Atomic structures of silicene layers grown on Ag(111): scanning tunneling microscopy and noncontact atomic force microscopy observations. Sci. Rep. 3 (2013)
- 37. E. Salomon, R.E. Ajjouri, G.L. Lay, T. Angot, Growth and structural properties of silicene at multilayer coverage. J. Phys.: Condens. Matter **26**, 185003 (2014)
- 38. N. Sato, T. Nagao, S. Hasegawa, Si(111)- $(\sqrt{3} \times \sqrt{3})$ -Ag surface at low temperatures: symmetry breaking and surface twin boundaries. Surface Sci. **442**, 65–73 (1999)
- T. Shirai, T. Shirasawa, T. Hirahara, N. Fukui, T. Takahashi, S. Hasegawa, Structure determination of multilayer silicene grown on Ag(111) films by electron diffraction: evidence for Ag segregation at the surface. Phys. Rev. B 89, 241403 (2014)
- M. Shishkin, G. Kresse, Self-consistent GW calculations for semiconductors and insulators. Phys. Rev. B 75, 235102 (2007)
- 41. R. Stephan, M.C. Hanf, P. Sonnet, Spatial analysis of interactions at the silicene/Ag interface: first principles study. J. Phys.: Condens. Matter 27, 015002 (2015)
- L. Tao, E. Cinquanta, D. Chiappe, C. Grazianetti, M. Fanciulli, M. Dubey, A. Molle, D. Akinwande, Silicene field-effect transistors operating at room temperature. Nat. Nanotechnol. 10, 227–231 (2015)

- 43. D. Tsoutsou, E. Xenogiannopoulou, E. Golias, P. Tsipas, A. Dimoulas, Evidence for hybrid surface metallic band in  $(4 \times 4)$  silicene on Ag(111). Appl. Phys. Lett. **103**, 231604 (2013)
- 44. E. Vlieg, A.V.D. Gon, J.V.D. Veen, J. MacDonald, C. Norris, The structure of Si(111)- $(\sqrt{3} \times \sqrt{3})$ r 30°-Ag determined by surface X-ray diffraction. Surface Sci. **209**, 100–114 (1989)
- P. Vogt, P. Capiod, M. Berthe, A. Resta, P. De Padova, T. Bruhn, G. Le Lay, B. Grandidier, Synthesis and electrical conductivity of multilayer silicene. Appl. Phys. Lett. 104, 021602 (2014)
- P. Vogt, P. De Padova, C. Quaresima, J. Avila, E. Frantzeskakis, M.C. Asensio, A. Resta, B. Ealet, G. Le Lay, Silicene: compelling experimental evidence for graphenelike two-dimensional silicon. Phys. Rev. Lett. 108, 155501 (2012)
- 47. Y.P. Wang, H.P. Cheng, Absence of a Dirac cone in silicene on Ag(111): first-principles density functional calculations with a modified effective band structure technique. Phys. Rev. B 87, 245430 (2013)
- 48. Y. Xu, B. Yan, H.J. Zhang, J. Wang, G. Xu, P. Tang, W. Duan, S.C. Zhang, Large-gap quantum spin Hall insulators in tin films. Phys. Rev. Lett. 111, 136804 (2013)
- 49. X.S. Ye, Z.G. Shao, H. Zhao, L. Yang, C.L. Wang, Intrinsic carrier mobility of germanene is larger than graphene's: first-principle calculations. RSC Adv. 4, 21216–21220 (2014)
- 50. L.D. Zhang, F. Yang, Y. Yao, Possible electric-field-induced superconducting states in doped silicene. Sci. Rep. **5** (2015)

# Chapter 9 Silicene on Ag(111) at Low Temperatures



Peng Cheng, Lan Chen and Kehui Wu

**Abstract** Following the successful preparation of silicene, the focusing issue is whether silicene indeed exhibits the exotic electronic properties predicted theoretically. To study the electronic structure of silicene, angle resolved photoelectron emission spectroscopy and scanning tunneling microscopy/spectroscopy are the two major experimental techniques. The development of cryogenic STM allows the investigation of physical phenomena that occur only at low temperatures or are best seen at low temperature, such as superconductivity, a quantum Hall effect, metal-insulator transition and charge density waves. However, it is equally important that low temperature environment provides a stable and well-regulated platform and greatly improves the performance of STM. In this chapter, we give an overview on the recent progress of silicene on Ag(111) at low temperatures by utilizing cryogenic STM.

#### 9.1 Introduction

Silicene, a single sheet of silicon atoms arranged in a honeycomb lattice, has attracted tremendous attention during the past few years. It is a new two-dimensional silicon allotrope, different from any silicon structure previously found in nature. The theoretical investigation on silicene actually dates back to year 1994, when Takeda and Shiraishi explored the silicon analogue of graphite and proposed that silicon can exist in a two-dimensional sheet [1]. In contrast to graphene where the A and B sublattices are in exactly the same plane, they pointed out the two sublattices in silicene are relatively shifted in the direction perpendicular to the atomic plane, forming a so-called low buckled structure. However, this work was before the discovery of graphene and not paid too much attention. Following the boom of graphene research, silicene has received renewed interest. In 2007, silicene as a silicon version of graphene was named by Guzmán-Verri and Lew Yan Voon, who developed a unified tight-binding

(TB) Hamiltonian for Si-based nanostructures and showed that silicene is a zero-gap semiconductor [2]. In 2009, silicene with a buckled geometry was confirmed to be dynamically stable by Cahangirov et al. [3]. Moreover, theoretical calculations show that silicene has graphene-like electronic band structure, supporting charge carriers behaving as massless Dirac fermions. Compared with graphene, silicene has a larger spin-orbit coupling strength, which may lead to a larger energy gap at the Dirac point and favor a detectable quantum spin Hall effect (QSHE) [4]. The breakthrough in experimental research on silicene took place in year 2012, when several groups reported in parallel the successful preparation of a silicene sheet. Among them Fleurence et al. reported the formation of silicene on ZrB<sub>2</sub> substrate [5], whereas other groups, including Vogt et al. [6], Lin et al. [7], and our group [8, 9], reported the growth of silicene on Ag (111).

Ag(111) is currently the most often used substrate for growing silicene films. Depending on the Si coverage and substrate temperature, silicene can form a variety of superstructures on Ag(111) surface, including  $4 \times 4$ ,  $\sqrt{13} \times \sqrt{13}$ ,  $2\sqrt{3} \times 2\sqrt{3}$  (with respect to Ag(111) surface lattice) and finally to a  $\sqrt{3} \times \sqrt{3}$  (with respect to silicene  $1 \times 1$ ) [6–9] (see also Chap. 7). The origination of silicene reconstructions is the low-buckled structure of silicene. Although silicene has a honeycomb lattices like graphene, the silicon atoms are not exactly located on the same plane, but instead forming a buckled structure. In free standing silicene, the Si atoms in sublattice A is upper buckled whereas those in B are lower buckled, forming a  $1 \times 1$  structure. Once the silicene sheet adsorbs on Ag(111) surface, the interaction between silicene and substrate results in rearrangement of the buckling degree, forming a variety of superstructures corresponding to different buckling patterns. It should be note that overall the honeycomb lattice of silicene is still preserved regardless the different patterns.

Following the successful preparation of silicene, the focusing issue is then whether silicene indeed exhibits the exotic electronic properties predicted theoretically. To study the electronic structure of silicene, angle resolved photoelectron emission spectroscopy (ARPES) and scanning tunneling microscopy/spectroscopy (STM/STS) were two major experimental techniques.

STM is a surface sensitive technique based on the concept of quantum tunneling [10–13]. The atomically resolved structure of a surface can be obtained by monitoring the tunneling current in an STM. Besides its unprecedented capability to study surface topography, information on electronic structure at a given location of a sample can also be obtained by STS. The scanning tunneling spectroscopy (STS) measures the energy resolved local density of state (LDOS) on surface with subatomic resolution. This capability is due to the exponential dependence of the tunneling current on the tip-sample separation and the proportionality of the differential conduction to the LDOS of the sample at the center of tip apex. STM with high energy resolution is needed to study effects determined by small energy scale. The smearing of electron occupation at Fermi level for both STM tip and sample limits the energy resolution. The thermal broadenings of peaks in dI/dV are  $3.5k_BT$  [14], where  $k_B$  and T are the Boltzmann constant and temperature, respectively. The development of cryogenic STM allows the investigation of physical phenomena that occur only at low temperatures or are best seen at low temperature, such as superconductivity, quantum Hall

effect, metal-insulator transition and charge density waves. However, it is equally important that low temperature environment provides a stable and well-regulated platform and greatly improves the performance of STM.

The cryogenic STM with high performance has been widely used in the characterization of metals, semiconductors and superconductors. Applying it to study of silicene, many intriguing properties have recently been unveiled. For silicene, the low temperature environment brings into new physical phenomena, and the low temperature behavious reveal more fascinating properties. For examples, on the  $\sqrt{3} \times \sqrt{3}$  silicene phases STS reveals pronounced quasiparticle interference patterns and linear dispersion was derived [9], together with the intriguing observation of suppressed backscattering [15], low temperature phase transition [16], and a superconducting-like energy gap [17]. These results demonstrated that silicene is a promising playing ground for exotic electronic properties as well as potential applications.

In this chapter, we give an overview on the recent progress of silicene on Ag(111) at low temperatures by utilizing cryogenic STM.

### 9.2 Electronic Structure of the 4 x 4 Phase by STS

At relatively low substrate temperature, the first perfectly ordered phase observed in experiments is silicene  $4 \times 4$  phase [6–8] (see also Chap. 7). As displayed in Fig. 9.1b, the STM image of  $4 \times 4$  phase exhibits triangular half unit cells (HUC) each consisting of three bright spots, which is quite similar to the well-known Si(111)  $-5 \times 5$  surface structure.

The  $4 \times 4$  structure can be understood by the so called "magic mismatch" between the lattice constant of Ag ( $a_{Ag} = 2.88 \text{ Å}$ ) and Si ( $a_{Si} = 3.84 \text{ Å}$ ), i.e.,  $4 \times a_{Ag} = 3 \times a_{Si}$ within 0.5% of error. Since both the Ag(111) surface and silicene are hexagonal lattices, a commensurate  $4 \times 4$  superstructure can be constructed by simply overlapping a low-buckled, freestanding silicene  $1 \times 1$  lattice on top of a Ag(111)  $-1 \times 1$  lattice in the same orientation. Such a magic commensuration results in minimal interface strain and thus stabilizes the silicene structure. Once the silicene  $-1 \times 1$  sheet is placed on the Ag(111) substrate, the buckling configuration will spontaneously rearrange to lower the surface energy. As a consequence, there will be six upper-buckled Si atoms per unit cell, while the other twelve Si atoms are all lower-buckled. Moreover, the three upper-buckled Si atoms in one HUC do not belong to the same sublattice with the three upper-buckled Si atoms in the other HUC, as illustrated in Fig. 9.1c. This is in contrast to the case of freestanding silicene where all upper-buckled (or lower-buckled) Si atoms constitute a sublattice. That the protrusions observed in STM correspond to upper-buckled Si atoms that are indeed geometrically higher can be further confirmed by atomic force microscopy (AFM) measurements [18].

 $<sup>^1\</sup>text{Note}$  that the  $4\times 4$  silicene phase is therefore also referred to as a  $3\times 3$  superstructure, e.g. in Chap. 5, 7 and 8.

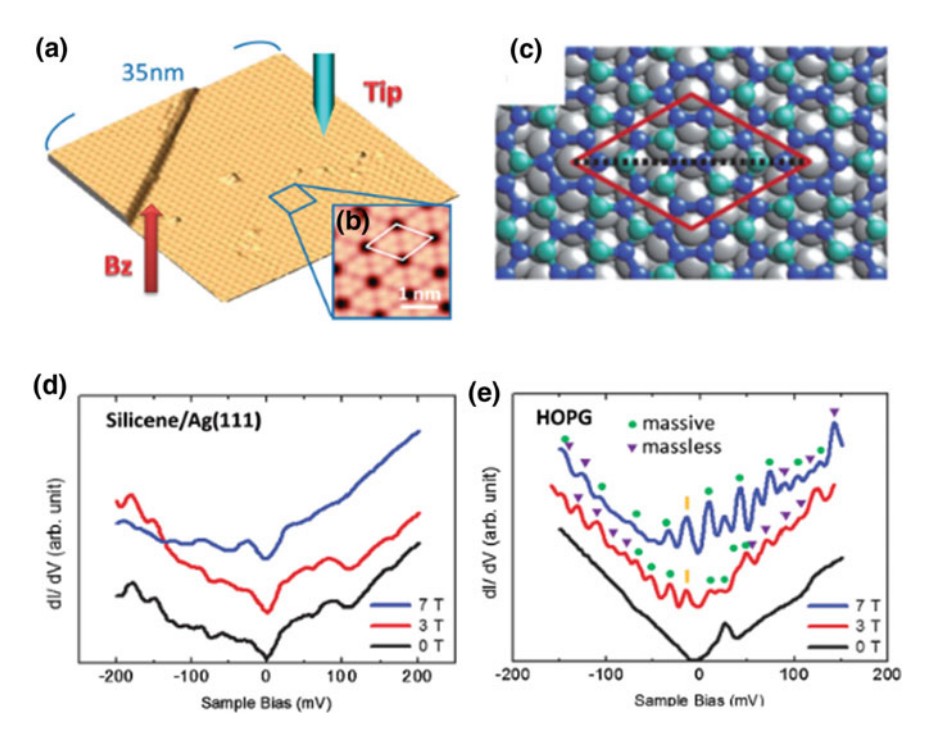


Fig. 9.1 a STM image of large area of silicene (sample bias voltage  $V_s = -0.70$  V and tunneling current  $I_t = 0.19$  nA. The image size is  $35 \times 35$  nm²). b High resolution STM image of the  $4 \times 4$  silicene ( $V_s = 0.50$  V and  $I_t = 0.30$  nA,  $3.65 \times 3.65$  nm²). The unit cell is shown by the white rhombus. c The geometric structures of the  $4 \times 4$  silicene. d The STS spectra of silicene for various magnetic fields perpendicular to the sample surface,  $B_z$ . e The STS spectra of HOPG for various  $B_z$ . The purple triangles and green circles show the peaks originating from the LLs of massless and massive Dirac fermions, respectively. The n = 0 LL is marked by the yellow bar and the n = 1 LL of massive Dirac fermions is not clearly resolved in 3 T due to low magnetic field. Reproduced with permission from Phys. Rev. Lett. 110, 076801 (2013)

After the successful sample preparation of  $4 \times 4$  phase, Vogt et al. reported, together with their silicene structure, possible existence of the Dirac cone and linear dispersion in the  $4 \times 4$  phase of silicene from ARPES measurements [6] (see also Sect. 7.4.2). Later, Avila et al. revisited the electronic structures of the silicene  $4 \times 4$  phase and further confirmed that the linear dispersion comes from silicene rather than Ag substrate [19].

However, there is still a fierce debate about whether the Dirac cone of monolayer silicene can be preserved on Ag(111) surface [20–27]. The key issue is that, once a monolayer silicene sheet is placed on a clean Ag(111) substrate, the strong interaction between the silicene film and the Ag substrate may significantly influence the surface electronic band structure. Combining STS measure and DFT calculations of  $4 \times 4$  phase, Lin et al. proposed that silicene on the Ag(111) surface would no longer be a 2D Dirac fermion system due to substrate-induced symmetry breaking [20].

Measuring the Landau levels (LLs) of the 4 × 4 phase under a magnetic field by using STS is the most direct way to judge whether the sample acquires the Dirac fermion. In normal metals and two-dimensional electron gases, Landau levels are equally spaced. While for Dirac fermions, Landau levels consist of a field-independent state at the Dirac point and a sequence of levels with squareroot dependence in both field and index, instead of the usual linear dependence. The cyclotron frequency ( $\omega_C$ ) of the Dirac fermion is given by  $\omega_C = \sqrt{2}v_F/\ell$ , and the nth LL appears at  $E_n = \hbar\omega_C\sqrt{n}$ , where  $v_F$  is the Fermi velocity, and  $\ell$  is the magnetic length ( $\ell = \sqrt{\hbar/eB_z}$ ). The energy  $E_n$  is measured relative to the Dirac point.

STS was proved to be a powerful tool to study the Landau quantization under magnetic fields [28–31]. Figures 9.1d, e show the evolution of the STS spectra taken for the  $4 \times 4$  silicene and highly-oriented pyrolytic graphite (HOPG) with an increase in the magnetic field perpendicular to the sample,  $B_z$ . From  $B_z = 0$  to 7 T, the spectrum of the  $4 \times 4$  silicene does not change essentially, and characteristic structures attributed to the Landau quantization are not found. Even in the wide range (-0.5 to +0.5V) spectra, no significant change can be found. In contrast, LLs appear in the HOPG, and their energy positions shift with  $B_z$ . The spectral evolution of the HOPG is reasonably rationalized by a combination of massless and massive Dirac fermions. Thus, they conclude that the electrons in the  $4 \times 4$  silicene lose both their two dimensionality and linear dispersion that are requisite for the Dirac fermion.

The size effects and the structural inhomogeneity can be ruled out while considering the absence of the LLs. To explain the absence of the LLs of 4  $\times$  4 phase, they investigated the electronic structure of silicene by DFT calculations and obtained the evolution of the band structure from freestanding lightly-buckled silicene, freestanding distorted silicene to the 4  $\times$  4 phase silicene. The electronic states associated with Si in the 4  $\times$  4 phase are strongly hybridized with the substrate states and demonstrating the lack of Dirac fermions in a single layer honeycomb lattice due to significant symmetry breaking.

## 9.3 The $\sqrt{3} \times \sqrt{3}$ Phase

As substrate temperature reaches 500 K, silicene islands with  $(\sqrt{3} \times \sqrt{3})R30^\circ$  periodicity (with respect to silicene  $-1 \times 1$  lattice) are observed on the surface [9] (see also Sect. 8.3). The STM image in Fig. 9.4a shows an island of silicene  $(\sqrt{3} \times \sqrt{3})R30^\circ$  phase across the step edges of the underlying Ag(111) surface without losing continuity. The high-resolution image (Fig. 9.4b) displays the honeycomb structure of silicene terrace. The lattice period of the honeycomb structure is about 0.64 nm, corresponding to a  $(\sqrt{3} \times \sqrt{3})R30^\circ$  honeycomb superstructure with respect to the  $1 \times 1$  lattice.

To explain the atomic structure of  $(\sqrt{3} \times \sqrt{3}) R30^\circ$  phase, we should mention the characteristic phase transition at low temperature (Fig. 9.4d), which will be described in Sect. 9.3.2 in detail [16]. When the silicene sample on substrate is cooled to liquid helium temperature (5 K), the silicene film is phase separated into triangular domains

P. Cheng et al.

with the two symmetric configurations divided by narrow domain boundaries. The  $(\sqrt{3}\times\sqrt{3})R30^\circ$  superstructure can then be explained by the double symmetric  $(\sqrt{3}\times\sqrt{3})R30^\circ$  reconstruction structures with dynamic flip-flop motion at high temperature. If ignoring the substrate, these two  $(\sqrt{3}\times\sqrt{3})R30^\circ$  superstructures have identical geometry and share the same central substrate atom for each hexagon unit. In every  $(\sqrt{3}\times\sqrt{3})R30^\circ$  unit cell, only one Si atom is buckled upward, whereas the rest five Si atoms have nearly identical lower height, resulting in a rhombic  $(\sqrt{3}\times\sqrt{3})R30^\circ$  superstructure. The two types of rhombic  $(\sqrt{3}\times\sqrt{3})R30^\circ$  superstructures coincide well with the two mirror-symmetric phases observed in the low temperature experiments. At higher temperature, the flip-flop motion between the two phases leads to an averaged, symmetric  $(\sqrt{3}\times\sqrt{3})R30^\circ$  phase.

The electronic structure of  $(\sqrt{3} \times \sqrt{3})R30^{\circ}$  phase has also been investigated by STS and many intriguing phenomenon were observed, including the pronounced quasiparticle interference patterns [9, 15], low temperature phase transition [16], and an superconducting-like energy gap [17].

# 9.3.1 Dirac Fermions Evidenced by Quasi-particle Interference in the $\sqrt{3} \times \sqrt{3}$ Phase

In contrast to the controversy about the electronic states of silicene  $4 \times 4$  phase, low-temperature electronic state measurements by STS conducted by Chen et al. have revealed that the  $\sqrt{3} \times \sqrt{3}$  phase exhibits a metallic surface state which can host Dirac fermions [9].

Scanning tunneling spectroscopy (STS) records differential tunneling conductance, dI/dV, as a measure of the local density of states at the tunneling energy. On a metallic surface, When disorders are introduced into the sample, the change in potential leads to the elastic electron scattering of the incident wave with a wave vector  $k_i$  into  $k_f = k_i + q$ , with  $k_i$  and  $k_f$  being on the same constant-energy contour (CEC). The quantum interference between the initial and final states results in a standing wave pattern whose spatial period is given by  $\lambda = 2\pi/|q|$ , which are often referred to as the "Friedel oscillations". The phenomena can be observed by STM as modulations of the differential tunneling conductance. When the STM images of standing waves are Fourier transformed, the scattering wave vector q becomes visible in the reciprocal space. This way, it simultaneously provides real-space and momentum-space information. STS has become a powerful tool to probe the surface state characteristics such as symmetry and dispersion [32, 33].

Similar as graphene, the Dirac cone of silicene are located at K points in the 2D Brillouin zone [3, 4]. The constant energy contours in reciprocal space are small circles centered at the K points (Fig. 9.2g). Quasiparticles can be scattered within the small circles (intravalley scattering) or between circles (intervalley scattering), resulting in standing waves (quasiparticle interference patterns) observed in dI/dV maps [34–36]. Interference patterns with short-wavelength are observed in STM

images of silicene, consistent with an intervalley scattering. The patterns exhibit closed packed protrusions (shown in Fig. 9.2b, c) in areas near the step edge and point defect, in contrast to the honeycomb structure observed in terrace of silicene island. The wave vectors of intervalley scattering are close in length to the wave vectors  $K_{1(2)}$ , which have a length of  $1/\sqrt{3}$  in reciprocal space, corresponding to a  $(\sqrt{3} \times \sqrt{3})R30^\circ$  periodicity in real space. The QPI pattern originating from the scattering center extends for a length of only a few nm.

The standing waves with long wavelength are observed near the edges of island of second layer silicene in dI/dV maps shown in Fig. 9.2e, f. The wavelength changes as a function of tip bias voltage. As the bias increases from -0.4 to -1.1V, the wavelength decreases correspondingly from 2.8 to 1.6 nm. The wavelike quasi-partical interference (OPI) patterns are attributed to the intra-valley scattering (Fig. 9.2g). The wave vector  $q_1$  of intravalley scattering connects points within a single constantenergy circle and determines the observed long wavelength interference pattern. Since  $q_1$  equals to the diameter of the constant energy contour of Dirac cone, the energy-momentum dispersion can be deduced from the E(k) curves in Fig. 9.2h, where  $2k = q_1$ . The fitting curve give the linear dispersion, with Fermi velocity  $v_F = (1.2 \pm 0.1) \times 10^6$  m/s. The k = 0 energy intercept gives the Dirac energy,  $E_F - E_D = 0.52 \pm 0.02 \,\text{eV}$ , consistent with the position of the DP in the dI/dVspectra. The linear  $E \sim k$  dispersion proves the existence of the Dirac cone in electronic band structures of silicene. The surprising large Fermi velocity, comparable with that of graphene [34, 37], suggests the prospective applications comparable with those that have been proposed or realized in graphene. The observation of QPI patterns, consistent with analysis based on the theoretical band structure of silicene, is additional proof that the underlying atomic structure of the film is graphene-like, with only some buckling that does not change the basic electronic structure of the film.

A linear dispersion near Fermi level is far from a complete description of the Dirac fermion state. In Dirac systems such as graphene or three dimensional (3D) topological insulators, existence of quasiparticle chirality is even more important. In graphene, chirality is introduced to project the pseudospin in the direction of the momentum [38]. Due to the quasiparticle chirality, the backscattering of quasiparticle within a valley (same K point, intravalley) or between two valleys (K and K' points, intervalley) (Fig. 9.2g) should be strongly suppressed because the backscattering will reverse the chirality of the quasiparticle. As a consequence, the behaviors of decay of standing waves from a straight step edge for Dirac fermion systems are different from conventional 2D electron gas. For 2D electron gas, the decay factor of standing waves is -0.5 [32], while in graphene or the surface of a topological insulator, the chirality of quasiparticles results in suppression of backscattering and a faster decay. A decay factor of  $\alpha = -1.5$  had been reported for graphene [36], and  $\alpha = -1.5$ and -1 had been reported for 3D topological insulators [39, 40]. Suppression of backscattering can be regarded as fingerprints of Dirac systems with quasiparticle chirality.

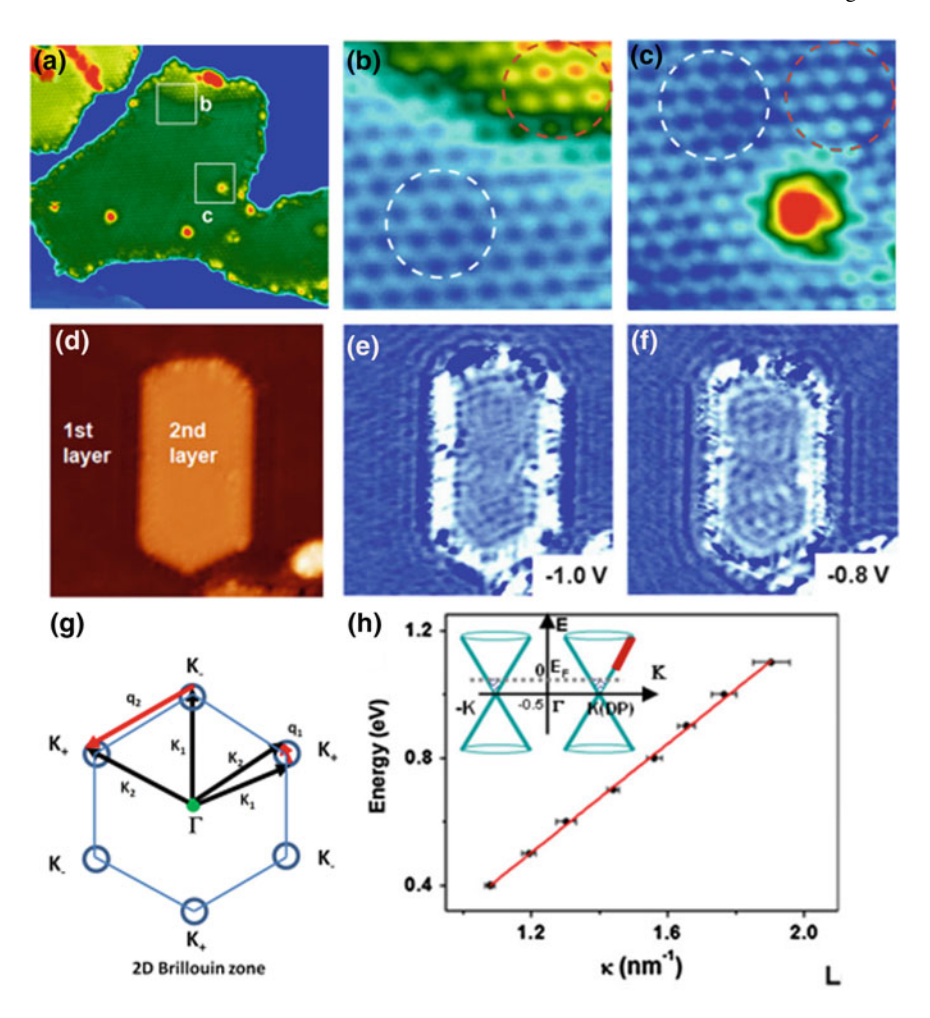


Fig. 9.2 a STM image ( $V_t = -1.1 \text{ V}$ ) of a  $50 \times 45 \text{ nm}^2$  area of silicene  $\sqrt{3} \times \sqrt{3}$  island. **b**, **c** Enlarged STM images of the areas marked by the white squares in (**a**), respectively. The white and red circles represent the normal honeycomb structure and hexagonal closed packed patterns induced by intervalley scattering of quasiparticles, respectively. **d** The STM image ( $V_t = -1.0 \text{ V}$ ) of  $40 \times 40 \text{ nm}^2$  of one monolayer silicene  $\sqrt{3} \times \sqrt{3}$  phase containing an island of second layer. **e** and **f** dI/dV maps of the same area as (**d**) taken at  $V_t = -1.0 \text{ V}$  and  $V_t = -0.8 \text{ V}$ , respectively. **g** Schematic of the 2D Brillouin zone [blue (thin gray) lines], constant energy contours [blue (gray) rings] at K points, and the two types of scattering vectors:  $\mathbf{q}_1$  [intravalley, short red (dark gray) arrow] and  $\mathbf{q}_2$  [intervalley, long red (dark gray) arrow]. **h** Energy dispersion as a function of K for silicene  $\sqrt{3} \times \sqrt{3}$  phase determined from the wavelength of standing waves in dI/dV maps. Reproduced with permission from Phys. Rev. Lett. 109, 056804 (2012)

The decaying behavior of QPI patterns from the step edges of a  $\sqrt{3} \times \sqrt{3}$  silicene film was reported by Feng et al. [15]. The dI/dV intensity as a function of the distance from the armchair and zigzag step edges at various energies are shown in Fig. 9.3a–f.

The data were fitted using an exponential decaying equation  $\delta \rho(x) \propto \cos(2kx + \varphi)x^{\alpha}$ [32], which is generally applicable for Friedel oscillations of LDOS in a surface state band, where k is the wave vector of the standing wave,  $\varphi$  is a phase shift associated with the scattering potential, and  $\alpha$  is the decay factor. The best fitting parameter of  $\alpha = -1.5$  for armchair edge ( $\Gamma$ -K direction), and  $\alpha = -1.0$  for zigzag edge ( $\Gamma$ -M direction) were obtained. The observation of strong decay of LDOS oscillation in silicene suggests that the quasiparticle in silicene is chiral, otherwise, the decay of QPI from a step edge should obey a power law with a decay factor of 0.5, as that in conventional 2D electron gas systems. The faster decay of LDOS oscillation should be due to scattering of electrons between states with nonparallel or even antiparallel pseudospins. In topological insulator of  $Bi_2Te_3$ , the decay factors are -1.5 in  $\Gamma$ -K direction and -1.0 in  $\Gamma$ -M direction, which dramatically coincides with the silicene. It was also noticed that in multilayer silicene, similar and persistent QPI patterns and decaying behavior have been observed on terraces with different thickness, indicating that the observed QPI is indeed originating from the metallic surface state instead of from the bulk or substrate.

Furthermore, other properties of Dirac cone of silicene can be revealed by the standing waves scattering from point defects. Feng et al. [15] deposited 0.001 monolayer (defined as single layer of silicene with lattice constant 0.38 nm) hydrogen atoms on silicene, which are adsorbed on top of Si atoms to form Si-H bonds. The hybridization of Si atoms is thus changed from sp<sup>2</sup> to sp<sup>3</sup> [41], which will change the local potential and create a scattering center. After hydrogen adsorption, the typical dI/dV map shows significant QPI patterns, as shown in Fig. 9.3g. A striking aspect of the map is that the waves around point defects exhibit a hexagonal rather than circular shape. This unique feature can be revealed more clearly by fast Fourier transformation (FFT) of dI/dV maps into k space (Fig. 9.3h). A hexagon is found in the center with the edges in  $\Gamma$ -K direction and vertices in  $\Gamma$ -M direction. In graphene, the CEC of Dirac cone at K and K' points in BZ at low energy is isotropic and circular, but it is trigonally warped at higher energies [42]. The orientation of warping is different for K and K' points. It is thus easy to assume that similar trigonal warping may exist in the Dirac cone of silicene. However, the trigonally warped CECs cannot explain the hexagonal shape of LDOS oscillations observed in both real space and k space for silicene. To better understand the Dirac cone warping in silicene, the electronic band structure of silicene was explored by using first principle calculations. Due to the formation of the  $(\sqrt{3} \times \sqrt{3})R30^{\circ}$  superstructure of silicene, the K and K' points in the Brillouin zone of  $(1 \times 1)$  phase are folded onto the  $\Gamma$  point of  $(\sqrt{3} \times \sqrt{3})$ R30° phase. As a consequence, the six Dirac cones with different orientations of warping at K and K' points of  $(1 \times 1)$  phase are folded onto the  $\Gamma$  point of  $(\sqrt{3} \times \sqrt{3})$ R30° phase and give rise to one Dirac cone, which should be hexagonally warped (Fig. 9.3i).

Therefore, the scattering wave vector q varies along the opposite edges, and will result in a hexagon with edges toward  $\Gamma$ -K direction and vertices toward  $\Gamma$ -M direction (for BZ of  $1 \times 1$  structure) in k-space maps. On the other hand, the backscattering should be suppressed due to the states with antiparallel pseudospins, which will give QPI with faster decay rate. Additionally, occurrence of the intraval-

P. Cheng et al.

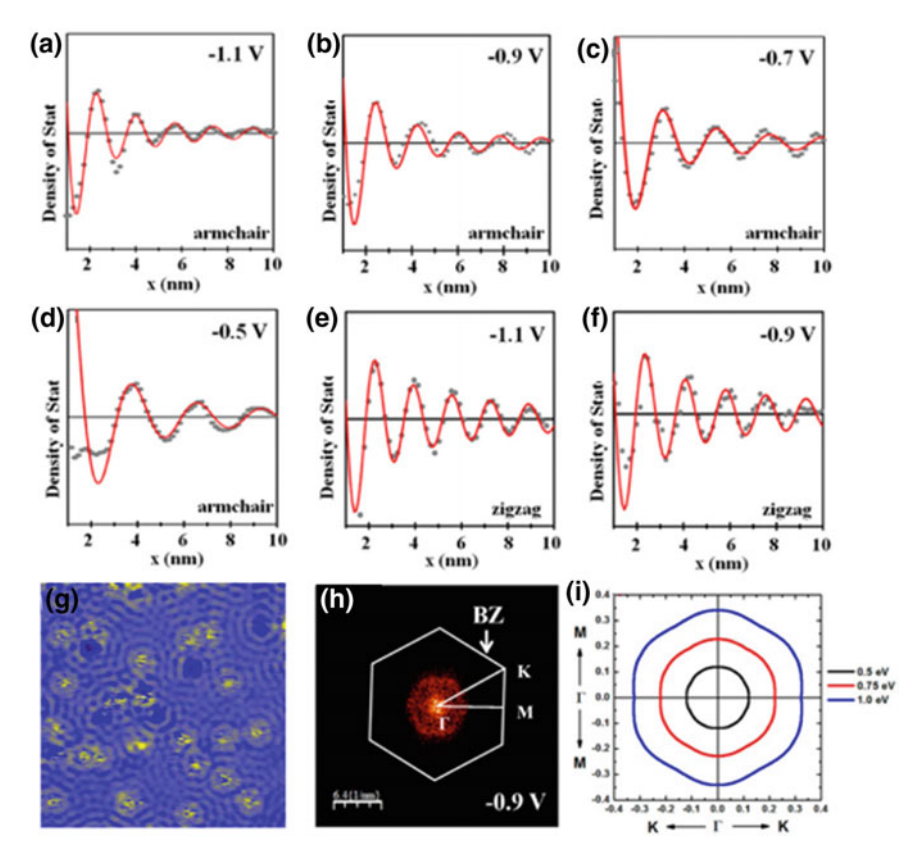


Fig. 9.3 a-f LDOS on monolayer silicene as function of distance from the step edges of silicene  $\sqrt{3} \times \sqrt{3}$  phase at different energies. The data were acquired near armchair edge (a-c) and zigzag edge (d-f). Grey dots: experimental values; red lines: fits to the data. g dl/dV map ( $V_t = -0.9 \text{ V}$ ) of surface of hydrogenated silicene showing standing wave patterns induced by hydrogen sites. h Fourier transform of (g). A hexagon of  $1 \times 1$  Brillouin zone is superimposed. i Constant energy contour of Dirac cone of silicene  $\sqrt{3} \times \sqrt{3}$  phase obtained from DFT calcultions. Reproduced with permission from ACS Nano 7, 9049 (2013)

ley backscattering requires a pseudospin-flip process induced by strong scattering potentials such as the point defects and step edges. For weaker scattering potential such as substrate step beneath the continuous silicene sheets, no QPI patterns had been observed in experiment, which can be viewed as a result of protection by quasiparticle chirality.

The emergence of the QPI patterns resulting from both intervalley and intravalley scattering proves that quasiparticles in silicene behave as massless Dirac fermions. For comparison, although other monolayer silicene phases are also expected to be metallic, QPI patterns have never been observed on their surfaces. Moreover, these results unambiguously reveal that the Dirac cone in silicene is hexagonally warped, and with chirality.

# 9.3.2 Dynamic Phase Transition of the $\sqrt{3} \times \sqrt{3}$ Phase

As we mentioned before, the  $(\sqrt{3} \times \sqrt{3})R30^{\circ}$  phase was found to undergo a phase transition to two types of mirror-symmetric boundary-separated rhombic phases at temperatures below 40 K. The monolayer silicene film on Ag(111) exhibits a honeycomb structure with a period of 0.64 nm (Fig. 9.4b), corresponding to the  $(\sqrt{3} \times \sqrt{3})$ R30° superstructure with respect to the silicene 1 × 1 lattice, for sample temperature at 77 K or up to room temperature [9]. The  $(\sqrt{3} \times \sqrt{3})$ R30° structure can be confirmed by the low energy electron diffraction (LEED) pattern and four predominant orientations of silicene with reference to the [110] direction of Ag(111): 0°, 10°, and 30° were found. More intriguingly, when the sample is cooled to liquid helium temperature (5 K), a dramatic structural phase transition occurs, which is characterized by the appearance of atomic chains forming interconnected triangles. A close inspection reveals that these are boundaries separating two symmetric domains, as shown in Fig. 9.4d. At 77 K, the two neighboring protrusions in each honeycomb unit cell are equally bright. While upon the phase transition, one of them becomes much brighter than the other, showing an apparently rhombic superstructure (Fig. 9.4e). As there are two possible configurations, the surface is phase separated into triangular domains with either one of the two symmetric configurations, separated by narrow domain boundaries where the neighbor protrusions are identically bright. Temperature-dependent experiments show that the phase transition takes place at about 40 K.

The phase transition can be described by a "super-buckling model". It has been known that free-standing silicene maintains a non-planar, so called low-buckled (LB) geometry. When silicene is adsorbed on Ag(111) surface, it further adopts two mirror symmetric  $(\sqrt{3} \times \sqrt{3})R30^\circ$  rhombic super-buckled structures, as illustrated in Fig. 9.4c, f. The low transition barrier between these two phases enables dynamic flip-flop motion at high temperature, resulting in the  $(\sqrt{3} \times \sqrt{3})R30^\circ$  honeycomb structure observed by STM.

Further, Chen et al. performed STS measurements on the  $(\sqrt{3} \times \sqrt{3})$ R30° phase silicene at 5 K [16]. The typical dI/dV curves over wide energy range (from -1.5 to +1.5 V) taken at 5 K reveal similar electronic structures with at 77 K. Besides the pronounced peak at 0.9 V, there is a small dip located at about 0.5 V, which is attributed to the position of DP of silicene. The similar electronic structures of the two phases confirm that their basic structures are identical (Fig. 9.5a).

The dI/dV curve over a narrow energy range around Fermi energy  $(E_F)$  (from 120 to 120 mV) is substantially different at 5 K, as shown in Fig. 9.5b. The spectra obtained on silicene shows a characteristic gap about 70 meV centered exactly at  $E_F$  and two significant shoulder peaks at both sides, while the spectra taken on Ag(111) do not exhibit any gap signature at  $E_F$ . Thus, the gap is not induced by the Ag(111) substrate or STM tip. Also, the STS spectra are measured on different locations of the silicene surface and the gap exhibits high spatial homogeneity. It is possible that the gap may be a superconducting one and the two shoulders are coherence peaks. The observed superconductivity was further explored by varying the sample temperature.

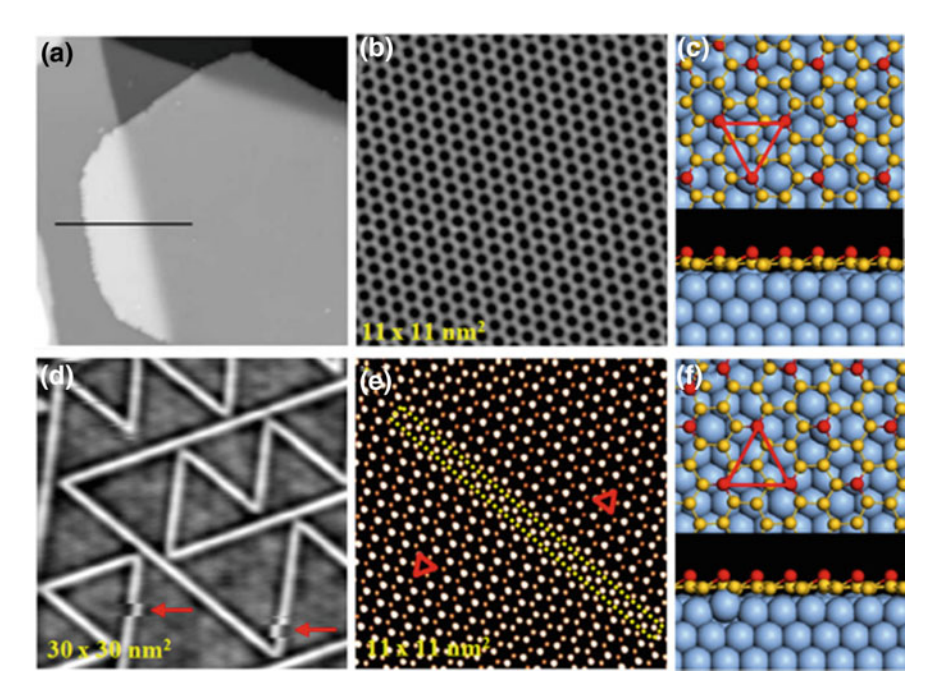
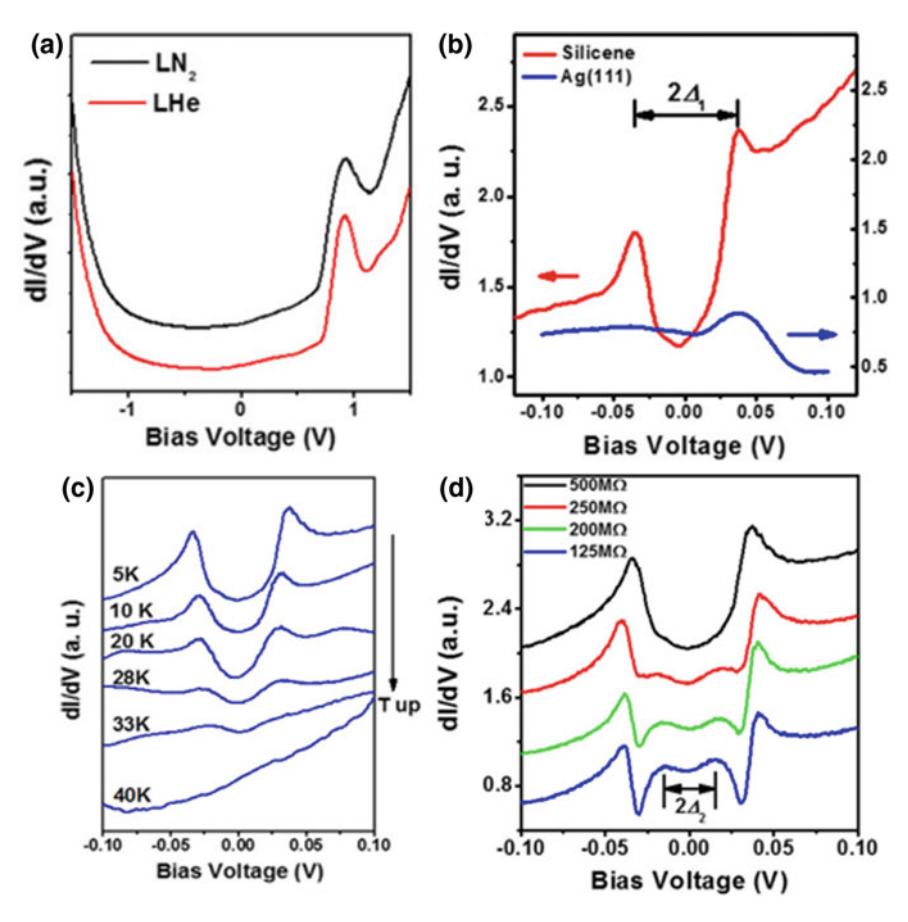


Fig. 9.4 a The STM topography image of a large area  $(65 \times 65 \text{ nm}^2)$  consisting of a sheet of silicene on Ag(111) crossing two substrate steps. Reproduced with permission from Phys. Rev. Lett. 109, 056804 (2012). **b** High-resolution STM image  $(V_t = 1.0 \text{ V})$  of the surface of silicene  $\sqrt{3} \times \sqrt{3}$  phase taken at 77 K. The honeycomb structure is clearly observed. **d** STM image  $(V_t = -2.0 \text{ V})$  of silicene  $\sqrt{3} \times \sqrt{3}$  phase taken at 5 K. **e** The filtered high-resolution STM image with high contrast  $(V_t = 0.1 \text{ V})$  of silicene  $\sqrt{3} \times \sqrt{3}$  phase taken at 5 K. **e** and **f** Models of two energy-degenerated  $\sqrt{3}$  reconstructed structures of silicene sheet on Ag(111). Color code: Blue, yellow, and red spheres denote Ag atoms, Si atoms in lower layer, and Si atoms in higher layer, respectively. The red triangles denote the units of  $\sqrt{3}$  silicene structures. **b**-**f** reproduced with permission from Phys. Rev. Lett. 110, 085504 (2013)

A sequence of dI/dV curves measured over the same monolayer silicene island at different temperatures (Fig. 9.5c) shows that the coherence peaks can be clearly observed up to 28 K. When the temperature is increased to 33 K, the superconducting gap is still observable, but the two coherence peaks start to disappear, indicating the superconducting critical temperature of silicene is about 35–40 K. Additionally, when the tip approaches the surface, the tunneling conductance in the middle of the gap region is lifted (Fig. 9.5d), consistent with expected Andreev reflection in this superconductor-metal junction [43]. This provides another evidence of superconductivity in silicene. Another finding is the emergence of a smaller gap about 30 meV around  $E_F$  when the tip gets close to the surface, which implies that silicene on Ag(111) surface may be a two-band superconductor, similar as MgB<sub>2</sub> [44]. Another possibility is that the smaller gap may be results from the proximity effect. However, these features still need further confirmation.



**Fig. 9.5** a dI/dV curves of silicene  $\sqrt{3} \times \sqrt{3}$  phase with large energy range taken at 77 K and 5 K. b dI/dV curves of silicene  $\sqrt{3} \times \sqrt{3}$  phase and Ag(111) with narrow energy range taken at 5 K. c Temperature dependence of dI/dV curves at same silicene film. d dI/dV curves of silicene  $\sqrt{3} \times \sqrt{3}$  phase taken at different tunneling resistance of tunneling junction between tip and surface. Reproduced with permission from Appl. Phys. Lett. 102, 081602 (2013)

The triangular domain boundaries can also serve as quasiparticle scattering centers to result in pronounced standing wave patterns in STS maps, exhibiting strong QPI patterns because of intravalley scattering in a single Dirac cone. From the bias dependent wavelength of the standing waves, the quasiparticle energy-momentum dispersion relation E(k) was deduced and a linearly energy-momentum dispersion relation was found, with Fermi velocity  $v_F = (0.97 \pm 0.02) \times 10^6 \, \text{m/s}$ . The k=0 energy intercept gives the Dirac energy,  $E_F - E_D = 0.50 \pm 0.02 \, \text{eV}$ , in consistency with the position of DP in dI/dV spectra very well. The electronic structure of silicene is similar to each other for the low temperature and high temperature phases, except for a slightly smaller Fermi velocity for the phase at 5 K than that at 77 K.

The dynamic  $(\sqrt{3} \times \sqrt{3})$ R30° phase of silicene on Ag(111) is energetically stable and contains linear dispersion in the electronic bands. Therefore, it must share the same nontrivial topological properties as the freestanding, low buckled silicene. The stronger buckling of the  $(\sqrt{3} \times \sqrt{3})$ R30° superstructure than that of the freestanding 1 × 1 phase may result in stronger SOC, which will help to realize the QSHE [4] and the QAHE [45]. Moreover, understanding the structure of silicene on metal surfaces will build a base for investigating other important physical phenomena such as superconductivity.

## 9.3.3 Multilayer Silicene on Ag(111)

"Multilayer silicene" films, with increasing thickness more than 30 layers, were successfully fabricated on Ag(111) by Chen et al. [46]. As we mentioned before, monolayer silicene film grown on Ag(111) surface exhibits a variety of different structural phases such as  $4 \times 4$ ,  $\sqrt{13} \times \sqrt{13}$ ,  $\sqrt{7} \times \sqrt{7}$ ,  $2\sqrt{3} \times 2\sqrt{3}$  (with respect to Ag(111) surface lattice) and  $\sqrt{3} \times \sqrt{3}$  (with respect to silicene 1 × 1). In contrast, "multilayer silicene" films only exhibit  $\sqrt{3} \times \sqrt{3}$  honeycomb superstructure (see also Sects. 5.5 and 8.4). The identical  $\sqrt{3} \times \sqrt{3}$  honeycomb superstructure strikingly persists on the surface up to the maximum thickness that have ever been obtained. The line profile shows that the apparent height of the first  $\sqrt{3} \times \sqrt{3}$  layer varies significantly from 0 to 0.48 nm with bias, whereas the height of second  $\sqrt{3} \times \sqrt{3}$ layer, 0.31 nm, is almost constant. This can be explained by the fact that the local density of states (LDOS) is different on the  $\sqrt{3} \times \sqrt{3}$  layer surface and the Ag(111). On the other hand, the almost constant height for thicker  $\sqrt{3} \times \sqrt{3}$  layers indicates the same LDOS for different  $\sqrt{3} \times \sqrt{3}$  layers. The atomically resolved STM images (Fig. 9.6a) near the step edges revealed the ABC stacking sequence of Si layers for all different layer thickness (Fig. 9.6b). In addition, the layer distance, 0.31 nm, coincides with the layer distance in bulk Si(111) layers. Both the above two facts point to a conclusion that the so-called "multilayer silicene" is actually a bulk-like Si(111) film, but with  $\sqrt{3} \times \sqrt{3}$  honeycomb reconstruction on its surface.

Typical dI/dV curves obtained on surfaces with different thickness, as shown in Fig. 9.6d, reveal similar features: a pronounced peak at positive bias 0.9–1.1 V and a DOS onset at negative bias 0.7–0.9 V. While the film thickness increases, the positions of the peak and LDOS onset both shift slightly to the right. The differential conductance (dI/dV) maps show obviously standing waves corresponding to quasiparticle interference (QPI) patterns. Such QPI patterns can be observed on Si films of all different thicknesses, even above 30 ML. This indicates that the metallic surface state is delocalized, and it should originate from the  $\sqrt{3} \times \sqrt{3}$  superstructure on the surface, and not from the Ag(111) substrate. There are two types of step edges: zigzag and armchair. The dI/dV map (shown in Fig. 9.6e) taken at same area as Fig. 9.6c shows QPI patterns near both step edges. The energy-momentum dispersion relation E(k) curves deduced from standing waves near armchair and zigzag step edges correspond to dispersions at Γ-K and Γ-M directions of Brillouin zone (BZ),

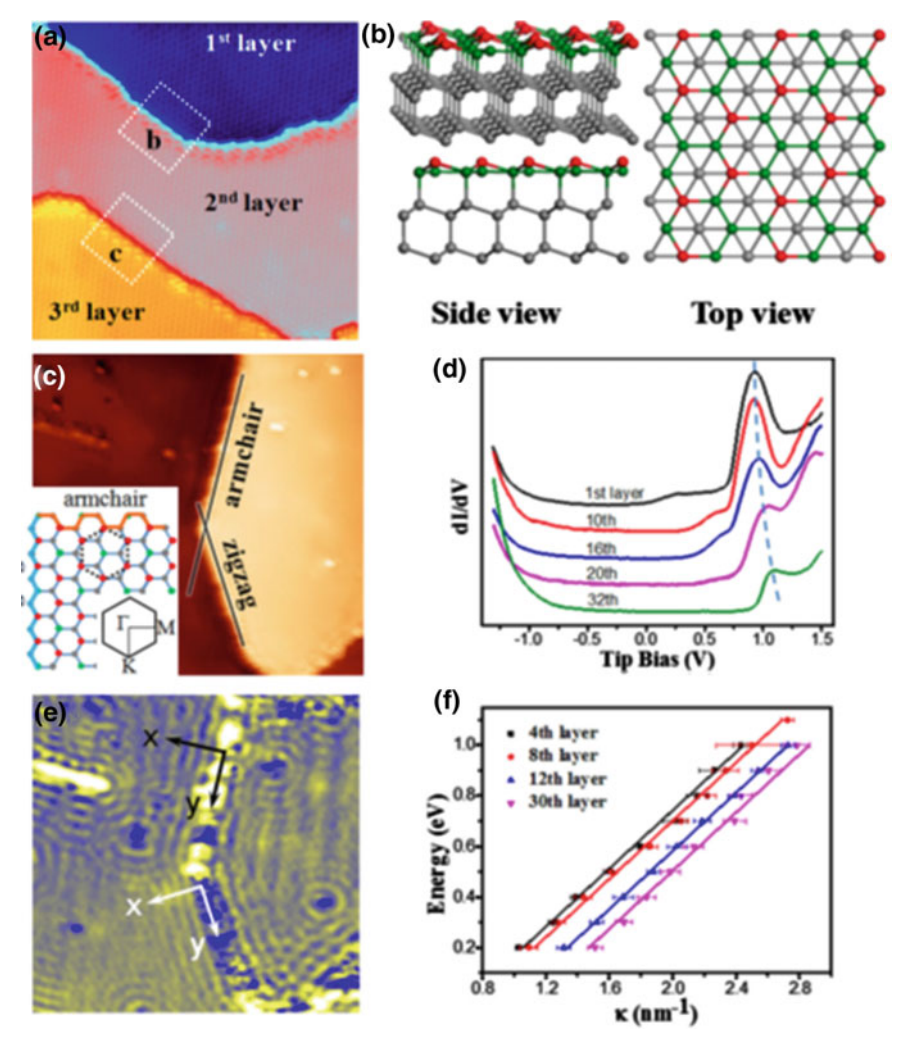


Fig. 9.6 a The STM image ( $V_t = 1.2 \text{ V}, I = 100 \text{ pA}, 25 \times 25 \text{ nm}^2$ ) of Si film with three continuous terraces. b The side and top view of the atomic model of Si film with  $\sqrt{3} \times \sqrt{3}$  reconstruction. c STM image ( $V_t = -0.4 \text{ V}, I = 100 \text{ pA}, 45 \times 45 \text{ nm}^2$ ) obtained on top of Si film of 20 ML, containing an island with both armchair and zigzag step edges. Inset: the atomic model of  $\sqrt{3} \times \sqrt{3}$  superstructure of Si. d dI/dV curves obtained on surface of Si films with different thickness. The curves are vertically shifted for clarity. e dI/dV map ( $V_t = -0.4 \text{ V}, I = 200 \text{ pA}, 45 \times 45 \text{ nm}^2$ ) of the same area as (c) showing obvious standing wave. f E(k) curves (armchair edge) obtained on surface of Si films with different thickness on Ag(111) surface. Reproduced with permission from Sci. Rep. 5, 13590 (2015)

respectively. Figure 9.6f shows the curves along  $\Gamma$ -K for films with thickness of 4, 8, 12 and 31 ML. All the curves exhibit linear energy-momentum dispersion with

194 P. Cheng et al.

the same slopes, but are right shifted with increasing thickness, which coincides well with the right shift of peak position in dI/dV curves shown in Fig. 9.6d.

In addition, Chen et al. reported that the silicene film can be peeled off by the STM tip, exposing the surface of the underneath layer. The high resolution STM image shows the atomic structures of the underneath layer to be  $\sqrt{3} \times \sqrt{3}$  phase, identical to the top layer. This phenomenon clarifies the existing debates that whether the  $\sqrt{3} \times \sqrt{3}$  structure (on both 2-ML and multilayer silicene film surfaces) is a pure silicone structure, or it is simply the well-known Si(111)( $\sqrt{3} \times \sqrt{3}$ )-Ag structure that was conventionally observed in a single crystal Si(111) surface with 1 ML Ag adatoms, as suggested by Shirai et al. [47] As we know, the Si(111)( $\sqrt{3} \times \sqrt{3}$ )-Ag structure consists of only one layer of Ag atoms on top of pure Si(111) substrate, and it forms at temperature above 700 K. Supposing that the  $\sqrt{3} \times \sqrt{3}$  structure comes from Si(111)( $\sqrt{3} \times \sqrt{3}$ )-Ag, when the top layer was removed, we should not observe the reconstruction on the underneath layer, which is a pure silicon surface. Therefore, ( $\sqrt{3} \times \sqrt{3}$ )R30° reconstruction is not the Si(111)( $\sqrt{3} \times \sqrt{3}$ )-Ag, but is an intrinsic structure of pure Si.

#### 9.4 Conclusions

After the experimental synthesis of silicene sheet on Ag(111) in 2012, there have been many significant achievements in this field. In this brief review, we summarized some basic properties of silicene which have been established by utilizing cryogenic STM, combining with theoretical calculations. However, the research of silicene is still at its early stage. Theoretical works proposed various intriguing properties of silicene, including QSHE, QAHE and unconventional properties tuned by external electric and magnetic fields. These predictions put forward great challenges to material synthesis and experimental measurements and there will be much work to do to realize the potential application of this dramatic system.

#### References

- 1. K. Takeda, K. Shiraishi, Phys. Rev. B 50, 14916 (1994)
- 2. G.G. Guzman-Verri, L.C. Lew Yan Voon, Phys. Rev. B 76, 075131 (2007)
- 3. S. Cahangirov, M. Topsakal, E. Aktürk, H. Şahin, S. Ciraci, Phys. Rev. Lett. 102, 236804 (2009)
- 4. C.C. Liu, W.X. Feng, Y.G. Yao, Phys. Rev. Lett. 107, 076802 (2011)
- A. Fleurence, R. Friedlein, T. Ozaki, H. Kawai, Y. Wang, Y. Yamada-Takamura, Phys. Rev. Lett. 108, 245501 (2012)
- P. Vogt, P. De Padova, C. Quaresima, J. Avila, E. Frantzeskakis, M.C. Asensio, A. Resta, B. Ealet, G. Le Lay, Phys. Rev. Lett. 108, 155501 (2012)
- C.L. Lin, R. Arafune, K. Kawahara, N. Tsukahara, E. Minamitani, Y. Kim, N. Takagi, M. Kawai, Appl. Phys. Express 5, 045802 (2012)
- 8. B.J. Feng, Z.J. Ding, S. Meng, Y.G. Yao, X.Y. He, P. Cheng, L. Chen, K.H. Wu, Nano Lett. 12, 3507 (2012)

- 9. L. Chen, C.C. Liu, B.J. Feng, X.Y. He, P. Cheng, Z.J. Ding, S. Meng, Y.G. Yao, K.H. Wu, Phys. Rev. Lett. **109**, 056804 (2012)
- 10. G. Binnig, H. Rohrer, Helv. Phys. Acta 55, 726 (1982)
- 11. G. Binnig, H. Rohrer, Ch. Gerber, E. Weibel, Appl. Phys. Lett. 40, 178 (1982)
- 12. G. Binnig, H. Rohrer, Ch. Gerber, E. Weibel, Phys. Rev. Lett. 49, 57 (1982)
- 13. G. Binnig, H. Rohrer, Rev. Mod. Phys. 56, 615 (1987)
- 14. J. Lambe, R.C. Jaklevic, Phys. Rev. **165**, 821 (1968)
- B.J. Feng, H. Li, C.C. Liu, T.N. Shao, P. Cheng, Y.G. Yao, S. Meng, L. Chen, K.H. Wu, ACS Nano 7, 9049 (2013)
- L. Chen, H. Li, B.J. Feng, Z.J. Ding, J.L. Qiu, P. Cheng, L. Chen, K.H. Wu, S. Meng, Phys. Rev. Lett. 110, 085504 (2013)
- 17. L. Chen, B.J. Feng, K.H. Wu, Appl. Phys. Lett. 102, 081602 (2013)
- 18. A. Resta, T. Leoni, C. Barth, A. Ranguis, C. Becker, T. Bruhn et al., Sci. Rep. 3, 2399 (2013)
- 19. J. Avila, P. De Padova, S. Cho, I. Colambo, S. Lorcy, C. Quaresima et al., J. Phys.: Condens. Matter 25, 262001 (2013)
- C.L. Lin, R. Arafune, K. Kawahara, M. Kanno, N. Tsukahara, E. Minamitani, Y. Kim, M. Kawai, N. Takagi, Phys. Rev. Lett. 110, 076801 (2013)
- 21. Z.X. Guo, S. Furuya, J.I. Iwata, A. Oshiyama, Phys. Rev. B 87, 235435 (2013)
- 22. Z.X. Guo, S. Furuya, J.I. Iwata, A. Oshiyama, J. Phys. Soc. Jpn. 82, 063714 (2013)
- D. Tsoutsou, E. Xenogiannopoulou, E. Golias, P. Tsipas, A. Dimoulas, Appl. Phys. Lett. 103, 231604 (2013)
- 24. P. Gori, O. Pulci, F. Ronci, S. Colonna, F. Bechstedt, J. Appl. Phys. 114, 113710 (2013)
- S. Cahangirov, M. Audiffred, P. Tang, A. Iacomino, W.H. Duan, G. Merino, A. Rubio, Phys. Rev. B 88, 035432 (2013)
- 26. Y. Yuan, R.G. Quhe, J. Zheng, Y. Wang, Z. Ni, J. Shi, J. Lu, Physica E 58, 38 (2014)
- R.G. Quhe, Y. Yuan, J. Zheng, Y. Wang, Z. Ni, J. Shi, D. Yu, J. Yang, J. Lu, Sci. Rep. 4, 5476 (2014)
- R. Dombrowski, C. Wittneven, M. Morgenstern, R. Wiesendanger, Appl. Phys. A 66, S203 (1998)
- T. Matsui, H. Kambara, Y. Niimi, K. Tagami, M. Tsukada, H. Fukuyama, Phys. Rev. Lett. 94, 226403 (2005)
- 30. G.H. Li, E.Y. Andrei, Nat. Phys. 3, 623 (2007)
- 31. D.L. Miller, K.D. Kubista, G.M. Rutter et al., Science **324**, 924 (2009)
- 32. M.F. Crommie, C.P. Lutz, D.M. Eigler, Nature 363, 524 (1993)
- 33. Y. Hasegawa, Ph Avouris, Phys. Rev. Lett. **71**, 1071 (1993)
- 34. G.M. Rutter, J.N. Crain, N.P. Guisinger, T. Li, P.N. First, J.A. Stroscio, Science 317, 219 (2007)
- I. Brihuega, P. Mallet, C. Bena, S. Bose, C. Michaelis, L. Vitali, F. Varchon, L. Magaud, K. Kern, J.Y. Veuillen, Phys. Rev. Lett. 101, 206802 (2008)
- J. Xue, J. Sanchez-Yamagishi, K. Watanabe, T. Taniguchi, P. Jarillo-Herrero, B.J. LeRoy, Phys. Rev. Lett. 108, 016801 (2012)
- 37. C. Berger et al., Science **312**, 1191 (2006)
- A.H. Castro Neto, F. Guinea, N.M.R. Peres, K.S. Novoselov, A.K. Geim, Rev. Mod. Phys. 81, 109 (2009)
- J. Wang, W. Li, P. Cheng, C.L. Song, T. Zhang, P. Deng, X. Chen, X.C. Ma, K. He, J.F. Jia et al., Phys. Rev. B 84, 235447 (2011)
- Z. Alpichshev, J.G. Analytis, J.H. Chu, I.R. Fisher, Y.L. Chen, Z.X. Shen, A. Fang, A. Kapitulnik, Phys. Rev. Lett. 104, 016401 (2010)
- 41. M. Houssa, E. Scalise, K. Sankaran, G. Pourtois, V.V. Afanas'ev, A. Stesmans, Appl. Phys. Lett. 98, 223107 (2011)
- F.V. Tikhonenko, D.W. Horsell, R.V. Gorbachev, A.K. Savchenko, Phys. Rev. Lett. 100, 056802 (2012)
- 43. D. Daghero, M. Tortello, G.A. Ummarino, R.S. Gonnelli, Rep. Prog. Phys. 74, 124509 (2011)
- 44. X.X. Xi, Rep. Prog. Phys. **71**, 116501 (2008)
- 45. M. Ezawa, Phys. Rev. Lett. 109, 055502 (2012)

196 P. Cheng et al.

46. J. Chen, Y. Du, Z. Li, W.B. Li, B.J. Feng, J.L. Qiu, P. Cheng, S.X. Dou, L. Chen, K.H. Wu, Sci. Rep. 5, 13590 (2015)

47. T. Shirai, T. Shirasawa, T. Hirahara, N. Fukui, T. Takahashi, S. Hasegawa, Phys. Rev. B 89, 241403 (2014)

# Chapter 10 Synthesis of Silicene on Alternative Substrates



M. Houssa, E. Scalise, V. V. Afanas'ev and A. Stesmans

Abstract Silicene has so far been successfully grown on metallic substrates, like Ag(111),  $ZrB_2(0001)$  and Ir(111) surfaces. However, the characterization of its electronic structure is hampered by the metallic substrate. In addition, potential applications of silicene in nanoelectronic devices will require its growth/integration with semiconducting or insulating substrates. In this chapter, we review recent theoretical works about the interaction of silicene with several non-metallic templates, distinguishing between the weak van der Waals like interaction of silicene with e.g. AlN or layered metal (di)chalcogenides, and the stronger covalent bonding between silicene and e.g. ZnS surfaces. Recent experimental results on the possible growth of silicene on  $MoS_2$  are also highlighted and compared to the theoretical predictions.

### 10.1 Introduction

Very recently, the formation of silicene was reported on various metallic surfaces, like (111)Ag surfaces [1–6], (0001)ZrB<sub>2</sub> surfaces [7, 8] and (111)Ir [9] surfaces. The electronic properties of the silicene layer on (111)Ag was investigated using angle-resolved photoemission spectroscopy. These measurements revealed the presence of a linear dispersion in the band structure of silicene (so called Dirac cones) with a Fermi velocity of about  $1.3 \times 10^6$  m/s, as theoretically predicted for free-standing silicene. A recent breakthrough paved the way to the possible realization of silicene-based field effect transistors operating at room temperature [10], presenting ambipolar current-voltage characteristics, as expected for a gapless semiconductor.

M. Houssa (⊠) · V. V. Afanas'ev · A. Stesmans Department of Physics and Astronomy, University of Leuven, Celestijnenlaan 200D, 3001 Louvain, Belgium e-mail: Michel.Houssa@fys.kuleuven.be

E. Scalise

Department of Materials Science, University of Milano-Bicocca, U5-2023, Via R. Cozzi 55, 20125 Milano, Italy e-mail: scalise@unimib.it

The possible existence of silicene was so far reported on these metallic substrates. However, the characterization of the electronic and electrical properties of silicene on metallic substrates is very challenging, since these properties are then largely dominated by the metal. The growth of silicene on semiconducting or insulating substrates is required for their firm identification and complete characterization. In addition, potential applications of this novel 2D material in nanoelectronic devices will also require its growth and integration on non-metallic substrates.

We review here recent theoretical results, based on density-functional theory (DFT) calculations, pertaining to the interaction of silicene with non-metallic surfaces. We first discuss the weak (van der Waals) interaction of silicene with e.g. AlN and layered dichalcogenide substrates. On these templates, silicene is predicted to be either metallic or semi-metallic (with preserved Dirac cones at the k-points), depending on its buckling. Recent experimental results on the possible growth of silicene on MoS<sub>2</sub> are discussed and compared to the theoretical predictions.

We next discuss the covalent bonding of silicene on e.g. (0001)ZnS surfaces. The charge transfer occurring at the silicene/(0001) ZnS interface leads to the opening of an indirect energy band gap in silicene. Very interestingly, it is found that the nature (indirect or direct) and magnitude of its energy band gap can be controlled by an external electric field, a results potentially very interesting for field-effect devices.

# 10.2 Silicene/Substrate Interaction: Weak van der Waals Bonding

Layered semiconducting materials, with strong intra-layer covalent bonding and weak inter-layer van der Waals bonding, are expected to interact weakly with silicene, potentially preserving its peculiar electronic properties [11–19]. We discuss here the weak interaction of silicene with two different type of layered materials, namely graphite-like AlN [11, 12] and semiconducting transition metal dichalcogenides [13–16].

AlN is and insulator (energy band gap of about 6.5 eV [20]) which crystallizes in the wurtzite phase, with in-plane lattice parameters a = b = 3.11 Å and out-of-plane lattice parameter c = 4.98 Å [21]. Very interestingly, the polar (0001) AlN surface is predicted to evolve to a more stable graphite-like structure [11, 22], with the Al and N atoms adopting a sp²-hydridization, as shown in Fig. 10.1. The graphite-like form of AlN is insulating, with a computed energy band-gap of about 4.6 eV, and is more stable than the (0001) AlN polar surface by about 0.27 eV/atom [11]. This predicted structural and electronic "phase transition" in AlN is consistent with first-principles calculations on ultra-thin wurtzite films [22]. The driving force for the planarization and  $sp^2$ -hybridization of the AlN layers is the suppression of the strong dipole between the bottom and the top surface of the film, which are terminated either by anions or cations; this transition depends on the electronegativity difference between the anions and cations as well as the energy gap of the material, leading to a thick-

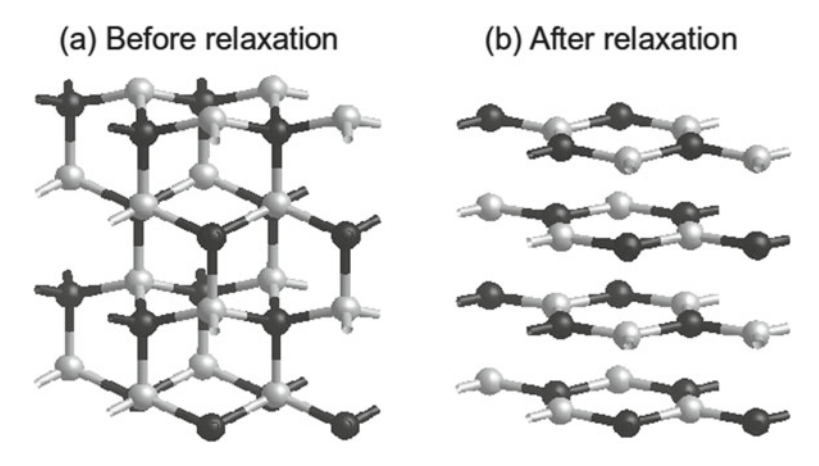


Fig. 10.1 Atomic configuration of a (0001) AlN slab model,  $\mathbf{a}$  in wurtzite form (before structural relaxation) and  $\mathbf{b}$  in graphite-like form (after relaxation). Light gray and dark gray spheres represent Al and N atoms, respectively

ness dependence of this transition [22]. The graphite-like form of AlN is predicted to be more stable than the (0001) wurtzite structure up to 24 layers, corresponding to a layer thickness of about 2.6 nm. Very interestingly, the possible growth of graphite-like AlN on Ag (111) surfaces has been recently observed experimentally [23].

The possibility of inserting a silicene "flake" (i.e. a silicene ribbon terminated by H atoms) in-between a graphite-like AlN lattice was then considered [11, 12]. In this configuration, the top AlN layer could serve as an efficient barrier against the diffusion of chemical species towards the silicene surface. The starting configuration corresponds to a compressively strained flat silicene ribbon inserted between two AlN layers, as shown in Fig. 10.2. During the energy relaxation, the Si-Si bond length increases and reaches its free-standing value of about 2.2 Å. After relaxation, the silicene layer is buckled, with a buckling distance of about 0.21 Å, which is lower than its predicted free-standing buckling distance (about 0.44 Å). In this configuration, the silicene layer weakly interacts with the AlN layers via van der Waals forces, the computation of the partial (Mulliken) atomic charges on the Si, Al, and N atoms indicating no net charge transfer between Si and the Al or N atoms. However, the weak interaction between the Si p<sub>z</sub> orbitals and the out-of-plane dipole formed between the Al and N atoms from the bottom and top AlN layers, respectively, is likely responsible for the reduced silicene buckling, as compared to its free-standing configuration. In this van der Waals like AlN/silicene/AlN heterostructure, silicene is predicted to be a gapless semiconductor, as shown in Fig. 10.3, due to the preserved  $sp^2-sp^3$  mixed hybridization of the Si atoms.

Van der Waals interactions play also a crucial role for the family of materials known as (layered) transition metal chalcogenides, having MoS<sub>2</sub> as the most noted representative. These materials are composed by metal-chalcogenide layers, having

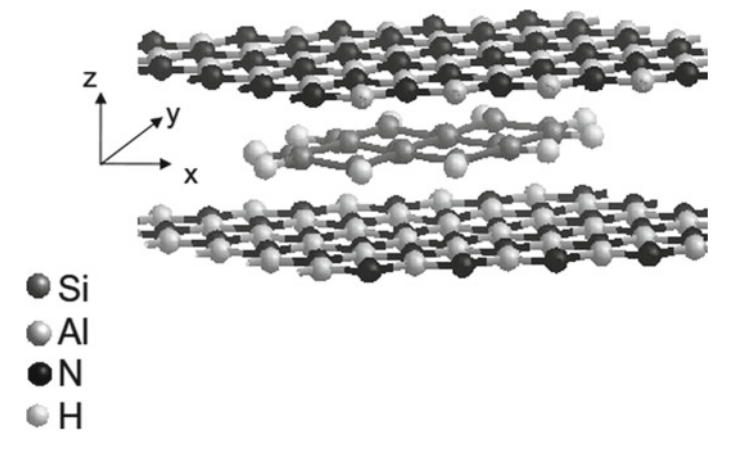
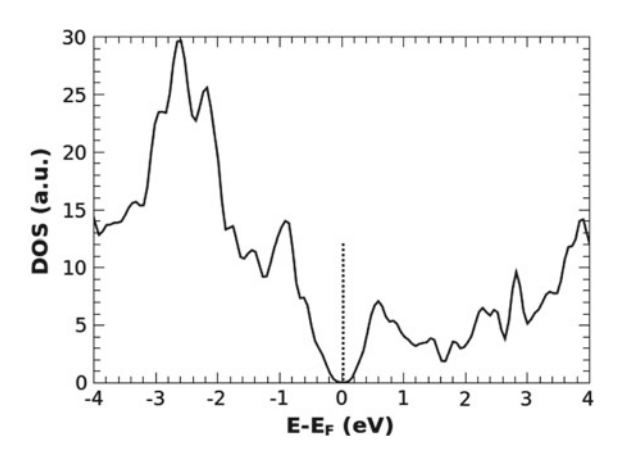


Fig. 10.2 Relaxed atomic configuration of a AlN/silicene/AlN (van der Waals) heterostructure

Fig. 10.3 Computed electronic density of states of the AlN/silicene/AlN heterostructure shown in Fig. 10.2



a hexagonal structure similar to silicene, which are kept together by the van der Waals interactions. Ionic-covalent bonds between the transition metal and the chalcogenide elements ensure the in-plane stability of the layers. Because of their layered structure, transition metal chalcogenide bulk crystals can be exfoliated in order to obtain few-layers thin flakes or even monolayers, with "ideal" surfaces having no dangling bonds. Thus, transition metal chalcogenides are perfect substrates for other (2D) layered materials, such as graphene, and optimal candidate as template for silicene.

 $MoS_2$  is an indirect band-gap semiconductor (gap = 1.2 eV [24]) and its hexagonal structure has an in-plane lattice parameter of 3.16 Å [24] (about 18.3% smaller than the lattice parameter of free standing silicene). Single layer  $MoS_2$  is a direct-gap semiconductor with a band-gap of about 1.9 eV [25–27]. Suspended mono-layer  $MoS_2$  has also been realized [28, 29] and its properties have been investigated both experimentally [25–27] and theoretically [30–32].

We placed flat silicene layers on bulk MoS<sub>2</sub> in order to study their interactions. First, the flat silicene was squeezed in order to match the lattice of MoS<sub>2</sub> and then different possible arrangements of the silicon atoms on the MoS2 surface were considered, as discussed in more details in [14]. The bulk MoS<sub>2</sub> substrate was modeled by using 4 MoS<sub>2</sub> layers, with the two bottom layers "frozen" at their bulk position. A supercell with about 15 Å vacuum layer was used for the DFT simulations. After energy relaxation, the silicene layer placed on MoS<sub>2</sub> turned out to be buckled, with the Si top and bottom atoms showing a vertical distance of about 1.9 Å (cf. Fig. 10.4). The energy difference between the various arrangements of silicene on MoS<sub>2</sub> is about 3 meV/atom, indicating a degeneracy of the different configurations and hence very weak (van der Waals) interactions between silicene and MoS<sub>2</sub>. The adhesion energy of the silicene layer on MoS2, estimated as the difference between the energy of the silicene/MoS<sub>2</sub> system and the sum of the energies of the isolated silicene layer and MoS<sub>2</sub> substrate, was calculated to be about 200 meV per unit cell. This is a value very close to the reported interlayer binding energy in bulk-layered materials, like graphite [33], thus confirming the vdW nature of the Si/MoS<sub>2</sub> interaction. The silicon/MoS<sub>2</sub> interlayer distance was predicted to be about 3.5 Å (cf. Fig. 10.4), a value comparable to the typical inter-layer distance in vdW-bonded layered materials, like MoS<sub>2</sub>, h-BN or graphite [33]. Both the Si buckling distance and the Si-MoS<sub>2</sub> distance are in very good agreement with experimental STM results (see Fig. 10.5), where the step profile between a Si domain and the MoS<sub>2</sub> substrate amounts to 3 Å and exhibits a feature at about 2 Å consistently with the highly buckled silicene arrangement (see the picture in Fig. 10.4c). Details about the experiments can be found in [3]. Although further experimental investigations are necessary to corroborate the growth of silicene on MoS<sub>2</sub>, the relatively good agreement between the experimental measurements on Si nanosheets with local hexagonal symmetry [16] and the computed structural properties of silicene on MoS<sub>2</sub> is a further confirmation of the weak interaction of silicene with MoS<sub>2</sub>.

The calculated buckling distance of the silicene layer on MoS<sub>2</sub> is very close to that obtained from the simulated highly buckled (HB) freestanding silicene structure [34], which contrary to the low buckled and flat layers, is predicted to be metallic. The calculated band structures and local density of states (LDOS) for silicene on bulk MoS<sub>2</sub> also indicate a metallic character, as shown in Fig. 10.6. Particularly, the LDOS shows that the density of states of the MoS<sub>2</sub> substrate still preserve a gap very close to that of the bare MoS<sub>2</sub>, while all the electronic states close to the Fermi level are due to the contribution of Si atoms, confirming that almost no hybridization between Si and Mo/S atomic orbitals is induced.

We next investigated the possibility of inserting a silicene layer in between two MoS<sub>2</sub> layers, forming a sandwich configuration. In this configuration, the top MoS<sub>2</sub> layer could serve as a capping layer against the diffusion of chemical species towards the silicene surface, similar to the case of AlN mentioned above. Also in this case, the starting configuration was a flat silicene layer inserted in between the two MoS<sub>2</sub> layers. Interestingly, an out-of plane buckling of the silicene layer was also observed after relaxation, with a Si–Si buckling distance very close to that calculated for the silicene layer on bulk MoS<sub>2</sub> (1.9 Å). The calculated interlayer Si/MoS<sub>2</sub> dis-

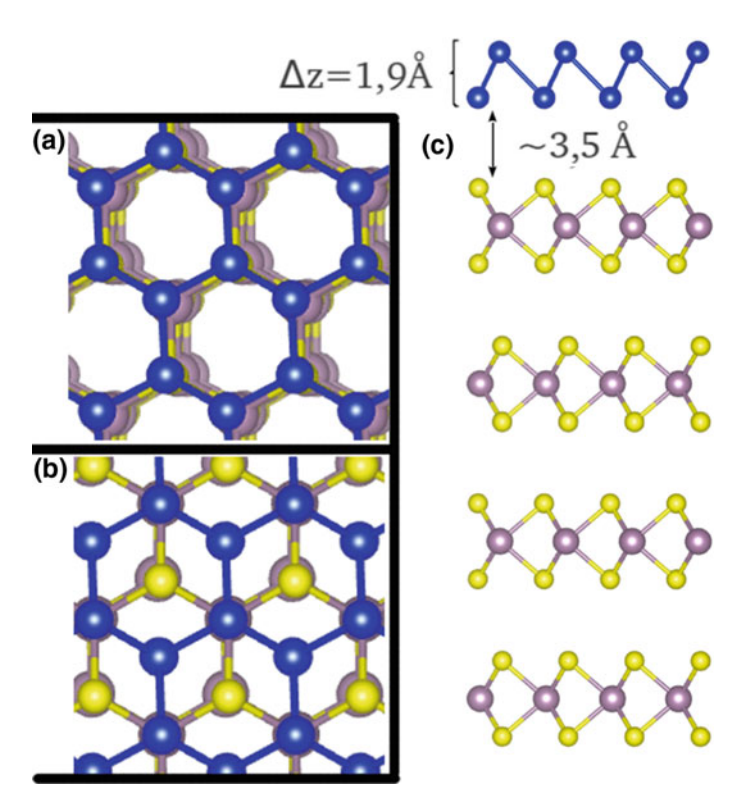


**Fig. 10.4** Relaxed atomic configuration of silicene on bulk MoS<sub>2</sub> (in **a** and **c** the top and side view is shown, respectively). In **b** the top view of a different configuration is also shown [14]. Blue, yellow and green spheres are Si, S and Mo atoms, respectively

tance, in the range of 3–3.5 Å, confirmed that vdW interactions between the silicene and the  $MoS_2$  layers are preserved also in the sandwich configuration. The relaxed  $MoS_2$ /silicene/ $MoS_2$  structure was predicted to be metallic, similarly to the case of silicene on  $MoS_2$ .

Finally, we studied the case of a silicene layer on a single layer  $MoS_2$  and no marked differences with respect to the case of silicene on bulk  $MoS_2$  were found, both from the structural and electronic point of view.

Bond buckling can dramatically alter the electronic properties of the silicene layer because of its impact on the Si–Si bonds. The high buckling of the silicene layer on MoS<sub>2</sub> essentially originates from the lattice mismatch between the silicene layer (in its free standing low buckled form) and the MoS<sub>2</sub> (about 18% of lattice mismatch). In order to possibly obtain a silicene layer with lower buckling, we investigated other substrates than MoS<sub>2</sub>, with very similar structural properties but larger in-plane lattice parameter, namely MoSe<sub>2</sub> and MoTe<sub>2</sub>. Similarly to MoS<sub>2</sub>, bulk MoSe<sub>2</sub> and MoTe<sub>2</sub> are indirect bandgap materials, with a gap of about 1.1 and 1.0 eV, respectively [35, 36]. The unit cell of the hexagonal structure of MoSe<sub>2</sub> and MoTe<sub>2</sub> has an in-plane

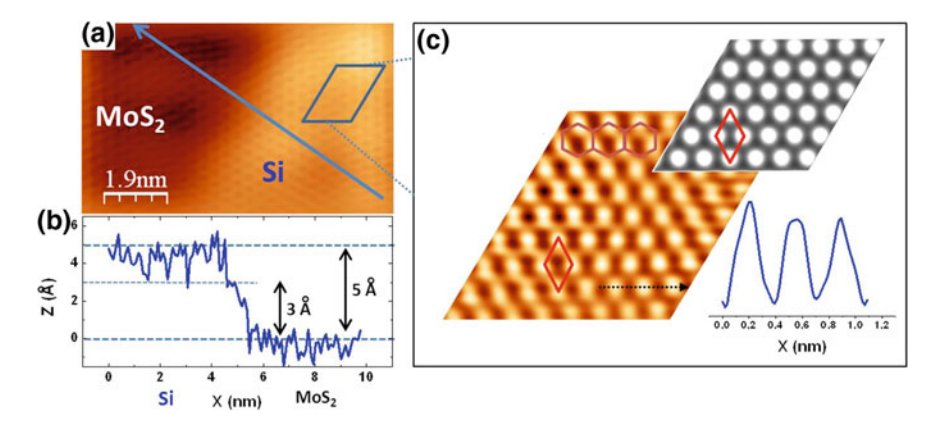


**Fig. 10.5** a Higher resolution STM image of a partially Si-covered  $MoS_2$  surface [16]. The left side and the right side of the image correspond to a portion of bare  $MoS_2$  and a Si covered region, respectively. A line profile taken across the two terraces, measuring the amplitude of the step, is shown in (b). In c the magnified topography after (fast Fourier transform) filtering evidences the hexagonal surface. A simulated STM image of silicene on  $MoS_2$  is shown as (top) inset. A line profile following the black arrow drawn in the STM image is plotted in the bottom inset

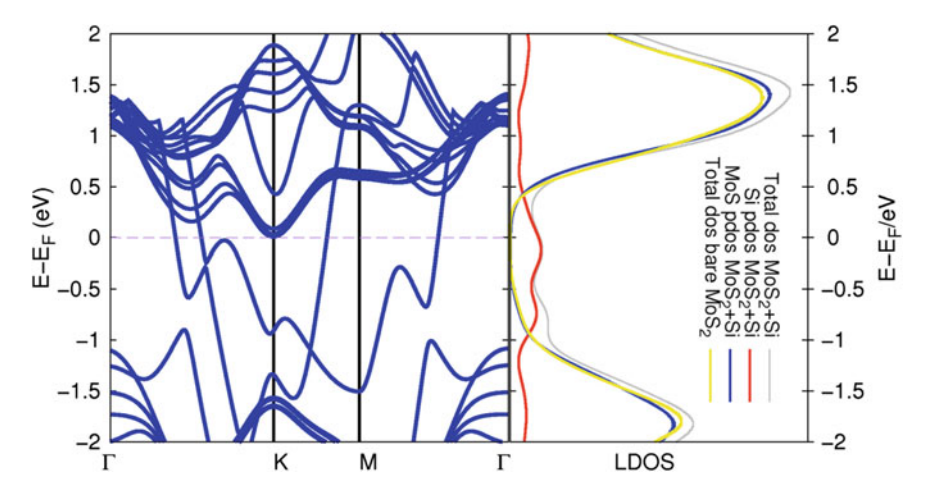


Fig. 10.6 Band structures and local density of states of the Silicene/MoS<sub>2</sub> structure [14]

lattice parameter of about 3.3 and 3.5 Å, respectively, i.e. about 15% and 9% smaller than free standing silicene.

Like in the  $MoS_2$  case, we started with different initial atomic configurations, which after energy relaxation showed almost the same total energy, typically within 10 meV/atom. For all the studied configurations, the flat silicene layer, both on  $MoSe_2$  and  $MoTe_2$ , buckled after the atomic relaxation, with a buckling distance of about 1 Å on  $MoSe_2$  and 0.7 Å on  $MoTe_2$ ; this latter value is very close to the buckling estimated for the  $3 \times 3$  silicene layer on Ag(111)[1]. Very interestingly, its calculated

M. Houssa et al.

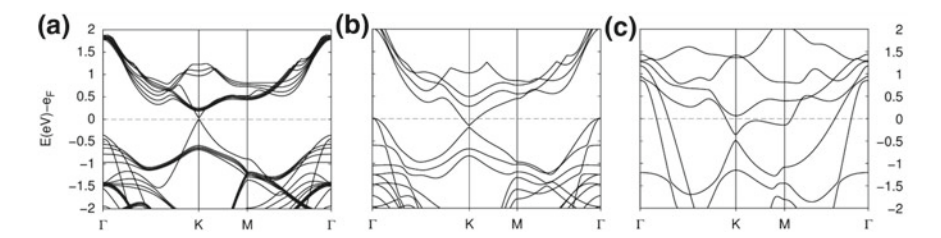


Fig. 10.7 Electronic band structure of the silicene layer on bulk MoTe<sub>2</sub> (a), monolayer MoTe<sub>2</sub> (b) and MoSe<sub>2</sub> (c) [14]

electronic band structure (see Fig. 10.7a) revealed that silicene on bulk MoTe<sub>2</sub> is a gapless-semiconductor, due to the typical  $sp^2$ -like hydridization of the Si atoms in low-buckled silicene [37]. Contrary, the calculations of silicene on a monolayer MoTe<sub>2</sub> or placed in between two MoTe<sub>2</sub> layers revealed that silicene presents a higher buckling ( $\sim 0.77 \text{ Å}$ ) compared to the case of bulk MoTe<sub>2</sub> substrate, due to the stronger interaction of the silicene layer with the MoTe<sub>2</sub> monolayer. This was confirmed by the adhesion energy of silicene in the two systems, which is about 5% higher for silicene on monolayer MoTe<sub>2</sub> than silicene on bulk MoTe<sub>2</sub>. Consequently, silicene on a MoTe<sub>2</sub> monolayer or in between two MoTe<sub>2</sub> layers is metallic, as shown in Fig. 10.7b, though with preserved Dirac cones at the K points. Similarly, the study of silicene on bulk MoSe<sub>2</sub> as well as on MoSe<sub>2</sub> monolayer or in-between two MoSe<sub>2</sub> layers revealed that these systems are metallic (see Fig. 10.7c), due to the substantial higher buckling of silicene on MoSe<sub>2</sub> with respect to silicene on MoTe<sub>2</sub>.

## 10.3 Silicene/Substrate Interaction: Covalent Bonding

The formation of covalent bonds between silicene and an underlying substrate can result in the partial or complete  $sp^3$  hybridization of the Si atoms, and consequently, in the opening of an energy gap in its electronic structure-like e.g. in silicene functionalized by the adsorption of ad-atoms [38–43]; we discuss here the covalent bonding between silicene and ZnS surfaces [44, 45], as a typical example of a stronger interaction (compared to the weak van der Waals bonding) between silicene and a non-metallic substrate.

ZnS crystallizes in the Wurtzite phase [21, 46] and is a semiconductor, with a direct energy band-gap of about 3.8 eV. Interestingly, its in-plane lattice constant (3.81 Å) is very close to the computed one of free-standing silicene, (about 3.9 Å), ZnS thus appearing as an ideal non-metallic template for the growth of silicene. A (0001) polar ZnS surface is considered here as a possible template for silicene [44]. A slab model with 8 atomic layers (64 atoms) and with a 15 Å vacuum layer was used for the DFT simulations. Displacements of the top and bottom ZnS layers was observed during atomic relaxation, resulting in a surface reconstruction very

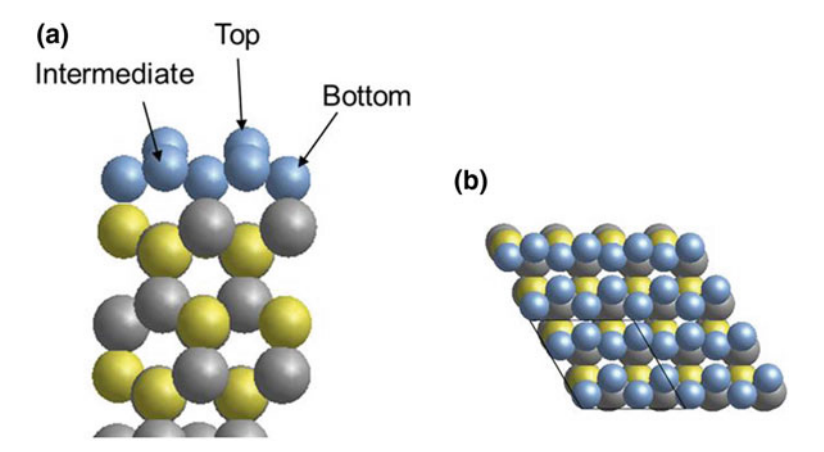
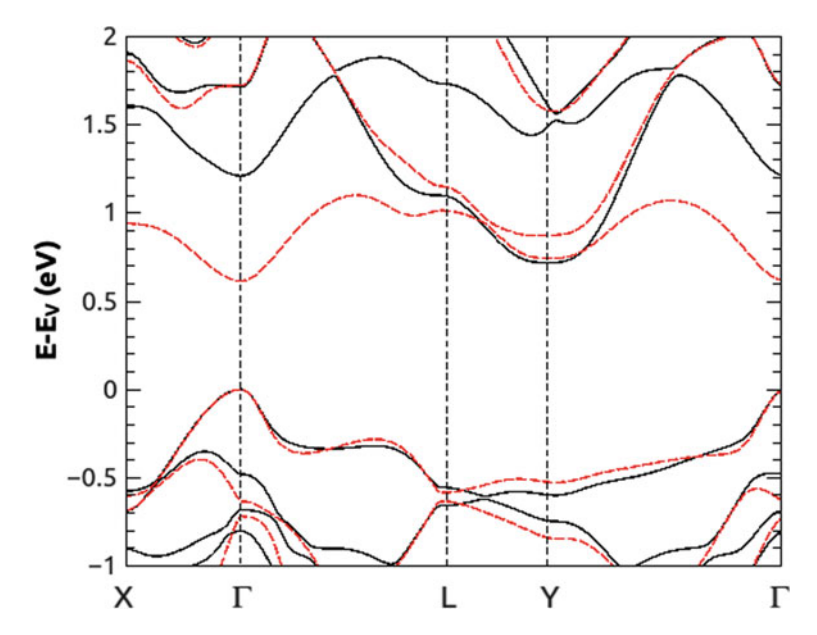


Fig. 10.8 Side view (a) and top view (b) of the relaxed silicene/(0001) ZnS slab model. Yellow, gray and blue spheres are S, Zn and Si atoms, respectively

similar to the one of the non-polar (1010) ZnS surface [47, 48], as discussed in more details in [44, 49]. The reconstructed (0001) ZnS surface is semiconducting, with a computed energy gap of about 2.5 eV, and is predicted to be more stable than the non-reconstructed polar surface for layers up to about 6.6 nm [49]. Note that the polar (non-reconstructed) ZnS surface is metallic, due to the pining of the Fermi level by the anion surface states, like in ZnO [50, 51]. On such a polar surface, silicene is also predicted to be metallic [52].

To study the interaction of silicene with the reconstructed (0001) ZnS surface, a flat silicene layer was placed on top of the surface, followed by atomic relaxation. Different possible arrangements of the Si atoms on the (0001) ZnS surface were considered, as discussed in more details in [31]. The most energetically stable structure is presented in Fig. 10.8, and corresponds to a hexagonal arrangements of the Si atoms placed at intermediate positions between top and hollow sites of the ZnS hexagons. Two Si-S bonds and two Si-Zn bonds are formed, with a charge transfer essentially involving the 3p<sub>z</sub> orbitals of the Si atoms and the 4 s states of Zn and 3p states of S, the bonded Si atoms thus adopting an  $sp^3$ -like character. Four other Si atoms are not bonded to the ZnS surface, two of these atoms lying at about 2.64 Å from the surface (marked "intermediate" on Fig. 10.8) and two other atoms lying at about 3.33 Å from surface (marked "top" on Fig. 10.8). The charge transfer at the silicene/(0001) ZnS interface leads to an excess of negative (Mulliken) charge of about 0.18 IeI on the top Si atoms, with respect to the intermediate Si atoms, resulting in the formation of a dipole at this interface. The average Si-Si distance (2.30 Å) is very similar to the one of free-standing silicene.

The silicene/(0001)ZnS interface is predicted to be semiconducting, with a computed indirect energy band gap of about 0.7 eV, as shown in Fig. 10.9. The energy gap opening in silicene is due to the charge transfer and partial  $sp^3$  hybridization of the Si atoms bonded to the Zn or S atoms on the surface. The effect of an out-



**Fig. 10.9** Computed energy band structure of the silicene/(0001) ZnS slab model, without (solid black lines) and with (dashed red lines) an external electric field of 0.6 V/Å in the direction perpendicular to the interface. The reference (zero) energy level corresponds to the top of the valence band  $E_V$  of silicene

of-plane electric field on the energy band structure of the system is also illustrated in Fig. 10.9 (dashed lines). A periodic zigzag potential was applied in the direction perpendicular to silicene/(0001) ZnS interfaces to study the effect of an out-of-plane electric field on the electronic properties of this system [44]. The electric field has a substantial effect on the conduction band near the  $\Gamma$  point, leading to a transition from an indirect ( $\Gamma$  to Y point) to direct (at  $\Gamma$  point) energy band gap in silicene, for an electric field of about 0.5 V/Å, as indicated in Fig. 10.10. The electric-field dependence of the energy band gap of the silicene layer is related to the modulation of the electric dipole at the silicene/ZnS interface [45].

# 10.4 Concluding Remarks

The recent progress on the growth and characterization of silicene on different substrates, are very encouraging. However, so far, silicene has been successfully grown on metallic surfaces. Its possible integration in future nanoelectronic devices will require its growth on non-metallic substrates. In this chapter, we have reviewed recent theoretical works on the interaction between silicene and non-metallic surfaces. The weak van der Waals interaction between silicene and e.g. transition metal

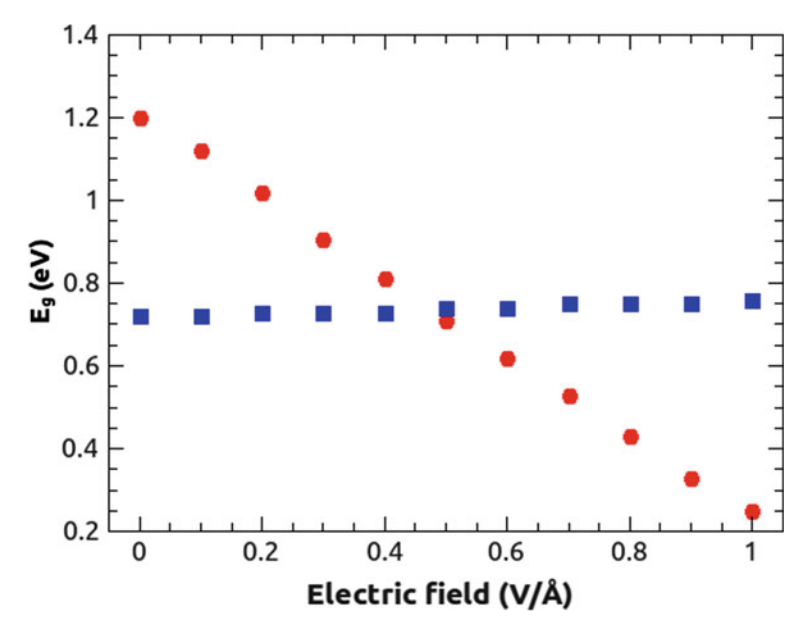


Fig. 10.10 Computed direct (filled circles) and indirect (filled squares) energy band gaps of the silicene/(0001) ZnS slab model, as a function of the external electric field applied to the system

dichalcogenides can potentially preserves the electronic properties of free-standing silicene, which is predicted to be a gapless semiconductor, like graphene. Very recently, encouraging results have been reported on the possible growth of silicene on  $MoS_2$ . However, DFT simulations indicate that silicene on  $MoS_2$  is highly buckled and metallic. Low buckled silicene, with preserved Dirac cones, is predicted to be grown on e.g.  $MoTe_2$ , a prediction which still needs experimental confirmation. These results could pave the way to so-called silicene-based van der Waals heterostructures for high performances and low-power nanoelectronic applications.

On the other hand, the covalent bonding of silicene on e.g. ZnS surfaces leads to the opening of an energy gap in its electronic structure. Very interestingly, the magnitude and nature (direct or indirect) of this energy gap is predicted to be controlled by an out-of-plane electric field. This theoretical prediction is potentially very interesting for silicene-based logic devices.

**Acknowledgements** This work has been financially supported by the European Project 2D-NANOLATTICES, within the Future and Emerging Technologies (FET) program of the European Commission, under the FET-grant number 270749, as well as the KU Leuven Research Funds, project GOA/13/011. We are grateful to A. Molle (MDM Laboratory), A. Dimoulas (NCSR Demokritos), G. Pourtois (imec), B. van den Broek and K. Iordanidou, (KU Leuven) for their valuable contributions to this work and for stimulating discussions.

208 M. Houssa et al.

### References

P. Vogt, P. De Padova, C. Quaresima, J. Avila, E. Frantzeskakis, M.C. Asensio, A. Resta, B. Ealet, G. Le Lay, Phys. Rev. Lett. 108, 155501 (2012)

- B. Feng, Z. Ding, S. Meng, Y. Yao, X. He, P. Cheng, L. Chen, K. Wu, Nano Lett. 12, 3507 (2012)
- 3. D. Chiappe, C. Grazianetti, G. Tallarida, M. Fanciulli, A. Molle, Adv. Mat. 24, 5088 (2012)
- H. Enriquez, S. Vizzini, A. Kara, B. Lalmi, H. Oughaddou, J. Phys, Condens. Matter 24, 314211 (2012)
- D. Tsoutsou, E. Xenogiannopoulou, E. Golias, P. Tsipas, A. Dimoulas, Appl. Phys. Lett. 103, 231604 (2013)
- P. Moras, T.O. Mentes, P.M. Sheverdyaeva, A. Locatelli, C. Carbone, J. Phys.: Condens. Matter 26, 185001 (2014)
- A. Fleurence, R. Friedlein, T. Ozaki, H. Kawai, Y. Wang, Y. Takamura, Phys. Rev. Lett. 108, 245501 (2012)
- 8. C.C. Lee, A. Fleurence, Y. Yamada-Takamura, T. Ozaki, R. Friedlein, Phys. Rev. B 90, 075422 (2014)
- 9. L. Meng, Y. Wang, L. Zhang, S. Du, R. Wu, L. Li, Y. Zhang, G. Li, H. Zhou, W.A. Hofer, M.J. Gao, Nano Lett. 13, 685 (2013)
- L. Tao, E. Cinquanta, D. Chiappe, C. Grazianetti, M. Fanciulli, M. Dubey, A. Molle, D. Akinwande, Nat. Nanotech. 10, 227 (2015)
- 11. M. Houssa, G. Pourtois, V.V. Afanas'ev, A. Stesmans, Appl. Phys. Lett. 97, 112106 (2010)
- M. Houssa, G. Pourtois, M.M. Heyns, V.V. Afanas'ev, A. Stesmans, J. Electrochem. Soc. 158, H107 (2011)
- 13. Y. Ding, Y. Wang, Appl. Phys. Lett. 103, 043114 (2013)
- E. Scalise, M. Houssa, E. Cinquanta, C. Grazianetti, B. van den Broek, G. Pourtois, A. Stesmans, M. Fanciulli, A. Molle, 2D Mater. 1, 011010 (2014)
- 15. L.Y. Li, M.W. Zhao, J. Phys. Chem. C 118, 19129 (2014)
- D. Chiappe, E. Scalise, E. Cinquanta, C. Grazianetti, B. van den Broek, M. Fanciulli, M. Houssa, A. Molle, Adv. Mater. 26, 2096 (2014)
- 17. J.J. Zhu, U. Schwingenschlögl, A.C.S. Appl, Mat. Interf. 6, 11675 (2014)
- 18. L. Linyang, W. Xiaopeng, Z. Xiaoyang, Z. Mingwen, Phys. Lett. A 377, 2628 (2013)
- 19. S. Kokott, P. Pflugradt, L. Matthes, F. Bechstedt, J. Phys.: Condens. Matter 26, 185002 (2014)
- M. Badylevich, S. Shamuilia, V.V. Afanas'ev, A. Stesmans, Y.G. Fedorenko, C. Zhao, J. Appl. Phys. 104, 093713 (2008)
- 21. Y.-N. Xu, W.Y. Ching, Phys. Rev. B 48, 4335 (1993)
- 22. C.L. Freeman, F. Claeyssens, N.L. Allan, J.H. Harding, Phys. Rev. Lett. 96, 066102 (2006)
- P. Tsipas, S. Kassavetis, D. Tsoutsou, E. Xenogiannopoulou, E. Golias, S.A. Giamini, C. Grazianetti, D. Chiappe, A. Molle, M. Fanciulli, A. Dimoulas, Appl. Phys. Lett. 103, 251605 (2013)
- 24. K.K. Kam, B. Parkinson, J. Chem. Phys. **86**, 463 (1982)
- 25. K.F. Mak, C. Lee, J. Hone, J. Shan, T.F. Heinx, Phys. Rev. Lett. 105, 136805 (2010)
- A. Splendiani, L. Sun, Y. Zhang, T. Li, J. Kim, C.Y. Chim, G. Galli, F. Wang, Nano Lett. 10, 1271 (2010)
- S.W. Han, H. Kwon, S.K. Kim, S. Ryu, W.S. Yun, D.H. Kim, J.H. Hwang, J.-S. Kang, J. Baik, H.J. Shin, S.C. Hong, Phys. Rev. B 84, 045409 (2011)
- 28. J.N. Coleman, M. Lotya, A. O'Neill, S.D. Bergin, P.J. King, U. Khan, K. Young, A. Gaucher, S. De, R.J. Smith, I. V. Shvets, S.K. Arora, G. Stanton, H.-Y. Kim, K. Lee, G.T. Kim, T. Duesberg, G.S. Hallam, J.J. Boland, J.J. Wang, J.F. Donegan, J.C. Grunlan, G. Moriarty, A. Shmeliov, R.J. Nicholls, J.M. Perkins, E.M. Grieveson, K. Theuwissen, D.W. McComb, P.D. Nellist, V. Nicolosi, Science 331, 568 (2011)
- K.S. Novoselov, D. Jiang, F. Schedin, T.J. Booth, V.V. Khotkevich, S.V. Morozovand, A.K. Geim, PNAS 102, 10451 (2005)

- 30. S. Lebegue, O. Eriksson, Phys. Rev. B 79, 115409 (2009)
- 31. T. Li, G. Galli, J. Phys. Chem. C 111, 16192 (2007)
- 32. C. Ataca, H. Sahin, E. Akturk, S. Ciraci, J. Phys. Chem. C 115, 3934 (2011)
- D.C. Langreth, M. Dion, H. Rydberg, E. Schroeder, P. Hyldgaard, B.I. Lundqvis, Int. J. Quant. Chem. 101, 599–610 (2005)
- S. Cahangirov, M. Topsakal, E. Akturk, H. Sahin, S. Ciraci, Phys. Rev. Lett. 102, 236804(1)–236804(4) (2009)
- 35. J.A. Wilsonand, A.D. Yoffe, Adv. Phys. 18, 193-335 (1969)
- 36. T. Boker et al., Phys. Rev. B **64**, 235305(1)–235305(11) (2001)
- 37. E. Cinquanta et al., J. Phys. Chem. C 117, 16719 (2013)
- 38. L.C. Lew Yan Voon, E. Sandberg, R.S. Aga, A.A. Farajian, Appl. Phys. Lett. 97, 163114 (2010)
- M. Houssa, E. Scalise, K. Sankaran, G. Pourtois, V.V. Afanas'ev, A. Stesmans, Appl. Phys. Lett. 98, 223107 (2011)
- R. Quhe, R. Fei, Q. Liu, J. Zheng, H. Li, C. Xu, Z. Ni, Y. Wang, D. Yu, Z. Gao, J. Lu, Sci. Rep. 2, 853 (2012)
- 41. Y. Ding, Y. Wang, Appl. Phys. Lett. **100**, 083102 (2012)
- 42. B. van den Broek, M. Houssa, E. Scalise, G. Pourtois, V.V. Afanas'ev, A. Stesmans, Appl. Surf. Sci. 291, 104 (2014)
- 43. T.P. Kaloni, N. Singh, U. Schwingenschlögl, Phys. Rev. B 89, 035409 (2014)
- 44. M. Houssa, B. van den Broek, E. Scalise, G. Pourtois, V.V. Afanas'ev, A. Stesmans, Phys. Chem. Chem. Phys. 15, 3702 (2013)
- S.S. Li, C.W. Zhang, S.S. Yan, S.J. Hu, W.X. Ji, P.J. Wang, P. Li, J. Phys.: Condens. Matter 26, 395003 (2014)
- 46. M.J. Weber (ed.), Handbook of Laser Science and Technology (CRC Press, Cleveland, 1986)
- 47. J.E. Northrup, J. Neugebauer, Phys. Rev. B 53, R10477 (1996)
- 48. A. Filippetti, V. Fiorentini, G. Cappellini, A. Bosin, Phys. Rev. B 59, 8026 (1999)
- 49. X. Zhang, H. Zhang, T. He, M. Zhao, J. Appl. Phys. 108, 064317 (2010)
- A. Wander, F. Schedin, P. Steadman, A. Norris, R. McGrath, T.S. Turner, G. Thornton, N.M. Harrison, Phys. Rev. Lett. 86, 3811 (2001)
- 51. B. Meyer, D. Marx, Phys. Rev. B 67, 035403 (2003)
- 52. M. Houssa, B. van den Broek, E. Scalise, G. Pourtois, V.V. Afanas'ev, A. Stesmans, ECS Trans. 53, 51 (2013)

# Chapter 11 Surface Functionalization of Silicene



Jijun Zhao and Kehui Wu

**Abstract** For two-dimensional (2D) materials, an attractive feature is that all the atoms of the materials are exposed on the surface. Thus tuning the structure and properties by surface treatments becomes straightforward. Similar as graphene, the nearly zero-gap character of silicene hinders its applications in electronic and optoelectronic devices. In the case of graphene, functionalization through hydrogenation, halogenation, oxidation, have been widely explored in order to modify the electronic structure of graphene. However, the stable aromatic  $\pi$ -bond network of graphene makes it very inert and difficult to bond with foreign atoms. For example, hydrogen atoms on graphene usually form clusters instead of an ordered structure. In contrast, silicene possesses hybrid  $sp^2$ - $sp^3$  bonding, which is more readily to be modified or functionalized. Since the early stage of silicene research, theoretical investigations on the hydrogenation, halogenation, and oxidation of silicene have been widely reported in literature. Recently, increasing experimental successes have been achieved on functionalization of silicene. It is now imperative to review the progresses in the fast-growing field. In this chapter, we will discuss hydrogenation, halogenation oxidization individually. In each section, we first describe those theoretical predictions and then illustrate recent experimental successes. Finally, we will give some overview and outlook of this field.

#### 11.1 Introduction

For two-dimensional (2D) materials, an attractive feature is that all the atoms of the materials are exposed on the surface. Thus tuning the structure and properties by

K. Wu (⊠)

Institute of Physics, Chinese Academy of Sciences, No. 8 Zhongguancun South 3rd Str., Beijing, Haidian 100080, China e-mail: khwu@iphy.ac.cn

J. Zhao

Key Laboratory of Materials Modification by Laser, Ion and Electron Beams, Dalian University of Technology, Dalian 116024, China

surface treatments becomes straightforward. Similar as graphene, the nearly zerogap character of silicene hinders its applications in electronic and optoelectronic devices. In the case of graphene, functionalization through hydrogenation, halogenation, oxidation, have been widely explored in order to modify the electronic structure of graphene. However, the stable aromatic  $\pi$ -bond network of graphene makes it very inert and difficult to bond with foreign atoms. For example, hydrogen atoms on graphene usually form clusters instead of an ordered structure [1]. In contrast, silicene possesses hybrid  $sp^2-sp^3$  bonding, which is more readily to be modified or functionalized. Since the early stage of silicene research, theoretical investigations on the hydrogenation, halogenation, and oxidation of silicene have been widely reported in literature. Recently, increasing experimental successes have been achieved on functionalization of silicene. It is now imperative to review the progresses in the fast-growing field. In this chapter, we will discuss hydrogenation, halogenation oxidization individually. In each section, we first describe those theoretical predictions and then illustrate recent experimental successes. Finally, we will give some overview and outlook of this field.

## 11.2 Hydrogenation

Hydrogenation can convert  $sp^2$  hybridized silicon atom into  $sp^3$  state and provide a straightforward way to open the band gap of silicene [2, 3]. There are two major configurations of fully hydrogenated silicene (namely, silicane): chair and boat, which are presented in Fig. 11.1 and have been confirmed to be stable, just like that of graphane [4, 5]. In the chair configuration, neighboring hydrogen atoms sit alternatively above and below the basal plane. The boat one has alternative paired hydrogen atoms, or hydrogen dimers. From density functional theory (DFT) calculations, the chair configuration is more stable than the boat one by 25 meV/atom [2] or 30 meV/atom [6]. After full hydrogenation, the bucking height of silicene sheet increases from 0.44 to 0.72 Å [2], indicating that the  $sp^3$  hybridization is moderately enhanced. The calculated formation energy of silicane with chair configuration is only 0.032 eV per atom with respect to bulk silicon solid with H<sub>2</sub> gas, which is much smaller than that of monolayer silicene (0.779 eV per atom) [7]. The dynamical stabilities of the chair and boat configurations of silicane sheets have been verified by first-principles phonon dispersion calculations [3, 8–10]. From DFT calculation, the energy barrier for dissociative adsorption of a H<sub>2</sub> molecule on silicene sheet is 1.75 eV [11], which means that the H<sub>2</sub> molecule does not dissociate spontaneously on the silicene surface.

In previous theoretical calculations, the electronic structures of silicane have been extensively investigated with various methods, including DFT with different treatments of exchange-correlation interactions [2, 3, 6, 10, 12–14], various tight binding (TB) models [8, 15, 16], as well as many-body Green's function approach within the *GW* approximation. The theoretical values of band gaps are summarized in Table 11.1 and the representative band structures from LDA calculations are shown in Fig. 11.2. Silicane with chair configuration is an indirect semiconductor (Fig. 11.2a), while the boat one is a direct semiconductor (Fig. 11.2b). According to more accurate HSE and

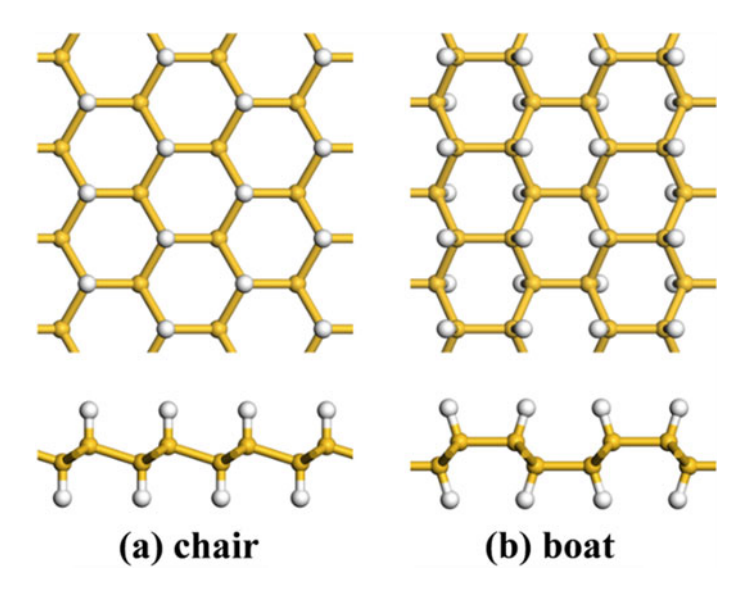


**Fig. 11.1** Top view (upper) and side view (lower) of silicane in **a** chair and **b** boat configurations. The yellow balls represent Si atoms and the white balls represent H atoms

**Table 11.1** Band gaps (eV) of two-side and one-side hydrogenated silicene with different configurations (shown in Figs. 11.1 and 11.3) from the theoretical calculations using different methods (GGA denotes either PW91 or PBE)

Method	Two-side hydrogenation		One-side hydrogenation		
	Chair	Boat	Chair	Boat	Zigzag
ТВ	2.2 [15], 2.31 [16]	1.93 [16]			
LDA	2.0 [2, 3]	1.6 [3]			
GGA	2.11 [312], 2.19 [10], 2.36 [6], 2.37 [14]	1.6 [6]	0.84 [6], 0.95 [12], 0.94 [17]	0.53 [6]	0 [6]
HSE06	4.0 [3], 3.51 [6]	3.3 [3], 2.41 [6]	1.79 [6], 1.74 [17]	1.14 [6]	0 [6]
GW	3.8 [3]	2.9 [3]			

GW calculations, the band gaps of chair-like (boat-like) silicane are in the range of  $3.5 \sim 4.0 (2.4 \sim 3.3)$  eV. For the chair-like silicane, the effective masses for electron and hole carriers are  $0.04 m_0$  and  $0.076 m_0$  ( $m_0$  is the electron mass), respectively [16].

The intrinsic mechanical properties of silicane have been investigated by Peng and De using first-principles calculations [9]. Compared to silicene, silicane has lower in-plane stiffness (53.8 N/m) and lower Poisson ratio (0.24); in other words, full hydrogenation of the silicene moderately reduces its intrinsic strength and Poisson

J. Zhao and K. Wu

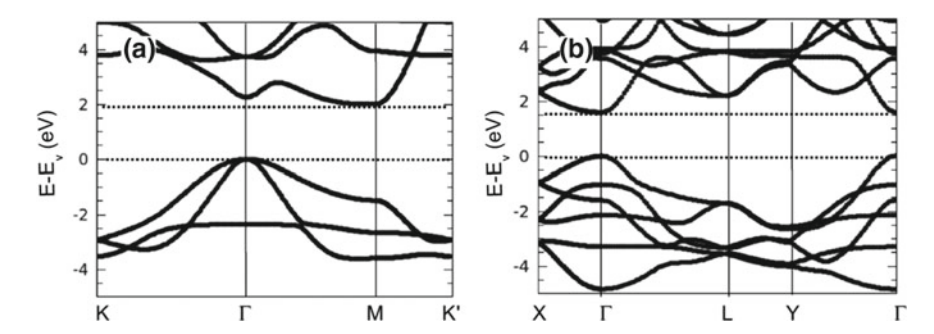


**Fig. 11.2** Energy band structures, calculated using LDA functional, for **a** chair silicane, **b** boat silicane. The reference (zero) energy level corresponds to the top of the valence band. Reproduced with permission from [3]. Copyright 2016, American Institute of Physics

ratio. Due to the increased buckling roughness of 59% by hydrogenation, the ultimate strains increase by 29%, 33%, and 24% under armchair, zigzag, and biaxial deformations, respectively. Meanwhile, hydrogenation has little effect on the ultimate tensile strengths of silicene layer.

In addition to silicane with two-side hydrogenation, one-side semihydrogenated silicene have also been investigated by many first-principles calculations [6, 12, 17, 18]. Again, its dynamical stability has been confirmed by the fact that no imaginary phonon branch occurs in the phonon dispersions curve. As shown in Fig. 11.3, there are three most possible configurations of half-hydrogenated silicene: (a) zigzag conformer with the H atoms absorbed on silicon zigzag chains alternately, (b) boat conformer with the H atoms distributed in pairs, (c) chair conformer with the H atoms sitting alternately on only one side of the sheet. According to the DFT calculation [6], the zigzag conformer is more stable than the boat and chair conformers by 33 and 180 meV/atom, respectively. The computed band gaps of half-hydrogenated silicene with various configurations are summarized in Table 11.1. Both chair-like and boat-like semihydrogenated silicene sheets are semiconductors with direct band gaps [6, 12, 17, 18]. Using HSE06 method, the band gaps of 1.79 eV (chair) and 1.14 eV (boat) [6] are only about half of the fully hydrogenated silicene with the same configuration.

One unique feature of the one-side semihydrogenated silicene is the ferromagnetism in the chair-like conformer, in which every unsaturated Si atom carries a magnetic moment of 1  $\mu_B$ . In contrast, the most stable zigzag configuration is metallic and non-magnetic. The different magnetic orderings in half-hydrogenated silicene conformers originate from coupling of the  $p_z$  orbitals of the unsaturated Si atoms. In short, hydrogenation paves a novel way to tailor the electronic and magnetic properties of silicene and shows great potentials for future nanoelectronics and spintronics.

Starting from silicane with substantial band gap, silicane can be further doped and functionalized. Doping by boron or phosphorus atoms in the chair-like silicane with dopant concentration between 1.4 and 12.5% was theoretically explored by Pi et al. [19]. By substitutional B- or P- doping, silicane is transformed from an indirect-gap

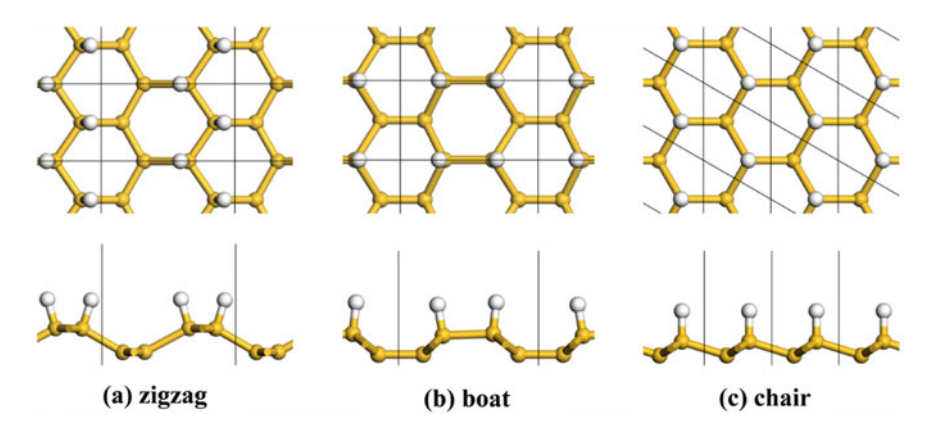


Fig. 11.3 Top view (upper) and side view (lower) of the atomic structures for: a zigzag semihydrogenated silicene; b boat-like semihydrogenated silicene; c chair-like semihydrogenated silicene. The yellow balls and white balls represent Si and H atoms, respectively. The black lines show the unit cell

semiconductor into a direct semiconductor, and the band gap reduces with increasing dopant concentration. More interestingly, doping can reduce the effective mass of holes and electrons and thus enhance the carrier mobility in silicane.

Using first-principles calculations, it was shown that the substitutional doping by N and B impurities is an effective approach to functionalize silicane and convert the pristine silicane into *n*-type and *p*-type semiconductor, respectively [20]. Additionally, it was further demonstrated that chemical functionalization of various elements (N, P, S, Li, Na, K, Mg and Ca) can enhance the photocatalytic water-splitting activity of silicane for the hydrogen evolution reaction and oxygen evolution reaction [21].

Beyond monolayer silicene, hydrogenation on the bilayer and few-layer silicene sheets have also been theoretically explored by DFT calculations [22–24]. For instance, Liu et al. [23] demonstrated that the electronic and optical properties of hydrogenated few-layer silicene sheets strongly rely on the thickness and stacking modes. The formation energy increases with decreasing number of layers owing to the higher surface/volume ratio. Because of the quantum confinement effect, there is an increased trend of band gap with the reduction of layer thickness, leading to a blue shift of optical absorption edge in the hydrogenated few-layer silicene.

Although theoretical studies on silicene hydrogenation are extensive, only a few experimental works on hydrogenation of silicene have been reported so far. Compared with free-standing silicene that is used as a model system for hydrogenation, experimentally available silicene is always prepared on certain kind of substrates. Thus two important substrate effects have to be considered. Firstly, the hydrogen atoms can only adsorb on one side of the silicene surface unless they are able to penetrate through the silicene film and go into the interface. Currently, there is no evidence of such behavior, thus one-side hydrogenation model is more realistic for comparison with the experimental results. Secondly, the interaction between silicene

J. Zhao and K. Wu

and the substrate can often result in complex superstructures, such as the  $4\times 4$ ,  $\sqrt{13}\times\sqrt{13}$ R19°, and  $2\sqrt{3}\times2\sqrt{3}$  superstructures formed by monolayer silicene on Ag(111). These superstructures are due to the rearrangement of the buckling pattern of Si atoms in the low-buckled silicene network. Since the theoretical calculation indicated that hydrogenation can substantially increase the bucking height of silicene sheet [2], the buckling pattern may also be affected by hydrogenation. However, so far, theoretical studies have not yet include consideration of the initial buckling configuration of silicene on substrates.

As the most well studied system, monolayer silicene on Ag(111) substrate is a good model system for the investigation of silicene hydrogenation. Depending on the preparation condition, several monolayer silicene phases can form on Ag(111) surface, such as  $4 \times 4$ ,  $(\sqrt{13} \times \sqrt{13})$ R13.9°,  $2\sqrt{3} \times 2\sqrt{3}$  reconstructions with respect to the Ag(111)-1 × 1 lattice [25–37], and  $(\sqrt{3} \times \sqrt{3})$ R30° with respect to silicene-1 × 1 lattice [26, 30]. Of these phases the 4 × 4 is the simplest and most well understood one, in which a 3 × 3-Si supercell is placed commensurately with a 4 × 4-Ag supercell.¹ The hydrogenation of monolayer silicene with Si(3 × 3)/Ag(4 × 4) phase on Ag(111) has been studied by Wu's group [38]. By introducing atomic hydrogen to the UHV chamber and exposing the 4 × 4 phase to a saturated hydrogen dose at room temperature, a perfectly ordered structure with the same 4 × 4 periodicity was observed in scanning tunneling microscopy (STM) images, as displayed in Fig. 11.4a for a large area image. The distance between the nearest bright spots is about 3.8 Å, corresponding to the lattice constant of silicene-1 × 1.

Intuitively, adsorption of H atoms on upper-buckled Si atoms only changes its degree of buckling slightly. The resulting STM pattern after hydrogenation should resemble that of the clean 4 × 4 surface of silicene. However, high resolution image of the hydrogenated structure in Fig. 11.4b manifests two inequivalent HUCs: one with six bright spots, the other with only one bright spot in the middle. This is different from the 4  $\times$  4 silicene, but reminiscent of the rarely observed  $\beta$ -4  $\times$  4 phase (correspondingly, the normal  $4 \times 4$  phase is referred to as  $\alpha$ -4  $\times$  4) [39]. This observation can be understood considering the fact that the  $\beta$ -4  $\times$  4 phase prefers to stay in the strained area of a pure silicene sheet. Because the adsorption of H atoms will increase the degree of buckling of Si atoms and thus increases the strain, the  $\beta$  phase can turn to be more stable as compared with the  $\alpha$  phase after hydrogenation. As shown in Fig. 11.5, the perfect agreement between theoretical model and experimental STM images also supports that both the  $\alpha$ -4  $\times$  4 and  $\beta$ -4  $\times$ 4 are pure silicon structures. Moreover, the fully half-hydrogenated silicene sheet can be completely restored to its original state by annealing the sample to about 450 K. The adsorption-desorption cycle can be repeated many times without degradation of the silicene film if the ultrahigh vacuum system is clean enough.

Monolayer silicene with the  $2\sqrt{3} \times 2\sqrt{3}$  phase on Ag(111) was also hydrogenated by applying the same hydrogenation procedures and studied by STM [40].

 $<sup>^1</sup>$ Note that the 4  $\times$  4 silicene phase is therefore also referred to as a 3  $\times$  3 superstructure, e.g. in Chaps. 5, 7 and 8

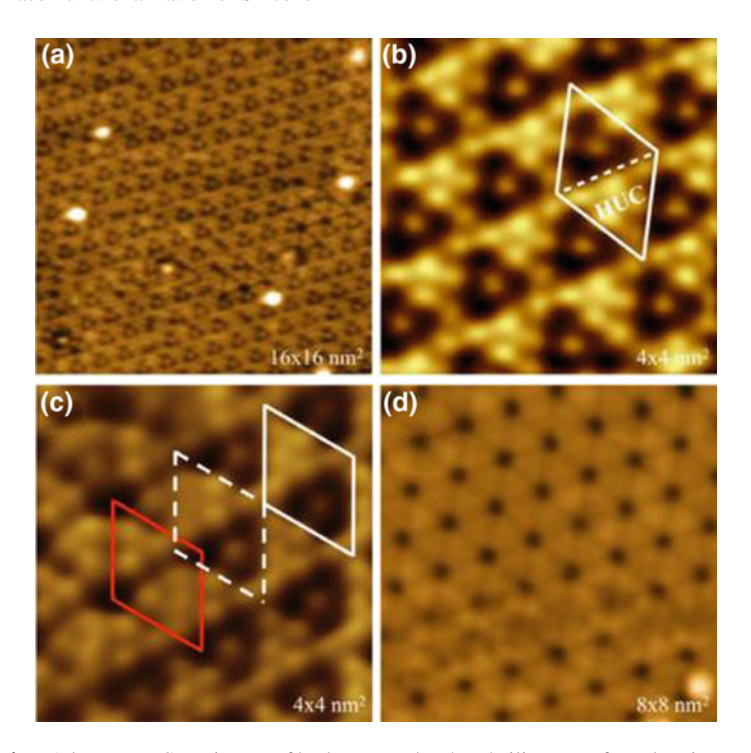


Fig. 11.4 a A large area STM image of hydrogenated  $\alpha$ -4  $\times$  4 silicene surface showing an ordered 4×4 structure. b Zoom-in STM image of hydrogenated  $\alpha$ -4  $\times$  4 phase. The white rhombus marks an apparent unit cell of the structure. There are six bright protrusions in one HUC and one protrusion in the other HUC. c STM image showing the comparison between the position of apparent UCs of clean and hydrogenated  $\alpha$ -4  $\times$  4. The red and white rhombuses correspond to clean  $\alpha$ -4  $\times$  4 UC and the hydrogenated  $\alpha$ -4  $\times$  4 UC, respectively. A translation of the white UC (dot line) does not match with the red one. d The clean  $\alpha$ -4  $\times$  4 surface is fully recovered after annealing the surface at 450 K. Reproduced with permission from [38]. Copyright 2016, American Physical Society

As displayed in Fig. 11.6, at a saturation H dosage the  $2\sqrt{3} \times 2\sqrt{3}$  silicene has been converted to an ordered structure consisting of hexagonal close packed (HCP) spots. The HCP spots has a lattice period of about 3.8 Å, identical to the lattice constant of silicene-1  $\times$  1. Such a resulting structure can be understood by a half-silicane model where the Si atoms in one of the Si sublattice are all terminated by H atoms, and become upper-buckled, whereas another sublattice is lower-buckled in contact with the Ag(111) substrate. The lower buckled Si sublattice has no H atoms attached to it as it is not accessible by H atoms from the surface. The clean silicene  $2\sqrt{3} \times 2\sqrt{3}$  phase is a partially disordered phase, where perfect  $2\sqrt{3} \times 2\sqrt{3}$  only exist in small Moiré-like domains, and the areas between the ordered  $2\sqrt{3} \times 2\sqrt{3}$  domains appear to be quite disordered and defective. However, the formation of a complete, single domain  $1 \times 1$  half-silicane surface after hydrogenation indicates that although the  $2\sqrt{3} \times 2\sqrt{3}$  phase appears defective, it is essentially composed of a continuous honeycomb lattice of Si, while the disorder is related to the buckling pattern.

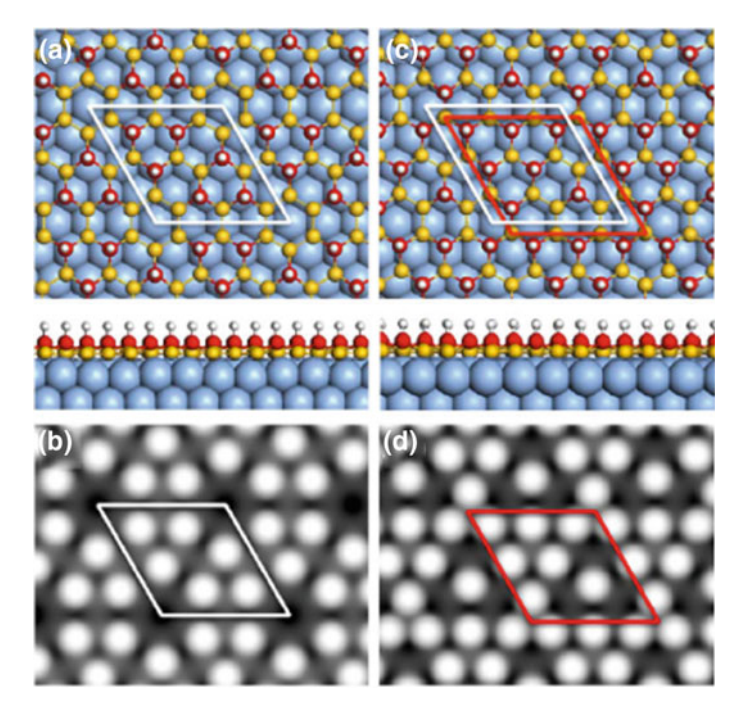


Fig. 11.5 a and b are the structural model and the simulated STM image of hydrogen-terminated  $\alpha$ -4 × 4 and  $\beta$ -4 × 4 model, respectively. c and d are the structural model and the simulated STM image of hydrogen-terminated  $\alpha$ -4 × 4 and  $\beta$ -4 × 4 models, respectively. In c the white and red rhombuses corresponding to the positions of apparent UCs of  $\alpha$ -4 × 4 and  $\beta$ -4 × 4 phases, respectively, which are shifted relatively. Note that in a and c, the lateral position of Si atoms are fixed unchanged and only the buckling configuration has changed, resulting in the change of the position of apparent Ucs. Reproduced with permission from [38]. Copyright 2016, American Physical Society

Another obvious feature of the hydrogenated  $2\sqrt{3} \times 2\sqrt{3}$  surface is the hole, or vacancy sites corresponding to missing single H atoms, as shown in Fig. 11.6. Detailed analysis shows that most of the hole sites are arranged in a periodic  $\sqrt{7} \times \sqrt{7}$  pattern with respect to silicene-1  $\times$  1, as shown by the white rhombus in Fig. 11.6. Notably, the  $\sqrt{7} \times \sqrt{7}$  periodicity with respect to silicene-1  $\times$  1 is identical to a  $(2\sqrt{3} \times 2\sqrt{3})$ R30° periodicity with respect to Ag(111)-1  $\times$  1. So that these holes is a result of the commensuration between the silicene lattice and the Ag(111) lattice. Besides the ordered monoatomic holes, there are another two types of holes shown in Fig. 11.6. The second type is formed by two holes sitting side by side, and the third type consists of a bright spot at the center surrounded by three holes. The above three types of holes are referred to as mono, double and triple holes, respectively. Note that the triple hole site is very similar as the darker half- unit cell in the hydrogenated silicene 4  $\times$  4 phase. The formation mechanism of these hole sites was discussed with DFT calculations [40].

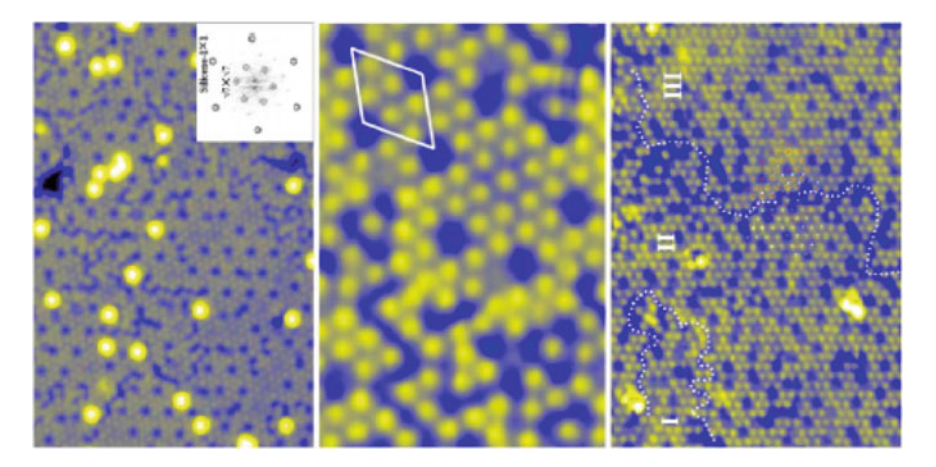


Fig. 11.6 Full hydrogenation of the silicene  $(2\sqrt{3} \times 2\sqrt{3})$ R30 phase on Ag(111). (a) STM image of the fully hydrogenated silicene  $(2\sqrt{3} \times 2\sqrt{3})$ R30 phase. The inset is the result of FFT of (a), showing six spots corresponding to silicene-1 × 1 lattice. (b) High-resolution STM image (of the hydrogenated  $(2\sqrt{3} \times 2\sqrt{3})$ R30 phase. The white rhombus marks the periodically ordered hole sites with  $\sqrt{7} \times \sqrt{7}$  structure with respect to the silicene 1 × 1 lattice, which agrees well with the  $\sqrt{7} \times \sqrt{7}$  spots observed in the inset of (a). (c) STM image of the hydrogenated silicene  $(2\sqrt{3} \times 2\sqrt{3})$ R30 phase shows three domains (marked by I, II,and III). The domain boundaries are labeled by white dotted lines. The small white and red dots correspond to the lattice of the bright spots in II and III domains, respectively. One lattice is exactly located in the hollow site of the other lattice

The resulting half-silicane structure corresponds to one of the Si sublattice terminated by H atoms. This implies that there should be a same possibility for the two different Si sublattices to be hydrogenated. As a result, the hydrogenated silicene- $(2\sqrt{3}\times2\sqrt{3})\text{R}30^\circ$  will separate into different domains, where either the A sublattice or B sublattice hydrogenated. Indeed, the STM image of Fig. 11.6c shows a hydrogenated silicene surface that appears at a first sight to have well-ordered single domain. But by careful inspection one notices that there are three domains, separated by two domain boundaries that are labeled by white dotted lines. The positions of bright spots in neighboring domains (both HCP lattices) indicate that one HCP lattice is exactly located in the hollow site of the other HCP lattice, which is exactly what we expect from the above sublattice-hydrogenation picture: A and B sublattices are located in the hollow sites of each other.

Similar hydrogenation result was also obtained by Wang et al. [41] in the same  $2\sqrt{3} \times 2\sqrt{3}$  phase on Ag(111) surface. In their experiment, the angle resolved photoelectron emission spectroscopy (ARPES) data were obtained from the hydrogenated silicene, as shown in Fig. 11.7. Apart from the dispersive Ag *sp* band from the Ag(111) substrate, there are two additional bands S1 and S2, which can be assigned to half-silicane. These bands are in good agreement with the calculated bands of free-standing half-silicane. And a clear indication of the gap opening is confirmed.

The hydrogenation of silicene is interesting not only for modifying the structure and electronic properties, but also helps to clarify some fundamental issues related

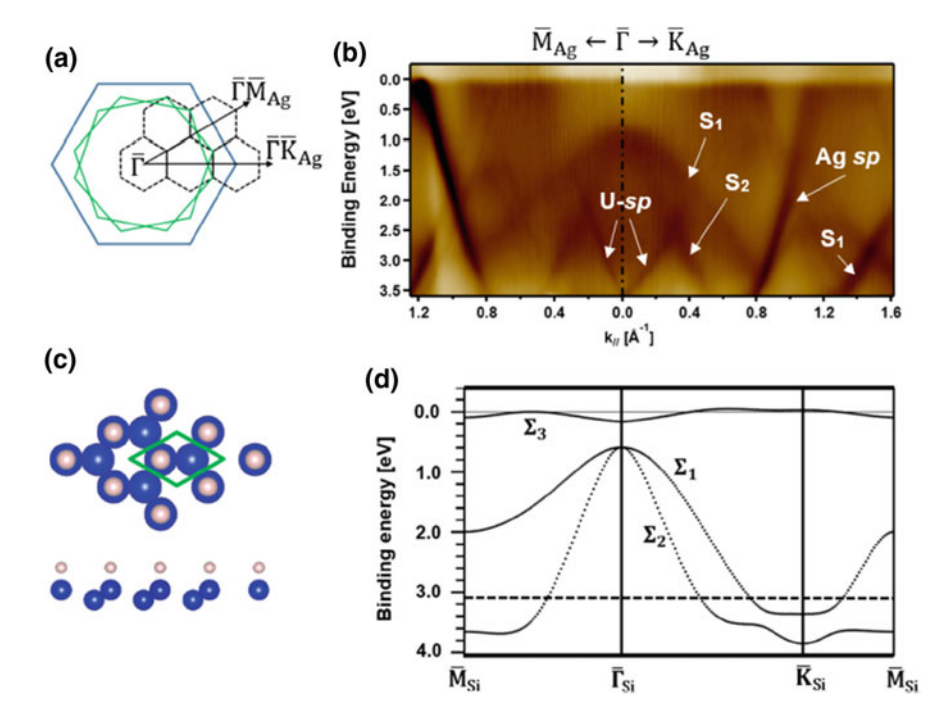
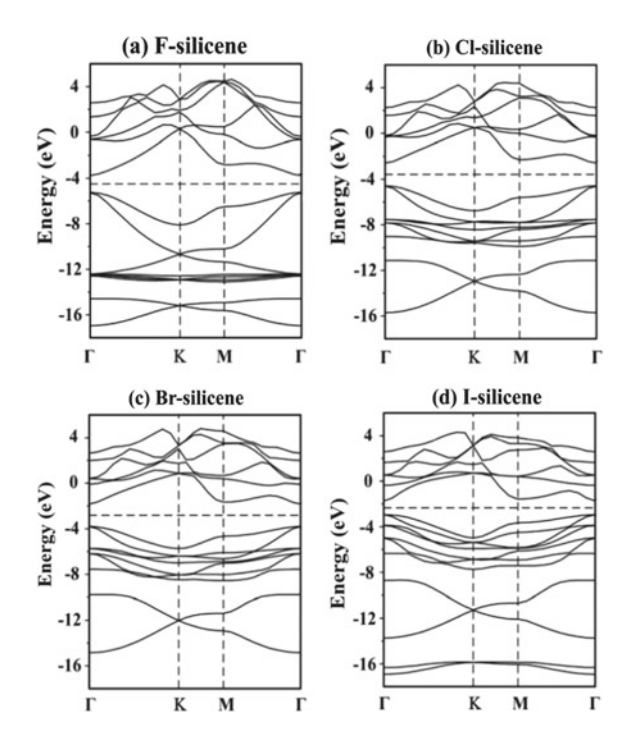


Fig. 11.7 a SBZs of  $(1\times 1)$  Ag(111) (blue),  $(2\sqrt{3}\times 2\sqrt{3})$  reconstruction (black), and two  $(1\times 1)$  half-silicane SBZs rotated by  $\pm 10.9^\circ$  (green). b ARPES data from half-silicane obtained at a photon energy of  $26\,\mathrm{eV}$  along  $\overline{\varGamma}\to\overline{\mathrm{M}}_{\mathrm{Ag}}$  and  $\overline{\varGamma}\to\overline{\mathrm{K}}_{\mathrm{Ag}}$  of the Ag $(1\times 1)$  SBZ. S1 and S2 are two dispersive bands which originate from half-silicane. The label Ag-sp indicates Ag bulk emission and U-sp points at dispersive features due to umklapp scattering of the Ag-sp emission by  $(2\sqrt{3}\times 2\sqrt{3})$  reciprocal lattice vectors. c Top and side views of a half-silicane model with hydrogen adsorbed on one of the two hexagonal sublattices of free-standing silicene. The green diamond represents the  $(1\times 1)$  silicane unit cell, and blue and pink balls represent Si and H atoms, respectively. The bond length between Si and H atoms is  $1.52\,\mathrm{A}^\circ$ , and the -z of the two Si sublattices is  $0.68\,\mathrm{A}^\circ$ . d Calculated band structure of the half-silicane model in (c). The dashed line indicates the binding energy limit of the ARPES measurement

with silicene. Recently, the nature of silicene monolayer on Ag(111) has been questioned by some researchers as being actually a Ag–Si alloy phase. Prevot et al. [42] explored in situ STM measurement during the growth of silicene films. They found that the morphology of Ag(111) surface suffers a significant change during growth, which may correspond to strong Ag mass transport. Hence, they suggested that Ag atoms should be incorporated into the resulting silicene film to form Ag–Si alloy. However, mass transport is not a direct proof of the incorporation of Ag in silicene film. The fact that the hydrogen adsorption phenomena can be nicely explained by existing silicene model supports the pure silicene model without Ag–Si alloying. Moreover, the local  $1 \times 1$  structure of half-silicane is so compact that it is hard to insert Ag atoms into it. Therefore, there is no alloy model which can explain these existing STM observations, supporting the silicene monolayers on Ag(111) are pure Si sheets instead of Si–Ag alloy phases.

Fig. 11.8 Energy band structures for a F-silicene, b Cl-silicene, c Br-silicene and d I-silicene. The Fermi level is labeled with a dashed line. Reproduced with permission from [43]. Copyright 2016, Royal Society of Chemistry



## 11.3 Halogenation

Chemisorption of halogen elements is another effective way to open a band gap in silicene. Similar to silicane, the chair configuration is more stable than the boat configuration for X-silicene (X=F, Cl, Br and I). The band structures of the chair-like X-silicene systems are presented in Fig. 11.8. Using sX-LDA methods, all X-silicene are direct semiconductors with band gaps of 1.469 eV, 1.979 eV, 1.950 eV and 1.194 eV for F, Cl, Br and I, respectively [43]. The variation trend of  $E_g$  can be ascribed to the competition of Si–Si and Si–X bond strengths.

Among X-silicene, the F-silicene with chair configuration has been intensively studied by first-principles calculations. The theoretically predicted band gaps fall in a rather wide range, i.e.,  $0.70\,\text{eV}$  (PBE) [10],  $1.2\,\text{eV}$  (M06L) [44],  $1.469\,\text{eV}$  (sX-LDA) [43],  $1.6\,\text{eV}$  (HSE) [44],  $2.33\,\text{eV}$  (GW $_0$ ) [10]. Moreover, a new configuration for F-silicene, so called Z-line (Fig. 11.9), is nearly energetically degenerate with the chair configuration [10]. In this conformer, F atoms are adsorbed along zigzag lines alternatively on both sides of silicene; in other words, it has the buckling alternated by the zigzag lines, losing the symmetry of pristine silicene. As shown in Fig. 11.9, the Z-line configuration of F-silicene is also a direct semiconductor with band gap of  $0.82\,\text{eV}$  at PBE level or  $2.64\,\text{eV}$  at  $GW_0$  level, which is slightly larger than that of the chair conformer by  $\sim 15\%$ .

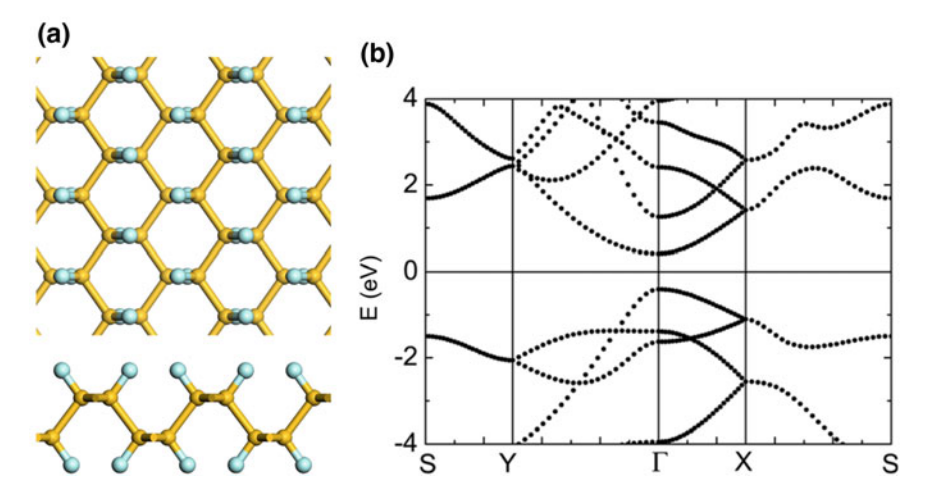


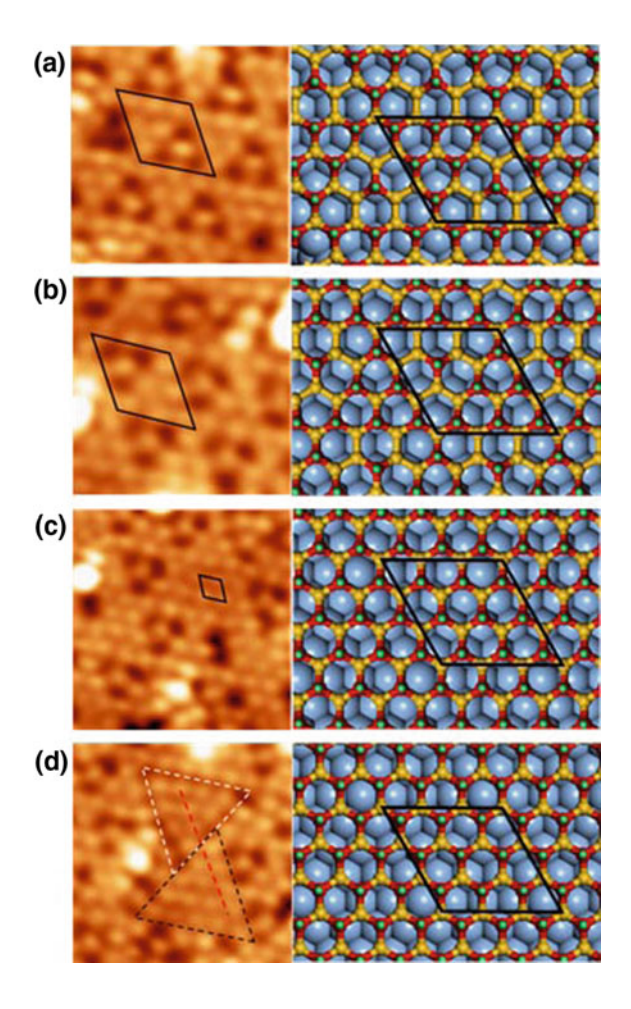
Fig. 11.9 a Atomic structure and b band structure of F-silicene in Z-line configuration. The yellow balls and light blue balls represent Si and F atoms, respectively. Reproduced with permission from [10] Copyright 2016, American Institute of Physics

In addition to full halogenation, Wang et al. [45] explored half-fluorinated silicene sheets using spin-polarized DFT calculations. They considered the zigzag, chair, and boat configurations and found that they are all dynamically stable from the phonon dispersion curves. Similar to the case of half-hydrogenated silicene, the zigzag configuration is the most stable conformer. Half-fluorinated silicene with zigzag and boat configurations are direct semiconductors with band gaps of 0.411 and 0.824 eV (HSE03), respectively. Indeed, partial fluorination provides an effective way to tune electronic structure (especially band gap) in silicene-based materials. Combining first-principles calculations with the cluster expansion approach, Huang et al. [46] predicted that the band gaps of homogenous  $SiF_x$  alloys with two-side functionalization could be continually modulated from 0 to 1.59 eV. On the other hand, the chair-like half-halogenated silicene shows antiferromagnetic behavior, with each unsaturated Si atom carrying a magnetic moment of 0.84  $\mu_B$  for F, 0.24  $\mu_B$  for Cl, and 0.11  $\mu_B$  for Br, respectively [18].

On the experimental side, the chlorination of monolayer silicene on Ag(111), with initial surface reconstructions including  $4\times 4$ ,  $(\sqrt{13}\times\sqrt{13})$ R13.9°,  $(2\sqrt{3}\times2\sqrt{3})$ R30° phases, has been systematically studied by Li et al. using STM [47]. At low coverage, chlorine atoms tend to adsorb on the upper-buckled Si atoms without changing the buckling configuration of the silicene lattice, whereas at high coverage the buckling configuration will change, and new ordered structures as well as ordered defect patterns form, similar as the hydrogenation of silicene.

For the  $4 \times 4$  silicene phase, increasing Cl atoms to a saturation dosage, the  $4 \times 4$ - $\alpha$  silicene will transform to two types of superstructures, as illustrated in Fig. 11.10. The first structure is similar to the fully hydrogenated silicene  $4 \times 4$ : six bright spots in one HUC and one bright spot in another HUC [38]. Similar as hydrogenated

Fig. 11.10 STM images of chlorinated silicene 4 × 4 surface and corresponding structure models. a and b correspond to the same structure, but the orientation of the triangular HUCs is flipped. c and d show two 1 × 1 structures corresponding to two different upper buckled sublattices



silicene  $4 \times 4$  model, the chlorinated silicene structure also consists of six upper buckled Si atoms in one HUC and one Si in another HUC, all of them terminated by Cl atoms. In another word, it is a silicene  $4 \times 4$ - $\beta$  with all upper-buckled Si atoms terminated by Cl atoms. It is noted that the areas in Fig. 11.10a and b correspond to the same structure, but the orientation of the triangular HUCs is flipped. This is because when the transformation from  $4 \times 4$ - $\alpha$  to the inequivalent  $4 \times 4$ - $\beta$  occurs, there will be two possible configurations, which are mirror symmetric with respect to each other, as in areas 10(a) and 10(b).

In areas in Fig. 11.10c and d, one observes local triangular domains consisting of close packed protrusions in a  $1 \times 1$  periodicity. The observation of  $1 \times 1$  structure indicates that the pristine silicene-1  $\times$  1 lattice is recovered by Cl adsorption, with all the upper buckled Si atoms terminated by Cl atoms, as illustrated in the right panels of Fig. 11.10c and d. Because during the transformation from  $4 \times 4$ - $\alpha$  to  $1 \times 1$ , the

J. Zhao and K. Wu

system can chose either one of the two sublattices as the upper-buckled sublattlice, there will be also two mirror symmetric  $1 \times 1$  domains. This is indeed observed in the experiment, as shown in Fig. 11.10d. The two triangular  $1 \times 1$  domains are relatively shifted by half of the lattice constant of silicene  $1 \times 1$ , which is the lateral shift between the two sublattices.

The fully chlorinated silicene- $\sqrt{13} \times \sqrt{13}$  phase is displayed in Fig. 11.11. Two characteristic features can be revealed. Firstly, the majority of the surface has been transformed into a close packed  $1 \times 1$  structure. Secondly, many dark defect sites occur on the surface. Interestingly, most defects are arranged in a periodic  $\sqrt{7} \times \sqrt{7}$  patterns (with respect to silicene- $1 \times 1$ ). It is noted that the  $\sqrt{7} \times \sqrt{7}$  periodicity with respect to silicene  $1 \times 1$  coincides with the  $\sqrt{13} \times \sqrt{13}$  periodicity of the Ag(111) substrate, indicating the defect pattern is a result of the registration of the film lattice to the substrate lattice. Most defects appear as single dark site, which we call as monomer defect. There are also two-atom and three-atom defects, referred to as dimer and trimer defects. In particular, the trimer defects are quite popular on the surface, and they can be locally arranged in a compact  $\sqrt{7} \times \sqrt{7}$  periodic pattern, as shown in Fig. 11.6e. The structure and formation mechanism of these periodic defect sites can be understood based on analysis of the overlapping geometry of the silicene and Ag(111) lattices [47].

The chlorination of  $(2\sqrt{3}\times2\sqrt{3})R30^\circ$  gives a similar ordered silicene-1  $\times$  1 structure as the hydrogenation of the silicene- $(2\sqrt{3}\times2\sqrt{3})R30^\circ$  phase, which also results in an ordered silicene-1  $\times$  1. [40] The production of pristine silicene-1  $\times$  1 lattice by hydrogenation and chlorination prove that the original  $(2\sqrt{3}\times2\sqrt{3})R30^\circ$  phase consists of a complete silicene honeycomb lattice. The apparent defective area in the original silicene- $(2\sqrt{3}\times2\sqrt{3})R30^\circ$  surface is caused by the disorder in the buckling configuration.

It is also notable that although the chlorination of silicene- $\sqrt{13} \times \sqrt{13}$  and  $2\sqrt{3} \times \sqrt{13}$  $2\sqrt{3}$  both result in 1  $\times$  1 structures, the chlorinated  $2\sqrt{3} \times 2\sqrt{3}$  surface appears significantly more defective as compared with the  $\sqrt{13} \times \sqrt{13}$  case. The reason can be understood as the adsorption of a Cl atom on top of an upper buckled Si atom will pull the Si atom further outward, and thus increases its degree of buckling, similar as the adsorption of H on silicene [2]. As a result, both H and Cl adsorption will increase the compressive stress in the silicene film. On the other hand, the lattice mismatch between silicene and the Ag(111) substrate is different for different silicene phases. In the  $2\sqrt{3} \times 2\sqrt{3}$  phase, the silicene lattice is compressed, while in both  $4 \times 4$  and  $\sqrt{13} \times \sqrt{13}$  phase, the silicene-1  $\times$  1 lattice is expanded by Ag(111) substrate (the mismatch between lattice parameters: silicene- $\sqrt{7} \times \sqrt{7/\text{Ag}(111)}$ - $2\sqrt{3} \times 2\sqrt{3} \approx 1.02$ , silicene- $\sqrt{7} \times \sqrt{7}/Ag(111)$ -  $\sqrt{13} \times \sqrt{13} \approx 0.98$ , silicene- $3 \times 1.02$  $3/Ag(111)-4 \times 4 \approx 0.997$ ). This means that the adsorption of Cl on  $4 \times 4$  and  $\sqrt{13} \times 10^{-1}$  $\sqrt{13}$  phase is preferable because it helps to compensate the tensile stress and restore the silicene-1  $\times$  1 lattice. In contrast, adsorption of Cl on silicene-2 $\sqrt{3}$   $\times$  2 $\sqrt{3}$ would result in further compression of the silicene-1  $\times$  1 lattice, and thus making it more unstable. This may be the reason why chlorinated  $2\sqrt{3} \times 2\sqrt{3}$  phase is more defective than chlorinated  $4 \times 4$  and  $\sqrt{13} \times \sqrt{13}$  phases.

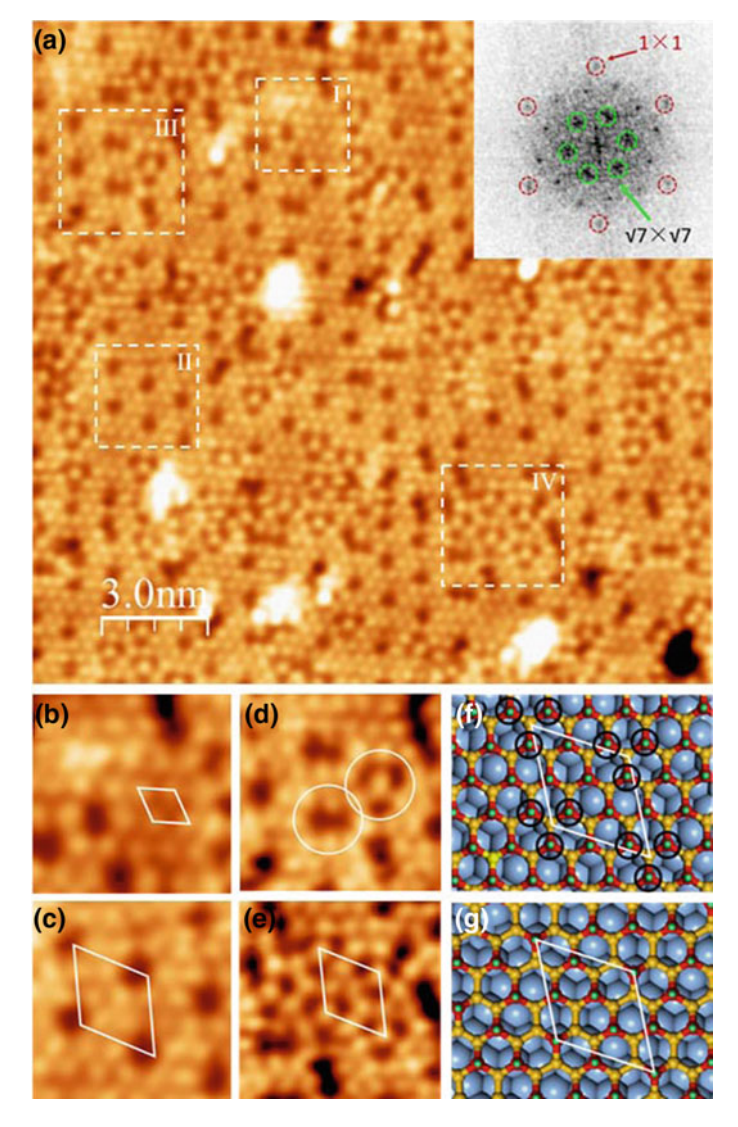


Fig. 11.11 Fully chlorinated silicene- $\sqrt{13} \times \sqrt{13}$  phase. a Typical STM image of  $\sqrt{13} \times \sqrt{13}$  phase after fully chlorinated (tip bias 0.2 V, tunneling current 50 pA). The inset is the FFT of the image showing both  $1 \times 1$  and  $\sqrt{7} \times \sqrt{7}$  patterns (with respect to silicene- $1 \times 1$ ). b-e Enlarged STM images of areas I-IV in (a). f Model of the silicene- $1 \times 1$  structure in (b), with black circles corresponding to possible defect sites. g Structure model of trimer defects arranged in a  $\sqrt{7} \times \sqrt{7}$  pattern (with respect to the silicene- $1 \times 1$ ). The white rhombuses in (f, g) represent unit cell of  $\sqrt{13} \times \sqrt{13}$  phase

J. Zhao and K. Wu

### 11.4 Oxidization

Owing to its high chemical activity, adsorption of oxygen adatoms and molecules can be used to probe and modulate local electronic states in silicene. Oxidation of silicene into silicene oxide is thus one of the major steps towards functionalization of silicene. Meanwhile, chemical stability exposed in air is a critical concern to the device applications of silicene. To address all these issues, the oxidation of silicene has been extensively studied both experimentally and theoretically.

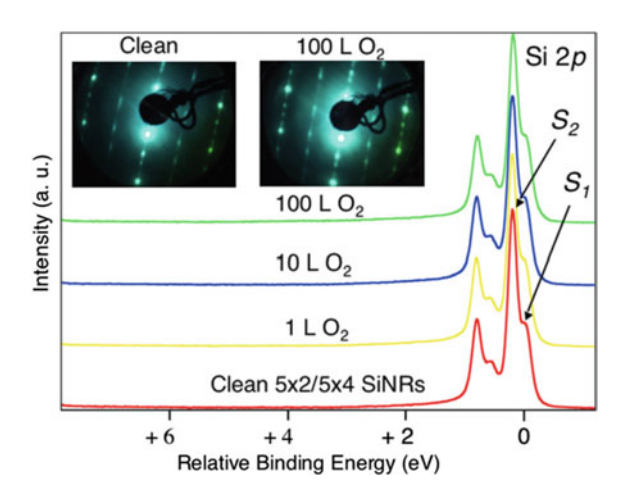
On the theoretical side, the stability of freestanding silicene sheets under oxygen environment was explored by Liu et al. [48, 49]. According to their first-principles calculations, an  $O_2$  molecule can be easily chemisorbed on pristine silicene by dissociating into two O atoms without any energy barrier. Such dissociation reaction is an exothermic process with reaction heat of about  $4.046 \sim 5.355$  eV per  $O_2$ , while the dissociated O atoms form strong Si–O bonds with silicon atoms. Compared with pristine silicene, fully hydrogenated silicene is more stable upon oxidization due to the existence of two energy barriers of 0.268 and 0.249 eV.

Morishita and Spencer [50] further investigated the microscopic mechanism of the reaction of  $O_2$  with  $4\times4$  silicene on a Ag(111) substrate using ab initio molecular dynamics (AIMD) simulations. They found barrierless oxygen chemisorption pathways around the outer Si atoms of the silicene overlayer. Therefore oxygen can easily react with a Si atom to form Si–O–Si configuration. In the case of high oxygen dose that involves multiple  $O_2$  molecules in the oxidation process, a synergistic effect between the molecular dissociation and subsequent structural rearrangements is found to accelerate the oxidation process and to enhance self-organized formation of  $sp^3$ -like tetrahedral Si–O configurations. These theoretical results help explain the inconsistent experimental observations of the oxidation of silicene on Ag(111) substrate, where different flux (or pressure) and temperature of oxygen gas could induce distinct oxidation processes.

Similar to its graphene counterpart, oxidization is also an effective way of tuning band gap of silicene in a wide range. Intuitively, the local electronic structure can be modulated from zero-gap state to semiconducting state by varying the oxygen level and changing the adsorption site of oxygen adatoms on silicene. In this regard, Pi et al. [51] investigated the structures, thermodynamic stability, and electronic properties of silicene oxides by incorporating atomic oxygen (O) and hydroxyl (OH) onto silicene lattice in many possible bonding configurations. It was found that the oxidation of silicene in the oxygen atmosphere most likely leads to the formation of the single-side over-bridging configuration, while boat-like OH and umbrella-like OH configurations are likely produced when OH is the oxidizing agent. If both O and OH exist, fully oxidized silicene may be readily produced. Depending on the specific bonding configuration and concentration of O and OH, the partially and fully oxidized silicene could be metallic, semimetallic, semiconducting and insulating.

In a pioneering experimental study, De Padova et al. [52] investigated the room temperature oxidation of Si nanoribbons (SiNRs) synthesized on Ag(110) surface by high-resolution Si 2p core level photoemission spectroscopy and low-energy electron

**Fig. 11.12** Normal emission  $(\vartheta = 0^\circ)$  Si 2p core levels for a grating of silicene NRs after increasing oxygen exposures. The LEED patterns  $(E_p = 57 \text{ eV})$  were collected on the bare grating and after the oxygen exposition of 100 L. Reproduced with permission from [52]. Copyright 2016, IOP Publishing



diffraction. As shown in Fig. 11.12, the Si spectra are practically unaffected up to an exposure of 100 Langmuir (L), where the region between 1.0 and 4.5 eV below the Si 2p core level is completely free of oxidation states. The oxidation process occurs only at high oxygen exposures up to 1000 L, typically higher than that on Si(111)  $7 \times 7$  surface by four orders of magnitude, suggesting the strong resistance of SiNRs towards oxidation.

Oxidation of epitaxial silicene sheets (with domains of  $4 \times 4$  and  $\sqrt{13} \times \sqrt{13}$  superstructures) fabricated on an Ag(111) substrate was also investigated by monitoring the Si 2p XPS photoemission line [53]. In an ultrahigh vacuum environment up to  $1000 \, \text{L}$  of oxygen dose, silicene sheets were found to be chemically stable, but undergo oxidation upon exposure to ambient air. For device applications of silicene, the oxidation might be prevented by encapsulations of the silicene layer with an ultrathin Al or aluminum oxide (Al<sub>2</sub>O<sub>3</sub>) of a few nm thickness. However, Friedlein et al. [54] deposited Al atoms onto epitaxial silicene on thin  $\text{ZrB}_2(0001)$  films grown on Si(111) and found that the aluminum oxide overlayers on silicene do not prevent but promote the oxidation of silicene instead. Under oxygen exposure up to a dose of 4500 L, the bare silicene is hardly affected, whereas aluminum oxide covered silicene becomes partially oxidized because of the dissociative chemisorption of O<sub>2</sub> molecules by Al atoms.

In addition to monolayer silicene, De Padova [55] demonstrated that thick epitaxial multilayer silicene films with a  $\sqrt{3} \times \sqrt{3} R(30^\circ)$  surface structure show only mild surface oxidation after 24 h exposure to ambient air in a combined experimental study using Auger electron spectroscopy, X-ray diffraction and Raman spectroscopy. Comparison of AES spectra shows that even after 24 h in air, the 43 MLs silicene film remains largely intact, being oxidized only at its top layers. Moreover, the characteristic G band at 523.26 cm<sup>-1</sup> and the broad D band between 430 and 500 cm<sup>-1</sup> were observed in the ex situ Raman spectrum of multilayer silicene film in air, which

228 J. Zhao and K. Wu

locate at the same positions for the  $Al_2O_3$  capped multilayer silicene and can be also related to the in situ Raman feature of bilayer silicene on Ag(111) [56].

A series of studies of the oxidation processes on monolayer silicene in different phases have been reported by Du and co-workers [56–58]. In their studies, the correlation between buckled silicene surface and oxygen adatoms has been identified by using a low-temperature STM and in situ Raman spectroscopy, while the electronic structures of oxidized silicene have been revealed by ARPES as well as XPS. The formation of the Si–O bonds on surface of silicene was investigated under well-controlled oxidation conditions with various oxygen doses.

The STM images of oxidized silicene in  $4 \times 4$ ,  $2\sqrt{3} \times 2\sqrt{3}$ , and  $\sqrt{13} \times \sqrt{13}$ structures are presented in Fig. 11.13. It can be found that the initial oxygen absorption behavior on silicene monolayers in different phases is dominated by their buckling structures, that is, Si-O bonds dominate the  $\sqrt{13} \times \sqrt{13}$  and  $2\sqrt{3} \times 2\sqrt{3}$  phases and Si–O–Si is the major oxidation form on  $4 \times 4$  phase during the initial oxidation stage. In the  $\sqrt{13} \times \sqrt{13}$  and  $2\sqrt{3} \times 2\sqrt{3}$  phases, oxygen adatoms occupy the top sites. During oxidation of  $4 \times 4$  phase, the oxygen adatoms prefer to reside at the bridge sites. Note that the silicene oxides are distinct to silicon oxide. With increment of oxygen dose, silicene monolayers are eventually fully oxidized owing to the mixed  $sp^2/sp^3$  hybridization. The binding energy between epitaxial silicene layer and Ag(111) surface is weaker than the binding energy for Si-O. Therefore, the oxygen adatoms prefer to bond firstly with Si atoms in silicene sheet instead of Ag atoms in the metal substrate. Due to the characteristic  $sp^3$  hybridization of Si, energetically stable Si-O-Si bonds are expected for all phases when silicene is exposed to high oxygen dose, e.g., 600 L. Interestingly, silicene monolayer crumples during oxidation and results in some "silicene free" areas. This observation suggests that, by taking this advantage, silicene oxide layer could be possibly detached from Ag(111) substrate and become quasi freestanding, which was demonstrated in a recent study of oxidization of bilayer silicene by the same group.

The electronic structures of oxidized silicene have been characterized by STS and ARPES, and further studied by DFT calculations. The ARPES results are displayed in Fig. 11.14. Before oxidation, the saddle-shape metallic hybrid surface band (HSB) was observed in epitaxial monolayer silicene, which can be attributed to the hybridization of Si and Ag orbitals that resembles the  $\pi$ -band dispersion in graphene. The saddle point of the surface state is about 0.15 eV below the Fermi level. ARPES investigation also reveals that the metallic HSB is decayed upon oxidation in silicene with an oxygen dose of 600 L. Meanwhile, the well-defined Shockley surface state and Ag-sp bands revive in the oxidized silicene/Ag(111) sample. An asymmetric band with the highest energy level of about -0.6 eV is also observed in ARPES features, suggesting formation of an energy gap due to oxidation.

In the same sample, STS measurements were performed on areas of Ag(111) surface and silicene oxide. An energy gap of 1.2 eV is opened on silicene oxide, whereas bare Ag(111) surface shows a typical metallic characteristics. Therefore, the asymmetric state can be attributed to the valence band originated from silicene oxide. These results coincide with the STM observations that amorphous silicon oxide covers most area of the Ag(111) surface. Note that Shockley surface state in

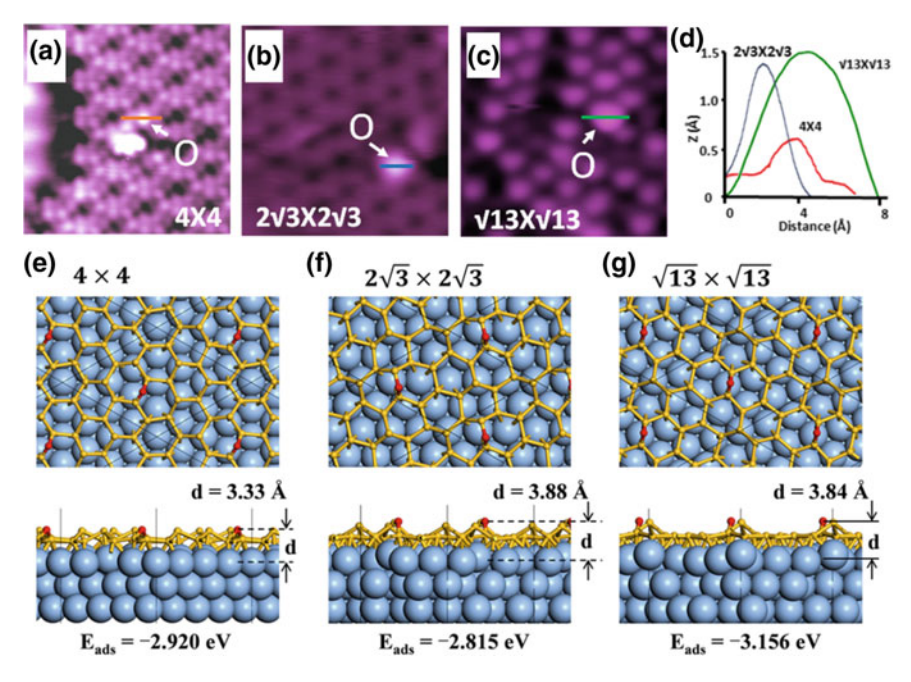
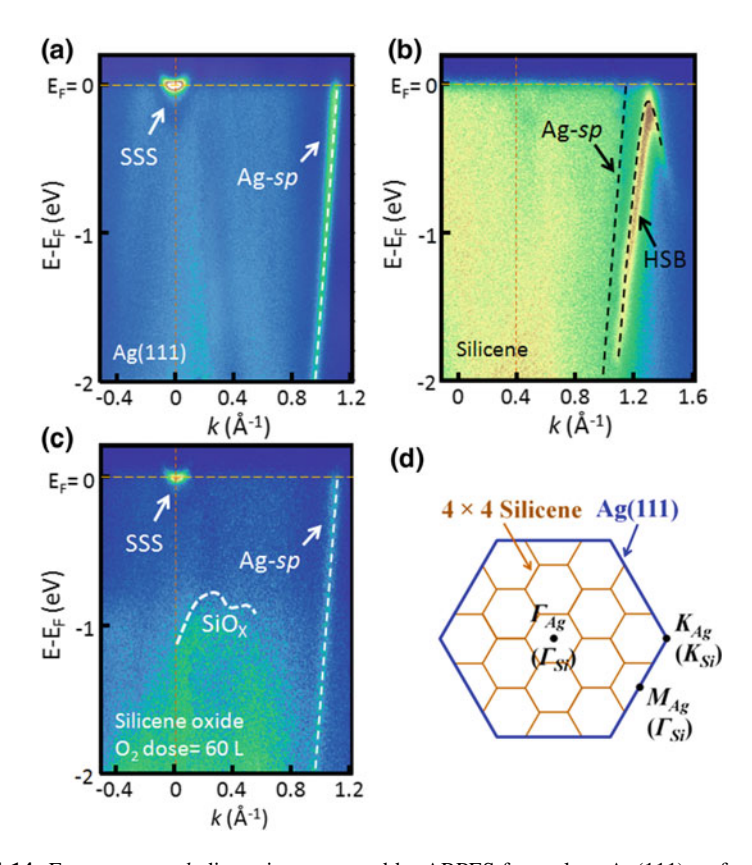


Fig. 11.13 STM images of oxidized silicene in  $\mathbf{a} 4 \times 4$ ,  $\mathbf{b} 2\sqrt{3} \times 2\sqrt{3}$ , and  $\mathbf{c} \sqrt{13} \times \sqrt{13}$  structures (scanning area  $4 \times 4$  nm²,  $V_{\text{bias}} = -0.2$  V, I = 4 nA). The oxygen adatoms prefer to reside on top-layer Si atoms in the initial oxidation.  $\mathbf{d}$  Line profiles of oxygen adatoms on silicene corresponding to the lines in the STM images in ( $\mathbf{a}$ ), ( $\mathbf{b}$ ), and ( $\mathbf{c}$ ), respectively.  $\mathbf{e} - \mathbf{g}$  DFT simulations (top and side views) of atomic structures for oxygen adatoms on Ag(111) supported silicene monolayers in different superstructures:  $\mathbf{e} 4 \times 4$ ,  $\mathbf{f} 2\sqrt{3} \times 2\sqrt{3}$ ,  $\mathbf{g} \sqrt{13} \times \sqrt{13}$ . The black rhombuses in the top views represent the unit cell. Red: oxygen; yellow: silicon; blue: silver. Reproduced with permission from [57]. Copyright 2016, American Chemical Society

metal surface is extremely surface sensitive that can reflect modifications of surface atomic and electronic properties. In the ARPES result, revived Shockley surface state in oxidized sample shows that oxygen would preferentially react with Si instead of Ag, in the case of low oxygen dose. Consequently, Si–O bonds easily replace the Ag–Si bonds.

Very recently, Du and co-workers [59] reported a quasi-free-standing silicene layer that has been successfully obtained through oxidization of bilayer silicene on the Ag(111) surface. Both STM images and DFT calculations show that the oxygen atoms prefer to intercalate into the underlayer of silicene instead of adsorb on top silicene layer, resulting in isolation of the top layer of silicene from the substrate. As a consequence of much less interaction with the substrate, the top layer of silicene exhibits the signature of a  $1 \times 1$  honeycomb lattice and hosts massless Dirac fermions as evidenced by ARPES measurement and confirmed by DFT calculations. The oxidized silicon buffer layer is expected to serve as an ideal dielectric layer for electric



**Fig. 11.14** Energy versus k dispersion measured by ARPES for **a** clean Ag(111) surface, **b**  $4 \times 4$  silicene grown on Ag(111), and **c** oxidized silicene on Ag(111), respectively. SSS in (**a**) and (**b**) denotes the Shockley surface state. HSB in (**b**) denotes the hybrid surface band. **d** Schematic of BZ for  $4 \times 4$  silicene grown on Ag(111): blue and orange honeycomb structures correspond to Ag(111) and  $4 \times 4$  silicene, respectively. Reproduced with permission from [58]. Copyright 2016, Macmillan Publishers Limited

gating in electronic devices, paving a new way toward silicene-based nanoelectronic and spintronic devices.

## 11.5 Conclusion and Perspective

Compared with the hydrophobic and chemically inert surface of graphene, silicene sheets exhibit higher chemical activities, resulting in easy tunability of their physical, chemical and electronic properties via chemical functionalization. Secondly, as native silicene surface is sensitive to exposure to air, any future application of silicene in nanodevices should inevitably involve a protection layer, or a sandwich structure with

the silicene layer in the center. Thus studying the interaction between silicene and other materials or adsorbates is a fundamental issue and desires more investigations, both theoretically and experimentally.

### References

- R. Balog, B. Jørgensen, J. Wells, E. Lægsgaard, P. Hofmann, F. Besenbacher, L. Hornekær, J. Am. Chem. Soc. 131, 8744 (2009)
- L.C. Lew Yan Voon, E. Sandberg, R.S. Aga, A.A. Farajian, Hydrogen compounds of group-IV nanosheets. Appl. Phys. Lett. 97:163114 (2010)
- M. Houssa, E. Scalise, K. Sankaran, G. Pourtois, V.V. Afanas'ev, A. Stesmans, Electronic properties of hydrogenated silicene and germanene. Appl. Phys. Lett. 98, 223107 (2011)
- J.O. Sofo, A.S. Chaudhari, G.D. Barber, Graphane: a two-dimensional hydrocarbon. Phys. Rev. B 75, 153401 (2007)
- S. Lebègue, M. Klintenberg, O. Eriksson, M.I. Katsnelson, Accurate electronic band gap of pure and functionalized graphane from GW calculations. Phys. Rev. B 79, 245117 (2009)
- P. Zhang, X.D. Li, C.H. Hu, S.Q. Wu, Z.Z. Zhu, First-principles studies of the hydrogenation effects in silicene sheets. Phys. Lett. A 376, 1230–1233 (2012)
- H. Liu, N. Han, J. Zhao, Band gap opening in bilayer silicene by alkali metal intercalation. J. Phys. Condens. Matter 26, 475303 (2014)
- V. Zólyomi, J.R. Wallbank, V.I. Fal'ko, Silicane and germanane: tight-binding and first-principles studies. 2D Mater. 1:011005 (2014)
- 9. Q. Peng, S. De, Elastic limit of silicane. Nanoscale 6, 12071–12079 (2014)
- Y. Ding, Y. Wang, Electronic structures of silicene fluoride and hydride. Appl. Phys. Lett. 100, 083102 (2012)
- W. Wu, Z. Ao, T. Wang, C. Li, S. Li, Electric field induced hydrogenation of silicene. Phys. Chem. Chem. Phys. 16, 16588–16594 (2014)
- C.-W. Zhang, S.-S. Yan, First-principles study of ferromagnetism in two-dimensional silicene with hydrogenation. J. Phys. Chem. C 116, 4163–4166 (2012)
- T.H. Osborn, A.A. Farajian, O.V. Pupysheva, R.S. Aga, L.C. Lew Yan Voon, Ab initio simulations of silicene hydrogenation. Chem. Phys. Lett. 511:101–105 (2011)
- G. Cao, Y. Zhang, J. Cao, Strain and chemical function decoration induced quantum spin hall effect in 2D silicene and Sn film. Phys. Lett. A 379, 1475–1479 (2015)
- G.G. Guzman-Verri, L.C. Lew Yan Voon, band structure of hydrogenated Si nanosheets and nanotubes. J. Phys. Condens. Matter 23:145502 (2011)
- B. van den Broek, M. Houssa, E. Scalise, G. Pourtois, V.V. Afanas'ev, A. Stesmans, Firstprinciples electronic functionalization of silicene and germanene by adatom chemisorption. Appl. Surf. Sci. 291, 104–108 (2014)
- 17. X.Q. Wang, H.D. Li, J.T. Wang, Induced ferromagnetism in one-side semihydrogenated silicene and germanene. Phys. Chem. Chem. Phys. 14, 3031–3036 (2012)
- 18. F.-B. Zheng, C.-W. Zhang, The electronic and magnetic properties of functionalized silicene: a first-principles study. Nanoscale Res. Lett. **7**, 422 (2012)
- X. Pi, Z. Ni, Y. Liu, Z. Ruan, M. Xu, D. Yang, Density functional theory study on boron- and phosphorus-doped hydrogen-passivated silicene. Phys. Chem. Chem. Phys. 17, 4146–4151 (2015)
- C.J. Rupp, S. Chakraborty, R. Ahuja, R.J. Baierle, The effect of impurities in ultra-thin hydrogenated silicene and germanene: a first principles study. Phys. Chem. Chem. Phys. 17, 22210–22216 (2015)
- C.J. Rupp, S. Chakraborty, J. Anversa, R.J. Baierle, R. Ahuja, Rationalizing the hydrogen and oxygen evolution reaction activity of two-dimensional hydrogenated silicene and germanene. ACS Appl. Mater. Interfaces 8, 1536–1544 (2016)

- 22. B. Huang, H.-X. Deng, H. Lee, M. Yoon, B.G. Sumpter, F. Liu et al., Exceptional optoelectronic properties of hydrogenated bilayer silicene. Phys. Rev. X 4, 021029 (2014)
- Y. Liu, H. Shu, P. Liang, D. Cao, X. Chen, W. Lu, Structural, electronic, and optical properties of hydrogenated few-layer silicene: size and stacking effects. J. Appl. Phys. 114, 094308 (2013)
- R. Wang, S. Wang, X. Wu, The formation and electronic properties of hydrogenated bilayer silicene from first-principles. J. Appl. Phys. 116, 024303 (2014)
- P. Vogt, P. De Padova, C. Quaresima, J. Avila, E. Frantzeskakis, M.C. Asensio et al., Silicene: compelling experimental evidence for graphene like two-dimensional silicon. Phys. Rev. Lett. 108, 155501 (2012)
- B. Feng, Z. Ding, S. Meng, Y. Yao, X. He, P. Cheng et al., Evidence of silicene in honeycomb structures of silicon on Ag(111). Nano Lett. 12, 3507–3511 (2012)
- C.-L. Lin, R. Arafune, K. Kawahara, N. Tsukahara, E. Minamitani, Y. Kim et al., Structure of silicene grown on Ag(111). Appl. Phys. Express 5, 045802 (2012)
- H. Jamgotchian, Y. Colignon, N. Hamzaoui, B. Ealet, J.Y. Hoarau, B. Aufray et al., Growth of silicene layers on Ag(111): unexpected effect of the substrate temperature. J. Phys. Condens. Matter 24, 172001 (2012)
- D. Chiappe, C. Grazianetti, G. Tallarida, M. Fanciulli, A. Molle, Local electronic properties of corrugated silicene phases. Adv. Mater. 24, 5088–5093 (2012)
- L. Chen, C.-C. Liu, B. Feng, X. He, P. Cheng, Z. Ding et al., Evidence for Dirac fermions in a honeycomb lattice based on silicon. Phys. Rev. Lett. 109, 056804 (2012)
- 31. H. Enriquez, S. Vizzini, A. Kara, B. Lalmi, H. Oughaddou, Silicene structures on silver surfaces. J. Phys. Condens. Matter **24**, 314211 (2012)
- 32. X. Xun, Z. Jincheng, D. Yi, S. Eilers, G. Peleckis, Y. Waikong et al., Epitaxial growth mechanism of silicene on Ag(111), in 2014 International Conference on Nanoscience and Nanotechnology (ICONN), Adelaide, SA IEEE (2014). p. 28–30
- 33. J. Sone, T. Yamagami, Y. Aoki, K. Nakatsuji, H. Hirayama, Epitaxial growth of silicene on ultra-thin Ag(111) films. New J. Phys. 16, 095004 (2014)
- 34. A. Resta, T. Leoni, C. Barth, A. Ranguis, C. Becker, T. Bruhn et al., Atomic structures of silicene layers grown on Ag(111): scanning tunneling microscopy and noncontact atomic force microscopy observations. Sci. Rep. 3, 2399 (2013)
- 35. E. Cinquanta, E. Scalise, D. Chiappe, C. Grazianetti, B. van den Broek, M. Houssa et al., Getting through the nature of silicene: an  $sp^2-sp^3$  two-dimensional silicon nanosheet. J. Phys. Chem. C **117**, 16719–16724 (2013)
- 36. J. Zhuang, X. Xu, Y. Du, K. Wu, L. Chen, W. Hao et al., Investigation of electron-phonon coupling in epitaxial silicene by in situ Raman spectroscopy. Phys. Rev. B. **91**, 161409 (2015)
- C. Grazianetti, D. Chiappe, E. Cinquanta, M. Fanciulli, A. Molle, Nucleation and temperaturedriven phase transitions of silicene superstructures on Ag(111). J. Phys. Condens. Matter 27, 255005 (2015)
- 38. J. Qiu, H. Fu, Y. Xu, A.I. Oreshkin, T. Shao, H. Li et al., Ordered and reversible hydrogenation of silicene. Phys. Rev. Lett. **114**, 126101 (2015)
- Z.-L. Liu, M.-X. Wang, J.-P. Xu, J.-F. Ge, G.L. Lay, P. Vogt et al., Various atomic structures of monolayer silicene fabricated on Ag(111). New J. Phys. 16, 075006 (2014)
- J. Qiu, H. Fu, Y. Xu, Q. Zhou, S. Meng, H. Li et al., From silicene to half-silicane by hydrogenation. ACS Nano 9, 11192 (2015)
- 41. Wang et al., PRB 93, 081406R (2016)
- G. Prévot, R. Bernard, H. Cruguel, Y. Borensztein, Monitoring Si growth on Ag(111) with scanning tunneling microscopy reveals that silicene structure involves silver atoms. Appl. Phys. Lett. 105, 213106 (2014)
- 43. N. Gao, W.T. Zheng, Q. Jiang, Density functional theory calculations for two-dimensional silicene with halogen functionalization. Phys. Chem. Chem. Phys. 14, 257–261 (2012)
- 44. P.A. Denis, Stacked functionalized silicene: a powerful system to adjust the electronic structure of silicene. Phys. Chem. Chem. Phys. 17, 5393–5402 (2015)
- 45. X. Wang, H. Liu, S.-T. Tu, First-principles study of half-fluorinated silicene sheets. RSC Adv. 5, 6238–6245 (2015)

- 46. B. Huang, H.J. Xiang, S.-H. Wei, Chemical functionalization of silicene: spontaneous structural transition and exotic electronic properties. Phys. Rev. Lett. 111, 145502 (2013)
- 47. W. Li et al. PRB 2016
- G. Liu, X.L. Lei, M.S. Wu, B. Xu, C.Y. Ouyang, Is silicene stable in O<sub>2</sub>?—First-principles study of O<sub>2</sub> dissociation and O<sub>2</sub>-dissociation—induced oxygen atoms adsorption on free-standing silicene. Europhys. Lett. 106, 47001 (2014)
- G. Liu, X.L. Lei, M.S. Wu, B. Xu, C.Y. Ouyang, Comparison of the stability of free-standing silicene and hydrogenated silicene in oxygen: a first principles investigation. J. Phys. Condens. Matter 26, 355007 (2014)
- 50. T. Morishita, M.J. Spencer, How silicene on Ag(111) oxidizes: microscopic mechanism of the reaction of O<sub>2</sub> with silicene. Sci. Rep. **5**, 17570 (2015)
- 51. R. Wang, X. Pi, Z. Ni, Y. Liu, S. Lin, M. Xu et al., Silicene oxides: formation, structures and electronic properties. Sci. Rep. **3**, 3507 (2013)
- 52. P. De Padova, C. Quaresima, B. Olivieri, P. Perfetti, G. Le Lay, Strong resistance of silicene nanoribbons towards oxidation. J. Phys. D Appl. Phys. **44**, 312001 (2011)
- A. Molle, C. Grazianetti, D. Chiappe, E. Cinquanta, E. Cianci, G. Tallarida et al., Hindering the oxidation of silicene with non-reactive encapsulation. Adv. Funct. Mater. 23, 4340–4344 (2013)
- R. Friedlein, H. Van Bui, F.B. Wiggers, Y. Yamada-Takamura, A.Y. Kovalgin, M.P. de Jong, Interaction of epitaxial silicene with overlayers formed by exposure to Al atoms and O<sub>2</sub> molecules. J. Chem. Phys. 140, 204705 (2014)
- P. De Padova, C. Ottaviani, C. Quaresima, B. Olivieri, P. Imperatori, E. Salomon et al, 24 h stability of thick multilayer silicene in air. 2D Mat. 1:021003 (2014)
- J. Zhuang, X. Xu, Y. Du, K. Wu, L. Chen, W. Hao et al., Investigation of electron-phonon coupling in epitaxial silicene by in situ Raman spectroscopy. Phys. Rev. B 91, 161409 (2015)
- 57. Y. Du, J. Zhuang, H. Liu, X. Xu, S. Eilers, K. Wu et al., Tuning the band gap in silicene by oxidation. ACS Nano 8, 10019–10025 (2014)
- 58. X. Xu, J. Zhuang, Y. Du, H. Feng, N. Zhang, C. Liu et al., Effects of oxygen adsorption on the surface state of epitaxial silicene on Ag(111). Sci. Rep. 4, 7543 (2014)
- 59. Du et al., Sci. Adv. 2, e1600067 (2016)

# Chapter 12 Encapsulated Silicene Field-Effect Transistors



Li Tao, Eugenio Cinquanta, Carlo Grazianetti, Alessandro Molle and Deji Akinwande

**Abstract** Besides theoretical studies, experimental investigations on silicene began with the synthesis of silicene on ceramic or metallic catalyst substrates such as ZrB<sub>2</sub>, Ir and Ag. Among various reported methods, the epitaxial growth of silicene sheet atop Ag(111) has received increasing attention and a derivative approach of using evaporated Ag(111) film as catalyst on a cleavable substrate will be specifically discussed in this Chapter for the ease of following device studies. Despite these research progresses in silicene synthesis, there is a lack of experimental investigation on silicene devices. One of the most key challenges is the material preservation during device fabrication and measurement process. This chapter will summarize recent understanding and progress in air-stability of silicene and viable device fabrication choices, to enable the debut of the first silicene field-effect transistor. A survey will be conducted on experimental probing of electrical properties of silicene via scanning tunneling microscopy, angle-resolved photoemission spectroscopy, and experimental transport measurement on field-effect transistors. These results not only provide experimental feedback to existing theoretical studies, but also encourages further interest in novel device concepts and prospects of silicene and other emerging 2D materials like germanene, stanene and phosphorene.

#### 12.1 Introduction

Since the pioneering work on graphene [1, 2], research on graphene-like two-dimensional (2D) crystalline materials has evolved to an emerging field crossing fundamental science and practical engineering [3, 4]. Owing to their distinct prop-

L. Tao · D. Akinwande (⊠)

Microelectronics Research Centre, The University of Texas at Austin, Austin, TX 78758, USA e-mail: deji@ece.utexas.edu

Present Address

L. Tao

School of Materials Science and Engineering, Southeast University, Nanjing 211189, China

E. Cinquanta · C. Grazianetti · A. Molle

Laboratorio MDM, IMM-CNR, Via Camillo Olivetti 2, Agrate Brianza, 20864 Catania, Italy

© Springer Nature Switzerland AG 2018

235

P. Vogt and G. Le Lay (eds.), Silicene, NanoScience and Technology,

L. Tao et al.

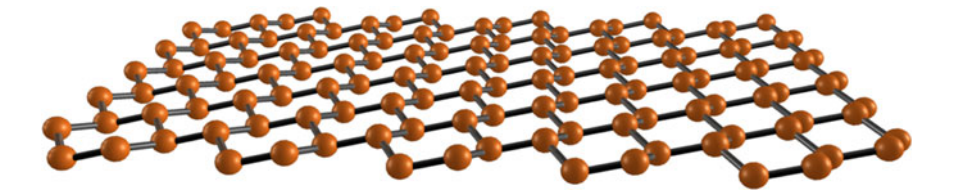


Fig. 12.1 Buckled honeycomb lattice structure of silicene

erties arising from the specific 2D physical character and chemical composition, 2D materials hold great promise for future nanoelectronics, spintronics, straintronics, optoelectronics, sensors, and energy related applications [4–7]. Besides the recent upsurge in studies on hexagonal boron nitride, transition metal dichalcogenides (TMDs) and metal oxides [3–5, 8], there is very limited experimental research on group IV elemental graphene analogues such as silicene and germanene. Free Standing (FS)-silicene, a 2D crystal, is composed of silicon atoms arranged in a buckled honeycomb lattice (Fig. 12.1) that had been predicted [9, 10] even before the 2004 reports on graphene [1, 2]. The theoretical calculations based on tight binding [11, 12] (TB) or density functional theory (DFT) [13–15], have predicted a semiconductor Dirac band structure for FS-silicene (quasi-2D silicon) similar to graphene. Regardless of the similar orbital configurations for group-IV elements,  $sp^3$  rather than  $sp^2$  hybridization is more favorable for silicon in contrast to carbon [16] thus inducing vertical distortions in the silicene lattice [19]. The buckled nature of silicene due to  $sp^3$  hybridization leads to a greater interface interaction (than graphene) that can result in a sizeable band-gap (e.g. attaching hydrogen to form silicane) and offer desirable electronic and optoelectronic properties [15, 17]. As a result, monolayer FSsilicene is expected to be a promising 2D material for electronic devices or sensors. Due to its buckled physical structure and relatively stronger spin-orbit coupling, theoretical calculations also suggest FS-silicene should afford novel phenomena such as quantum spin Hall effect [18], piezo-magnetism [19], giant magnetoresistance [20], enhanced optical absorption [21] and strain-related thermal conductivity [22] distinguished from the commonly studied prototypical 2D material, graphene.

Besides theoretical studies, experimental investigations on silicene began with the synthesis of silicene on ceramic or metallic catalyst substrates such as  $ZrB_2$  [23], Ir [24] and Ag [25–29] as introduced in Chap. 5. Among various reported methods, the epitaxial growth of silicene sheet atop Ag(111) [30–32] has received increasing attention and a derivative approach of using evaporated Ag(111) film as catalyst on a cleavable mica [17, 33, 34] substrate will be specifically discussed in Sect. 12.2 for the ease of following device studies. Despite these research progresses in silicene synthesis, there is a lack of experimental investigation on silicene devices. One of the most key challenges is the material preservation during device fabrication and measurement process. Section 12.3 will summarize recent understanding and progress in air-stability of silicene and viable device fabrication choices, to enable the debut of the first silicene field-effect transistor. Consequently, in Sect. 12.4, a survey will

be conducted on experimental probing of electrical properties of silicene via scanning tunneling microscopy (STM) [31, 33, 35, 36], angle-resolved photoemission spectroscopy (ARPES) [32, 35], and experimental transport measurement on field-effect transistors (FETs) [37]. These results not only provide experimental feedback to existing theoretical studies, but also encourages further interest in novel device concepts and prospects of silicene and other emerging 2D materials like germanene [38], stanene [39] and phosphorene [6, 40]. In addition, the allotropic affinity of silicene with crystal bulk silicon suggests a more direct integration path with ubiquitous semiconductor technology unlike other 2D crystals that are historically not mainstream microelectronic materials.

# 12.2 Epitaxy of Silicene on Cleavable Ag (111)/Mica Substrate

In 2005 and 2007, Lendri et al. reported self-aligned silicon quantum wires on Ag(110) [25] and silicon nanostructures on Ag(001) [26]. These works employed a ultra-high vacuum (UHV) synthesis approach highly similar to the epitaxial growth of silicene, which was proposed to exist by few theoretical studies several years later in 2007–2009 [11, 13]. Le Lay group grew graphene-like silicon nanoribbons on Ag(110), indicating a possible formation of silicene for the first time in 2010 [28] (see also Chap. 6). Two years later, several groups (e.g. Vogt et al. [32], Lin et al. [31], Feng et al. [30] and Chiappe et al. [33]) demonstrated the epitaxial synthesis of silicene on single crystal Ag(111) (Chap. 7). This opens the road for practical device study as Ag(111) holds great promise to obtain a continuous silicene sheet instead of nanoscale wires or ribbons previously shown on Ag(110). As a result, there had been increasing investigations (e.g. Acun et al. [41], Moras et al. [42], and Mannix et al. [43].) on the technical details of silicene growth on Ag(111) that enable more thorough understanding and control of this process.

A most recent progress was made to epitaxially grow silicene on 300-nm thick Ag(111) film on mica substrate instead of single crystal Ag(111) bulk, allowing a mechanical cleaving way to transfer silicene for device fabrication [37]. Such a silicene synthesis was performed in a UHV chamber (base pressure  $10^{-10}$ – $10^{-11}$  mbar) system equipped with three interconnected chambers for sample processing, chemical analysis and in-situ STM characterization. Several cycles of Ar<sup>+</sup> ion sputtering (1 keV) was first performed on Ag(111) to reveal a clean surface, and subsequent annealing at 530 °C for 30 min was introduced. Silicene sheet was deposited on processed Ag(111) surface from a heated crucible in the built-in evaporator at a temperature between 250–270 °C with a rate of 2–6 ×  $10^{-2}$  monolayer/min. Silicene growth on Ag(111)/mica substrate was monitored by a real-time reflection high-energy electron diffraction (RHEED) at 30 keV and in-situ STM with a typical tip voltage of -1.4 V and tunneling current of 0.5 nA. Figure 12.2a shows a RHEED pattern of pristine (1 × 1) Ag(111) surface after

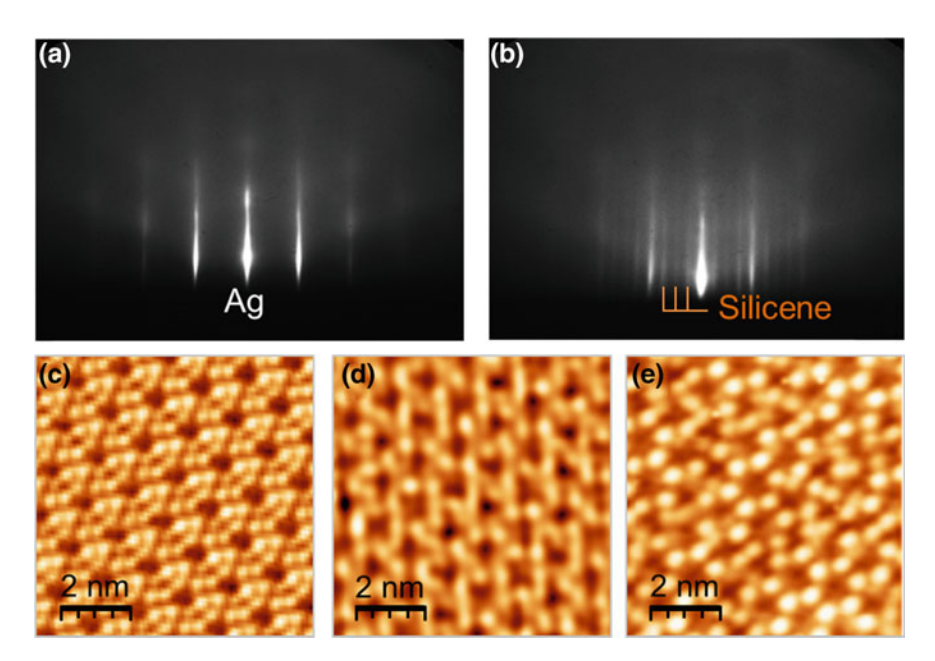


Fig. 12.2 In-situ materials characterization of silicene synthesis. Real-time reflection high-energy electron diffraction (RHEED) on  $\bf a$ , Ag(111), and  $\bf b$ , silicene on Ag(111) (the azimuth is along the [11-2] Ag surface direction and the emergence of extra-streaks in the RHEED pattern in panel  $\bf b$  results from the silicene epitaxy). In-situ scanning tunnelling microscopy (STM) shows three main Si over layers:  $\bf c$ , (4 × 4),  $\bf d$ , ( $\sqrt{13} \times \sqrt{13}$ ), and  $\bf e$ , (2 $\sqrt{3} \times 2\sqrt{3}$ ) superstructures. The STM images are  $10 \times 10$  nm<sup>2</sup> and were acquired with a sample bias of -1.4 V and tunnelling current of 0.5 nA

Ar<sup>+</sup> plasma cleaning and annealing. After the growth of monolayer 2D silicon on Ag(111), a new set of sub-streaks in Fig. 12.2b appeared in between aforementioned main streaks, resulting from silicene crystalline grown on Ag(111). Depending on whether silicon atoms are sequentially sitting in between or on top of Ag atoms, characteristic patterns of silicene domains with respect to the Ag unit cell include  $(4 \times 4)$ ,  $(\sqrt{13} \times \sqrt{13})$  and  $(2\sqrt{3} \times 2\sqrt{3})$  that have been well-distinguished by STM [31, 33, 35] as seen in Fig. 12.2c, d. This epitaxial growth leads to a variety of coexisting silicene domains with different periodic order whose amount depends on the deposition temperature [33, 41, 42]. For instance, a uniform  $2\sqrt{3} \times 2\sqrt{3}$  superstructure (Fig. 12.2e) can be obtained with increased deposition temperature at 270 °C in a recent report by Carlo et al. [44]. This outcome is in consistent with a recent report by Moras et al. [42], who exhaustively accounts for the multiphase character of the silicene monolayer by systematically measuring the amount of each silicene phase as a function of the growth temperature. Above certain temperature, Acun et al. [41] reported instability of silicene grown on Ag(111) (for a detailed discussion see Chap. 7).

Although the scope of this chapter will still be focused on the monolayer silicene in the following content, the synthesis of few layer or multilayer silicene on Ag(111) is also a topic of great interests (see also Sects. 5.5 and 8.4). Mannix et al. [43] provided a thorough discussion on the epitaxy of silicene on Ag(111), and identified a  $\sqrt{7} \times \sqrt{7}$  superstructure (referred to the Si periodicity and equivalent to  $2\sqrt{3} \times 2\sqrt{3}$  and  $\sqrt{13} \times \sqrt{13}$  superstructures referred to the Ag(111) periodicity) in the monolayer regime and  $\sqrt{3} \times \sqrt{3}$  reconstruction in the bilayer or multilayer regime. It should be noted that a scientific debate is currently emerging on what is the correct crystallographic nature of the  $\sqrt{3} \times \sqrt{3}$  phase (e.g. whether it is graphite-like as suggested by De Padova et al. [45] or diamond Si(111)-like as proposed by Mannix et al. [43] and Shirai et al. [46]).

# 12.3 Air-Stability of Silicene Post Synthesis and During Transfer

## 12.3.1 $Al_2O_3$ Capping of Silicene

Despite the progress in epitaxy of large area silicene on Ag(111), there was a key challenge to keep silicene intact post synthesis as it exhibited a destructive reactivity once under ambient condition. Alessandro et al., investigated such degradation of silicene with O dosing in UHV environment and upon exposure to air [34]. Based on their X-ray photoelectron spectroscopy (XPS) monitoring of the Si 2p photoemission line, epitaxial silicene grown on Ag(111) stays chemically stable upon O exposure up to 1000 L (1 L=1 s at  $1 \times 10^{-6}$  Torr) but it undergoes a progressive oxidation in air. In consistent with low reactivity of silicene nanoribbons [29], XPS observes a scarce oxidation degree of silicene sheet on Ag(111) in UHV environment that can be presumably related to slow oxidation pathways via crystal defects or phase boundaries mentioned in 12.1. Nevertheless, an instant change of silicene composition (with XPS indicating Si-O bond) occurred once exposed to air. To address this air-stability issue, Alessandro et al., developed a non-reactive capping procedure [34] via the in-situ co-deposition of Al and O<sub>2</sub> to form an Al<sub>2</sub>O<sub>3</sub> layer post silicene synthesis. In contrary to uncapped epitaxial silicene on Ag(111) suffering from degradation immediately after air exposure, Al<sub>2</sub>O<sub>3</sub> capping adopted silicene samples remain intact as seen in the detailed ex situ Raman characterization below.

Raman spectroscopy was employed to verify the integrity of silicene on Ag(111) after removal from the UHV synthesis environment. Raman spectra of differently-oriented silicene superstructures are dominated by the presence of a sharp and intense peak in the 515–522 cm<sup>-1</sup> range, induced by the symmetric stretching of Si–Si atoms in planar hexagons ( $E_{2g}$  vibrational modes) [17, 47]. In addition, the different buckling amount and distribution is the carrier of the  $A_{1g}$  vibrational modes (breathing-like modes), which in turns give rise to the asymmetric shoulder in the 450–500 cm<sup>-1</sup> range unlike bulk Si (Fig. 12.3). More in details, the spectrum of the 4 × 4 superstruc-

240 L. Tao et al.

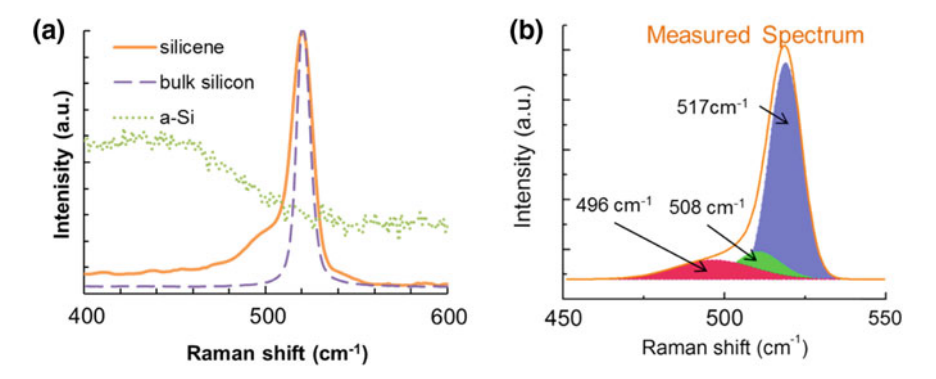


Fig. 12.3 Raman characterization on **a** silicene compared to amorphous silicon (a-Si) and bulk silicon; **b** decomposition of a measured Raman spectrum agrees with theoretical computation of  $E_{2g}$  and  $A_{1g}$  modes (centred at 517, 508 and 496 cm<sup>-1</sup>) representing a mixed-phase silicene. Raman spectroscopy serves as a good cross-reference to STM for distinguishing silicene from a-Si phase

ture is characterized by a remarkable intensity for the asymmetric shoulder, reflecting the high degree of intrinsic disorder due to the large amount of buckled atoms (30%) present in its unit cell (see also Sect. 7.4.3). On the other hand, the spectrum of the  $2\sqrt{3}\times2\sqrt{3}$  is dominated by  $E_{2g}$  modes at 522 cm $^{-1}$ , while the  $A_{1g}$  ones just bears a negligible intensity, reflecting the planarity of this silicene superstructure [17]. By comparing Raman spectra of the different superstructures as a function the excitation energy, resonant and non-resonant behaviors can be respectively associated with the  $4\times4$  and the  $2\sqrt{3}\times2\sqrt{3}$  superstructure of Ag-supported silicene, which hint at different electronic band structures [17, 48]. This can be potentially used as a benchmark to assess the influence of the substrate or to recognize different superstructures in the vibrational properties of silicene.

The  $Al_2O_3$  capping procedure, as part of the encapsulation design in following Sect. 12.4.1, can be generally applied to any silicene configuration, irrespective of the support substrate, and it leads to the fabrication of atomically sharp and chemically intact silicene. This approach makes epitaxial silicene accessible to a broad number of ex situ diagnostic and potentially suitable to gated device configurations.

# 12.3.2 Ag-Si Interaction

With  $Al_2O_3$  capping layer as an effective protection for epitaxial silicene on Ag(111) catalyst, the next question along the line for device studies is: could synthesized silicene be easily transferred to insulating substrates for device studies? Tao et al. [37] revealed that it is unfeasible for silicene to go through the conventional polymer coating/protective layer lift-off transfer employed for graphene and other 2D materials [49, 50], because even  $Al_2O_3$  capped silicene degrades (oxidizes) readily as the Ag

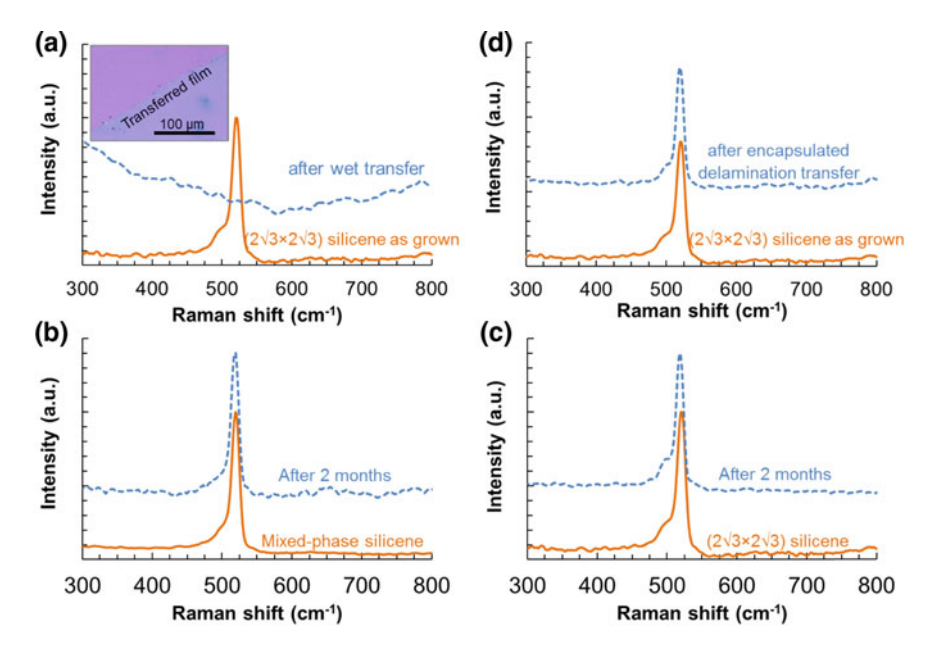


Fig. 12.4 Raman monitor on the air-stability of Ag-supported silicene. a Raman spectra of  $(2\sqrt{3} \times 2\sqrt{3})$  silicene as grown (solid curve) and after wet transfer (dash curve). Inset shows silicene film on SiO<sub>2</sub>/Si substrate by wet transfer. b, c Raman scans on  $(\sqrt{13} \times \sqrt{13})$  and  $(4 \times 4)$  mixed-phase silicene and  $(2\sqrt{3} \times 2\sqrt{3})$  silicene before (solid curve) and after 2-month storage (dash curve) in 30-mbar rough vacuum at room temperature. d Raman signatures of  $(2\sqrt{3} \times 2\sqrt{3})$  silicene as grown (solid curve) and 7 days after our encapsulated delamination transfer (dash curve)

interface is removed by wet etching (Fig. 12.4a). To verify that the removal of Ag(111) film is the major cause for the degradation of Al<sub>2</sub>O<sub>3</sub> capped silicene, they monitored the ex situ Raman characteristics of Al<sub>2</sub>O<sub>3</sub> capped silicene on Ag(111)/mica stored in a rough vacuum (30 mbar) at room temperature. The Raman signatures of silicene remain intact, indicating chemical stability when supported by the Ag(111) film, over two months (Fig. 12.4b, c). Inspired by this observation, a new method was conceived for silicene transfer to overcome the stability challenge associated with suspended silicene. The key innovation is to preserve silicene/Ag(111) interface after separation from the growth substrate (mica) followed by the integration onto a device substrate, the details of which will be discussed in the following Sect. 12.4. As a proof-ofprinciple for this idea, Raman spectra of capped silicene/Ag(111) taken 7 days after the transfer (Fig. 12.4d) shows the same signatures as the freshly grown sample. Another merit of this observation on the stability of Ag-supported silicene is that it provided an original evidence from experiments supporting DFT calculations on that p-d hybridization between Ag and Si preserves the stability of silicene grown on Ag (111) [51] and such interaction could substantially affect the material properties of silicene [52, 53]. Details of Ag-Si interaction are covered in Chap. 7 and Sect. 8.2.

Besides the substrate coupling effect, the intrinsic structure of silicene also plays an important role in the stability of silicene. Silicene with mostly  $(4 \times 4)$  superstructure experienced more rapid degradation than samples composed of  $(2\sqrt{3}\times2\sqrt{3})$  superstructure. Considering the difference in the amount of buckled atoms 30% for  $(4\times4)$  versus 14% for  $(2\sqrt{3}\times2\sqrt{3})$  [17], one can deduce that the stability of silicene also depends on the  $sp^2$  to  $sp^3$  ratio: the larger the  $sp^3$  composition, the higher the chemical reactivity; the larger the  $sp^2$  composition, the more stable it is. The inevitable presence of  $sp^3$  component in silicene eventually drives the degradation of working device within a couple of minutes when exposed to the air after measurement. The instability of Ag-remove silicene will be illustrated in the following Sect. 12.4.2, and it agrees with the spontaneous structural transition [54] and local reconstruction [55] of silicene expected by recent fundamental studies. It is warranted to improve silicene stability for reliable devices with future research on Si–Ag interface, intrinsic structure (i.e. number of layers and phase) of silicene and immediate capping upon device fabrication.

# 12.4 Silicene Devices: Fabrication, Measurement and Electronic Properties

Ever since the successful synthesis of silicene, there is always a booming interest in understanding the electronic properties that will have a tremendous impact on the development of potential nanoelectronics. Strong efforts had been made to theoretical studies and there are several recent experimental probing of material structure or electronic properties of silicene using in-situ STM [31, 33, 35, 36] or ARPES [32, 35] referring to related content in Sects. 6.5 and 7.4. For example, Chiappe et al. [33] measured bell-shape current-voltage (bias through STM tip) response of silicene on Ag(111) and Vogt et al. [32] and De Padova et al. [35] observed ARPES data possibly due to the existence of Dirac cone. Nevertheless, ex situ measurement of a practical device is of great importance to provide experimental evidences to guide the understanding of the electronic band structure of silicene. This section will introduce the most recent progress on the debut of silicene transistors [37] that hold great promise for potentially practical applications.

## 12.4.1 Silicene Encapsulated Delamination and Native Ag Electrodes (SEDNE) Process

Recall the Sects. 12.3.1 and 12.3.2 of this chapter, air-stability is the key issue to build practical silicene devices. Towards overcoming this issue, it is essential to preserve pristine silicene by keeping the Ag-Si interface on one side and having the  $Al_2O_3$  protection layer on the other side. In this light, Tao et al. [37] devised a synthesis-

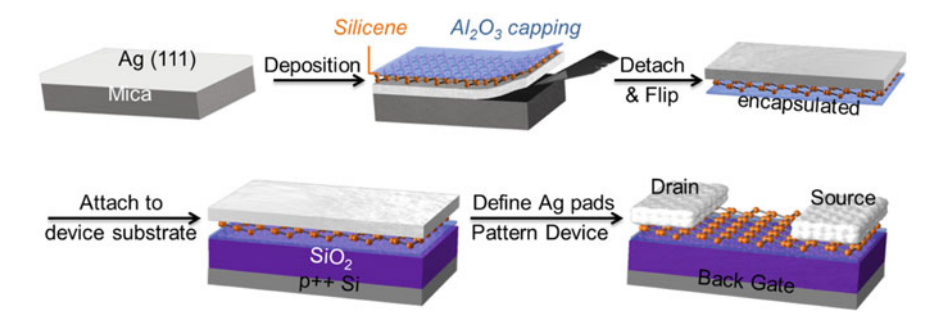


Fig. 12.5 Silicene encapsulated delamination with native electrode (SEDNE) process that includes the following key steps: epitaxial growth of silicene on crystallized Ag(111) thin film, in-situ  $Al_2O_3$  capping, encapsulated delamination transfer of silicene, and native contact electrodes formation to enable back-gated silicene transistors

transfer-fabrication process denoted as Silicene Encapsulated Delamination with Native Electrodes (SEDNE). A schematic illustration of the SEDNE process is shown in Fig. 12.5, which includes the following key innovations: (i) epitaxial silicene synthesis on deposited Ag(111) thin film instead of expensive single crystal bulk Ag, (ii) encapsulated delamination transfer of silicene sandwiched between  $Al_2O_3$  and native Ag thin films that affords the recycle of mica substrate and (iii) reuse of the native Ag(111) film to stabilize silicene and serve as contact electrodes.

The process flow of SEDNE runs as following steps below. Starting from epitaxial silicene on Ag(111)film/mica, a blade (or a tape) initiated a gap at the edge of the sample in between the Ag and mica interface, peeling off the Al<sub>2</sub>O<sub>3</sub>/silicene/Ag film stack. This encapsulated silicene in between Al<sub>2</sub>O<sub>3</sub> and Ag was then placed on a device substrate (e.g. 90-nm thick SiO<sub>2</sub> on p<sup>++</sup> Si) with the Al<sub>2</sub>O<sub>3</sub> layer facing downward in contact with the SiO<sub>2</sub> layer. Silicene channel as well as source/drain electrodes (in native Ag catalyst film) were patterned via e-beam lithography followed by etching to enable back-gate transistor devices. To prevent a rapid degradation/oxidation of silicene observed in commonly used Ag etchant like nitric acid, a potassium iodide and iodine based etchant was developed in-house. This gains a short but sufficient time window for capturing the charge transportation behaviour in Ag-free silicene. The microscopic image in Fig. 12.6a shows a representative backgated silicene transistor device with contact lines formed in the original Ag layer on  $2\sqrt{3} \times 2\sqrt{3}$  silicene. On the dashed box area, zoom-in AFM scan (Fig. 12.6b) reveals the Ag source and drain pads at both ends of the silicene channel (false color for enhanced contrast). Electrical characterization were subsequently performed using the highly-doped silicon substrate as the back-gate as depicted in Sect. 12.4.2.

SEDNE process provides an effective platform that can be generally applied to a broad spectrum of air-sensitive 2D materials, for instance its Group IV and V cousins such as but not limited to germanene, stanene and phosphorene. In the rest of this chapter, electronic properties of silicene will be discussed in detail from experimental measurement of FETs made via SEDNE process.

244 L. Tao et al.

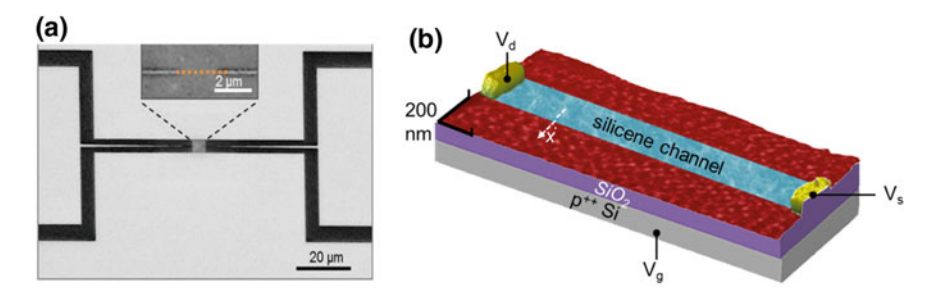


Fig. 12.6 a scanning electron microscope (dash line in inset denotes the silicene channel) and b Three dimensional rendering of atomic force microscope image on a silicene field-effect transistor device close to the dash line region in a, including the channel (false-coloured for visual guide) and source/drain contacts defined in native Ag film.  $V_g$ ,  $V_s$ , and  $V_d$  are the gate, source and drain voltages respectively in electrical measurements

## 12.4.2 Electrical Characterization of Silicene Field-Effect Transistors

Tao et al. [37] conducted electrostatic transfer and output measurements of backgated silicene transistors on a probe station/analyser using  $V_d=20~\rm mV$  with  $V_g$  swept from -2 to 2 V under ambient conditions. In brief, the electrical measurements on silicene transistors reveal transport behaviors similar to graphene. A linear output (Fig. 12.7a) is typically observed from the FET characteristic (drain current  $I_d$  versus drain-source bias  $V_d$  for a fixed gate bias  $V_g=0$ ). As a compelling evidence of Dirac-like band structure, Fig. 12.7b shows ambipolar transfer behavior with gate overdrive voltage ( $V_g-V_{\rm Dirac}$ ) from device #1 (Fig. 12.7a) that has a mixed phase silicene.  $V_{\rm Dirac}$  is defined as the voltage value where maximum resistance (or minimum current) occurs [56]. In addition, a representative V-shape of drain current versus gate voltage from device #2 on the same mixed phased silicene is shown in Fig. 12.7c, which also exhibits quasi-symmetric bell shape resistance profile with gate modulation (maximum to minimum current  $I_{\rm MAX}/I_{\rm MIN}$ ) of about one order of magnitude.

Using a well-accepted diffusive model [56, 57] for graphene FETs, the total device resistance R is:

$$R = R_{\text{contact}} + R_{\text{channel}} = R_{\text{contact}} + \frac{N_{sq}}{C} = R_{\text{contact}} + \frac{N_{sq}}{e\mu\sqrt{n_0^2 + n_G^2}}$$
(12.1)

where  $R_{channel}$  is the contact resistance,  $R_{channel}$  is the channel resistance,  $N_{sq}$  equals to the ratio of channel length divided by width, C is the gate dielectric capacitance,  $\mu$  is the field-effect mobility,  $n_0$  is the residual carrier concentration (charged impurities at  $V_{\rm Dirac}$ ) and  $n_G$  is the carrier concentration resulting from the difference between

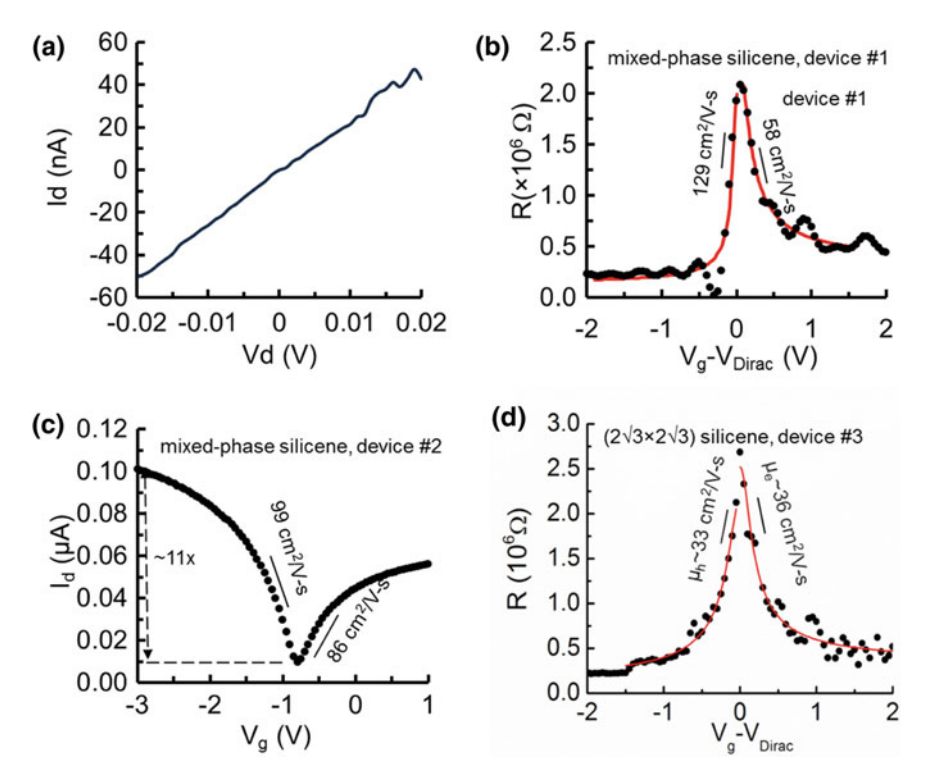


Fig. 12.7 Room-temperature electrical characterization of silicene transistor devices. a Low-field linear  $I_d$  versus  $V_d$  response at  $V_g=0$  and b resistance (R) versus override voltage ( $V_g-V_{\rm Dirac}$ ) of silicene device #1. Measured transfer characteristics (dots) are in good agreement with a widely-used ambipolar diffusive transport model (line), which yields extracted low-field hole and electron carrier mobilities of 129 and 58 cm²/V-s respectively. c The  $I_d$  versus  $V_g$  curve of silicene device #2 displays ambipolar electron-hole symmetry with extracted hole and electron mobilities at 99 and 86 cm²/V-s, respectively. Both Device #1 and #2 are from mix-phase silicene with similar residual carrier density at ~3–7 × 109 cm²-². d R versus ( $V_{gv}V_{\rm Dirac}$ ) on silicene device #3 ( $2\sqrt{3}$  ×  $2\sqrt{3}$  silicene). The extracted low-field carrier mobilities are 33 and 36 cm²/V-s for electrons and holes respectively with residual carrier concentration at 8–9 × 109 cm²-². All three devices exhibited a gate modulation over one order of magnitude with typical channel length of 1.8  $\mu$ m and width of 230 nm and fixed  $V_d=20$  mV for all the measurements

 $V_G$  and  $V_{\text{Dirac}}$  defined below in (12.2) with  $v_F$  Fermi velocity value for silicene is estimated as  $1.3 \times 10^8$  m/s:

$$V_G - V_{\text{Dirac}} = \frac{e}{C} n_G + \frac{\hbar v_F \sqrt{\pi n_G}}{e}$$
 (12.2)

Applying (12.1) to transport measurement data in (Fig. 12.7b, d), field-effective mobilities of hole and electron are extracted as 129 and 58 cm<sup>2</sup>/V-s respectively with residual carrier concentration at the Dirac point of  $2.6-7.2 \times 10^9$  cm<sup>-2</sup> for device

L. Tao et al.

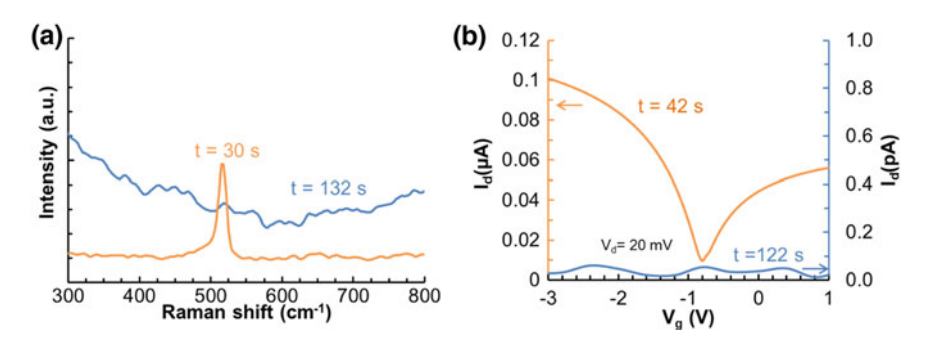


**Fig. 12.8** Air-stability of silicene transistor: **a** Raman spectroscopy and **b** electrical measurement of the Ag-free mixed-phase silicene channel observable immediately after Ag removal. The silicene channel exposed on the top-side to ambient conditions degrades in about 2 min

#1. On device #2, extracted mobilities for hole and electron are 99 and 86 cm²/V-s respectively with residual carrier concentration at the Dirac point of 3.5– $7.6 \times 10^9$  cm<sup>-2</sup>. Device #3 with  $(2\sqrt{3} \times 2\sqrt{3})$  silicene exhibited similar ambipolar behaviour and more symmetric bell shape resistance profile (Fig. 12.7d) compared to devices #1 and #2 mixed-phase silicene described in the main text. Particularly, an  $I_{MAX}/I_{MIN}$  of ~11 and extracted field-effect mobility ~35 cm²/V-s, with residual carrier concentration at the Dirac point of 8– $9 \times 10^9$  cm<sup>-2</sup>. This observation on device #3, together with device #1 and #2, supports the predicted Dirac electronic structure of silicene. The lower mobility with respect to devices #1 and #2 can be due to a more pronounced tendency for the  $(2\sqrt{3} \times 2\sqrt{3})$  superstructure to show defects and clustering due to the higher formation temperature and dewetting, therein conferring a relatively lower degree of long range structural order. In statistics, mobility values measured from different devices are of the order  $100 \text{ cm}^2/\text{V-s}$ , which is within the estimated range of 10– $1000 \text{ cm}^2/\text{V-s}$  for supported silicene in theoretical predictions [58–60].

It's worth to note that the silicene FET became unstable once Ag is removed from silicene for the same reason explained in previous Sect. 12.3.2. Real-time Raman observation reveals that the Ag-free silicene in device #2 still exhibits ambipolar transport in ~40 s, and then degrades afterwards within ~2 min when exposed to air after Ag removal (Fig. 12.8). This additional observation agrees with the spontaneous structural transitions [54] and local reconstruction [55] of silicene suggested in recent fundamental studies. Further experimental studies are essential for ensuring long-term device stability for practical applications under ambient operation. Promising research avenues include controlling the intrinsic structure (i.e. phase and the number of layers) of silicene, and immediate thin film capping of post-fabrication silicene devices.

To rule out the possibility of channel current from Ag residue that might remain during etching to form contact pads, a control group of devices (with thin Ag residue and without silicene) was made under the same conditions and showed three orders higher metallic output with no ambipolar behavior or leakage (Fig. 12.9). Once fully degraded or oxidized, silicene device exhibits open circuit. As a result, one can

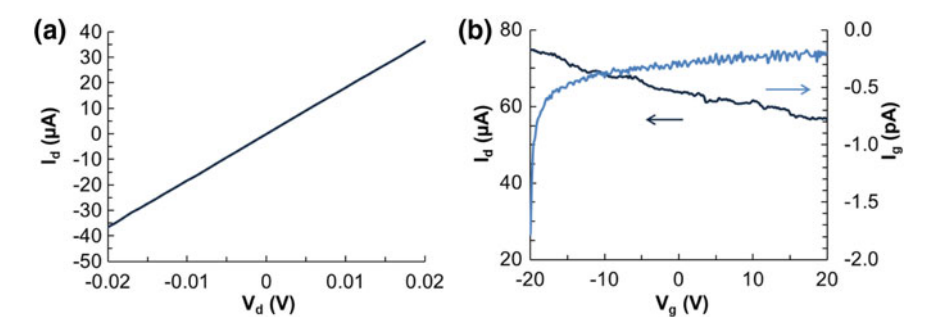


Fig. 12.9 Electrical characterization of control group devices with 1–2 nm residual Ag. a Smooth drain current ( $I_d$ ) versus voltage ( $V_d$ ) curve showing linear metallic behaviour with a resistance of ~570  $\Omega$ . b  $I_d$ - $V_g$  curve showing no ambipolar feature, negligible gate control and negligible gate leakage current ( $I_g$ )

conclude that the observed ambipolar character is indeed a nature of silicene channel (Table 12.1). Although there have been theoretical calculations [15, 36, 52, 53, 59, 60] on electrical behavior of silicene transistors, this is the first experimental evidence that clarifies the electronic transport behavior of the silicene FETs in the following aspects. First, the transport measurement of silicene devices provided a clear evidence of the existence of Dirac-cone in Ag-removed silicene similar to graphene. There was no experimental observation of ambipolar charge transport in prior reports on Ag-supported silicene [52], although it has been commonly expected in many theoretical studies [11, 12, 59, 61]. Despite there is the wide consensus in recognizing the metallic nature of Ag-supported epitaxial silicene [62–65], the observed ambipolar behavior in the silicene FETs is conversely consistent with a graphene-like electronic transport which resembles the expected response of an Ag-removed silicene.

Second, the mobility values obtained on silicene transistors are significantly lower than graphene counterparts given the same device configuration. This provides experimental evidence revealing an increased role of out-of-plane acoustic phonons in electron transport in silicene as predicted by the theory [59]. This arises because of the buckled geometry of silicene lattice, unlike planar graphene, leading to enhanced electron-phonon interaction from out-of-plane acoustic phonons that reduce the mobility of charge carriers in silicene lattice. Consequently, the Fermi velocity and mobility values of silicene would be significantly lower than graphene. Third, the electrical results support theoretical calculations [12, 14, 15] on that silicene experiences  $sp^2$  behavior like graphene, whereas the bond length and angle preserve an  $sp^3$ -like structure [17]. However, it must be kept in mind that mobility degradation can also stem from structural imperfection or disorder (e.g. point and line defects, clustering) which are intrinsic of the silicene epitaxy and can be nonetheless minimized by post-deposition thermal treatments. Moreover, it should be mentioned that the presence of different silicene phases in the channel gives rise to domains and then grain boundaries whose importance as scattering mechanism was thoroughly recognized in the case of polycrystalline graphene [66].

248 L. Tao et al.

 Table 12.1
 Comparison of silicene transistors with 4 control group devices

Device configuration	Id-Vd	Id-Vg	Key notes
S Silicene D	60 40 20 0 -0.02 -0.01 0.02	0.12 0.10 0.08 0.04 0.02 0.00 0.04 0.02 0.00 0.04 0.02 0.00 0.04 0.02 0.00	Ambipolar; μ~100 cm2/V-s
S Ag D residue D	40 20 320 -40 -60 -0.02 -0.01 0 0.01 0.02	80 40 20 -10 -5 0 5 10 V <sub>9</sub> (V)	Metallic behaviour
s a-Si min	-0.8 -0.9 -1.0 -1.1 -0.02 -0.01 0 0.01 0.02	0.5 0.5 0.3 0.2 -10 -5 0 5 10	
S Al <sub>2</sub> O <sub>3</sub> D	120 80 90 20 0 -0.02 -0.01 V <sub>q</sub> (V) 0.01 0.02	150 100 50 -50 -10 -5 0 5 10	Open circuits
S degraded D slicene	30 20 10 -10 -20 -30 -30 -30 -30 -30 -30 -30 -30 -30 -3	§ 50 0 0 0 0 0 0 0 0 0 0 0 0 0 0 0 0 0 0	

The buckled structure in silicene allows additional modification on conductivity and mobility from intrinsic material structure in contrast to pure  $sp^2$  bonded graphene. Moreover, a sizable band gap that can be created by a vertical electrical field [58, 67, 68] in a single monolayer silicene (in contrast to graphene that requires a bilayer), adsorption of hydrogen (resulting in the so-called silicane [69]) or doping with foreign atoms [15]. The tunable band gap of silicene holds great promise to enable digital switching transistors. In this respect, further optimization of the silicene atomic structure is demanded in order to boost the carrier mobility which in turn can be limited by linear or point defects in the pristine silicene lattice. The experimental study on the proof-of-principle silicene FET also suggests that future research on interface engineering, such as high-k thin dielectric also serving as a capping layer [34] and contact resistance between silicene and different metals, would be essential for advancing device performance.

# 12.4.3 Fundamental Physics Revealed by Prelim Electrical Measurements

A long time debate on the electronic structure of silicene is that: does it really have a band gap and how large it is if so? The debut of silicene FET devices brought in experimental data, limited though, to shed some light on this, and a general approach is to link the experimentally extracted residual carrier density values together with estimated Fermi velocity of silicene back into the density of states function. Tao et al. [37] followed this approach with their experimental data and further estimated a rather small band gap of silicene as a Dirac semiconductor as depicted below.

The residual carrier density  $(n_o)$  is the total electron and hole density at the Dirac point.  $n_o$  of a Dirac semiconductor is given by the sum of the populated states, adapted from Chap. 3, (3.44) in [70]

$$n_o = 2 \int_{\Delta/2}^{E_{max}} g(E) F(E, E_F) dE$$
 (12.3)

where  $\Delta$  is the small band gap within an order of magnitude of thermal energy. The factor of two accounts for the contribution of electrons and holes, and  $E_{max}$  represents the maximum relevant energy. g(E) and  $F(E, E_F)$  are the energy (E) dependent density of states and Fermi-Dirac population function respectively.  $g(E) = 8\pi/(hv_F)^2 E$ , and  $F(E, E_F) = 1/(1 + e^2((E - E_F)/KT))$ , where h is Planck's constant, K is Boltzmann's constant, K is temperature, and K0 is the Fermi velocity. At the equilibrium Dirac point, K1 is temperature, and the residual carrier density is due to thermal activation, assuming negligible impurity doping, which is the case for silicene devices reported by Tao et al. [37]. In addition, without loss of accuracy, the upper limit of (12.3) can be taken to infinity because of the rapid decline of the Fermi-Dirac exponential tail at high energies. Equation (12.3) then reduces to:

250 L. Tao et al.

$$n_o = \frac{16\pi}{(hv_E)^2} \int_{\Delta/2}^{\infty} \frac{E}{1 + e^{\frac{E}{KT}}} dE$$
 (12.4)

For the case of graphene with zero band gap, (12.4) simplifies to  $n_0 = (4(kT)^2\pi^3)/(3(hv_F)^2)$ , a quantity that depends only on a single material parameter,  $v_F$ , and amounts to a constant  $\sim 1.5 \times 10^{11}$  cm<sup>-2</sup> at 20 °C room temperature [70]. Here, the substantially lower residual carrier density indicates a small band gap is present. Solving (12.4) for experimental  $n_0 \sim 8 \times 10^9$  cm<sup>-2</sup> yields  $\Delta \sim 0.21$  eV within the range of band gap opening (0.0–0.4 eV) predicted by Pflugradt et al. [71]. The Fermi velocity of silicene was taken from recent measurement to be  $v_F \sim 1.3 \times 10^8$  cm/s [32]. The value of  $\Delta$  calculated here must be considered a rough estimate particularly because of the assumption that the Dirac dispersion is largely preserved. While this is supported by recent density DFT [71] and ARPES [32] of silicene, specific studies are needed to understand the silicene–dielectric surface interaction, the nature, value and dependence of silicene's electronic structure and band gap on temperature, substrates, and external fields. Most importantly, these studies are now in principle feasible based on the SEDNE concept described in this chapter that can enable the realization of experimental silicene devices.

### 12.5 Summary and Outlook

This chapter reviewed the epitaxial synthesis of silicene (2D silicon) on Ag(111)/mica with in-situ and ex situ characterizations showing silicene signature with multi-phase character. Raman spectroscopy and analysis of characteristic modes elucidated the material property and stability of silicene, which are largely affected by the  $Al_2O_3$  capping layer on top and Ag(111) catalyst film under the silicene. SEDNE process, affords intact silicene while transferring onto device substrate and reuse of mica substrates for silicene growth. Such a synthesis-transfer-fabrication integrated platform enabled the debut of silicene transistor device, demonstrating the first direct experimental proof to support theoretical predictions on the Dirac-cone with extracted mobility values within reasonable range of theoretical calculations. Most importantly, the first proof-of-concept device opens promising future for a silicene based nanotechnology and various applications such as bandgap engineering, optoelectronics, ferroelectric devices and quantum spin Hall insulator with a briefly outlook below.

Although free-standing silicene is regarded as gapless like graphene and germanene [72, 73], its buckled structure unlike flat graphene allows more tunable bandgap (at a small extent) either by external electric field of surface/interface modification. This potentially existing small bandgap due to the buckled structure in silicene with controlled crystal structure enables the study on opto-electronic properties of silicene that could pave the way for photocurrent generation with buckled 2D materials [74]. A recent TB study proposes that a thermal field could enhance the effect of the electric field to open a band gap, making silicene a better candidate

for room temperature electronic applications [75]. Recent studies indicated that the interface engineer of ferroelectric tunnel junctions [76] can result in enhanced tunneling electroresistance, e.g. with graphene electrode [77], silicene as an analogue to graphene holds great promise in improving such ferroelectric devices for next generation non-volatile memory and logic devices. The research experience with silicene can be relevantly extended to other elemental 2D materials such as the recently reported germanene [38, 78] (see Chap. 13).

#### References

- K.S. Novoselov, A.K. Geim, S.V. Morozov, D. Jiang, Y. Zhang, S.V. Dubonos, I.V. Grigorieva, A.A. Firsov, Electric field effect in atomically thin carbon films. Science 306(5696), 666–669 (2004)
- C. Berger, Z. Song, T. Li, X. Li, A.Y. Ogbazghi, R. Feng, Z. Dai, A.N. Marchenkov, E.H. Conrad, P.N. First, W.A. de Heer, Ultrathin epitaxial graphite: 2D electron gas properties and a route toward graphene-based nanoelectronics. J. Phys. Chem. B 108(52), 19912–19916 (2004)
- 3. R. Mas-Balleste, C. Gomez-Navarro, J. Gomez-Herrero, F. Zamora, 2D materials: to graphene and beyond. Nanoscale **3**(1), 20–30 (2011)
- S.Z. Butler, S.M. Hollen, L. Cao, Y. Cui, J.A. Gupta, H.R. Gutiérrez, T.F. Heinz, S.S. Hong, J. Huang, A.F. Ismach, E. Johnston-Halperin, M. Kuno, V.V. Plashnitsa, R.D. Robinson, R.S. Ruoff, S. Salahuddin, J. Shan, L. Shi, M.G. Spencer, M. Terrones, W. Windl, J.E. Goldberger, Progress, challenges, and opportunities in two-dimensional materials beyond graphene. ACS Nano 7(4), 2898–2926 (2013)
- Q.H. Wang, K. Kalantar-Zadeh, A. Kis, J.N. Coleman, M.S. Strano, Electronics and optoelectronics of two-dimensional transition metal dichalcogenides. Nat. Nanotech. 7(11), 699–712 (2012)
- L. Li, Y. Yu, G.J. Ye, Q. Ge, X. Ou, H. Wu, D. Feng, X.H. Chen, Y. Zhang, Black phosphorus field-effect transistors. Nat. Nanotech. 9, 372–377 (2014)
- A.P. Nayak, S. Bhattacharyya, J. Zhu, J. Liu, X. Wu, T. Pandey, C. Jin, A.K. Singh, D. Akinwande, J.-F. Lin, Pressure-induced semiconducting to metallic transition in multilayered molybdenum disulphide. Nat. Commun. 5, 3731 (2014)
- 8. H.-Y. Chang, S. Yang, J. Lee, L. Tao, W.-S. Hwang, D. Jena, N. Lu, D. Akinwande, High-performance, highly bendable MoS<sub>2</sub> transistors with high-k dielectrics for flexible low-power systems. ACS Nano 7(6), 5446–5452 (2013)
- K. Takeda, K. Shiraishi, Theoretical possibility of stage corrugation in Si and Ge analogs of graphite. Phys. Rev. B 50(20), 14916–14922 (1994)
- E. Durgun, S. Tongay, S. Ciraci, Silicon and III-V compound nanotubes: structural and electronic properties. Phys. Rev. B 72(7), 075420 (2005)
- G.G. Guzmán-Verri, L.C. Lew Yan Voon, Electronic structure of silicon-based nanostructures. Phys. Rev. B 76(7), 075131 (2007)
- G.G. Guzmán-Verri, L.C. Lew Yan Voon, Band structure of hydrogenated Si nanosheets and nanotubes. J. Phys. Cond. Matter 23(14), 145502 (2011)
- S. Cahangirov, M. Topsakal, E. Aktürk, H. Şahin, S. Ciraci, Two- and one-dimensional honeycomb structures of Silicon and Germanium. Phys. Rev. Lett. 102(23), 236804 (2009)
- S. Lebègue, O. Eriksson, Electronic structure of two-dimensional crystals from ab initio theory. Phys. Rev. B 79(11), 115409 (2009)
- 15. R. Quhe, R. Fei, Q. Liu, J. Zheng, H. Li, C. Xu, Z. Ni, Y. Wang, D. Yu, Z. Gao, J. Lu, Tunable and sizable band gap in silicene by surface adsorption. Sci. Rep. 2, 853 (2012)
- U. Röthlisberger, W. Andreoni, M. Parrinello, Structure of nanoscale silicon clusters. Phys. Rev. Lett. 72(5), 665–668 (1994)

- E. Cinquanta, E. Scalise, D. Chiappe, C. Grazianetti, B. van den Broek, M. Houssa, M. Fanciulli,
   A. Molle, Getting through the nature of silicene: an sp<sup>2</sup>-sp<sup>3</sup> two-dimensional silicon nanosheet.
   J. Phys. Chem. C 117(32), 16719–16724 (2013)
- C.-C. Liu, W. Feng, Y. Yao, Quantum spin hall effect in silicene and two-dimensional germanium. Phys. Rev. Lett. 107(7), 076802 (2011)
- Y.D. Nelson, O.O. Kingsley, K.A. Sampson, C.A. Akosa, A. Emmanuel, D.A. Clement, A.B. Abdulhakeem, I. Emmanuel, B.N. Stany, T.O. Joshua, O.O. Anthony, F. Olu Emmanuel, O.U. Josephine, V.W. Umesh, Silicene and transition metal based materials: prediction of a two-dimensional piezomagnet. J. Phys. Cond. Matter 22(37), 375502 (2010)
- C. Xu, G. Luo, Q. Liu, J. Zheng, Z. Zhang, S. Nagase, Z. Gao, J. Lu, Giant magnetoresistance in silicene nanoribbons. Nanoscale 4(10), 3111–3117 (2012)
- F. Bechstedt, L. Matthes, P. Gori, O. Pulci, Infrared absorbance of silicene and germanene. Appl. Phys. Lett. 100(26), 261906 (2012)
- Q.-X. Pei, Y.-W. Zhang, Z.-D. Sha, V.B. Shenoy, Tuning the thermal conductivity of silicene with tensile strain and isotopic doping: a molecular dynamics study. J. Appl. Phys. 114(3), 033526 (2013)
- A. Fleurence, R. Friedlein, T. Ozaki, H. Kawai, Y. Wang, Y. Yamada-Takamura, Experimental evidence for epitaxial silicene on diboride thin films. Phys. Rev. Lett. 108(24), 245501 (2012)
- L. Meng, Y. Wang, L. Zhang, S. Du, R. Wu, L. Li, Y. Zhang, G. Li, H. Zhou, W.A. Hofer, H.-J. Gao, Buckled silicene formation on Ir(111). Nano Lett. 13(2), 685–690 (2013)
- C. Leandri, G.L. Lay, B. Aufray, C. Girardeaux, J. Avila, M.E. Dávila, M.C. Asensio, C. Ottaviani, A. Cricenti, Self-aligned silicon quantum wires on Ag(110). Surf. Sci. 574(1), L9–L15 (2005)
- C. Léandri, H. Oughaddou, B. Aufray, J.M. Gay, G. Le Lay, A. Ranguis, Y. Garreau, Growth of Si nanostructures on Ag(001). Surf. Sci. 601(1), 262–267 (2007)
- A. Kara, H. Enriquez, A.P. Seitsonen, L.C. Lew Yan Voon, S. Vizzini, B. Aufray, H. Oughaddou, A review on silicene—new candidate for electronics. Surf. Sci. Rep, 67(1), 1–18 (2012)
- B. Aufray, A. Kara, S. Vizzini, H. Oughaddou, C. Léandri, B. Ealet, G. Le Lay, Graphene-like silicon nanoribbons on Ag(110): a possible formation of silicene. Appl. Phys. Lett. 96(18), 183102 (2010)
- P. De Padova, P. Perfetti, B. Olivieri, C. Quaresima, C. Ottaviani, G.L. Lay, 1D graphene-like silicon systems: silicene nano-ribbons. J. Phys. Condens. Matter 24(22), 223001 (2012)
- 30. B. Feng, Z. Ding, S. Meng, Y. Yao, X. He, P. Cheng, L. Chen, K. Wu, Evidence of silicene in honeycomb structures of silicon on Ag(111). Nano Lett. 12(7), 3507–3511 (2012)
- 31. C.-L. Lin, R. Arafune, K. Kawahara, N. Tsukahara, E. Minamitani, Y. Kim, N. Takagi, M. Kawai, Structure of silicene grown on Ag(111). Appl. Phys. Exp. **5**(4), 045802 (2012)
- P. Vogt, P. De Padova, C. Quaresima, J. Avila, E. Frantzeskakis, M.C. Asensio, A. Resta,
   B. Ealet, G. Le Lay, Silicene: compelling experimental evidence for graphene like two-dimensional silicon. Phys. Rev. Lett. 108(15), 155501 (2012)
- D. Chiappe, C. Grazianetti, G. Tallarida, M. Fanciulli, A. Molle, Local electronic properties of corrugated silicene phases. Adv. Mater. 24(37), 5088–5093 (2012)
- A. Molle, C. Grazianetti, D. Chiappe, E. Cinquanta, E. Cianci, G. Tallarida, M. Fanciulli, Hindering the oxidation of silicene with non-reactive encapsulation. Adv. Funct. Mater. 23(35), 4340–4344 (2013)
- P. De Padova, O. Kubo, B. Olivieri, C. Quaresima, T. Nakayama, M. Aono, G. Le Lay, Multilayer silicene nanoribbons. Nano Lett. 12(11), 5500–5503 (2012)
- B. Feng, H. Li, C.-C. Liu, T.-N. Shao, P. Cheng, Y. Yao, S. Meng, L. Chen, K. Wu, Observation
  of Dirac cone warping and chirality effects in silicene. ACS Nano 7(10), 9049–9054 (2013)
- L. Tao, E. Cinquanta, D. Chiappe, C. Grazianetti, M. Fanciulli, M. Dubey, A. Molle, D. Akinwande, Silicene field-effect transistors operating at room temperature. Nat. Nanotech. 10(10), 227–231 (2015)
- 38. L. Li, S.-Z. Lu, J. Pan, Z. Qin, Y.-Q. Wang, Y. Wang, G.-Y. Cao, S. Du, H.-J. Gao, Buckled germanene formation on Pt(111). Adv. Mater. **26**(28), 4820–4824 (2014)

- 39. Y. Xu, B. Yan, H.-J. Zhang, J. Wang, G. Xu, P. Tang, W. Duan, S.-C. Zhang, Large-gap quantum spin hall insulators in tin films. Phys. Rev. Lett. 111(13), 136804 (2013)
- 40. H. Liu, A.T. Neal, Z. Zhu, Z. Luo, X. Xu, D. Tománek, P.D. Ye, Phosphorene: an unexplored 2D semiconductor with a high hole mobility. ACS Nano 8(4), 4033–4041 (2014)
- A. Acun, B. Poelsema, H.J.W. Zandvliet, R. van Gastel, The instability of silicene on Ag(111).
   Appl. Phys. Lett. 103(26) (2013)
- P. Moras, T.O. Mentes, P.M. Sheverdyaeva, A. Locatelli, C. Carbone, Coexistence of multiple silicene phases in silicon grown on Ag(111). J. Phys. Condens. Matter 26(18), 185001 (2014)
- A.J. Mannix, B. Kiraly, B.L. Fisher, M.C. Hersam, N.P. Guisinger, Silicon growth at the twodimensional limit on Ag(111). ACS Nano 8(7), 7538–7547 (2014)
- C. Grazianetti, D. Chiappe, E. Cinquanta, M. Fanciulli, A. Molle, Nucleation and temperaturedriven phase transitions of silicene superstructures on Ag(111). J. Phys. Cond. Matter 27(25), 255005 (2015)
- P. Paola De, O. Carlo, Q. Claudio, O. Bruno, I. Patrizia, S. Eric, A. Thierry, Q. Lucia, R. Claudia, V. Alessandro, M.-M. Maurizio, G. Amanda, P. Barbara, L. Guy Le, 24 h stability of thick multilayer silicene in air. 2D Mater, 1(2), 021003 (2014)
- 46. T. Shirai, T. Shirasawa, T. Hirahara, N. Fukui, T. Takahashi, S. Hasegawa, Structure determination of multilayer silicene grown on Ag(111) films by electron diffraction: evidence for Ag segregation at the surface. Phys. Rev. B 89(24), 241403 (2014)
- 47. E. Scalise, M. Houssa, G. Pourtois, B. van den Broek, V. Afanas'ev, A. Stesmans, Vibrational properties of silicene and germanene. Nano Res. 6(1), 19–28 (2013)
- E. Scalise, E. Cinquanta, M. Houssa, B. van den Broek, D. Chiappe, C. Grazianetti, G. Pourtois, B. Ealet, A. Molle, M. Fanciulli, V.V. Afanas'ev, A. Stesmans, Vibrational properties of epitaxial silicene layers on (111) Ag. Appl. Surf. Sci. 291(0), 113–117 (2014)
- L. Tao, J. Lee, H. Chou, M. Holt, R.S. Ruoff, D. Akinwande, Synthesis of high quality monolayer graphene at reduced temperature on hydrogen-enriched evaporated copper (111) Films. ACS Nano 6(3), 2319–2325 (2012)
- J.W. Suk, W.H. Lee, J. Lee, H. Chou, R.D. Piner, Y. Hao, D. Akinwande, R.S. Ruoff, Enhancement of the electrical properties of graphene grown by chemical vapor deposition via controlling the effects of polymer residue. Nano Lett. 13(4), 1462–1467 (2013)
- J. Gao, J. Zhao, Initial geometries, interaction mechanism and high stability of silicene on Ag(111) surface. Sci. Rep. 2, 861 (2012)
- 52. Z.-X. Guo, S. Furuya, J.-I. Iwata, A. Oshiyama, Absence and presence of Dirac electrons in silicene on substrates. Phys. Rev. B **87**(23), 235435 (2013)
- C.-L. Lin, R. Arafune, K. Kawahara, M. Kanno, N. Tsukahara, E. Minamitani, Y. Kim, M. Kawai, N. Takagi, Substrate-induced symmetry breaking in silicene. Phys. Rev. Lett. 110(7), 076801 (2013)
- 54. B. Huang, H.J. Xiang, S.-H. Wei, Chemical functionalization of silicene: spontaneous structural transition and exotic electronic properties. Phys. Rev. Lett. 111(14), 145502 (2013)
- V.O. Özçelik, S. Ciraci, Local reconstructions of silicene induced by adatoms. J. Phys. Chem. C 117(49), 26305–26315 (2013)
- S. Kim, J. Nah, I. Jo, D. Shahrjerdi, L. Colombo, Z. Yao, E. Tutuc, S.K. Banerjee, Realization of a high mobility dual-gated graphene field-effect transistor with Al<sub>2</sub>O<sub>3</sub> dielectric. Appl. Phys. Lett. 94(6), 062107-3 (2009)
- 57. K.N. Parrish, D. Akinwande, An exactly solvable model for the graphene transistor in the quantum capacitance limit. Appl. Phys. Lett. **101**(5), 053501 (2012)
- 58. Z. Ni, Q. Liu, K. Tang, J. Zheng, J. Zhou, R. Qin, Z. Gao, D. Yu, J. Lu, Tunable bandgap in silicene and germanene. Nano Lett. 12(1), 113–118 (2011)
- X. Li, J.T. Mullen, Z. Jin, K.M. Borysenko, M. Buongiorno, M.B. Nardelli, K.W. Kim, Intrinsic electrical transport properties of monolayer silicene and MoS<sub>2</sub> from first principles. Phys. Rev. B 87(11), 115418 (2013)
- 60. R. Wang, X. Pi, Z. Ni, Y. Liu, S. Lin, M. Xu, D. Yang, Silicene oxides: formation, structures and electronic properties. Sci. Rep. 3, 3507 (2013)

- P. De Padova, P. Vogt, A. Resta, J. Avila, I. Razado-Colambo, C. Quaresima, C. Ottaviani,
   B. Olivieri, T. Bruhn, T. Hirahara, T. Shirai, S. Hasegawa, M. Carmen Asensio, G. Le Lay,
   Evidence of Dirac fermions in multilayer silicene. Appl. Phys. Lett. 102(16), 163106 (2013)
- S. Cahangirov, M. Audiffred, P. Tang, A. Iacomino, W. Duan, G. Merino, A. Rubio, Electronic structure of silicene on Ag(111): strong hybridization effects. Phys. Rev. B 88(3), 035432 (2013)
- 63. D. Tsoutsou, E. Xenogiannopoulou, E. Golias, P. Tsipas, A. Dimoulas, Evidence for hybrid surface metallic band in (4 × 4) silicene on Ag(111). Appl. Phys. Lett. **103**(23), 231604 (2013)
- N.W. Johnson, P. Vogt, A. Resta, P. De Padova, I. Perez, D. Muir, E.Z. Kurmaev, G. Le Lay, A. Moewes, The metallic nature of epitaxial silicene monolayers on Ag(111). Adv. Funct. Mater. 24(33), 5253–5259 (2014)
- S.K. Mahatha, P. Moras, V. Bellini, P.M. Sheverdyaeva, C. Struzzi, L. Petaccia, C. Carbone, Silicene on Ag(111): a honeycomb lattice without Dirac bands. Phys. Rev. B 89(20), 201416 (2014)
- 66. A.W. Tsen, L. Brown, M.P. Levendorf, F. Ghahari, P.Y. Huang, R.W. Havener, C.S. Ruiz-Vargas, D.A. Muller, P. Kim, J. Park, Tailoring electrical transport across grain boundaries in polycrystalline graphene. Science **336**(6085), 1143–1146 (2012)
- N.D. Drummond, V. Zólyomi, V.I. Fal'ko, Electrically tunable band gap in silicene. Phys. Rev. B 85(7), 075423 (2012)
- Y. Liang, V. Wang, H. Mizuseki, Y. Kawazoe, Band gap engineering of silicene zigzag nanoribbons with perpendicular electric fields: a theoretical study. J. Phys. Cond. Matter 24(45), 455302 (2012)
- 69. J.-N. Ding, J.-X. Wang, N.-Y. Yuan, B. Kan, X.-S. Chen, Electronic band transformation from indirect gap to direct gap in Si–H compound. Chin. Phys. B **19**(7), 077103 (2010)
- H.-S.P. Wong, D. Akinwande, Carbon Nanotube and Graphene Device Physics (Cambridge University Press, Camberidge, 2011)
- 71. P. Pflugradt, L. Matthes, F. Bechstedt, Silicene-derived phases on Ag(111) substrate versus coverage: *Ab initio* studies. Phys. Rev. B **89**(3), 035403 (2014)
- 72. F. Schwierz, Graphene and beyond: two-dimensional materials for transistor applications. in *Proceedings of SPIE* (2015), pp. 94670 W-94670 W-9
- 73. F. Schwierz, J. Pezoldt, R. Granzner, Two-dimensional materials and their prospects in transistor electronics. Nanoscale **7**(18), 8261–8283 (2015)
- M. Buscema, J.O. Island, D.J. Groenendijk, S.I. Blanter, G.A. Steele, H.S.J. van der Zant, A. Castellanos-Gomez, Photocurrent generation with two-dimensional van der Waals semiconductors. Chem. Soc. Rev. 44(11), 3691–3718 (2015)
- 75. C. Lian, J. Ni, The effects of thermal and electric fields on the electronic structures of silicene. Phys. Chem. Chem. Phys. 17(20), 13366–13373 (2015)
- 76. Z. Wen, C. Li, D. Wu, A. Li, N. Ming, Ferroelectric-field-effect-enhanced electroresistance in metal/ferroelectric/semiconductor tunnel junctions. Nat. Mater. 12(7), 617–621 (2013)
- 77. H. Lu, A. Lipatov, S. Ryu, D.J. Kim, H. Lee, M.Y. Zhuravlev, C.B. Eom, E.Y. Tsymbal, A. Sinitskii, A. Gruverman, Ferroelectric tunnel junctions with graphene electrodes. Nat. Commun. 5, 5518 (2014)
- 78. G. Le Lay, E. Salomon, T. Angot, M. Eugenia Dávila, Increasing the lego of 2D electronics materials: silicene and germanene, graphene's new synthetic cousins, in *Proceedings of SPIE* (2015), pp. 94670U-94670U-5

# Chapter 13 Germanene: Silicene's Twin Sister



Pantelis Bampoulis, Lijie Zhang, Qirong Yao, Rik van Bremen, Caspar J. Walhout, Adil Acun, Arie van Houselt and Harold J. W. Zandvliet

**Abstract** Soon after the discovery of graphene, the first two-dimensional material, many other two-dimensional materials have been developed. Due to their  $s^2 p^2$  type of electronic structure the elements of the 'carbon' column of the periodic system i.e. silicon, germanium and tin have received a lot of attention as potential two-dimensional materials. The silicon, germanium and tin analogues of graphene are coined silicene, germanene and tinene or stanene, respectively, and share many properties with graphene. There are, however, also a few distinct differences with graphene. Here we will give a brief update on the current status of germanene. We briefly review the various routes to synthesize germanene and elaborate on its structural and electronic properties as well as its potential for application in future electronic devices.

#### 13.1 Introduction

The discovery of graphene, a single layer of  $sp^2$  hybridized carbon atoms arranged in a honeycomb registry, has resulted in a myriad of intriguing and exciting scientific breakthroughs. In addition, it initiated a complete new research field in materials science that deals with materials that are two-dimensional in nature, rather than three-dimensional [1, 2]. The fact that a single sheet of atoms is stable was already a great surprise, since the Mermin and Wagner theorem [3] states that a two-dimensional crystal is instable because of a lack of long-range order at any nonzero temperature. Later work revealed that the origin of the stability of graphene lies in the anharmonic

Physics of Interfaces and Nanomaterials, MESA+ Institute for Nanotechnology, University of Twente, P.O. Box 217, 7500 AE Enschede, The Netherlands e-mail: h.j.w.zandvliet@utwente.nl

P. Bampoulis · L. Zhang · Q. Yao · R. van Bremen · C. J. Walhout · A. Acun · A. van Houselt H. J. W. Zandvliet ( $\boxtimes$ )

coupling between in-plane and out-of-plane phonon modes, an effect that was not taken into account in the Mermin and Wagner theory.

Graphene is a semimetal, i.e. the material is gapless, but the density of states vanishes at the Fermi level. It should be noted here, however, that the spin-orbit coupling in graphene opens up a tiny spin-orbit gap, which is so small that it is not detectable at any temperature larger than about 0.3 K. The energy bands near the K and K' points of the Brillouin zone, the so-called Dirac points, have a linear, conelike shape. The electronic states of graphene near these Dirac cones are described by linear dispersion relations:

$$E = \hbar v_F k,\tag{13.1}$$

where k is measured with respect to the K and K' points of the Brillouin zone and  $v_F$  is the Fermi velocity. The Fermi velocity can be calculated using  $v_F = \frac{1}{2}\sqrt{3}\frac{a}{\hbar}t$ , where a is the lattice constant of the honeycomb lattice and t the nearest-neighbour hopping energy. Due to these linear energy bands the group velocity of the electrons is energy independent. The behaviour of these massless electrons are described by the Dirac equation, i.e. the relativistic variant of the Schrödinger equation. This Dirac equation is given by:

$$-i\hbar v_F \begin{pmatrix} 0 & \partial_x - i\partial_y \\ \partial_x + i\partial_y & 0 \end{pmatrix} \begin{pmatrix} \Psi_1 \\ \Psi_2 \end{pmatrix} = E \begin{pmatrix} \Psi_1 \\ \Psi_2 \end{pmatrix}, \tag{13.2}$$

where  $\Psi_{1,2}(r)$  refer to the amplitudes of the wave functions on the two triangular sublattices.

The discovery of graphene has triggered many scientists to search for other twodimensional 'Dirac' materials. The most appealing candidates can be found in the 'carbon' column of the periodic system, i.e. silicon, germanium and tin. These elements have an electronic configuration that is very similar to carbon and are therefore also expected to exhibit  $sp^2$  hybridization. And indeed, recent experimental efforts have revealed that the silicon, germanium and tin counterparts of graphene can be synthesized. Following the graphene nomenclature these two-dimensional materials are referred to as silicene, germanene and tinene or stanene, respectively. In 2010 this research field got an enormous boost by the successful experimental realization of silicene nanoribbons on Ag(110) surfaces by the Le Lay group [4, 5]. A few years later the same group managed to grow a silicene sheet on a Ag(111) surface [6].

Soon after the rise of silicene, several groups started to synthesis germanene. Germanene shares many interesting properties with its silicon counterpart. The atoms of both two-dimensional materials are arranged in a buckled honeycomb registry. The buckled honeycomb lattices of silicene and germanene are composed of two vertically displaced triangular sublattices (see Fig. 13.1). Despite this buckling, tight binding and density functional theory calculations have demonstrated that the Dirac properties of free-standing silicene and germanene are preserved. Near the K and K' points of the surface Brillouin zone the energy bands are linear in k. In the vicinity of these k-points the electrons behave as massless relativistic particles. The spin-orbit gap in germanene ( $\sim$ 24 meV) is predicted to be substantially larger than in

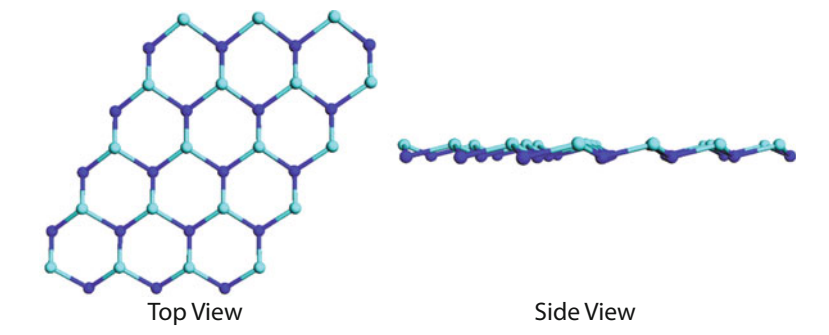


Fig. 13.1 Schematic model of germanene's buckled honeycomb lattice. Left: top view. Right: side view

graphene (<0.05 meV) and silicene ( $\sim$ 1.55 meV) and therefore germanene is an ideal candidate to exhibit the quantum spin Hall effect at experimentally accessible temperatures [7–9]. Furthermore, as a result of the buckled lattice of silicene and germanene it is much easier to open a band gap in these materials than in graphene, making these materials ideal candidates for the realization of field-effect based electronic devices. Despite these advantages, silicene and germanene also suffer from a number of severe disadvantages. Firstly, in contrast to graphene, germanene and silicene are not stable at ambient conditions. Secondly, germanene and silicene do not occur in nature and therefore these materials have to be synthesized.

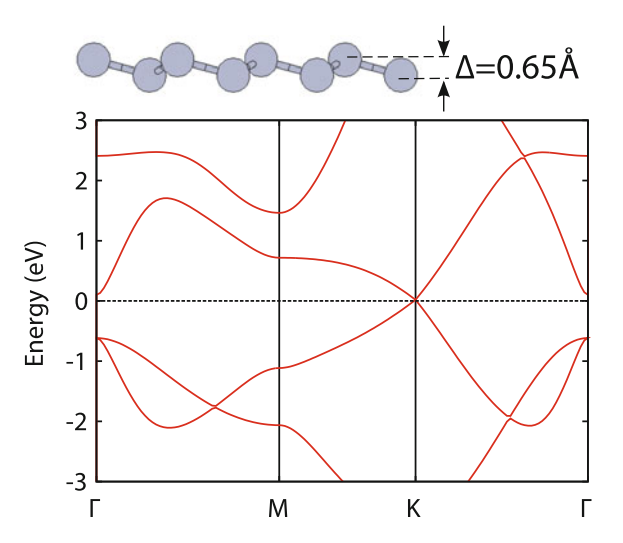
In this chapter we will attempt to give an update on the current status of germanene. The various routes to synthesize germanene are briefly reviewed. Subsequently, the structural and electronic properties of the grown germanene sheets are elucidated. In the second part of this chapter we briefly touch upon a few possibilities for future experiments on germanene sheets, such as the quantum spin Hall effect, topological phase transitions and the opening of a band gap.

#### 13.2 Germanene

# 13.2.1 First-Principles Calculations

In 1994 Takeda and Shiraishi [10] found that the lowest energy configuration of a single sheet of silicon and germanium atoms is a buckled honeycomb lattice. The silicon and germanium atoms are not perfectly  $sp^2$  hybridized, but exhibit a mixed  $sp^2/sp^3$  type of hybridization. The calculations of Takeda and Shiraishi revealed that these 'graphite-like' allotropes of silicon and germanium are semimetals. Despite the fact that Takeda and Shiraishi did not explicitly discuss the exact k-dependence of the electronic states near the Fermi level, it is obvious from their calculations that the energy bands are linear in k near the K and K' points of the surface Brillouin

**Fig. 13.2** Electronic band structure of free-standing germanene as obtained by density functional theory calculations. Zero energy corresponds to the Fermi energy. At the *K* points of the Brillouin zone two linear energy bands cross the Fermi level. Data taken from [13]



zone. More than a decade later Guzmán-Verri and Lew Yan Voon [11] performed tight binding calculations of silicene, and showed that silicene has Dirac cones at the K and K' points of the Brillouin zone. The buckling of silicene does not affect these Dirac cones and thus free-standing silicene is in principle a two-dimensional Dirac material. In 2009 Cahangirov et al. [12] showed that also free-standing germanene is a two-dimensional Dirac material. Interestingly, Cahangirov et al. [12] found two possible configurations for germanene. A low-buckled and high-buckled configuration. A more in depth theoretical analysis revealed that the phonon modes of the low-buckled configuration are real, whereas the high-buckled configuration has imaginary phonon modes in a large fraction of the Brillouin zone and hence this configuration has to be discarded. The electronic band structure of free-standing germanene, as obtained from density functional theory calculations, is shown in Fig. 13.2 (data taken from [13]). Interestingly, fully planar germanene is not semi-metallic, but metallic [13].

Graphene, silicene, germanene and stanene are predicted to belong to a new class of the so-called  $Z_2$  topological insulators that exhibits time-reversal symmetry. These materials are characterized by an interior that has a (spin-orbit) band gap, whereas the edges have spin-polarized topologically protected metallic states. In Sect. 13.3.2. we will elaborate on the intriguing properties of these  $Z_2$  topological insulators.

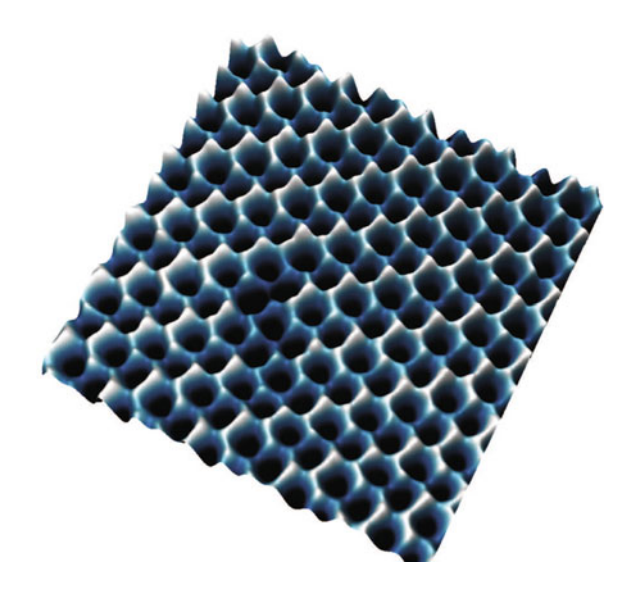
# 13.2.2 Synthesis

The first successful synthesis of germanane, i.e. hydrogen terminated germanene, was reported in 2013 by Bianco et al. [14]. Germanane is a very appealing material because it has a direct band gap of about 1.5 eV and the predicted effective masses are very small resulting in high carrier mobilities. Bianco et al. [14] produced germanane

sheets using topochemical deintercalation of CaGe<sub>2</sub>. The germanane crystallites are thermally stable, do not oxidize and single layer germanane sheets can be obtained via exfoliation.

One year later three experimental papers on the synthesis of germanene were published, followed by two more papers in 2015 and 2016, respectively. In the first paper Li et al. [15] deposited germanium on a Pt(111) surface. The authors found a  $\sqrt{19} \times \sqrt{19}$  reconstruction, which they interpreted as a buckled germanene layer. This interpretation has, however, recently been questioned by Švec et al. [16], who suggested that the  $\sqrt{19} \times \sqrt{19}$  reconstructed layer on Pt(111) is not germanene, but rather a surface alloy consisting of Ge<sub>3</sub>Pt tetramers. A few months after the first report on the synthesis of germanene a second paper appeared by Dávila et al. [17]. In this article germanium was deposited on a Au(111) substrate. Dávila et al. [17] found a  $\sqrt{7} \times \sqrt{7}$  reconstructed adlayer that they ascribed to germanene. These authors based their assignment on results obtained by a large arsenal of experimental techniques, including scanning tunneling microscopy, low energy electron diffraction and core level spectroscopy as well as density functional theory calculations. Shortly after the appearance of the Dávila et al. article another germanene article was published by Bampoulis et al. [18]. Bampoulis et al. deposited Pt on a Ge(110) substrate and subsequently annealed the substrate to a temperature of about 1100 K, i.e. just above the eutectic temperature of the PtGe alloy. Using low energy electron microscopy these authors showed that at temperatures exceeding 1040 K liquid-like droplets are formed on the Ge(110) surface. These liquid-like droplets are actually eutectic Pt<sub>0.22</sub>Ge<sub>0.78</sub> droplets. Upon cooling down, the eutectic phase undergoes spinodal decomposition into a pure Ge and a Ge<sub>2</sub>Pt phase. The surplus Ge segregates to the surface of the solidifying Ge<sub>2</sub>Pt droplets and forms a buckled honeycomb structure, which the authors interpreted as germanene. Scanning tunneling microscopy experiments revealed a nearest neighbor distance between the Ge atoms of  $2.5 \pm 0.1$  Å and a buckling of 0.2 Å. In 2015 a paper was published by Derivaz et al. [19] on the growth of a germanium layer on an Al(111) surface. The authors interpreted the  $3 \times 3$  reconstructed layer as germanene. The  $3 \times 3$  reconstructed layer covers the whole Al(111) surface and has domain sizes as large as 100 nm. In all the above mentioned cases [15, 17, 19] only reconstructed germanene superlattices were resolved in the scanning tunneling microscopy images. Only Bampoulis et al. [18] managed to atomically resolve the buckled honeycomb unit cell of germanene. In Fig. 13.3 a scanning tunneling microscopy image of this buckled honeycomb lattice is shown. The individual germanium atoms as well as the honeycomb unit cell of germanene are well-resolved. The measured nearest-neighbor distance between the germanium atoms of  $2.5 \pm 0.1$  Å agrees well with the theoretical predictions for free-standing germanene [12]. The buckling of 20 pm is, however, smaller than the 65 pm buckling predicted for free-standing germanene [12, 13]. In a follow-up study Zhang et al. [20] showed that the density of states of these germanene sheets has a V-shape, which is one of the hallmarks of a two-dimensional Dirac system. Unfortunately, the density of states does not completely vanish at the Dirac point. Early 2016 Dávila and Le Lay [21] reported the growth of a few monolayers of germanene on a Au(111) substrate. The germanene sheet has a  $3\sqrt{3} \times 3\sqrt{3}$  periodicity.

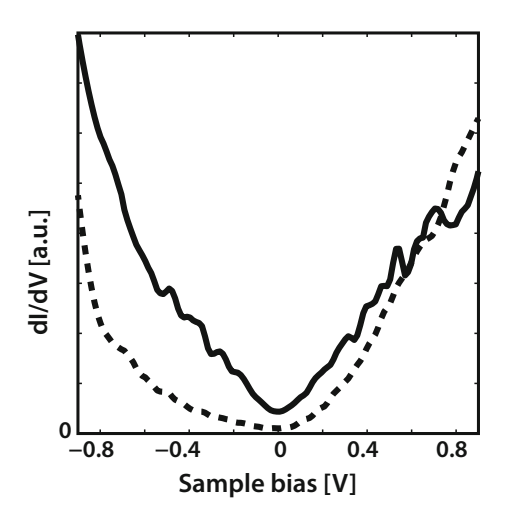
Fig. 13.3 a Scanning tunneling microscopy image recorded at a sample bias of 0.5 V and a tunnel current of 0.2 nA (data obtained from [18]). The image size is 4.5 nm  $\times$  4.5 nm. The nearest neighbor distance between the Ge atoms is 2.5  $\pm$  0.1 Å and the buckling is 0.2 Å



A reconstructed  $3\sqrt{3}\times3\sqrt{3}$  germanene unit cell coincides with an  $8\times8$  unit cell of the underlying Au(111) substrate. High-resolution angle resolved photoemission spectroscopy measurements revealed that this few layer thick germanene possesses Dirac cones. As pointed out by the authors it is essential to have a stack of a few layers of germanene. The predicted unique Dirac character of free-standing germanene can only be preserved if the interaction with the underlying substrate is sufficiently weak. It is evident that the germanene-germanene Van der Waals interaction is much weaker than the germanene-Au(111) interaction.

So far, all the germanene sheets were synthesized on metallic substrates [15, 17–21]. Metallic substrates are usually detrimental for the two-dimensional Dirac nature of the germanene sheets, because germanene's relevant electronic states near the Fermi level can hybridize with the electronic states of the underlying metallic substrate. In 2016 the first successful synthesis of germanene on molybdenum disulfide, a band gap material, was reported by Zhang et al. [22]. Using scanning tunneling spectroscopy these authors found that the density of states exhibits a V-shape, which is reminiscent of a two-dimensional Dirac system (see Fig. 13.4). Unfortunately, the density of states did not completely vanish at the Fermi level. Density functional theory calculations revealed that this metallic character is due to two electronic states that originate from two parabolic bands that cross the Fermi level at the  $\Gamma$  point of the surface Brillouin zone. In another, closely related, density functional theory study Amlaki et al. [23] showed that the topological insulator character of germanene remains intact upon the interaction with molybdenum disulfide.

Fig. 13.4 Differential conductivities of a germanene layer synthesized on a molybdenum disulfide substrate (solid line) and a bare molybdenum disulfide (dashed line). The spectra are recorded at room temperature with the same scanning tunneling microscopy tip. The setpoints are -1.4 V and 0.6 nA (data taken from [22])



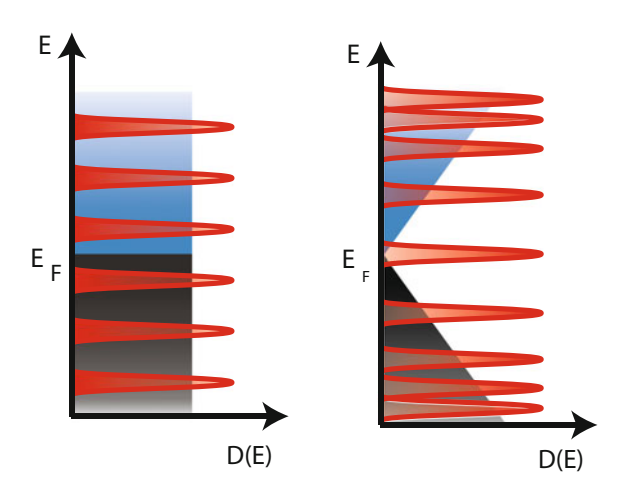
## 13.3 Future Experiments

In this section we briefly touch upon a few tantalizing experiments that can be performed once germanene is successfully synthesized on a band gap material. The first two experiments deal with the anomalous quantum Hall effect and the quantum spin Hall effect, respectively. In the last example we elaborate on the various possibilities to open a band gap in germanene. The realization of a band gap that exceeds about 0.3–0.4 eV is very interesting from a technological point of view since it opens the door to germanene-based field-effect devices.

# 13.3.1 Anomalous Quantum Hall Effect

Germanene and silicene are predicted to be two-dimensional Dirac materials. The most prominent difference between a two-dimensional Dirac material and a two-dimensional electron gas is the dispersion relation. In the case of a two-dimensional electron gas the energy dispersion relation is quadratic in k, whereas the energy dispersion relation is linear in k for a two-dimensional Dirac material. The dispersion relation of the energy bands below the Fermi level can be measured with angle resolved photoemission spectroscopy and therefore this technique seems to be the technique of choice if one wants to distinguish a two-dimensional electron gas from a two-dimensional Dirac system. There are, however, a few caveats. Firstly, the observation of only a part of the dispersion curve is not always sufficient to discriminate between a linear and a quadratic dispersion relation because the difference between both dispersion relations can be quite small. Secondly, it is usually quite difficult to distinguish substrate-related and germanene-related bands, since both bands are

**Fig. 13.5** Landau levels for a 2D electron gas (left) and a 2D Dirac system (right)



susceptible to hybridization effects. Alternatively, the energy dispersion relation can be measured by scanning tunneling spectroscopy using the quasi particle interference method. Although this technique provides information on the energy dispersion relation below as well as above the Fermi level, this technique suffers from the same aforementioned problems as angle-resolved photoemission spectroscopy. It should be noted here that attempts to measure quasi particle interference patterns near the step edges of germanene have failed [24]. To date, the exact origin of the absence of these quasi particle interference patterns for germanene remains unclear.

The most conclusive and straightforward way to discriminate between a two-dimensional electron gas and a two-dimensional Dirac system is a measurement of the energy spectrum of the Landau levels upon the application of an external magnetic field, i.e. the quantum Hall effect. In the case of a conventional two-dimensional electron gas the Landau levels are equidistantly spaced, whereas the Landau levels of a two-dimensional Dirac system are proportional to  $\sqrt{B_Z(n+\frac{1}{2}\pm\frac{1}{2})}$ . Here  $n=0,1,2,\ldots$  is the quantum number and  $B_z$  the magnetic field [25](see Fig. 13.5). The  $\pm\frac{1}{2}$  term is related to the chirality of the Dirac electrons. The electrons are chiral because their direction of motion is tied to the direction of the (pseudo)spin. This chirality is a direct consequence of the symmetry of the honeycomb lattice. In contrast to a two-dimensional electron system, a two-dimensional Dirac system exhibits a state at the Fermi level, i.e. at zero energy (n=0) and the minus sign in the equation). The existence of a zero-energy Landau level leads to an anomalous quantum Hall effect with a half-integer quantization of the Hall conductivity, rather than an integer quantization.

## 13.3.2 Quantum Spin Hall Effect

In 2005 Kane and Mele [26, 27] proposed that graphene is a  $Z_2$  topological insulator. The spin-orbit coupling in graphene results in the opening of a tiny gap at the Dirac points. Kane and Mele [26, 27] predicted that graphene exhibits a novel quantum state of matter, which is referred to as the quantum spin Hall phase. The quantum spin Hall phase is a time reversal invariant electronic state that is characterized by a band gap in the bulk of the material and spin-polarized topologically protected edge states. The quantum spin Hall effect should not be confused with the conventional integer quantum Hall effect. In the latter case an external magnetic field is required for the occurrence of the edge states. The quantum spin Hall effect, however, does not require an external magnetic field. The spin-orbit coupling results in an internal magnetic field that couples to the spin of the electrons. The spin-up electrons spin around in a clock-wise fashion, whereas the spin-down electrons around in a counter-clock-wise fashion or vice versa. This asymmetry will result into two spin-polarized conduction channels at the edges of the material that propagate in opposite directions, the socalled gapless and topologically protected helical edge modes. The quantum spin Hall phase is characterized by a vanishing charge Hall conductance and a quantized spin Hall conductance of  $\frac{2e}{4\pi}$ .

Unfortunately the spin-orbit gap in graphene is so small (<0.05 meV) that verification of the quantum spin Hall phase requires extremely low temperatures. Germanene, which is predicted to belong to the same class of topological insulators, exhibits a substantially larger spin-orbit gap and therefore it is much easier to detect the quantum spin Hall effect. There are various ways to prove the existence of the quantum spin Hall effect in germanene. The most straightforward way is to measure the electronic band structure in the vicinity of the Fermi level using scanning tunnelling spectroscopy. Scanning tunnelling spectroscopy provides the spatial and energy resolution that are required to separate the gapped from gapless regions. This experiment does, however, not unambiguously prove the existence of the quantum spin Hall phase. The most conclusive experiment is to directly measure the transport along the edges of the topological insulator. The charge transport along the edges, preferably step edges, of a two-dimensional material can be measured with a four-probe scanning tunnelling microscope. In order to interpret these transport measurements properly, the separation between the probes should be smaller than the elastic mean free path of the charge carriers. For a charge carrier mobility of the order of 100000 cm<sup>2</sup> V<sup>-1</sup> s<sup>-1</sup> the elastic mean free path is about 1  $\mu$ m. Expressions for the four-terminal and two-terminal conductance can be derived within the framework of a straightforward Landauer-Büttiker analysis. By applying this Landauer-Büttiker analysis one finds for the four-terminal and two-terminal conductance  $G_{14,23} = \frac{I_{14}}{V_{23}} = \frac{2e^2}{h}$  and  $G_{14,14} = \frac{I_{14}}{V_{14}} = \frac{2e^2}{3h}$ , respectively [28].

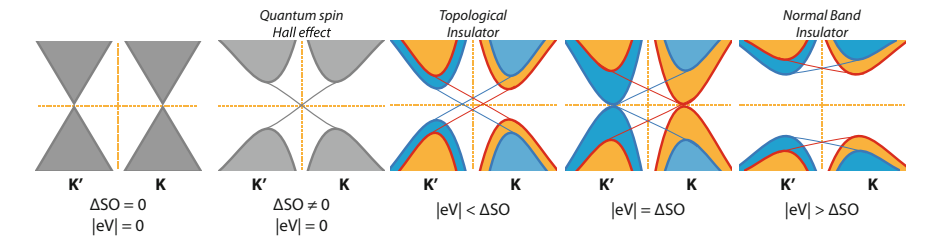


Fig. 13.6 Schematic diagram of the band structure of germanene near the K and K' points of the surface Brillouin zone. From left to right: without spin-orbit gap, with spin-orbit gap, applied electric field smaller than the critical value, applied electric field equal to the critical value and applied electric field larger than the critical value

# 13.3.3 Topological Phase Transitions and Band Gap Engineering

As discussed above free-standing germanene is in principle a two-dimensional topological insulator. The spin-orbit coupling in germanene leads to the opening of a small band gap at the K and K' points of the surface Brillouin zone. This gap can be opened further by transferring charge from one triangular sublattice to the other triangular sublattice (see Fig. 13.6). This transfer of charge is much easier to realize in germanene than in graphene, because germanene is buckled, whereas graphene is fully planar.

The band gap at the Dirac points of the Brillouin zone of germanene due to the application of an electric field E=eV in a direction normal to the germanene sheet is given by:

$$E_{\sigma}(k) = \pm \sqrt{(v_F \hbar k)^2 + (\Delta_{SO} + \frac{1}{2} \xi \sigma e V)^2}$$
 (13.3)

where  $\sigma=\pm 1$  refers to the spin and  $\xi=\pm 1$  to the K and K' points, respectively.  $\Delta_{SO}$  denotes the spin-orbit coupling. From (13.3) it is immediately clear that there are two branches of solutions, one with a band gap  $|\Delta_{SO}+\frac{1}{2}\xi\,{\rm eV}|$  and another with a band gap  $|\Delta_{SO}-\frac{1}{2}\xi\,{\rm eV}|$ . At the critical field, i.e.  $\Delta_{SO}=\frac{1}{2}\,{\rm eV}$ , the smaller gap closes, whereas the other gap opens further (see Fig. 13.6 for a simple schematic diagram). Beyond this critical field the small gap reopens again resulting in a transition from a topological insulator to a semimetal and finally to a normal band insulator [29–33]. As suggested by Ezawa [34] the application of an inhomogeneous electric field, for instance by using a scanning tunnelling microscopy tip, would allow the creation and manipulation of topologically protected edge modes in the interior of the material rather than at its edges.

One of the major drawbacks of graphene is that it has no band gap. The absence of a band gap disqualifies graphene as the key ingredient of a field-effect transistor (FET), for which a band gap of at least 300–400 meV is required in order to realize acceptable on-off current ratios at room temperature. The opening of such a band

gap in graphene by interaction with a substrate or adsorbed molecules has proven to be ineffective and the band gap opening by chemical modification of graphene seriously degrades its charge carrier mobility. Graphene electronics must therefore be based on transistors with radically new designs, such as the 'vertical geometry' tunneling transistor, which operates through tunneling of electrons between two graphene layers [35].

In this paragraph we have elaborated on the opening of a band gap by the application of an external electric field in germanene. There are, however, several other routes to open a band gap in germanene: (1) by the interaction with a substrate, (2) the adsorption or intercalation of atoms or molecules at one side of the germanene sheet [36], (3) one can try to modify the electronic structure of germanene by applying an external strain [37] and (4) by applying simultaneously an external strain and an electric field [38]. All these methods have in common that they try to exploit the broken symmetry of the germanene honeycomb lattice by inducing charge at one sublattice or shifting charge from one sublattice to the other. The interaction of germanene with a substrate or the selective adsorption or intercalation of atoms/molecules at one side of the germanene can significantly affect germanene's electronic properties [39] such as the electronic states near the Fermi level and the carrier mobilities. For field-effect applications the degradation of the carrier mobilities is, however, one of the most severe threats [40, 41]. As a final remark we like to stress that germanene is, in contrast to graphene, not stable at ambient conditions and therefore germanene needs to be protected against oxidation. Capping or encapsulating should preferably be done with a band gap material that has a weak Van der Waals interaction with the germanene layer. Suitable candidates are for instance hexagonal boron nitride, molybdenum disulfide and tungsten diselenide.

#### 13.4 Conclusions and Outlook

It is evident that the research field of germanene is still in its infancy. The study of germanene has just begun, its promises have not yet been materialized, and the extent of its potential for new devices and physics remains largely unexplored. So far, germanene has only been synthesized on substrates and it remains to be seen if one ever succeeds in creating free-standing germanene. The coupling with a substrate will in general result in a degradation of the 'graphene-like' properties of germanene. Bearing this in mind we first have to unambiguously demonstrate that germanene synthesized on a substrate is indeed a two-dimensional Dirac material. The anomalous quantum Hall effect is in this respect probably the most decisive test experiment. Once the two-dimensional Dirac nature of germanene has been confirmed the next logical step is to figure out whether germanene has a spin-orbit gap and how large this gap is. For a sufficient large spin-orbit gap (larger than a few meV) it will be extremely valuable to verify if germanene possesses indeed the predicted spin-polarized topologically protected edge states.

From a technological point of view, there are also a few requirements that should be met before it makes sense to consider the realization of germanene based field-effect devices. In order to realize germanene based field-effect devices the following two requirements should be met: the band gap should be larger than about 300–400 meV in order to realize a sufficiently large on/off ratio and germanene's charge carrier mobilities should be sufficient high (>1000 cm $^2$  V $^{-1}$  s $^{-1}$ ). There are several ways to open a gap in germanene such as the application of an electric field, adsorption or intercalation of atoms or molecules at one side of the material, coupling to a substrate and the application of an external strain.

**Acknowledgements** PB and AA thank the Nederlandse Organisatie voor Wetenschappelijk Onderzoek for financial support. LZ and QY thank the China Scholarship Council for financial support and RB and HJWZ thank the stichting voor Fundamenteel Onderzoek der Materie for financial support.

#### References

- K.S. Novoselov, A.K. Geim, S.V. Morozov, D. Jiang, Y. Zhang, S.V. Dubonos, I.V. Grigorieva, A.A. Firsov, Science 306, 666 (2004)
- 2. A.K. Geim, K.S. Novoselov, Nat. Mat. 6, 183 (2007)
- 3. N.D. Mermin, Phys. Rev. 176, 250 (1968)
- B. Aufray, A. Kara, S. Vizzini, H. Oughaddou, C. Léandri, B. Ealet, G. Le Lay, Appl. Phys. Lett. 96, 183102 (2010)
- P. De Padova, C. Quaresima, C. Ottaviani, P.M. Sheverdyaeva, P. Moras, C. Carbonne, D. Topwal, B. OLivieri, A. Kara, H. Oughaddou, B. Aufray and G. Le Lay. Appl. Phys. Lett. 96, 261905 (2010)
- P. Vogt, P. De Padova, C. Quaresima, J. Avila, E. Frantzeskakis, M.C. Asensio, A. Resta, B. Ealet, G.L. Lay, Phys. Rev. Lett. 108, 155501 (2012)
- 7. C.-C. Liu, H. Jiang, Y. Yao, Phys. Rev. B 84, 195430 (2011)
- 8. Y. Yao, F. Ye, X.-L. Qi, S.-C. Zhang, Z. Zhang, Phys. Rev. B. 75, 041401 (2007)
- 9. C.-C. Liu, W. Feng, Y. Yao, Phys. Rev. Lett. 107, 076802 (2011)
- 10. K. Takeda, K. Shiraishi, Phys. Rev. B 50, 14916 (1994)
- 11. G.G. Guzmán-Verri, L.C. Lew Yan Voon, Phys. Rev. B **76**, 075131 (2007)
- 12. S. Cahangirov, M. Topsakal, E. Aktürk, H. Şahin, S. Ciraci, Phys. Rev. Lett. 102, 236804 (2009)
- A. Acun, L. Zhang, P. Bampoulis, M. Farmanbar, M. Lingenfelder, A. van Houselt, A.N. Rudenko, G. Brocks, B. Poelsema, M.I. Katsnelson, H.J.W. Zandvliet, J. Phys. Condens. Matter 27, 443002 (2015)
- E. Bianco, S. Butler, S. Jiang, O.D. Restrepo, W. Windl, J.E. Golberger, ACS Nano 7, 4414 (2013)
- L. Li, S.-Z. Lu, J. Pan, Z. Qin. Y.-Q. Wang, Y. Wang, G. Cao, S. Du, H.-J. Gao, Adv. Mater. 26, 4820 (2014)
- M. Švec, P. Hapala, M. Ondráček, P. Merino, M. Blanco-Rey, P. Mutombo, M. Vondráček, Y. Polyak, V. Cháb, J.A. Martín, Gago, P. Jelínek, Phys. Rev. B 89, 201412(R) (2014)
- 17. M.E. Dávila, L. Xian, S. Cahangirov, A. Rubio, G. Le Lay, New J. Phys. 16, 095002 (2014)
- P. Bampoulis, L. Zhang, A. Safaei, R. van Gastel, B. Poelsema, H.J.W. Zandvliet, J. Phys. Condens. Matter 26, 442001 (2014)
- 19. M. Derivaz, D. Dentel, R. Stephan, M.-C. Hanf, A. Mehdaoui, P. Sonnet, C. Pirri, Nano Lett. 15, 2510 (2015)

- L. Zhang, P. Bampoulis, A. van Houselt, H.J.W. Zandvliet, Appl. Phys. Lett. 107, 111605 (2015)
- 21. M.E. Dávila, G. Le Lay, Sci. Rep. 6, 20714 (2016)
- L. Zhang, P. Bampoulis, A.N. Rudenko, Q. Yao, A. van Houselt, B. Poelsema, M.I. Katsnelson, H.J.W. Zandvliet, Phys. Rev. Lett. 116 (2016)
- 23. T. Amlaki, M. Bokdam, P.J. Kelly, Phys. Rev. Lett. 116 (2016)
- C.J. Walhout, A. Acun, L. Zhang, M. Ezawa, H.J.W. Zandvliet, J. Phys. Condens. Matter 28, 284006 (2016)
- M.I. Katsnelson, Graphene: Carbon in Two Dimensions (Cambridge University Press, Cambridge, 2012)
- 26. C.L. Kane, E.J. Mele, Phys. Rev. Lett. 95, 146802 (2005)
- 27. C.L. Kane, E.J. Mele, Phys. Rev. Lett. 95, 226801 (2005)
- M. König, S. Wiedmann, C. Brüne, A. Roth, H. Buhmann, L.W. Molenkamp, X.-L. Qi, S.-C. Zhang, Science 318, 766 (2007)
- 29. M. Ezawa, New J. Phys. 16, 065015 (2012)
- 30. M. Ezawa, Eur. Phys. J. B 86, 139 (2013)
- 31. M. Ezawa, Phys. Rev. Lett. 109, 055502 (2012)
- 32. M. Ezawa, Phys. Rev. Lett. 110, 026603 (2013)
- 33. N.D. Drummond, V. Zólyomi, V.I. Fal'ko, Phys. Rev. B 85, 075423 (2012)
- 34. M. Ezawa, New J. Phys. 14, 033003 (2012)
- L. Britnell, R.V. Gorbachev, R. Jalil, B.D. Belle, F. Schedin, A. Mishchenko, T. Georgiou, M.I. Katsnelson, L. Eaves, S.V. Morozov, N.M.R. Peres, J. Leist, A.K. Geim, K.S. Novoselov, L.A. Ponomarenko, Science 335, 947 (2012)
- 36. T.P. Kaloni, G. Schreckenbach, M.S. Freund, J. Phys. Chem. C 118, 25200 (2014)
- 37. T.P. Kaloni, U. Schwingenschlögl, Chem. Phys. Lett. 583, 137 (2013)
- 38. J.A. Yan, S.-P. Gao, R. Stein, G. Coard, Phys. Rev. B 91, 245401 (2015)
- 39. P. Zhou, L.Z. Sun, Sci. Rep. 6, 27830 (2016)
- 40. H.J.W. Zandvliet, Nano Today 9, 691 (2014)
- 41. L. Tao, E. Cinquanta, D. Chiappe, C. Grazianetti, M. Fanciulli, M. Dubey, A. Molle, D. Akinwande, Nat. Nanotechnol. 10, 227 (2015)

Symbols	Ambipolar transfer behavior, 244
4×4, 216	Amorphous aluminium, 156
$\sqrt{7} \times \sqrt{7} / \sqrt{13} \times \sqrt{13}$ , 104	Amorphous silicon (a-Si), 135
•	Amorphous silicon oxide, 229
A	Amphiphilic character, 12
AA stacking, 94	Andreev reflection, 111, 190
ABC stacking, 192	Angle Resolved Photoelectron Emission
Ab initio, 140	Spectroscopy (ARPES), 101, 180, 219
Ab initio Molecular Dynamics (AIMD), 226	Angle-Resolved Photoemission Spectroscopy
Absorption, 77	(ARPES), 121, 237
AB stacking, 94	Anharmonic terms, 150
Acoustic branches, 37	Anisotropic honeycomb lattice, 65
Adhesion energy, 140, 201	Annealing, 132, 237
Ag, 130, 236	Anthracene, 15
Ag(110), 130	Antiferromagnetic exchange magnetization, 49
Ag(111), 100, 130, 197	Antiferromagnetic manganese
(111)Ag, 197	chalcogenophosphates, 49
$Ag(111)(1 \times 1), 130$	Antiferromagnetic semiconductors, 116
Ag lattice constant, 119	Ar <sup>+</sup> ion-sputtering, 132, 237
Ag MNN, 136	Armchair and zigzag step edges, 186
Ag–Si alloy, 220	Armchair (ASiNRs), 116
Ag sp band, 162, 145, 219	Aromaticity, 1
AIN, 198	A symmetry, 147
Air-stability, 236, 239, 242	Atomic force microscopy, 133
Alkaline-earth-metal silicides, 116	Auger electron spectroscopy, 136
Allotropes, 130	
Al <sub>2</sub> O <sub>3</sub> , 24, 243	В
Al <sub>2</sub> O <sub>3</sub> capped, 228	Back folding, 170
Al <sub>2</sub> O <sub>3</sub> capping, 239	Back-gate transistor, 243
$\alpha$ -4×4, 216	Backscattering, 185
α-silicene, 143	Ball-and-stick model, 140
Aluminum oxide $(Al_2O_3)$ , 227	Ballistic transport, 59
Ambient conditions, 156, 244	Band gap, 144
Ambipolar behavior, 246	Band gap tuning, 13
Ambipolar current-voltage characteristics, 197	Band insulator, 38, 39

© Springer Nature Switzerland AG 2018 P. Vogt and G. Le Lay (eds.), *Silicene*, NanoScience and Technology, https://doi.org/10.1007/978-3-319-99964-7

Basis set superposition error, 12	Chiral edges, 56
Beard-beard edges, 66	Chlorinated silicene, 223
Benzene, 2	Chlorination, 222
Bernal-stacked bilayer graphene, 92	Cl, 221
Berry connection, 50	Cluster, 134
Berry curvature, 50	Cluster expansion approach, 222
$\beta$ -4×4, 216	Cohesive energy, 166
$\beta$ -silicene, 143	Compressive stress, 224
Bethe-Salpeter equation, 83	Conduction band, 33
Bi <sub>2</sub> Te <sub>3</sub> , 187	Cone-like bands, 145
Bilayer graphene, 92	Constant-Energy Contour (CEC), 184
Bilayer Si(111), 165	Cooper minimum, 144
Bilayer silicene, 94, 228	Core level photoemission spectroscopy, 227
Black phosphorous, 147	Coulomb interactions, 83
Bloch functions, 77	Counterpoise correction, 12
Bloch wave vector, 87	Covalent bonding, 198
Boat configuration, 29, 212	Covalent bonds, 204
Boat-like conformer, 14	Covalent chemical bonds, 140
Boltzmann constant, 180	Creation and annihilation operators, 30
Bond angles, 16	Critical temperature, 190
Bond length, 131	Crystalline Si, 116
Bond shortening, 140	$C_{3\nu}$ , 17
Boron, 100	$C_{6\nu}$ symmetry point group, 142
Boron nitride, 25	Cyclic molecules, 1
Borophene, 100	Cyclotron frequency, 183
Boundary conditions, 81	Cyclotron nequency, 185
Br, 221	D
Bridge site, 166	_
2	Dangling bonds, 120, 166
Brillouin-zone, 130	D band, 146, 148, 228
Buckling, 75, 142, 216	1D Brillouin zone, 122
Bulk-edge correspondence, 55	2D Brillouin zone, 75
Bulk silicon, 131	2D-3D phase transition, 137
Burning match, 120	2D electron gas, 187
BZ corners, 38	2D interband structure, 85
C	$D_{3d}$ , 142
C	$D_{3d}$ geometry, 7
Calculations, 140	D <sub>6h</sub> geometry, 7
Capped silicene, 241	1,1-dimethyl $SiC_5H_5$ , 2
Capping layer, 201	1,1'-Disila-4,4'-biphenyl, 2
Carbon compounds, 140	2D-lattices, 130
Carrier concentration, 244	Degeneracies, 37
CaSi <sub>2</sub> , 164	Delamination, 242
Chair configuration, 212	Dense-SiNRs arrays, 119
Chair-like conformer, 14	Density Functional Theory (DFT), 8, 25, 140,
III–VI chalcogenides, 25	198, 236
Charge density, 139	Density Functional Theory (DFT) calculations
Charge density waves, 181	101, 131, 212
Charge transfer, 164	Density of States (DOS), 138, 175, 249
Charge transport, 11	Deposition temperature, 238
Chemical potential, 140	DFT-GGA calculations, 121
Chemical stability, 241	DFT-PBE, 173
Chemisorb, 226	Diamond, 132
Chern number, 43, 50	Diamond-like Si, 147
Chiral, 119	Diamond-like structure, 12

Diamond silicon, 171	Exfoliation, 130
Dielectric function, 75	Exothermic process, 166
Dielectric tensor, 76, 80	External electric field, 34
Differential conductance (dI/dV), 192	
Differential conduction, 180	F
Differential reflectance spectroscopy, 124	F, 221
Differential tunneling conductance, 184	Fast Fourier transformation (FFT), 187
Dimer and trimer defects, 224	Fermi-Dirac population function, 249
Dirac cone, 46, 129, 143, 242	Fermi level, 27, 129
Dirac Hamiltonian, 47	Fermi-liquid approximation, 87
Dirac mass, 49, 57	Fermi velocity, 26, 76, 144, 170, 185, 197, 245
Dirac particles, 145	Ferroelectric tunnel junctions, 251
Dirac point, 46, 183, 245	Ferromagnetism, 214
Dirac semiconductor, 249	Field effect, 197
Dirac-type dispersion, 27	Field-effect mobility, 244
Dirac-type electron, 24	Field-Effect Transistor (FET), 156, 164, 237
Direct semiconductors, 221	Filled states STM images, 142
Disilenes, 131	Fingerprint, 17
Disorder, 153, 240	First-principles, 25
Disordered areas, 154	First-principles calculations, 164
Dissociation reaction, 226	Flat bands, 68
Domain boundaries, 148	Flip-flop motion, 165
Doping, 214	Flower pattern, 101, 138, 160
Down spin, 58	Fluorination, 222
Drain current I <sub>d</sub> , 244	Force-constant approach, 28
Drain pads, 243	Friedel oscillations, 184, 187
Drain-source bias $V_d$ , 244	F-silicene, 221
3D SiNRs, 124	F symmetry, 149
Dumbbell structure, 166	Full Dumbbell Silicene (FDS), 167
	Full width at half maximum, 135
E	Functionalization, 212
E-beam lithography, 243	
Eclipsed (eLDS) and staggered (sLDS) layered	G
dumbbel silicite, 172	Gapless semiconductor, 199
Edge state, 44, 117	Gap opening, 164, 219
Effective-medium theory, 78	Gate dielectric capacitance, 244
Effect topological quantum transistor, 59	Gate overdrive voltage, 244
Ehrenreich-Cohen formula, 77	Gauge potential, 50
Electrical measurements, 244	G band, 228
Electric field, 37	Genuine Chern numbers, 54
Electron-hole coupling, 86	Germanane, 83
Electron-hole exchange, 83	Germanene, 43, 100, 237, 251
Electron-Phonon Coupling (EPC), 149	Germanium, 100
Electron-phonon interaction, 151, 247	Giant magnetoresistance, 236
Embedded islands, 135	G mode, 151
Encapsulation, 227, 240	Graphane, 14, 25, 83
Energy-momentum dispersion, 185	Graphene, 8
Energy relaxation, 201	Graphite, 173
Epitaxial growth, 236	Graphite-like AlN, 199
Epitaxial silicene, 131, 239	Gravimetric capacity, 14
E symmetry, 148	Green function, 61
Exchange-correlation functional, 25, 26	Growth, 100
Excitonic effects, 83, 93	$G_0W_0$ , 175
Excitonic insulator, 84	GW approximation, 212

Н	Inequivalent Triangle (IET) structure, 170
H <sub>2</sub> , 212	Infrared (IR) spectroscopy, 17, 92
Hafnene, 100	Inner edges, 56
Hafnium, 100	In-plane, 148
Haldane interaction, 49	In-plane dielectric constant, 175
Half-hydrogenated, 214	In-plane modes, 132
Half-silicane, 219	In situ, 137
Halogenation, 221	In situ Raman spectroscopy, 123
Harmonic oscillators, 85	Insulating, 227
H-BN, 201	Intravalley scattering, 184
Hedin GW approximation, 83	Intrinsic disorder, 154
Hellmann-Feynman theorem, 49	Ionic-covalent bonds, 200
Herical edges, 56	Ir, 236
Hexagonal boron nitride, 236	Ir(111), 110, 130
Hexagonal Brillouin zone, 24	(111)Ir, 197
Hexagonal Close Packed (HCP), 217	Isolated SiNRs, 118
Hexasilabenzene, 2	I(V) spectra, 120
Hexasilaprismane, 8	-(·) -F,
Hexasilicon ring, 11	J
High-buckled geometries, 75	Jackiw-Rebbi mode, 58
High-k thin dielectric, 249	such in record mode, 50
Highly Buckled (HB) freestanding silicene,	K
201	K <sub>//</sub> , 122
Highly-doped silicon, 243	Kane–Mele spin-orbit (SO) coupling, 24
Highly-Oriented Pyrolytic Graphite (HOPG),	Kirchhoff law, 59
162, 183	Kohn-Sham eigenvalues, 75
High resolution electron energy loss	Kohn-Sham equation, 75
spectroscopy, 147	Kohn-Sham wave functions, 175
Hole conductors, 12	k-point, 26
HOMO, 8	K points, 204
HOMO-LUMO gap, 12	<i>K</i> points, 129, 143
Honeycomb-Chained-Triangle (HCT) model,	K-projection technique, 164
100, 108	Kubo formula, 49
Honeycomb-Chain Trimer (HCT) structure,	•
170	L
Honeycomb Dumbbell Silicene (HDS), 166	Landauer formalism, 59
Honeycomb structure, 130	Landau levels, 162, 183
Hoppings, 65	Landau quantization, 183
Hubbard Hamiltonian, 117	Langmuir, 119
Hybrid functionals, 29	Large Honeycomb Dumbbell Silicene (LHDS)
Hybrid orbitals, 131	168
Hydrogen, 32, 119	Layered materials, 200
Hydrogenated graphene, 14	Layered silicene, 108
Hydrogenation, 15, 212	Layer lift-off, 240
Hydroxyl (OH), 226	Leakage, 246
_	Linear bands, 162
I	Linear electronic dispersion, 106
I, 221	Line profile, 140
Imaginary frequencies, 26	Liquid helium temperature, 184
Imaginary phonon branch, 214	Local Density Approximation (LDA), 25, 26,
Independent-particle approximation, 77	75
Independent-quasiparticle approximation, 77,	Local Density of State (LDOS), 139, 180, 201
89	Local electron density, 142
Indirect-gap semiconductor, 37	Local-field effects, 80

Logic devices, 251	Nearest neighbor hopping, 32, 45
Lone-pair, 5	Nielsen-Ninomiya theorem, 46
Low-bias conductance, 61	Non-contact AFM, 139, 160
Low-buckled, 142	Non-metallic substrates, 198
Low-buckled geometries, 75	Non-volatile memory, 251
Low Energy Electron Diffraction (LEED), 100, 132, 160	<i>N</i> -type, 215
Low Energy Electron Microscopy (LEEM),	0
100, 137	Occupied molecular orbitals, 8
Low-frequency limit, 86	OH groups, 116
L(T)O, 123	Ohm law, 79
L(T)O mode, 132	O <sub>2</sub> molecule, 226
LUMO, 8	Optical absorbance, 86
	Optical absorption edge, 215
M	Optical conductivity, 79
Magnetic-like domains, 119	Optical local-field effects, 83
Magnetic moment, 222	Optical properties, 74
Majorana fermions, 111	Optoelectronic properties, 175, 250
Many-body effects, 83	Optoelectronics, 236
Many-body Green's function approach, 212	2nd-order band, 151
Many-body self-energy corrections, 173	Outer edge, 57
Massless Dirac fermions, 230	Out-of-plane acoustic phonons, 247
Massless particles, 129	Out-of plane buckling, 201
•	
Maxwell equations, 80 Mechanical cleaving, 237	Out of plane phonon mode 132
	Out-of-plane phonon mode, 132
Meissner effect, 84	Out-of-plane vibration, 147
Metal-insulator transition, 181	Oxidation, 106, 145, 239
Metallic, 227	Oxidization, 226
Metal oxides, 236	Oxygen, 120
MgB <sub>2</sub> , 190	n.
Mica, 236, 237	P
Mirror planes, 142	Pauli matrices, 38
Mixed $sp^2$ and $sp^3$ hybridisation, 24	Peeled off, 194
Moiré-like, 217	Pentagraphene, 125
Moiré-like pattern, 136	Perdew–Burke–Ernzerhof (PBE), 25
Moiré-pattern, 153	$2\sqrt{3} \times 2\sqrt{3}$ phase, 216
Momentum-space information, 184	Phase transition, 189
Monomer defect, 224	Phenanthrene, 15
MoS <sub>2</sub> , 147, 173, 198	Phonon band, 134
MoSe <sub>2</sub> , 147, 202	Phonon dispersion, 28, 37
MoTe <sub>2</sub> , 202	Phonon-phonon interaction, 151
M point, 28	Phonon scattering, 151
Multilayer silicene, 192, 227, 239	Phonon symmetries, 147
Multilayer SiNRs, 121	Phosphorene, 65, 237
Multi-phase regime, 152	Photocatalytic water-splitting, 215
	Photoemission spectroscopy, 133
N	Photovoltaic applications, 176
Nanodikes, 124	$\pi$ -band , 6, 116, 228
Nanoelectronics, 214, 236	$\pi$ bond, 132
Nano-junction, 121	$\pi$ -conjugated molecules, 1
Nano-particles, 136	Piezo-magnetism, 236
Nanoribbon, 55, 101	$\pi$ -stacking interactions, 13
Nanotrenches, 124	$\pi^*$ (upper branch) and $\pi$ (lowerbranch)
	bands, 121
Naphthalene, 15	vanus, 121

Plane-wave basis set, 36	R
Plane-wave cutoff energy, 37	Raman-active phonon mode, 147
Point group, 6	Raman intensities, 17
Poisson ratio, 213	Raman selection rules, 146, 147
Polarizability, 16	Raman shift, 146
Polarization dependent Raman measurements,	Raman spectroscopy, 16, 133, 227, 239
142	Real part, 96
Polar surface, 205	Reconstructed silicene, 101
Polyacenes, 12	Reflection, 77
Polycrystalline graphene, 247	Reflection High-Energy Electron Diffraction
Polymer coating, 240	(RHEED), 237
Pontryagin number, 53	Reflection High Energy Positron Diffraction
p <sub>z</sub> orbitals , 199	(RHEPD), 104, 160
Porto notation, 146	Reorganization Energy, 11
Positron diffraction, 133	Rotation angles, 136
Probe station, 244	Rotation axis, 142
Projector-Augmented-Wave (PAW), 26	
Projector-Augmented Wave (PAW) method,	S
74	Saddle-point, 92
Proximity effect, 190	Saddle-point exciton, 74
Pseudo Jahn-Teller effects, 6	Saddle-shape metallic hybrid surface band
Pseudopotentials, 26	(HSB), 228
P-type, 215	s and $p$ orbitals, 32
Pyramidal cross section, 121	Scanning Tunneling Microscopy (STM), 133, 180, 237
Q	Scanning Tunneling Spectroscopy (STS), 111,
QSH phase, 63	162, 180
Quadratic bands, 36	Scattering intensity, 146
Quantized conductance, 59	Screening, 35
Quantum Anomalous Hall (QAH), 54	Second rank tensor, 147
Quantum Anomalous Hall Effect (QAHE), 192	Segregated layer, 109
Quantum Anomalous Hall (QAH) insulator, 44	Self-assembling, 119
Quantum confinement effect, The, 215	Semiconducting, 227
Quantum Espresso code, 74	Semiconducting state, 226
Quantum Hall effect, 181	Semimetal, 37
Quantum Spin Hall (QSH), 44, 54, 156	Semimetallic, 48, 227
Quantum Spin Hall Effect (QSHE), 192, 236	Sensors, 236
Quantum Spin-Valley Hall (QSVH) insulator,	Shockley surface state, 228
54	Si ad-layer, 137
Quantum tunneling, 180	Si-Ag bonds, 135
Quantum Valley-Hall (QVH) insulator, 44	Si allotropes, 149
Quantum-well states, 36	Si crystallites, 152
Quartet state, 6	σ bond, 6, 119
Quasi-flat band, 70	SiH <sub>x</sub> , 119
Quasi-free-standing, 108, 228	Silaaromatic, 2
Quasi-free-standing silicene, 229	Silabenzene, 2
Quasi-Partical Interference (QPI), 185	Silabenzvalene, 2
Quasiparticle chirality, 185	Silanaphthalene, 2
Quasiparticle corrections, 76	9-silaphenanthrene, 2
Quasiparticles 184	Silicane, 28, 83, 117, 212, 249 Silicane, 43
Quasiparticles, 184 OVH phase, 63	Silicene, 43 Silicene/Ag interface, 152
V TII PHUOV, VV	51110111111111111111111111111111111111

Silicene cluster, 18	Spin-valleytronics, 44
Silicene devices, 236	Stability, 156
Silicene Encapsulated Delamination with	Stacking, 94, 172
Native Electrodes (SEDNE), 243	Standing waves, 185
Silicene transistors, 242	Stanene, 43, 100, 237
Silicide, 130	Stokes theorem, 51
Silicon nanotubes, 14	Straintronics, 236
Siloxenes, 116	Stranski-Krastanov, 100
Si LVV, 136	Structural relaxations, 140
Si-multilayers, 106	Sublattice-asymmetry, 24
Si nanoribbons (SiNRs), 16, 130, 227	Sublattice buckling, 24
Single- and double-strand SiNRs, 125	Sublattice polarisation, 35
Single crystal Ag(111), 237	Sublattices, 48, 140
Single crystals, 100	Sub-ML deposition, 137
Single-domain epitaxial silicene, 109	Substrate-induced symmetry breaking, 182
Single-shot GW, 29	Substrate interaction, 198
SiO <sub>2</sub> , 156, 243	Super-buckling model, 189
Si pentamers, 125	Supercell, 11
Si segregation, 109	Superconducting state, 84
Si-Si bond, 199	Superconductivity, 180, 189
Si-Si distance, 103	Superconductor-metal junction, 190
Si-Si in plane distance, 140	Superposition, 136
Sizeable band-gap, 236	Supramolecular chemistry, 9
Slab model, 204	Surface alloy, 101
Slater–Koster approach, 30	Surface-enhanced Raman scattering, 18
SO coupling, 37	Symmetry breaking, 143, 170
SO gap, 37	Synthesize, 130
Sommerfeld constant, 86	
Sommerfeld finestructure constant, 85	T
$sp^3$ , 12	Terraces, 136
sp <sup>2</sup> bonding, 75	Tersoff-Hamann approximation, 138
$sp^3$ bonding, 75	Tetrahedral bonding, 172
$sp^2$ - $Sp^3$ bonding, 212	Thermal coefficient, 150
$sp^2$ graphite, 12	Thermal conductivity, 236
$sp^2$ -hybridization, 198	Three dimensional (3D) topological insulators
$sp^3$ hybridization, 228	185
$sp^2$ - $sp^3$ hybridization, 115	Tight Binding (TB), 1, 45, 236
$sp^2$ hybrid orbital, 5	Tight-binding Hamiltonian, 30, 46
$sp^2/sp^3$ -like, 131	Tin, 100
$sp^2$ to $sp^3$ ratio , 242	Tip-Enhanced Raman Scattering (TERS), 18
Spectral weight, 95	Topochemical removal, 116
Specular HREELS, 110	Topological defects, 117
Spin current, 56	Topological distinct phases, 55
Spin filter, 117	Topological edge, 55
Spin gap, 117	Topological insulator, 24, 38, 39, 43, 111
Spin index, 47	Topological Kirchhoff law, 44, 58
Spin Orbit Coupling (SOC), 76, 117	Topologically protected, 59
Spin polarization, 117	Topological non-trivial characteristics, 117
Spin-polarized Quantum Anomalous Hall	Topological properties, 39
(SQAH) insulators, 54	Topological stability, 59
Spintronic devices, 230	Topological superconductors, 43
Spintronics, 214, 236	Total charge density, 175
•	

Total device resistance, 244	V-like shape, 122
Total-energy calculations, 125	Volumetric capacity, 14
Trans-bent structure, 6	
Transfer-matrix method, 81	$\mathbf{W}$
Transistors, 197	Wavenumber, 150
Transition Metal Dichalcogenides (TMDs),	Wet etching, 241
25, 198, 236	Wetting layer, 107
Transmission, 77	Wigner-Seitz cell, 142
Transmittivity, 91	WSe <sub>2</sub> , 147
Transport measurement, 237	Wurtzite phase, 198
Trichlorocyclotrisilane, 2	
Trigonal Dumbbell Silicene (TDS), 166	X
Trigonal warping, 187	$\bar{X}$ point, 206
Triple degeneracy, 132	X-ray diffraction, 108, 131
Tristable Si(111) bilayer, 170	X-ray Photoelectron Spectroscopy (XPS), 239
Tunable band gap, 46	X-silicene, 221
Tunnelling voltage, 138	
Two-band superconductor, 190	Y
Two-dimensional electron systems, 43	<i>Y</i> point, 206
U	${f Z}$
UHV chamber, 216	Zero-energy conductance, 64
Ultra-High Vacuum (UHV), 119, 237	Zero-gap, 144
Ultra-thin wurtzite films, 198	Zero-gap semiconductor, 16, 92
Unified tight-binding (TB) Hamiltonian, 180	Zero-gap state, 226
Unoccupied molecular orbitals, 8	Zigzag (ZSiNRs), 116
Unsaturated organic molecules, 5	Zigzag-beard edges, 66
Up spin, 58	Zigzag edges, 56
	Zigzag silicene nanoribbon, 59
V	Zirconium diboride, 100
Vacancy sites, 218	ZnO, 205
Valence band, 33	ZnS, 204
Valley index, 51	(0001)ZnS, 198
Van der Waals bonding, 198	Zone-centre Raman mode, 149
Van der Waals forces, 106, 199	ZrB <sub>2</sub> , 130, 236
Van der Waals interaction, 92, 173	$ZrB_2(0001), 109$
Van Hove singularities, 77	(0001)ZrB <sub>2</sub> , 197
Vibrational properties, 132, 145, 240	ZrC(111), 110
Vibronic coupling, 7, 8	
Vienna Ab initio Simulation Package (VASP),	
8, 74	